Temperature and Rate Dependent Finite Strain Behavior of Poly(ethylene terephthalate) and Poly(ethylene terephthalate)-glycol above the Glass Transition Temperature

by

Rebecca B. Dupaix

B.S. Mechanical Engineering, Utah State University, 1998

S.M. Mechanical Engineering,
Massachusetts Institute of Technology, 2000

Submitted to the Department of Mechanical Engineering
in partial fulfillment of the requirements for the degree of

Doctor of Philosophy
at the
MASSACHUSETTS INSTITUTE OF TECHNOLOGY
September 2003

Author .....
Mechanical Engineering
July 10, 2003

Certified by .....
Mary C. Boyce
Professor of Mechanical Engineering
Thesis Supervisor

Accepted by .....
Ain A. Sonin
Chairman, Department Committee on Graduate Students

Temperature and Rate Dependent Finite Strain Behavior of Poly(ethylene terephthalate) and Poly(ethylene terephthalate)-glycol above the Glass Transition Temperature

by

Rebecca B. Dupaix

Submitted to the Department of Mechanical Engineering
on July 10, 2003, in partial fulfillment of the
requirements for the degree of
Doctor of Philosophy

Abstract

Poly(ethylene terephthalate) is widely used for consumer products such as drawn fibers, stretched films, and soda bottles. Much of its commercial success lies in the fact that it crystallizes at large strains during warm deformation processing. The imparted crystallinity increases its stiffness and strength, improves its dimensional stability, and increases its density. The crystallization process and the stress-strain behavior above the glass transition depend strongly on temperature, strain rate, strain magnitude, and strain state. A robust constitutive model to accurately account for this stress-strain behavior in the processing regime is highly desirable in order to predict and computationally design warm deformation processes to achieve desired end product geometries and properties.

This thesis aims to better understand the material behavior above the glass transition temperature in the processing regime. It examines the strain rate, strain state, and temperature dependent mechanical behavior of two polymers: PET and PETG, an amorphous non-crystallizing copolymer of PET, in order to isolate the effects of crystallization on the stress-strain behavior. Experiments over a wide range of temperatures and strain rates were performed in uniaxial and plane strain compression. A constitutive model of the observed rate and temperature dependent stress-strain behavior was then developed. The model represents the material's resistance to deformation with two parallel elements: an intermolecular resistance to flow and a resistance due to molecular network interactions. The model predicts the temperature and rate dependence of many stress-strain features of PET and PETG very well, including the initial modulus, flow stress, initial hardening modulus, and dramatic strain hardening. The modeling results indicate that the large strain hardening behavior of both materials can only be captured by including a critical orientation parameter to halt the molecular relaxation process once the network achieves a spe-

cific level of molecular orientation. This suggests that much of the strain hardening in PET is due to molecular orientation and not to strain-induced crystallization. An example blow molding process is simulated to demonstrate the industrial applicability of the proposed model.

Thesis Supervisor: Mary C. Boyce
Title: Professor of Mechanical Engineering

Acknowledgments

I wish to thank my thesis advisor, Mary C. Boyce, for her continued guidance through my graduate education; my thesis committee: Simona Socrate, Greg Rutledge, and Gareth McKinley, for thoughtful discussions and flexibility in finding time for my committee meetings; Tom Pecorini and Fred Colhoun from Eastman Chemical, not only for the many material samples, but also for helpful meetings and discussions; and the National Science Foundation and Eastman Chemical for financial support of my graduate work.

On a more personal note I am very thankful for the friendships of all of my colleagues at MIT, especially Mats, Franco, Nuo, Hang, Rajdeep, Adam, Una, Ray, Simona, and many others who have come and gone. You all made coming to work fun, even when it was otherwise drudgery.

I could hardly begin to thank all of my friends and family members, so I will keep it simple by sticking with the most important: Mom and Dad, thanks for your continual encouragement, I love you both. And most importantly to Brian. We made it, didn't we? Thank you for not letting me drop out when things were tough and I was stressed and we were trying to plan our wedding. Thank you for taking such good care of me when I came down with mono. I may have been able to get to this point without you, but it certainly would not have been as much fun nor as much of an adventure. Thank you for being so perfect for me; for inspiring me and lifting me up, for bringing flowers to my thesis defense, and for simply loving me. Thanks for everything!

Contents

List of Figures

List of Tables

0.1 Notation

Symbol	Description	Used
a	Length of a primitive chain segment	Eqn. 4.53
a	Length of one side of the anisotropic unit cell	p. 268
$\mathbf{a}$	Vector representing one side of the anisotropic unit cell	p. 268
α	Fitting exponent in Ogden model	p. 50
α	Pressure coefficient	Eqn. 4.13
α_{max}	Maximum angle between chain and principal axes	Eqn. 4.44
α_{min}	Orientation parameter (complement of α_{max})	Eqn. 4.45
α_c	Critical orientation where molecular relaxation ceases	Eqn. 4.47
α_0	Orientation angle prior to deformation	Eqn. 4.47
b	Length of one side of the anisotropic unit cell	p. 268
$\mathbf{b}$	Vector representing one side of the anisotropic unit cell	p. 268
B	Bulk modulus	Eqn. 4.25
$\mathbf{B}^N$	Left Cauchy-Green tensor, network, resistance B	Eqn. 4.17
$\beta_\rho^{(i)}$	Inverse Langevin function of $\rho^{(i)}/N$	Eqn. 6.5
β_P	Inverse Langevin function of P/N	Eqn. 6.6
c	Number of molecules per unit volume	Eqn. 4.53
c	Length of one side of the anisotropic unit cell	p. 268
$\mathbf{c}$	Vector representing one side of the anisotropic unit cell	p. 268
C	Coefficient in Bergstrom-Boyce reptation model	Eqn. 4.21
$\mathbf{C}$	Right Cauchy-Green strain tensor	Eqn. 6.4
$\mathbf{C}_B^F$	Right Cauchy-Green tensor, flow, resistance B	Eqn. 6.18
C_{01}	Coefficient in Mooney-Rivlin equation	p. 50
C_{10}	Coefficient in Mooney-Rivlin equation	p. 50
D	Temperature Coefficient	Eqn. 4.22
$\tilde{\mathbf{D}}_A^p$	Plastic rate of stretching in resistance A	Eqn. 4.7
$\tilde{\mathbf{D}}_B^F$	Plastic rate of stretching in resistance B	Eqn. 4.16
δ_{ij}	Kronecker delta	Eqn. B.3

Symbol	Description	Used
E	Young's modulus	Eqn. 4.25
$\mathbf{E}$	Lagrangian strain field	p. 269
ε	True strain	Eqn. 4.9
η	Viscosity	Eqn. 4.40
$\mathbf{F}$	Deformation gradient	Eqn. 4.1
$\mathbf{F}^e$	Elastic deformation gradient	p. 237
$\mathbf{F}^v$	Viscous deformation gradient	p. 237
$\mathbf{F}_A$	Deformation gradient in resistance A	Eqn. 4.1
$\mathbf{F}_A^e$	Elastic deformation gradient in resistance A	Eqn. 4.3
$\mathbf{F}_A^p$	Plastic deformation gradient in resistance A	Eqn. 4.3
$\mathbf{F}_B$	Deformation gradient in resistance B	Eqn. 4.1
$\mathbf{F}_B^N$	Network deformation gradient in resistance B	Eqn. 4.14
$\mathbf{F}_B^F$	Flow deformation gradient in resistance B	Eqn. 4.14
g	Temperature dependent coefficient in power-law relaxation	Eqn. 4.44
G_0	Factor in Doi-Edwards model	Eqn. 4.50
ΔG	Activation energy	Eqn. 4.12
γ	Shear strain	Eqn. 4.40
$\dot{\gamma}_{0A}$	Pre-exponential factor	Eqn. 4.12
$\dot{\gamma}_A^p$	Plastic shear rate in resistance A	Eqn. 4.8
$\dot{\gamma}_B^F$	Plastic shear rate in resistance B	Eqn. 4.18
h	Temperature dependent coefficient in power-law relaxation	Eqn. 4.45
I_1	First strain invariant	p. 50
I_2	Second strain invariant	p. 50
$\mathbf{I}$	Identity tensor	p. 269
J_A	Volume change in resistance A	Eqn. 4.11
J_B	Volume change in resistance B	Eqn. 4.17
k	Boltzmann's constant	Eqn. 4.12
L	Contour length	Eqn. 4.53
$\mathbf{L}_A$	Velocity gradient in resistance A	Eqn. 4.6

Symbol	Description	Used
$\mathbf{L}_A^e$	Elastic velocity gradient in resistance A	Eqn. 4.7
$\tilde{\mathbf{L}}_A^p$	Plastic velocity gradient in resistance A	Eqn. 4.7
$\mathbf{L}_B$	Velocity gradient in resistance B	Eqn. 4.15
$\mathbf{L}_B^N$	Elastic velocity gradient in resistance B	Eqn. 4.16
$\tilde{\mathbf{L}}_B^F$	Plastic velocity gradient in resistance B	Eqn. 4.16
$\mathscr{L}^{-1}$	Inverse Langevin function	Eqn. 4.17
$\mathscr{L}^e$	Fourth order tensor of elastic constants	Eqn. 4.11
λ	Stretch	p. 50
$\lambda_1, \lambda_2, \lambda_3$	Principal stretches	p. 50
λ_k	Relaxation time	Eqn. 1.1
λ_N	Network stretch in resistance B	Eqn. 4.17
λ_F	Flow stretch in resistance B	Eqn. 4.21
λ_T	Total stretch	p. 178
$\bar{\lambda}_{NC}$	Critical network stretch	Eqn. 4.36
λ^*	Strain rate dependence of critical network stretch	Eqn. 4.37
λ_a^*	Fitting parameter for strain rate dependence of $\bar{\lambda}_{NC}$	Eqn. 4.38
λ_b^*	Fitting parameter for strain rate dependence of $\bar{\lambda}_{NC}$	Eqn. 4.38
λ_c^*	Fitting parameter for strain rate dependence of $\bar{\lambda}_{NC}$	Eqn. 4.38
λ_a	Stretch along the material axis $\mathbf{a}$	Eqn. 6.6
λ_b	Stretch along the material axis $\mathbf{b}$	Eqn. 6.6
λ_c	Stretch along the material axis $\mathbf{c}$	Eqn. 6.6
m	Temperature dependence of critical network stretch	Eqn. 4.37
m	Power-Law model strain-rate sensitivity coefficient	Eqn. 4.42
m_a	Fitting parameter for temperature dependence of $\bar{\lambda}_{NC}$	Eqn. 4.38
m_b	Fitting parameter for temperature dependence of $\bar{\lambda}_{NC}$	Eqn. 4.38
m_c	Fitting parameter for temperature dependence of $\bar{\lambda}_{NC}$	Eqn. 4.38
$m(t)$	Memory function	Eqn. 1.1
M	Linearization of flow stress plot	Eqn. 4.30

Symbol	Description	Used
μ	Shear modulus	p. 50
μ'	Relaxation modulus	Eqn. 4.50
μ_{gl}	Shear modulus in the glassy regime	Eqn. 4.26
μ_r	Shear modulus in the rubbery regime	Eqn. 4.26
n	Power law exponent	Eqn. 4.42
n_y	Number of error points	Eqn. 4.35
N	Number of rigid links between entanglements	Eqn. 4.17
$\mathbf{N}_A$	Normalized deviatoric stress in resistance A	Eqn. 4.8
$\mathbf{N}_B$	Normalized deviatoric stress in resistance B	Eqn. 4.18
ν	Chain density	Eqn. 4.17
ν_p	Poisson's ratio	Eqn. 4.25
p	Hydrostatic pressure	Eqn. 4.13
P	Undeformed length of a chain	Eqn. 6.2
$\mathbf{P}^{(i)}$	Vector representing chain i in the anisotropic model	p. 268
PSR	Planar stretch ratio	Eqn. 7.2
Q	Second temperature parameter	Eqn. 4.22
$\mathbf{Q}$	Orientation tensor	Eqn. 4.50
R	Gas constant	Eqn. 4.22
$\mathbf{R}_A^e$	Elastic rotation in resistance A	Eqn. 4.4
$\mathbf{R}_A^p$	Plastic rotation in resistance A	Eqn. 4.5
$\mathbf{R}_B^F$	Flow rotation in resistance B	Eqn. 6.17
$\rho^{(i)}$	Deformed length of chain i	Eqn. 6.4
s	Shear resistance	Eqn. 4.12
$\tilde{s}$	Pressure-modified shear resistance	Eqn. 4.13
σ	Stress	Eqn. 4.34
$\sigma_{\alpha\beta}$	Componenet of the stress tensor	Eqn. 4.50
σ_i	Stress at point i	Eqn. 4.34
t	Current time	Eqn. 4.50
t'	Reference time	Eqn. 4.50

Symbol	Description	Used
T_d	Time constant	Eqn. 4.52
T_g	Glass transition temperature	p. 42
$\mathbf{T}$	Cauchy stress	Eqn. 4.24
$\tilde{\mathbf{T}}$	Second Piola-Kirchhoff stress	Eqn. 6.9
$\mathbf{T}_A$	Cauchy stress in resistance A	Eqn. 4.11
$\mathbf{T}'_A$	Deviatoric Cauchy stress in resistance A	Eqn. 4.9
$\mathbf{T}_B$	Cauchy stress in resistance B	Eqn. 4.17
$\mathbf{T}'_B$	Deviatoric Cauchy stress in resistance B	Eqn. 4.19
τ	Shear stress	Eqn. 4.40
τ_A	Magnitude of shear stress in resistance A	Eqn. 4.9
τ_B	Magnitude of shear stress in resistance B	Eqn. 4.19
τ_p	Time constant	Eqn. 4.51
θ	Absolute temperature	Eqn. 4.12
θ_g	Glass transition temperature	Eqn. 4.26
θ_g^*	Reference transition temperature	Eqn. 4.28
$\Delta\theta$	Change in temperature fitting parameter	Eqn. 4.26
$\mathbf{u}$	Unit vector tangent to a chain segment	Eqn. 4.55
$u_j^{(i)}$	Displacement of node i in the j direction	Eqn. 7.1
$\mathbf{U}_B^F$	Flow right stretch in resistance B	Eqn. 6.17
$\mathbf{V}_A^e$	Elastic left stretch in resistance A	Eqn. 4.4
$\mathbf{V}_A^p$	Plastic left stretch in resistance A	Eqn. 4.5
w	Strain energy function in Valanis and Landel model	p. 50
w_0	Constant related to non-zero entropy in initial configuration	Eqn. 6.5
$w_{entropy}$	Entropic contribution to the strain energy function	Eqn. 6.5
$w_{repulsion}$	Repulsive contribution to the strain energy function	Eqn. 6.6
W	Strain energy	p. 50
$W(\mathbf{x})$	Strain energy density	Eqn. 6.7
W_0	Constant related to non-zero entropy in initial configuration	Eqn. 6.8

Symbol	Description	Used
$\tilde{\mathbf{W}}_A^p$	Plastic spin in resistance A	Eqn. 4.7
$\tilde{\mathbf{W}}_B^F$	Plastic spin in resistance B	Eqn. 4.16
X_g	Shear modulus slope with temperature	Eqn. 4.26
$\mathbf{X}_i$	Unit vector representing a global coordinate system	p. 268
ξ	Glass transition shift factor	Eqn. 4.28
Y_i	Error in stress at point i	Eqn. 4.34
y	Normalized error in stress at point i	Eqn. 4.34
$\bar{y}$	Averaged absolute normalized error	Eqn. 4.35
Z	Linearization of flow stress plot	Eqn. 4.30
ζ	Glass transition shift factor	Eqn. 4.28

Chapter 1

Introduction

Poly(ethylene terephthalate) (PET) is widely used in many high-volume commercial and consumer applications. Examples include films, fibers, and food containers such as soda bottles. The widespread success in using PET for these applications has been attributed to the ability of PET to crystallize upon deformation at the temperatures and strain rates used during processing. This strain- or stress-induced crystallization increases the density of the material, increases its resistance to gas permeability, aids in long term dimensional stability, and imparts anisotropy to the final product. A consequence of anisotropy is increased stiffness and strength of the polymeric product in certain preferential directions. An example is increased tensile strength along the axis of a drawn fiber. Poly(ethylene terephthalate)-glycol (PETG), a non-crystallizing amorphous copolymer of PET, does not occupy the same industrial niche as PET, precisely because it lacks the ability to undergo strain-induced crystallization. Instead, its uses are directed toward applications involving large, thermoformed parts, such as point-of-purchase display panels or vending machine faces.

As PET continues to be used in manufacturing processes, a cost-motivated need arises for ways to predict material behavior a priori, both in terms of material behavior during processing, as well as end product mechanical behavior. Essentially, mechanical engineers must be able to simulate an entire manufacturing process numerically, using a method such as finite element analysis. This enables them to know the processing parameters (temperatures, pressures, loads, and strain rates) required

to produce a valid part before costly molds are cut or even more expensive equipment is purchased.

Current models of the deformation behavior of PET under processing loading conditions span a range in level of detail and scope. Largely, constitutive models for the finite strain stress-strain behavior of PET and many polymers are based on curve fits to small sets of data (for instance at one strain rate over a range of temperatures) and the validity of these models outside of the initial experimental parameters must be questioned. Particular areas of difficulty are the overall behavior of polymers at very large deformations, their strong dependence on rate and temperature, and the incorporation of strain-induced crystallization effects into the models.

This thesis aims to make progress in some of these areas by better understanding the effects of strain rate, strain state, temperature, and crystallization through mechanical experiments. That understanding is then applied to developing a constitutive model based on the underlying physical mechanisms. By conducting experiments on PET and a non-crystallizing copolymer, poly(ethylene terephthalate-glycol) (PETG), effects of crystallization on the stress-strain behavior can be isolated. Uniaxial and plane strain compression experiments have been conducted on these two polymers, with specific emphasis on the temperature region just above the glass transition. Temperature and strain rate were varied to obtain a large sampling of the mechanical behavior of the polymers. Compression experiments allowed for obtaining a uniform sample temperature and for controlling true strain rate during the experiments. Experiments at constant true strain rate were conducted to capture the inherent material response to the deformation. These results are presented in Chapters 2 and 3.

A constitutive model for the temperature and rate dependent stress-strain behavior above the glass transition temperature has been developed specifically for PETG. Details of this development are given in Chapter 4. The model represents the material's resistance to deformation as two resistances in parallel, an intermolecular resistance to flow, and a resistance due to molecular network stretch and orientation. A new reptation model is developed to account for molecular relaxation which occurs as the polymer deforms at high temperatures. The model for molecular relaxation

incorporates an internal state variable to monitor molecular orientation using an orientation angle parameter which evolves with deformation. This model is compared with classical results of Doi and Edwards (1986). In Chapter 5 this constitutive model is adapted to fit the behavior of PET, showing those areas where strain-induced crystallization may play a role. Chapter 6 expands on further modelling developments incorporating an evolving anisotropy of the relaxed configuration or 'natural state' of the polymer.

A final section in this thesis includes results from finite element simulations using the model presented in chapter 4. In these simulations parameters such as temperature, pressure, and stretch rod history are varied to show the effect of each processing parameter on the simulation output. Results are qualitatively compared with actual bottle blowing experiments.

1.1 Experimental Background

The mechanical behavior of PET has been extensively studied over the years. From early drawing experiments by Marshall and Thompson (1954) to modern in situ FTIR and WAXS experiments on PET films (see, for example Middleton, et al. (2001)), PET has remained a popular topic for research as its industrial prominence has grown. Yet, in spite of the large quantity of literature relating to experimental characterization of PET, many aspects of its mechanical behavior remain elusive. Strain-induced crystallization is the principal feature which has both created the industrial niche for PET and has simultaneously kept the attention of fifty years of experimentalists.

Early work by Flory (1947, 1956) on stretch-induced and equilibrium crystallization in polymers was followed by experimental work of Thompson (1959), in which fibers were drawn between rollers over a hot plate. Significant differences in crystallinity and birefringence were observed depending on the thermal and mechanical history of the fibers. Attempts to develop a theory for this observed behavior associated crystallization with a strain hardening process which was independent of time and temperature. This theoretical approach was unsuccessful at capturing the be-

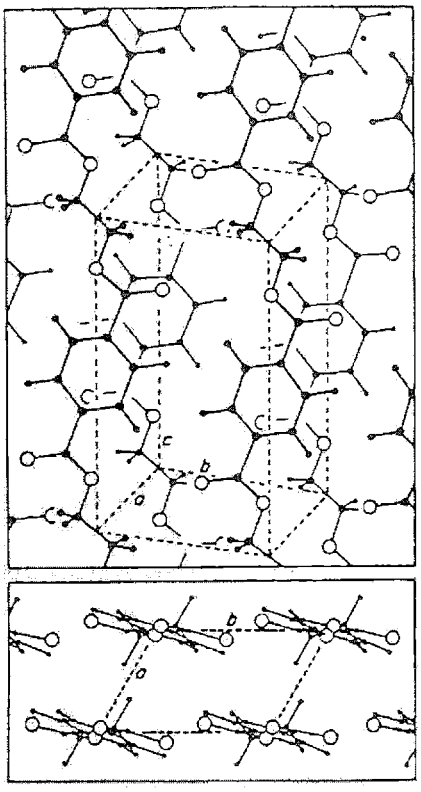

Figure 1-1: Crystal structure of PET (from Daubeny, Bunn, and Brown (1954))

havior of the PET fibers, but the idea that crystallization causes strain hardening has remained a common thread in work on PET. About the same time as Thompson's work, Daubeny, Bunn, and Brown (1954) published results of x-ray studies on PET. This paper detailed the triclinic crystal structure of PET, including the dimensions of the crystal, and commented on morphological explanations for such behavior as the high melting point of PET. The triclinic crystal structure is shown in figure 1-1 and the pertinent crystallographic planes are shown in figure 1-2. The dimensions of the unit cell are a=4.56 Å, b=5.94 Å, c=10.75 Å, $\alpha = 98.5^\circ$, $\beta = 118^\circ$, and $\gamma = 112^\circ$ (deP. Daubeny et al. 1954).

During the next twenty years, research on PET sampled various aspects of its behavior, focusing on measuring and understanding the role of molecular orientation in the polymer's deformation behavior. Work by Ward and Pinnock centered on the evolution of molecular orientation in PET during stress-relaxation experiments and the correlation with stress-optical relations (1966). Other work of Foot and Ward investigated the effect of initial orientation on drawing behavior by observing the

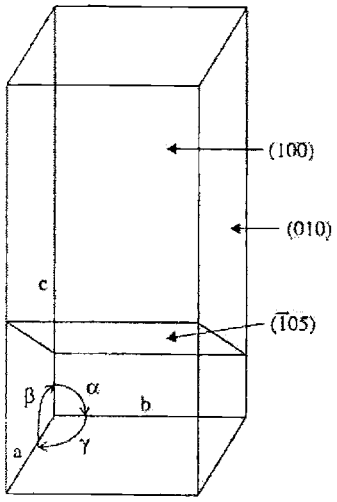

Figure 1-2: Crystallographic planes of a PET crystal (from Llana (1998))

material's natural draw ratio (Ward 1967; Foot and Ward 1975). They found that the natural draw ratio was dependent on the initial molecular orientation and that a correlation existed between the draw ratio and the degree of final molecular alignment. Purvis, Bower, and Ward applied polarized Raman scattering to determine the molecular orientation of PET films and fibers (Purvis et al. 1973; Bower and Ward 1982). De Vries, Bonnebat, and Beautemps (1977) conducted a wide range of uni- and biaxial extension experiments on polymer films, including on PET. They looked specifically at the effect of molecular orientation (as determined through birefringence measurements) on such mechanical properties as modulus, tensile strength, and impact resistance. They observed an approximately linear relation between Young's modulus and birefringence and observed an increase in tensile strength with orientation. Duckett, Rabinowitz, and Ward (1970) looked at the effect of strain rate and temperature on yielding of PET. Yield stress was found to increase monotonically with increasing strain rate and with decreasing temperature, as shown in figure 1-3. Note that the glass transition and melting temperatures of PET are approximately 80 ° C and 270 ° C, respectively.

It wasn't until the mid 1970's that the emphasis on PET research returned to crystallization. Siegmann (1980) studied melt crystallization of PET, including the

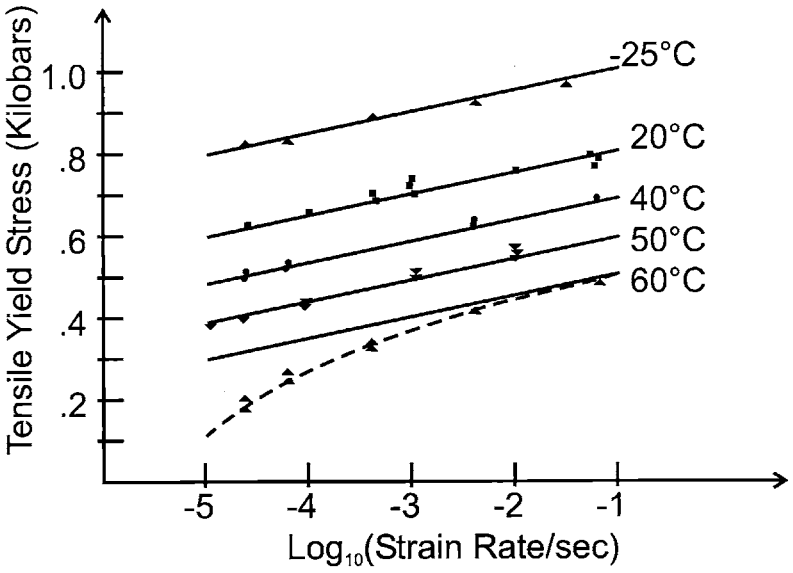

Figure 1-3: Tensile yield stress of PET (from Duckett, et al. (1970))

effect of pressure on the developed crystallinity. Two types of crystal morphology were observed: folded-chain crystals and extended chain crystals. The thin folded-chain lamellae were observed to be in the range of 90-150 Å and the extended chain lamellae were found with striated surfaces, up to several microns thick. Sun, Pereira, and Porter (1984) invested crystallization kinetics of cold extruded PET. They found that crystallization temperature decreased, crystallization rate rapidly increased, and activation energy decreased with the final draw ratio of the sample. Roland and Sonnenschein (1991) performed drawing experiments on PET near the glass transition to determine the molecular-weight dependence of crystallization. They found that the molecular configuration associated with the onset of strain-induced crystallization was independent of molecular weight.

A paper by Bellare, Cohen, and Argon (1993) looked at the development of crystallographic texture in initially semicrystalline PET as a function of deformation. They observed an initially spherulitic morphology, approximately 20 μm in diameter, which began to evolve as samples were deformed above a compression ratio of 1.8. At higher deformations, the spherulites became elongated, orienting toward the flow direction. The crystallographic texture within the spherulites also evolved as the

samples were further deformed, into stacks of fragmented crystalline lamellae. These lamellae were oriented toward the flow direction, as well. This oriented morphology led to an orthotropic symmetry in the final material samples.

Lee, et al. (1996) investigated the isothermal crystallization of PET at 110 ° C using small angle x-ray scattering. They observed 3 stages of crystallization: (1) thin lamellae are dispersed in a disordered array, (2) new lamellae become inserted between existing lamellae to start forming a stack, and (3) stacks then grow rapidly. A schematic representing these stages in the development of a spherulite in PET is shown in figure 1-4. In all three stages, the observed lamellae had a nearly constant thickness of 2.3 nm, initially dispersed in an isolated domain on the order of 20 nm in radius. This domain was seen to grows linearly with time and formed the basis of the lamellar sections in the evolving spherulitic morphology. A paper by Jog (1995) presents a review of crystallization in PET, including isothermal crystallization, which is modeled using the Avrami equation, and strain induced crystallization. Isothermal crystallization is often quantified in terms of a crystallization rate, which experiences a maximum around 174 ° C, at which point the crystallites can most easily nucleate and grow. At higher temperatures, it is difficult for stable crystallites to form and at lower temperatures, molecular mobilitiy is substantially decreased. Strain-induced crystallization is observed to occur at much higher rates (by an order of magnitude) than crystallization from an isotropic, amorphous state. During deformation processing, PET develops a metastable molecular ordering, which proceeds to crystallize under appropriate environmental conditions. The structure of the crystallites is often referred to as a shish kebab structure, or fully extended chain crystals. The crystallization process involves rotation, alignment, and perfection of the crystalline regions. During annealing of ordered PET samples, the initial orientation factor and temperatures at deformation and during annealing are the most important factors in crystallization rate and degree of crystallinity obtained.

Buckley and Salem (1987) performed low-strain, high temperature heat treatment on PET fibers to look at crystallization behavior. They observed a high temperature mechanical relaxation in semicrystalline PET which they associated with entangle-

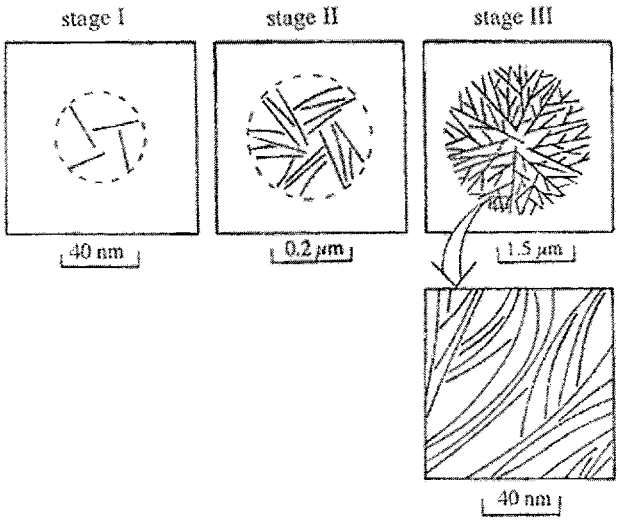

Figure 1-4: Evolution of Crystal Structure in PET (from Lee, et al. (1996))

ment slippage. The position of this α' relaxation was found to be highly sensitive to the thermomechanical history of the sample.

Several groups have looked at the effect of annealing on PET after deformation. Fischer and Fakirov (1976) annealed both undrawn and drawn PET to observe the development of crystallinity at various annealing temperatures. Misra and Stein (1979) conducted research specifically looking at stress-induced crystallization in PET drawn near the glass transition temperature. In this work, crystallinity was determined using density, WAXD and Small angle light scattering experiments. They observed that crystallinity increased in the deformed material when it was subsequently annealed. A rod-like crystal structure which developed during drawing later evolved into spherulites during this annealing process. All of their experiments were on PET drawn at one strain rate. Greener et al. (1995) performed a study on heatsetting of oriented PET films. In their work, they remarked that crystallinity increases linearly with heatset temperature. Additionally, WAXD patterns were observed to sharpen with increasing heatset temperature and crystallite size and in-plane crystalline orientation also increased with heatset temperature. Figure 1-5 shows how the crystallite size varied with heatset temperature, from approximately 35 Å at a heatset temper-

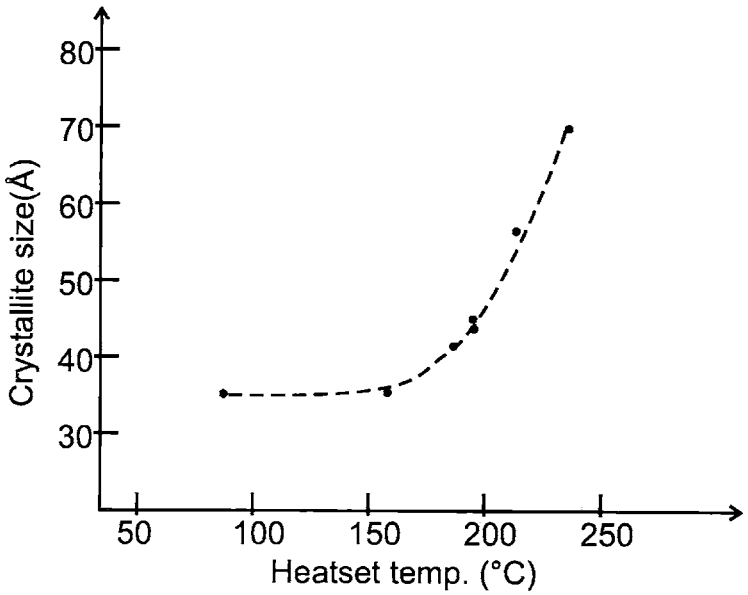

Figure 1-5: Crystallite size versus heatset temperature (from Greener, et al. (1995))

ature of 90 ° C to double that at a heatset temperature of 240 ° C.

Another group looking at crystallization kinetics in PET fibers was Peszkin and Shultz (1986). They annealed PET fibers at temperatures ranging from 100 ° C to 200 ° C and under a small tensile force (2 to 5 g) and observed through shrinkage and birefringence measurements that a competition existed between chain-recoiling and crystallization. They found that crystallization kinetics increased with higher temperatures and higher tension. Also, chain orientation was found to increase with tension. Petermann and Rieck (1987) looked at the effect of annealing on crystallinity in PET. Their results indicated that a higher annealing temperature led to greater crystallinity and orientation, higher tensile strength and tensile modulus, but lower elongation at break. They observed a micellar morphology.

Rietsch, Duckett, and Ward (1979) studied the tensile drawing behavior of PET at temperatures ranging from 20 ° C to 80 ° C. Cold drawn PET was observed to neck at a natural draw ratio of 4.3, which to a good approximation is independent of rate and temperature (elongation rates ranged from 0.05 cm/min to 5 cm/min, with a sample gage length of 4.75 mm). Hot-drawn PET, on the other hand, was observed to deform

homogeneously. Sweeney, et al. (1999) looked at applying a necking criterion to the behavior of PET. They concluded that necking would occur in PET below 60 ° C and would not occur above 80 ° C. They also noted that in intermediate temperatures, necking would occur only at high strain rates. This is evidence of the rate-dependence of the glass transition temperature.

Long and Ward (1991a, 1991b) looked at tensile drawing of PET and shrinkage force studies. They found that by determining a network draw ratio, properties of deformed PET could be correlated with different deformation histories. Gordon, Duckett, and Ward (1994) similarly studied two-stage uniaxial and constant-width stretching of PET. They observed that the results can be consistently interpreted using a molecular network model.

Ajji and coworkers (1994) performed uniaxial tension experiments on PET films at 80 ° C over a range of strain rates and to different final strains. They observed from DSC measurements that crystallinity increased at an approximate draw ratio of 3. At higher strain rates, this draw ratio shifted to lower values. Similarly, Dargent, Grenet, and Auvray (1994) used DSC and X-ray diffraction to monitor crystallization in samples deformed at a strain rate of 0.14 sec^{-1} and a temperature of 100 ° C. They observed strain-induced crystallization to occur above a critical stretch of 2.8. They also observed changes in melting, glass transition, and crystallization temperatures with strain: melting temperature increased weakly with extension ratio, the glass transition region became broader and shifted to increasing temperatures with extension, and the DSC crystallization peak shifted to lower temperatures with extension.

Salem (1994) conducted experiments over a range of strain rates (0.01 to 2.1 sec^{-1}) and temperatures above T_g (83 ° C to 96 ° C) to look at the relation between crystallinity and the final draw ratio. Crystallinity was determined using density measurements. It was found that lower strain rates delay the onset of crystallization to higher draw ratios. Additionally, Salem observed that crystallinity versus log-time curves could simply be shifted on top of one another. Clauss and Salem (1995) observed orientation in uniaxially drawn PET. Experiments were performed at 90 ° C and they observed that orientation develops faster at higher strain rates.

Jabarin (1984) conducted biaxial experiments on PET in 1984 to look at the effect of various parameters on birefringence. Results showed that molecular orientation and mechanical properties of the drawn films were a strong function of strain rate, final strain, molecular weight, and draw temperature. He found that for a given rate and final strain level, birefringence decreased with increases in temperature. He also determined that mechanical properties such as yield stress and ultimate tensile stress were directly related to the level of molecular orientation in the tensile direction.

Cakmak, et al. (1986, 1987, 1989) biaxially stretched PET films above the glass transition temperature to look at orientation and crystallinity. They observed that crystallinity increased with increasing final stretch and with annealing and that the crystal structure is perfected during annealing. They also found that in order to attain the same level of molecular orientation at 100 ° C as at 80 ° C, the sample must be stretched further. Le Bourvellec, et al. (1986, 1987) conducted similar experiments also looking at orientation and crystallinity. Their results indicated that crystallinity and crystallization kinetics depended on the degree of molecular orientation in the polymer. This meant that PET deformed at higher temperatures crystallized more slowly due to the fact that more molecular relaxation had occurred.

Matthews, et al. (1997) conducted biaxial drawing experiments on PET at 85 ° C with the goal being to fit a constitutive model to the data. Strain rates ranging from 0.5 sec^{-1} to 5.0 $\times$ 10^{-4} sec^{-1} were used. They found that strain hardening played a significant role in the stress-strain behavior beyond a draw ratio of about 2.2. Adams, Buckley, and Jones (1998) also conducted biaxial stretching experiments on PET, looking at how yield stress varies with strain rate above the glass transition temperature. In another paper (Adams et al. 2000), they extended their experiments to a wider range of temperatures in order to develop a constitutive model for the behavior of PET.

Dargent, et al. (1999) also performed stretching experiments on PET sheets to look at both crystallinity (based on DSC measurements) and birefringence (based on analysis of reflection-mode pole figures from spectroscopic measurements). They found that crystallinity changed little after a draw ratio of 3.5, but that birefrin-

gence continues to increase dramatically to much larger draw ratio. Matthews, et al. (1999) conducted roll drawing experiments on PET at high temperatures (130 ° C to 190 ° C). They found that the mechanical properties of the film were independent of the draw temperature at a given draw ratio. They suggested that this is because crystallinity increases with increasing temperature, but orientation decreases with increasing temperature, and that the two competing effects lead to the temperature independence.

A series of papers in 1992 by Clauss and Salem (Clauss and Salem 1992; Salem 1992a; Salem 1992b) and Jabarin (1992), looked at the relation between strain hardening and crystallization in PET. In Salem's work (1992b) the rate-dependence of crystallization in PET was investigated. He concluded from density measurements and wide angle X-ray scattering data that crystallization begins at the inflection point in the stress-strain curve and shifts to higher draw ratios and lower stress levels as the strain rate decreases. He also observed that crystallite size increased with draw ratio, crystallite sizes ranging from 2.5 to 4.0 nm. Jabarin (1992) also looked at rate-dependence, along with temperature-dependence of crystallization, but found that strain-induced crystallization occurred during stretching when samples were stretched to a strain below the strain hardening region.

Chandran and Jabarin published a series of three papers (1993a, 1993b, 1993c) on biaxial orientation of PET. In this work, a large series of experiments were performed on PET biaxially stretched both sequentially and simultaneously. Experimental data was reported for a variety of temperatures and strain rates, giving a solid foundation for the features of the stress-strain curves in these deformation modes. Similar experiments were performed by Gohil and Salem (1993) to look at the evolution of orientation and mechanical properties in each direction. They observed some difference between sequentially versus simultaneously stretched films, specifically that after a stretch of 2.7 in the second stretch direction, sequentially stretched chains begin to realign in that direction.

Tassin, Vigny and coworkers (Tassin et al. 1999; Vigny et al. 1999) performed sequential biaxial stretching experiments on PET followed by annealing. Specimens

were stretched at temperatures ranging from 85 ° C to 115 ° C at a drawing speed of 0.75 sec^{-1} in the first stretch direction. In the second stretch direction, stretching temperatures of 105, 115, and 125 ° C were used and applied loads ranged from 15 to 25 MPa. Annealing was then done at 200 ° C for up to 20 sec. X-ray diffraction and infrared dichroism were used to observe changes in crystallinity and orientation. They found that crystallinity increased with increase in draw ratio and that crystallization appeared at lower draw ratios for lower temperatures. Also, the chain axes were more aligned with increasing draw ratio or decreasing temperature. Upon subsequent stretching in the transverse direction, the crystals were found to rotate toward the transverse direction.

In another paper by Salem (1995) he looked at the difference in crystallization between tensile experiments at constant extension rate and those at constant strain rate. He observed that crystallization onset is at shorter times and that crystallization rate is higher for constant strain rate experiments. Salem (1998, 1999) conducted further constant-force and constant-extension ratio experiments on PET to look at orientation, crystallinity, and the development of microstructure. He found that much of the deformation during roll drawing, took place in the range of the maximum strain rate. In this range, the time available for molecular relaxation and crystallization is short, which leads to higher orientation and lower crystallinity than in a constant extension rate experiment. He also finds the same effect when drawing at lower temperatures, where molecular relaxation and crystallization are less favored than at high temperatures. Similar work by Lu and Hay(2001) gave the same results, that increasing strain rate or decreasing temperature promoted crystallization and orientation.

Guan, Saraf, and Porter (1987) compared biaxial stretching with uniaxial compression of PET. They found that in compression PET develops more planar orientation and more strain induced crystallization than in biaxial stretching. Work by Guan, et al. (1992) compared crystallization during biaxial stretching with uniaxial compression. Uniaxial compression resulted in more crystallization, however in both types of experiments the draw rate was held constant, so that in extension the strain rate was

decreasing during the experiment and in compression the strain rate was increasing.

In 1996, one research group began investigating the claim that strain-induced crystallization occurs during drawing. Blundell, et al. (1996) published results of tensile tests on PET in which x-ray patterns were recorded during the deformation process. This paper, combined with subsequent papers (Blundell et al. 1999; Blundell et al. 2000; Mahendrasingam et al. 1999; Mahendrasingam et al. 2000) suggested that, except in the case of quite slow experiments, strain-induced crystallization does not occur until the moment when deformation stops. They suggest that the crystallization which previous researchers had concluded was occuring during deformation, in fact had occurred during the quench process. Later work by Schrauwen, et al. (2000) confirmed the in situ experiments of Blundell, Mahendrasingam, et al. as they also observed that PET did not show any crystallization during drawing.

Work by Kim, et al. (1997) looked at orientation in commercially produced films. They observed that amorphous chains and crystallites are most fully aligned in the center of the films, but near the edges are more poorly aligned. They also found that crystallites tended to be more completely aligned in the film than the amorphous chains, and suggested that this was because crystallites could more easily rotate and align away from the first stretch direction and into the second stretch direction than the amorphous chains. They found a strong dependence of the elastic modulus on the orientation distribution of those amorphous chains.

Compression experiments, on the other hand, have been conducted by a few researchers to look at the deformation behavior of PET. Zaroulis and Boyce (1997) conducted one of the first such sets of experiments. This work was specifically focused in the glassy regime up to the glass transition temperature and looked at the material behavior over a variety of strain rates, including both uniaxial compression and plane strain compression experiments. Work by Llana and Boyce (Llana 1998; Llana and Boyce 1999) continued this effort by adding substantial experimental results above the glass transition temperature, and by performing WAXD and DSC experiments to look at crystallization as a function of temperature, rate, and strain state. Their experiments were in the range of 90 $^{\circ}$ C to 105 $^{\circ}$ C and at strain rates

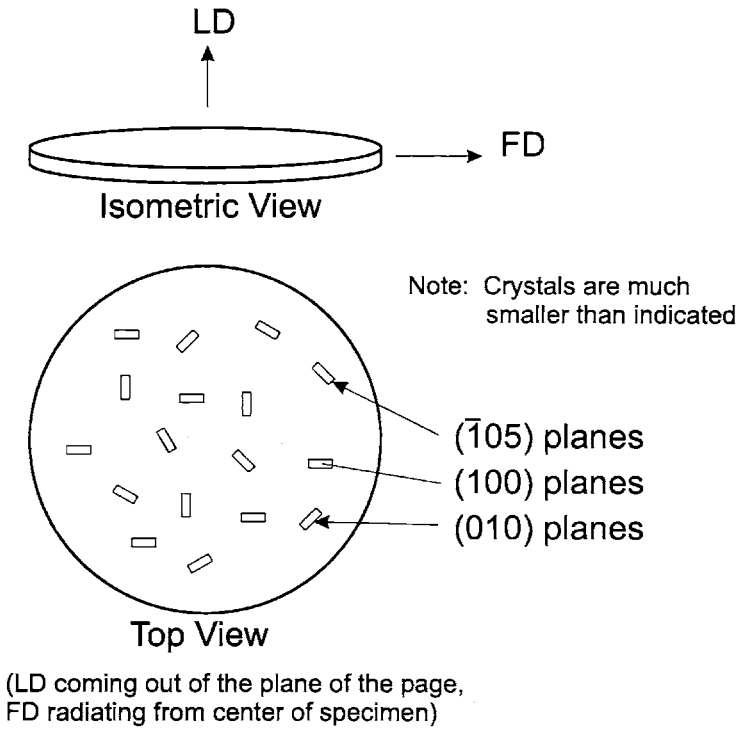

Figure 1-6: Orientation of crystals in uniaxial compression (from Llana and Boyce (1999))

ranging from -0.005 to -2.0 sec^{-1}. They observed that the stress-strain behavior exhibited a sequence of four characteristic features: (1) a relatively high initial stiffness, (2) a rollover in the stress-strain curve to flow, (3) an increase in stress with continuing strain, (4) a dramatic increase in stress with strain at high strains. Each depended strongly on strain rate, temperature, and strain state, and crystallinity was found to increase with increasing strain rate and decreasing deformation temperature in both uniaxial and plane strain compression. The crystallographic texture was observed through WAXD measurements to be consistent with the molecular orientation associated with each state of deformation, as shown in figures 1-6 and 1-7.

Vigny, et al. (1999) performed plane strain tensile tests on PET at 90 ° C for purposes of developing a constitutive model which would incorporate crystallinity. Gorlier, et al. (2000, 2001) performed video-controlled, constant strain rate tensile experiments on PET. They observed that crystallinity developed much more rapidly

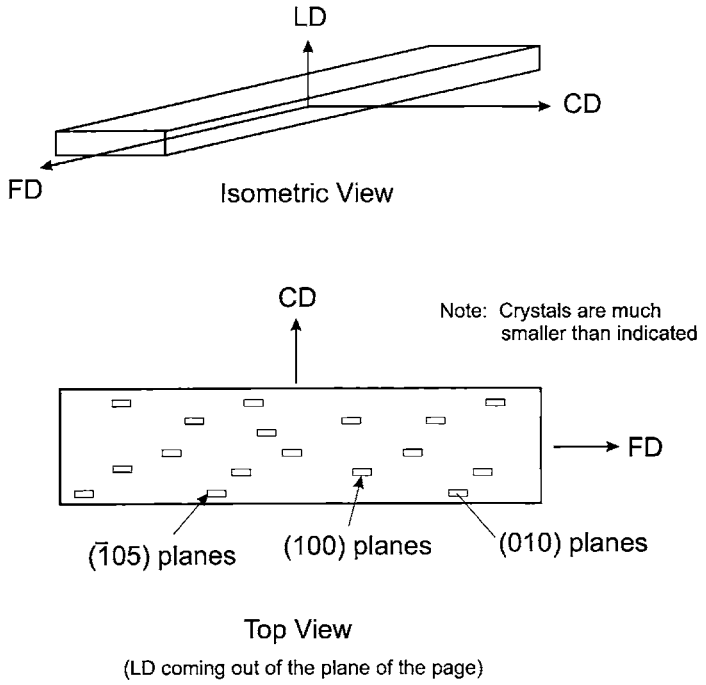

Figure 1-7: Orientation of crystals in plane strain compression (from Llana and Boyce (1999))

when the samples were quenched more slowly. They suggest that crystallization is not directly related to strain hardening but rather to the development of a mesophase. G'Sell (2000) performed similar experiments above T_g to observe the dependence of the stress-strain curves on strain rate.

Cole, Ajji, and Pellerin (2002) investigated the morphology of three cases of PET: amorphous (quenched from the melt), drawn (at 80 ° C and 2 cm/min) and subsequently quenched, and annealed at various temperatures (100 ° C to 200 ° C) for up to 24 h. Their results suggest that there is an intermediate stage of the material in which it is highly ordered, but not as closely packed as in the crystalline material. This intermediate stage is what results in strain induced crystallization.

The above summary of experimental literature related to PET illustrates the scientific interest in its behavior. Experiments on isothermal crystallization, annealing, and heatsetting treatments have been designed to identify the crystallolgraphic texture of PET. Other experiments have attempted to correlate deformation with

microstructural quantities such as molecular order or crystallinity using a variety of mechanical deformation histories combined with density, optical (birefringence), x-ray, and thermal (DSC) methods to observe changes in the microstructure. Challenges continually arise using these approaches because of the difficulty of quenching a sample quickly enough to remove the effects of crystallization during the brief annealing after deformation. Most recently research efforts have tried to resolve these issues by conducting simultaneous stretching and wide angle x-ray measurements. This approach has further illucidated the subject of strain-induced crystallization, indicating that at moderate to fast strain rates a meso-crystalline phase occurs during stretching, but actual crystallite development is delayed until the deformation process ceases. Once deformation halts, the crystallinity is seen to develop very rapidly (< 1 sec).

1.2 Constitutive Modeling Background

Constitutive modeling of the finite strain behavior of PET near the glass transition temperature has been evolving to gradually incorporate more of the observed mechanical behavior of the material. Some of these models have been developed strictly for the purpose of simulating a process, in which case a quick phenomelogical fit to data, a mathematically simple constitutive law, and a computationally efficient numerical scheme have taken priority. Other resesarchers have focused on trying to understand the underlying physics in order to develop a mechanistically based material model.

Much of the modeling of polymers relies on the concept of an underlying network of polymer chains. In rubbers, this network is created by physical crosslinks between the polymer molecules. In thermoplastic materials such as PET, this network is instead created by physical entanglements. Since these entanglements are not a chemical bond, there is the potential for chains to slip through their entanglements under an applied load, a process often called reptation.

The theory of rubber elasticity has been addressed by many sources, such as Treloar and Flory (Treloar 1975; Treloar 1976; Flory and Rehner 1943; Flory 1985).

Initially, polymer chains were treated using Gaussian statistics, but it was observed that as polymer chains were extended they eventually approached a limiting extensibility, causing the stress to rise dramatically. This could not be accounted for using Gaussian statistics, so in order to capture the behavior at very large stretches alternate, non-Gaussian statistical methods had to be used (see, for example Wang and Guth (1952) and Treloar (1975)).

The general approach to modeling rubbers is to treat them as hyperelastic materials and to develop an expression for the strain energy function. In general, this strain energy function is a function of the deformation gradient, but it is often simplified to be a function of the scalar invariants of the right or left Cauchy-Green strain tensor, or even of the principal stretch values. The strain energy function can then be differentiated to yield an expression relating the Piola-Kirchhoff stress to the deformation gradient.

Several models incorporate this approach phenomenologically. Treloar (1943) first proposed the neo-Hookean form of the strain energy: $W = \frac{1}{2}\mu(I_1 - 3)$. The Mooney-Rivlin (Mooney 1940; Rivlin 1948) form, $W = C_{10}(I_1 - 3) + C_{01}(I_2 - 3)$, incorporated a dependence on the second invariant but only gave a marginally better fit to experimental data than the neo-Hookean form. Valanis and Landel (1967) developed a strain energy function using the principal stretches, $W = w(\lambda_1) + w(\lambda_2) + w(\lambda_3)$. They found that for shear, $w = 2\mu \ln \lambda$ gave a good fit, but it was unable to adequately capture state-of-strain dependence. Ogden (1972) developed an isotropic strain energy function using strain energy invariants, which also depended on the principal stretches: $W(\alpha) = (\lambda_1^\alpha + \lambda_2^\alpha + \lambda_3^\alpha - 3)/\alpha$. The total strain energy is then the sum of each of these invariants, weighted by a modulus, μ: $W = \sum \mu_\alpha W(\alpha)$. This model could be fit to data using as many different values of α as needed.

Other models for rubber elasticity took a more mechanistic approach to developing a functional form for the strain energy. In these models, unit cells of a specific number of chains were proscribed. The material was assumed to deform affinely, such that the deformation of the unit cell and the resulting chain stretch was representative of the whole material. A good review of such models is given in ref. (Boyce and Arruda

2000). The main examples are the 3-chain, 4-chain, and 8-chain models. The 3-chain model proposed by Wang and Guth (1952) gives good results for uniaxial deformation, but is unable to capture other modes of deformation. The 4-chain model of Flory and Rehner (1943) gives a slight strain-state dependence due to the cooperative motion of the four chains, however the model is not symmetric with respect to principal stretch space. Hence, the results depend on the orientation of the 4-chain tetrahedron.

The Arruda-Boyce 8-chain model (1993b), on the other hand, both contains symmetry with respect to principal stretch space, and captures the cooperative chain motions associated with different deformation modes. It is therefore able to capture the strain state dependence of the mechanical behavior over the whole range of strain.

Ball, Doi, Edwards, and coworkers (Ball et al. 1981; Edwards and Vilgis 1986) began looking at the effect of entanglements in addition to crosslinks in rubber elasticity. They developed expressions for the free energy associated with an entanglement and began discussing concepts of a tube or primitive path, along which a polymer chain is constrained to move. This was followed by the classical book of Doi and Edwards (1986) which detailed the concept of reptation in polymer dynamics. This book summarized and expanded on previous work by de Gennes (1979) and earlier papers by Doi and Edwards (1978, 1980). Bergstrom and Boyce (1998) used the principles of the Doi-Edwards model to model the large strain time-dependent behavior of rubbers.

In models for thermoplastics, such as PET, which exhibit a huge rate and temperature dependence, constitutive models are generally hyperelastic-viscoplastic in nature. A model by Buckley, Jones, and Gerlach (Buckley and Jones 1995; Buckley et al. 1996; Gerlach et al. 1998), for example, used a summation of bond-stretching stress and conformational stress to account for the material behavior. The bond-stretching portion employed linear elasticity and Eyring viscous flow. The conformational (entropic) portion made use of the Edwards-Vilgis model (1986). This model was able to capture the change in behavior with temperature, from glassy behavior at low temperatures to rubbery behavior at higher temperatures above the glass transition temperature. This general model was then fit to biaxial extension data for PET.

They found that the model did very well at capturing the mid-strain range well, but did not fare particularly well at capturing the initial yield stress nor the large strain hardening at large extensions.

Dooling, et al. (1998) applied a similar model to PMMA, specifically trying to model creep just below the glass transition temperature. They found their results to be good for moderate time scales (up to 100 seconds), but found deviations at larger times. The model was extended by Adams, et al. (2000) to account for strain-induced crystallization in PET. This model was able to capture the experimentally observed trends quite well, with the limitation that the model was fit to data at one extension rate, and therefore its ability to capture strain-rate dependence is unclear.

In a model for PVC, Sweeney and Ward (1995) incorporated the Ball network model with a rate dependence which allowed the number of sliplinks (a parameter in the Ball model) to vary with strain rate. A similar approach was taken by Matthews et al. (1997) for PET. They found that the model only worked well up to a draw ratio of about 2.2 as it was unable to account for the strain hardening at large strain levels in PET. A model by Vigny, et al. (1999) obtains a strain-rate sensitivity coefficient from data from plane strain tensile tests on PET and uses this in a power-law type viscoplastic element. They incorporate crystallinity by proscribing the number of entanglements to increase as crystallization occurs.

A model by Boyce, Socrate, and Llana (2000) also took the deformation to be composed of two parts: one due to intermolecular interactions and the other due to intramolecular or network interactions. The intermolecular part was composed of a linear-elastic spring, and a viscous element which modeled yielding as a thermally activated process using an Arrhenius-type equation. The network part was composed of a network spring element (the 8-chain model), and a viscous element which represented reptation. The reptation element used was that of Bergstrom and Boyce (1998). The model also attempted to incorporate strain-induced crystallization by identifying a critical network stretch at which crystallization would occur. At this point, reptation ceased and the shear resistance of the material began to increase. This model was able to capture data over a wide range of temperatures and strain rates, but specifically

the crystallization portion of the model was quite phenomenological.

This model was extended by Ahzi, et al. (2002) to explicitly include the contribution of a crystalline phase to the overall response. This was done by treating the intermolecular resistance as a composite framework with the crystalline and amorphous phases as two seperate resistances. The resistances were coupled through three different analog representations: an upper bound, a lower bound, and a self-consistent approach. Crystallization rate was expressed using a non-isothermal phenomenological expression based on the modified Avrami equation and predicted results gave good agreement with experimental results.

Another area of modeling for PET is from the perspective of the fluid mechanics community. An extensive review of the field of non-Newtonian fluid mechanics can be found in the books by Bird, et al. (1987, 1987). Doufas, McHugh, et al. have recently published a series of papers on fiber spinning and film blowing of PET and other polymers (Doufas et al. 1999; Doufas et al. 2000; Doufas et al. 2000; Doufas and McHugh 2001b; Doufas and McHugh 2001a; McHugh and Doufas 2001). They use the Giesekus model (Giesekus 1982; Wiest 1989) incorporating finite chain extensibility for the amorphous polymer melt. They include a rate equation for crystallization which reduces to the Avrami equation for quiescent conditions. Their crystallization model employs a transformation over time of amorphous chain segments into a semi-crystalline phase. That semi-crystalline phase is taken to consist of rigid rods which orient in the flow direction. They obtain good comparison with experimental results, but the model contains many empirical constants without physical meaning.

Work by Coppola, et al. (2001) on flow-induced crystallization modeled the behavior using the Doi-Edwards model with the Independent Alignment Approximation (DE-IAA) combined with the Lauritzen-Hoffman equation for the crystallite nucleation rate in polymers below their melting temperature. They found that, compared with linear elastic dumbbells and FENE-P dumbbells, the DE-IAA model gave the best overall agreement with data. They suggest that this is because crystallization is enhanced more by the level of orientation of the dumbbells than by the amount of stretch experienced by the dumbbells.

1.3 Blow Molding Simulation Background

A few papers have experimentally investigated the bottle blowing process. Kim (1984, 1985) conducted reheat blow molding experiments with 2 liter PET bottles. The aim was to look at the effect of preheat time and equilibration time on the morphological, oxygen barrier, and overall bottle properties. Results showed that after preheating, the bottle wall temperature was greater on the outer surface than the inner (as measured using Cu- constantan thermocouples); however, after 10 to 30 seconds of equilibration time, the inner surface temperature had increased and the outer decreased to create optimal drawing conditions. Overall observations included that colder bottles tend to pearl on the inner wall surface (indicating chain scission) and warmer bottles tend to haze on the outer wall surface (due to spherulites developing). No clear trend was seen in oxygen permeability.

Bonnebat, Roullet, and de Vries (1981) looked at the effect of molecular weight on the stretch blow molding of PET. They found a significant effect, principally because molecular weight influences the natural draw ratio of the polymer. They conducted free blow experiments on PET with different molecular weights to observe the longitudinal and transverse stretches versus bottle volume as a function of molecular weight. They found that resins with lower molecular weight require thicker and shorter preforms.

Axtell and Haworth (1994) looked at the strain rate and temperature dependence of PET's rheological behavior in the range of blow molding simulations and plotted the results using a stress-growth function (an alternative to elongational viscosity which is used in cases where steady-state is not achieved and when elastic properties significantly affect the deformation process). They observed that the curves (stress-growth function versus time on a log-log plot) all superposed up until a critical strain, which they associated with the onset of strain-induced crystallization. They also looked at blow molding and commented that strain-induced crystallization was essential in bottle formation, in that it imparted a uniform wall-thickness and enhanced the physical properties of the molded bottles. They found that crystallinity

increased with increasing blow pressure.

Venkateswaran, Cameron, and Jabarin (1998a) investigated the effect of varying the temperature profile on the properties of reheat blown PET bottles. They found that the tensile modulus decreased with increasing processing temperature, and that the tensile energy absorption increased with increasing processing temperature. They found a higher hoop-direction birefringence on the inner wall surface than the outer surface. Bottle sidewall density and crystallinity increased with increasing processing temperature, though the oxygen permeability was not significantly affected.

Cakmak, et al. (1984, 1985b, 1985a) looked at orientation in both commercial and lab bottles. They found that 90 ° C produced more uniform orientation along the bottle length than either 80 ° C or 100 ° C. They observed that higher pressure leads to greater orientation and that the orientation is primarily equi-biaxial in nature. Additionally, birefringence was greater on the inside surface than on the outside surface of the bottle. In a set of experiments which looked at crystallinity in commercial bottles, they observed that bottles contain a high level of crystallinity and that they exhibit anisotropic mechanical behavior through the bottle wall thickness. This is due to higher transverse stretching on the inner surface of the bottle.

Chung (1983) and Caldicott (1999) discussed the principles of preform design for blow molding. In his paper, Chung discusses such design parameters as wall thickness, and uses heat transfer arguments to specify maximum and minimum wall thickness for a preform. Mold removal requires specific taper angles. Large stretch ratios are needed so that the final product has sufficient molecular orientation to give it the required strength and stiffness. He also noted that non-circular cross-sections create added complications such as preform-mold alignment and non-uniform temperature distribution issues. Caldicott suggests future design challenges for bottle blowing: wide-mouth jars, higher temperature containers, pasteurized beer bottles, and so forth.

Other experiments have been performed to study the extrusion blow molding process. One example is work of Choi, Spruiell, and White (1989) in which they examined orientation in blow-molded high and low density polyethylene bottles. They found

that bottles tended to be thicker at the neck than the bottom due to gravitational effects. The thickness of the bottles increased with decreasing temperature. Bottles inflated at higher pressure were seen to have a more uniform thickness along the length. In general, the birefringence of the bottles increased with increasing pressure and decreasing temperature.

Axtell and Haworth (1993) looked at extrusion blow molding of PETG. They noted that shear thinning behavior plus elongation stiffening made PETG a viable candidate for extrusion blow molding. They looked at different factors which influenced parison sag, such as output rate, melt temperature, and time.

Debbaut, Homerin, and Jivraj (1999) attempted to model extrusion blow molding of HDPE using a Lodge rubberlike constitutive model (see Lodge (1964)). It essentially consists of an integral viscoelastic constitutive equation in which the damping function is neglected and the memory function takes the form of a sum of decreasing exponential terms:

$$\begin{aligned} \mathbf{T} &= \int_{-\infty}^{t} m(t-t')[\mathbf{C}_t^{-1}(t') - \mathbf{I}]dt' \\ &= \int_{-\infty}^{t} \sum_{k=1}^{N} \frac{\eta_k}{\lambda_k^2}[\mathbf{C}_t^{-1}(t') - \mathbf{I}]dt' \end{aligned} \tag{1.1}$$

where $\mathbf{T}$ is the stress tensor, $m(t-t')$ is the memory function, $\mathbf{C}_t(t')$ is the right Cauchy-Green strain tensor, $\mathbf{I}$ is the identity tensor, η_k is a viscosity factor, and λ_k is a relaxation time. Their model was able to predict final shape easily, but was rather inaccurate at predicting thickness distributions. They attribute this to inaccuracy in the initial parison geometry, mold wall boundary conditions, and temperature variations. Liu (1999) similarly worked to simulate extrusion blow molding and attributed his discrepencies to parison sagging and to non-uniform temperatures.

The literature includes some attempts to simulate blow molding. One such paper is by McEvoy, Armstrong, and Crawford (1998). They used an elasto-viscoplastic constitutive model for the material behavior and simulated the deformation of a 48 gram preform inside a 2 liter bottle mold using axisymmetric finite elements. They compared bottle profiles both with and without a stretch rod and overall obtained

correct trends for the wall thickness profile of the final bottle. In a second paper by Menary, et al. (1999, 2000), three constitutive models were compared: a hyperelastic model, a creep model, and Buckley's model (1996). Of the three, Buckley's model worked the best, in terms of giving the most accurate thickness distributions and the most accurate free blow shape. Unfortunately, the Buckley model required the most computation time (48 hours, as compared with 12 hours and 10 minutes for the creep and hyperelastic models, respectively). They found the Buckley model to work well on both 330 mL and 2 L bottle simulations, though the simulation did not quite fill up the base of the 2 L mold. This is attributed to a different molecular weight PET which was used for the model as compared with the material the model was fit to. They also developed an algorithm for computing shelf life of a simulated bottle. Their results agreed fairly well with experimental shelf life data.

Erwin, Pollock, and Gonzalez (1983) attempted to model blow-molding by using a thin-wall shell (or membrane) theory. They used a phenomelogical fit of an invariant-based model from Ward (Ward 1983) to predict pressure as a function of hoop stretch and blow time. The general form of the strain energy function was:

$$W = \sum_{i,j=0}^{\infty} C_{ij}(I_1 - 3)^i(I_2 - 3)^j \tag{1.2}$$

where W is the strain energy, C is a coefficient, and I_1 and I_2 are the first and second strain invariants, respectively. This strain energy function was fit to data from a biaxial stretching experiment at a similar extension rate as that experienced during blow molding (approximately 25,000 percent per minute). They found that higher pressure is required to begin the aneurysm during blowing than to continue the blow by a factor of two.

Schmidt, Agassant, and Bellet (1998) attempted to model the blow molding process using an Oldroyd-B fluid model, including a viscosity which varies sharply with tempreature and a pseudo-crystallinity correction to prevent the free blow from growing without bound radially.

Wang, Makinouchi, and coworkers (2000) used an empirical viscoplastic model for

PET in which the model is fit in a low strain and high strain regime and each of the model parameters is fit by a fourth-order polynomial. They compare this model with a simple power-law fluid and a single regime viscoplastic model (no strain hardening). Their model is able to capture the thickness distribution and final shape of a bottle blown inside a mold quite well, while the other two cannot.

Venkateswaran et al. (1998b) used PET film data to predict bottle properties. They used a time-temperature superposition to extrapolate to higher strain rates and different temperatures and used an average orientation function in their model, which considers only the end state of the polymer obtained by birefringence.

Marckmann, Verron, and Peseux (2001) used an adaptive mesh refinement technique and a "sticky" surface boundary condition for blow molding simulations. They used a Mooney-Rivlin model and obtained fair results for the thickness distribution. They assessed the need for a better material model and better initial thickness estimates.

Each of these models has attempted to capture some feature of the stretch blow molding process. As always, some simplifying assumptions have been used to make the problem approachable. It is quite clear, however, that the method in which items such as boundary conditions, temperature profiles, and pressure or stretch rod displacement histories are applied can also significantly affect the validity of a computer simulation.

1.4 PETG Background

Relatively little literature has been published relating to PETG. Papadopoulou and Kalfoglou (1997) looked at the miscibility of PET and PETG and found the two to be completely miscible at all concentrations. They found that annealing the blends caused the PET to crystallize and led to embrittlement of the material. Moskala (1996) examined the fatigue resistance of PETG upon adding impact modifiers. He found that the impact modifiers decreased the fatigue resistance, with larger particles causing a larger decrease by facilitating plastic growth. Ching, Li,

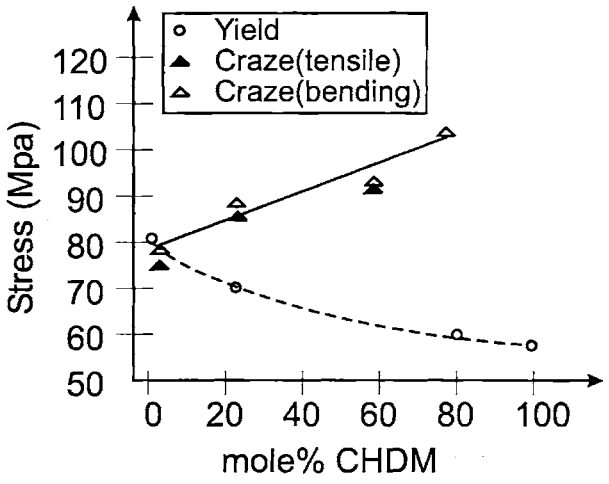

Figure 1-8: Yield and craze stress as a function of CHDM content (from Chen et al. (1999))

and Mai (2000) looked at fracture toughness of PETG. They found that the specific essential work of fracture was independent of gage length using double-edge-notched-tension specimens. They also observed a ductile to brittle transition at long gage lengths, though their paper did not suggest any mechanism to explain this observation. The specific essential work showed a small dependence on strain rate for loading rates lower than 1 mm/min (gage lengths ranged from 50 to 250 mm), and did not show a rate dependence at higher loading rates.

Work by Chen, Yee, et al. (1998, 1999) looked at the secondary relaxation, impact strength, and yield behavior of a series of polyester copolymer glasses, including PETG. They found that yield stress decreased as percent poly(1,4-cyclohexylene-dimethylene terephthalate) (PCT) increased (PETG is 69% PET, 31% PCT). The craze stress, on the other hand, increased as percent PCT increased. The tradeoff of yield stress decreasing and craze stress increasing led to a brittle-ductile transition. Figure 1-8 shows a summary of these results at room temperature and a strain rate of 22 sec^{-1}.

Unpublished work of Patton (1998) first looked at the effect of rate and temperature on the mechanical behavior of PETG. In this work, uniaxial and plane strain compression tests were performed over a range of temperatures (25 $^{\circ}$C to 100 $^{\circ}$C)

and over a range of strain rates. A strong dependence on both temperature and rate was observed for the material. The stress-strain curves followed similar trends to those reported for PET under similar testing conditions (1999), including a dramatic strain hardening at large levels of strain. An extension to this work was reported by Brown (Dupaix) (2000), which included a more extensive series of experiments and the initial development of a constitutive model to account for the behavior.

Recent work by Kattan, Dargent, et al. (2001, 2002) looked at strain-induced crystallization in PETG and aimed to compare the behavior of PET and PETG. They conducted experiments on both materials at a strain rate of 0.14 $sesc^{-1}$ and a temperature of 95 ° C. They found that very small levels of crystallinity (less than 3 percent) were attainable in PETG under normal drawing conditions. Upon annealing, it was possible to increase this level of crystallinity, but it was still substantially lower than that of PET. In their follow-up study comparing PET with PETG (Kattan et al. 2002), they observed that upon deformation both materials develop a significant amount of what they referred to as a rigid amorphous phase (35 % and 25 % in PET and PETG, respectively). This rigid amorphous phase was identified using thermally stimulated depolarisation current eperiments. After the formation of the rigid amorphous mesophase PET proceeded to crystallize whereas the PETG did not (measured crystallinities were 40 % for PET and 3% for PETG).

1.5 Summary

As has been discussed, the deformation behavior and morphological structure of PET has been widely studied. Constitutive models have advanced to be able to capture many of the features of the finite strain behavior of PET, but in many instances the incorporation of strain-induced crystallization into the models is highly empirical, and possibly inappropriate due to evidence that at many strain rates the material is not actually able to crystallize while the deformation is proceeding. A few example studies have attempted to characterize the blow molding process, but in all of these cases, the authors cite the need for better models to improve the predictive ability

of the simulations. Additionally, very little has been published on the mechanical behavior of PETG, and no constitutive models have been found in the literature which attempt to model the deformation behavior of PETG. This thesis is intended to begin to address these open issues.

Chapter 2

PETG Experiments

2.1 Introduction

In the polymer processing industry, poly(ethylene terephthalate) is a front-runner in terms of market volume and diversity of its applications. Those applications range from drawn fibers and films for clothing and photography to food storage applications, most notably that of carbonated beverage containers. The primary reason for its success in these applications is its ability to undergo strain-induced crystallization under appropriate conditions of temperature and strain rate.

Another polymer of less fame is an amorphous copolymer of PET, often called PETG. The letter G refers to the additional glycol group along the backbone of the copolymerizing agent, poly(1,4-cyclohexylenedimethylene terephthalate) (PCT) (see Figures 2-1 and 2-2). Specifically, PETG is a random copolymer consisting of 31 mol % PCT and 69 mol % PET. PETG is often used to produce large thermoformed parts such as vending machine faces and point-of-purchase display panels. PET and PETG both exhibit quite similar deformation behavior, have a similar glass transition temperature, are visually nearly indistinguishable, but there is one substantial difference: PET readily undergoes strain-induced crystallization, whereas in PETG crystallization is very difficult, if not impossible at processing temperatures. Two recent papers by Kattan, et al. (2001, 2002) address the difference in crystallizability between the two polymers.

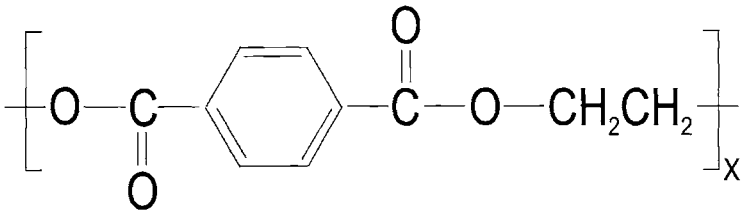

Figure 2-1: Chemical structure of PET

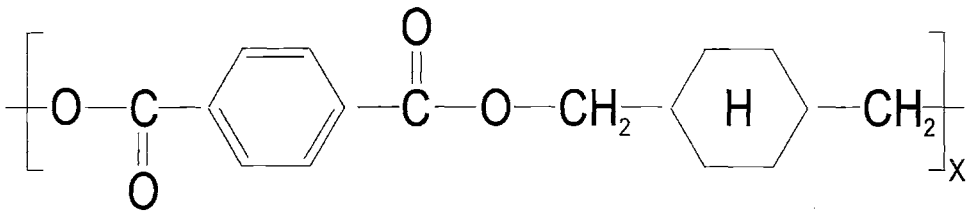

Figure 2-2: Chemical structure of PCT

In this chapter a thorough set of mechanical test data is presented for amorphous PETG over a wide range of temperatures and strain rates. In Chapter 3, analagous data for PET will be presented for comparative purposes. To date, there has been very little data presented in the literature with regard to the mechanical behavior of PETG (Brown 2000; Chen et al. 1999; Kattan et al. 2001; Kattan et al. 2002; Patton 1998). As a result, this comprehensive set of compression stress-strain curves can serve as a starting point for developing constitutive models for this material which has commercial applicability of its own. In Chapters 4 and 6 some constitutive modeling approaches to capture the trends observed in PETG will be presented and results will be compared with this experimental data.

2.2 Material

The material used in all experiments was PETG 6763 supplied by Eastman Chemical Co. with a weight average molecular weight of 38,888 and a polydispersity of 2. It was supplied in the form of 4 in. by 4 in. injection molded plaques of 1/8 in. nominal thickness, from which compression specimens were machined.

2.3 DSC

Differential scanning calorimetry (DSC) was performed using a Perkin Elmer DSC 7 at a constant heating rate of 10 ° C per minute. The equipment was calibrated with zinc and indium. DSC scans performed on the as-received material as well as on deformed material indicated that there was no crystallinity in the material, either before or after testing. DSC scans also identified the glass transition temperature for the material as 80 ° C.

2.4 DMA

Dynamic mechanical analysis (DMA) was performed on the as-received material. Specimens were cut using a Buehler Isomet cutoff saw at a very low cutting speed so as to prevent aging of the material. Specimens were approximately 30 mm long, 3.2 mm wide, and 1 mm thick. In DMA experiments, an oscillating force (tensile, bending, or torsional) is applied to the material at various frequencies. The temperature is gradually increased and the response of the material is measured. From the measured response, the shear (storage) modulus can be obtained as a function of temperature and frequency. Each sample was tested in a tensile mode at frequencies ranging from 1 Hz to 100 Hz and at temperatures ranging from 40 ° C to 110 ° C. The oscillating force had a mean value of 30 gf (.2943 N) with an amplitude of oscillation of 45 gf (.4415 N). The modulus data is shown in figures 2-3 and 2-4. The shift in the curve with frequency demonstrates a strain rate dependence of the glass transition temperature. When the material is deformed at higher frequencies, which corresponds to higher strain rates, the glass transition temperature shifts to higher temperatures.

With a knowledge of the DMA testing frequency, the elastic modulus, the specimen dimensions, and the magnitude of the cyclic load, an equivalent strain rate can be computed at various points on the DMA curves. These data points can then be compared with results from other tests, such as constant strain rate compression experiments. This is discussed in further detail in section 4.2.1.

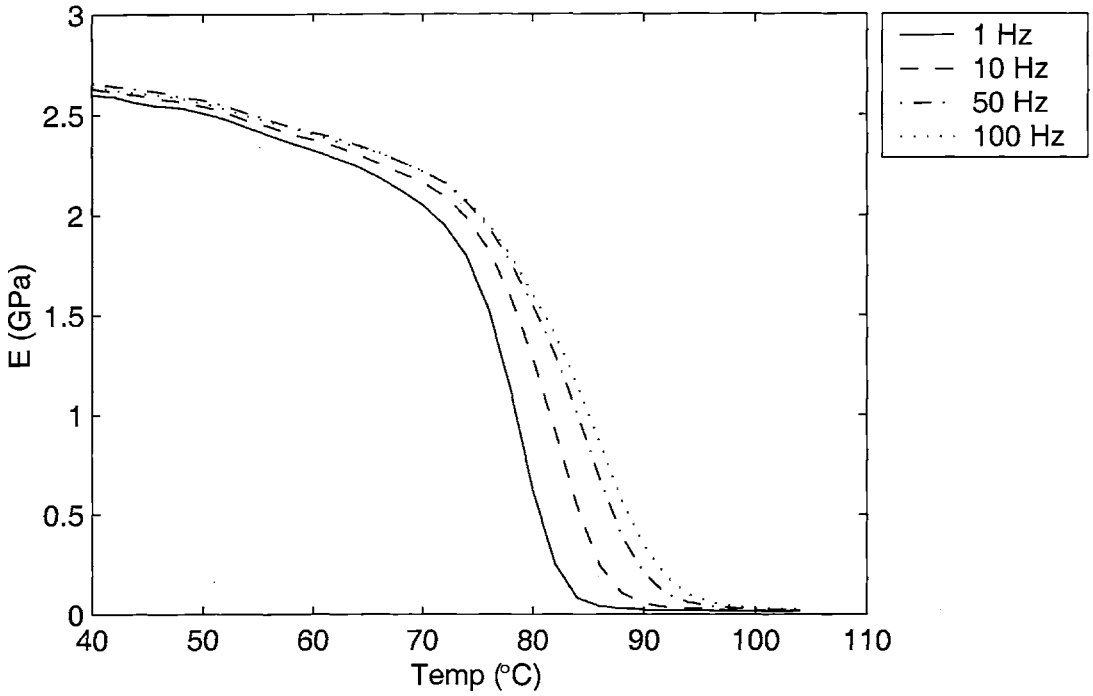

Figure 2-3: PETG DMA data

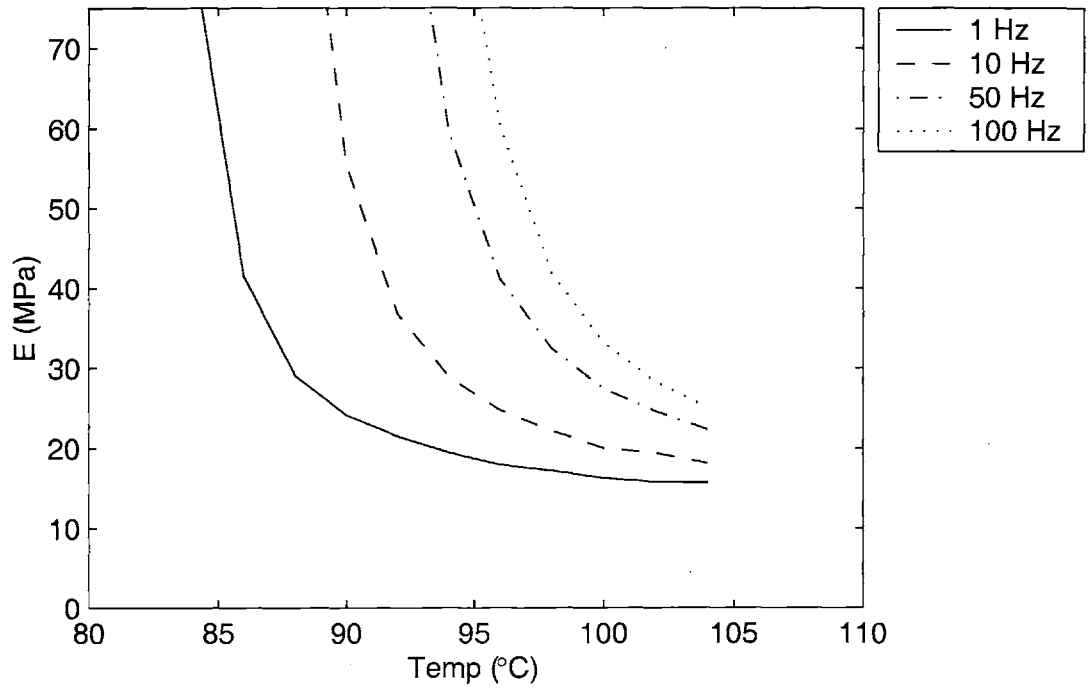

Figure 2-4: PETG DMA data, enlarged to show detail at high temperature

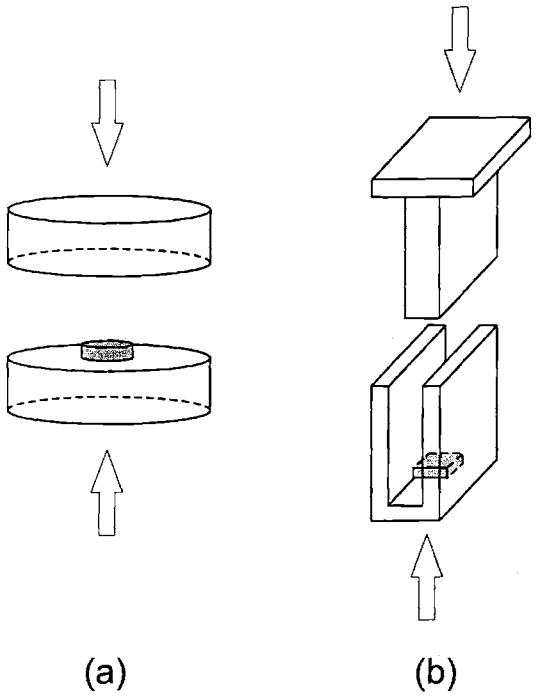

Figure 2-5: Compression experiment setup (a) Uniaxial compression (b) Plane strain compression

2.5 Compression Experiments

Two types of compression tests were performed: uniaxial and plane strain. Schematics of the two loading configurations are shown in figure 2-5. For the uniaxial tests, specimens were cut into circular disks 12.39 mm in diameter. For the plane strain experiments, square cross-section samples were cut to measure 9.55 mm on a side. The thickness of each specimen was that of the plaque thickness, nominally 1/8 in. (3.2 mm). For each test, WD-40, a common lubricant, was applied to the compression platens and a sheet of teflon was placed between the compression platens and the PETG sample to eliminate the effects of friction. Care was taken so that no lubricant contacted the test specimens. The specimens were brought to test temperature by use of an electric resistance heater. They were allowed to come to thermal equilibrium for a total of 20 minutes.

The compression experiments were performed using an Instron 1350 with servo-

hydraulic controls. The cross head speed was controlled using a personal computer running Windows NT and LabView. The vertical specimen displacement was measured using an extensometer and was fed back through the computer to control actuator displacement in order to eliminate load train compliance error. Specimens were compressed at a constant logarithmic strain rate to final strains ranging from -0.8 to -2.0 in the uniaxial experiments and to final strains from -0.8 to -1.3 in the plane strain experiments. After loading, the specimens were immediately unloaded using the same logarithmic strain rate.

The load was measured using a 10,000 lb. load cell and was acquired by standard data acquisition software during the experiments. True stress was determined from the initial cross-sectional area and by assuming no volume change for the polymer during plastic deformation. Thus,

$$CurrentArea = \frac{InitialArea * InitialHeight}{CurrentHeight} \tag{2.1}$$

$$TrueStress = \frac{MeasuredLoad}{CurrentArea} \tag{2.2}$$

Each test was performed at least twice in order to ensure repeatability. Tests were performed at strain rates ranging from -.005 sec^{-1} to -1.0 sec^{-1}. Attempting to perform experiments at higher strain rates resulted in oscillatory data apparently due to exciting a system natural frequency and were beyond the capability of this equipment. Temperatures were varied from 25 $^{\circ}$ C to 110 $^{\circ}$ C. In uniaxial compression experiments, temperature was measured using four thermocouples cemented to the compression platens. In plane strain compression experiments, temperature was measured using a single thermocouple in contact with the specimen. A simple computer program monitored the temperature readings from the thermocouples and adjusted the voltage supplied to the furnace to keep the specimen temperature constant at a preselected value.

Photographs showing undeformed PETG specimens as well as specimens deformed at room temperature to a final strain of 1.2 are shown in figures 2-6 and 2-7.

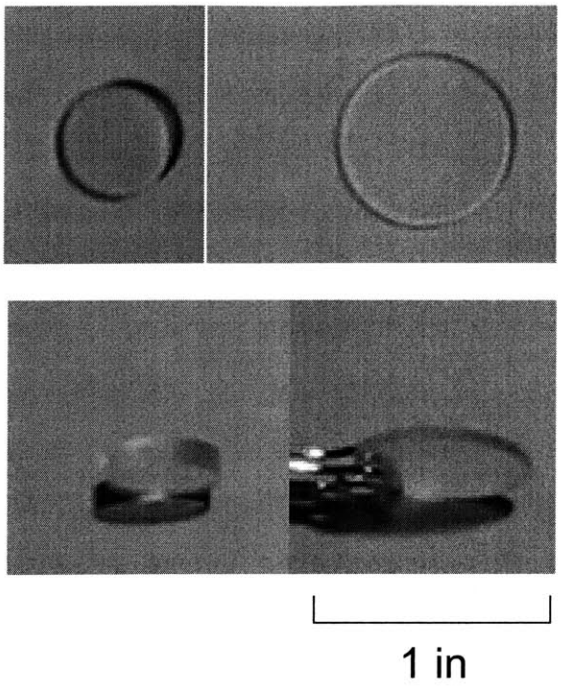

Figure 2-6: Uniaxial compression specimens

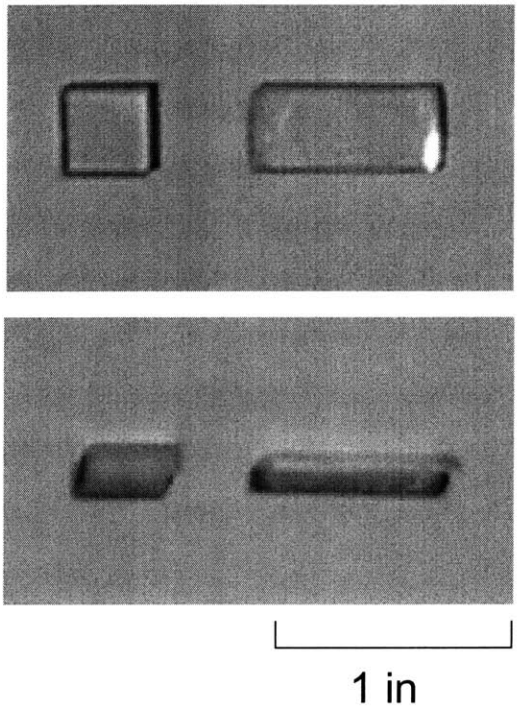

Figure 2-7: Plane strain compression specimens

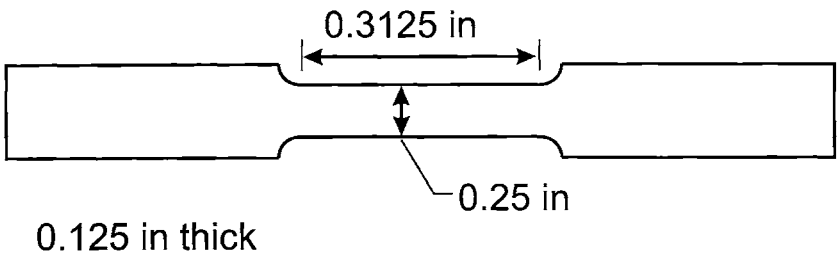

Figure 2-8: Tensile bar

2.6 Tensile Experiments

A few tensile tests were performed to compare with the experimental compression results. For these tests, small tensile bars were machined from larger bars. This was done so that the bars could be stretched to large extensions inside of an environmental chamber. The tensile bars had a gauge length of 0.3125 in. and a rectangular cross-section 0.25 in. wide by 0.125 in. thick (see figure 2-8). Tests were conducted at 90 ° C and 100 ° C and at a constant extension rate of 0.3125 in/sec, corresponding to a nominal initial strain rate of 1.0sec^{-1}. Tests were conducted on an Instron 5582 electro-mechanical system with an Instron model 3119-007 environmental chamber. Samples were allowed to come to thermal equilibrium for a total of 30 minutes.

During the experiments, the load required to deform the specimen and the crosshead displacement was measured and recorded. From these, it can be challenging to obtain true stress-true strain curves as the deformation may not be homogeneous. However, an average true stress can be calculated by assuming constant volume and by assuming that the material contracts in equal proportions in width and thickness. True logarighmic strain can be calculated from the measured crosshead displacement and the initial gage length.

2.7 Biaxial Stretching Experiments

Biaxial stretching experiments were conducted on a T.M. Long machine at Eastman Chemical. The samples were cut into 2 in. squares from .002 in. thick film material,

supplied by Eastman. Samples were tested at temperatures of 95 ° C, 100 ° C, and 105 ° C. The samples were held in place by grips on all four sides which employed a scissor-like mechanism to allow for large deformations in both directions. Specimens were heated by forced convection. They were held in position and heated for approximately 60 sec before being stretched. Specimen temperature was not directly measured, however, the temperature of the convective flow was kept at a constant value and the specimens were all heated for the same length of time. Specimens were deformed at a constant extension rate of 14 in/sec, corresponding to a nominal initial strain rate of 7sec^{-1}. Tests were conducted in three different deformation modes: equibiaxial extension, constrained-width tension, and sequential biaxial extension.

2.8 Results and Discussion

2.8.1 Compression Experiments

The results are shown in the following figures and are discussed below. Figures 2-9 through 2-21 show uniaxial compression data at each temperature. Figures 2-23 through 2-28 show the same data plotted at constant strain rate. Figures 2-29 through 2-33 show the effect of unloading at different final strains in uniaxial compression.

From these figures it can be observed that PETG exhibits the following general trends. First, the material has an initially stiff response which is highly temperature dependent. The modulus decreases moderately with increasing temperature but is fairly independent of strain-rate at temperatures below the glass transition temperature (T_g). In the transition region, the modulus drops dramatically with increasing temperature. This dropoff occurs at higher temperatures for specimens deformed at higher strain rates. At temperatures above the transition region, the modulus continues to drop as temperature rises, but the change is more moderate. The dependence is also mildly strain-rate dependent in this region (above T_g), with increasing strain rate leading to increased modulus.

Second, at temperatures below the glass transition temperature the polymer ex-

hibits a definite yield stress which increases with increasing strain rate and with decreasing temperature. This yield is followed by a considerable amount of strain softening. The amount of strain softening is relatively strain-rate independent, but decreases with increasing temperature. Effects of adiabatic heating due to plastic deformation can also become significant at temperatures below the glass transition. This effect is seen in figure 2-9 for room temperature data where at a strain on the order of 0.9, the high strain rate curves cross over the curves for lower rates.

At temperatures above the transition temperature, the stress-strain curves show a monotonic rise in stress with increasing strain, which is characteristic of rubber elastomers. The yield stress is no longer abrupt and instead the curve gently rolls over and the material begins to flow at a stress level on the order of 1-2 MPa. The magnitude of this flow stress also depends on strain rate and temperature. At higher temperatures and lower strain rates the roll over occurs at lower stress levels. Figures 2-16, 2-18, 2-20, and 2-22 show an enlarged view of the initial modulus and roll over to flow for the polymer at and above the glass transition temperature.

Figures 2-15 and 2-16 show the data at 80 ° C, approximately the glass transition temperature for PETG. This is a very illustrative set of curves, clearly demonstrating the strain rate dependence of the glass transition temperature. This strain rate dependence causes the glass transition temperature to effectively increase as the strain rate increased. In figure 2-15, it can be seen that at high strain rates, 80 ° C is still below the material's transition temperature, and the material exhibits the high yield stress and strain softening characteristic of polymers in the glassy state. At low strain rates, however, there is no apparent yield stress and the stress-strain curve rises monotonically. This indicates that at these lower strain rates the polymer is already above its glass transition at 80 ° C and hence exhibits rubbery polymeric behavior.

Third, after the strain softening region (or after the roll over to flow for tests above the transition temperature), the polymer begins to strain harden as the strain level is increased. Strain hardening is evident through both an initial hardening modulus in the flow region (at moderate strains) followed by a dramatic upturn in the stress-strain at very large strains. Strain hardening is more pronounced at lower

temperatures and higher strain rates. Additionally, with increasing temperature (and decreasing strain rate) the strain level at which the dramatic strain hardening occurs is postponed to higher strains.

In the constant strain rate figures (figures 2-23 to 2-28) the temperature dependence of the material is clearly discernible. At each of the strain rates, the initial yield or initial flow stress decreases as temperature increases. The hardening slope decreases with increasing temperature and the strain level at which the dramatic upswing in stress occurs is greater at higher temperatures.

Figures 2-29 to 2-33 show the material response as it is unloaded at different final strains. The data shows good repeatability and shows that at temperatures above the glass transition (see figures 2-32 and 2-33), much of the deformation is recovered upon unloading regardless of the final strain. Experimentally, it is difficult to determine how much of the deformation is actually recovered because upon unloading the bottom surface of the specimen remains in contact with the compression platen while the top surface is air quenched. This causes the rubbery specimens to curl up due to the thermal gradient during unloading so that the final specimen dimensions are difficult to measure. The effect is less pronounced in plane strain due to the test fixture remaining in contact with the specimen. Post test measurements using calipers indicate that the plane strain compression specimens recover to within 93% of their original height at temperatures above the glass transition. In contrast, at temperatures below the glass transition very little (on the order of 10 to 15 %) of the strain is recovered at all final strain levels.

Figure 2-17 demonstrates the strain rate dependence of strain recovery. Less recovery is observed upon unloading at lower strain rates than at higher strain rates. This is because at low rates more of the deformation is accommodated by molecular relaxation than at high rates, where deformation is due primarily to network orientation. Since the deformation due to molecular relaxation is permanent and the deformation due to orientation is recoverable, specimens which are deformed at higher rates are able to recover more. Again, due to the quenching phenomenon, it is difficult to pinpoint exact numbers, but at 90 $^{\circ}$ C, the material recovers by approximately

75% at -1.0 sec^{-1} and only recovers by 45% at -.005 sec^{-1}.

Since the specimens were unloaded immediately upon reaching the appropriate final strain, the initial unloading slope may be somewhat unreliable as a true measure of the material behavior of unloading at the given strain rate. There may be some additional creep in the measurement due to the turn around response of the actuator which could be removed by doing a brief hold before unloading the material.

Each of these trends is consistent with the trends exhibited by PET in compression, with the exception of strain recovery (Llana and Boyce 1999; Zaroulis and Boyce 1997). PET exhibits substantially less recovery at temperatures above the glass transition due to strain-induced crystallization. For example, at 90 ° C, -1.0 sec^{-1} PETG recovers by approximately 75%, whereas PET under the same conditions undergoes less than 50% recovery. A full set of compression data for PET and a thorough comparison between the two materials will be addressed in Chapter 3.

Figures 2-34 through 2-40 show plane strain compression data at each temperature. Figures 2-42 through 2-47 show the same data plotted at constant strain rate.

The plane strain compression data exhibits the same trends as were observed in the uniaxial compression data. In figures 2-48 through 2-51 the comparison of plane strain with uniaxial deformation modes is depicted. It was observed by comparing raw data from room temperature plane strain and uniaxial compression experiments that there was additional compliance and settling in the plane strain fixturing, which can be seen in figure 2-52. The initial modulus in plane strain should be slightly higher than in uniaxial compression. All plane strain data has been corrected for this fixturing compliance by assuming the compliance of the fixturing is linear with a modulus of 1.5 GPa (estimated from room temperature experiments). The corrected strain for each data point is then calculated by subtracting the compliance strain from the measured strain:

$$\varepsilon_{corrected} = \varepsilon_{measured} - \frac{\sigma_{measured}}{E_{fixturing}} \tag{2.3}$$

It is also interesting to note that the higher rate data exhibits the effects of ther-

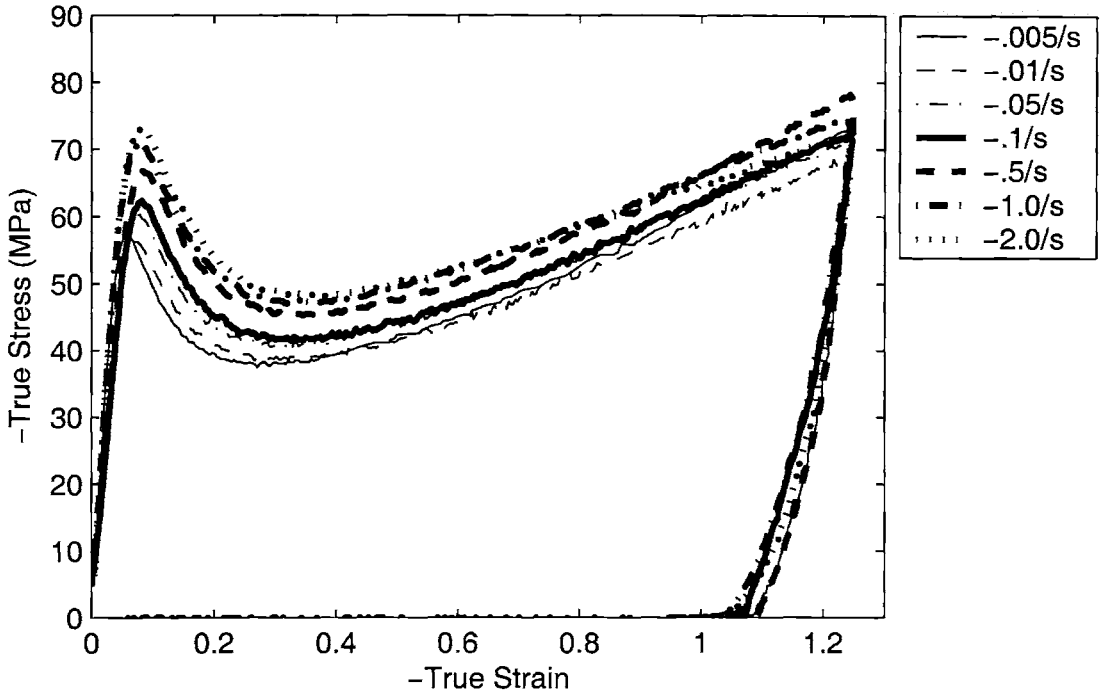

Figure 2-9: PETG Uniaxial compression data, Temperature = 25 ° C

mal softening due to adiabatic heating during deformation. This effect is present in both uniaxial compression and plane strain compression at low temperatures, but is more pronounced in plane strain due to the larger stress levels in the material. This effect manifests itself in the crossover of the stress-strain curves at large strains. For example, in figure 2-34, this can be observed as the -0.5 sec^{-1} data crosses over the -0.05 sec^{-1} data at a strain level of about -0.9. In the absence of thermal softening, the higher rate data would be expected to sustain a higher stress level throughout the deformation.

Figures 2-48 through 2-51 also demonstrate that in plane strain compression, the material begins to strain harden at a lower logarithmic strain level than in uniaxial compression.

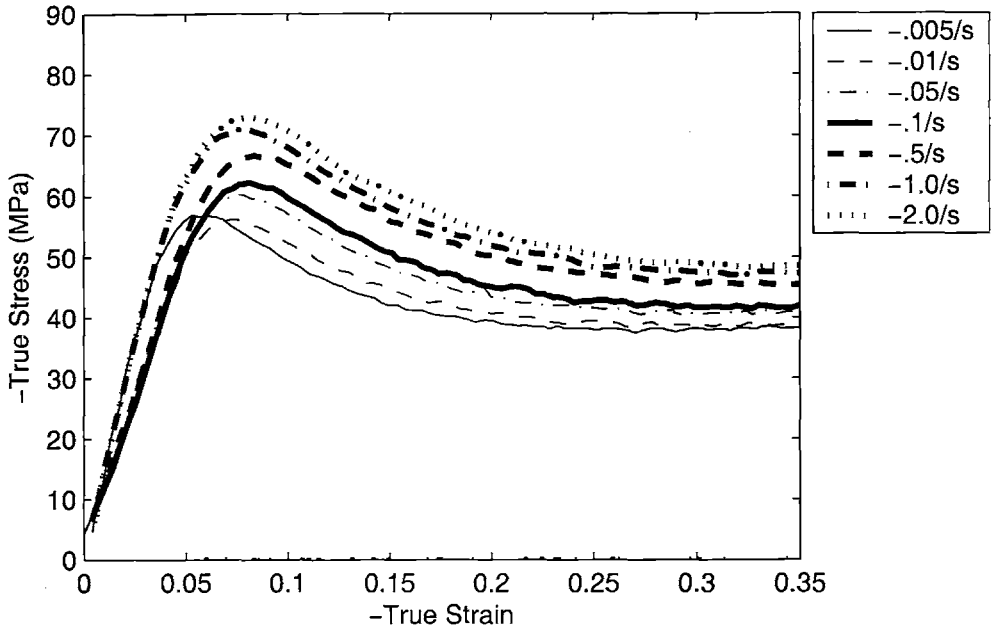

Figure 2-10: PETG Uniaxial compression data, Temperature = 25 ° C, enlarged to show small strain data

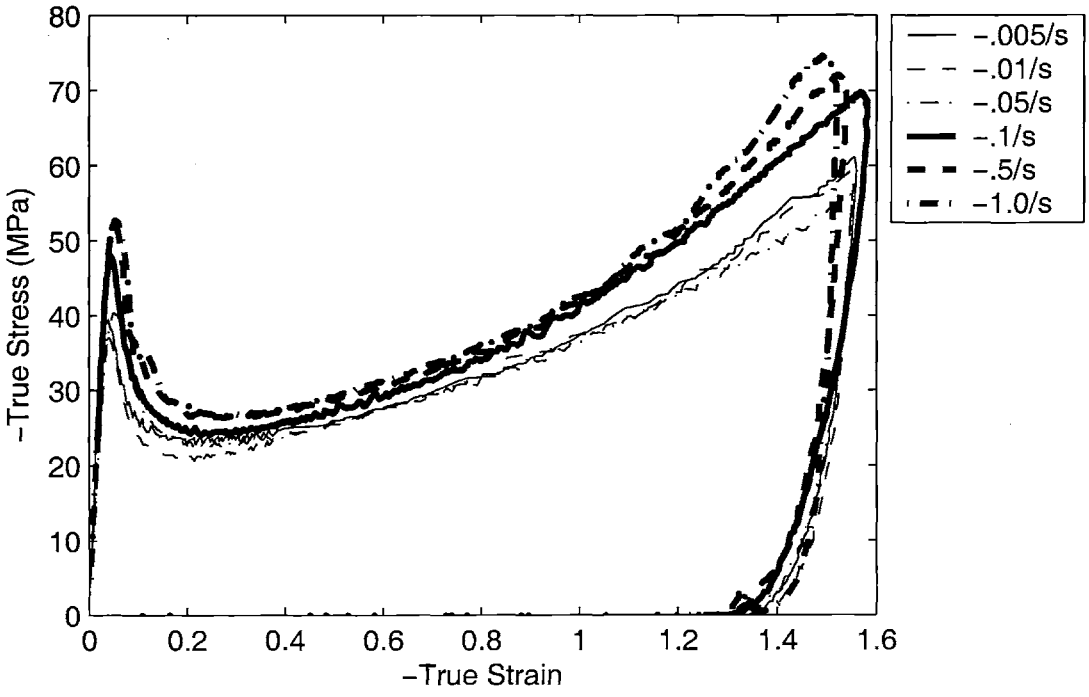

Figure 2-11: PETG Uniaxial compression data, Temperature = 60 ° C

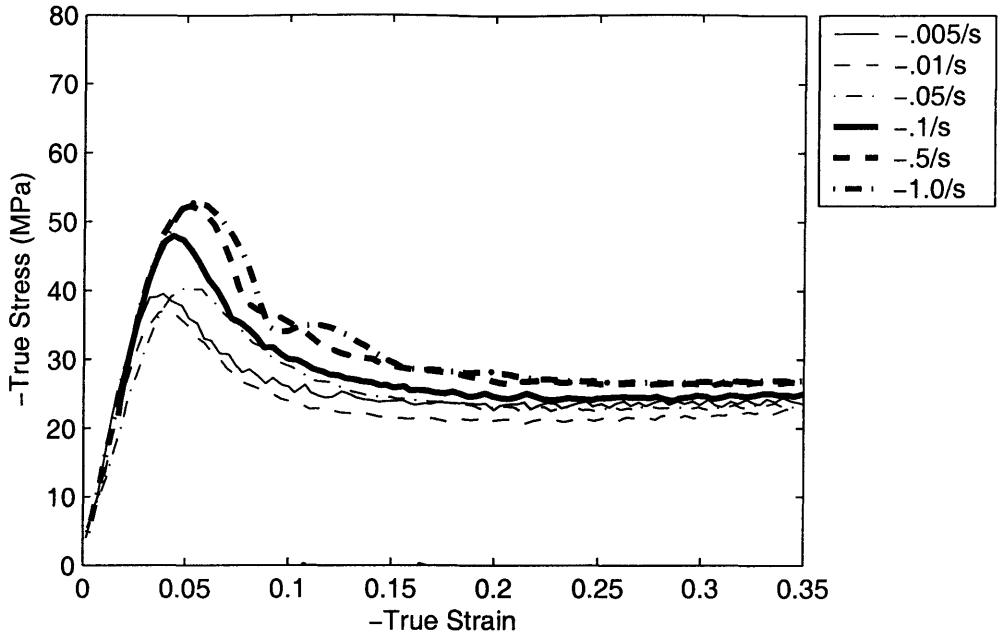

Figure 2-12: PETG Uniaxial compression data, Temperature = 60 ° C, enlarged to show small strain data

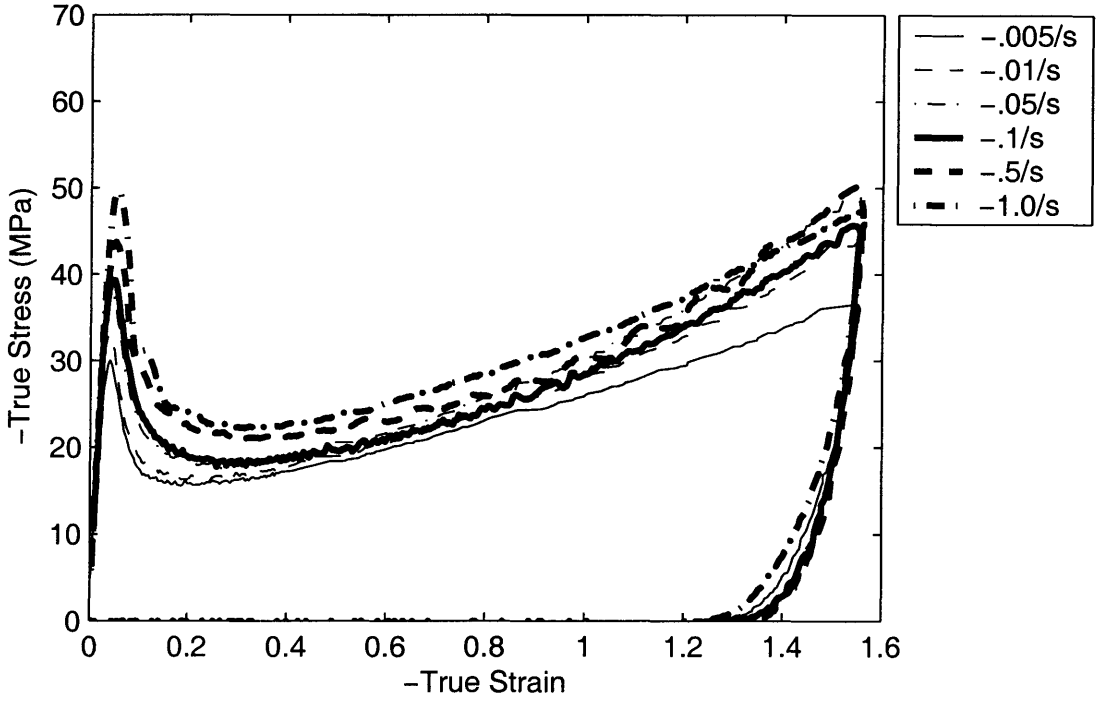

Figure 2-13: PETG Uniaxial compression data, Temperature = 70 ° C

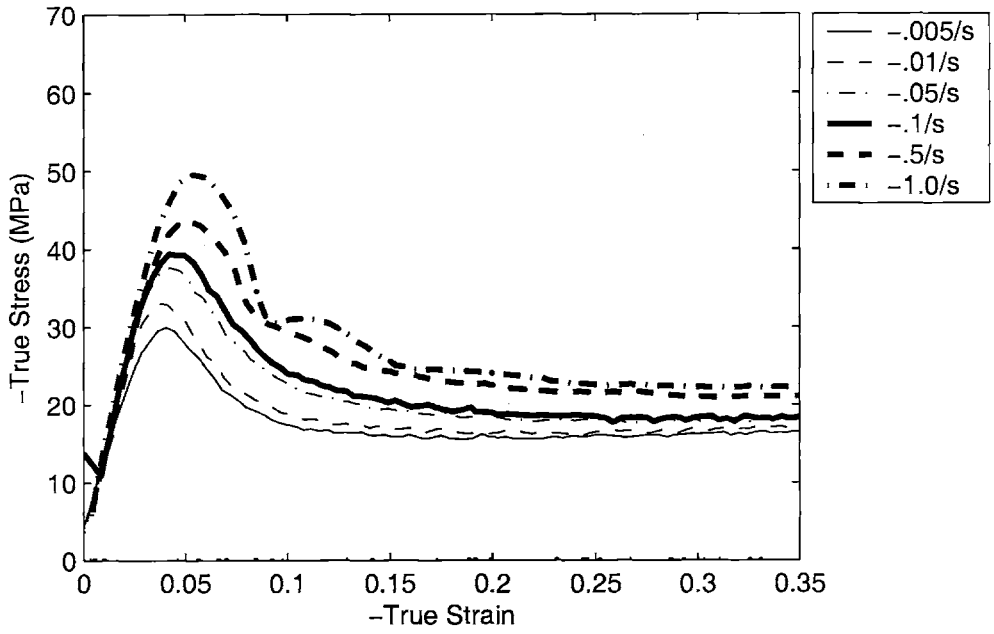

Figure 2-14: PETG Uniaxial compression data, Temperature = 70 ° C, enlarged to show small strain data

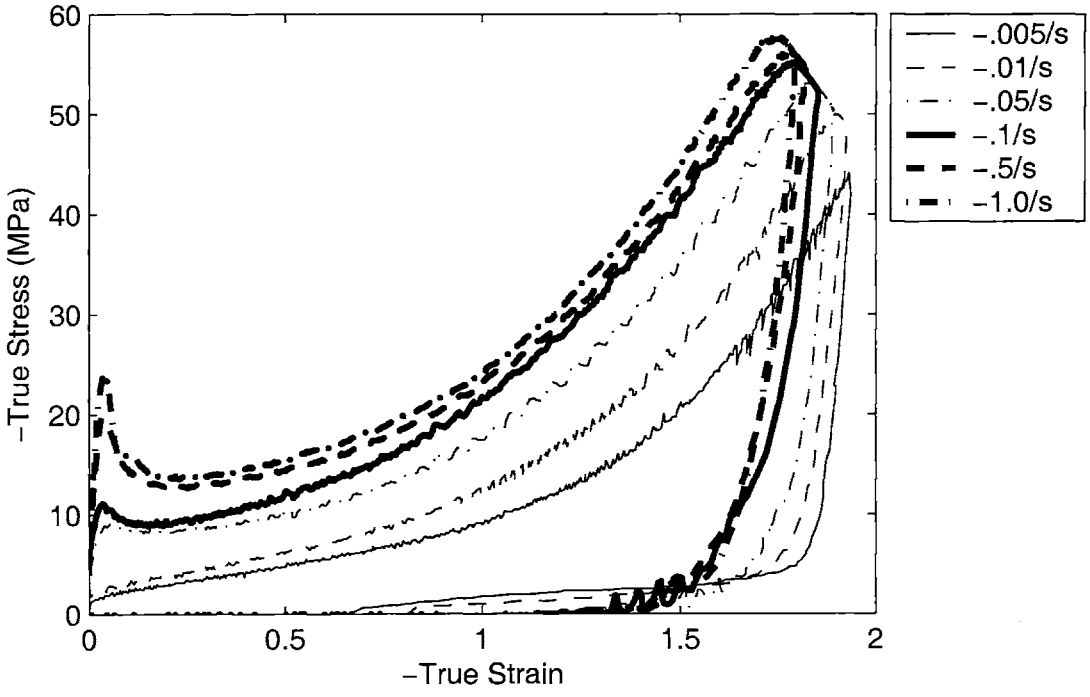

Figure 2-15: PETG Uniaxial compression data, Temperature = 80 ° C

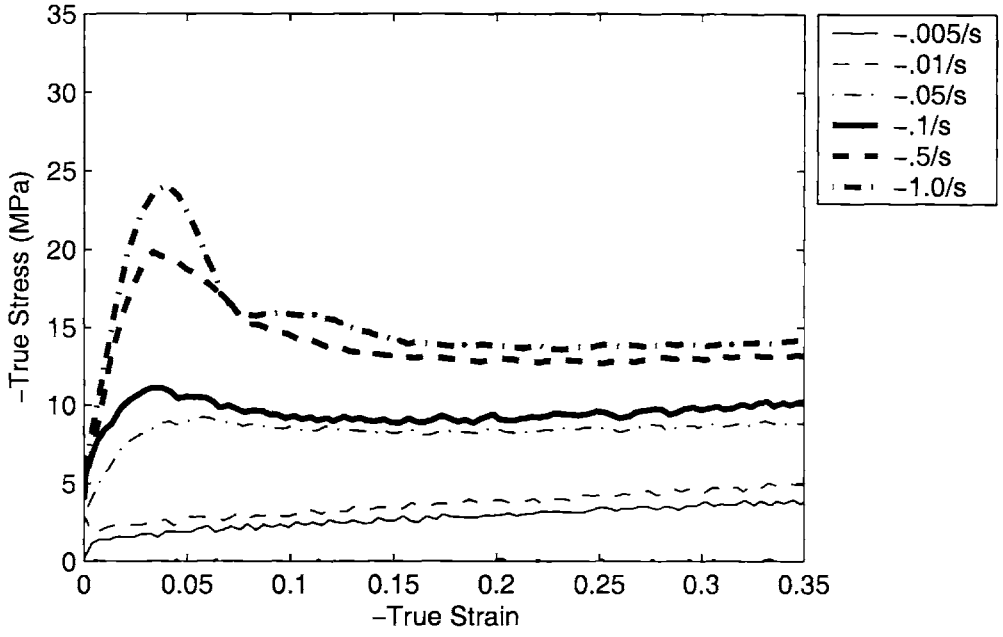

Figure 2-16: PETG Uniaxial compression data, Temperature = 80 ° C, enlarged to show initial modulus and flow stress

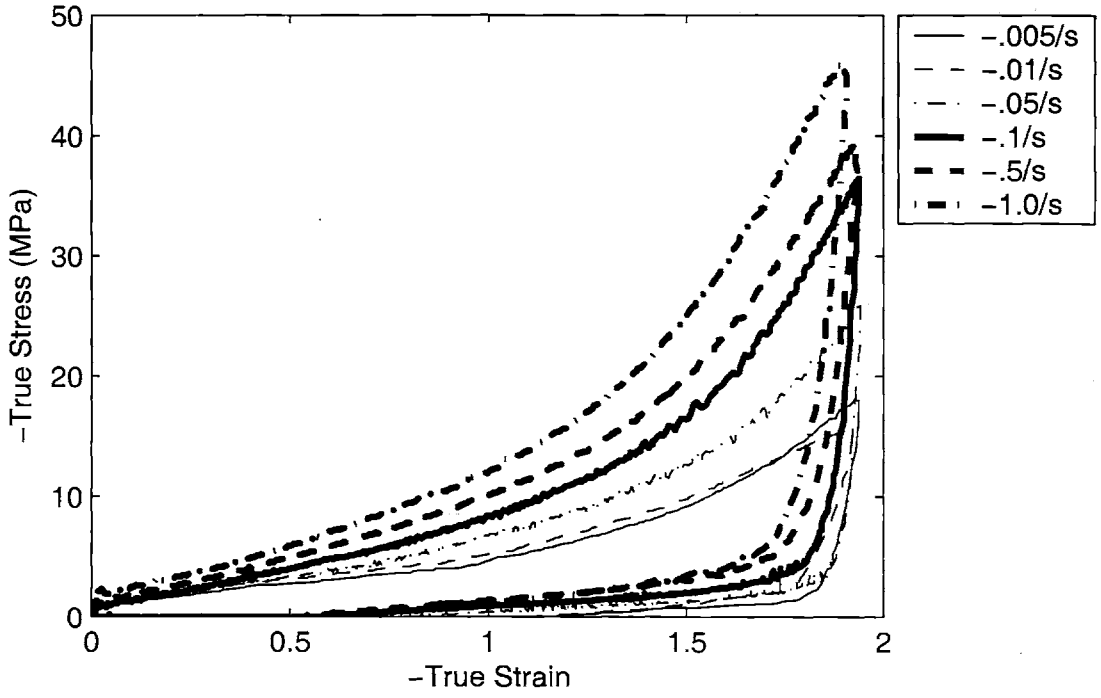

Figure 2-17: PETG Uniaxial compression data, Temperature = 90 ° C

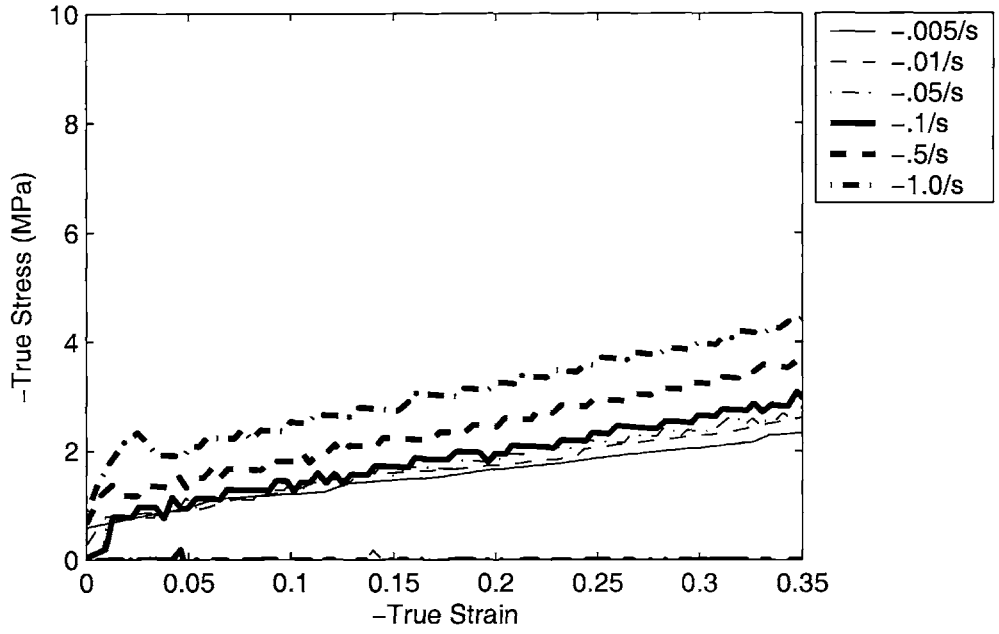

Figure 2-18: PETG Uniaxial compression data, Temperature = 90 ° C, enlarged to show initial modulus and flow stress

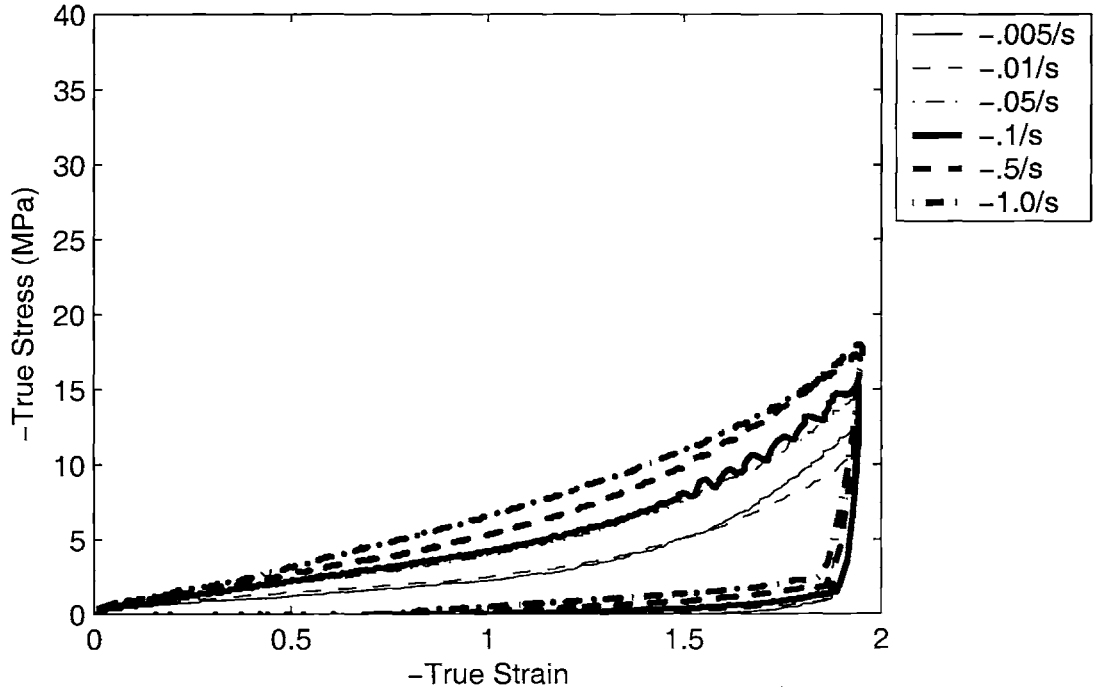

Figure 2-19: PETG Uniaxial compression data, Temperature = 100 ° C

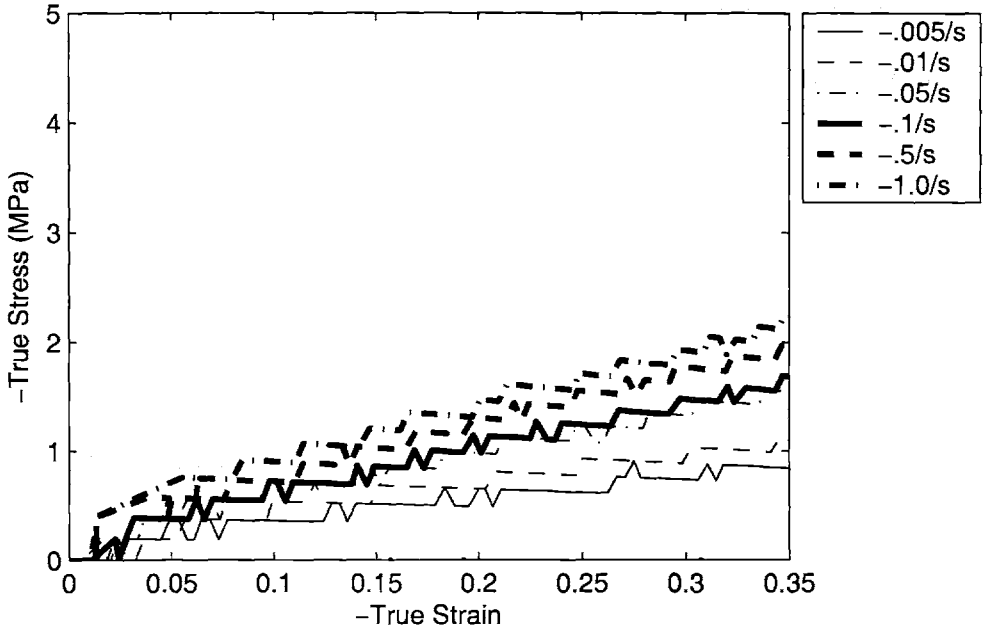

Figure 2-20: PETG Uniaxial compression eata, Temperature = 100 ° C, enlarged to show initial modulus and flow stress

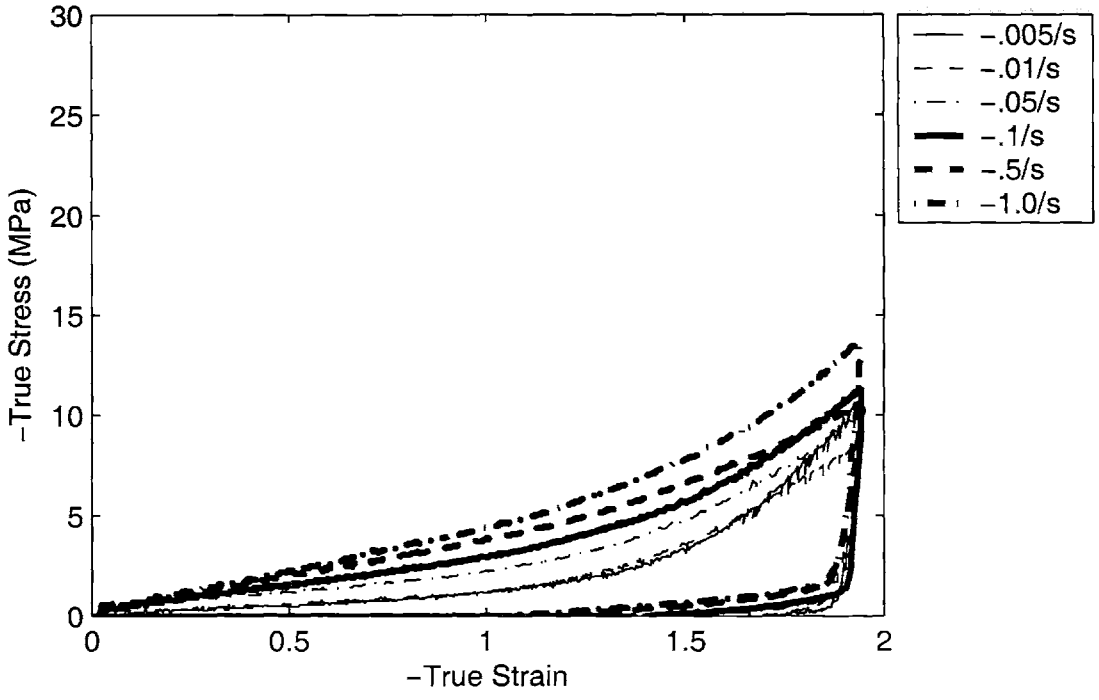

Figure 2-21: PETG Uniaxial compression data, Temperature = 110 ° C

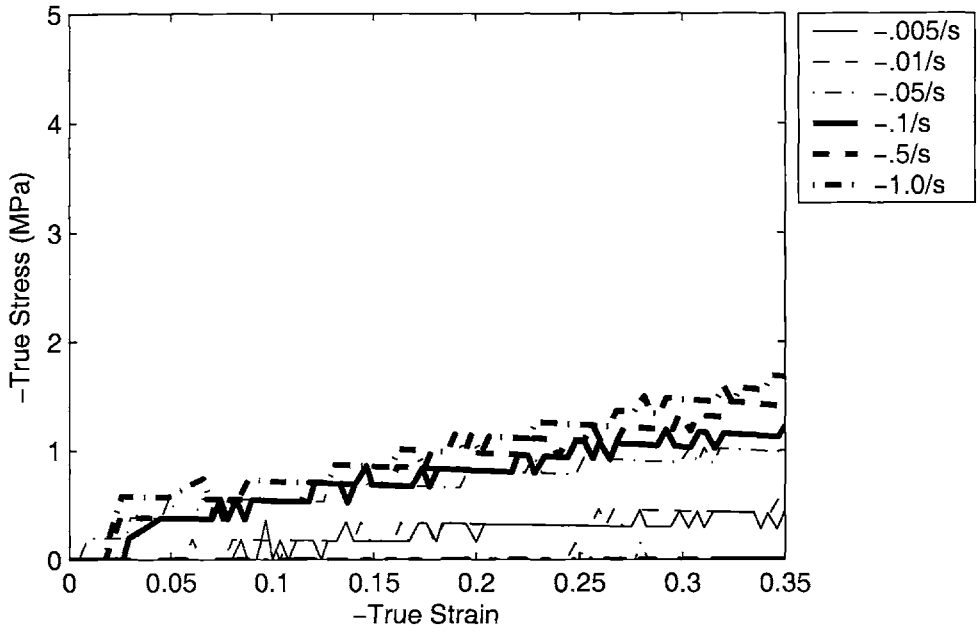

Figure 2-22: PETG Uniaxial compression data, Temperature = 110 ° C, enlarged to show initial modulus and flow stress

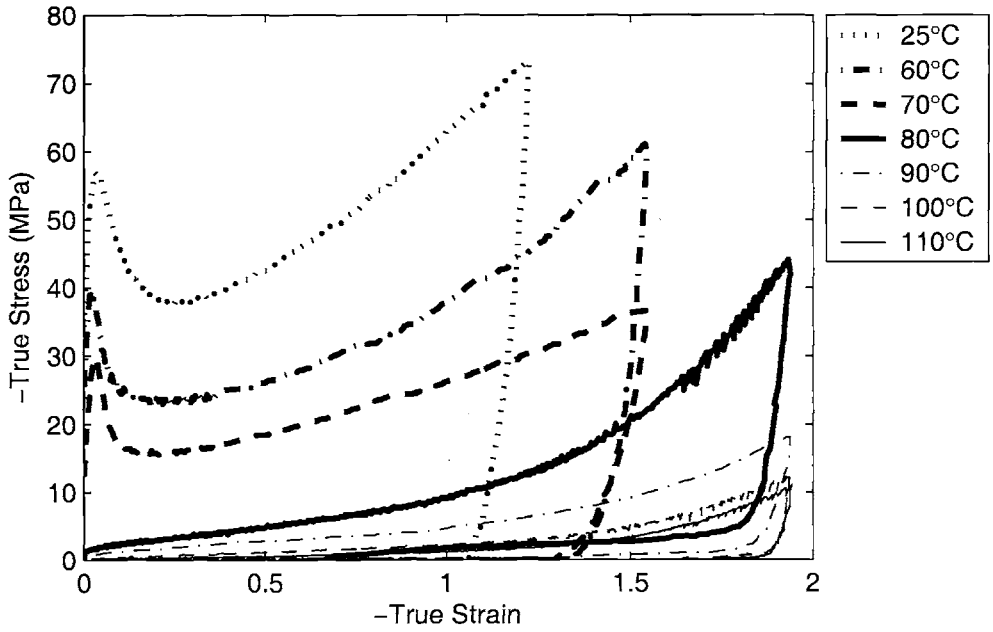

Figure 2-23: PETG Uniaxial compression data, $\dot{\varepsilon}$ = -.005/s

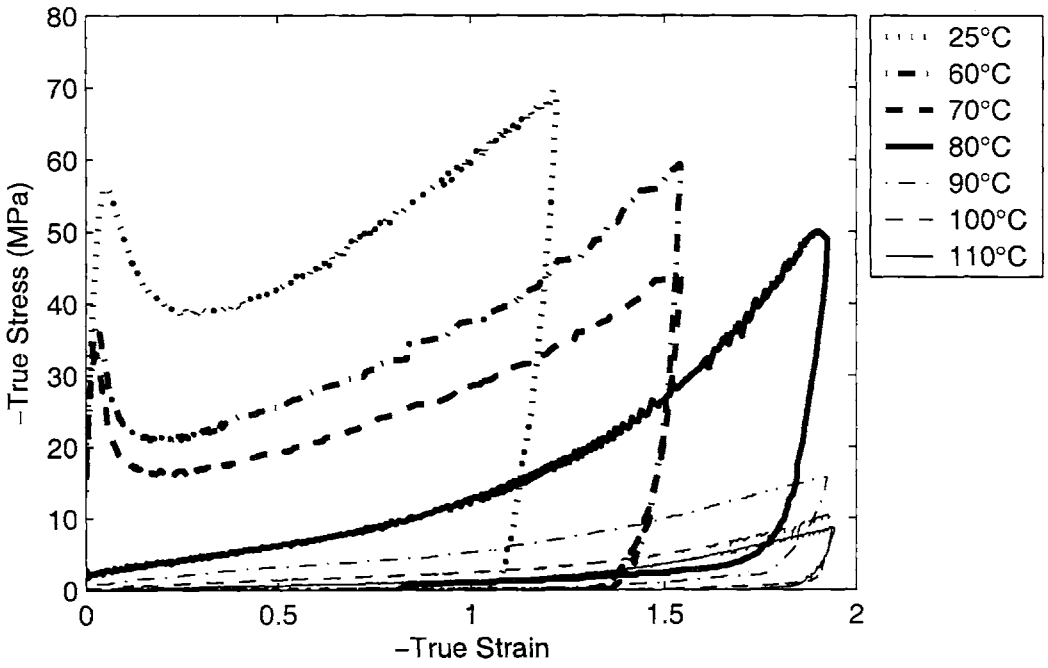

Figure 2-24: PETG Uniaxial compression data, $\dot{\varepsilon}$ = -.01/s

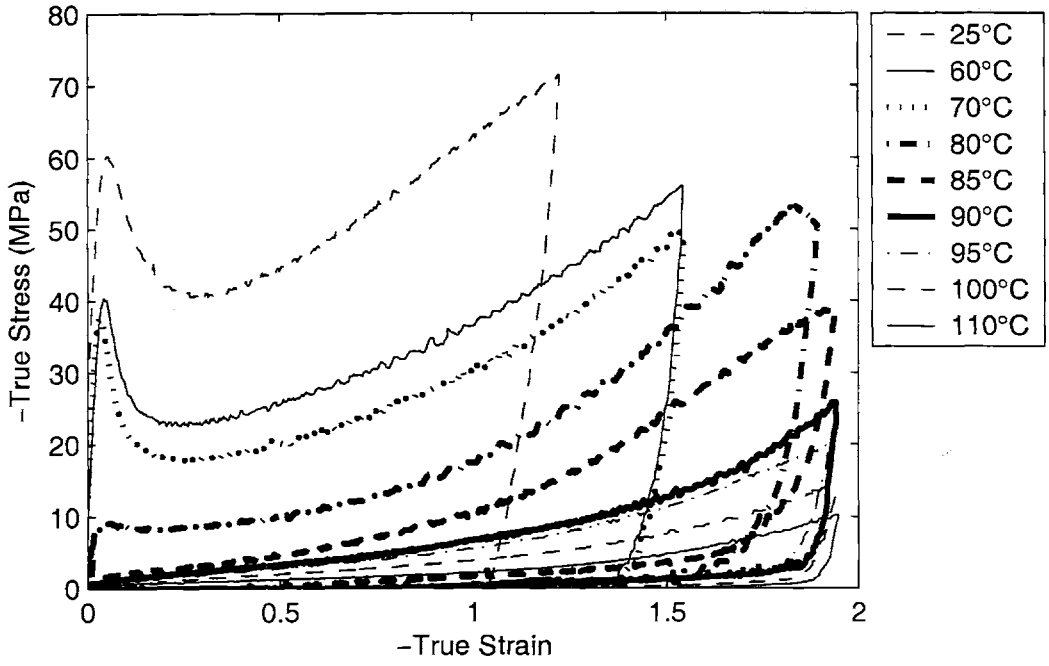

Figure 2-25: PETG Uniaxial compression data, $\dot{\varepsilon}$ = -.05/s

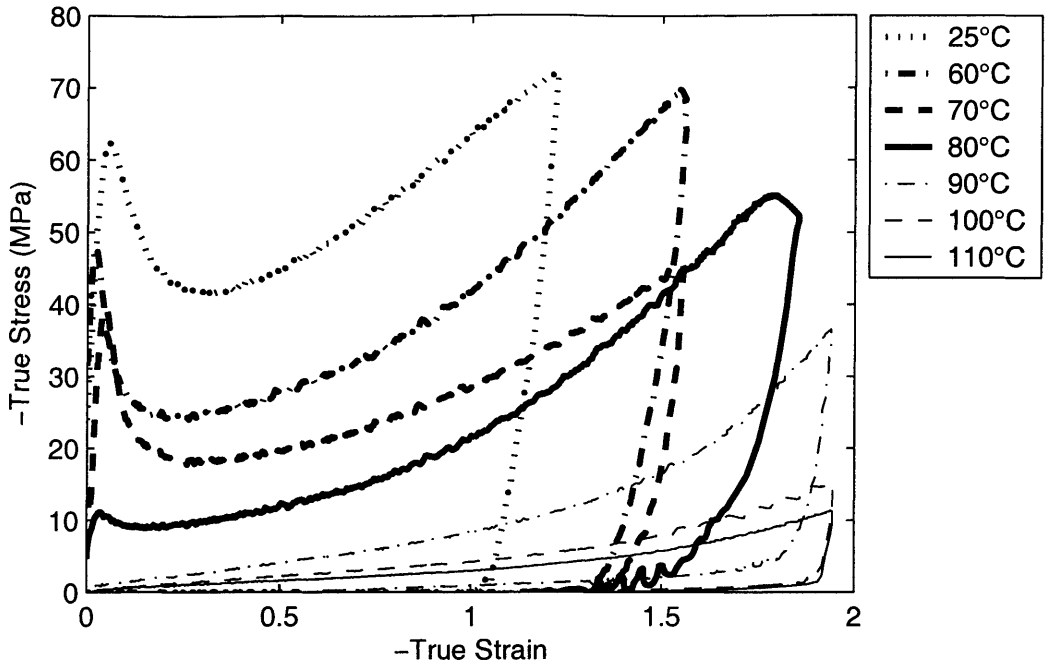

Figure 2-26: PETG Uniaxial compression data, $\dot{\varepsilon}$ = -.1/s

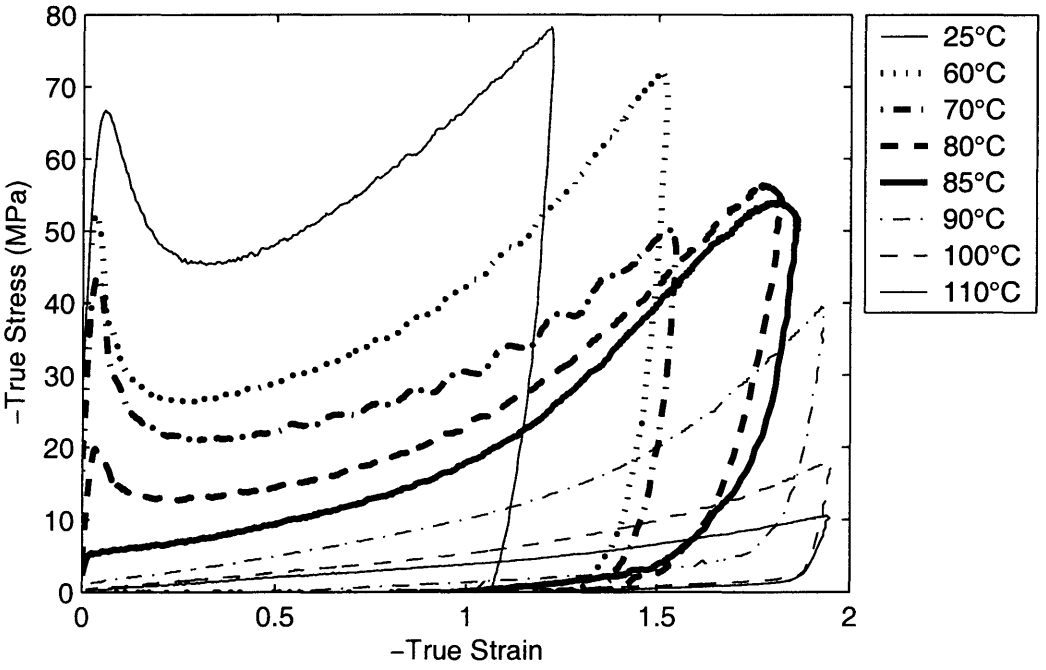

Figure 2-27: PETG Uniaxial compression data, $\dot{\varepsilon}$ = -.5/s

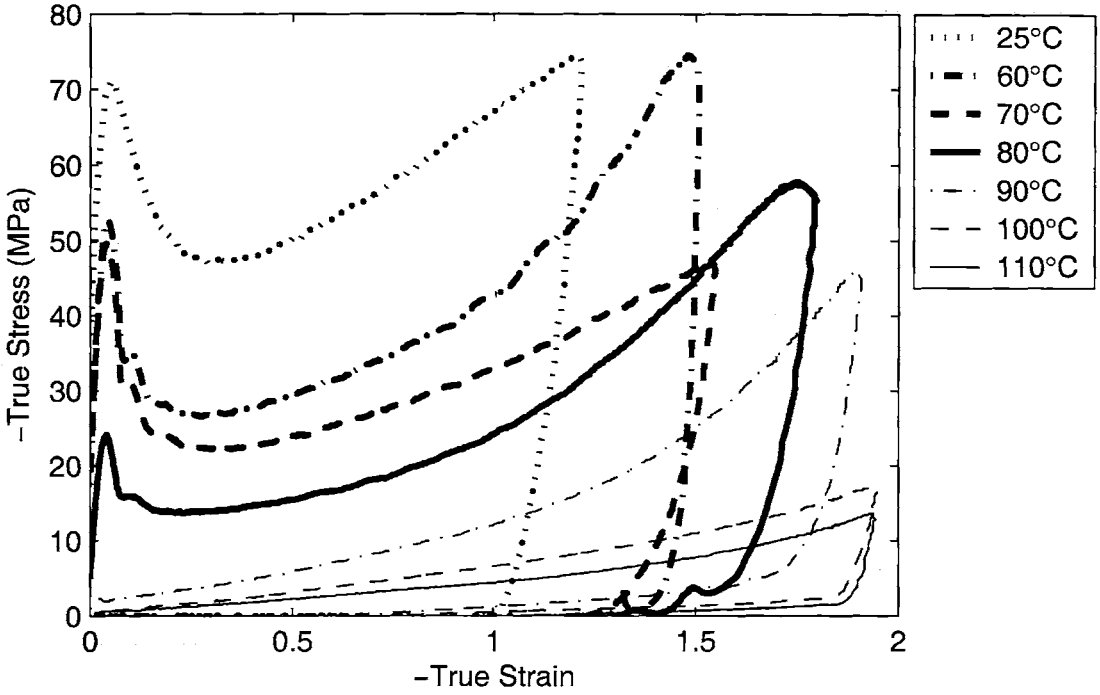

Figure 2-28: PETG Uniaxial compression data, $\dot{\epsilon}$ = -1.0/s

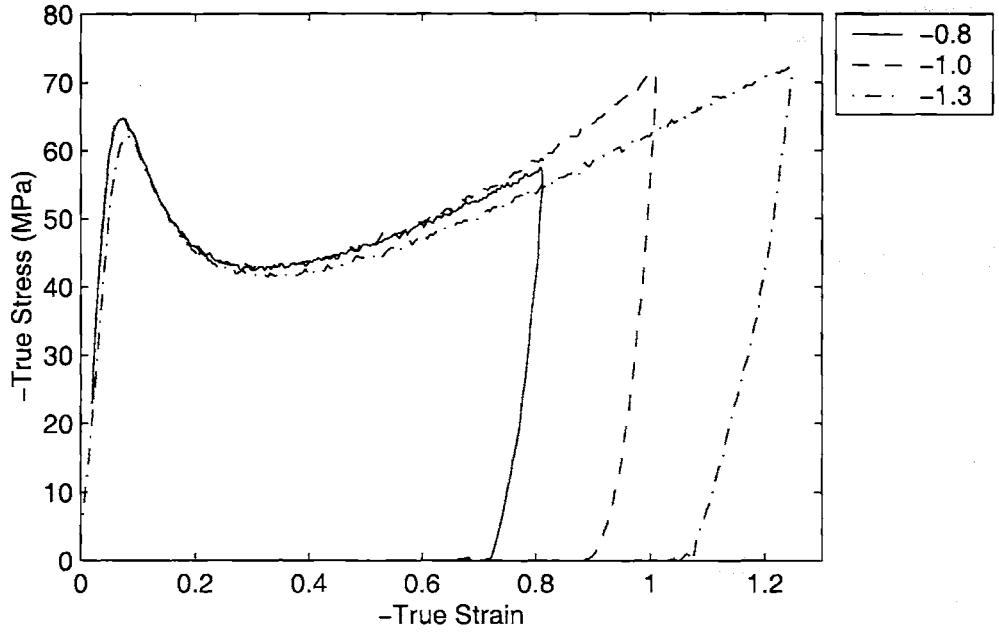

Figure 2-29: PETG Uniaxial compression data, Temperature = 25 ° C, $\dot{\epsilon}$ = -.1/s, Loaded to different final strains

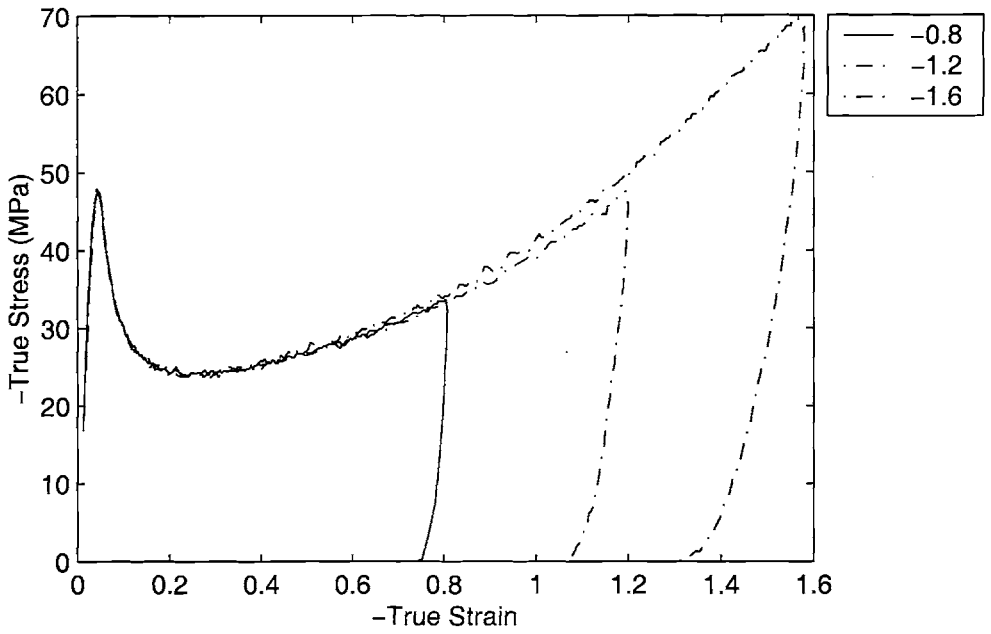

Figure 2-30: PETG Uniaxial compression data, Temperature = 60 ° C, $\dot{\varepsilon}$ = -.1/s, Loaded to different final strains

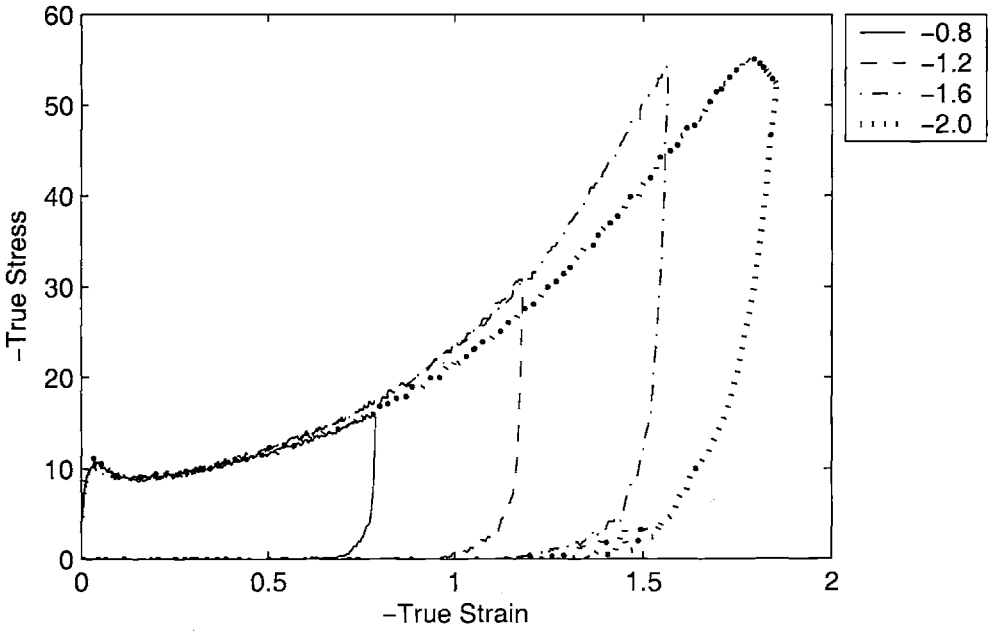

Figure 2-31: PETG Uniaxial compression data, Temperature = 80 ° C, $\dot{\varepsilon}$ = -.1/s, Loaded to different final strains

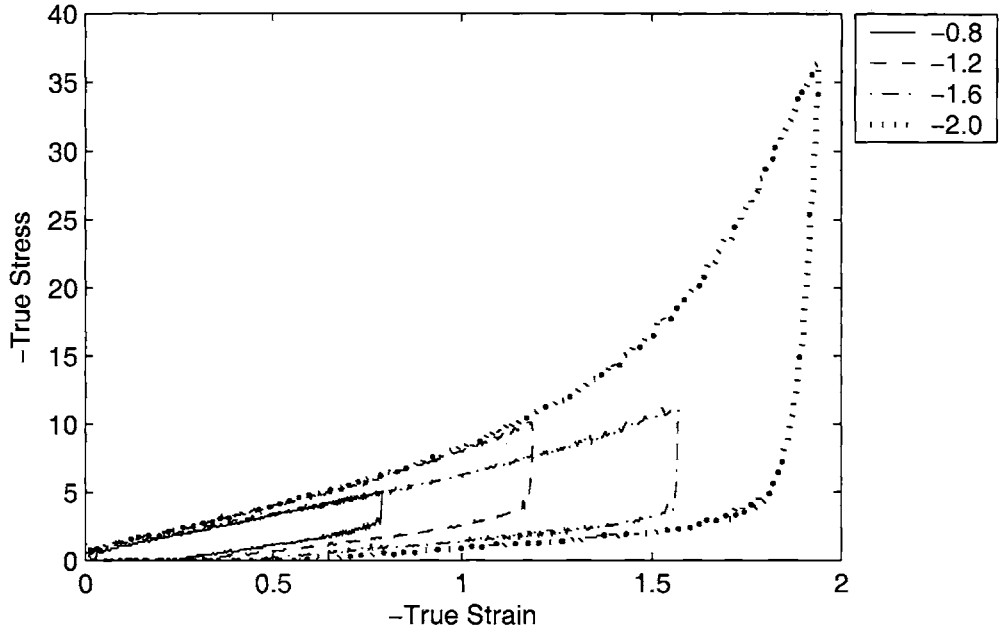

Figure 2-32: PETG Uniaxial compression data, Temperature = 90 ° C, $\dot{\varepsilon}$ = -.1/s, Loaded to different final strains

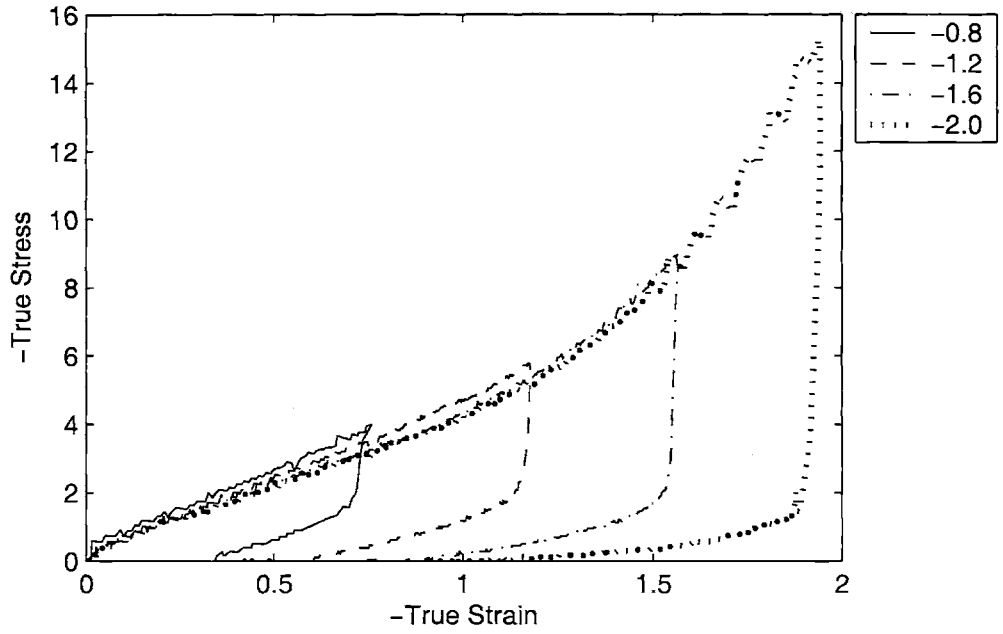

Figure 2-33: PETG Uniaxial compression data, Temperature = 100 ° C, $\dot{\varepsilon}$ = -.1/s, Loaded to different final strains

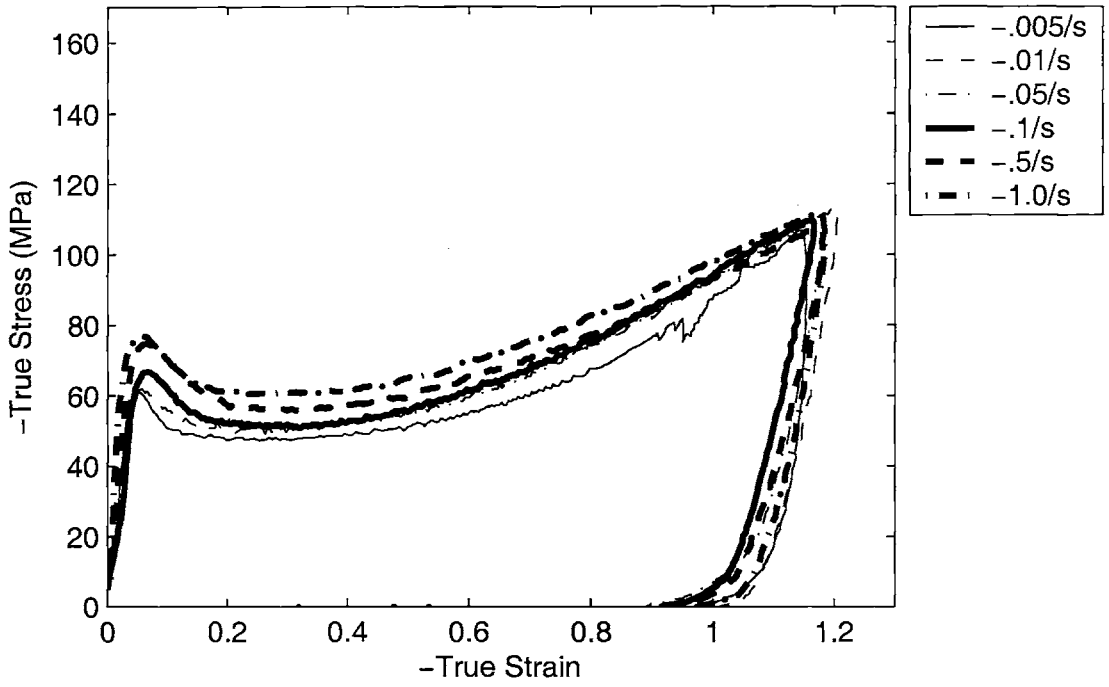

Figure 2-34: PETG Plane Strain Compression Data, Temperature = 25 ° C

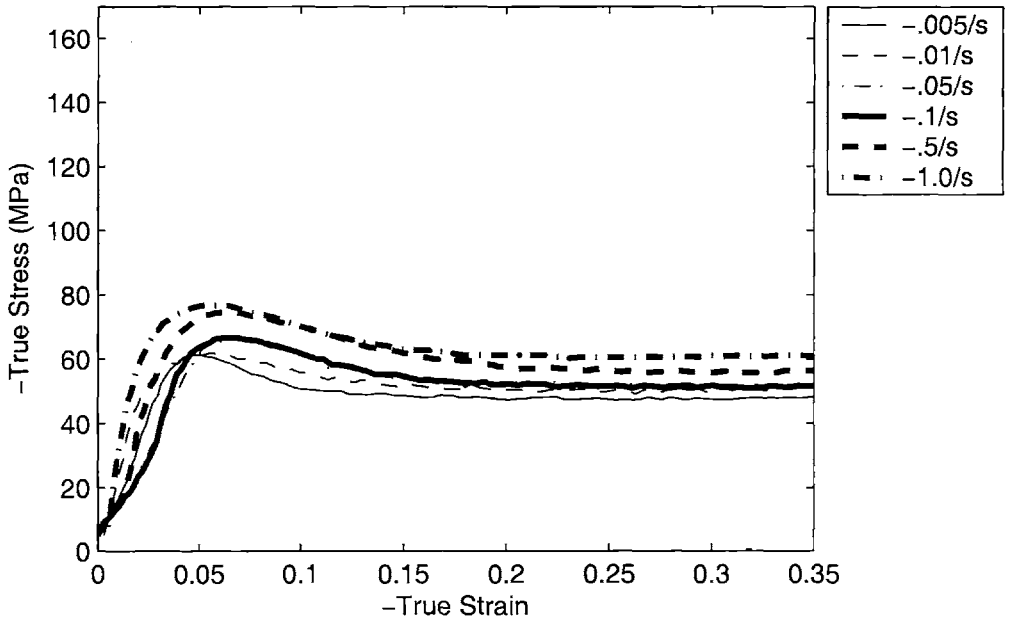

Figure 2-35: PETG Plane Strain Compression Data, Temperature = 25 ° C, Enlarged to show small strain data

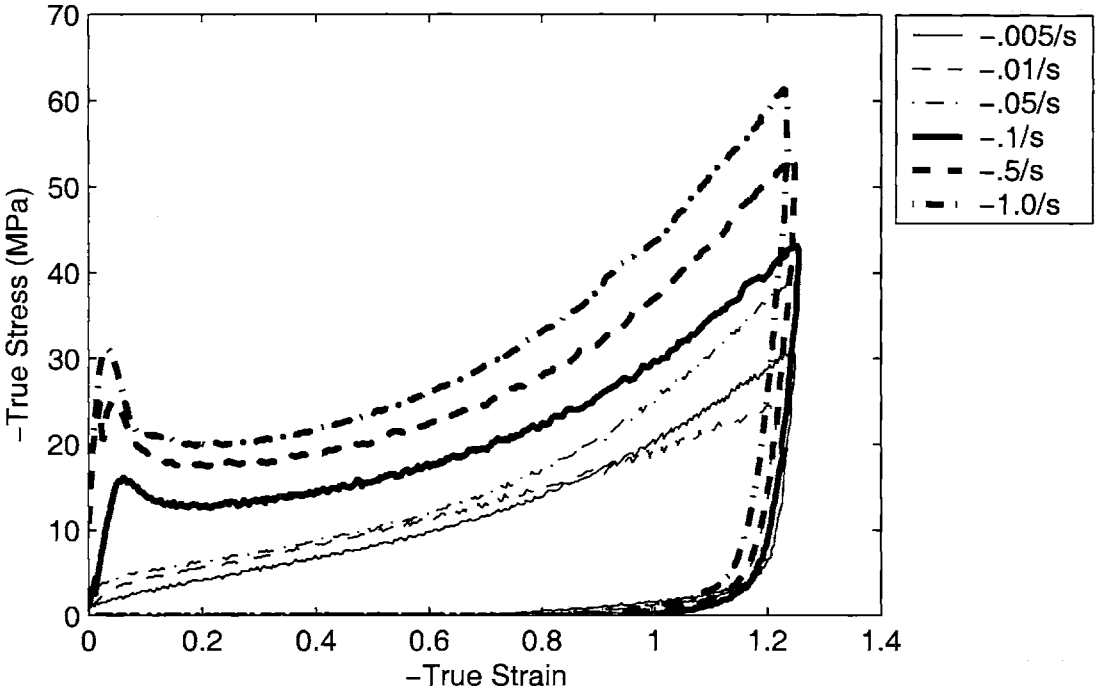

Figure 2-36: PETG Plane Strain Compression Data, Temperature = 80 ° C

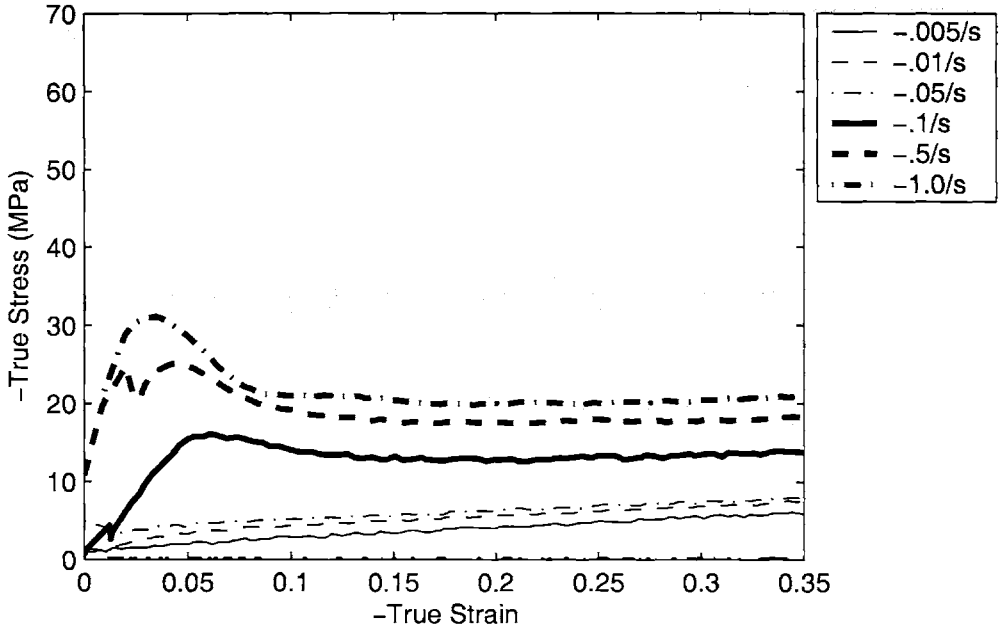

Figure 2-37: PETG Plane Strain Compression Data, Temperature = 80 ° C, Enlarged to show small strain data

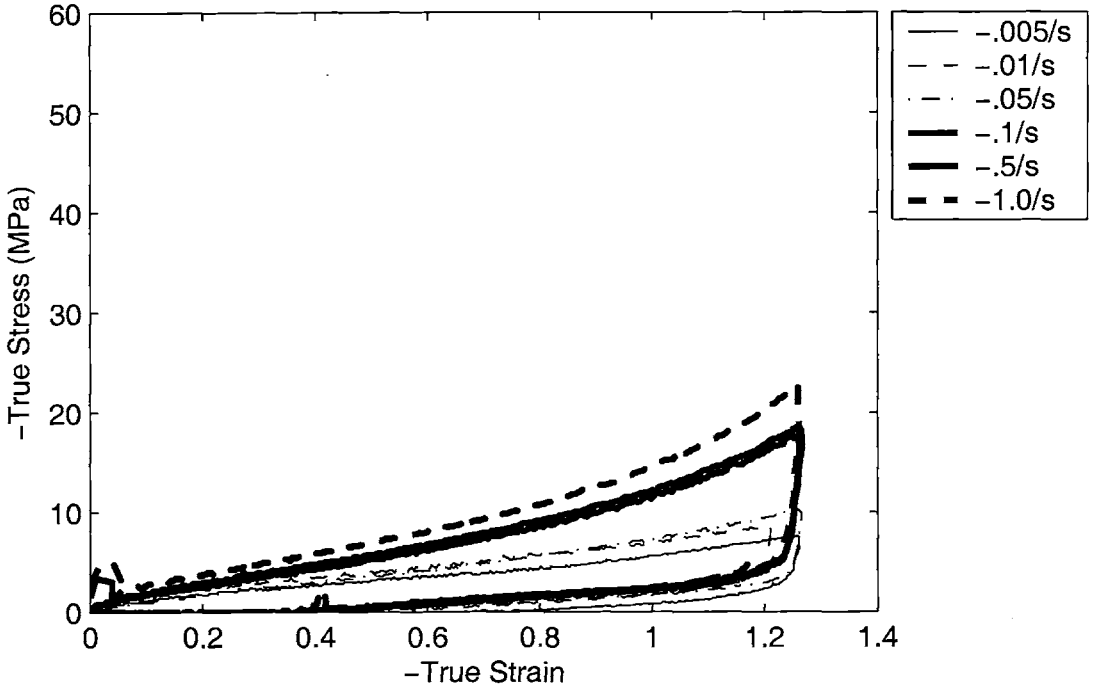

Figure 2-38: PETG Plane Strain Compression Data, Temperature = 90 ° C

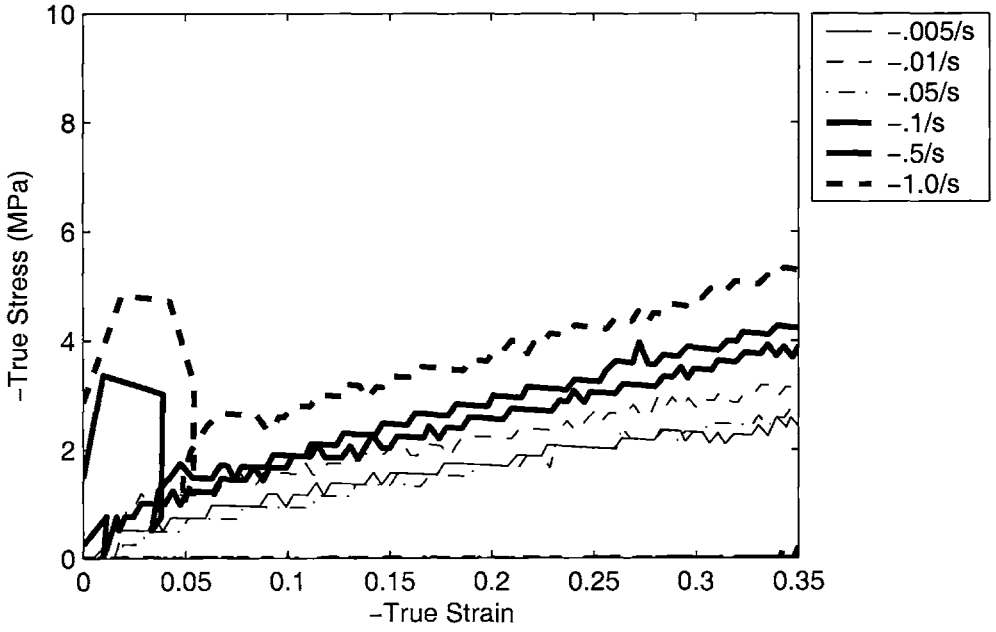

Figure 2-39: PETG Plane Strain Compression Data, Temperature = 90 ° C, Enlarged to show small strain data

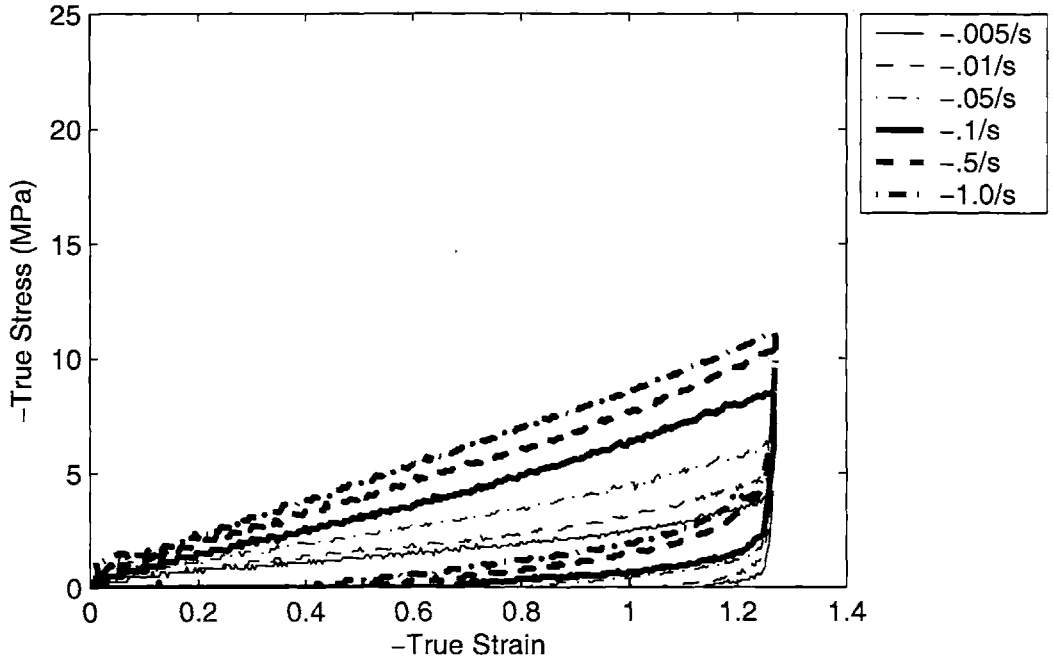

Figure 2-40: PETG Plane Strain Compression Data, Temperature = 100 ° C

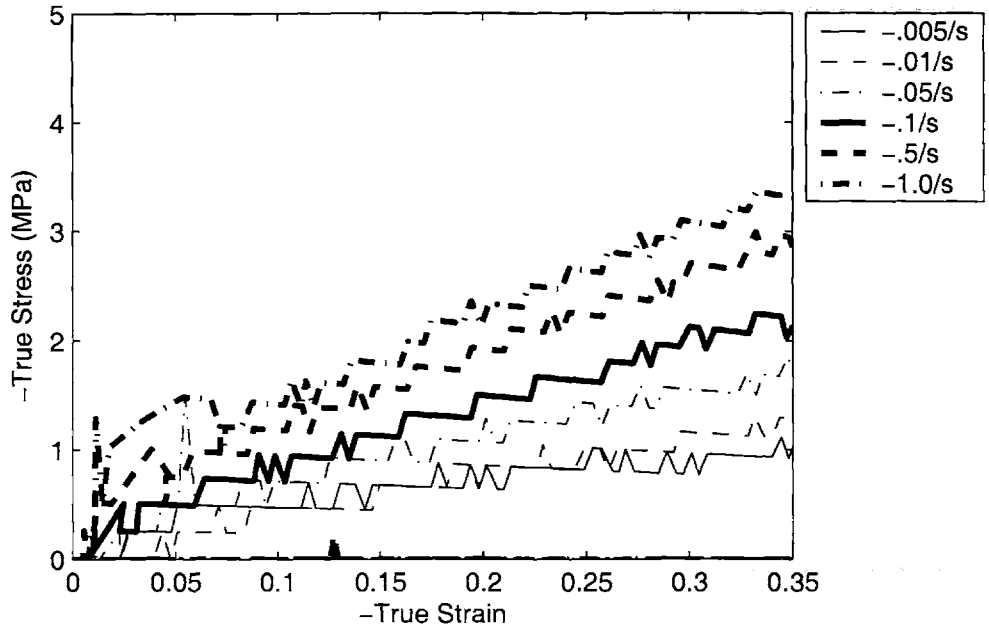

Figure 2-41: PETG Plane Strain Compression Data, Temperature = 100 ° C, Enlarged to show small strain data

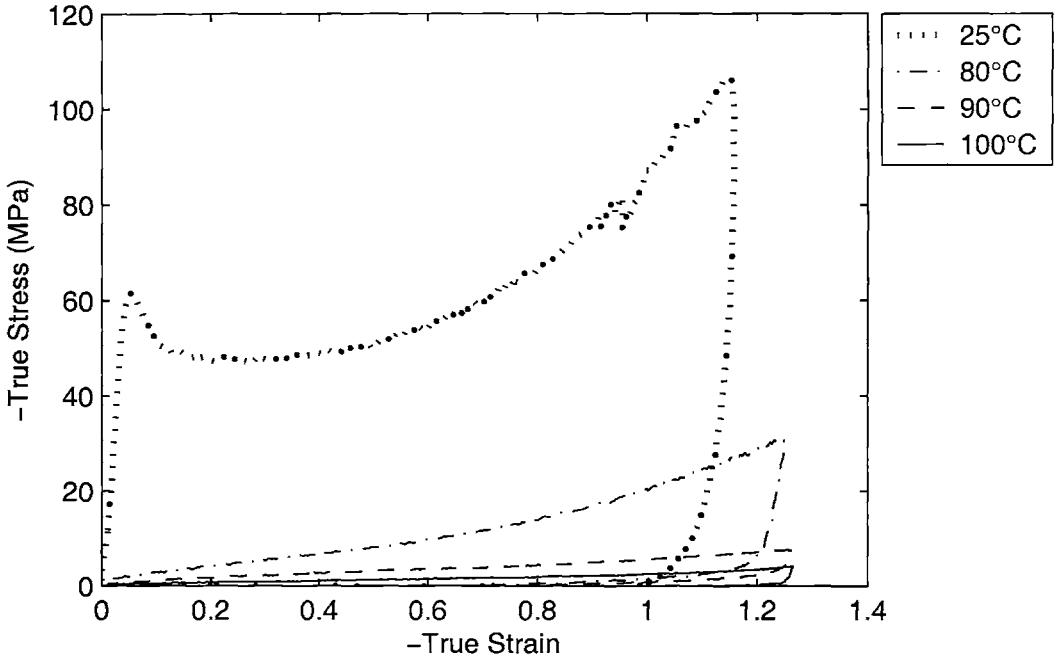

Figure 2-42: PETG Plane strain compression data, $\dot{\varepsilon}$ = -.005/s

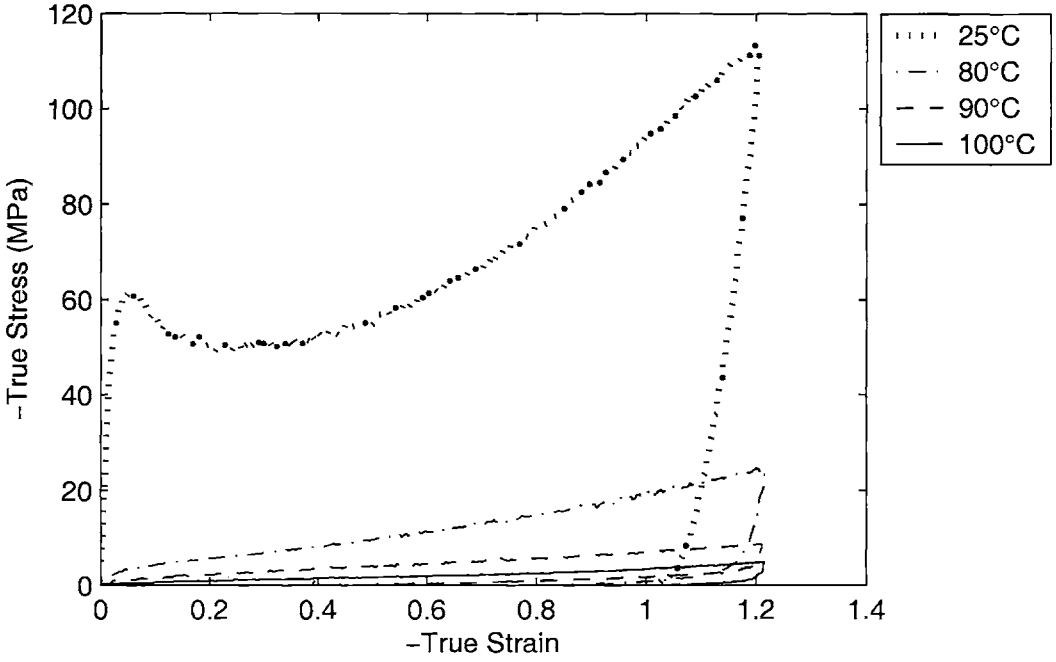

Figure 2-43: PETG Plane strain compression data, $\dot{\varepsilon}$ = -.01/s

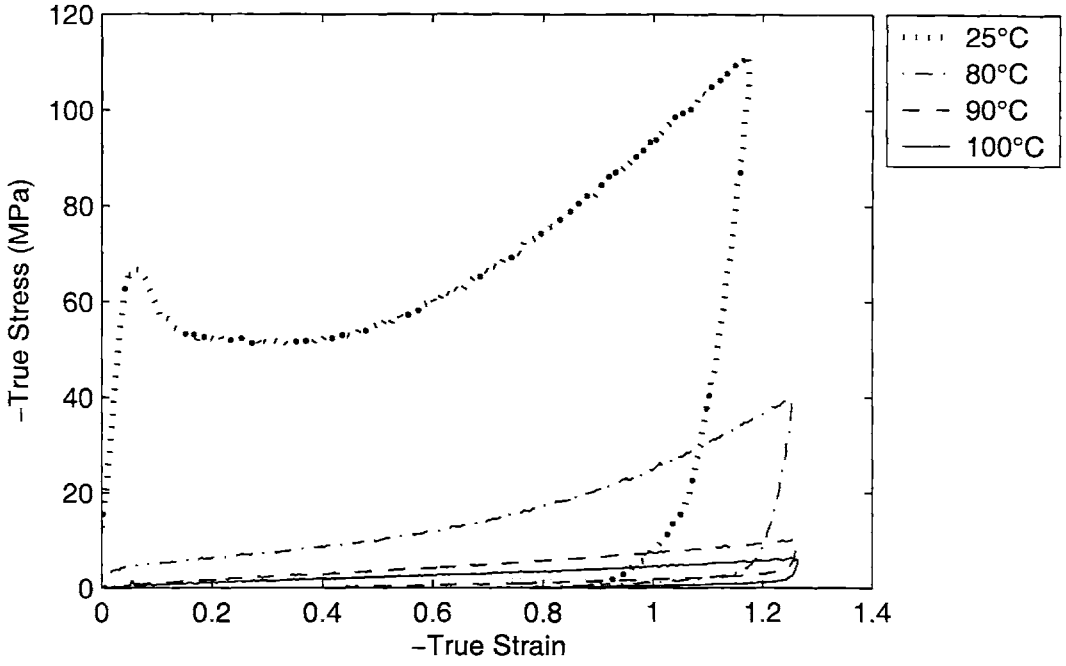

Figure 2-44: PETG Plane strain compression data, $\dot{\varepsilon}$ = -.05/s

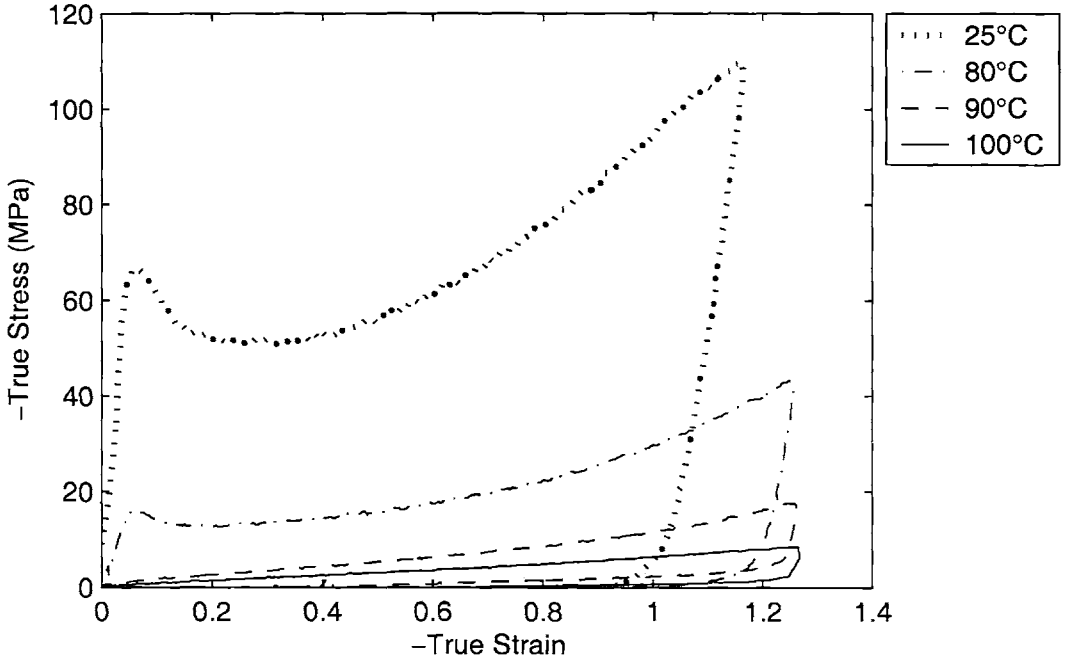

Figure 2-45: PETG Plane strain compression data, $\dot{\varepsilon}$ = -.1/s

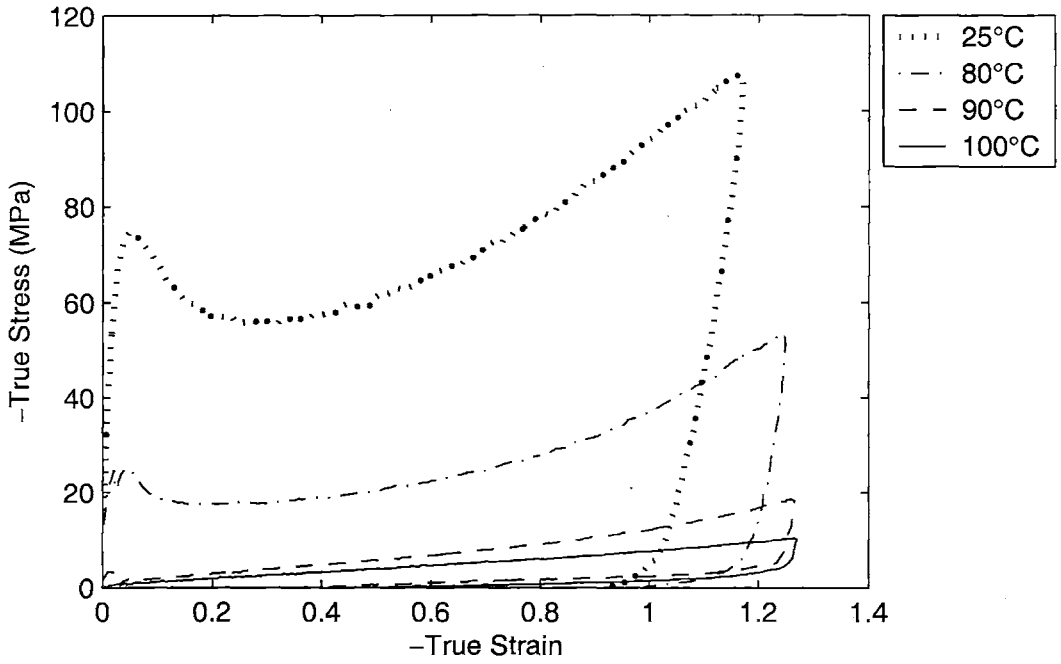

Figure 2-46: PETG Plane strain compression data, $\dot{\varepsilon}$ = -.5/s

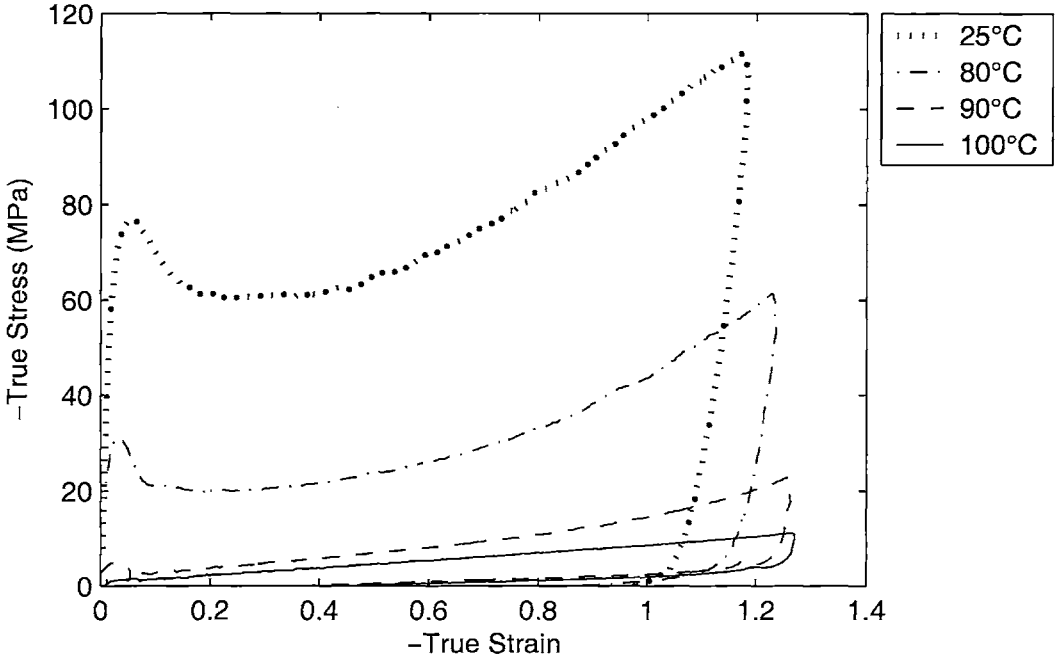

Figure 2-47: PETG Plane strain compression data, $\dot{\varepsilon}$ = -1.0/s

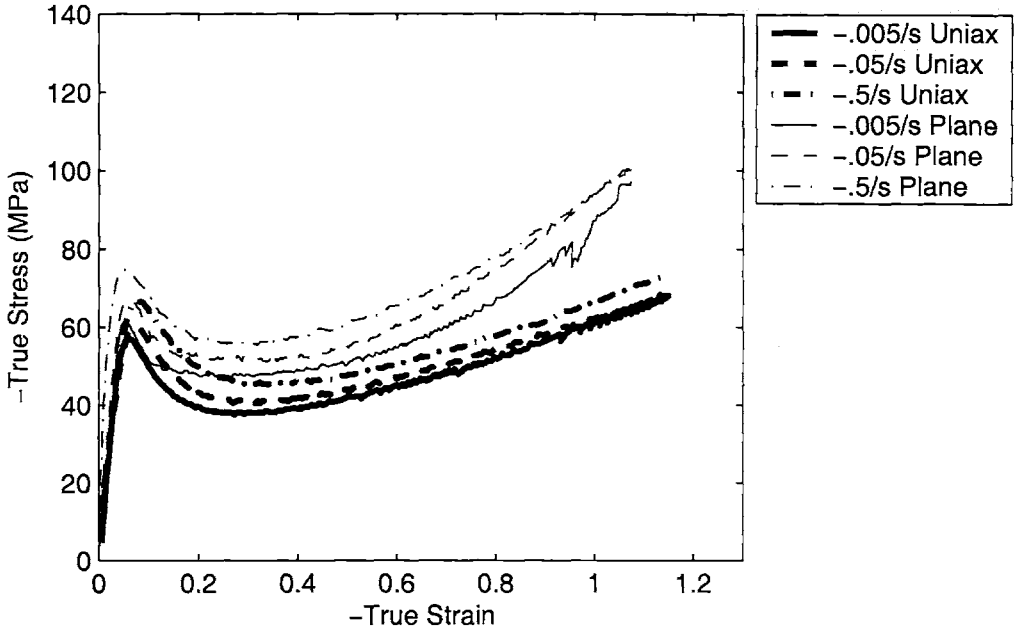

Figure 2-48: PETG Uniaxial and plane strain compression data, Temperature = 25 ° C

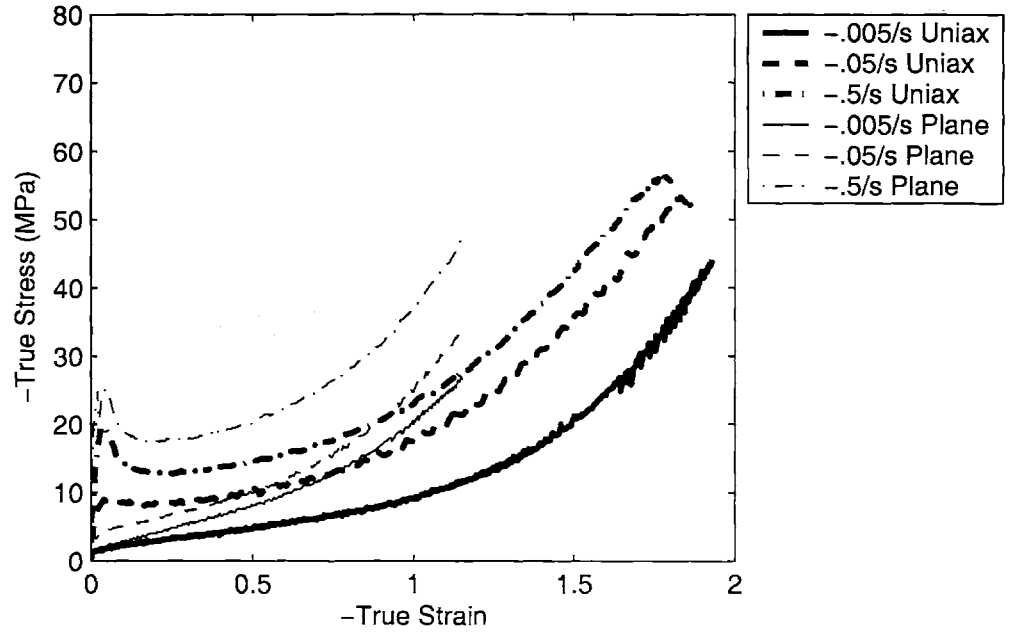

Figure 2-49: PETG Uniaxial and plane strain compression data, Temperature = 80 ° C

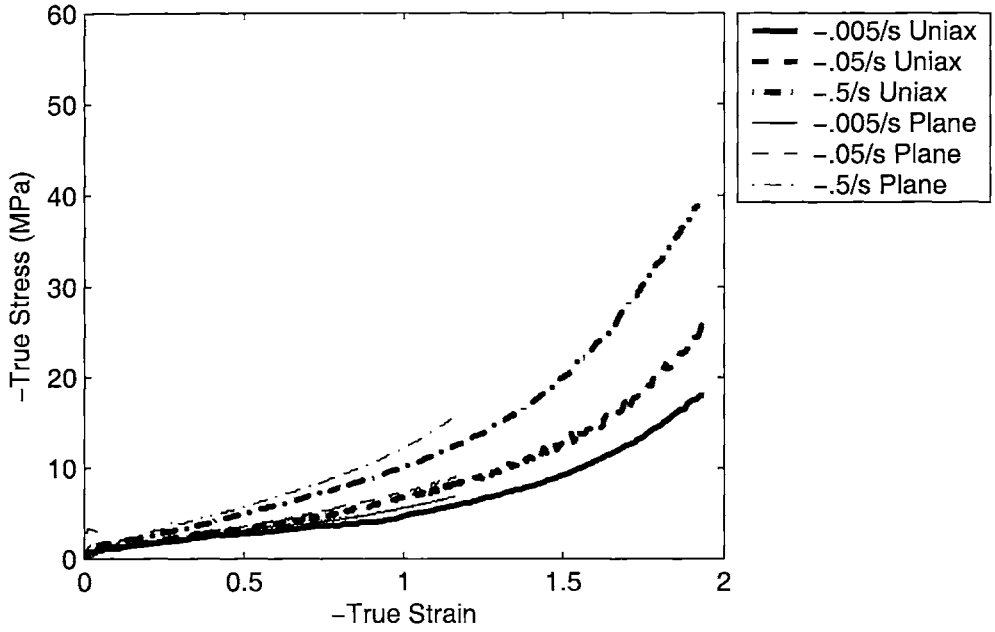

Figure 2-50: PETG Uniaxial and plane strain compression data, Temperature = 90 ° C

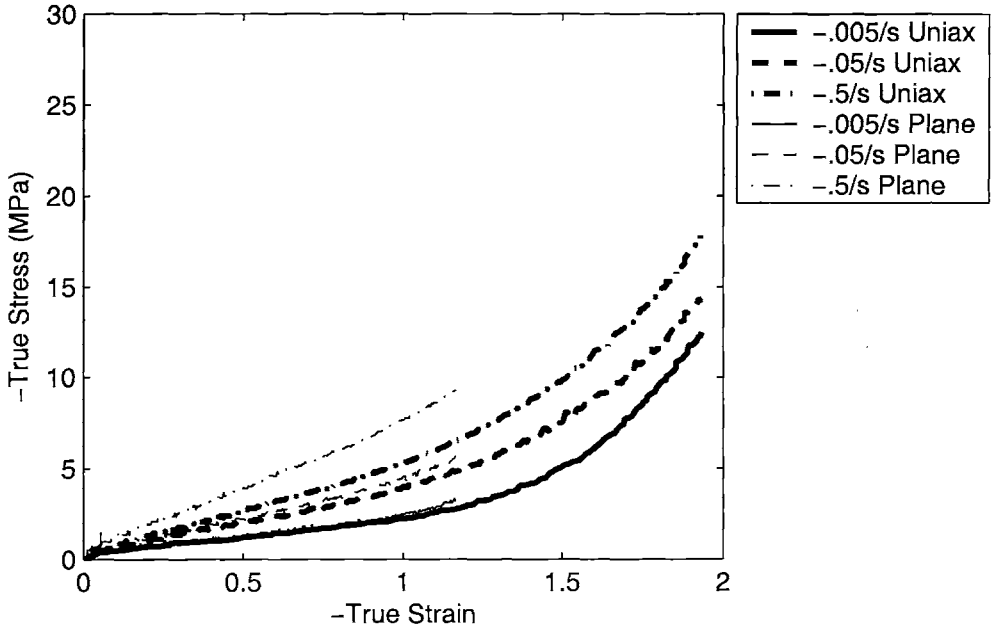

Figure 2-51: PETG Uniaxial and plane strain compression data, Temperature = 100 ° C

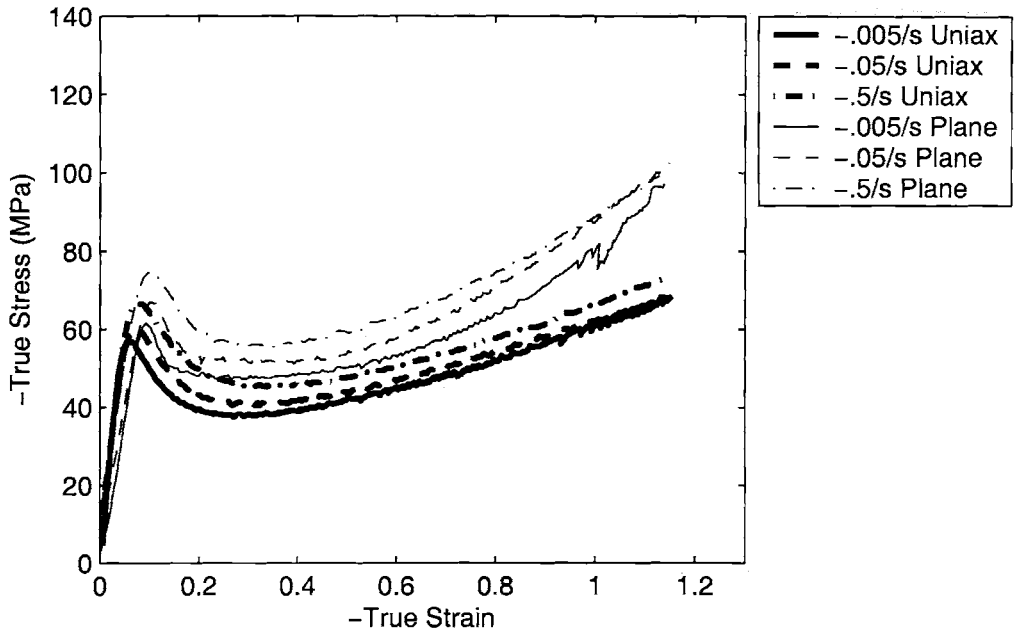

Figure 2-52: PETG Uniaxial and plane strain compression data, Temperature = 25 ° C, Illustrating additional compliance in the plane strain compression fixturing

2.8.2 Tension Experiments

Results from uniaxial tension tests on PETG are shown in Figures 2-53 to 2-57. In these experiments, deformation was nearly homogeneous–no neck developed and the whole specimen thinned until fracture or until the maximum extension allowed by the environmental chamber. Figure 2-53 shows the measured load displacement curves for tension tests at temperatures ranging from 90 ° C to 110 ° C. The general trends are as would be expected for the material behavior, i.e. the material becomes softer with increasing temperature. This softening is observed in terms of a more compliant initial modulus, a lower yield stress, and lower strain hardening. A drop in the curve is seen in these curves and is due either to inhomogeneity in the deformation or to the specimen slipping from the grips.

Figure 2-54 shows the calculated nominal stress-stretch curves for the same data. Nominal stress is computed simply as the load divided by the initial area in the gauge length. Stretch is computed as the current length (gage length plus crosshead

displacement) divided by the initial (gage) length. The data can be further reduced to yield a true stress-stretch curve by assuming uniform deformation and no volume change. In this manner the current area can be calculated using the axial stretch. This is the approach used to compute the stress shown in figures 2-55 to 2-57.

2.8.3 Biaxial Extension Experiments

In most of these experiments, the test was conducted until the sample fractured. The testing apparatus was capable of applying a stretch of 7 in each direction. Figure 2-58 shows the results of equibiaxial extension experiments conducted at 100 ° C and 105 ° C. These curves again show that the material is more compliant with increasing temperature. True stress values were calculated assuming constant volume and uniform deformation.

Figures 2-59 and 2-61 show the results of constrained width tension experiments conducted at 90 ° C, 100 ° C, and 105 ° C. These curves demonstrate the increase in material compliance with increasing temperature. True stress values were calculated assuming constant volume and uniform deformation.

An example of a sequential biaxial stretching experiment is shown in figures 2-62 and 2-64. The samples were stretched to a nominal stretch of 2 in the first stretch direction. In figure 2-62, engineering stress and strain are plotted as a function of time. In the stress-time plot, solid lines are stress values in the first stretching direction (X-direction) and dashed lines are the stress in the second (Y-) direction. In figure 2-63 true stress and true strain curves are plotted. The calculations are done assuming constant volume and uniform deformation. In figure 2-64 true stress and stretch ratio are plotted as a function of time. It can be observed in these figures that during stretching in the first direction, the stress rises in both the X- and Y-directions, though the stress is higher in the stretching direction. During the stretch in the second direction, the stress in that direction surpasses the stress in the first stretch direction and continues to rise until the end of the test.

The effect of temperature is to cause lower stress levels throughout the experiment. It should be noted that in the two test samples illustrated here, the sample drawn at

100 ° C broke rather early in the experiment, so it is unclear the effect of temperature at large extensions.

Similar curves are shown in figures 2-65 to 2-67 for a sequential stretching experiment in which the sample was stretched to a nominal stretch of 3 in the first stretch direction before being stretched in the second direction.

2.9 Summary of PETG Observations

In this chapter we have observed the rate, temperature, and strain state dependence of the mechanical behavior of PETG. In compression, the material exhibits four characteristic regions above the glass transition temperature: (1) a relatively stiff initial modulus, (2) a rollover to flow at around 2 MPa, (3) a gradual stiffening through the moderate strain regime, and (4) a dramatic upturn in strain at very large strain levels. Each of these features depends strongly on the temperature and rate of deformation. The initial modulus, flow stress, and initial hardening modulus all increase with decreasing temperature or increasing strain rate. The dramatic upturn in strain occurs at earlier strain levels with increasing strain rate or decreasing temperature. The material also exhibits a stiffer response and an earlier upturn in the stress-strain curve in plane strain compression than in uniaxial compression.

The tensile experiments illustrate similar temperature effects on the material behavior. It is difficult to directly compare tensile experiments with compression experiments, as the compression experiments were conducted at a constant strain rate and the tensile experiments were conducted at a constant extension rate. Hence, the tensile samples were subjected to a strain rate which decreased throughout the duration of the experiment.

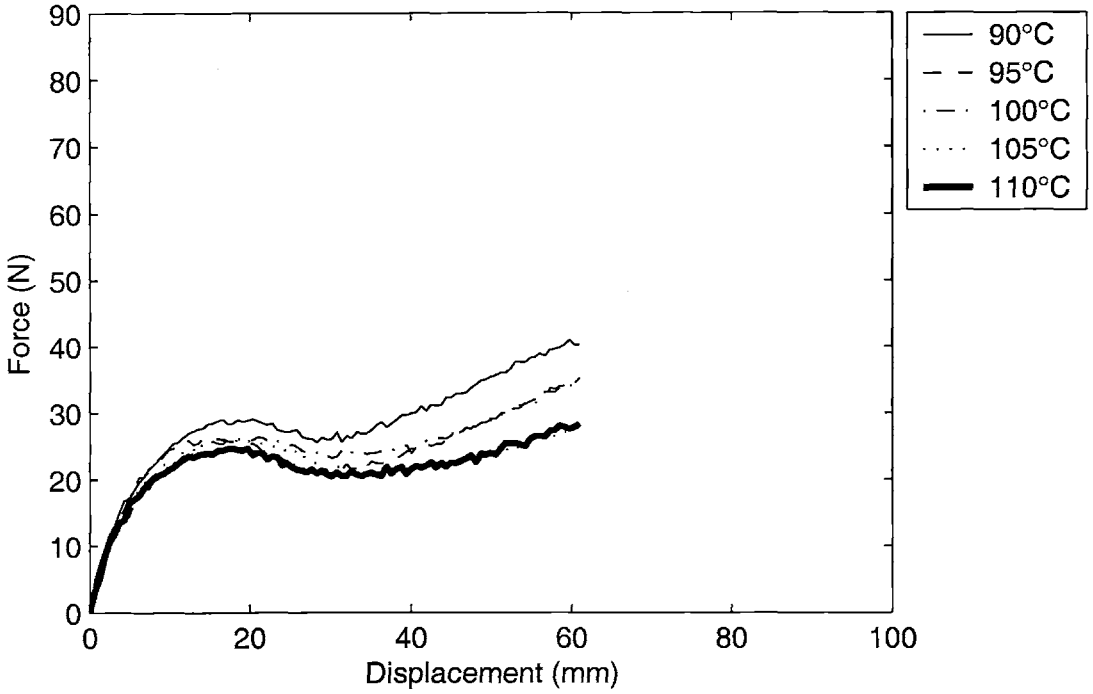

Figure 2-53: PETG Uniaxial tension, load-displacement

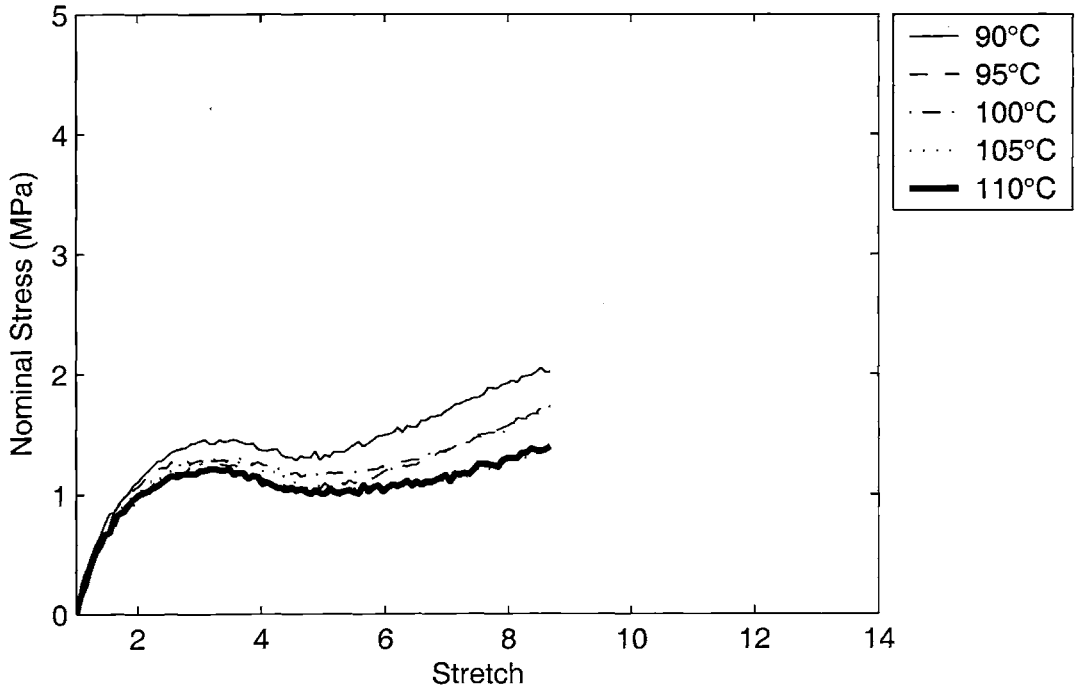

Figure 2-54: PETG Uniaxial tension, nominal stress-stretch

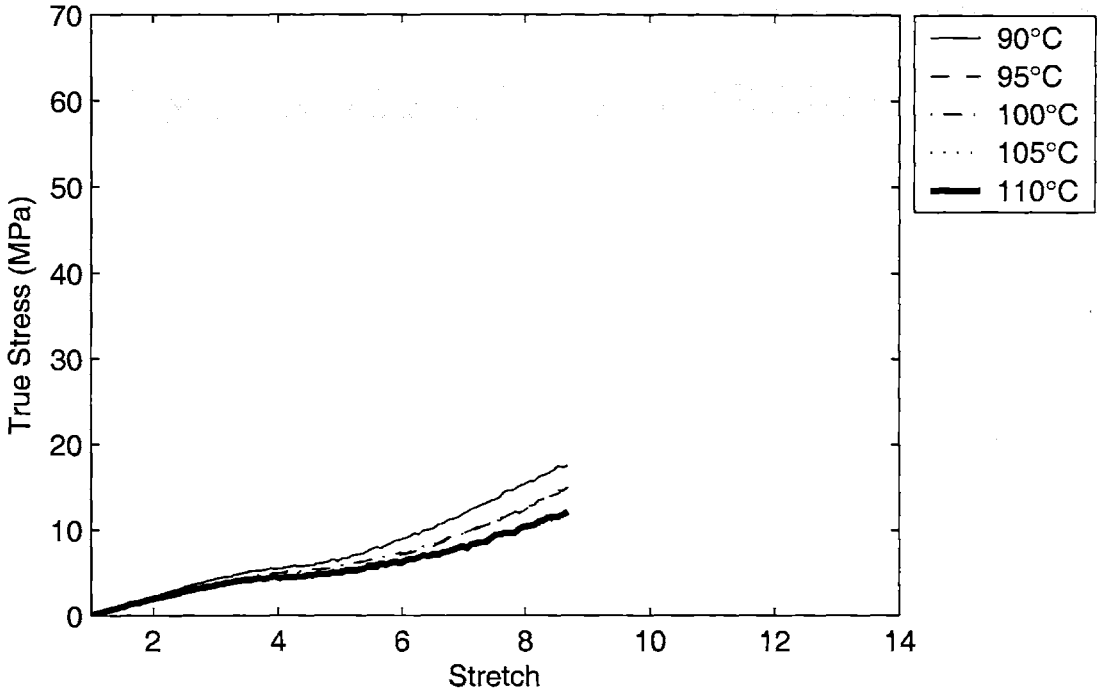

Figure 2-55: PETG Uniaxial tension, calculated true stress-stretch

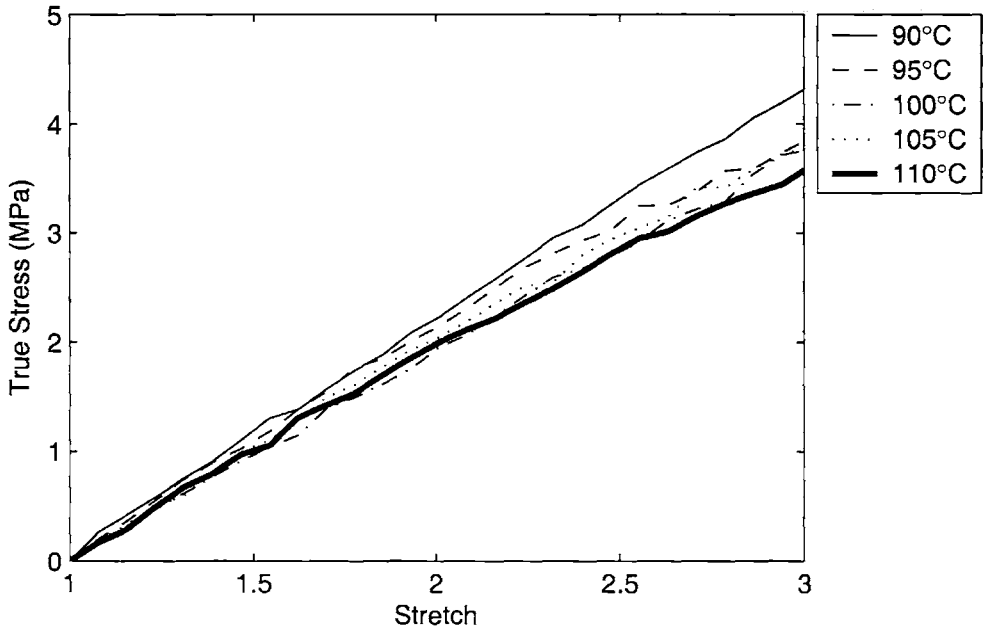

Figure 2-56: PETG Uniaxial tension, calculated true stress-stretch, enlarged

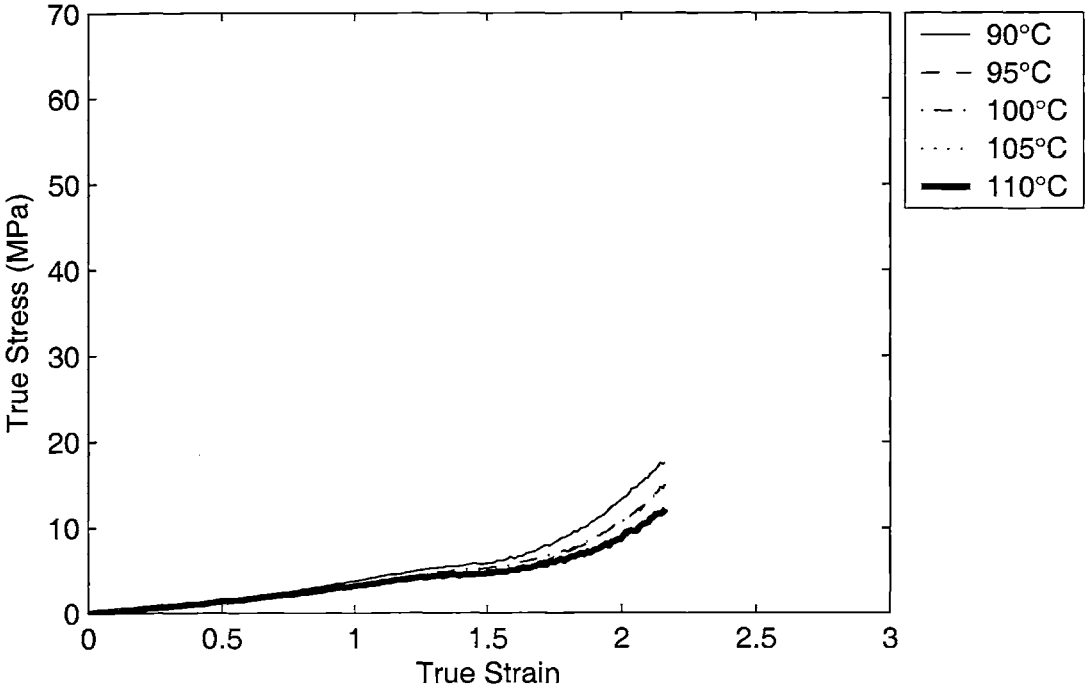

Figure 2-57: PETG Uniaxial tension, calculated true stress-true strain

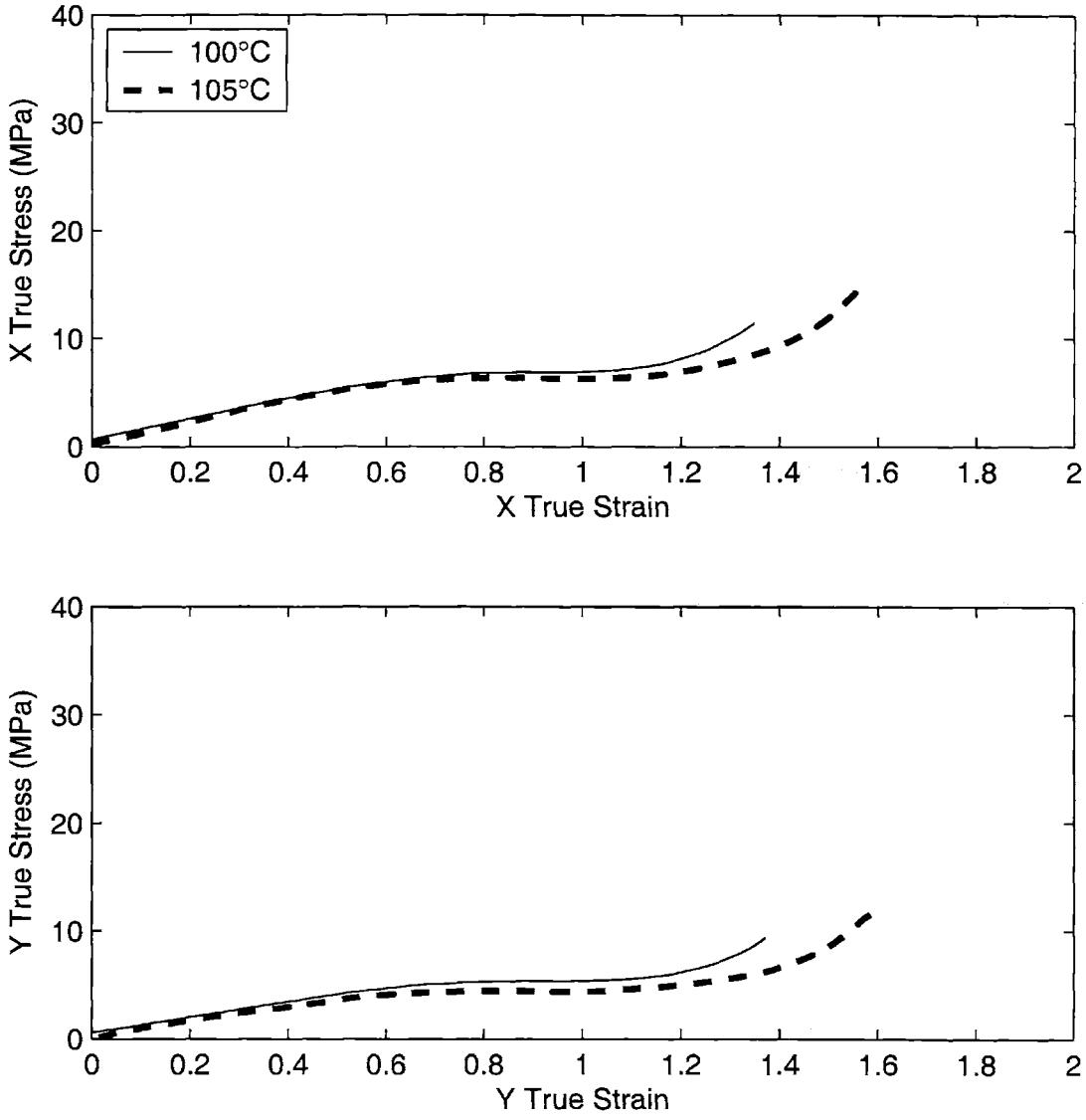

Figure 2-58: PETG Equibiaxial extension, true stress-strain, du/dt = 14 in/sec

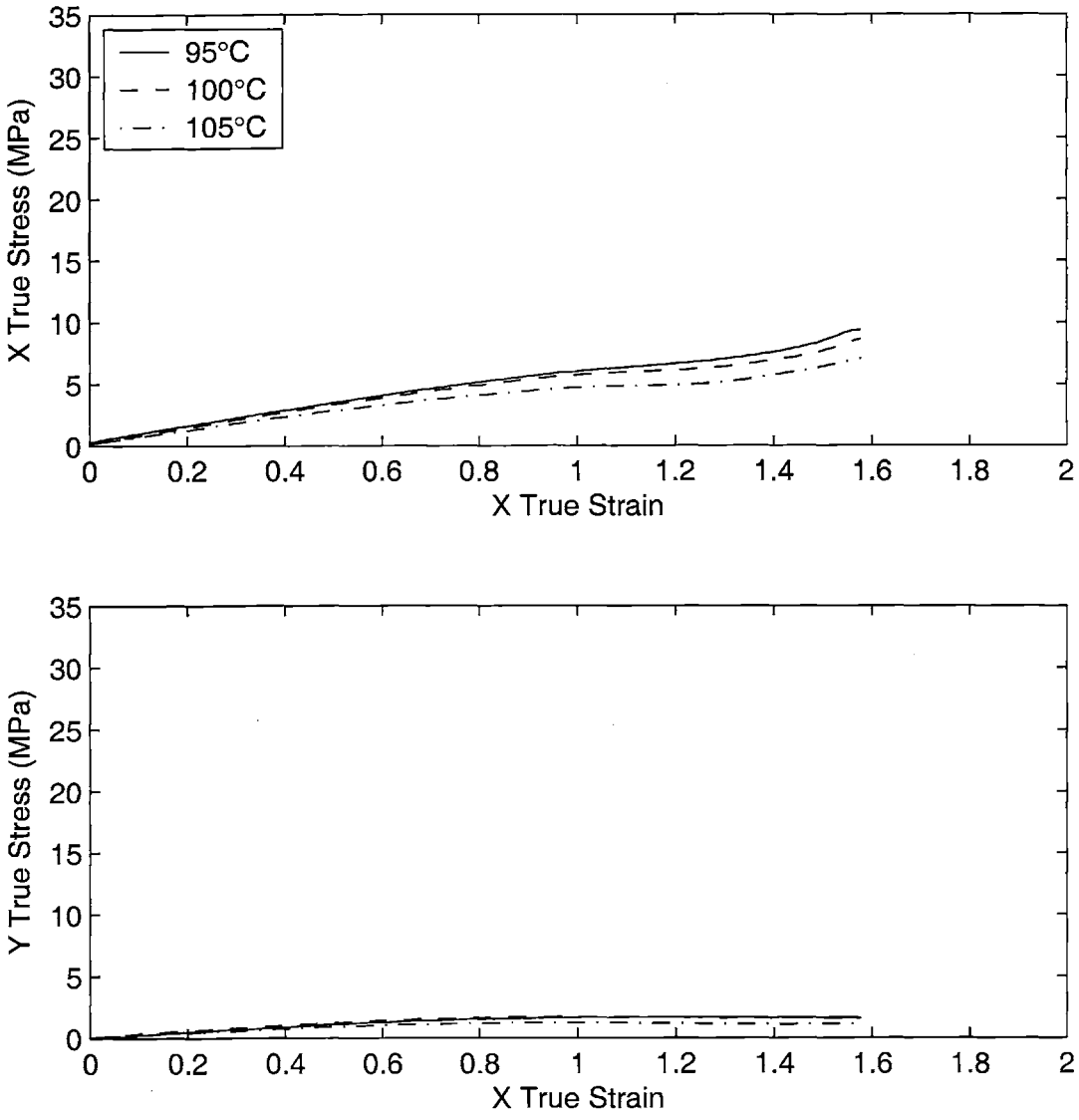

Figure 2-59: Constrained width tension, true stress-strain, du/dt = 14 in/sec

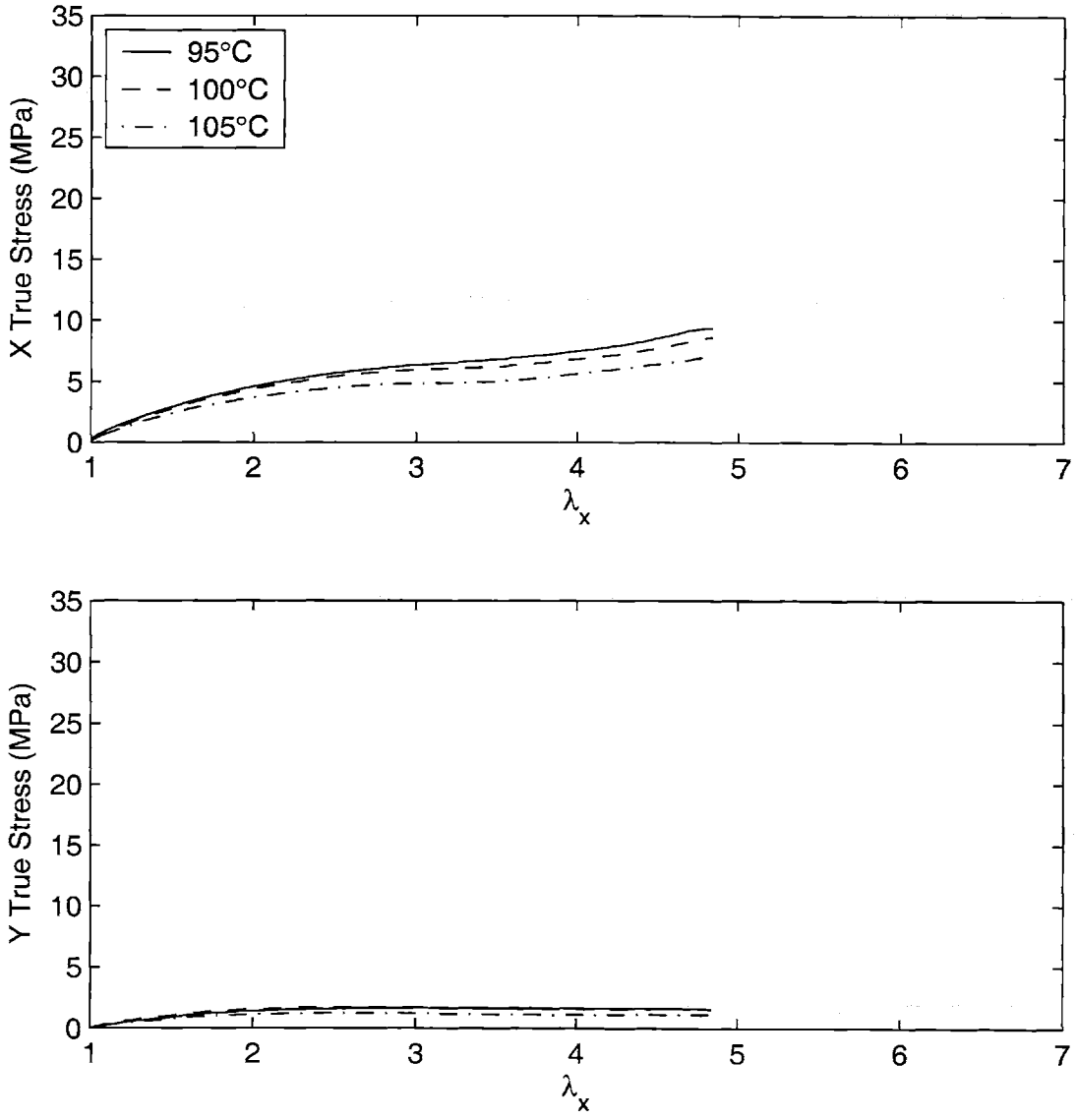

Figure 2-60: PETG Constrained width tension, true stress-stretch, du/dt = 14 in/sec

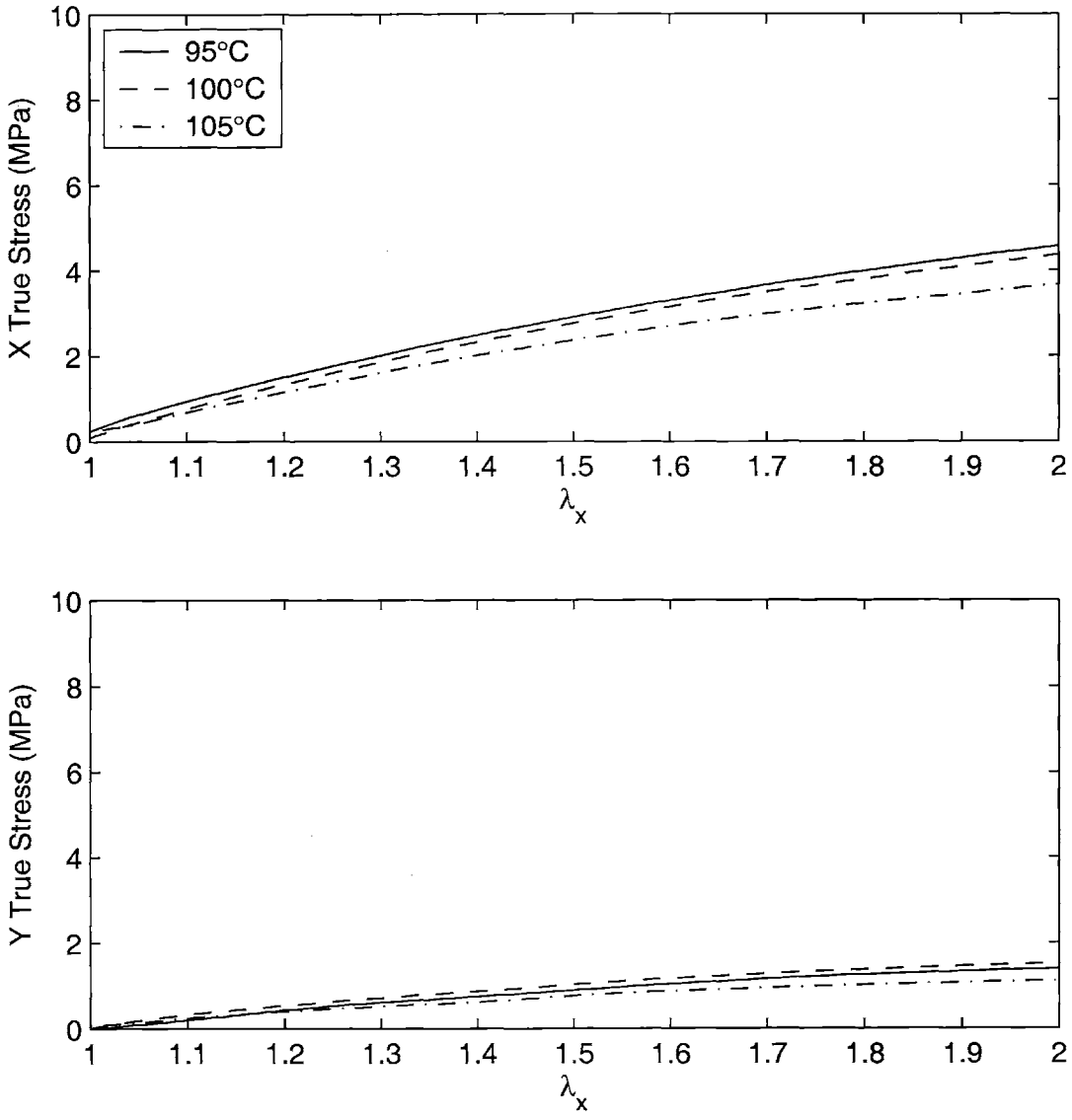

Figure 2-61: PETG Constrained width tension, true stress-stretch, du/dt = 14 in/sec, enlarged

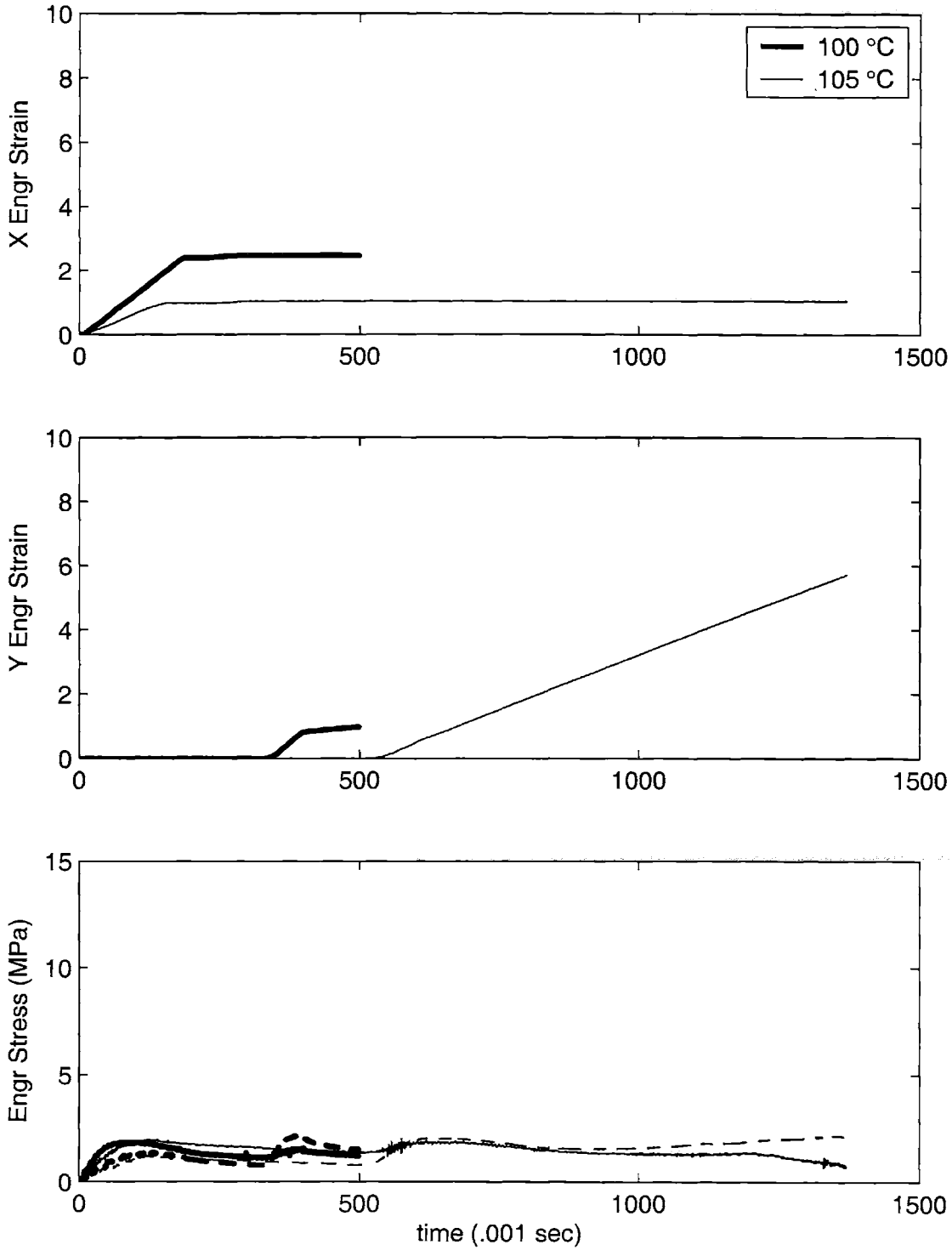

Figure 2-62: PETG Sequential biaxial extension, engineering stress-strain, $\lambda_x = 2$

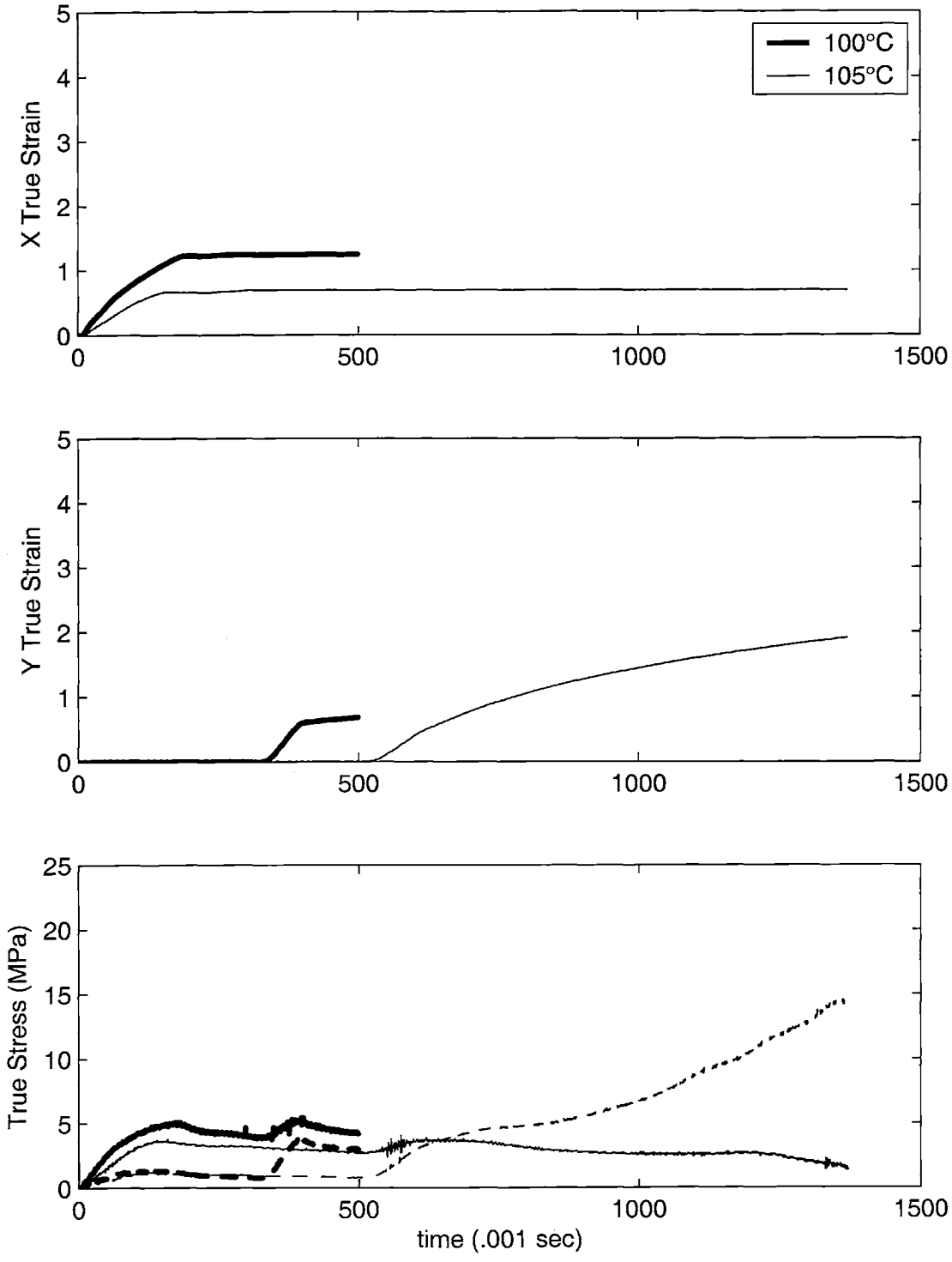

Figure 2-63: PETG Sequential biaxial extension, true stress-strain, $\lambda_x = 2$

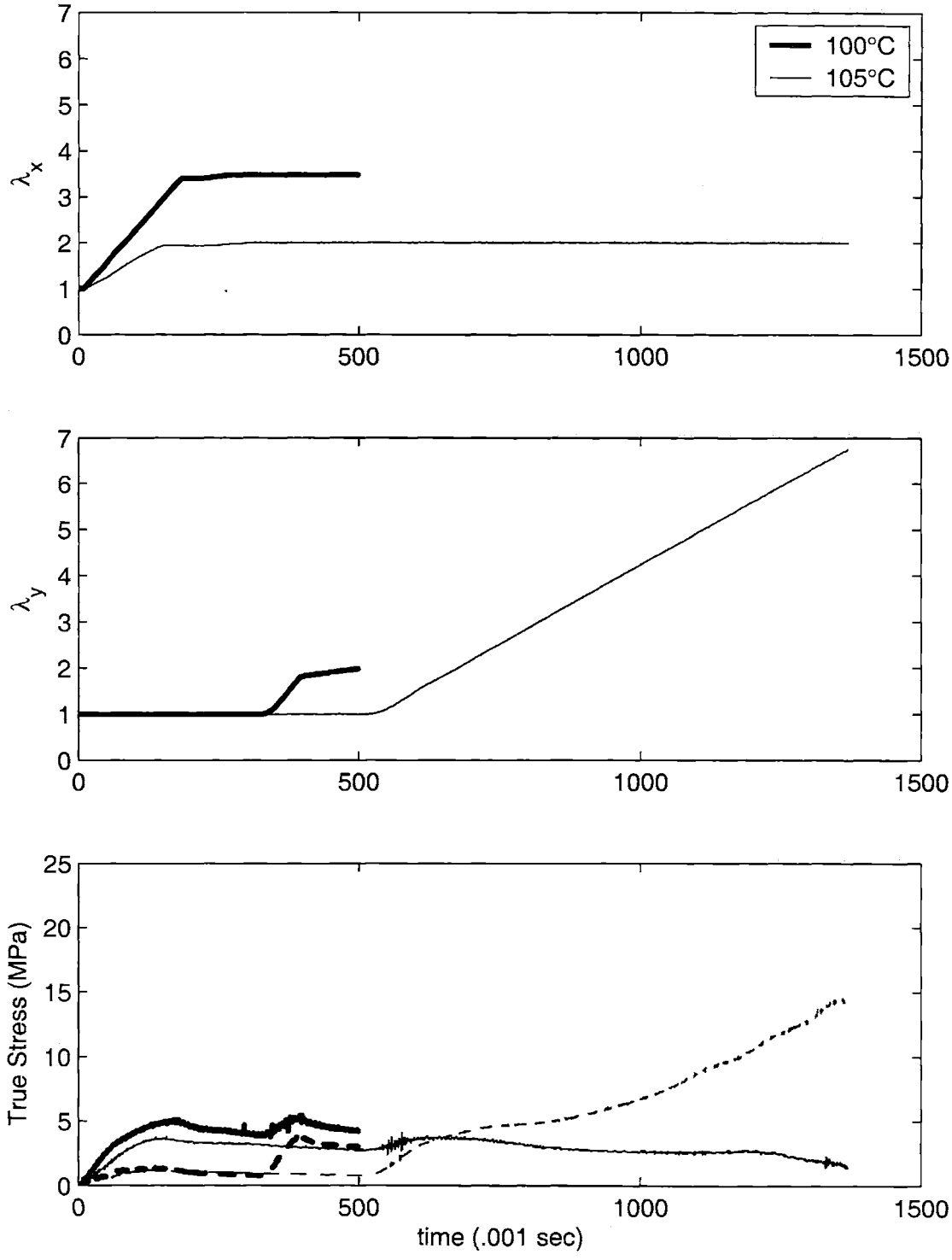

Figure 2-64: PETG Sequential biaxial extension, true stress-stretch, $\lambda_x = 2$

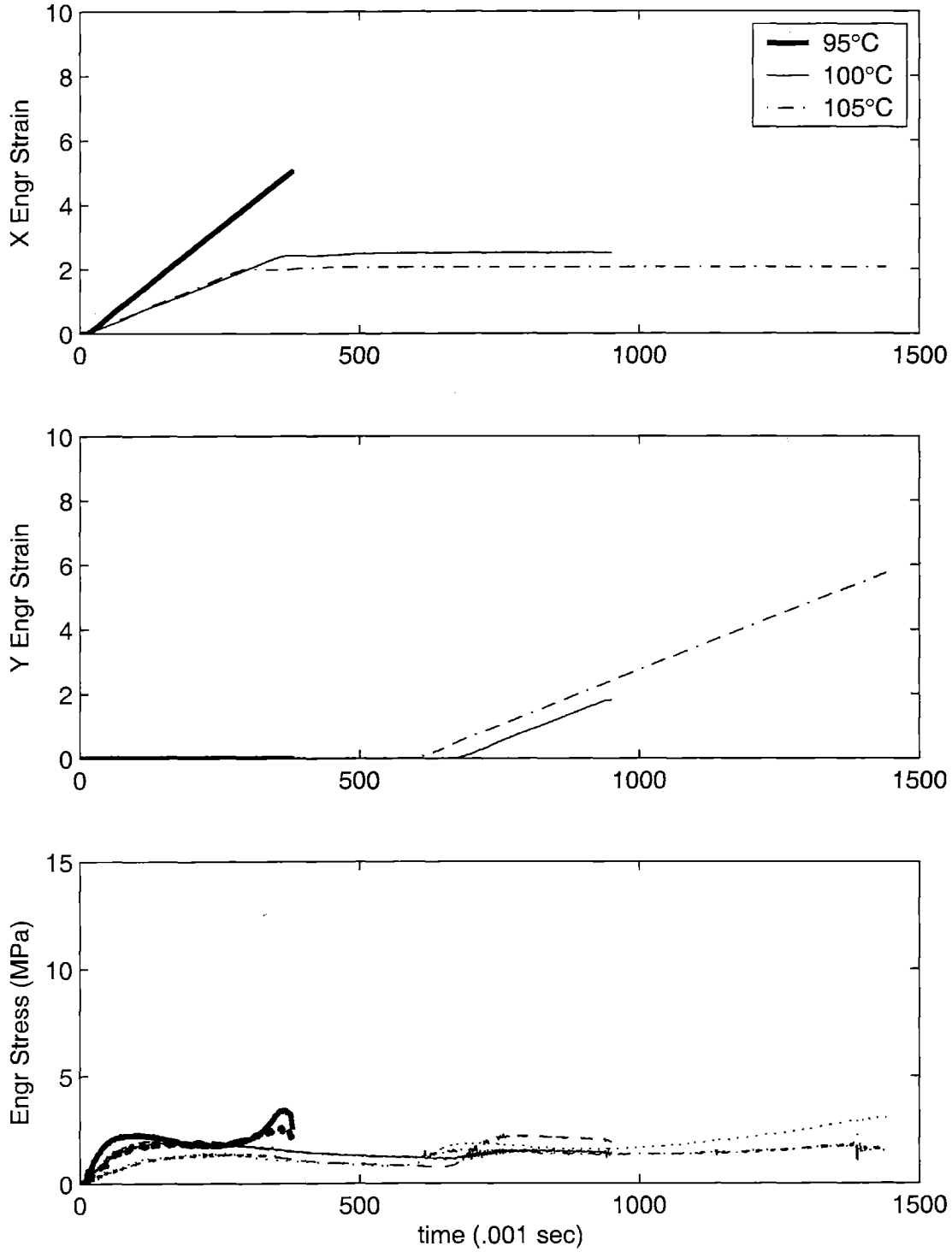

Figure 2-65: PETG Sequential biaxial extension, engineering stress-strain, $\lambda_x = 3$

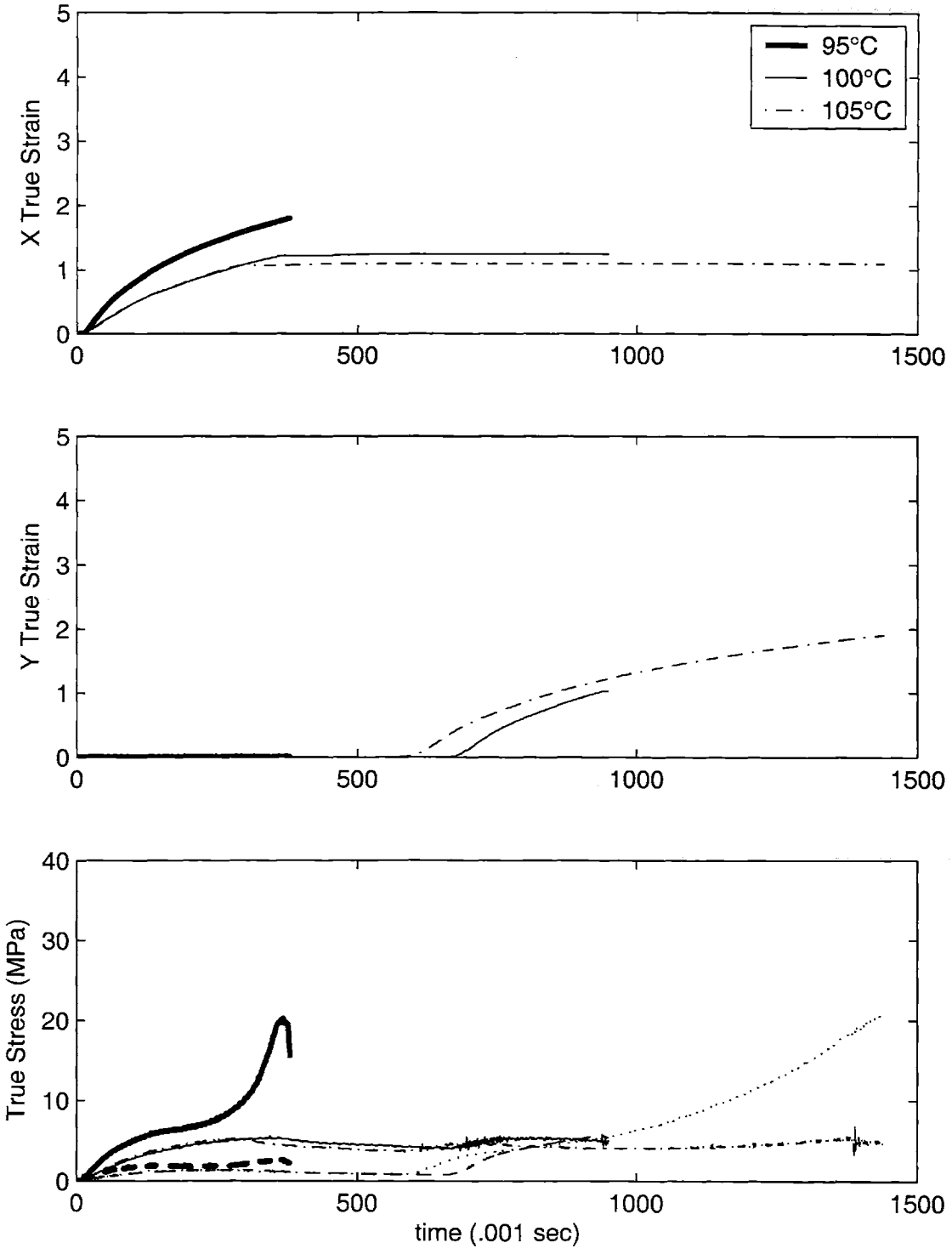

Figure 2-66: PETG Sequential biaxial extension, true stress-strain, $\lambda_x = 3$

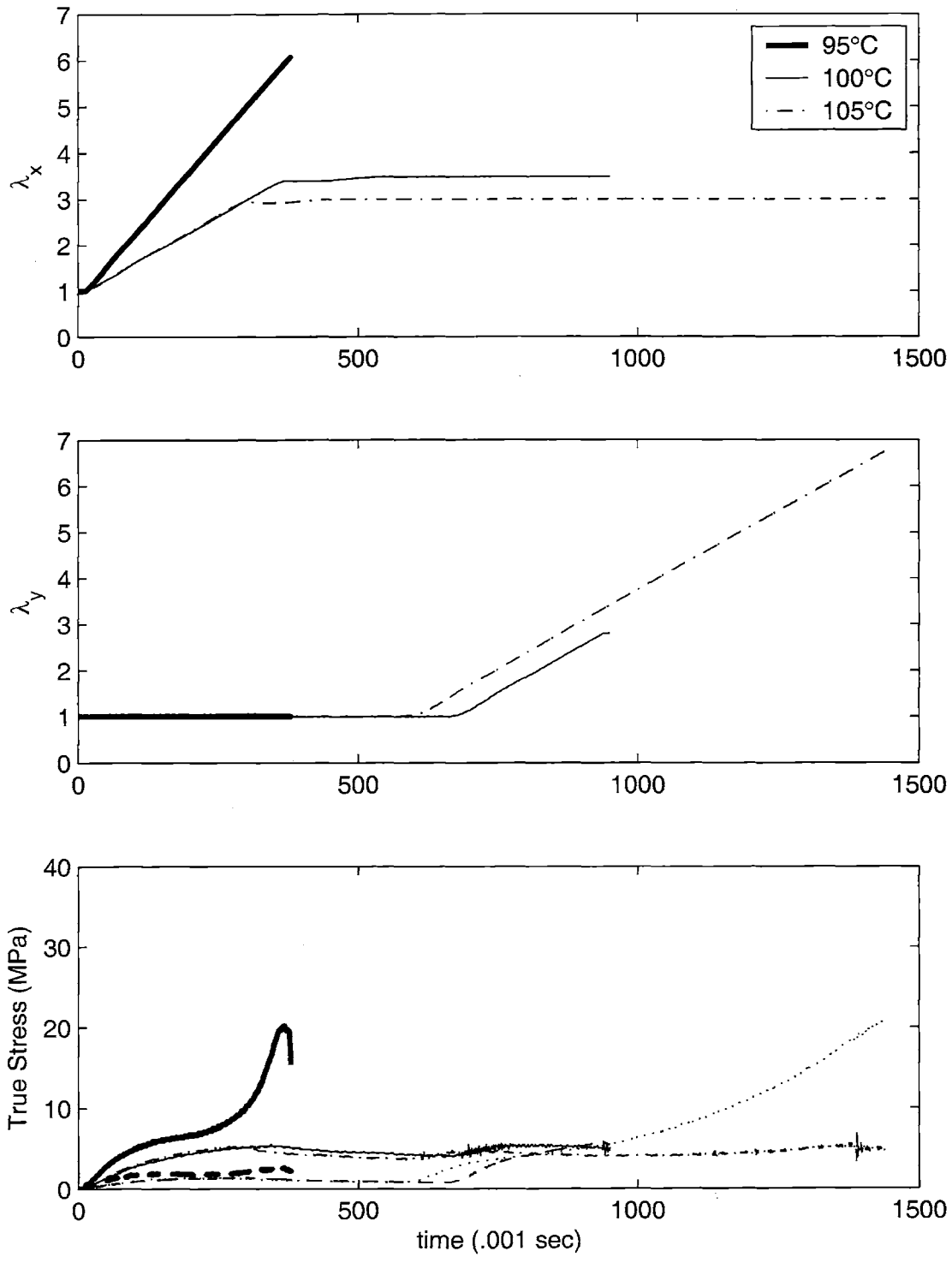

Figure 2-67: PETG Sequential biaxial extension, true stress-stretch, $\lambda_x = 3$

Chapter 3

PET Experiments

3.1 Introduction

Poly(ethylene terephthalate) is a widely used polymer for a variety of commercial applications. These applications range from drawn fibers and films for clothing and photography to carbonated beverage containers. A primary reason for its success in these applications is its ability to undergo strain-induced crystallization under appropriate conditions of temperature and strain rate. Because of its wide use, PET has been the subject of many research groups as referenced in Chapter 1.

In this chapter, experimental data for PET is presented for comparison to the behavior of PETG (ref. Chapter 2).

3.2 Material

The material used in all experiments was PET 9921 supplied by Eastman Chemical Co. with a weight average molecular weight of 51,365 and a polydispersity of 2. It was supplied in the form of 4 in. by 4 in. plaques of 1/8 in. nominal thickness, from which compression specimens were machined.

3.3 DSC

Differential scanning calorimetry (DSC) was performed using a Perkin Elmer DSC 7 at a constant heating rate of 10 ° C per minute. The equipment was calibrated with zinc and indium. DSC scans performed on the as-received material indicated that there was no crystallinity in the material.

3.4 Experimental Setup

The reader is referred to sections 2.5 to 2.7 for a complete description of the experimental setup. All experiments on PET followed a setup identical to that for PETG.

3.5 Results and Discussion

3.5.1 Compression Experiments

The results are shown in the following figures and are discussed below. Figures 3-1 through 3-14 show uniaxial compression data at each temperature. Figures 3-15 through 3-20 show the same data plotted at constant strain rate.

From these figures it can be observed that PET exhibits the same general trends as PETG. A thorough description of these features is provided in sec. 2.8.1, but a brief summary will be included here. First, the material has an initially stiff response which is highly temperature dependent, decreasing moderately with increasing temperature below and above the glass transition temperature and dropping dramatically with temperature in the transition region. There is also a strong strain rate dependence in the transition region, with increasing strain rate leading to a higher effective θ_g.

Second, at temperatures below the glass transition temperature the polymer exhibits a definite yield stress followed by strain softening. At temperatures above the transition temperature, the stress-strain curves show the monotonic rise in stress with increasing strain, which is characteristic of rubber elastomers. The magnitude of the yield and flow stresses depend on strain rate and temperature. At higher temperatures

and lower strain rates, yield (flow) occurs at lower stress levels. Figures 3-8, 3-10, 3-12, and 3-14 show an enlarged view of the initial modulus and roll over to flow for the polymer above the glass transition temperature.

Third, the polymer begins to strain harden as the strain level is increased. The material exhibits both an initial hardening modulus and a dramatic upturn in stress at very large strains.

In the constant strain rate figures (figures 3-15 to 3-20) the temperature dependence of the material is clearly discernible. At each of the strain rates, the initial yield or initial flow stress decreases as temperature increases. The hardening slope decreases with increasing temperature and the strain at which the dramatic upswing in stress occurs is greater at higher temperatures.

Figures 3-21 through 3-28 show plane strain compression data at each temperature. Figures 3-29 through 3-34 show the same data plotted at constant strain rate. The plane strain compression data indicates the same trends as were observed in the uniaxial compression data. In figures 3-35 through 3-38 the comparison of plane strain with uniaxial deformation modes is depicted.

Figures 3-35 through 3-38 also demonstrate that the deformation behavior of PET includes a very dramatic upswing in plane strain compression. This upswing is more pronounced than in uniaxial compression and much more dramatic than the behavior shown by PETG. This is likely due to strain-induced crystallization. While strain-induced crystallization is able to occur in PET regardless of the strain state, in plane strain the crystallites are completely aligned in one direction. In uniaxial compression, on the other hand, the crystallites are oriented within a plane perpendicular to the loading direction, but within the plane, the orientation of each crystallite is completely random (see figures 1-6 and 1-7 (Llana 1998; Llana and Boyce 1999)). This could explain why the plane strain data hardens so dramatically. In PETG, where strain-induced crystallization does not occur, this dramatic hardening is not seen in plane strain compression.

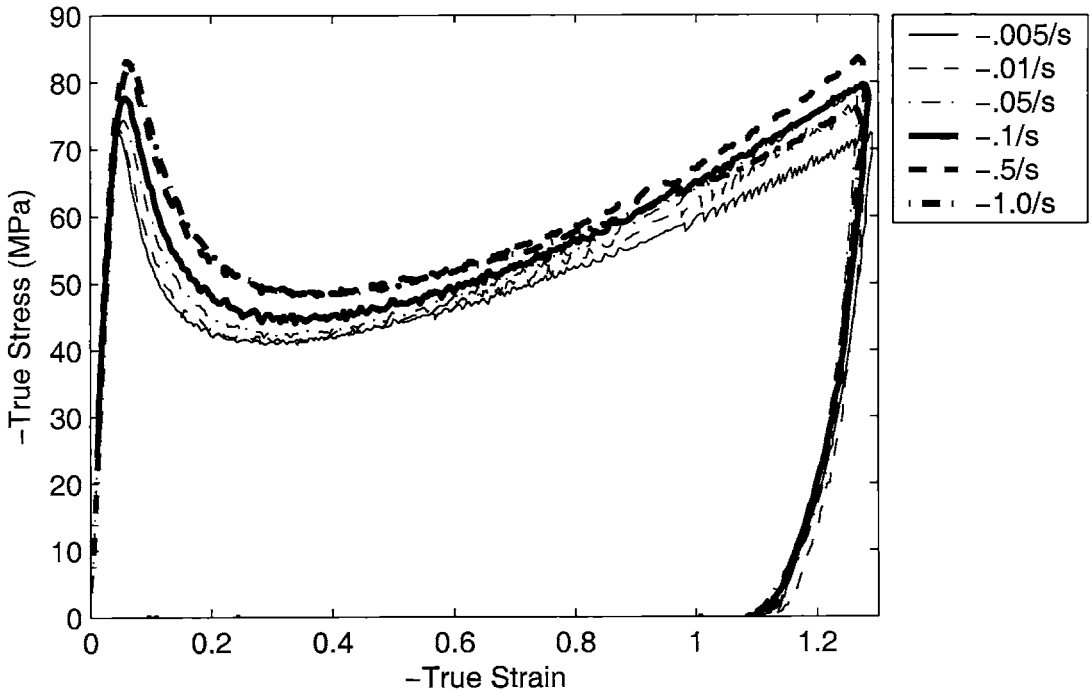

Figure 3-1: PET Uniaxial compression data, Temperature = 25 ° C

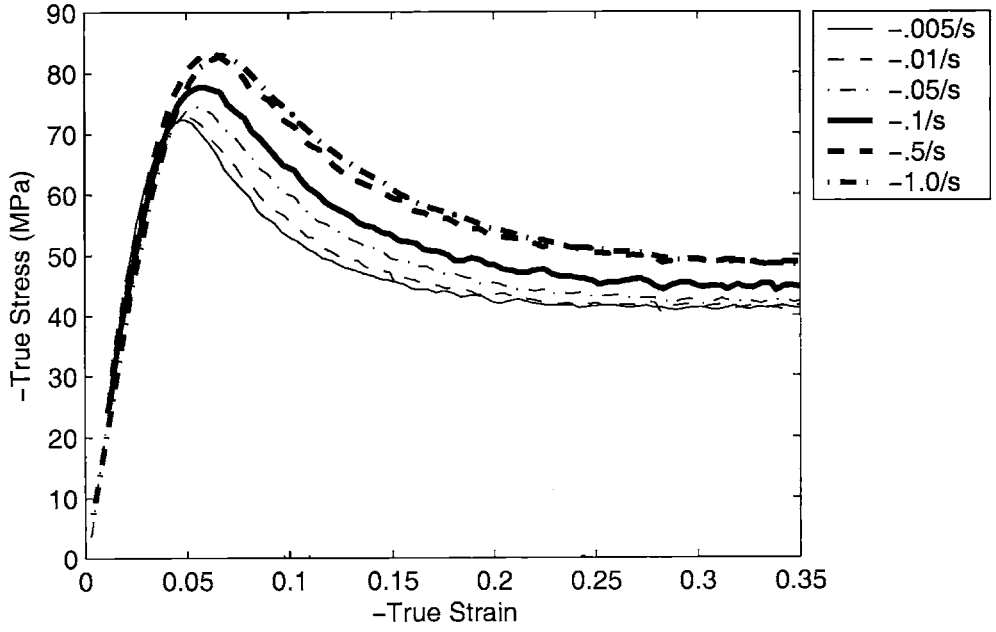

Figure 3-2: PET Uniaxial compression data, Temperature = 25 ° C, enlarged to show small strain data

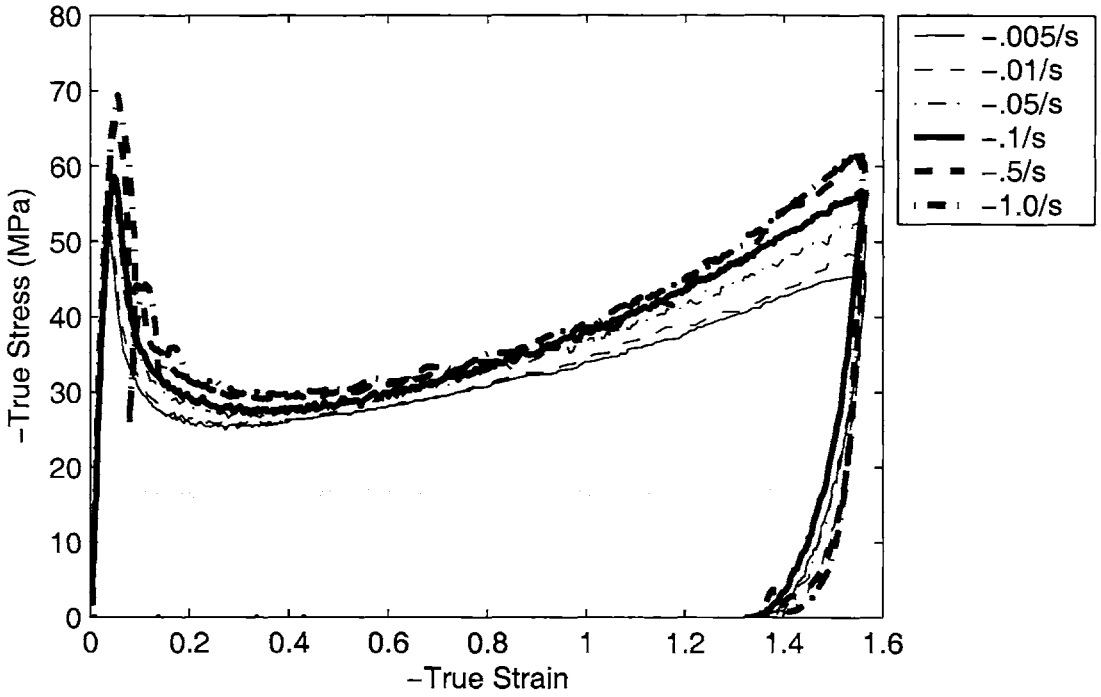

Figure 3-3: PET Uniaxial compression data, Temperature = 60 ° C

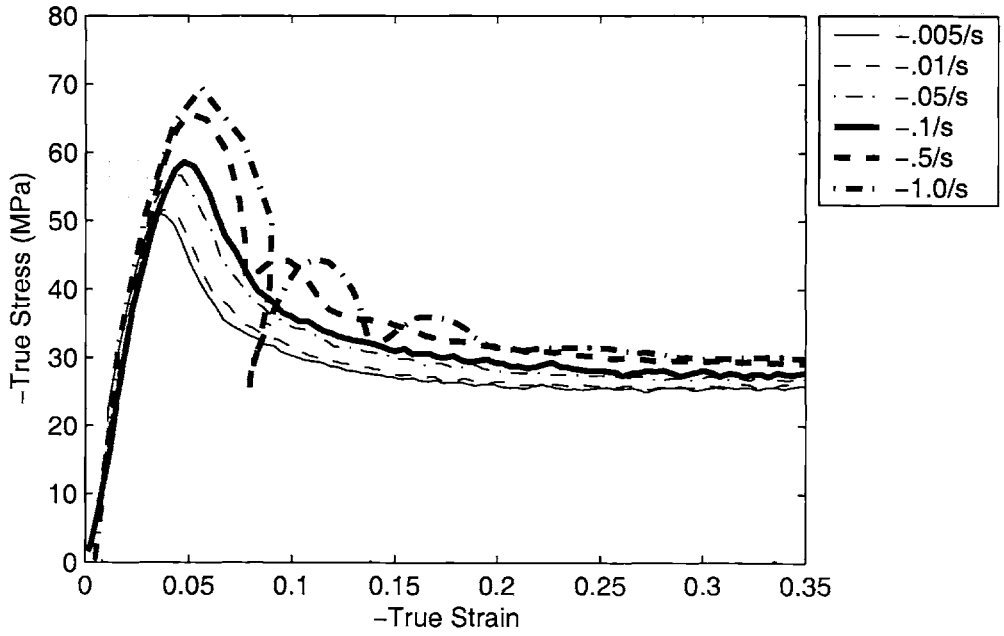

Figure 3-4: PET Uniaxial compression data, Temperature = 60 ° C, enlarged to show small strain data

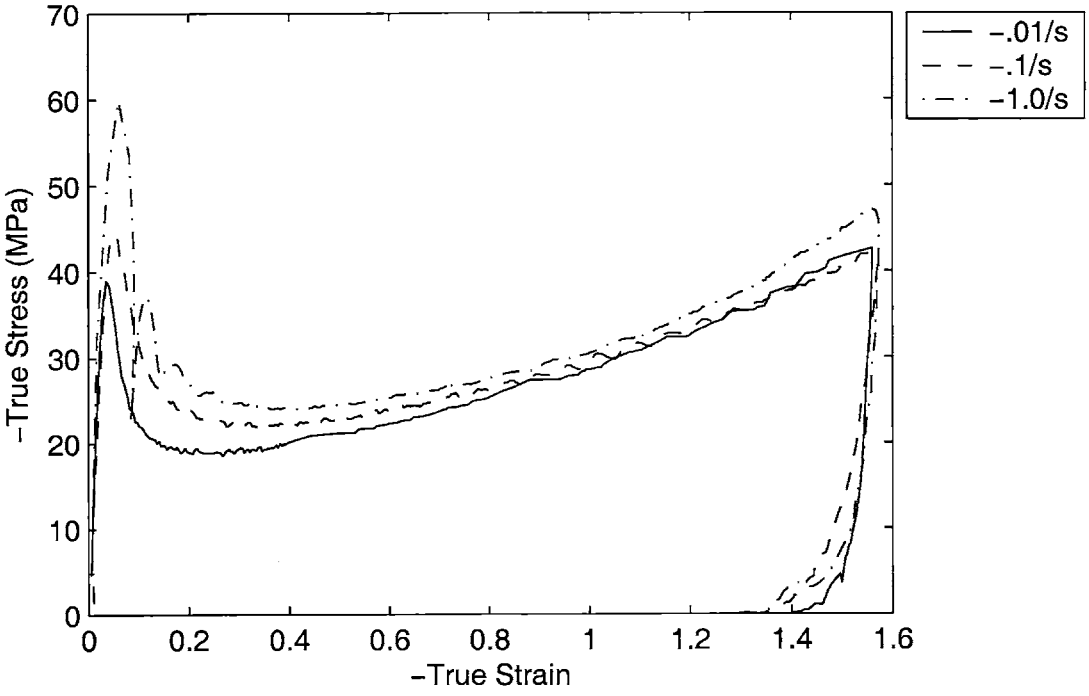

Figure 3-5: PET Uniaxial compression data, Temperature = 70 ° C

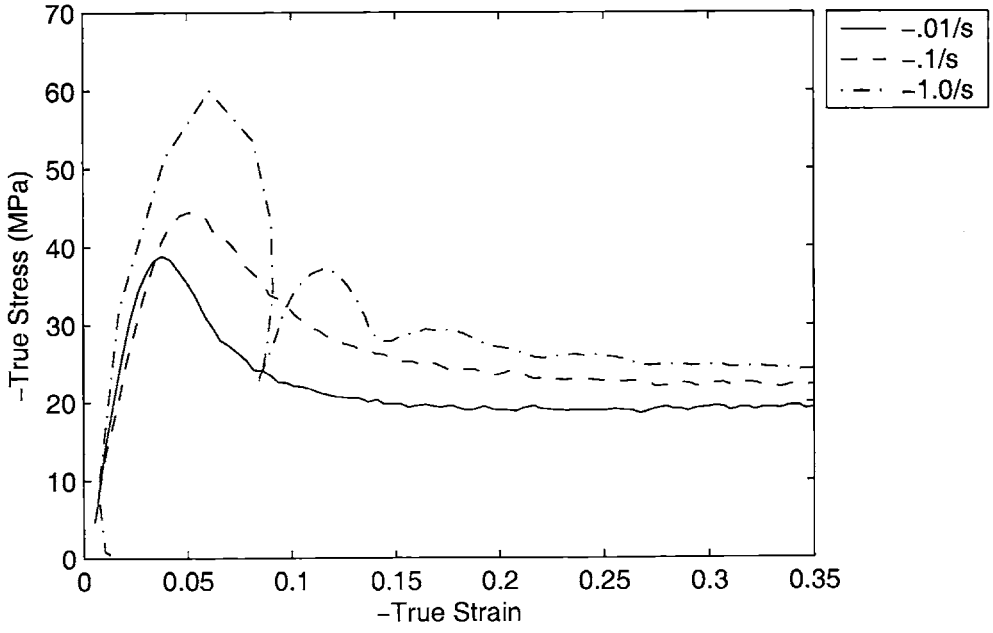

Figure 3-6: PET Uniaxial compression data, Temperature = 70 ° C, enlarged to show small strain data

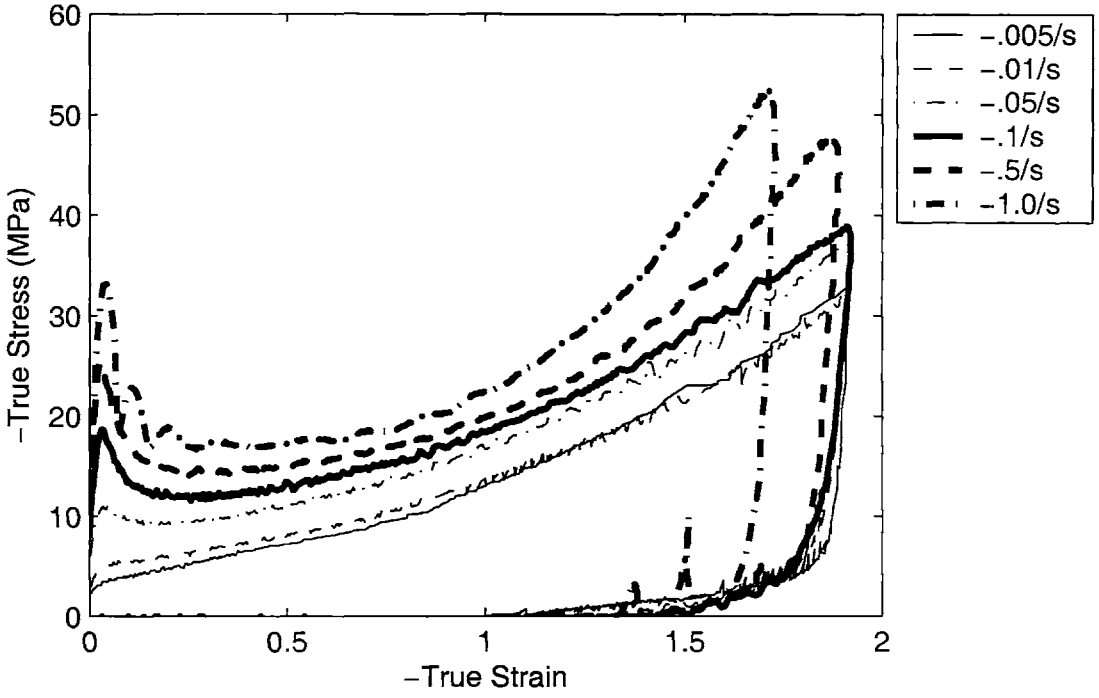

Figure 3-7: PET Uniaxial compression data, Temperature = 80 ° C

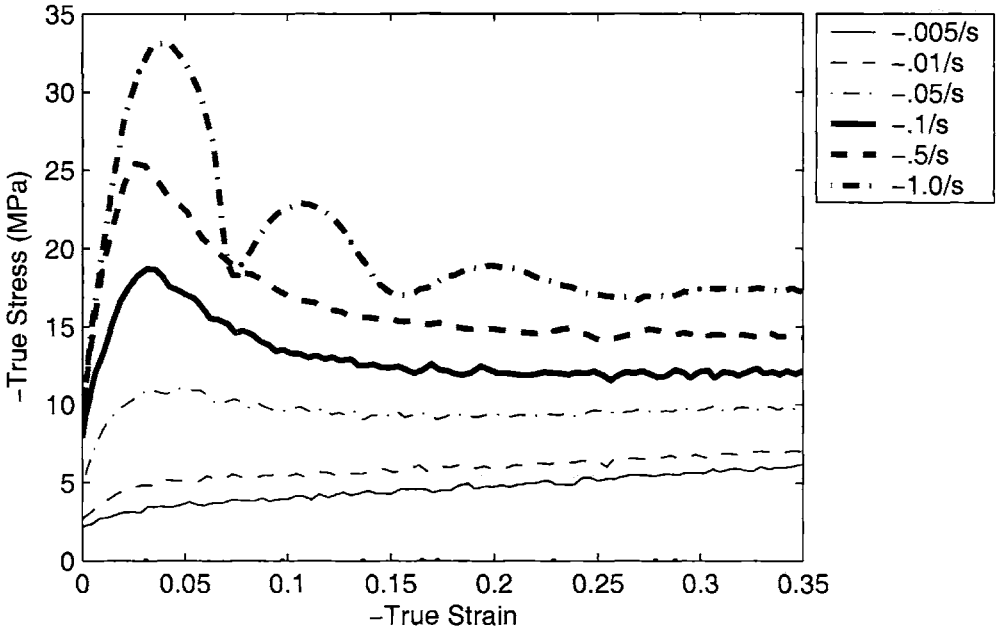

Figure 3-8: PET Uniaxial compression data, Temperature = 80 ° C, enlarged to show initial modulus and flow stress

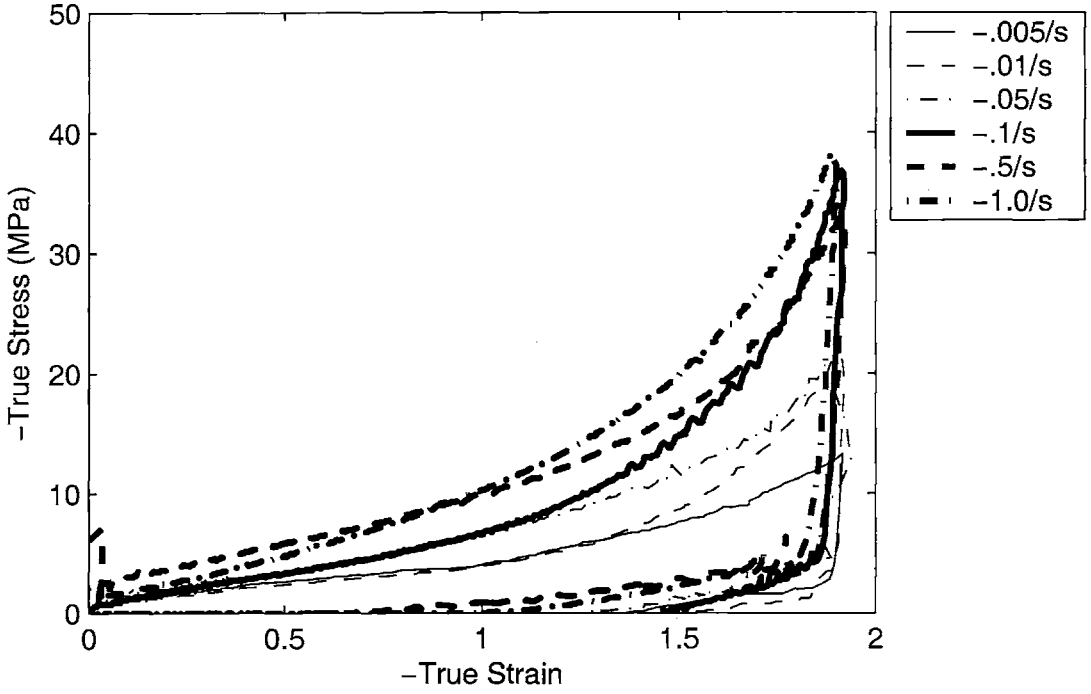

Figure 3-9: PET Uniaxial compression data, Temperature = 90 ° C

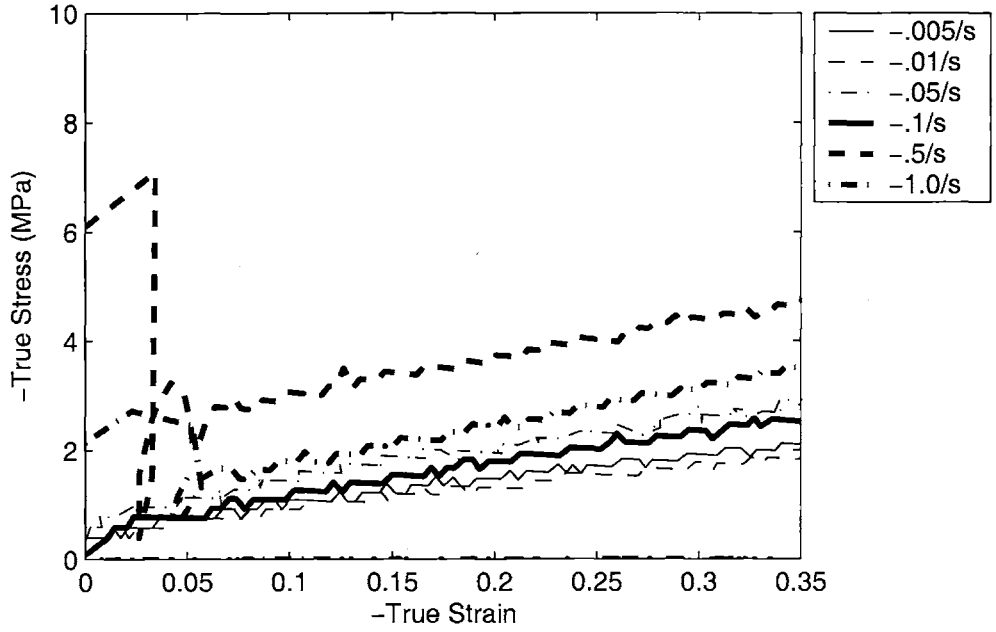

Figure 3-10: PET Uniaxial compression data, Temperature = 90 ° C, enlarged to show initial modulus and flow stress

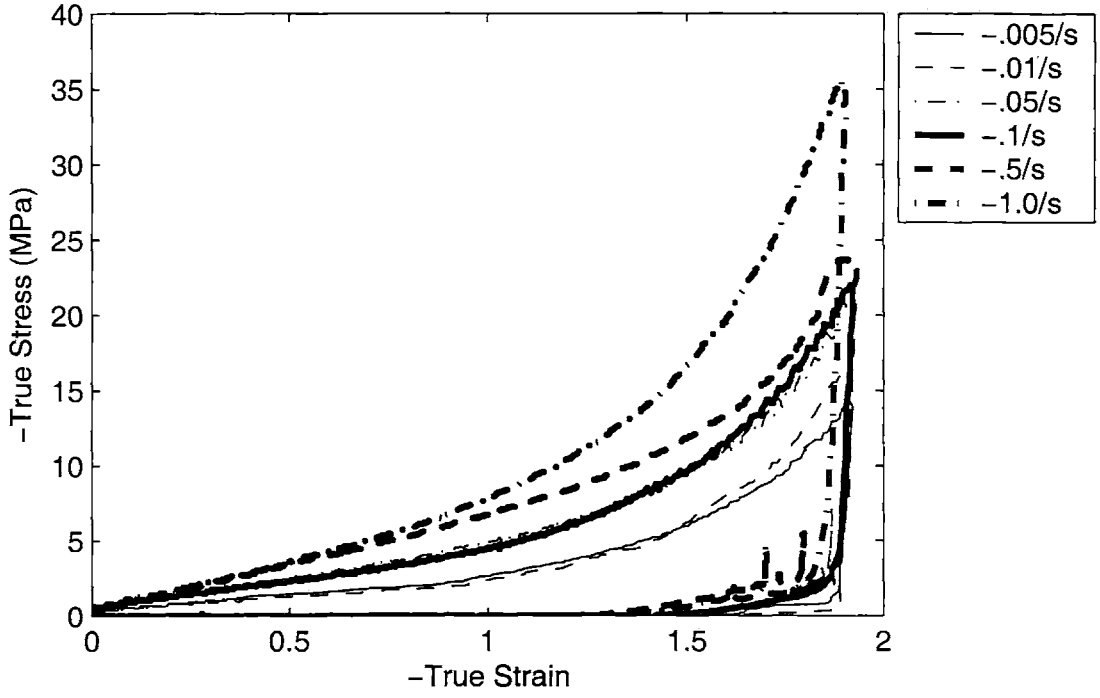

Figure 3-11: PET Uniaxial compression data, Temperature = 100 ° C

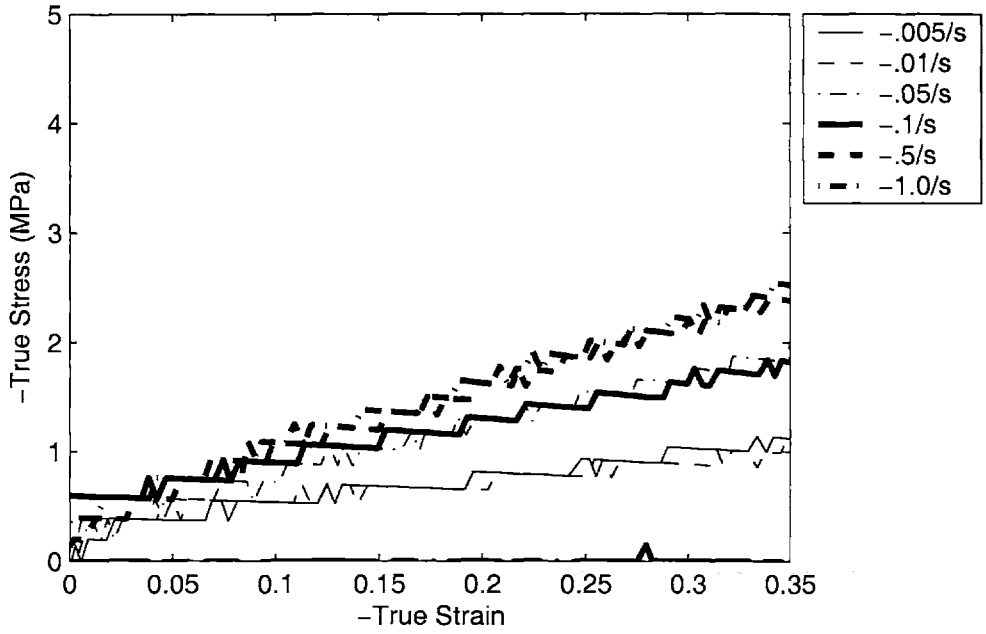

Figure 3-12: PET Uniaxial compression data, Temperature = 100 ° C, enlarged to show initial modulus and flow stress

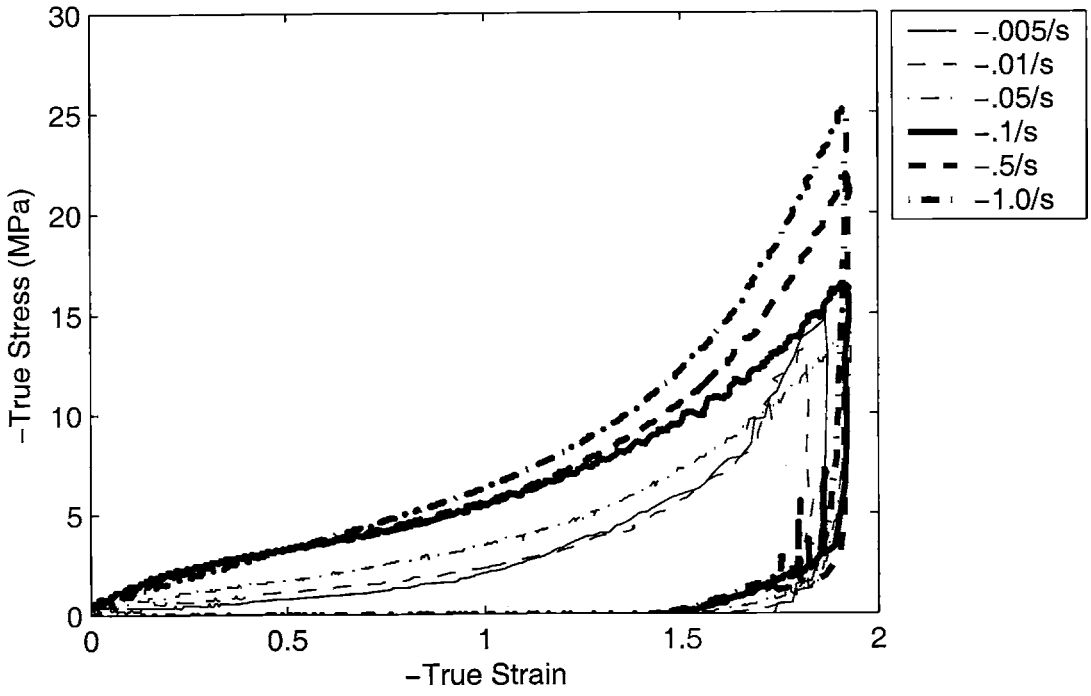

Figure 3-13: PET Uniaxial compression data, Temperature = 110 ° C

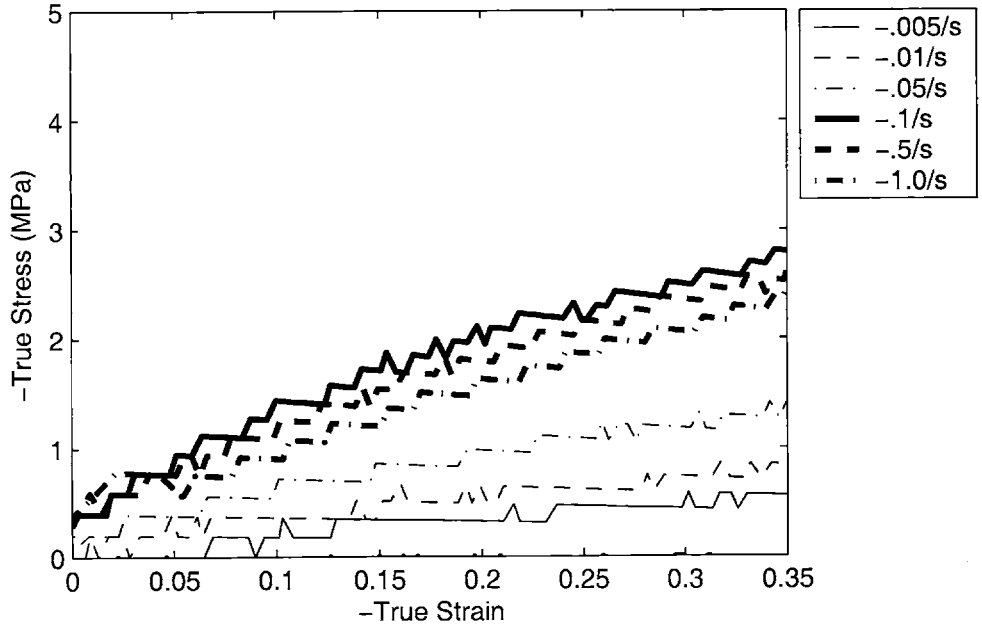

Figure 3-14: PET Uniaxial compression data, Temperature = 110 ° C, enlarged to show initial modulus and flow stress

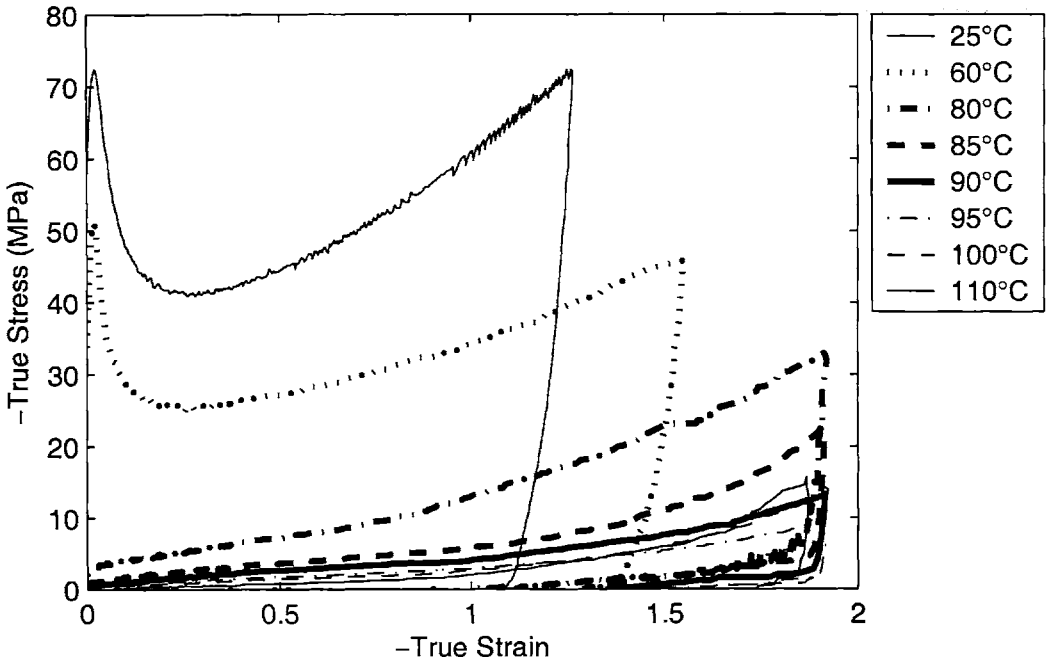

Figure 3-15: PET Uniaxial compression data, $\dot{\varepsilon}$ = -.005/s

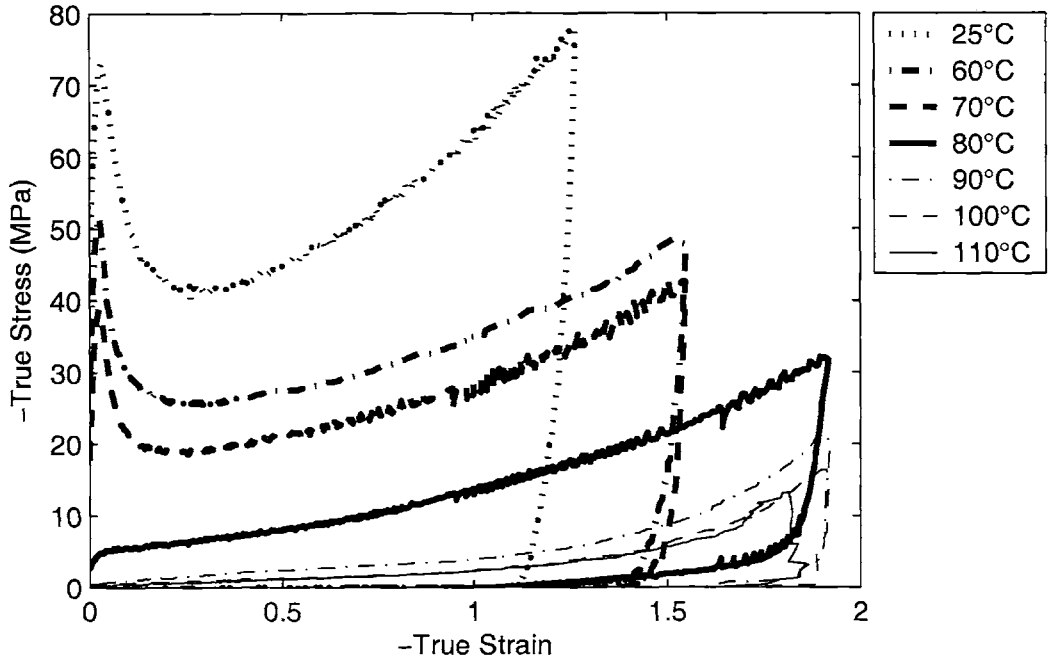

Figure 3-16: PET Uniaxial compression data, $\dot{\varepsilon}$ = -.01/s

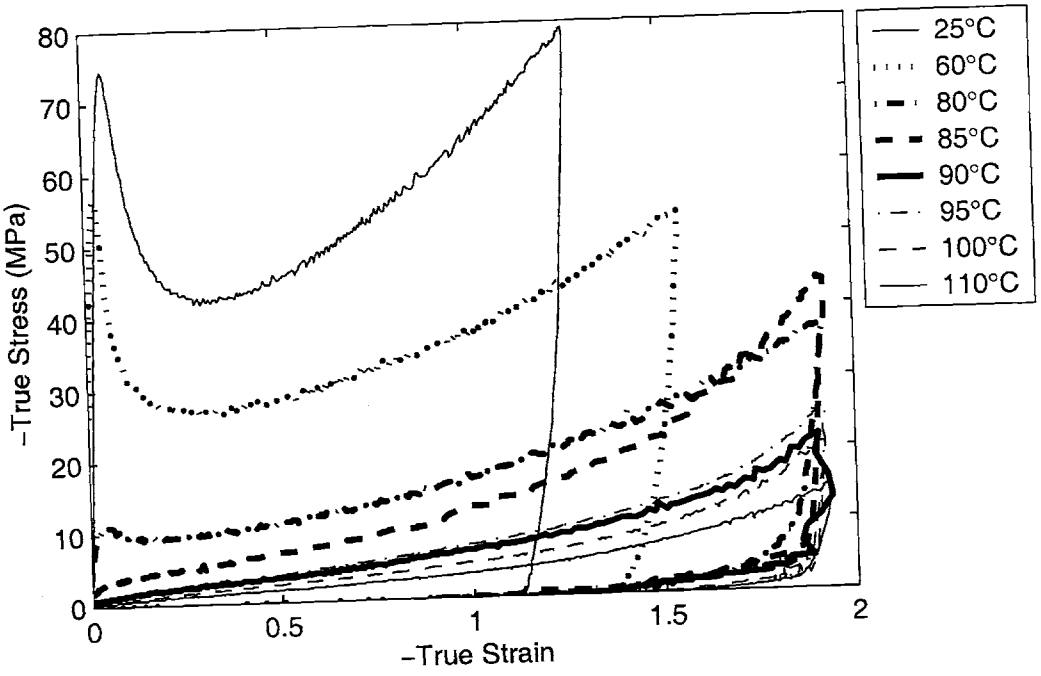

Figure 3-17: PET Uniaxial compression data, $\dot{\varepsilon}$ = -.05/s

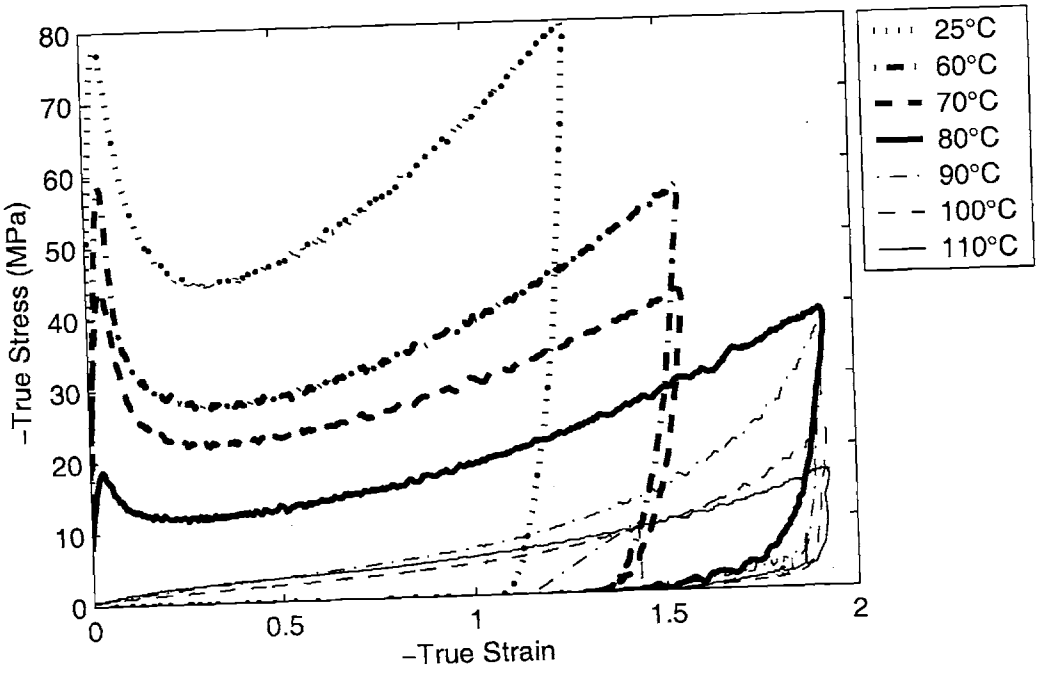

Figure 3-18: PET Uniaxial compression data, $\dot{\varepsilon}$ = -.1/s

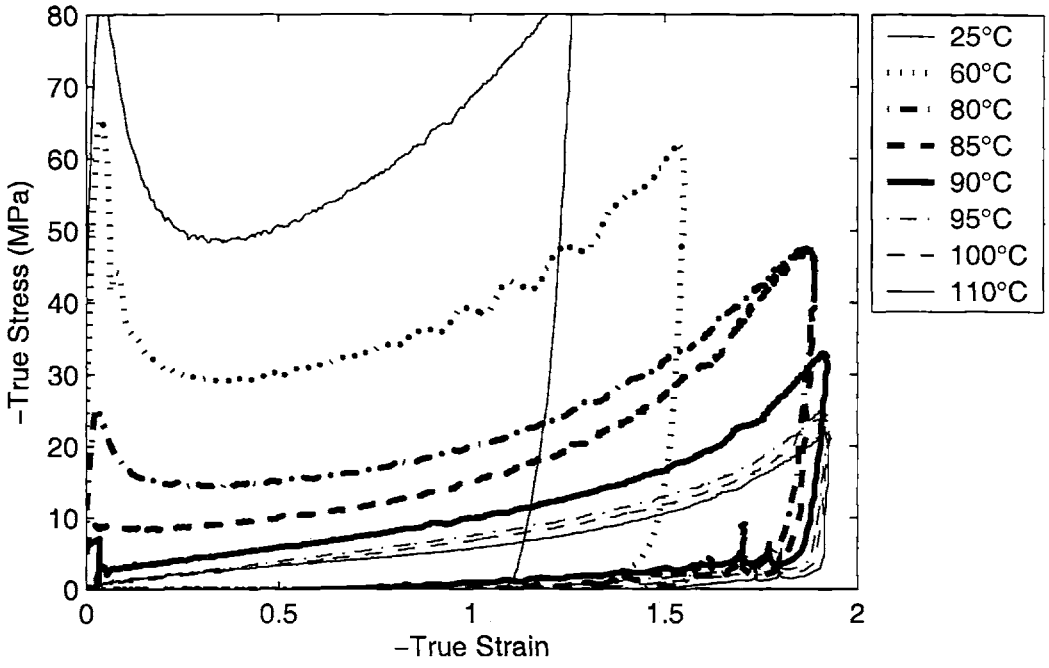

Figure 3-19: PET Uniaxial compression data, $\dot{\epsilon}$ = -.5/s

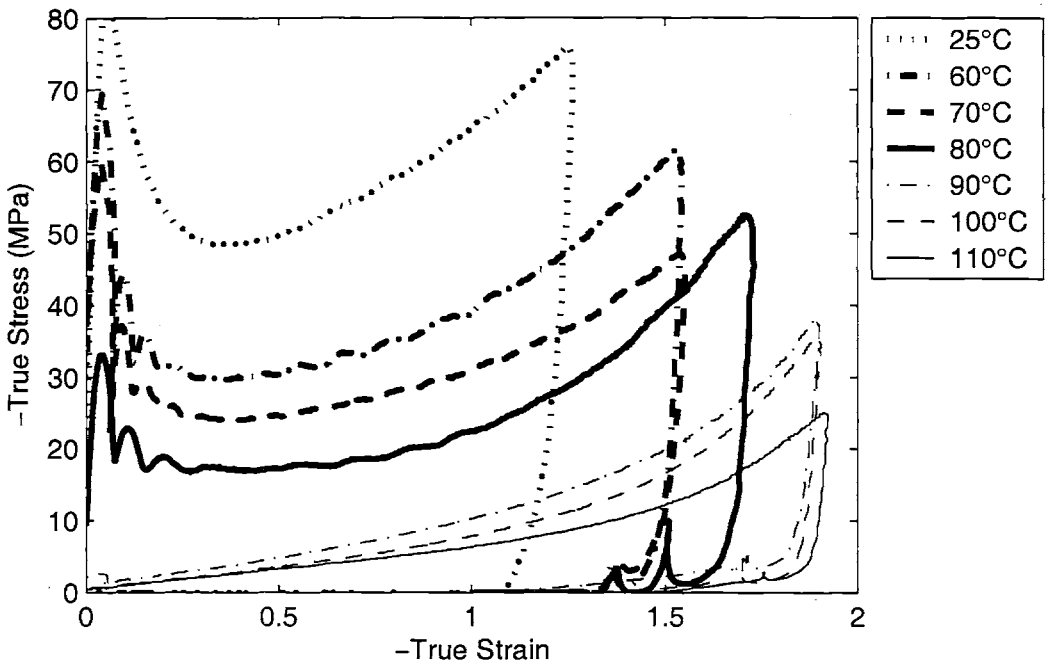

Figure 3-20: PET Uniaxial compression data, $\dot{\epsilon}$ = -1.0/s

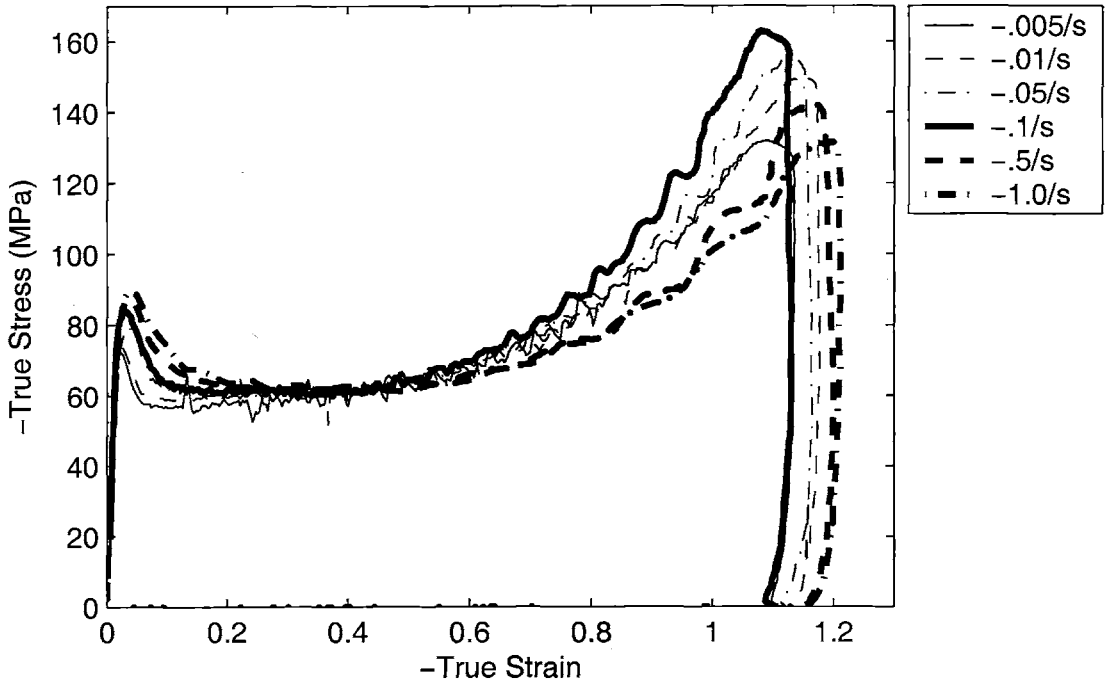

Figure 3-21: PET Plane strain compression data, Temperature = 25 ° C

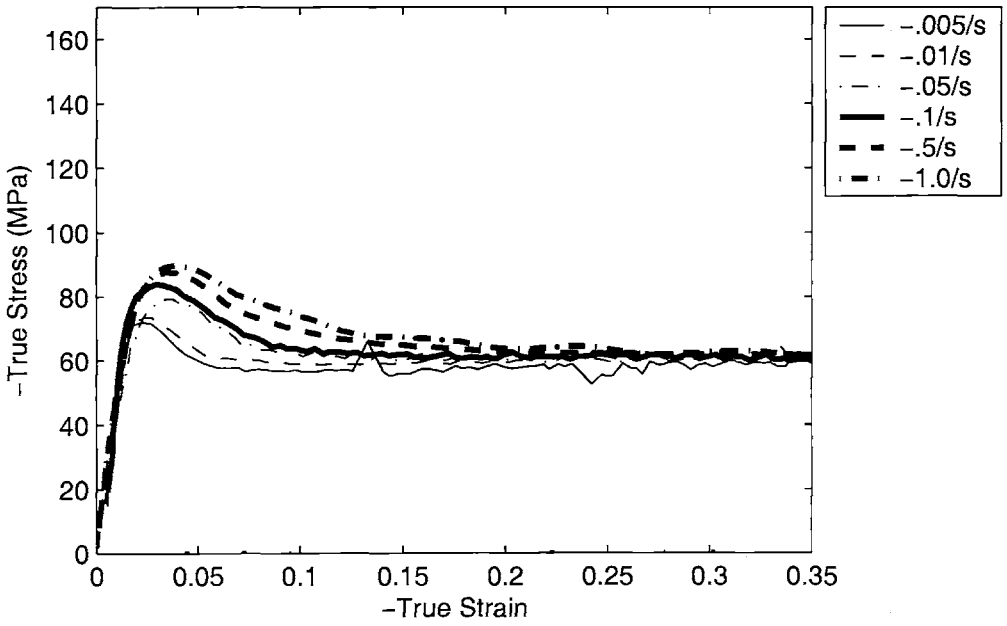

Figure 3-22: PET Plane strain compression data, Temperature = 25 ° C, enlarged to show small strain data

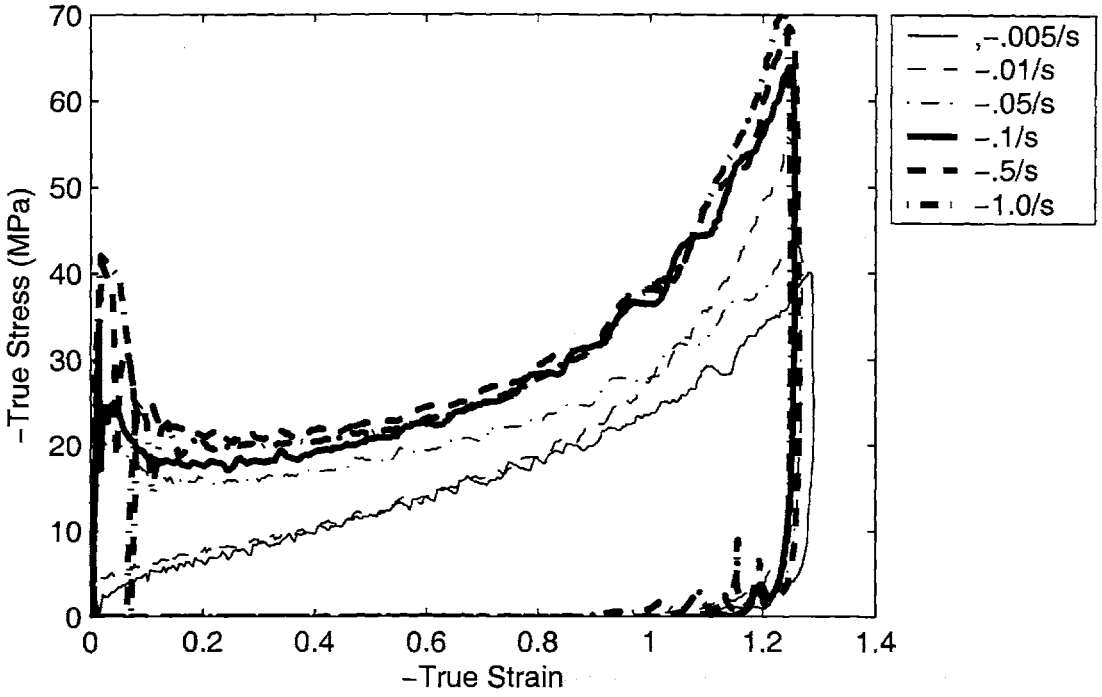

Figure 3-23: PET Plane strain compression data, Temperature = 80 ° C

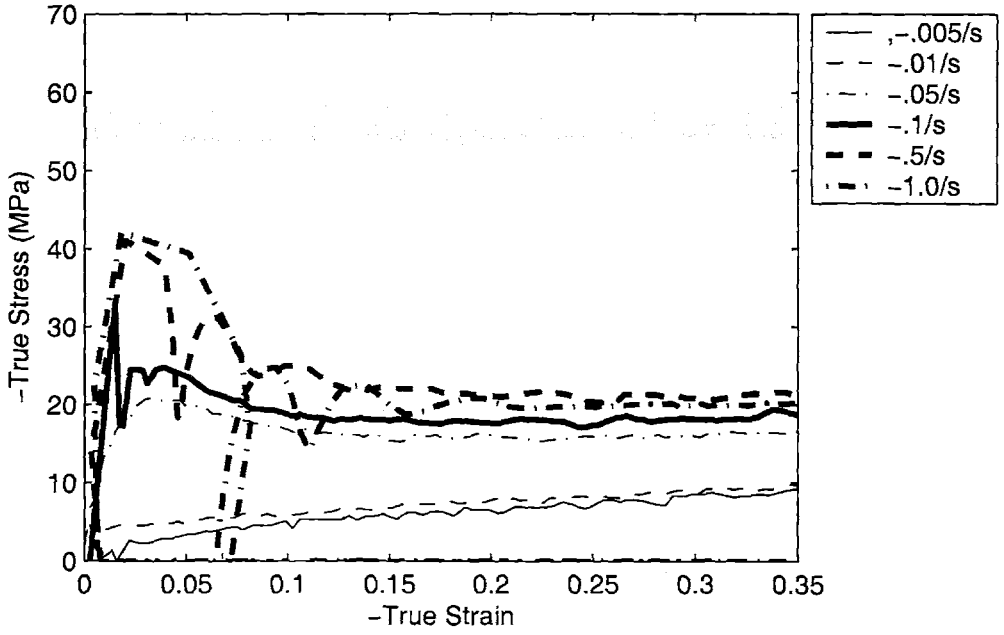

Figure 3-24: PET Plane strain compression data, Temperature = 80 ° C, enlarged to show small strain data

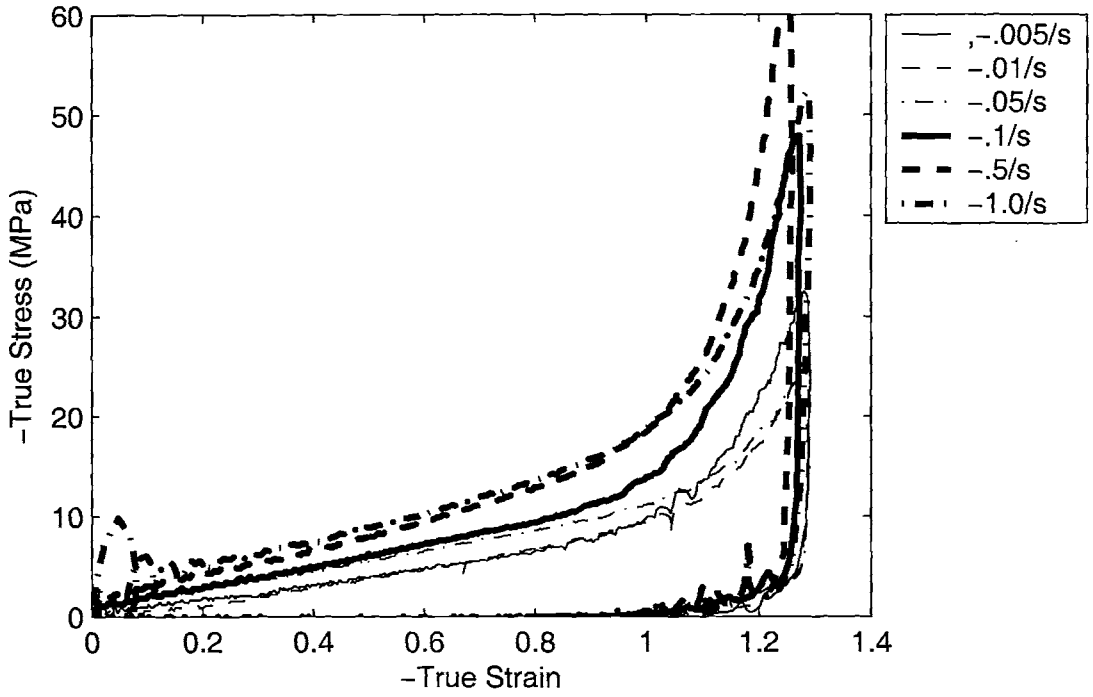

Figure 3-25: PET Plane strain compression data, Temperature = 90 ° C

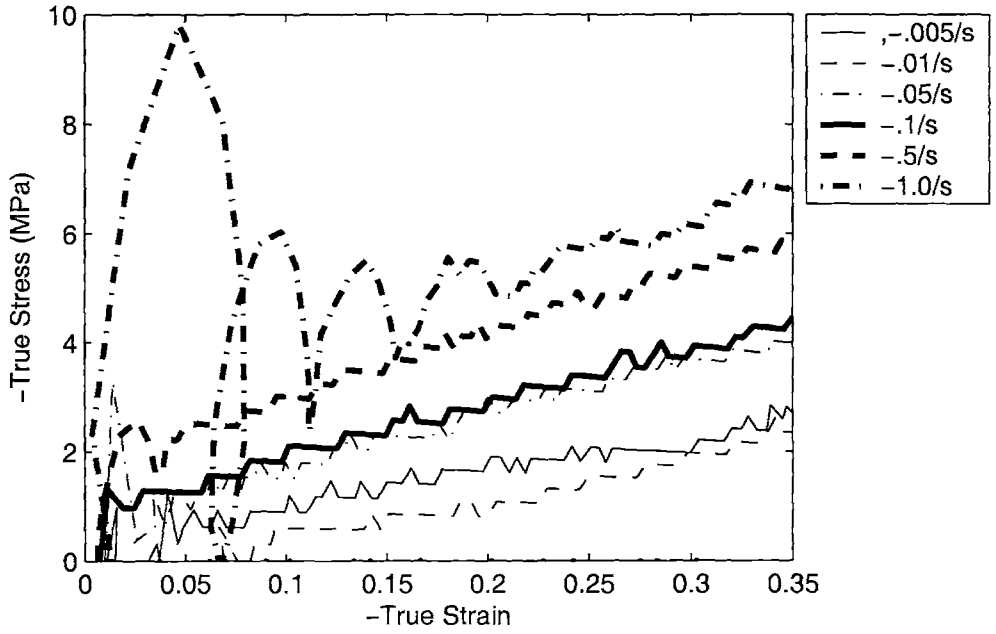

Figure 3-26: PET Plane strain compression data, Temperature = 90 ° C, enlarged to show small strain data

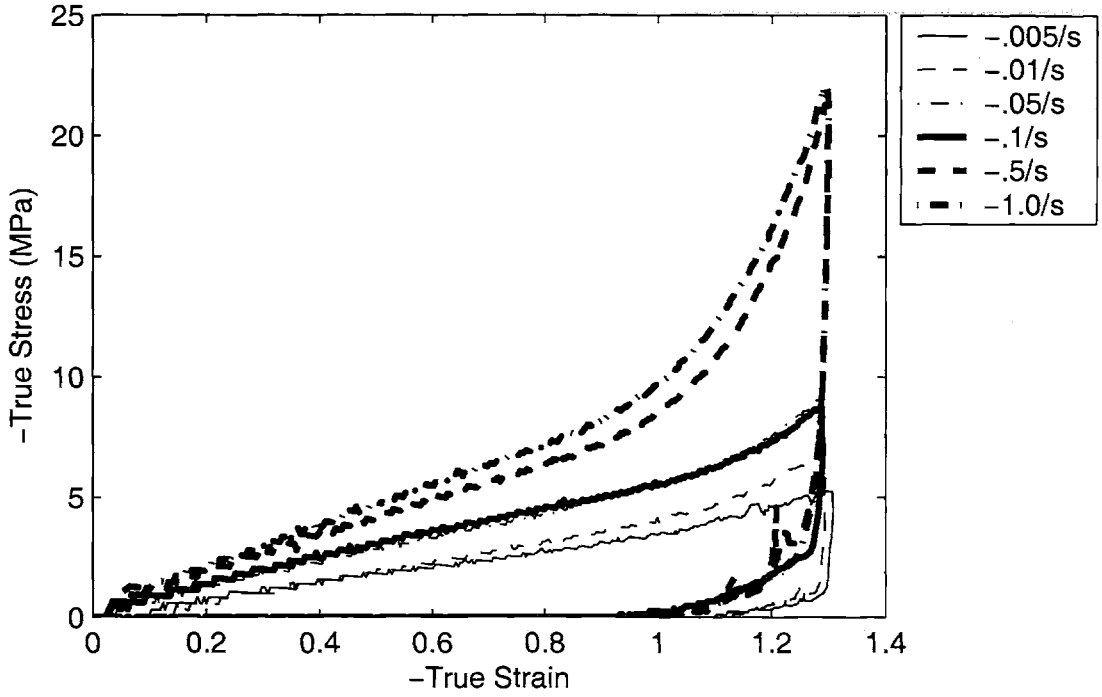

Figure 3-27: PET Plane strain compression data, Temperature = 100 ° C

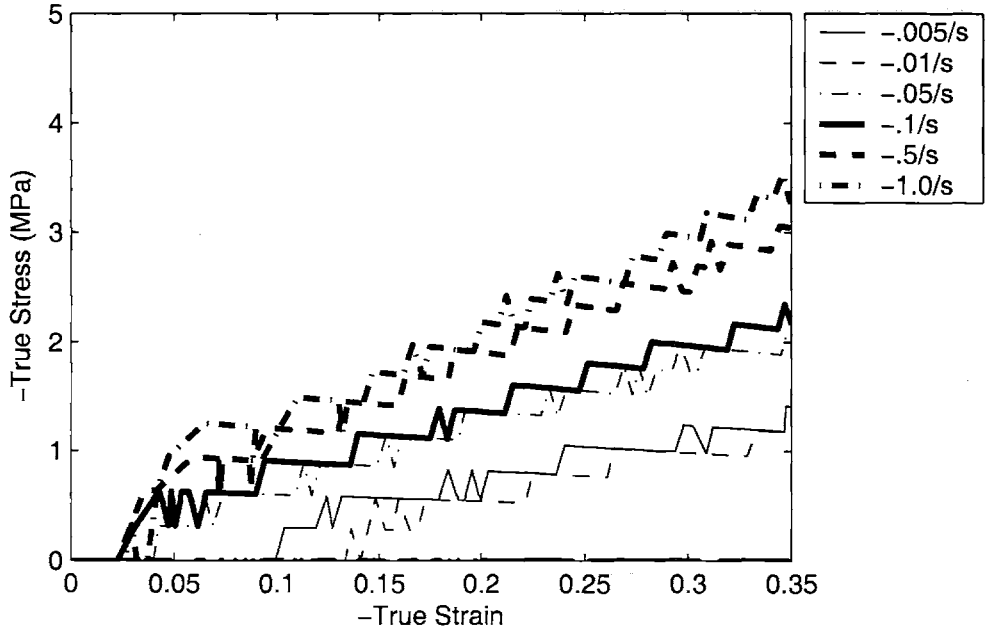

Figure 3-28: PET Plane strain compression data, Temperature = 100 ° C, enlarged to show small strain data

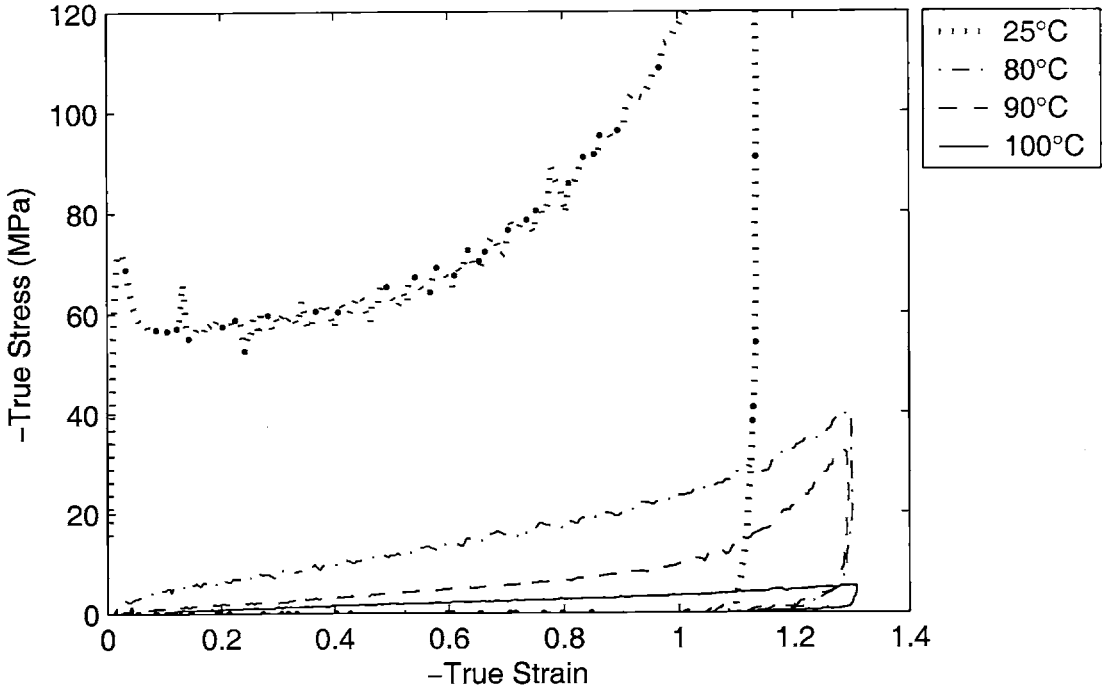

Figure 3-29: PET Plane strain compression data, $\dot{\varepsilon}$ = -.005/s

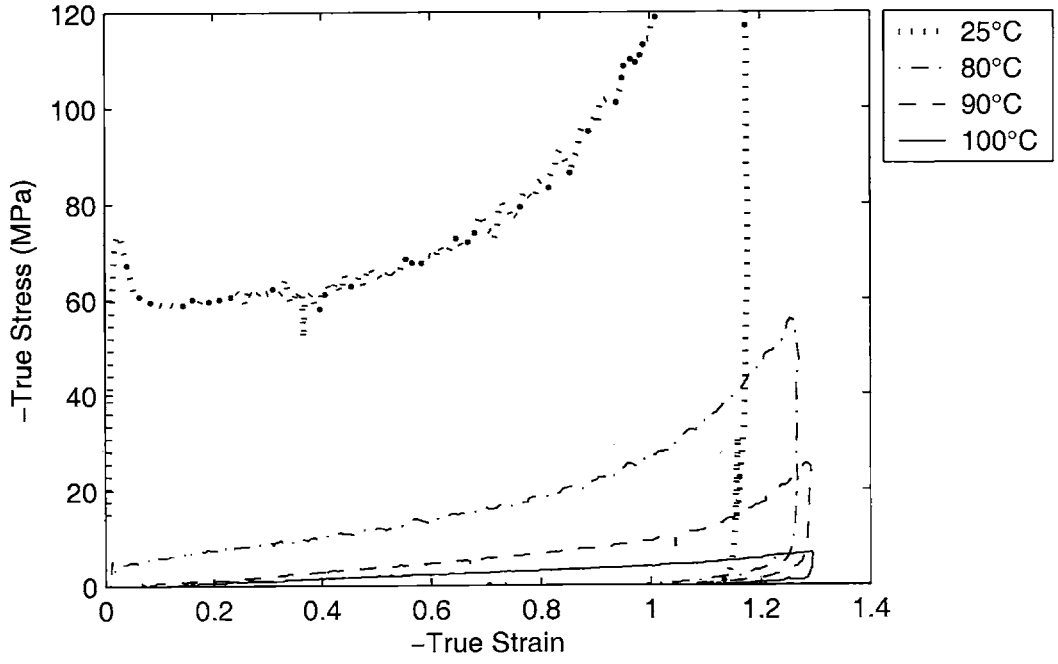

Figure 3-30: PET Plane strain compression data, $\dot{\varepsilon}$ = -.01/s

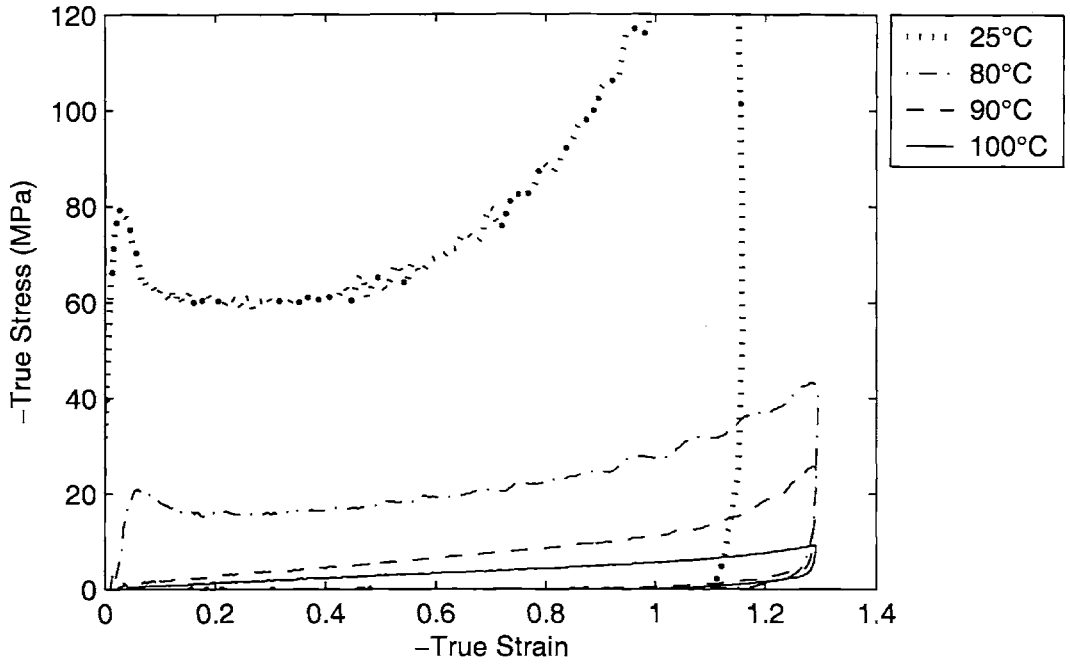

Figure 3-31: PET Plane strain compression data, $\dot{\varepsilon}$ = -.05/s

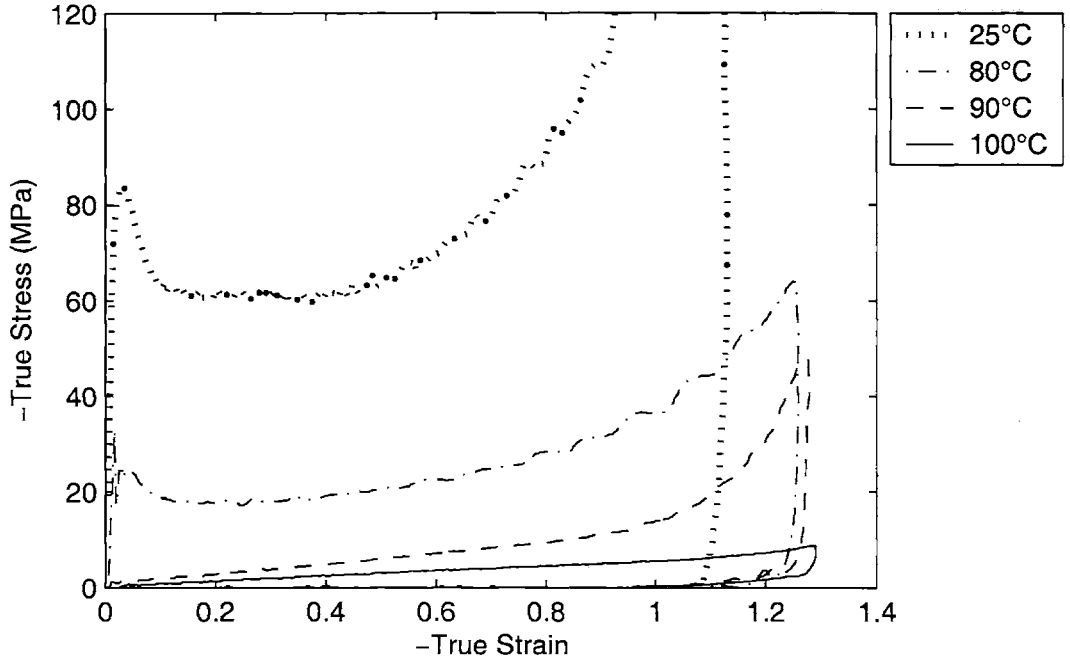

Figure 3-32: PET Plane strain compression data, $\dot{\varepsilon}$ = -.1/s

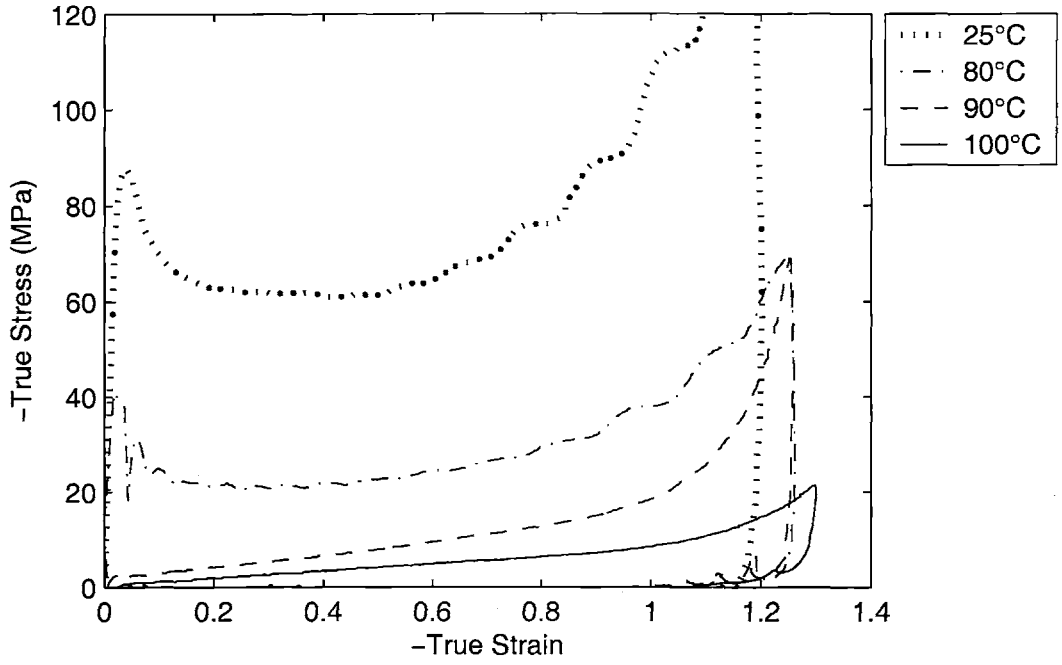

Figure 3-33: PET Plane strain compression data, $\dot{\varepsilon}$ = -.5/s

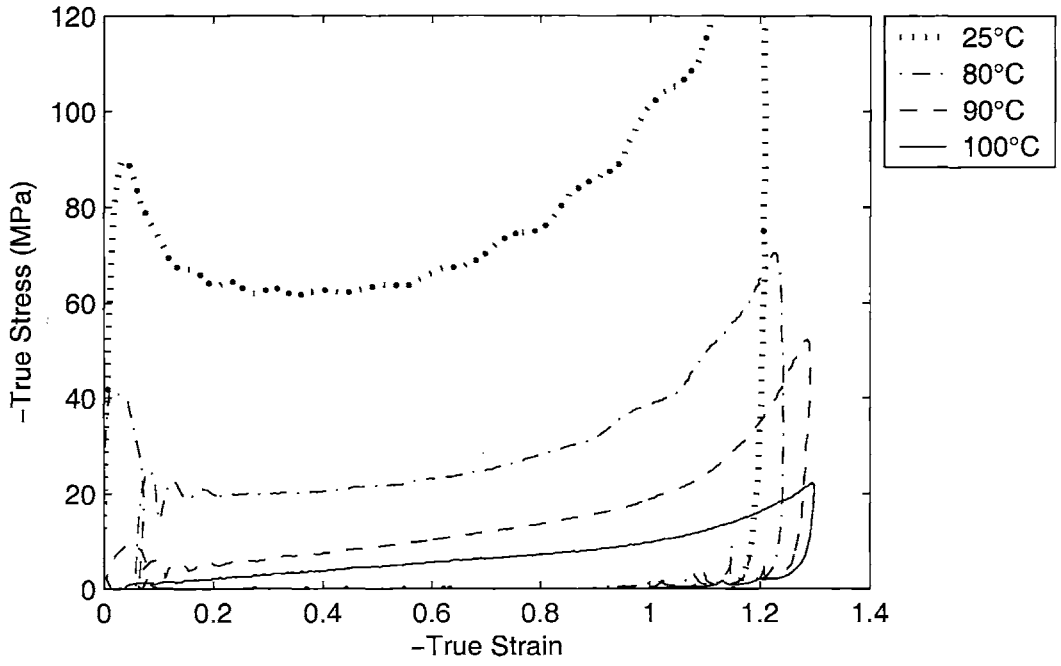

Figure 3-34: PET Plane strain compression data, $\dot{\varepsilon}$ = -1.0/s

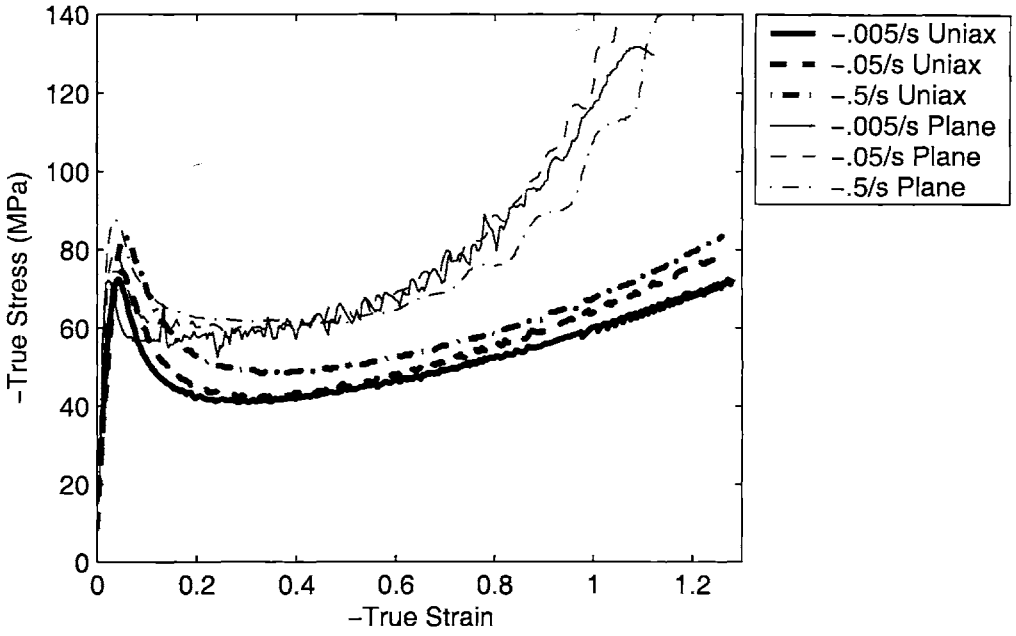

Figure 3-35: PET Uniaxial and plane strain compression data, Temperature = 25 ° C

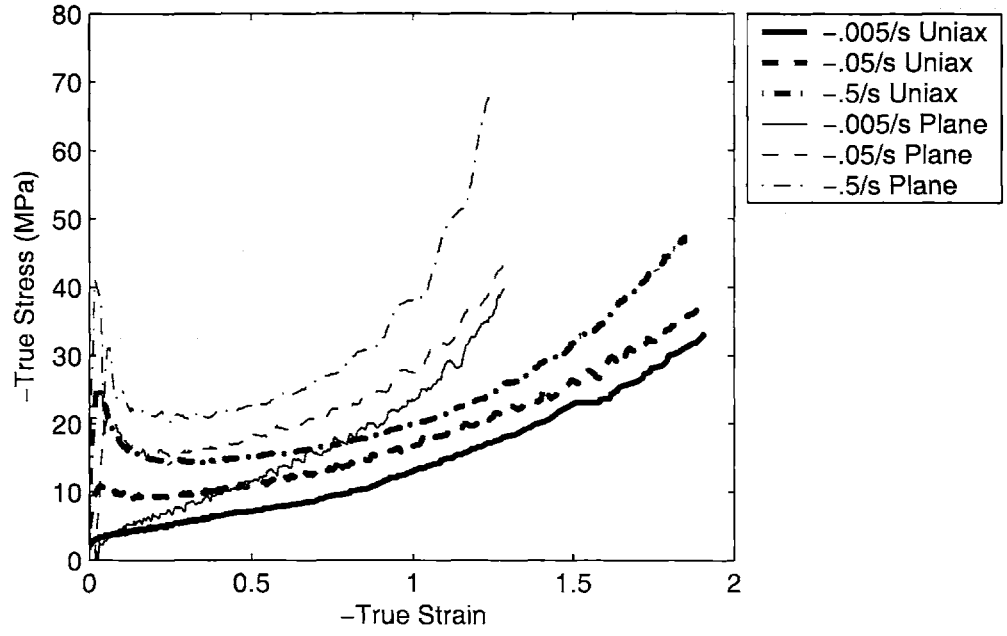

Figure 3-36: PET Uniaxial and plane strain compression data, Temperature = 80 ° C

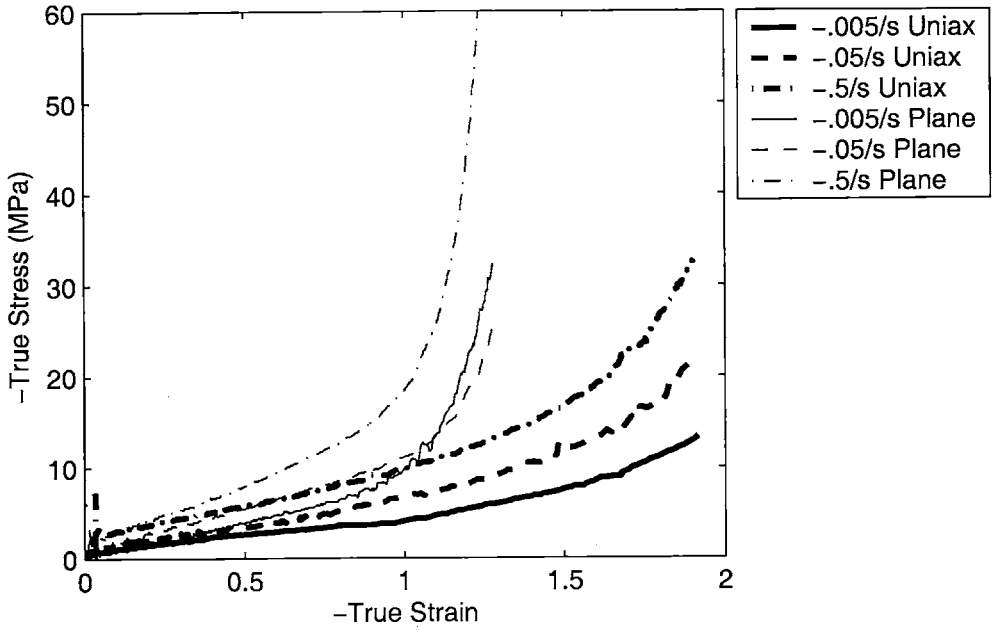

Figure 3-37: PET Uniaxial and plane strain compression data, Temperature = 90 ° C

3.5.2 Tension Experiments

Results from uniaxial tension tests on PET are shown in Figures 3-39 to 3-43. Figure 3-39 shows the measured load displacement curves for tension tests at temperatures of 90 ° C and 95 ° C. The general trends are as would be expected for the material behavior, i.e. the material becomes softer with increasing temperature. This softening is observed in terms of a more compliant initial modulus, a lower yield stress, and lower strain hardening. Deformation in these tensile experiments was overall homogeneous; no neck developed during deformation, rather, the entire specimen thinned until it broke or until the maximum extension allowed by the test equipment was reached.

Figure 3-40 shows the calculated nominal stress-stretch curves for the same data. Nominal stress is computed as simply the load divided by the initial area in the gauge length. Stretch is computed as the change in length (crosshead displacement) divided by the initial length (gauge length). The data can be further reduced to an averaged true stress-stretch curve by assuming uniform deformation and no volume change and

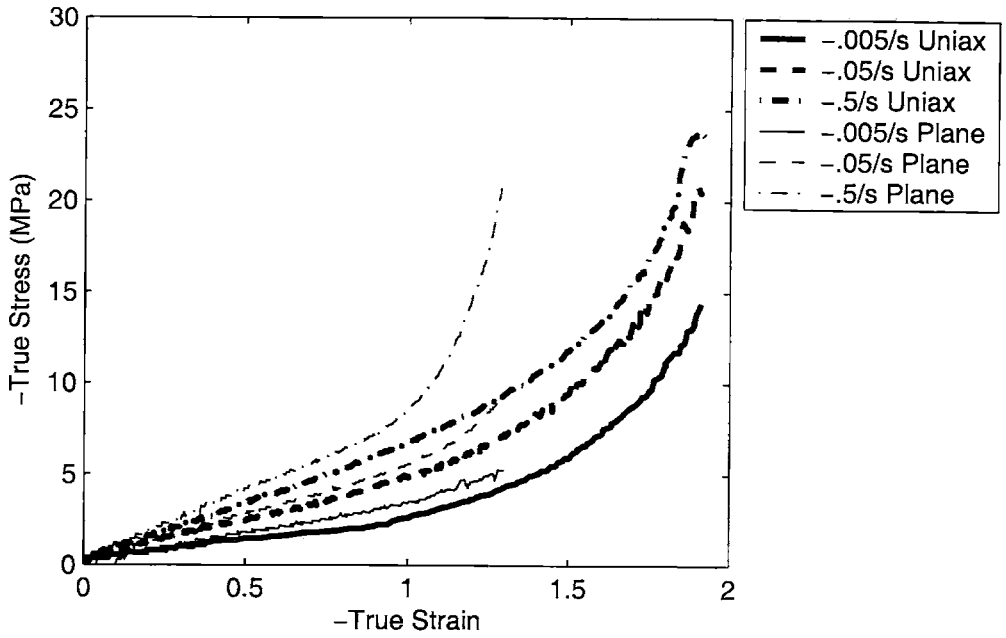

Figure 3-38: PET Uniaxial and plane strain compression data, Temperature = 100 ° C

thus the current area can be calculated knowing the axial stretch. Using this area to compute the stress gives the data in figures 3-41 to 3-43.

3.5.3 Biaxial Extension Experiments

Figure 3-44 shows the results of equibiaxial extension experiments conducted at 95 ° C, 100 ° C, and 105 ° C. These curves show that the material is more compliant with increasing temperature. True stress values were calculated assuming constant volume and uniform deformation.

Figures 3-45 to 3-47 show the results of constrained width tension experiments conducted at 95 ° C, 100 ° C, and 105 ° C. These curves again show that the material is more compliant with increasing temperature. True stress values were calculated assuming constant volume and uniform deformation.

An example of a sequential biaxial stretching experiment is shown in figures 3-48 and 3-50. In these experiments samples were stretched to a nominal stretch of 2 in the first stretch direction. In figure 3-48, engineering stress and strain are plotted

as a function of time. In the stress-time plot, solid lines are stress values in the first stretching direction (X-direction) and dashed lines are the stress in the second (Y-) direction. In figure 3-49 true stress and true strain curves are plotted. The calculations are done assuming constant volume and uniform deformation. In figure 3-50 true stress and stretch ratio are plotted as a function of time.

The effect of temperature is to cause lower stress levels throughout the experiment. It should be noted that in the two test samples illustrated here, the sample drawn at 100 ° C broke rather early in the experiment, so it is unclear the effect of temperature at large extensions.

Similar curves are shown in figures 3-51 to 3-53 but in these tests, the material was stretched to a nominal stretch of 3 in the first direction.

In each of these curves, it can be seen by comparison to corresponding figures in Chapter 2, that the PET data rises to a highter stress level at large strains than the PETG. This is generally attributed to strain-induced crystallization in PET. It should be noted, however, that the PETG curves do exhibit strain hardening, but the PETG films tended to fracture quite early in the experiments. It therefore cannot be concluded from these biaxial extension curves alone that the difference is due to crystallization. It could simply be due to a lower fracture resistance in PETG.

3.6 Summary of PET Observations

In this chapter we have observed the rate, temperature, and strain state dependence of the mechanical behavior of PET. In compression, the material exhibits four characteristic regions above the glass transition temperature: (1) a relatively stiff initial modulus, (2) a rollover to flow at around 2 MPa, (3) a gradual stiffening through the moderate strain regime, and (4) a dramatic upturn in strain at very large strain levels. Each of these features depends strongly on the temperature and rate of deformation. The initial modulus, flow stress, and initial hardening modulus all increase with decreasing temperature or increasing strain rate. The dramatic upturn in strain occurs at earlier strain levels with increasing strain rate or decreasing temperature. The ma-

terial also exhibits a stiffer response and an earlier upturn in the stress-strain curve in plane strain compression than in uniaxial compression. The tensile experiments illustrate similar temperature effects on the material behavior.

3.7 Comparison of PET and PETG Behavior

Careful comparison of the data in Chapter 2 for PETG with the previous sections for PET show that the overall mechanical behavior of PET and PETG are quite simiilar. Both materials exhibit all four stress-strain features above T_g and have similar dependencies on temperature, strain rate, and strain state. A few figures representing this data will be repeated here for comparison purposes. In figures 3-54 and 3-55 a similar dependence on strain rate is observed for the two materials. With an increase in strain rate, both materials exhibit a stiffer initial modulus, higher flow stress, increased strain hardening, and an earlier dramatic upturn in the stress-strain curve. Figures 3-56 and 3-57 show the temperature dependence of the behavior in the two materials. With increasing temperature, both materials exhibit a decrease in initial modulus and flow stress, less strain hardening, and the dramatic strain hardening is postponed to higher strain levels. Figures 3-58 through 3-61 show the state of strain dependence of PETG and PET. In both materials, the response of the material is stiffer in plane strain compression than in uniaxial compression. In PET it appears that there is a more dramatic increase in the strain hardening in plane strain compression. This is especially visible in the 90 $^\circ$ C data (figure 3-59. This is likely due to strain-induced crystallization or to the development of some highly ordered mesophase which is able to occur in PET, but not in PETG. Otherwise, the stress-strain behavior of the two materials is nearly identical.

An additional difference in the two materials is seen in extensional deformation modes, as shown in figures 3-62 and 3-63. PETG is unable to sustain deformations as large as PET without fracturing first. It is unclear whether this is due to strain-induced crystallization occuring in PET or if it is due to a lower fracture resistance in PETG.

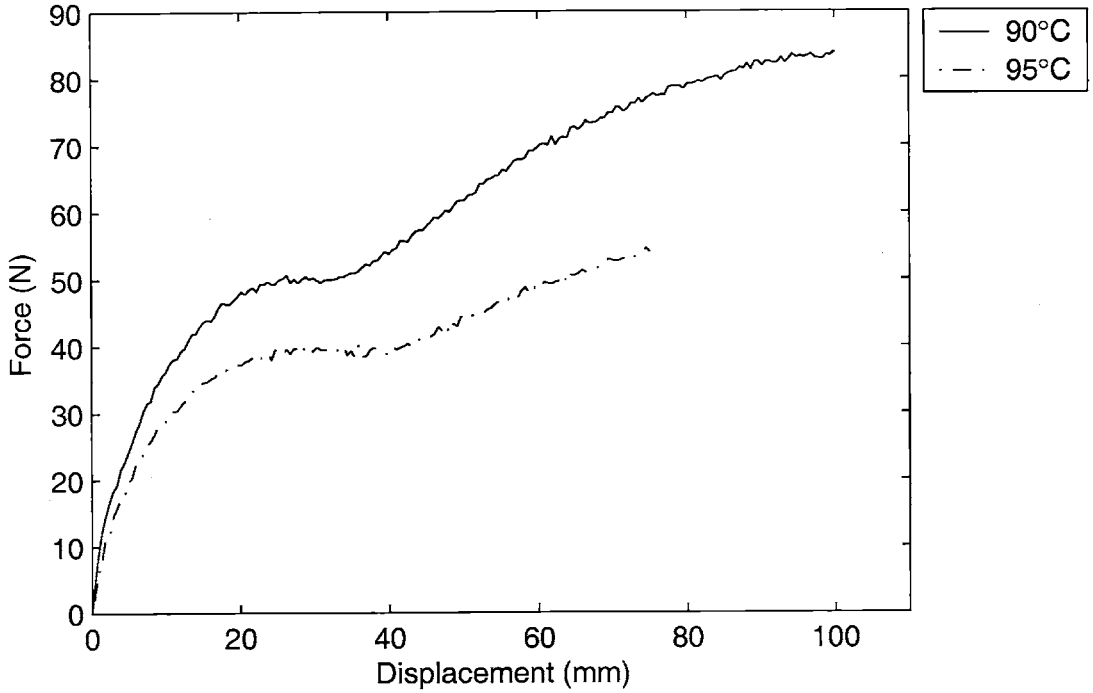

Figure 3-39: PET Tensile experiments, load-displacement

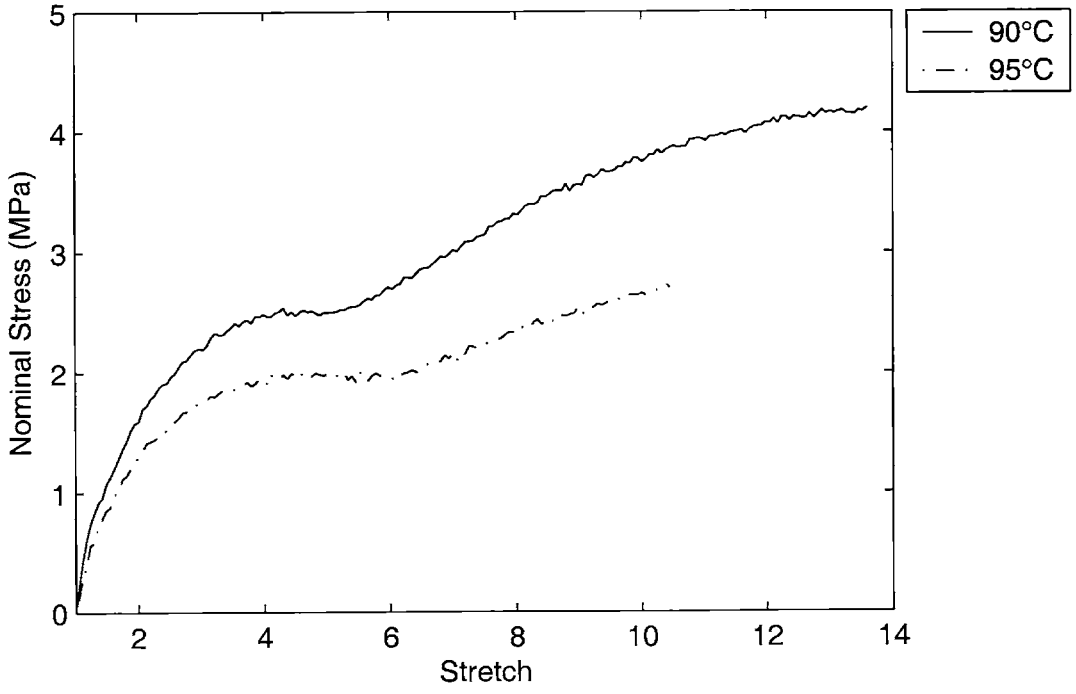

Figure 3-40: PET Tensile experiments, nominal stress-stretch

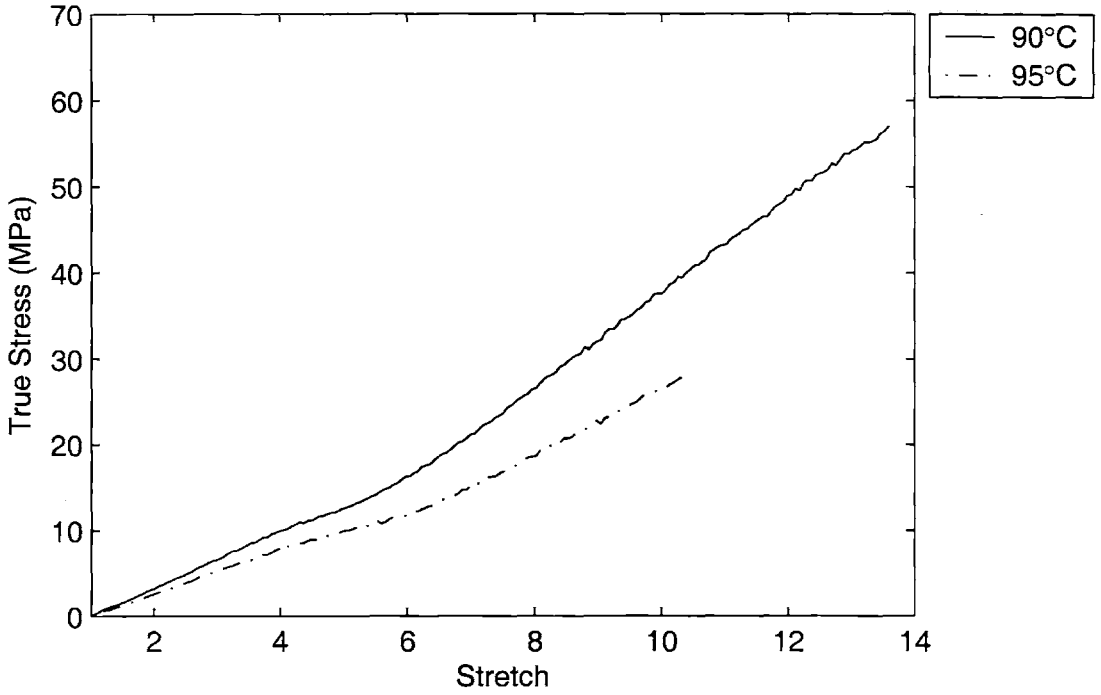

Figure 3-41: PET Tensile experiments, calculated true stress-stretch

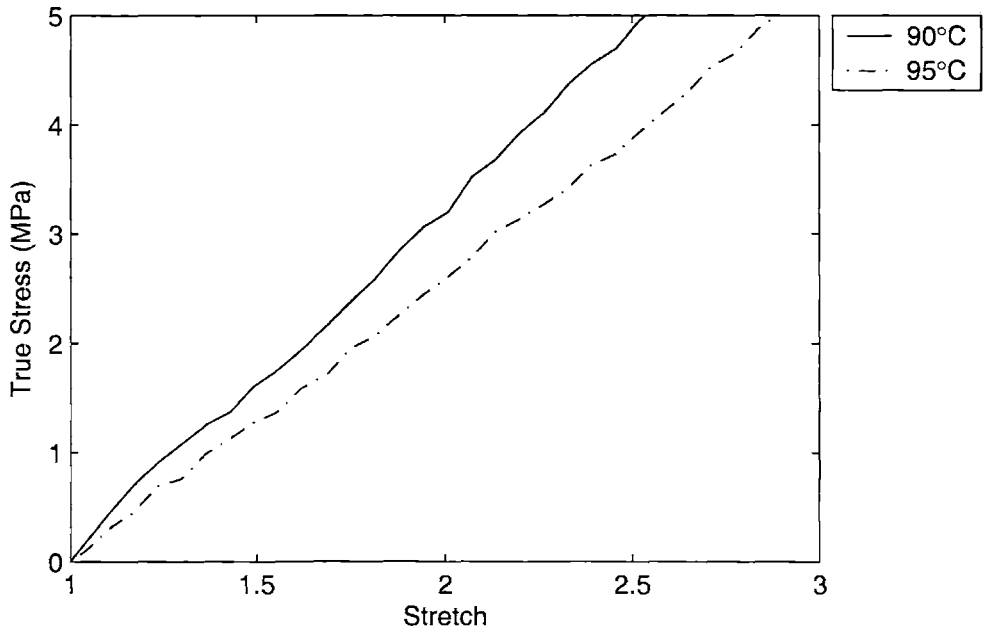

Figure 3-42: PET Tensile experiments, calculated true stress-stretch, enlarged

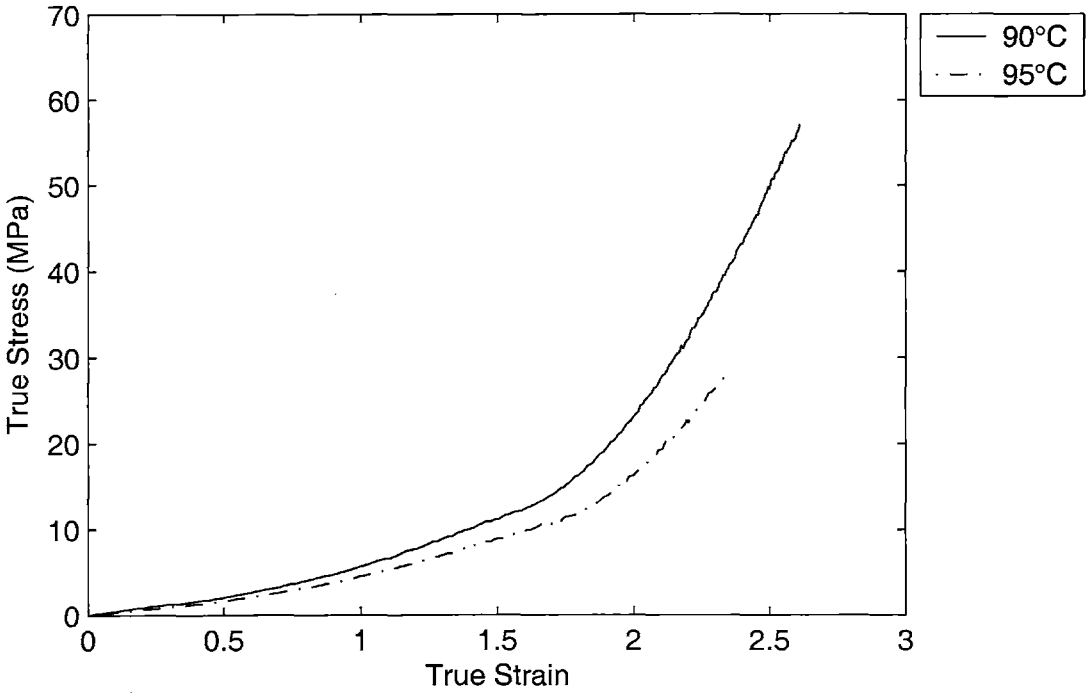

Figure 3-43: PET Tensile experiments, calculated true stress-true strain

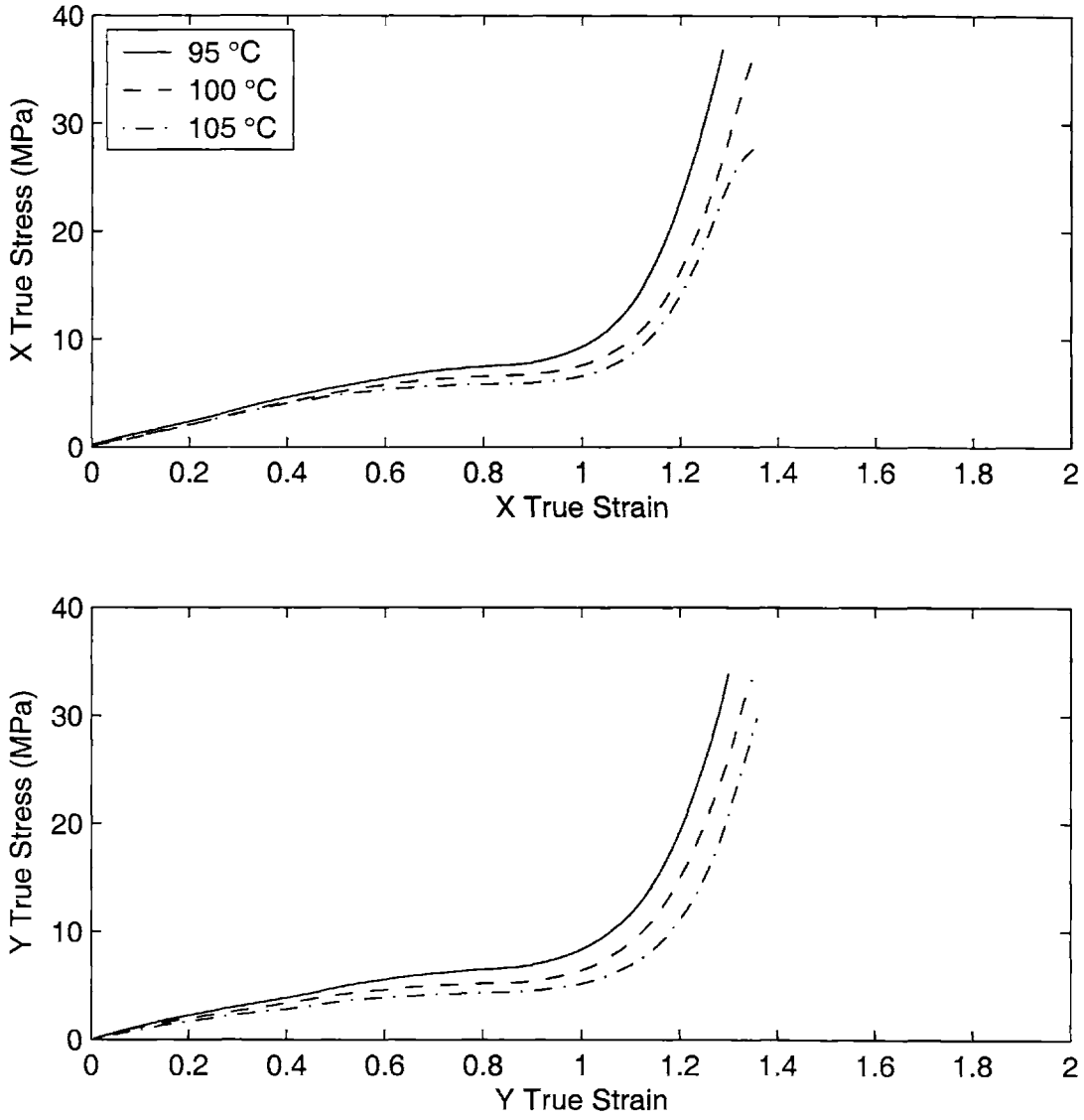

Figure 3-44: PET Equibiaxial extension, true stress-true strain, du/dt = 14 in/sec

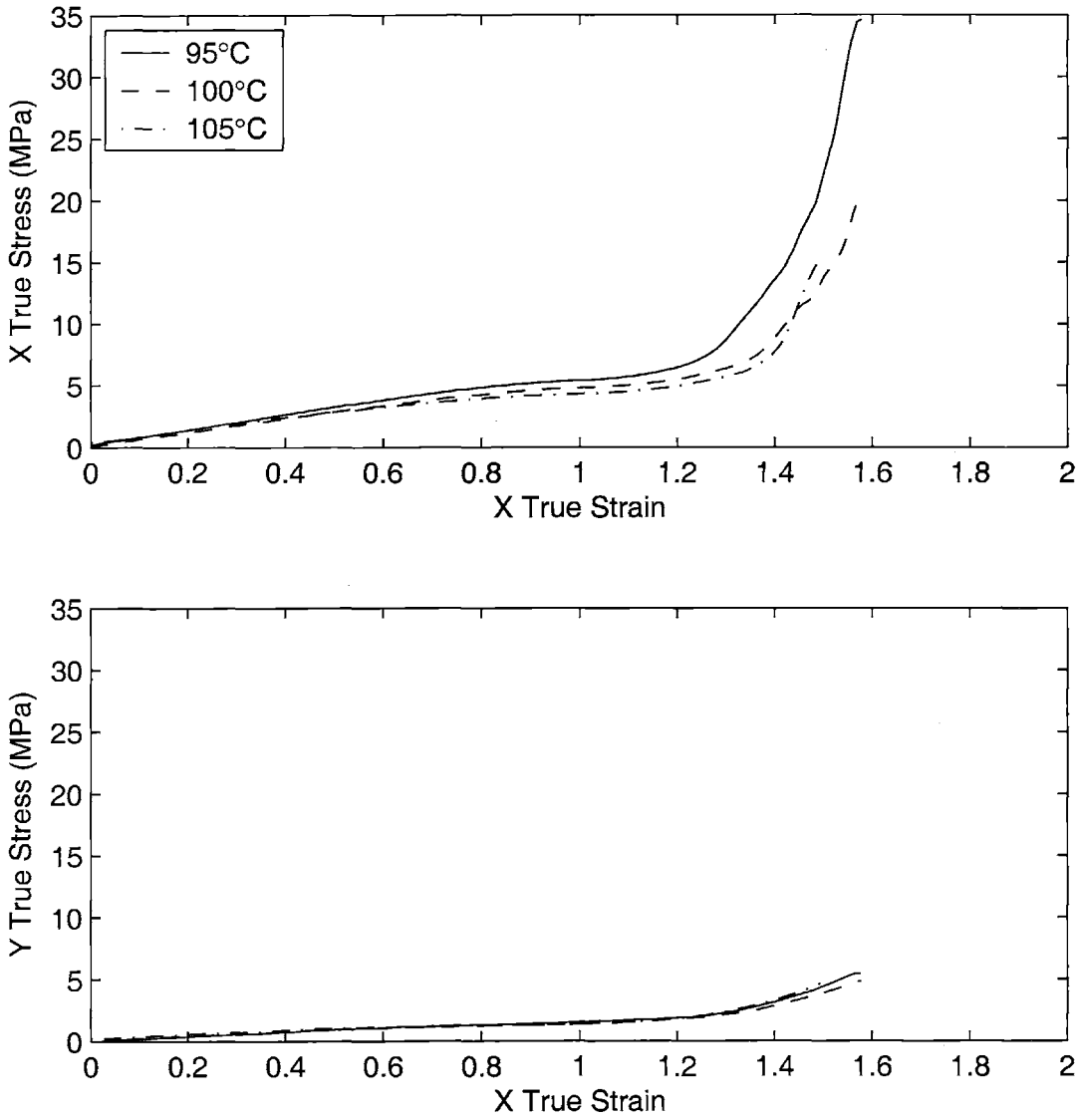

Figure 3-45: PET Constrained width tension, true stress-true strain, du/dt = 14 in/sec

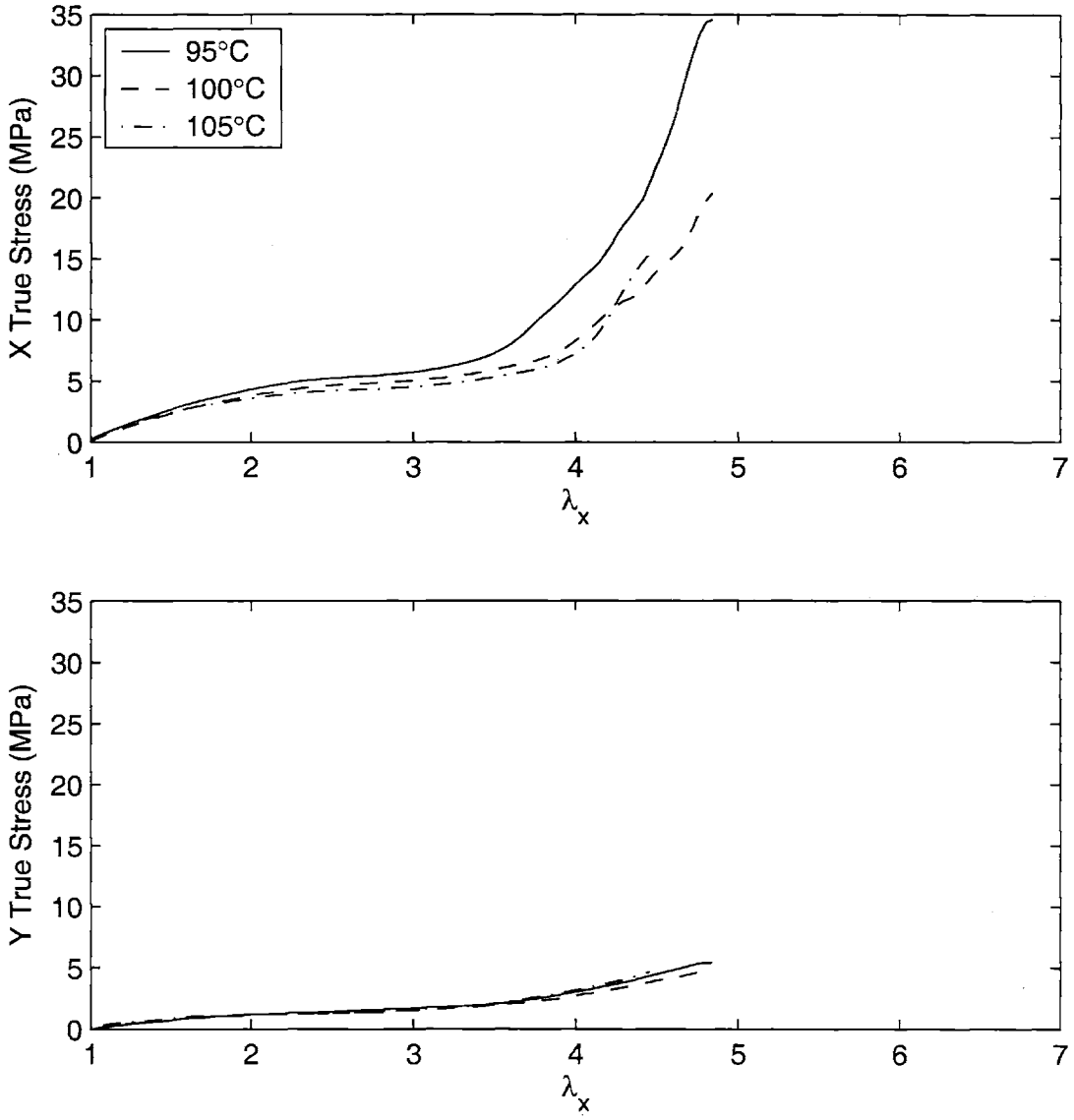

Figure 3-46: PET Constrained width tension, true stress-stretch, du/dt = 14 in/sec

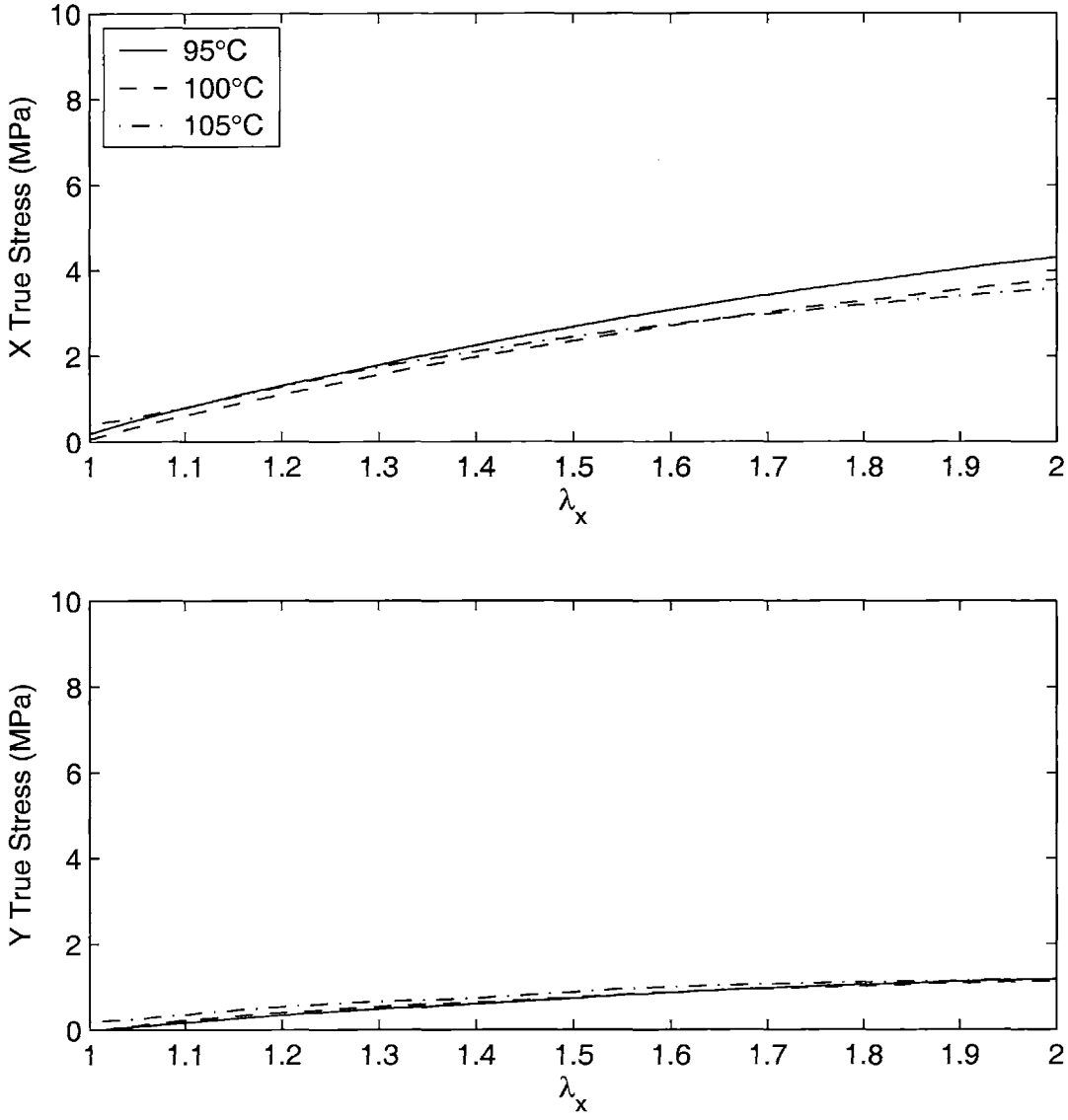

Figure 3-47: PET Constrained width tension, true stress-stretch, du/dt = 14 in/sec, enlarged to show small strain region

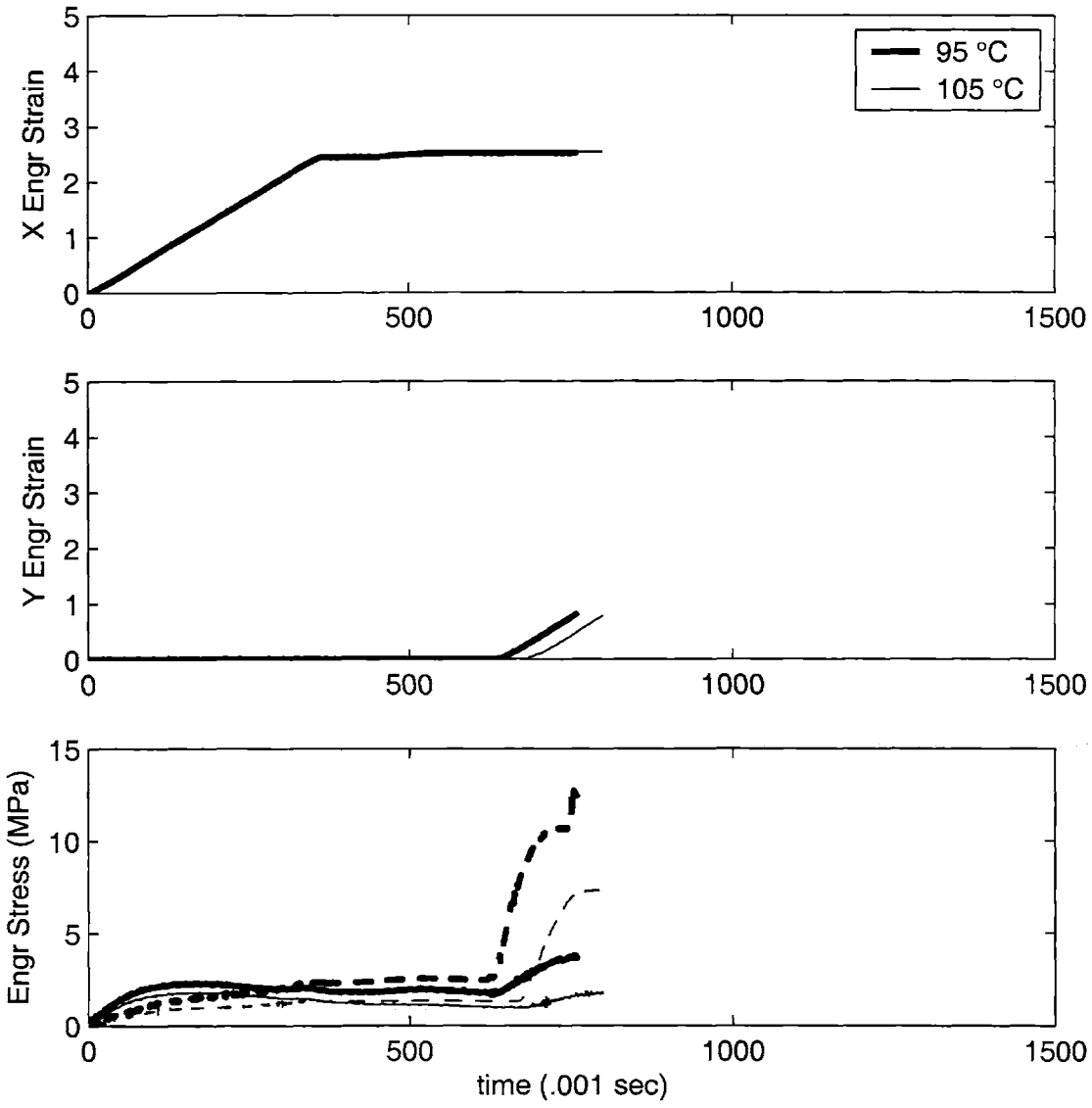

Figure 3-48: PET Sequential biaxial extension, engineering stress-strain, du/dt = 14 in/sec, $\lambda_x = 2$

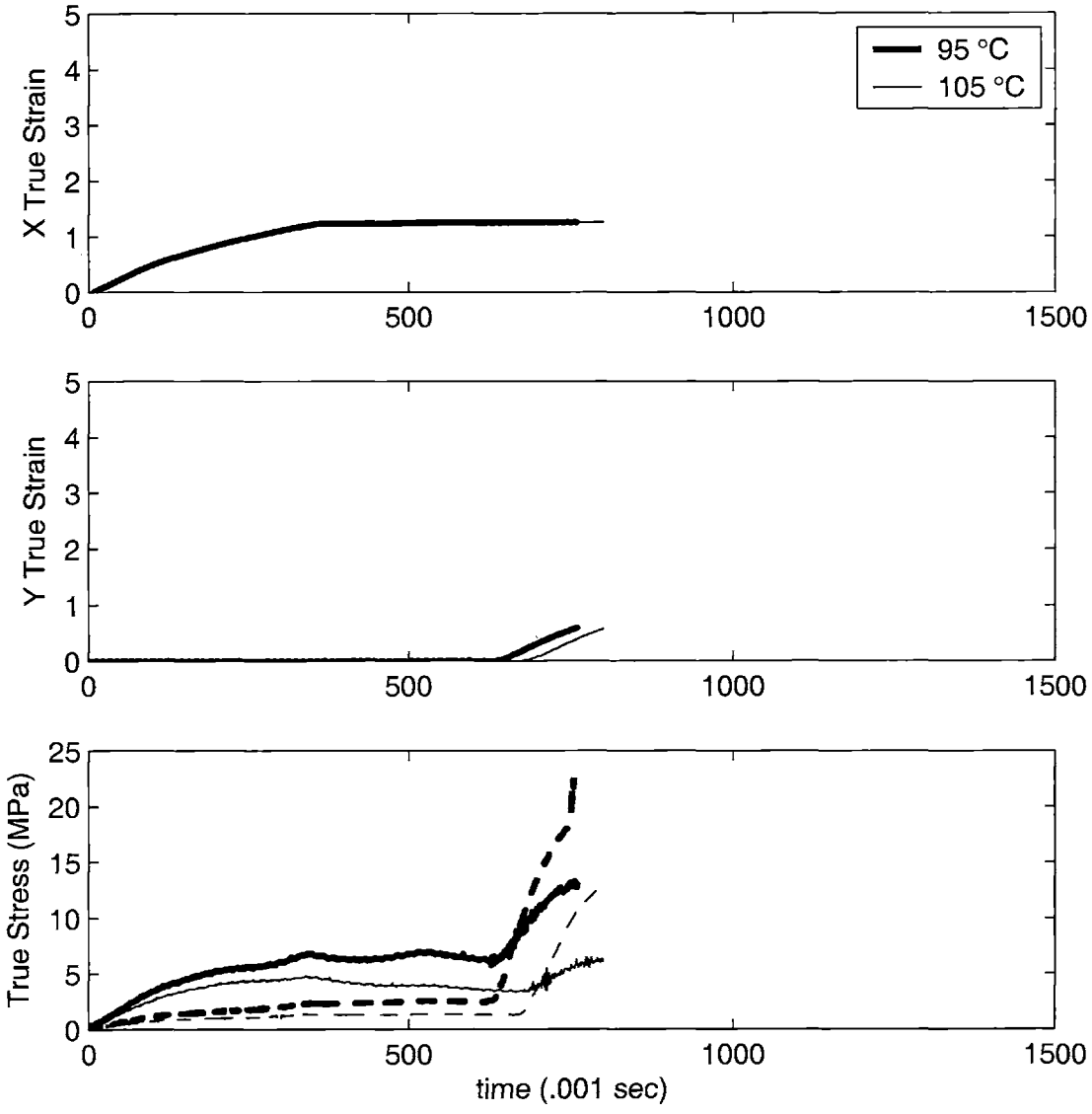

Figure 3-49: PET Sequential biaxial extension, true stress-strain, du/dt = 14 in/sec, $\lambda_x = 2$

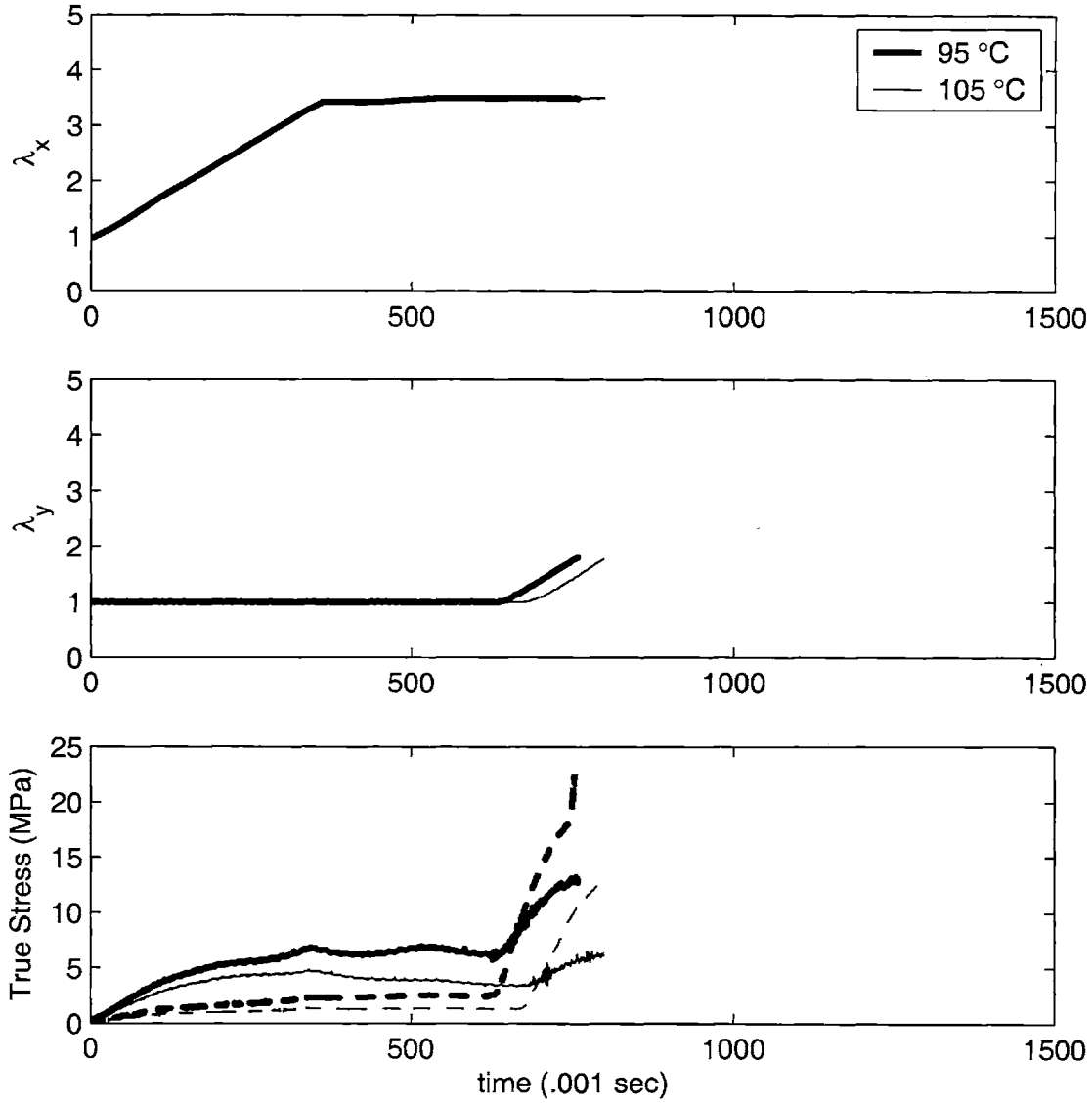

Figure 3-50: PET Sequential biaxial extension, true stress-stretch, du/dt = 14 in/sec, $\lambda_x = 2$

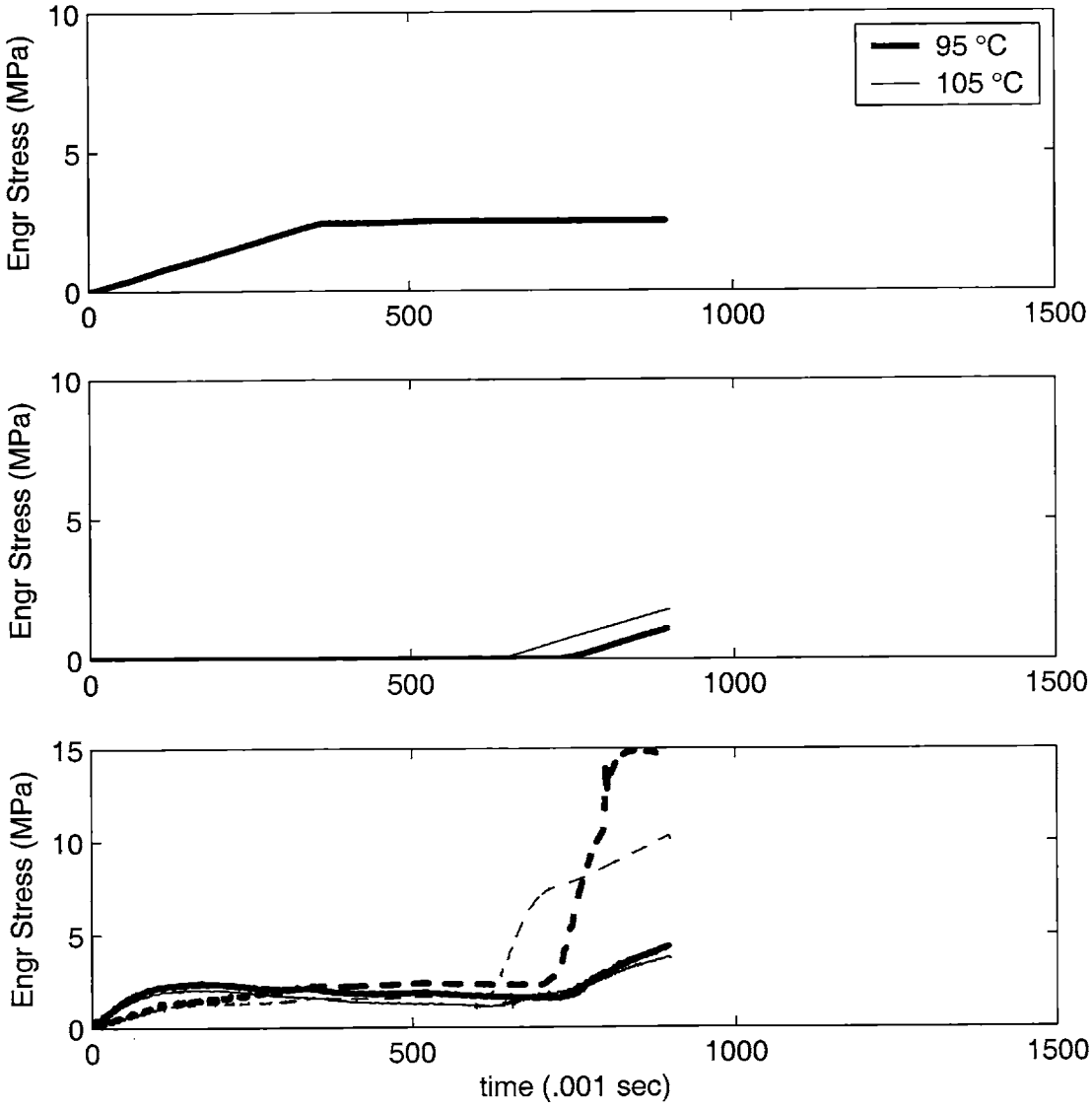

Figure 3-51: PET Sequential biaxial extension, engineering stress-strain, du/dt = 14 in/sec, $\lambda_x = 3$

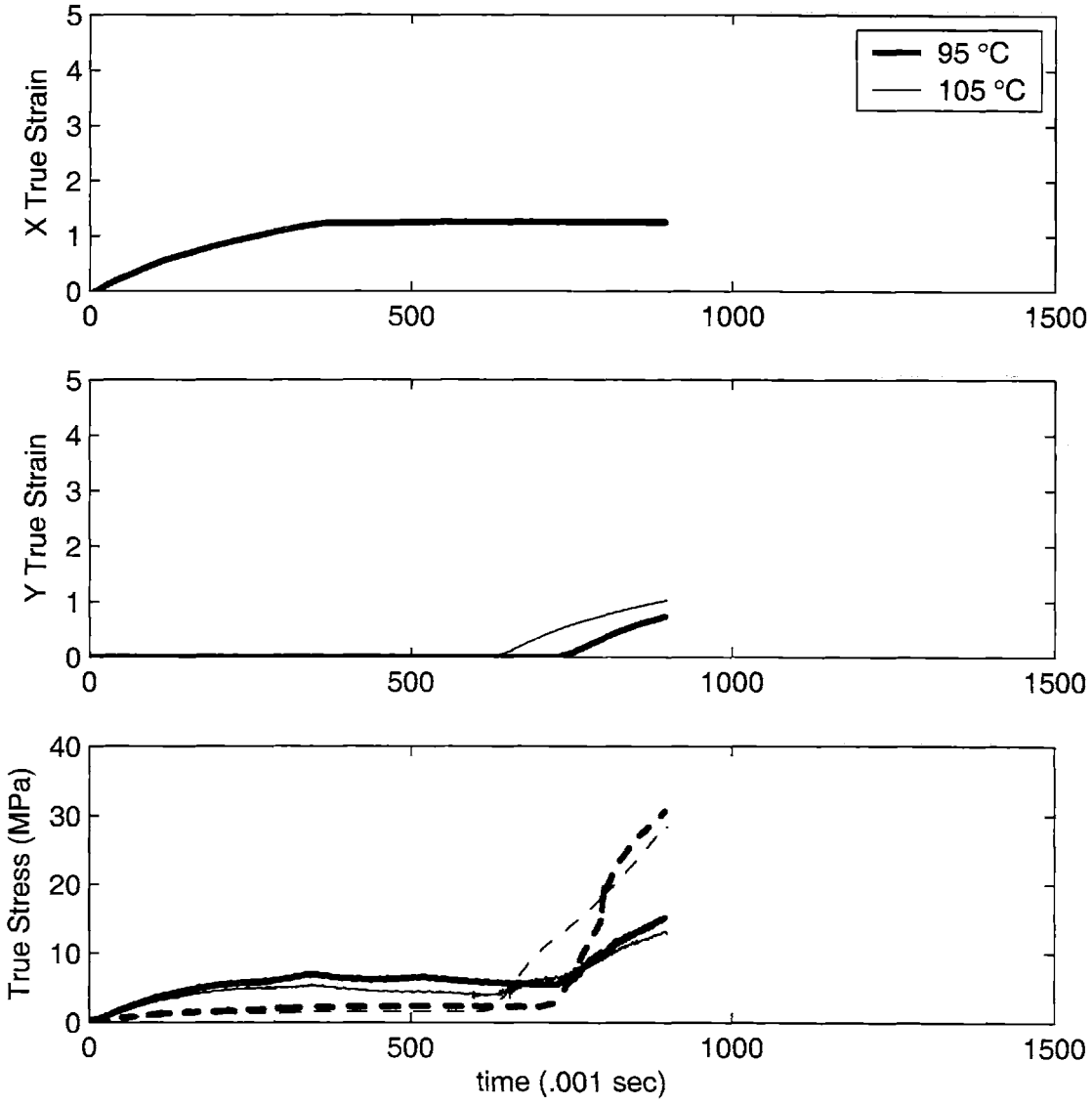

Figure 3-52: PET Sequential biaxial extension, true stress-strain, du/dt = 14 in/sec, $\lambda_x = 3$

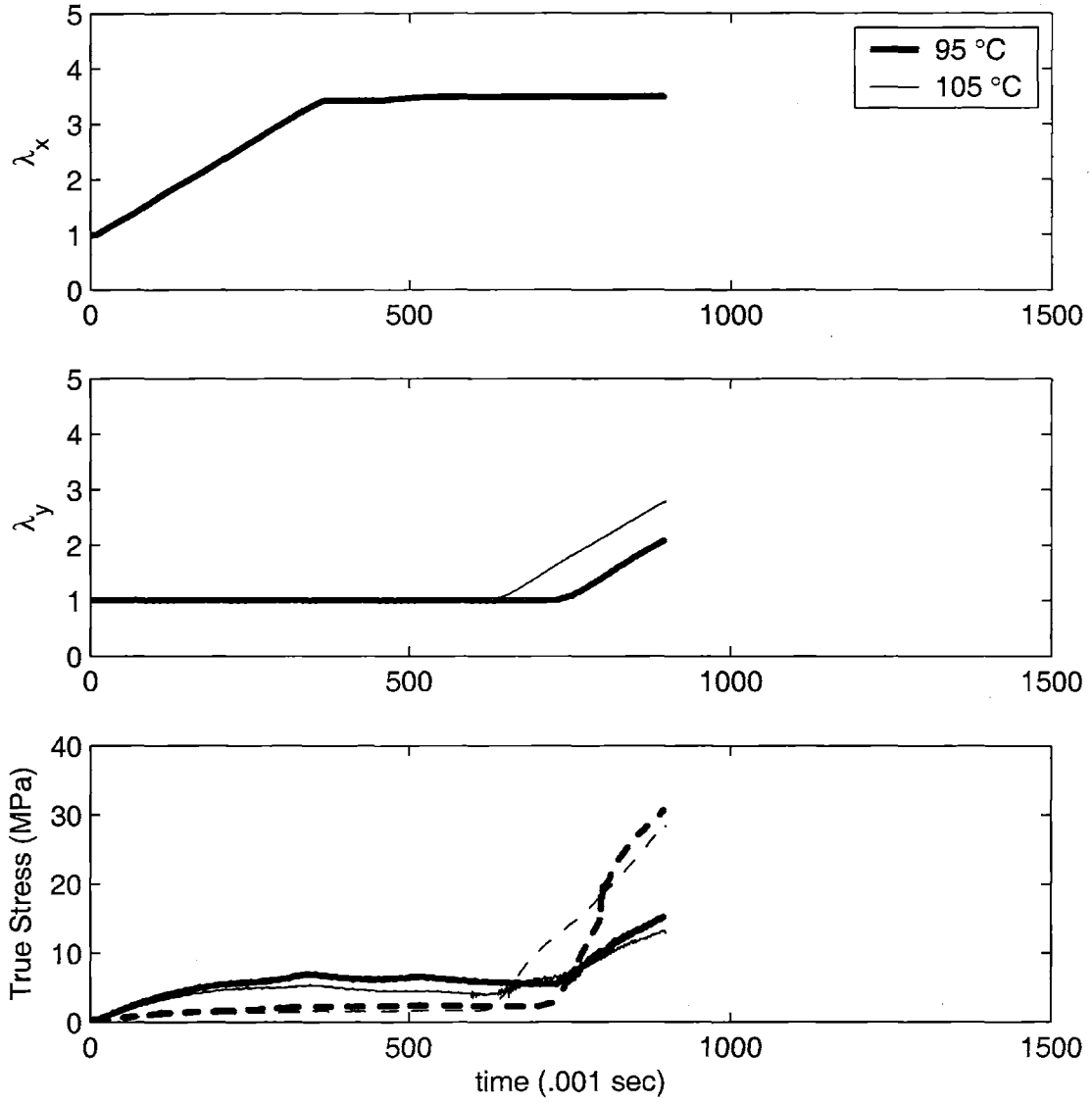

Figure 3-53: PET Sequential biaxial extension, true stress-stretch, du/dt = 14 in/sec, $\lambda_x = 3$

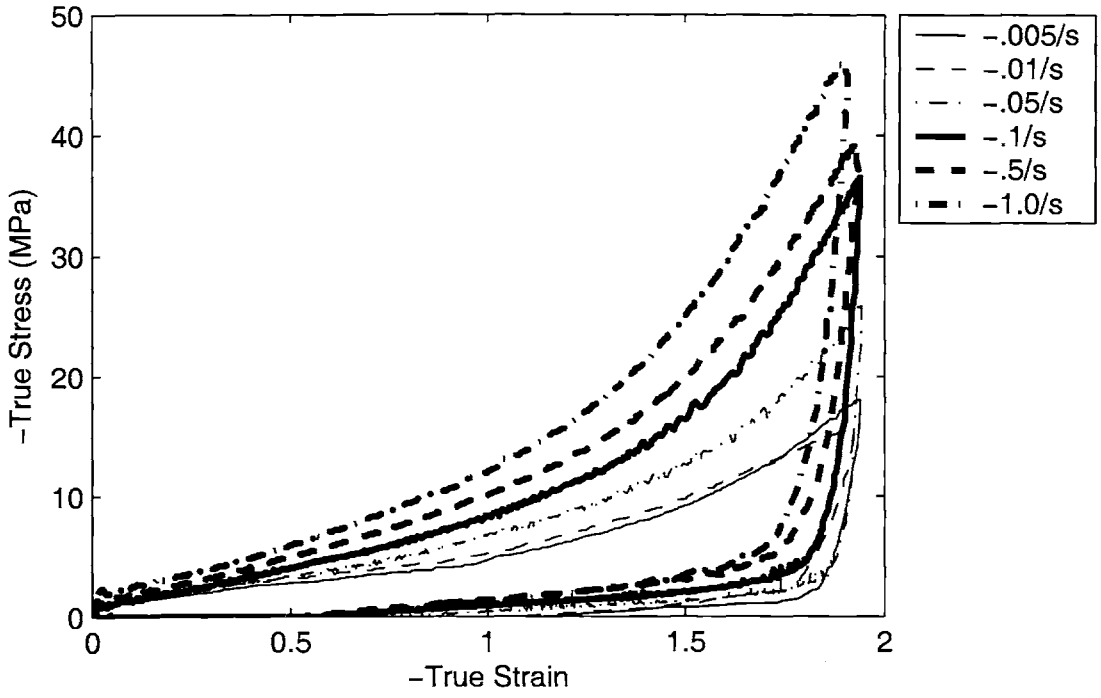

Figure 3-54: PETG Uniaxial compression data, Temperature = 90 ° C

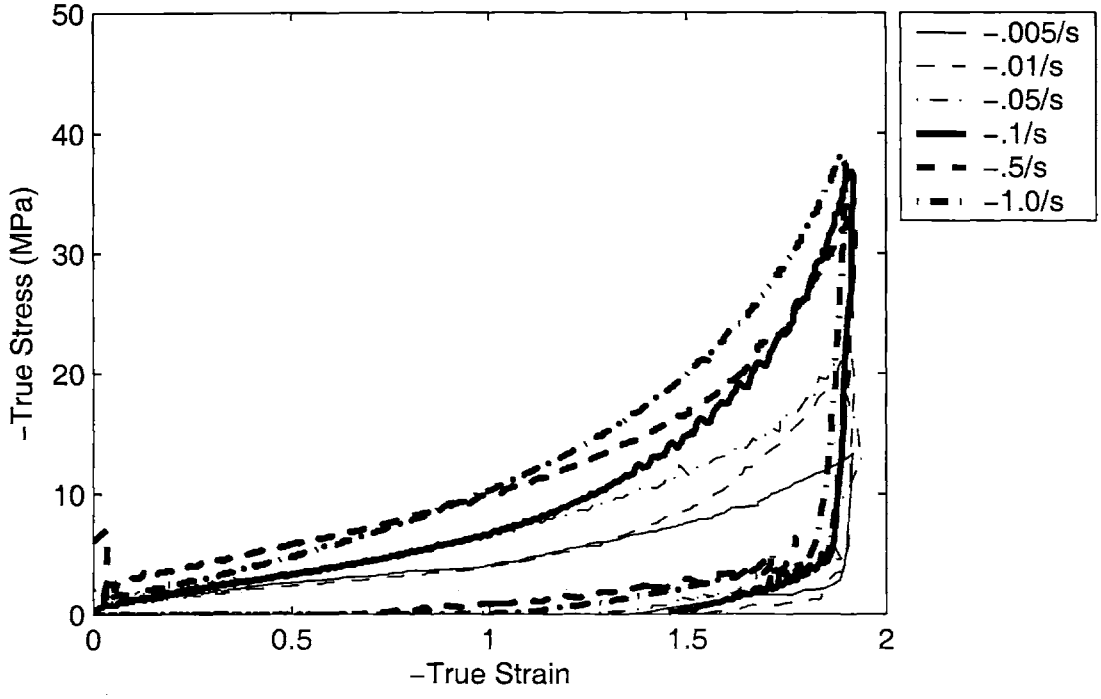

Figure 3-55: PET Uniaxial compression data, Temperature = 90 ° C

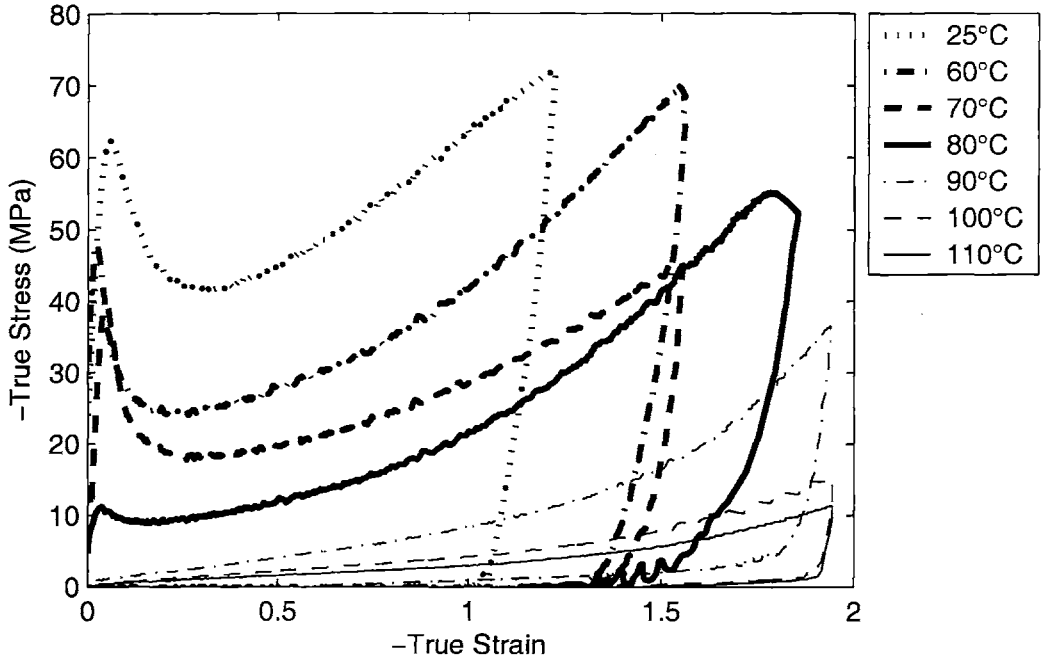

Figure 3-56: PETG Uniaxial compression data, $\dot{\varepsilon}$ = -.1/s

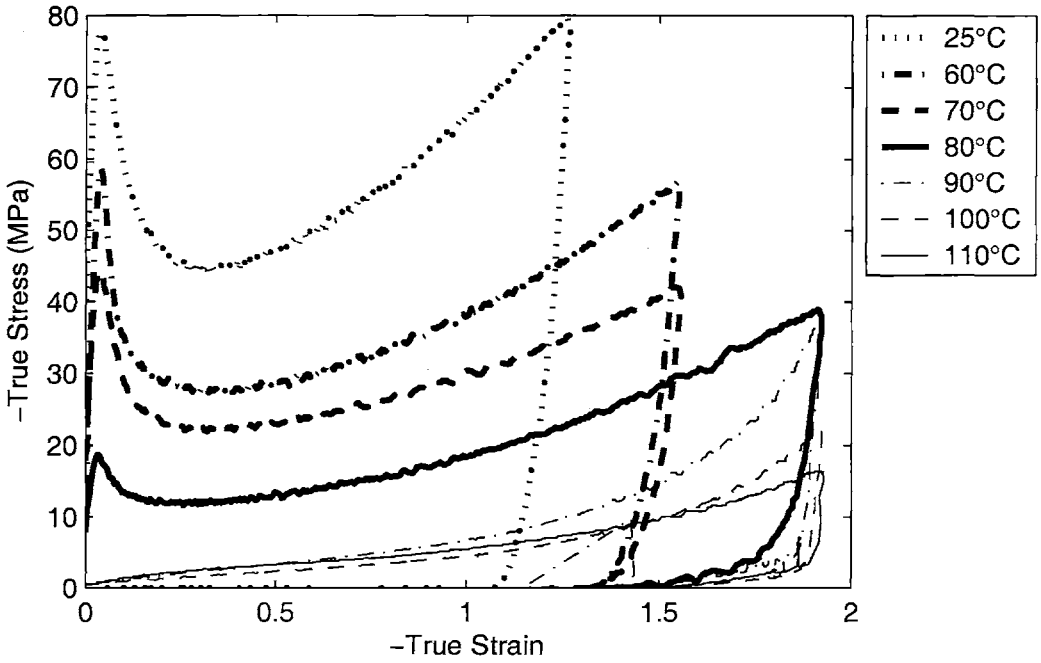

Figure 3-57: PET Uniaxial compression data, $\dot{\varepsilon}$ = -.1/s

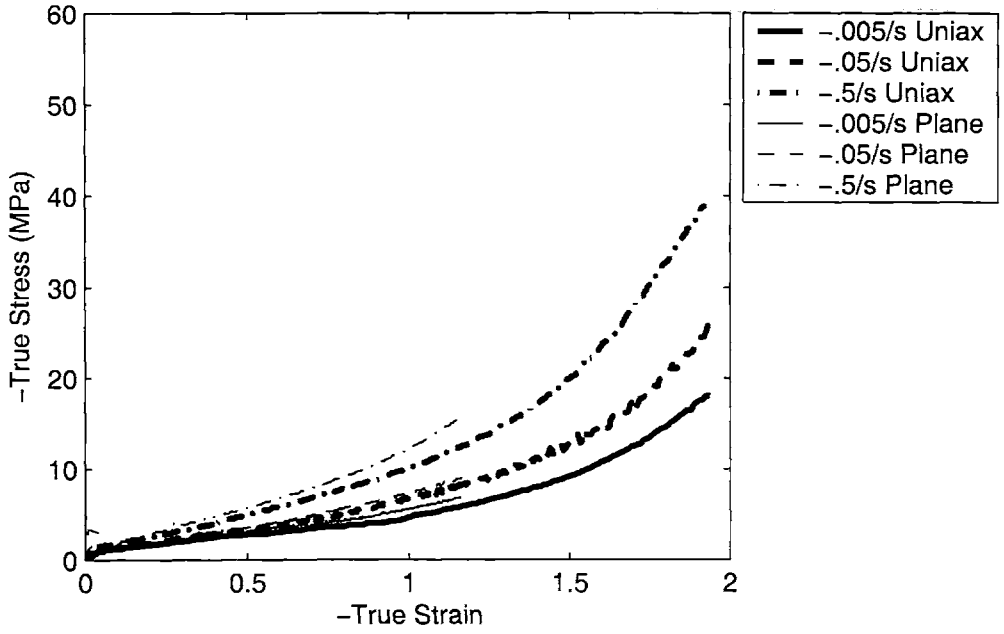

Figure 3-58: PETG Uniaxial and plane strain compression data, Temperature = 90 ° C

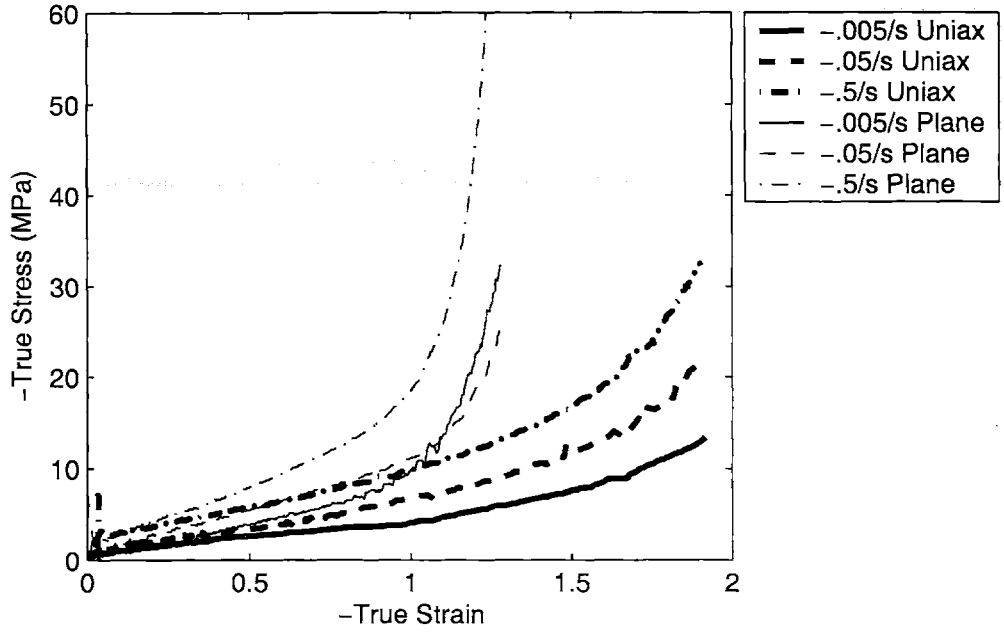

Figure 3-59: PET Uniaxial and plane strain compression data, Temperature = 90 ° C

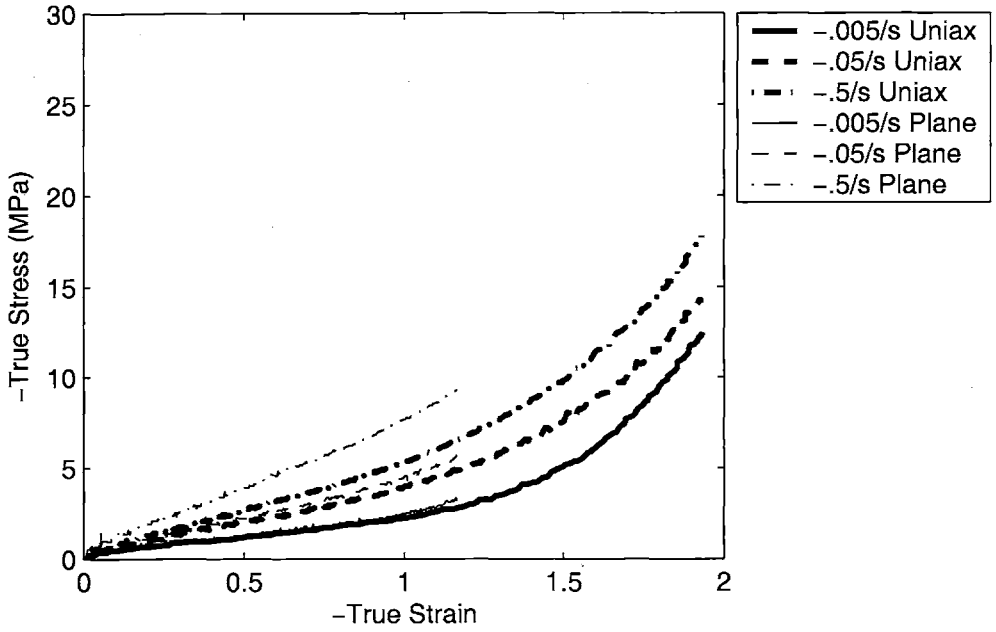

Figure 3-60: PETG Uniaxial and plane strain compression data, Temperature = 100 ° C

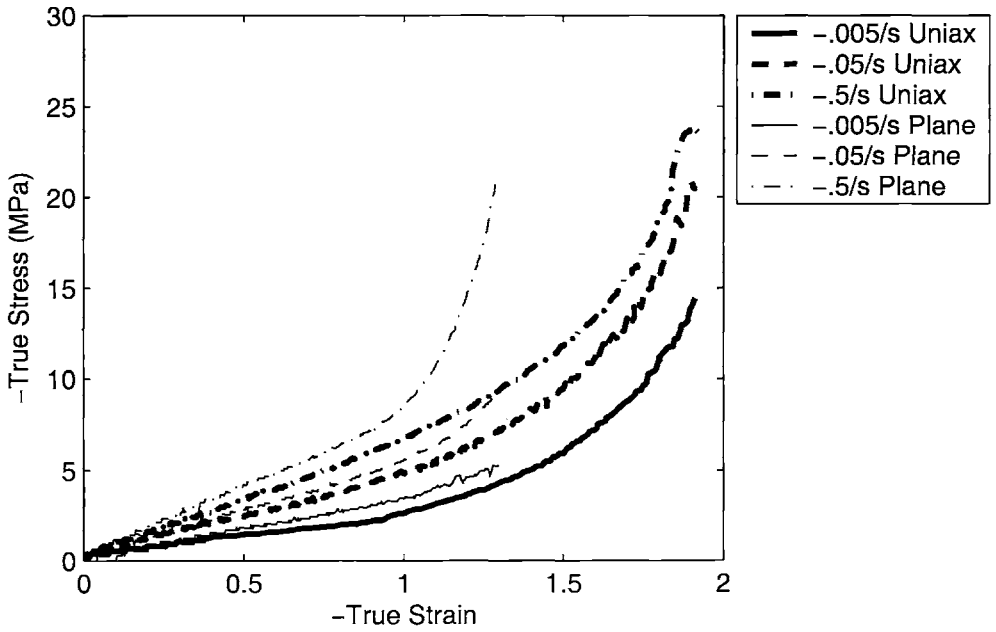

Figure 3-61: PET Uniaxial and plane strain compression data, Temperature = 100 ° C

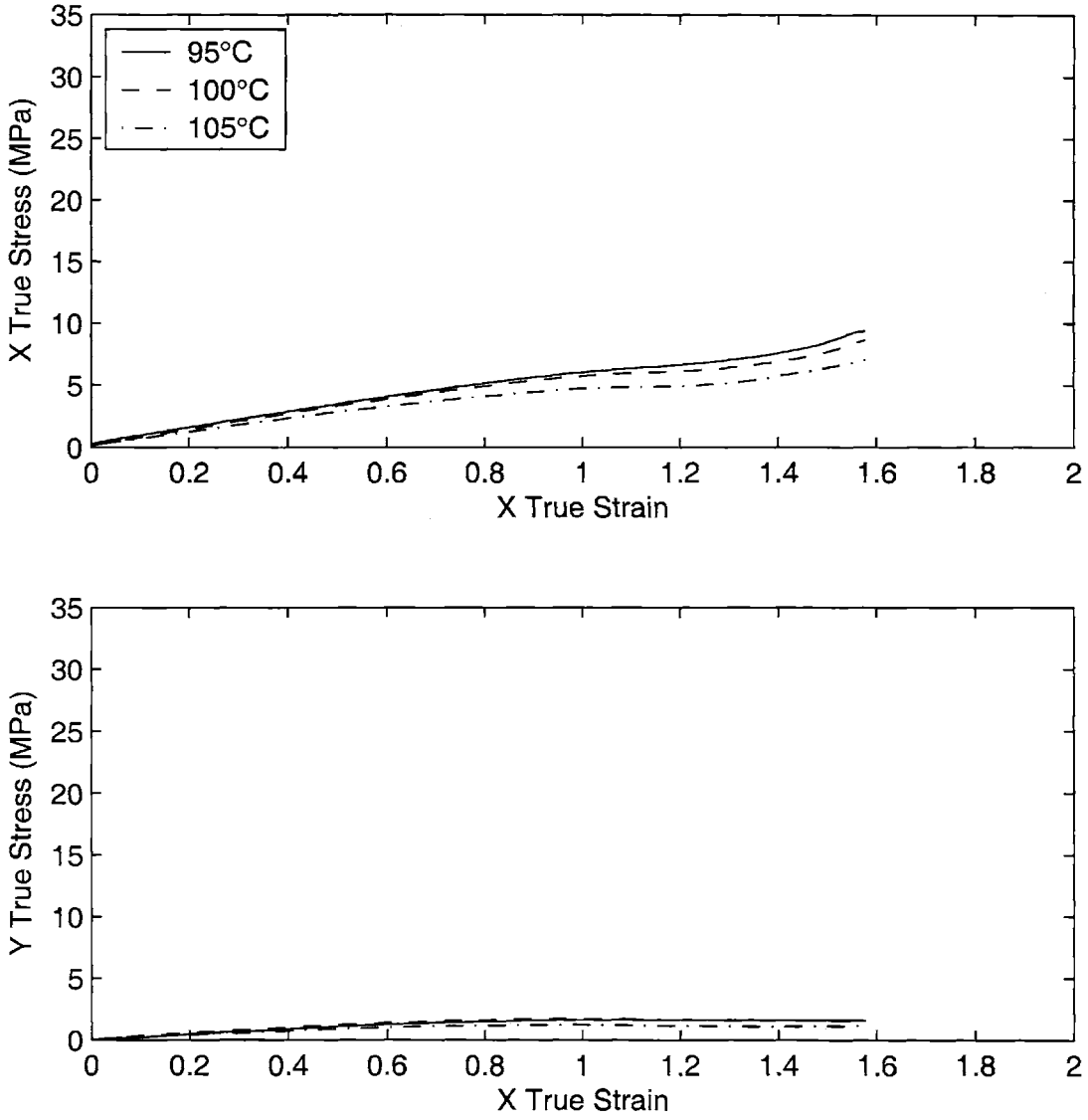

Figure 3-62: PETG Constrained width tension, true stress-strain, du/dt = 14 in/sec

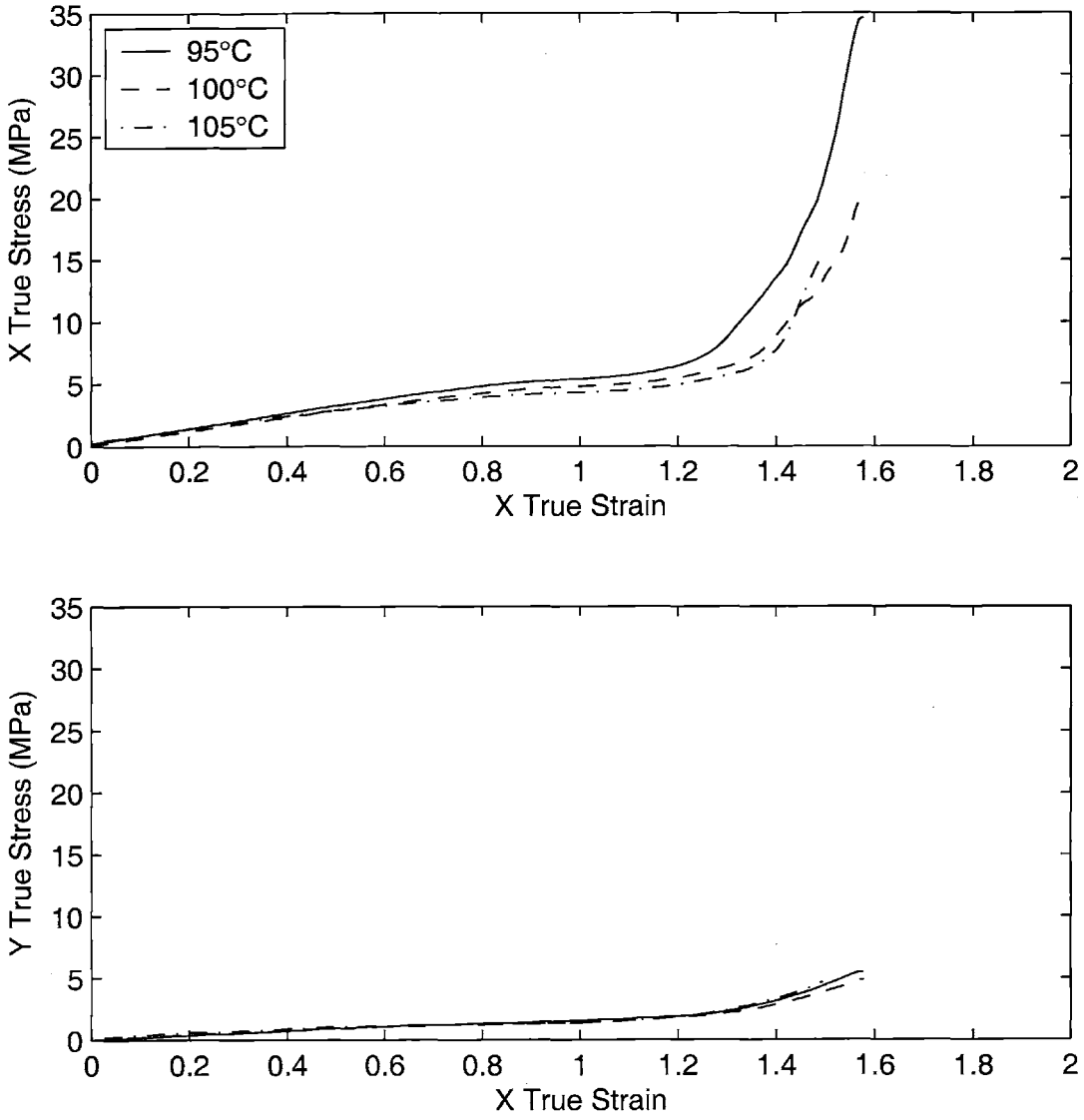

Figure 3-63: PET Constrained width tension, true stress-strain, du/dt = 14 in/sec

Chapter 4

Constitutive Model for PETG

In this chapter, we develop a constitutive model for the stress-strain behavior of PETG, focusing primarily on capturing the behavior at temperatures above the glass transition temperature. It should be noted that θ_g itself is rate dependent, as was illustrated by dynamic mechanical analysis experiments in Chapter 2. Broadly, there are two schools of modeling in this nearly melt-like regime of polymer deformation and flow: Non-Newtonian Fluid Mechanics, which tries to nonlinearize the viscosity and add elasticity, and Solid Mechanics, which tries to add viscous effects into an elastic or hyperelastic model. In this work, we will use the Solid Mechanics approach, but will discuss and compare results with the non-Newtonian fluids approach at the end of the chapter.

4.1 Background and Development

The overall framework for the constitutive model follows prior solid mechanics developments in modeling time dependent large strain deformation of polymers (Bergstrom and Boyce 1998; Boyce et al. 2000). In particular, the modeling approach and development of this thesis build on the work of Boyce, Socrate, and Llana (2000).

The constitutive response of the polymer can be interpreted as follows. In the presence of an applied load, the polymer resists deformation by two mechanisms: a resistance due to intermolecular forces and a network resistance due to molecular

orientation. This is shown schematically in figure 4-1 with the two distinct resistances represented as A and B.

Resistance A arises due to the intermolecular resistance between neighboring polymer segments. This gives the material its initial stiffness and results in a finite stress at which the polymer will flow, termed the flow stress. In resistance B, molecular network stretching and orientation of the polymer chains causes the polymer to stiffen at large strains. The nonlinear dashpot captures molecular relaxation at higher temperatures. Intermolecular contributions to the material behavior are due to changes in internal energy whereas the molecular network contributions are entropic in nature. The two resistances occur concurrently and are therefore modeled as being in parallel. Thus, the deformation gradient in each network is equal to the total deformation gradient,

$$\mathbf{F}_A = \mathbf{F}_B = \mathbf{F} \tag{4.1}$$

where the deformation gradient is defined as:

$$\mathbf{F} = \frac{\partial x}{\partial X} \tag{4.2}$$

where X represents the reference position and x the current position of a material point. The descriptions of the intermolecular (A) and intramolecular (B) resistances will be developed separately.

4.1.1 Resistance A: Intermolecular Interactions

The deformation gradient of resistance A is decomposed into elastic and plastic components in a multiplicative manner, as described by Lee (1969) and as illustrated schematically in figure 4-2.

$$\mathbf{F}_A = \mathbf{F}_A^e \mathbf{F}_A^p \tag{4.3}$$

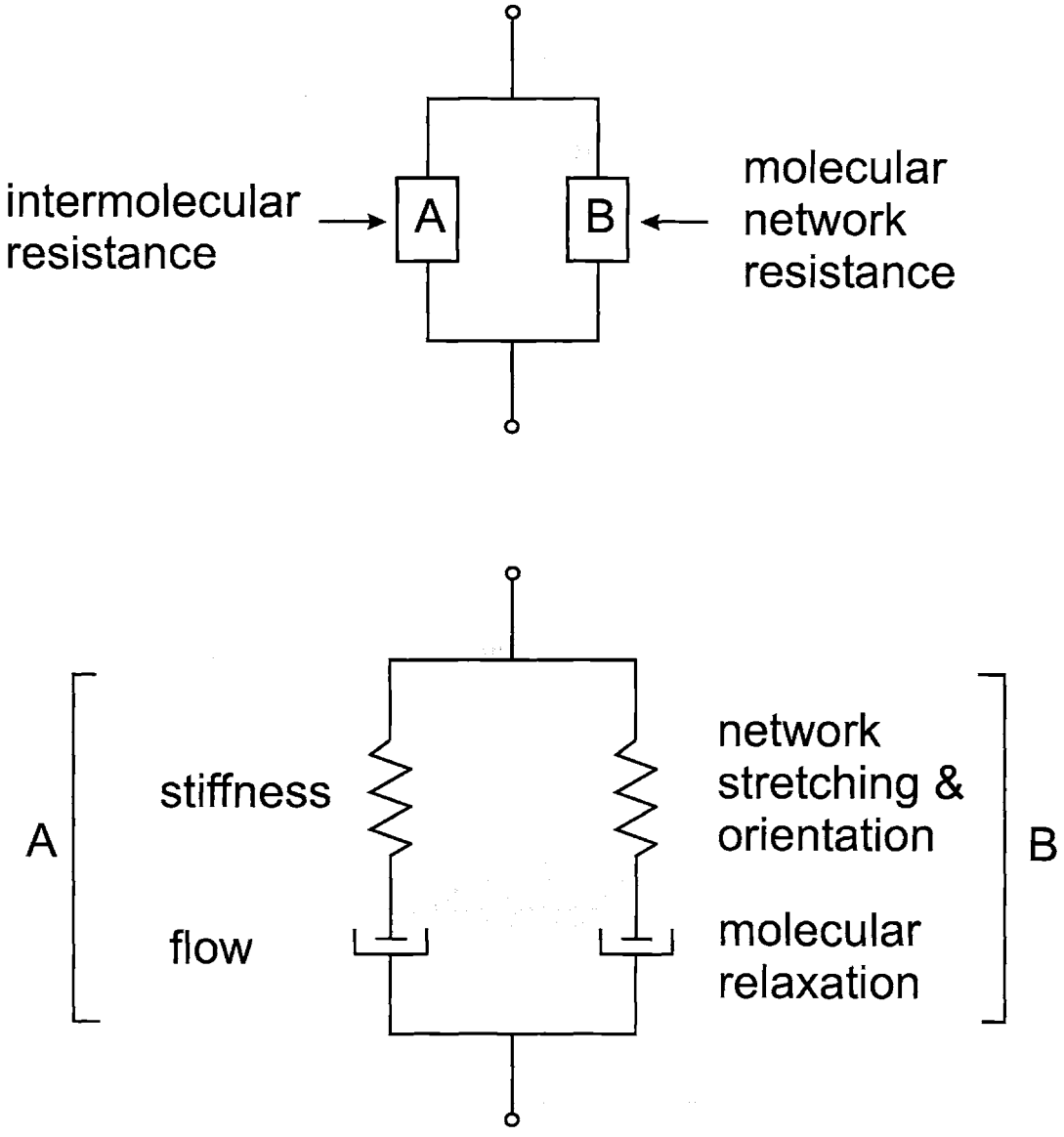

Figure 4-1: Schematic representation of the constitutive model

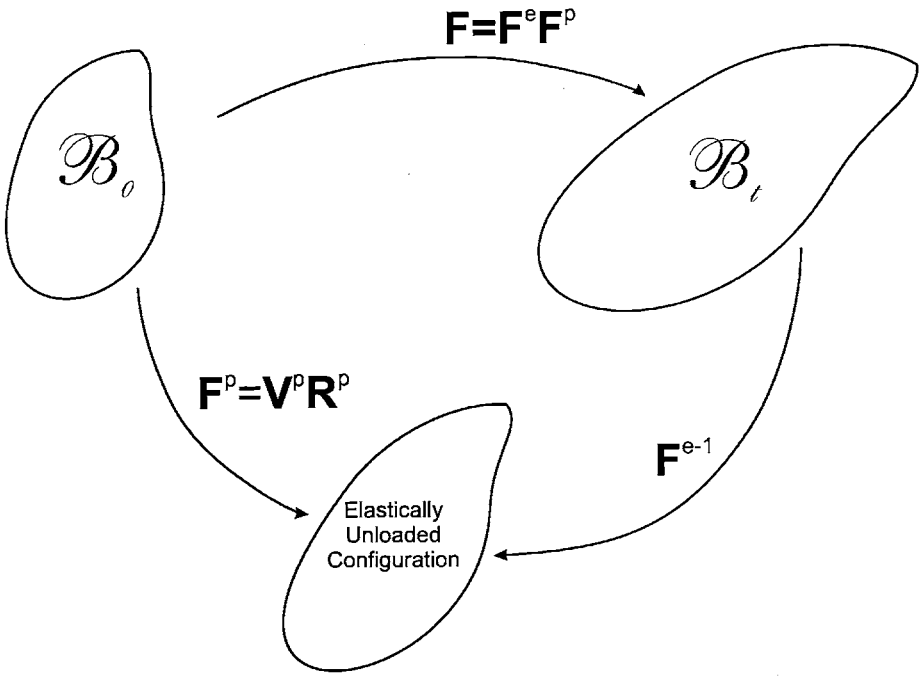

Figure 4-2: Kinematical description of elastic-plastic decomposition

and is then decomposed into stretch and rotation components using the polar decomposition

$$\mathbf{F}_A^e = \mathbf{V}_A^e \mathbf{R}_A^e \tag{4.4}$$

$$\mathbf{F}_A^p = \mathbf{V}_A^p \mathbf{R}_A^p \tag{4.5}$$

The rate kinematics are described by the velocity gradient, $\mathbf{L}_A$

$$\mathbf{L}_A = \dot{\mathbf{F}}_A \mathbf{F}_A^{-1} \tag{4.6}$$

By substitution of the elastic and plastic contributions to the deformation gradient this becomes

$$\mathbf{L}_A = \dot{\mathbf{F}}_A^e \mathbf{F}_A^{e-1} + \mathbf{F}_A^e \dot{\mathbf{F}}_A^p \mathbf{F}_A^{p-1} \mathbf{F}_A^{e-1} = \mathbf{L}_A^e + \tilde{\mathbf{L}}_A^p \tag{4.7}$$

Note that the plastic velocity gradient consists of a symmetric plastic rate of stretching and an antisymmetric plastic spin: $\tilde{\mathbf{L}}_A^p = \tilde{\mathbf{D}}_A^p + \tilde{\mathbf{W}}_A^p$. The representation is made

unique by prescribing the plastic spin in the loaded configuration to be zero: $\tilde{\mathbf{W}}_A^p = 0$.

The rate of stretching is constitutively described by

$$\tilde{\mathbf{D}}_A^p = \dot{\gamma}_A^p \mathbf{N}_A \tag{4.8}$$

Note that $\mathbf{N}_A$ is the normalized deviatoric stress in resistance A

$$\mathbf{N}_A = \frac{1}{\sqrt{2}\tau_A}\mathbf{T}'_A \tag{4.9}$$

$$\tau_A = \left[\frac{1}{2}\mathbf{T}'_A\mathbf{T}'_A\right]^{1/2} \tag{4.10}$$

$\mathbf{T}_A$ is the Cauchy stress and is related to the elastic deformation gradient by the constitutive relation

$$\mathbf{T}_A = \frac{1}{J_A}\mathscr{L}^e[\ln \mathbf{V}_A^e] \tag{4.11}$$

where $J_A = \det \mathbf{F}_A^e$ is the volume change, $\mathscr{L}^e$ is the fourth order tensor of elastic constants, and $\ln \mathbf{V}_A^e$ is the Hencky strain (Anand 1979). The plastic strain rate, $\dot{\gamma}_A^p$, is assumed to follow a thermally activated process

$$\dot{\gamma}_A^p = \dot{\gamma}_{0A} \exp\left[-\frac{\Delta G(1 - \tau_A/s)}{k\theta}\right] \tag{4.12}$$

where $\dot{\gamma}_{0A}$ is the pre-exponential factor, ΔG is the activation energy which must be overcome for flow to begin, s is the shear resistance, taken to be $.15\mu$ (μ is the shear modulus), k is Boltzmann's constant, and θ is the absolute temperature. The shear resistance can be further modified to account for pressure as in Boyce et al. (Boyce, Parks, and Argon 1988):

$$\tilde{s} = s(1 + \alpha p/s) \tag{4.13}$$

where the pressure $p = -\frac{1}{3}tr(\mathbf{T}_A)$ and α is the pressure coefficient.

Equations 4.1 to 4.13 complete the constitutive prescription for resistance A.

4.1.2 Resistance B: Network Interactions

Two mechanisms are involved in the deformation of resistance B: first, the stretching and orientation of the polymer chain network and second, molecular relaxation. Resistance B can be thought of as a non-linear spring in series with a viscous element (see figure 4-1). As such, the deformation of this element can also be multiplicatively decomposed into a network and flow portion:

$$\mathbf{F}_B = \mathbf{F}_B^N \mathbf{F}_B^F \tag{4.14}$$

The velocity gradient is then

$$\mathbf{L}_B = \dot{\mathbf{F}}_B \mathbf{F}_B^{-1} \tag{4.15}$$

$$\mathbf{L}_B = \dot{\mathbf{F}}_B^N \mathbf{F}_B^{N-1} + \mathbf{F}_B^N \dot{\mathbf{F}}_B^F \mathbf{F}_B^{F-1} \mathbf{F}_B^{N-1} = \mathbf{L}_B^N + \tilde{\mathbf{L}}_B^F \tag{4.16}$$

Again, $\tilde{\mathbf{L}}_B^F = \tilde{\mathbf{D}}_B^F + \tilde{\mathbf{W}}_B^F$ is made unique by setting the spin to zero, $\tilde{\mathbf{W}}_B^F = 0$.

The Arruda-Boyce eight-chain rubber elasticity model (Arruda and Boyce 1993a; Arruda and Boyce 1993b) is used to prescribe the stress arising from the network stretching and orientation of the polymer. Figure 4-3 illustrates how a collection of random polymer chains will each undergo elongation and a change in orientation with deformation. The 8-chain model attempts to capture the overall effect of stretching and orientation by using a unit cell model, which consists of 8 identical chains (as shown schematically in figure 4-4. The stretch of each chain in the network is given by an effective chain stretch, or the root-mean square of the distortional applied stretch: $\bar{\lambda}_N = [\frac{1}{3} tr(\bar{\mathbf{B}}^N)]^{1/2}$, where $\bar{\mathbf{B}}^N = \bar{\mathbf{F}}_B^N \bar{\mathbf{F}}_B^{NT}$, $\bar{\mathbf{F}}_B^N = (J_B)^{-1/3} \mathbf{F}_B^N$, and $J_B = \det \mathbf{F}_B^N$. The relationship between the chain stretch and the network stress is then

$$\mathbf{T}_B = \frac{1}{J_B} \frac{\nu k\theta}{3} \frac{\sqrt{N}}{\bar{\lambda}_N} \mathscr{L}^{-1} \left[\frac{\bar{\lambda}_N}{\sqrt{N}} \right] [\bar{\mathbf{B}}^N - (\bar{\lambda}_N)^2 \mathbf{I}] \tag{4.17}$$

The parameters in this expression are as follows: ν is the chain density (where a chain is defined as that portion of a polymer molecule between two entanglements), N is the number of rigid links between entanglements, and $\nu k\theta$ is a rubbery modulus, which

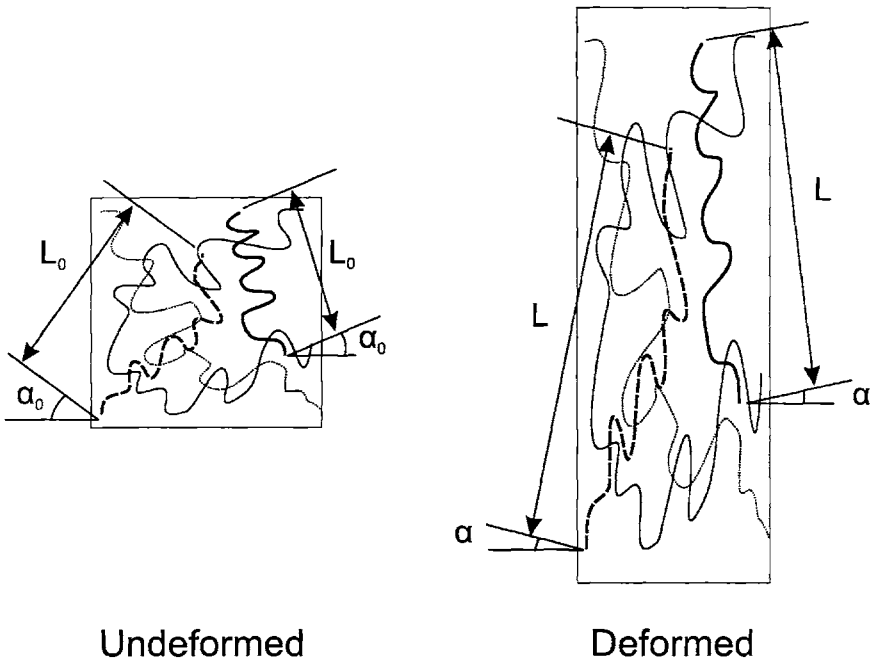

Figure 4-3: Schematic illustrating the stretching and orientation of chains in a random network

is proportional to the initial hardening modulus of the strain hardening curve, or the initial slope of the stress-strain curve at the onset of flow, before much stiffening or hardening has occurred. $\mathscr{L}^{-1}$ is the inverse Langevin function given by $\mathscr{L}(\beta) = \coth(\beta) - (1/\beta)$. This is derived from a non-Gaussian probability function which accounts for the fact that the chains have a finite extensibility. $\mathscr{L}^{-1}[\bar{\lambda}_N/\sqrt{N}]$ provides the functionality that as $\bar{\lambda}_N$ approaches $\sqrt{N}$, the stress rises dramatically.[1]

The rate of molecular relaxation is given by

$$\tilde{\mathbf{D}}_B^F = \dot{\gamma}_B^F \mathbf{N}_B \tag{4.18}$$

where $\mathbf{N}_B$ is

$$\mathbf{N}_B = \frac{1}{\sqrt{2}\tau_B}\mathbf{T}'_B \tag{4.19}$$

[1]For example, in axial tension, if stress rises very dramatically at $\lambda^* = X$, the chain stretch at that point is $\sqrt{\frac{1}{3}(X^2 + \frac{2}{X})}$, from which one obtains the value of $\sqrt{N}$.

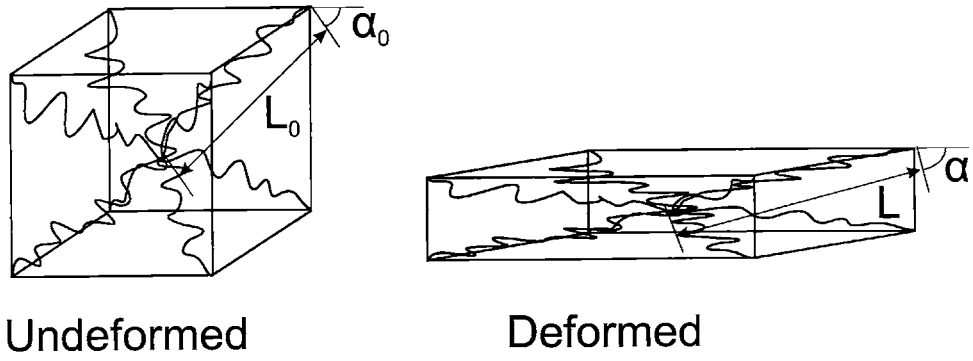

Figure 4-4: Schematic illustrating the 8-chain network model

$$\tau_B = \left[\frac{1}{2}\mathbf{T}'_B\mathbf{T}'_B\right]^{1/2} \tag{4.20}$$

and $\mathbf{T}_B$ is prescribed using the Arruda-Boyce model (eqn. 4.17). The only remaining unknown is the rate of relaxation, $\dot{\gamma}_B^F$, which must be constitutively prescribed. The assumed mechanism is chain reptation, the physical picture being one of polymer chains sliding through tube-like paths created by the entangled chains around them (see fig. 4-5). A model by Bergstrom and Boyce (1998) based on the Doi and Edwards (1986) theory of reptational motion is used to model this relaxation in ref. (Boyce et al. 2000):

$$\dot{\gamma}_B^F = C\left(\frac{1}{\lambda_F - 1}\right)\tau_B \tag{4.21}$$

where $\lambda_F = [\frac{1}{3}tr(\mathbf{F}_B^F\mathbf{F}_B^{FT})]^{1/2}$ is the flow stretch and the relaxation temperature dependence is captured by an exponential expression for C

$$C = D\exp\left\{-\frac{Q}{R\theta}\right\} \tag{4.22}$$

It will be shown that these relations for the molecular relaxation were not able to fully capture the strain rate dependence for PETG. The relation is therefore modified to better capture the observed strain rate dependence:

$$\dot{\gamma}_B^F = C\left[\left(\frac{1}{\lambda_F - 1}\right)\tau_B\right]^3 \tag{4.23}$$

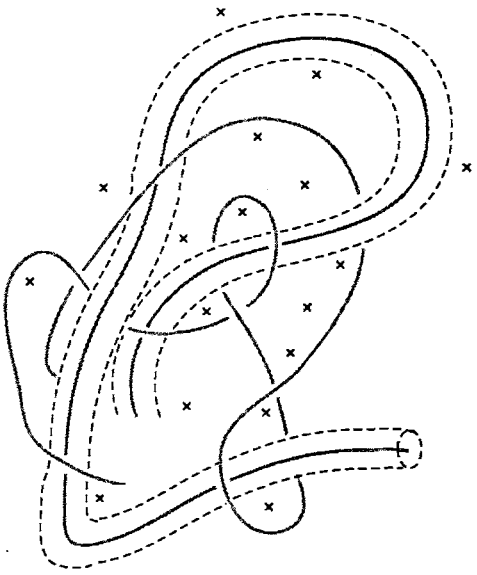

Figure 4-5: Illustration of the tube model

Equations 4.1 and 4.14 through 4.23 describe the constitutive behavior of resistance B.

Now the total stress acting on the system is the sum of the stresses in the two resistances

$$\mathbf{T} = \mathbf{T}_A + \mathbf{T}_B \tag{4.24}$$

4.2 Determining the Material Constants

4.2.1 Resistance A (Intermolecular)

The initial elastic response of the material is governed by the elastic element in resistance A. The initial modulus is determined from the stress-strain curves for uniaxial compression, in combination with a time-temperature relationship obtained from DMA experiments (see sec. 2.4). The equations are cast in terms of the shear modulus and the bulk modulus. Using uniaxial compression data at 25 ° C and at 90 ° C, the Young's modulus is found to be 1.25 GPa and 75 MPa, respectively. Assuming that the Poisson's ratio is approximately .33 at room temperature and .49 above the glass

transition temperature, the bulk modulus can be determined at each temperature using the relation between bulk modulus (B), Young's modulus (E), and Poisson's ratio (ν_p):

$$B = \frac{E}{3(1-2\nu_p)} \tag{4.25}$$

This gives a temperature independent value for the bulk modulus of 1.25 GPa. The temperature dependence of the shear modulus is approximated with a hyperbolic tangent function:

$$\mu = \frac{1}{2}(\mu_{gl} + \mu_r) - \frac{1}{2}(\mu_{gl} - \mu_r)\tanh(\frac{5}{\Delta\theta}(\theta - \theta_g)) + X_g(\theta - \theta_g) \tag{4.26}$$

where μ_{gl} is the modulus in the glassy region, μ_r is the modulus in the rubbery region, $\Delta\theta$ is related to the temperature range across which the glass transition occurs, θ_g is the glass transition temperature[2], and X_g is the slope outside the glass transition region (see figure 4-6). The constants μ_{gl}, μ_r, and $\Delta\theta$ are determined from the DMA data, which is scaled by a factor of 0.5 to correlate with the uniaxial compression experiments[3]. The data is then converted into shear modulus data using the relation

$$\mu = \frac{3EB}{9B - E} \tag{4.27}$$

[2]The glass transition temperature is defined here as the temperature at which the material softens from a glassy solid to a rubbery material. In the DMA data, this is indicated by the dramatic drop in modulus with temperature around 80 ° C. Since the drop does not occur instantaneously, but occurs gradually over about 5 ° C, the value of the glass transition temperature is taken as the temperature half way between where the low temperature plateau ends and the high temperature plateau begins in the DMA data.

[3]The factor 0.5 is chosen because it yields a good correlation between results from quasi-static compression experiments and dynamic DMA experiments. A theoretical correlation exists between the dynamic storage and loss modulii (G' and G'') and the elastic modulus of the material (E). To obtain this correlation, one must assume a form for the viscoelastic model (such as a Maxwell model). The relation between G' and G" and the model parameters (stiffness E and viscosity η) can then be derived by inserting the expression for the oscillating driving stress into the governing differential equation. For example, given $\sigma = \sigma_0 \exp(i\omega t) = (G' + iG'')\varepsilon$ as the driving stress, substitution into the Maxwell model yields the following relations: $G' = (E\omega^2\tau^2)/(1+\omega^2\tau^2)$ and $G'' = (E\omega\tau)/(1+\omega^2\tau^2)$, where $\tau = \eta/E$ is a time constant and ω is the frequency of oscillation. As we are only interested here in using the DMA data to obtain information about the temperature dependence of the elastic modulus, and not in prescribing a viscoelastic model to it, the empirical factor of 0.5 relating the dynamic to static modulus gives adequate information.

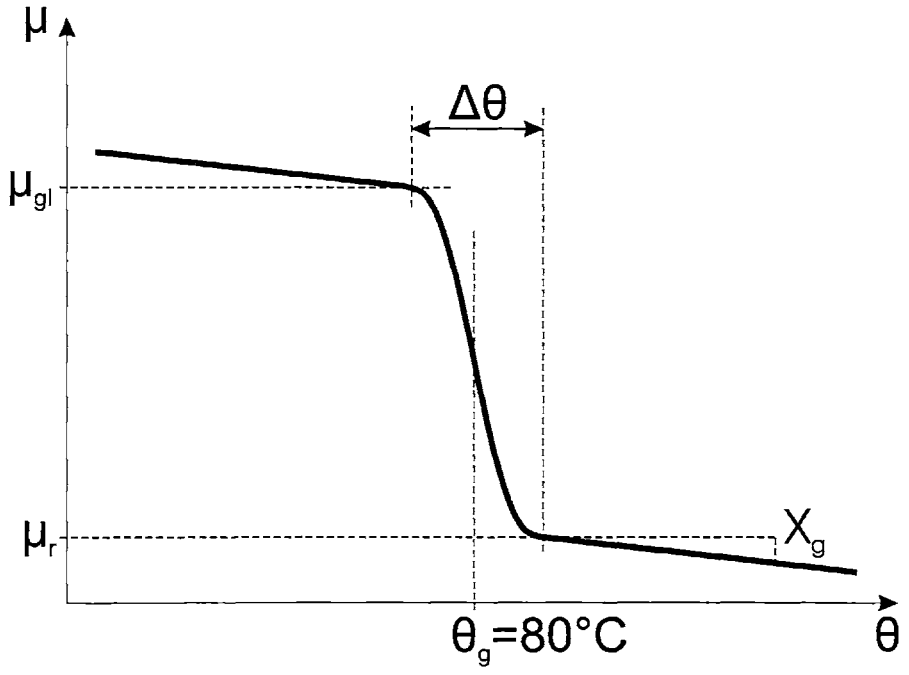

Figure 4-6: Description of initial modulus curve fit and parameters

For example, at 25 ° C, the DMA data gives a value for Young's modulus of 2.5 GPa. This corresponds to an initial modulus of 1.25 GPa in uniaxial compression, and from equation 4.27 the shear modulus is found to be .47 GPa at 25 ° C. A curve fit using the data points at $\dot{\varepsilon} = -.1$ sec^{-1} yields:

$$\begin{aligned} \mu_{gl} &= 455 \text{ MPa} \\ \mu_r &= 25 \text{ MPa} \\ \Delta\theta &= 30 \text{ K} \end{aligned}$$

The 90 ° C and 100 ° C data at $\dot{\varepsilon} = -.005$ sec^{-1} provides the information needed to determine the slope outside the transition region, X_g. This value is determined to be -0.4 MPa K^{-1} for PETG.

The initial modulus in the transition region is also strain-rate dependent. This is accounted for using time-temperature superposition to shift the glass transition temperature with strain rate. The following expression provides a good fit for the

relation between the glass transition temperature, θ_g, and the strain rate, $\dot{\gamma}_A^p$:

$$\theta_g = \begin{cases} \theta_g^* & : \quad \dot{\gamma}_A^p < 0.00173 \\ \xi \log_{10} \dot{\gamma}_A + \zeta + \theta_g^* & : \quad \dot{\gamma}_A^p \geq 0.00173 \end{cases} \tag{4.28}$$

The equivalent strain rate in resistance A, $\dot{\gamma}_A$, is approximated as $\sqrt{3}\dot{\varepsilon}$, with $\dot{\varepsilon}$ being the machine strain rate. θ_g^* is taken to be a reference transition temperature of 73 ° C. The values of ξ and ζ for PETG are 3 K and 8.2263 K, respectively.

Figures 4-7 and 4-8 show how the DMA data compares with data from uniaxial compression experiments. In figure 4-7 the DMA data is plotted along with points for each strain rate as determined from the DMA test setup, where the cyclic loading rate is converted into an equivalent strain rate. Figure 4-8 includes the data points from the uniaxial compression data. These indicate good agreement between the DMA and uniaxial test results. Figure 4-9 shows the curve fit at $\dot{\varepsilon} = -.1$ sec^{-1}, again indicating quite good agreement, and figure 4-10 shows the time-temperature superposition effect on the curve plotted with the data points from uniaxial compression data. Again, very good correlation is seen.

The rate dependence of the flow stress is incorporated using the equation for a thermally activated process:

$$\dot{\gamma}_A^p = \dot{\gamma}_{0A} \exp\left[-\frac{\Delta G(1 - \tau_A/s)}{k\theta}\right] \tag{4.29}$$

The intermolecular resistance, s, is temperature dependent, and is modeled as $s(\theta) = 0.15\mu(\theta)$, where μ is the initial shear modulus as determined above.

The constants $\dot{\gamma}_{0A}$ and ΔG are determined from the intial flow stress at each strain rate for a particular temperature. In this case, the 90 ° C data was used. Equation 4.29 is rearranged to a linear form

$$M \ln(\dot{\gamma}_A^p) - Z = \left(\frac{1}{k\theta}\left(\frac{\tau_A}{s} - 1\right)\right) \tag{4.30}$$

where M=1/ΔG and Z=Mln $\dot{\gamma}_{0A}$. A least squares fit of the data gives the values for

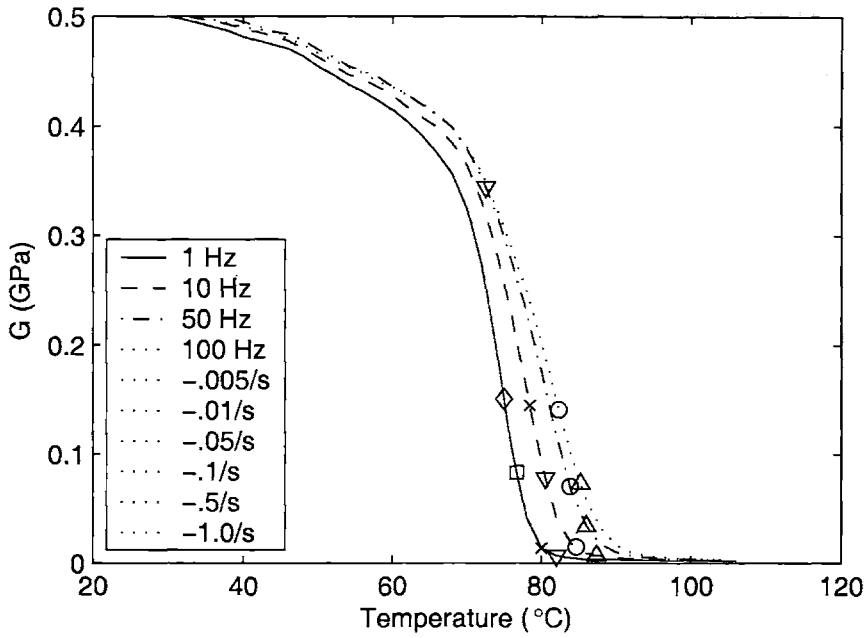

Figure 4-7: PETG DMA data and reduced data points for discrete strain rates

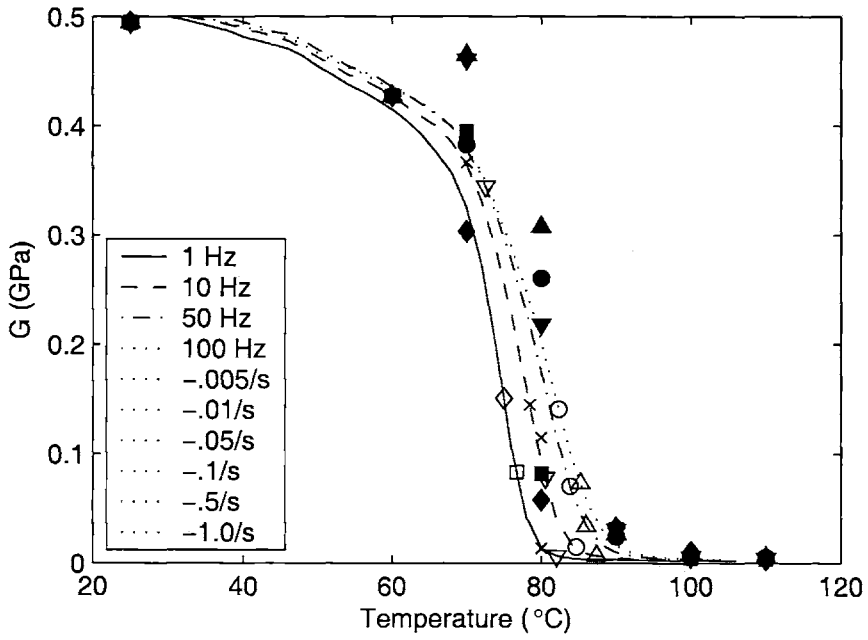

Figure 4-8: PETG DMA data combined with uniaxial initial modulus data (open symbols are DMA data at the indicated strain rates; filled symbols are the compression test data

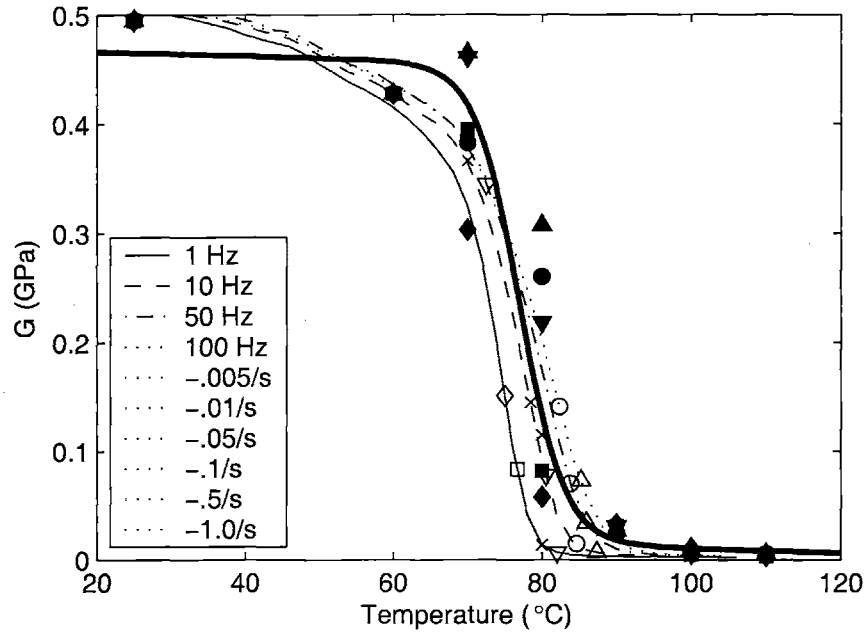

Figure 4-9: PETG DMA Data combined with uniaxial initial modulus data and curve fit (open symbols are DMA data at the indicated strain rates; filled symbols are the compression test data)

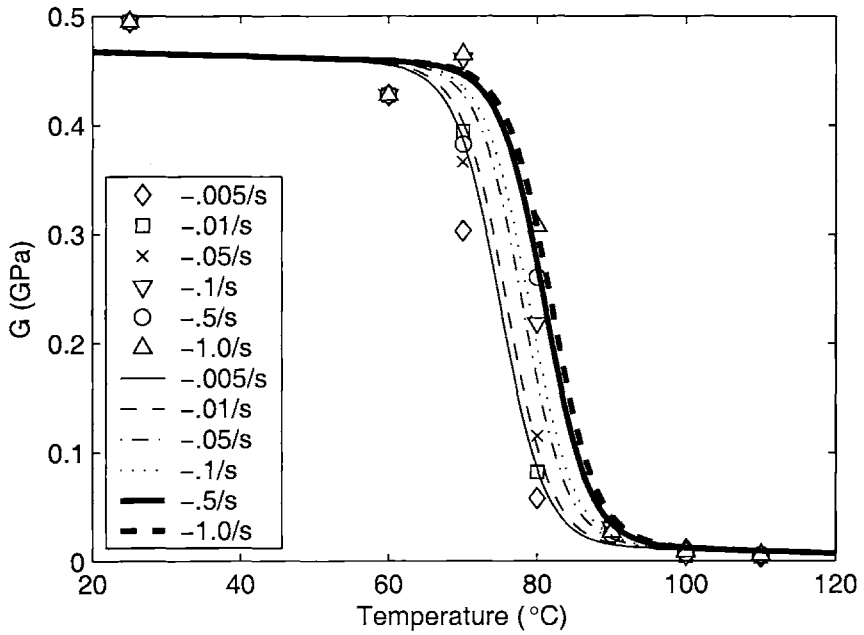

Figure 4-10: PETG Uniaxial initial modulus data and curve fit at various strain rates

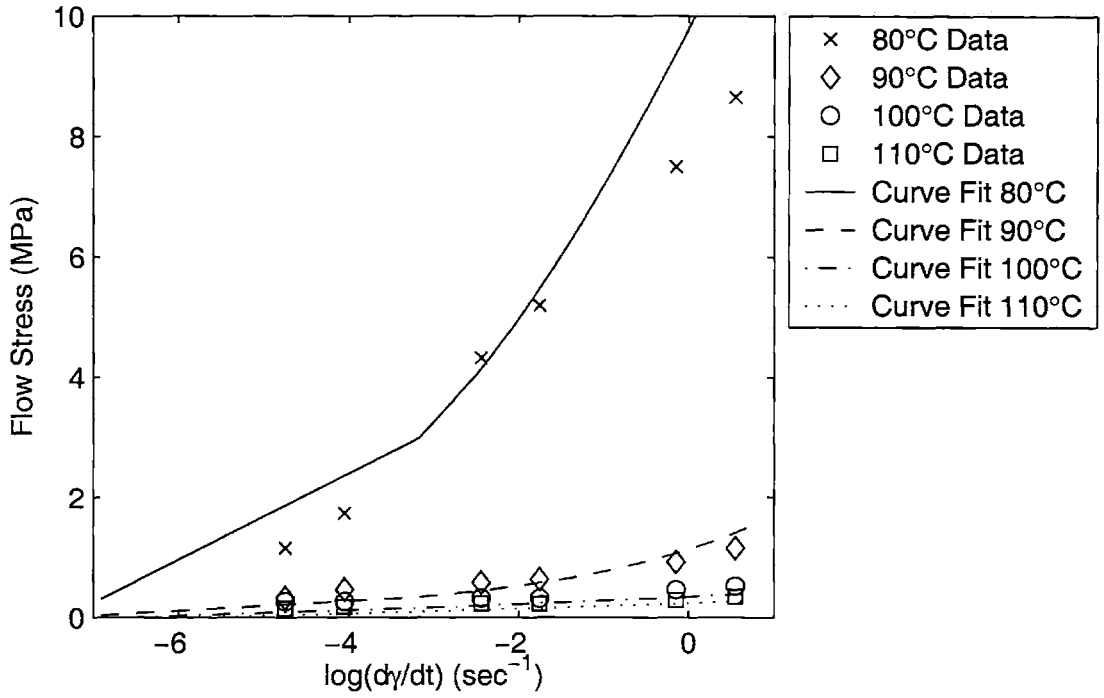

Figure 4-11: PETG Flow stress as a function of strain rate

M and Z, and in turn for ΔG and $\dot{\gamma}_{0A}$. For PETG, the values are:

$$\Delta G = 1.75 \times 10^{-19} \text{J}$$

$$\dot{\gamma}_{0A} = 2.0 \times 10^{12} \text{ sec}^{-1}$$

Figure 4-11 shows a plot of the flow stress, τ_A, as a function of the logarithm of the shear strain rate, $\ln \dot{\gamma}_A^p$, along with the least squares curve fit of the data. This figure demonstrates that very good agreement is obtained using the thermally activated mechanism. It is interesting to note that the curve fit is not a straight line. This is due to the rate dependence of the intermolecular resistance, s, which comes in through the rate dependence of the glass transition temperature and the shear modulus, as was discussed previously. The result is a non-linear curve for the flow stress as a function of the logarithm of the strain rate. The 80 ° C data shows particularly good correlation.

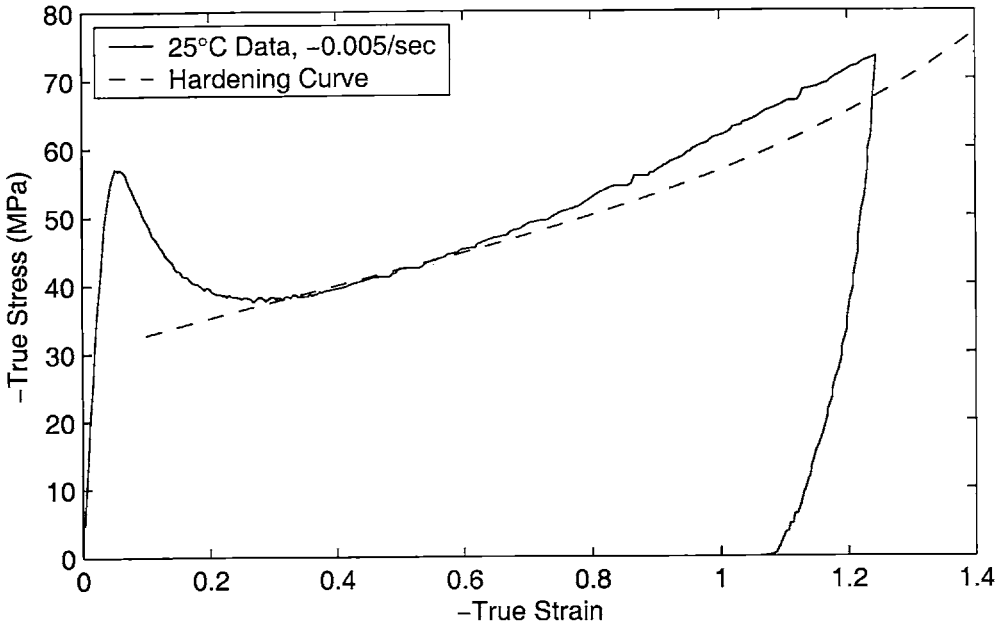

Figure 4-12: PETG Uniaxial Compression Data, Temperature = 25 ° C, $\dot{\epsilon} = -.005/s$, plotted with the strain hardening curve

4.2.2 Resistance B (Network)

The material properties needed for the hardening/stiffening portion of resistance B are an initial hardening slope, $\nu k\theta$, and the number of rigid links between entanglements, N, which correlates with the effective stretch where a dramatic upturn in stress occurs. Fitting to 25 ° C uniaxial compression data at $\dot{\epsilon}$= -0.1 $\sec^{-1}$ gives:

$$\begin{aligned} \nu k\theta &= 8.5 \times 10^6 \text{ Pa} \\ N &= 7.0 \end{aligned}$$

Figures 4-12 and 4-13 show how well the strain hardening is captured at 25 ° C in uniaxial compression. The agreement is quite good in plane strain compression as well. The lowest strain rate data (-0.005 $\sec^{-1}$) was used in order to avoid the effects of thermal softening due to adiabatic heating at higher temperatures.

The molecular relaxation in resistance B is temperature dependent and was orig-

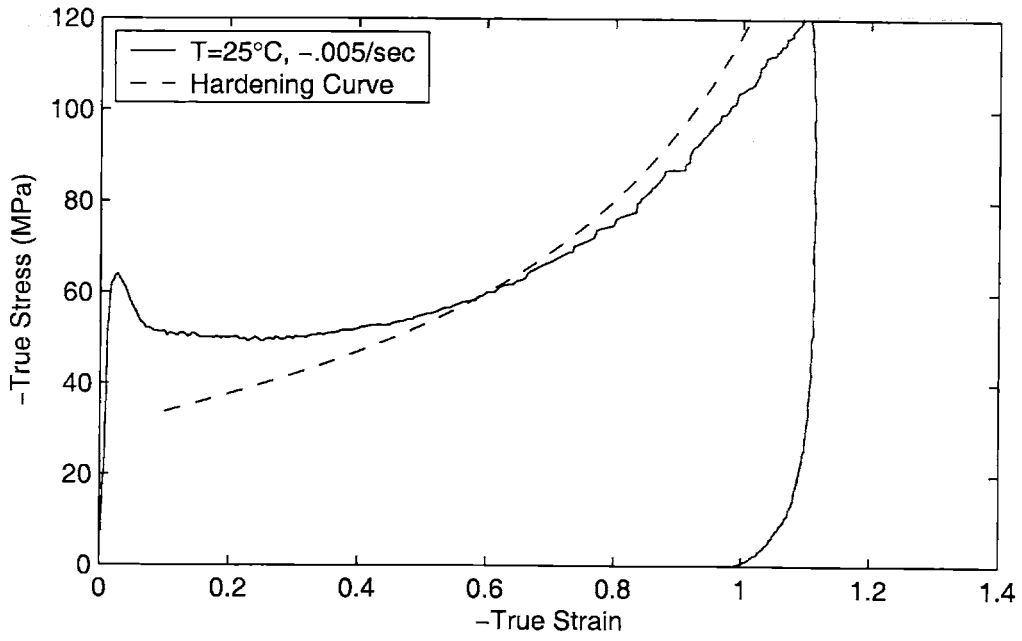

Figure 4-13: PETG Plane Strain Compression Data, Temperature = 25 ° C, $\dot{\varepsilon} = -.005/s$, plotted with the strain hardening curve

inally modeled as

$$\dot{\gamma}_B^F = C\left(\frac{1}{\lambda_F - 1}\right)\tau_B \tag{4.31}$$

with C being a temperature dependent parameter:

$$C = D\exp\left\{-\frac{Q}{R\theta}\right\} \tag{4.32}$$

Figure 4-14 shows the result of fitting the molecular relaxation coefficient, C, to the 90 ° C data at a strain rate of -.5 $\sec^{-1}$. This expression is inadequate in predicting the strain rate dependence of the material behavior at 90 ° C, as is evident from the extreme over-relaxation at the lower strain rates of -.05 $\sec^{-1}$ and -.005 $\sec^{-1}$.

To better capture the strain rate dependence, equation 4.31 is modified to be:

$$\dot{\gamma}_B^F = C\left[\left(\frac{1}{\lambda_F - 1}\right)\tau_B\right]^3 \tag{4.33}$$

Through trial and error curve fitting at 90 ° C, 100 ° C, and 110 ° C of the -0.5 $\sec^{-1}$

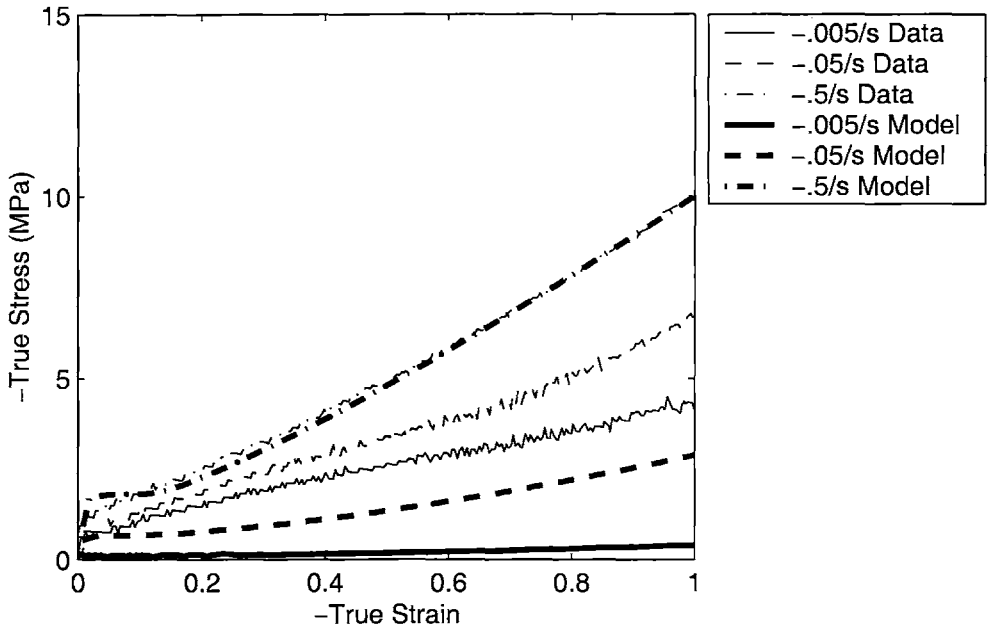

Figure 4-14: PETG Uniaxial Compression, Temperature = 90 ° C, Comparison of model prediction with experimental data

data the value of C at each temperature can be determined:

$$
\begin{aligned}
C(90\,^{\circ}C, -.5s^{-1}) &= 1.0 \times 10^{-23}(\mathrm{Pa}^3\ \mathrm{s})^{-1} \\
C(100\,^{\circ}C, -.5s^{-1}) &= 14.0 \times 10^{-23}(\mathrm{Pa}^3\ \mathrm{s})^{-1} \\
C(110\,^{\circ}C, -.5s^{-1}) &= 150.0 \times 10^{-23}(\mathrm{Pa}^3\ \mathrm{s})^{-1}
\end{aligned}
$$

and using a least-squares curve fit of these values, D and Q/R are obtained:

$$
\begin{aligned}
D &= 2.5 \times 10^{18}(\mathrm{Pa}^3\ \mathrm{s})^{-1} \\
Q/R &= 3.4574 \times 10^{4}\mathrm{K}
\end{aligned}
$$

This fully specifies the material properties needed for this model.

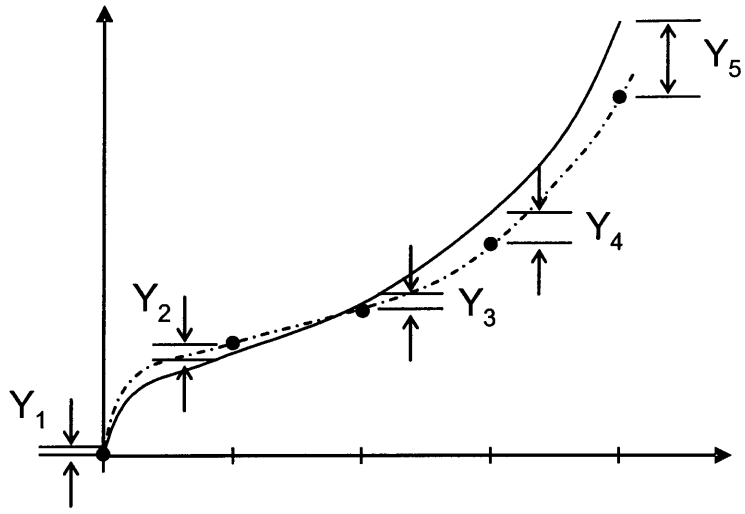

Figure 4-15: Illustration of error between simulation and experimental data

4.3 Error in Curve Fitting

In section 4.4 the simulation results using the previously defined material constants will be compared with experimental data. Before presenting this information, it will be useful to define an algorighm for quantifying the agreement between experimental data and the simulated curve. To do so, we begin by defining an error parameter to quantify the error between a simulated curve and the corresponding experimental data. This is illustrated in Figure 4-15.

The error in stress between simulation and experiment is measured at several discrete, equally-spaced strain values, in this case five error values are measured $(Y_1, \ldots, Y_5)$. Each error value is divided by the measured experimental stress value at that strain level:

$$y_1 = y\Big|_{\varepsilon=\varepsilon_1} = \frac{Y\Big|_{\varepsilon=\varepsilon_1}}{\sigma\Big|_{\varepsilon=\varepsilon_1}} = \frac{Y_1}{\sigma_1} \tag{4.34}$$

The absolute values of these normalized error values $(y_1, \ldots, y_5)$ are then averaged as follows:

$$\bar{y} = \frac{1}{n_y} \sum_{i=1}^{n_y} |y_i| \tag{4.35}$$

where n_y is the number of error points. It is clear that the error value will be different depending on the number of error points and the interval chosen to evaluate the error,

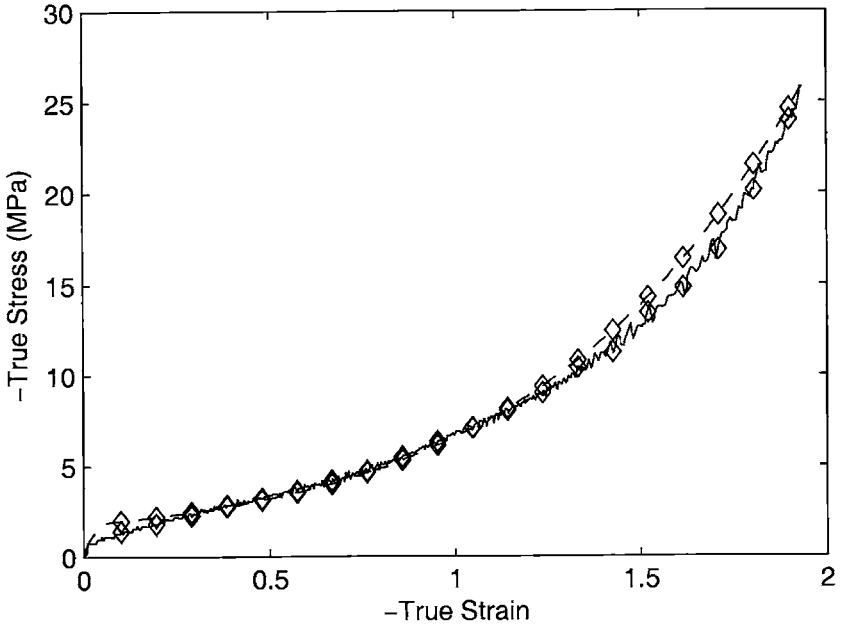

Figure 4-16: Illustration of error between simulation and experimental data (solid line is experimental data, dashed line is simulation, markers indicate points at which error is calculated)

so it is important to report both the number of points and the interval of interest when indicating the error of a particular curve fit.

As an example, in figure 4-16, experimental data for a uniaxial compression experiment at 90 ° C and -0.05/sec is shown (solid line) with the results of a simulation (dashed line). The error is calculated using $n_y = 20$, with data points equally spaced between ε=0.1 and ε=1.9. For this case, the error is calculated to be 0.0747, or 7.47 %. It can be seen in figure 4-16 that this represents an excellent curve fit over the entire strain range. The calculated error value using $n_y = 5$ is 12.54 %, using $n_y = 10$ is 8.20 %, using $n_y = 50$ is 6.92 %, using $n_y = 100$ is 6.54 %, and using $n_y = 200$ is 6.59 %. Based on these numbers, it appears that using fewer than fifty evaluation points over a strain range of 0 to 1.9 causes the calculated error to be dependent on the number of points, so for error calculation purposes we will use $n_y = 100$ from here on.

4.4 Comparison with Experimental Data

The following figures show the results of the computer simulation for uniaxial compression and plane strain compression. Figures 4-17 to 4-20 show results of the uniaxial compression simulations at each temperature from 80 ° C to 110 ° C. Figures 4-21 to 4-26 show the same results, plotted at constant strain rate. Figures 4-27 to 4-29 show the results at constant temperature for plane strain simulations.

The figures indicate that the material model captures the general trends of the stress-strain behavior of PETG quite well, including the initial modulus, roll over to flow, initial hardening slope, and strain hardening. The model is very good at predicting the temperature dependence of these various elements as well as the strain rate dependence. Figures 4-30 and 4-31 show enlarged views of the model predictions. Figure 4-30 shows the simulation at 90 ° C at different strain rates and indicates that as strain rate increases, the model correctly predicts that the initial modulus, flow stress, and hardening modulus all increase. Figure 4-31 shows the simulation at -.05 sec^{-1} at different temperatures. It demonstrates that the model correctly captures the decrease in initial modulus, flow stress, and initial hardening modulus with increasing temperature.

Figures 4-32 through 4-35 show the comparison between computer simulations and the experimental data for uniaxial compression. Figures 4-36 to 4-38 show the same comparison for plane strain. Table 4.1 lists the calculated error for each of the curves and figures 4-39 and 4-40 show these results graphically. The model does a fairly good job of predicting the deformation behavior up to a strain of about -1.0. The initial modulus and flow stress are predicted especially well at 80 ° C, as shown in figures 4-32 and 4-36. At higher strain levels, the model is not quite as effective at predicting the material behavior. In plane strain, the model tends to overpredict the strain hardening at large strains. In uniaxial compression, on the other hand, it appears that the model is predicting too much relaxation at large strain levels. For example, at 90 ° C (see figure 4-33), the model simply does not predict the dramatic strain hardening that is observed in experiments. The trend is less pronounced at

higher temperatures and high strain rates, but is still visible in the lower strain rates at 100 ° C and 110 ° C.

Since the material deformation is accommodated by a combination of strain due to the deforming network and strain due to molecular relaxation, the stress-strain curves can be decomposed into network stretch and flow stretch charts. This is approached as follows. Using the network stretch and orientation curve as a baseline for the material response in the absence of molecular relaxation, the strain hardening portion of each stress-strain curve is multiplicatively decomposed into network and flow portions. For example, under a particular set of test conditions, at a total logarithmic strain of -1.0 (an axial stretch, λ_T, of .368), the data gives the stress required to attain this strain. The baseline network stretch and orientation curve, however, indicates that, in the absence of molecular relaxation, this value of stress would have been reached at a much lower strain level, such as -0.7 (an axial stretch, λ_N, of .496) if network stretching and orientation were the only mechanism contributing to the polymer deformation. The remainder of the deformation is accounted for by molecular relaxation. The product of the network stretch and the flow stretch is therefore equal to the total stretch: $\lambda_N \lambda_F = \lambda_T$. In this example the flow stretch, λ_F, equals .741. This produces one point on the network stretch-flow stretch chart.

To illustrate, figure 4-41 shows the axial network stretch versus axial flow stretch curves for the 90 ° C experimental data. As deformation begins, the material has a network stretch and flow stretch equal to 1.0. As deformation progresses, it is accommodated by a combination of molecular relaxation and network stretching and orientation, and the relative amount that each contributes determines the slope of the curve. For the lower strain rates, the initial slope of the network stretch-flow stretch curve is steeper than at higher rates, indicating that more of the deformation is accommodated by molecular relaxation at low strain rates. This creates the general trend from the lower right to the upper left corner as strain rate increases. After the polymer reaches a certain level of network stretch (at approximately $\lambda_N = 0.6$ for -0.1 sec^{-1} in the 90 ° C data), the molecular relaxation appears to cease, indicated by the leveling off of the network stretch-flow stretch curve. This leveling off occurs at

earlier network stretch levels for lower strain rates.

Figures 4-42 through 4-44 show the network stretch versus flow stretch for uniaxial compression both for the experimental data and for the proposed model at various temperatures. The plots help to explain why the model does not capture the dramatic increase in strain hardening at large strains in uniaxial compression. In comparing the experimental data with the computer simulations, it can be seen that the current model (indicated by filled symbols) initially follows the same trend as the experimental data (indicated by open symbols), but is unable to capture the cessation of flow. In their work with PET, Llana and Boyce (1999) observed this phenomenon with PET and attributed it to the onset of strain-induced crystallization. While PETG is non-crystallizable, it seems to exhibit the same trend. In the next section, the model will be revised to incorporate this temperature and strain rate dependent cessation of flow to improve the ability of the model to capture the orientation hardening behavior of the material.

Figures 4-45 through 4-46 show the network stretch versus flow stretch for plane strain compression experiments and simulations. As was noted earlier, these plots consistently show how the model tends to overpredict the strain hardening in plane strain. Each of the simulated curves (filled symbols) lies above its corresponding experimental curve (open symbols), indicating that the simulation is predicting less molecular relaxation than is observed experimentally. It is also interesting to note that the plane strain curves do not exhibit such a distinct flow cutoff as was observed in the uniaxial compression experiments. This is likely because experiments were only carried out to a final strain of -1.3 due to the limited size of the plane strain compression fixture. It is suggested that if the experiments were carried out to higher strain levels, the same flow cessation would appear in the plane strain data as appears in the uniaxial data. This warrants additional testing in future work.

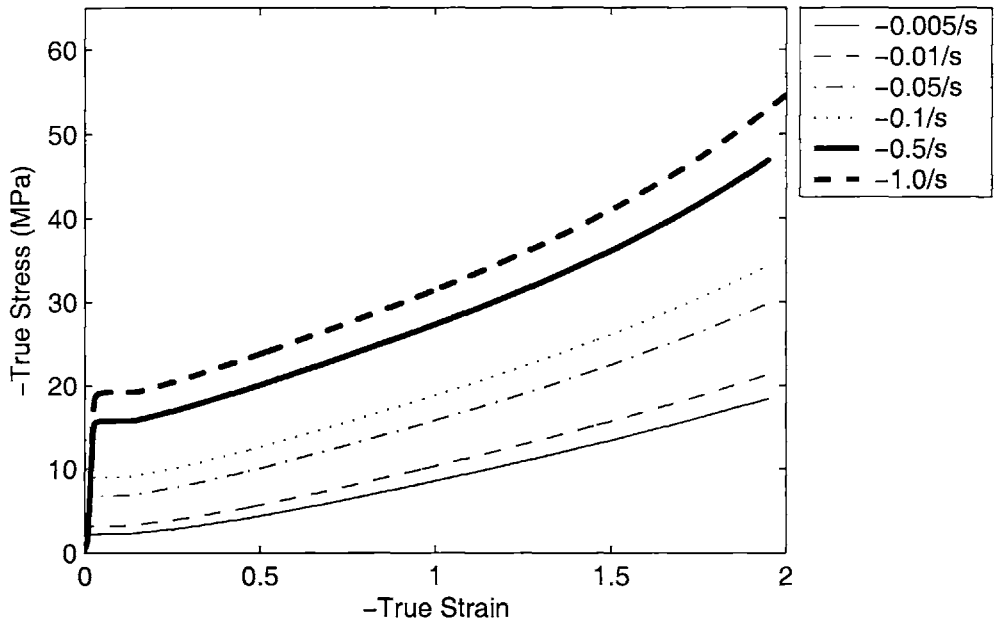

Figure 4-17: Uniaxial compression simulation, Temperature = 80 ° C

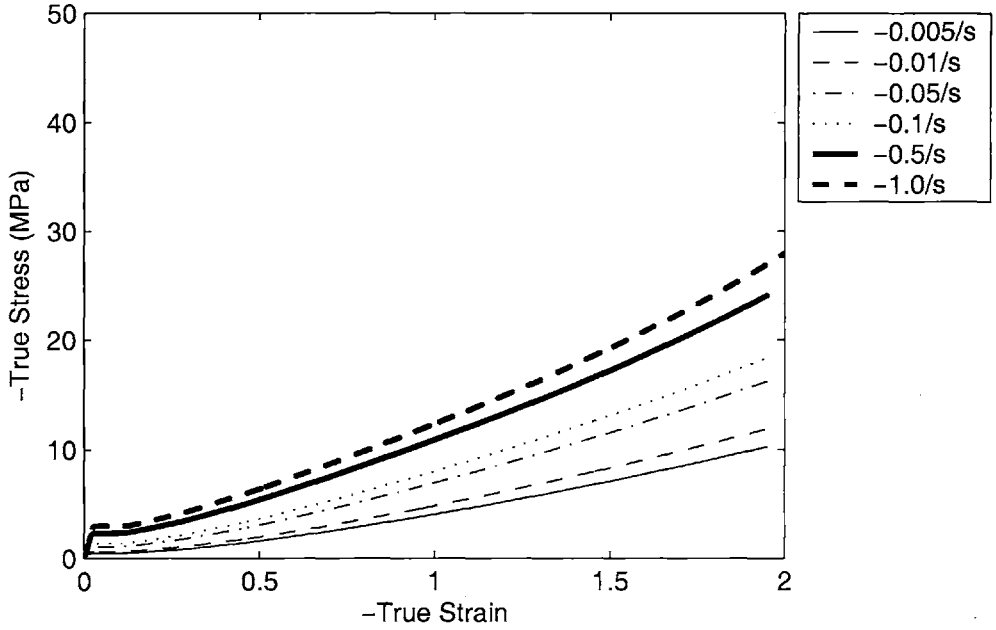

Figure 4-18: Uniaxial compression simulation, Temperature = 90 ° C

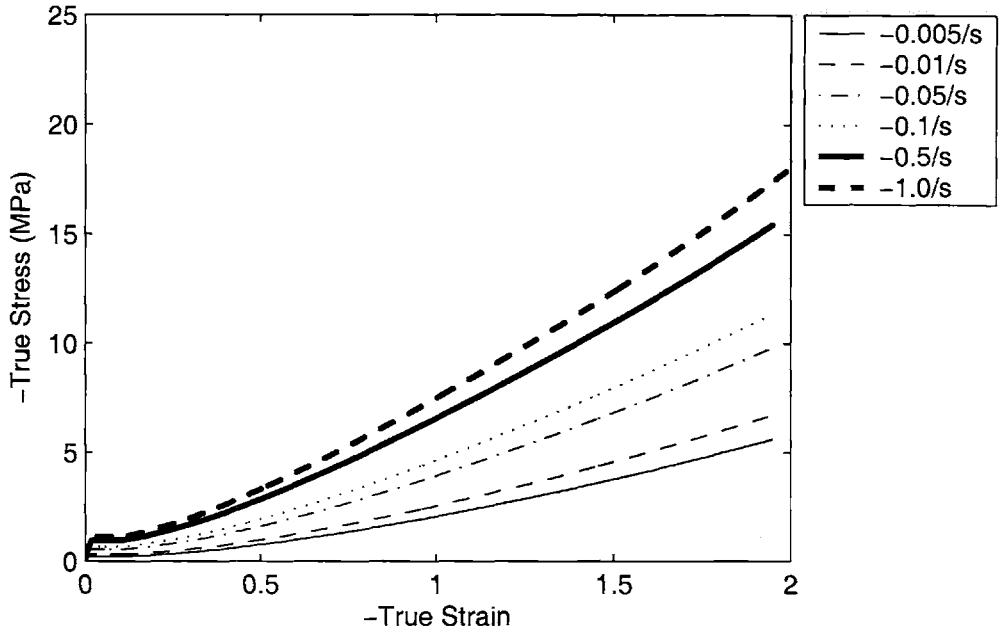

Figure 4-19: Uniaxial compression simulation, Temperature = 100 ° C

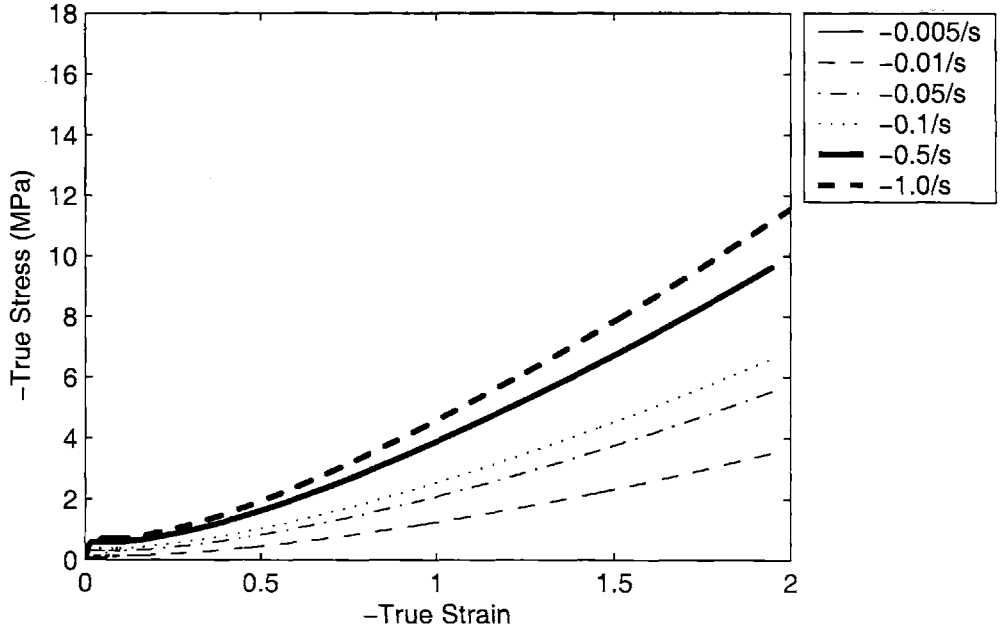

Figure 4-20: Uniaxial compression simulation, Temperature = 110 ° C

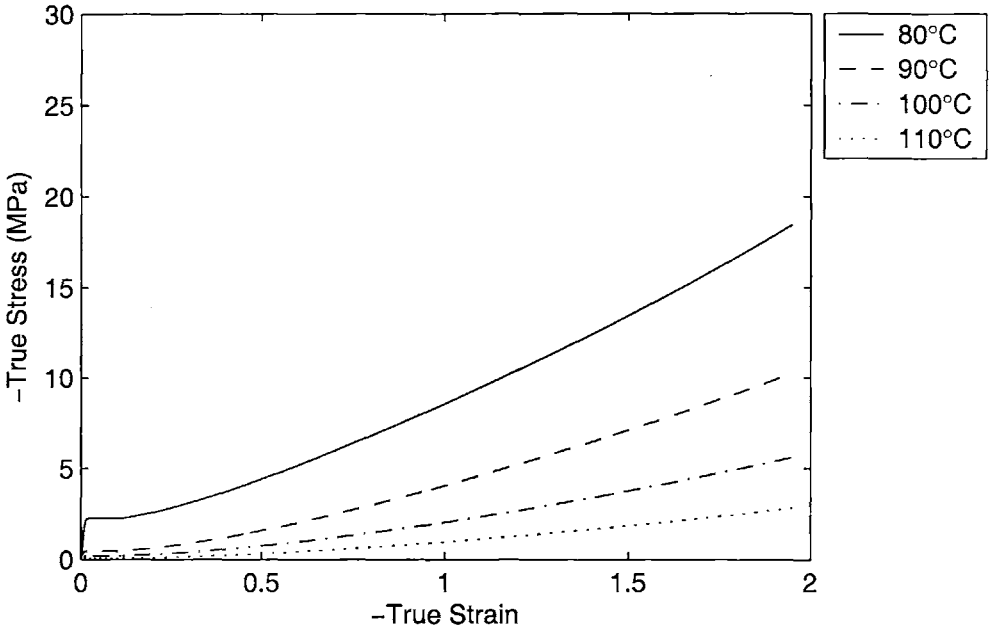

Figure 4-21: Uniaxial compression simulation, $\dot{\varepsilon}$ = -.005/s

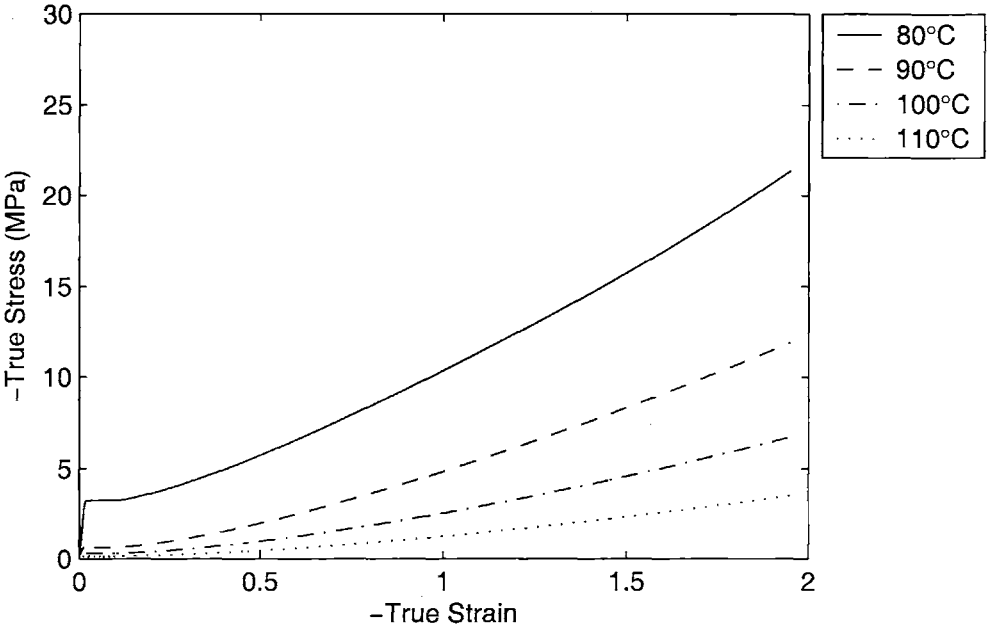

Figure 4-22: Uniaxial compression simulation, $\dot{\varepsilon}$ = -.01/s

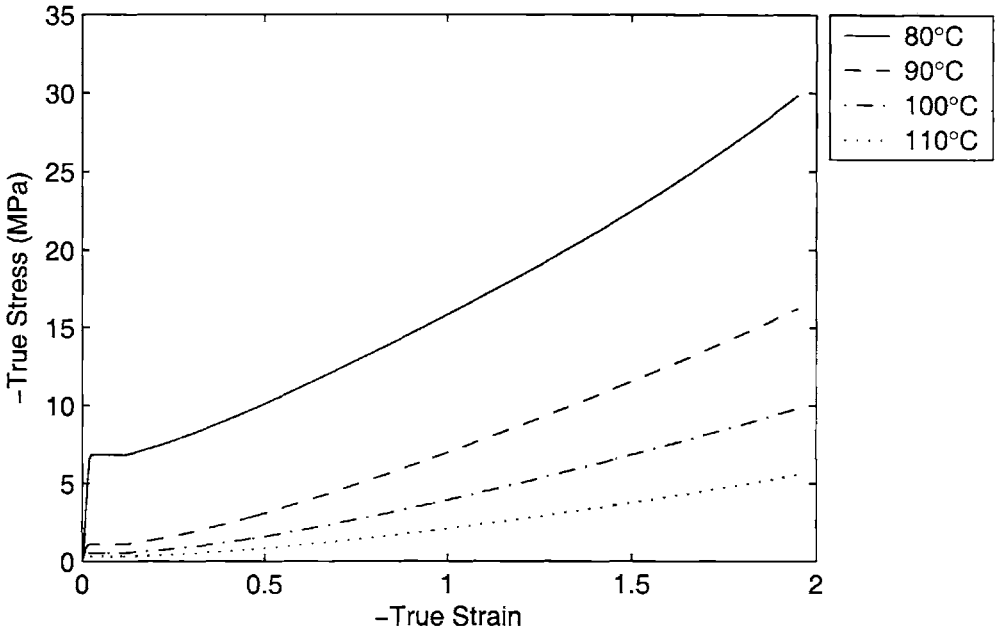

Figure 4-23: Uniaxial compression simulation, $\dot{\varepsilon}$ = -.05/s

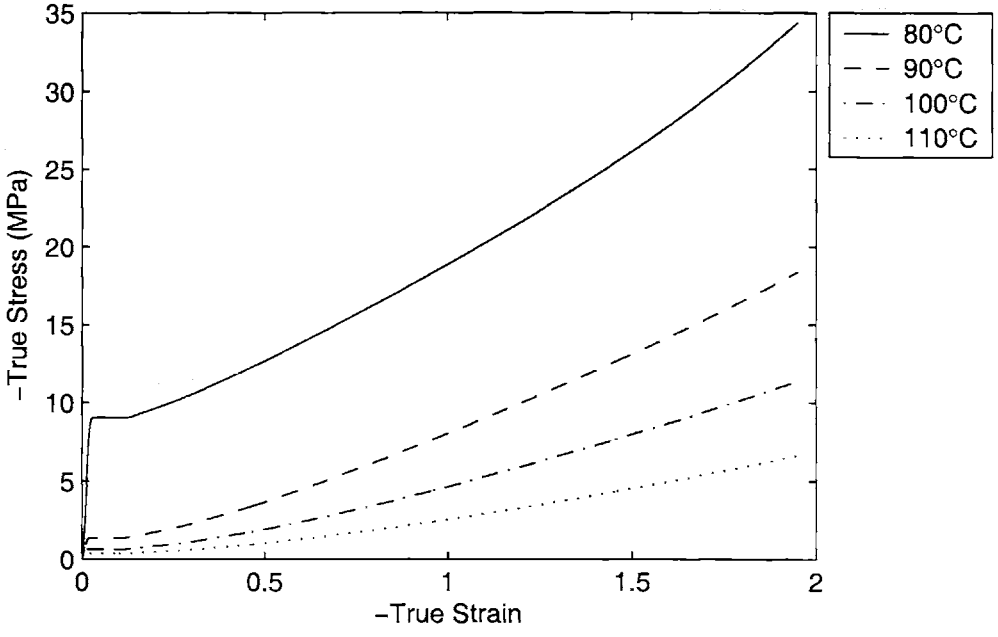

Figure 4-24: Uniaxial compression simulation, $\dot{\varepsilon}$ = -.1/s

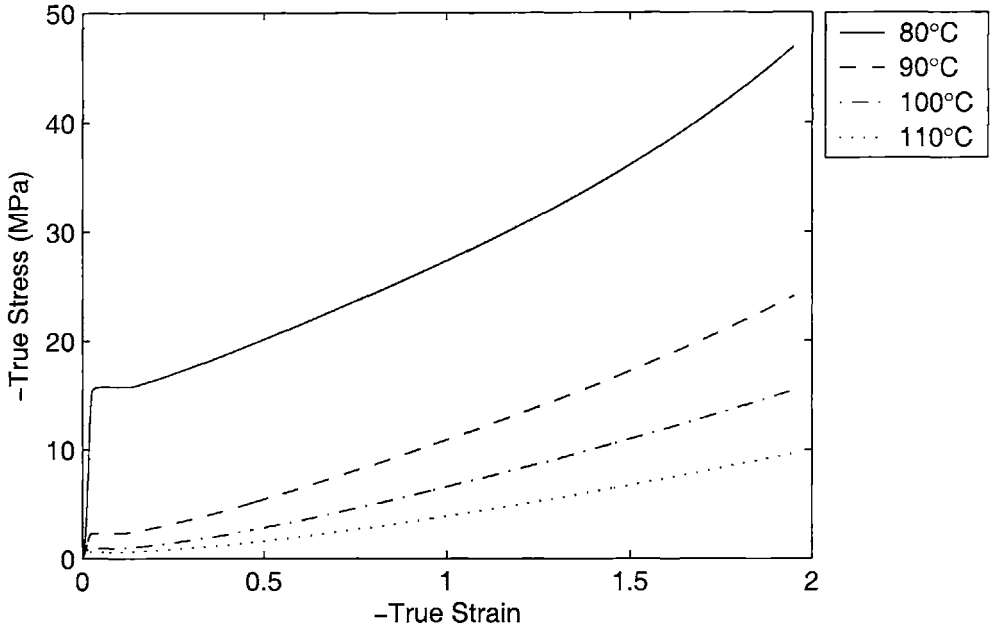

Figure 4-25: Uniaxial compression simulation, $\dot{\varepsilon}$ = -.5/s

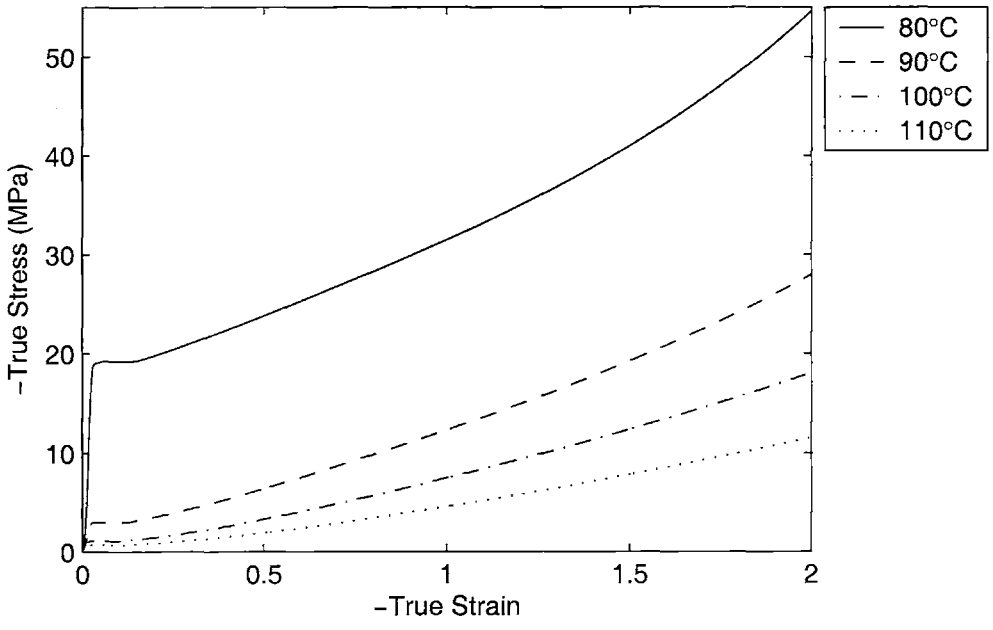

Figure 4-26: Uniaxial compression simulation, $\dot{\varepsilon}$ = -1.0/s

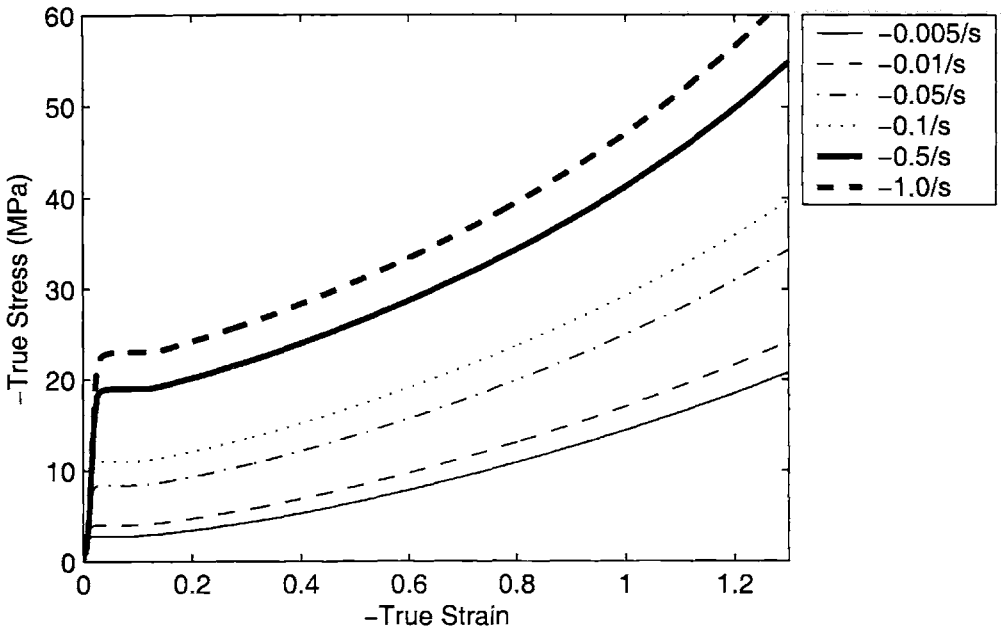

Figure 4-27: Plane strain compression simulation, Temperature = 80 ° C

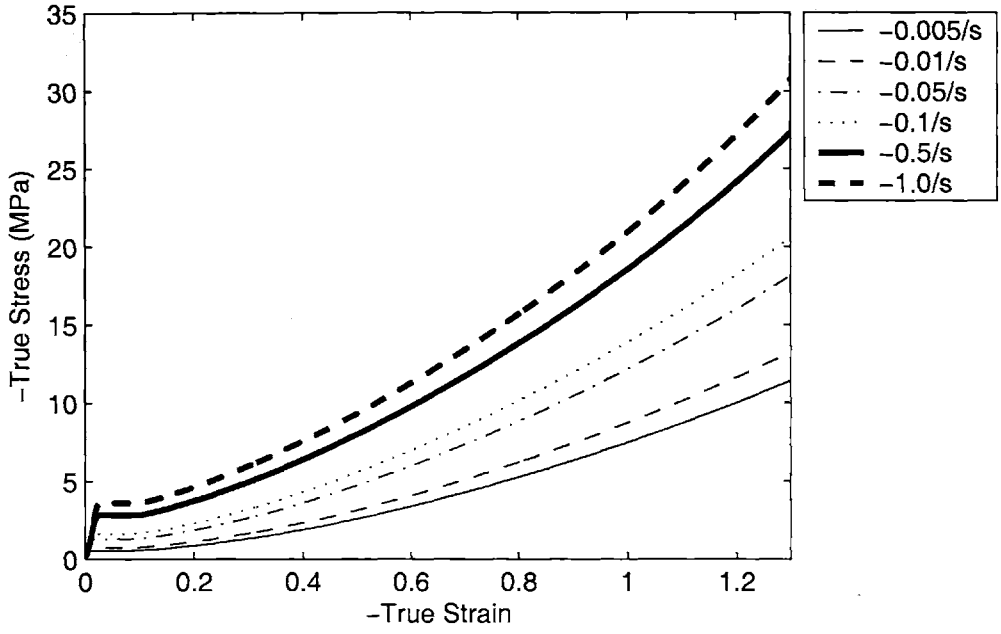

Figure 4-28: Plane strain compression simulation, Temperature = 90 ° C

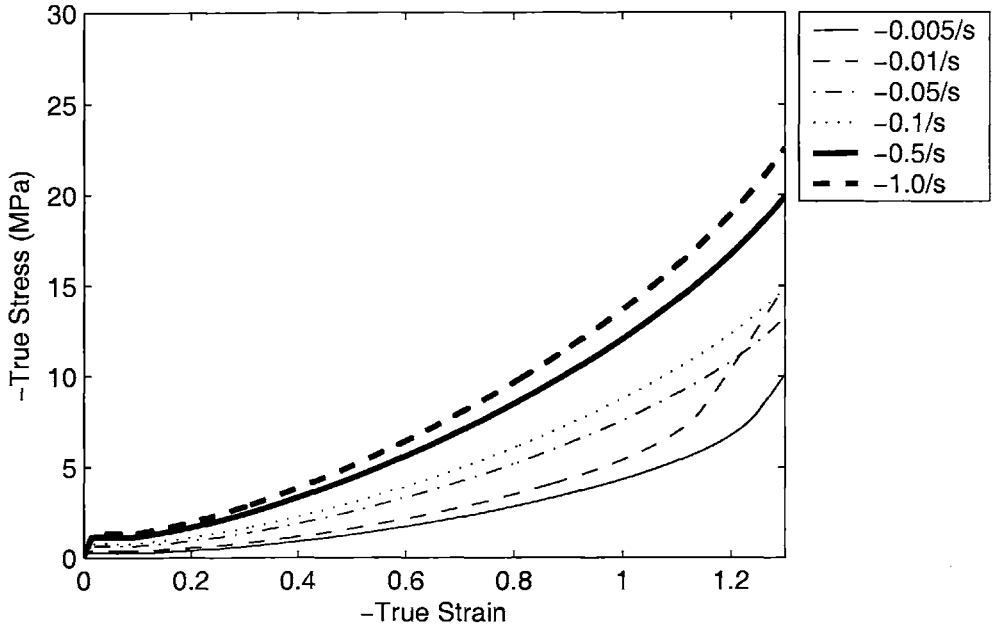

Figure 4-29: Plane strain compression simulation, Temperature = 100 ° C

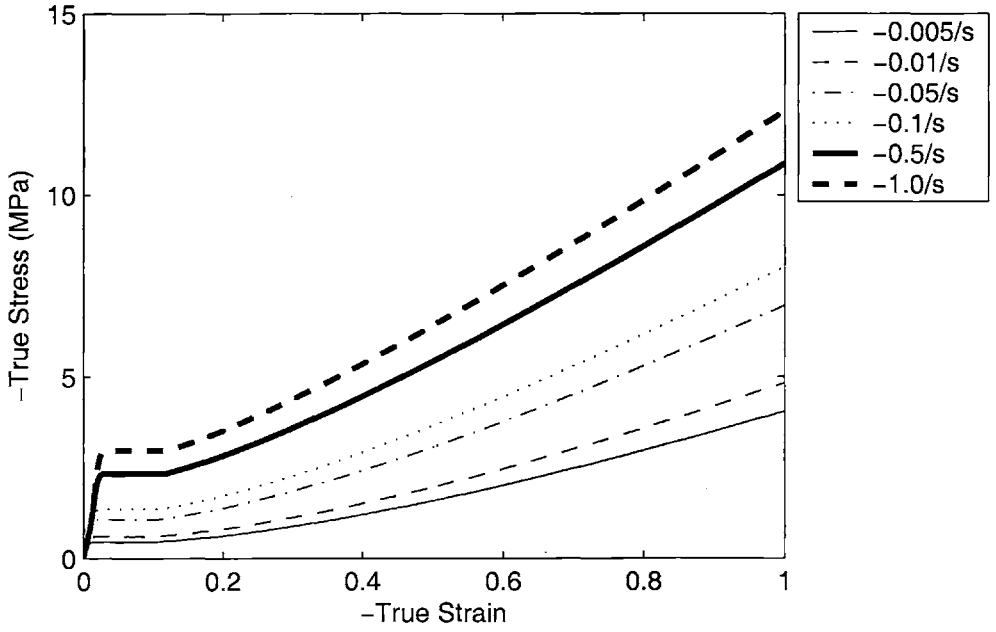

Figure 4-30: Uniaxial compression simulation, Temperature = 90 ° C, enlarged to show detail of initial modulus and flow stress

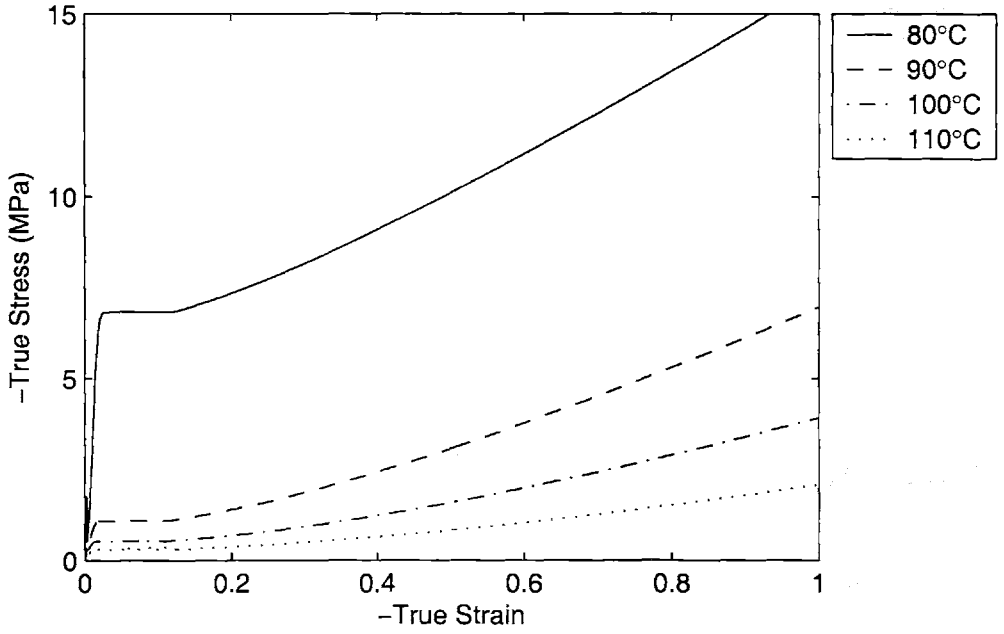

Figure 4-31: Uniaxial compression simulation, $\dot{\varepsilon}$ = -.05/s, enlarged to show detail of initial modulus and flow stress

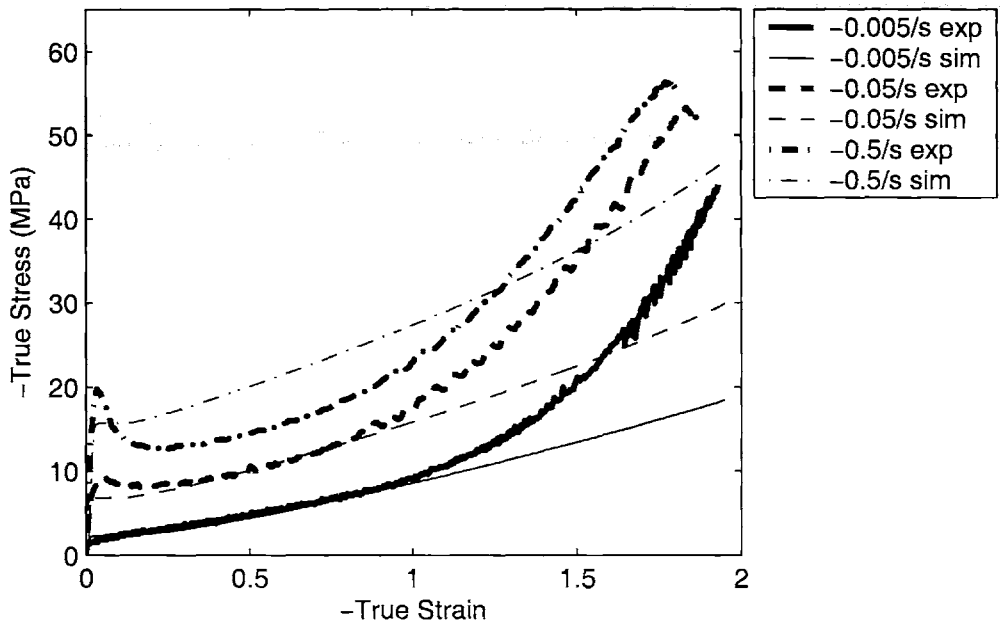

Figure 4-32: PETG Uniaxial compression, comparing simulation results with experimental data, Temperature = 80 ° C

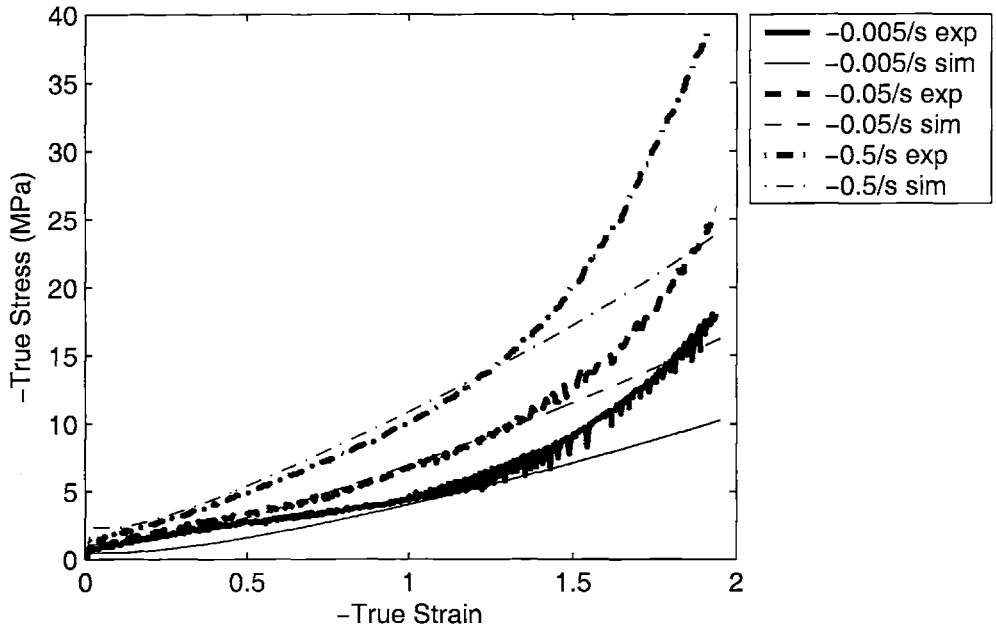

Figure 4-33: PETG Uniaxial compression, comparing simulation results with experimental data, Temperature = 90 ° C

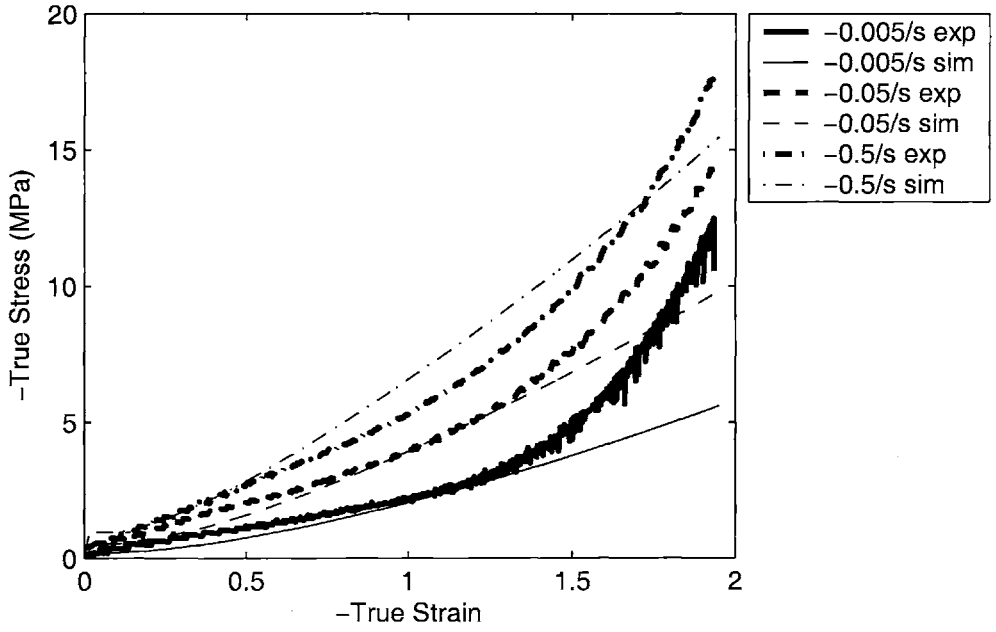

Figure 4-34: PETG Uniaxial compression, comparing simulation results with experimental data, Temperature = 100 ° C

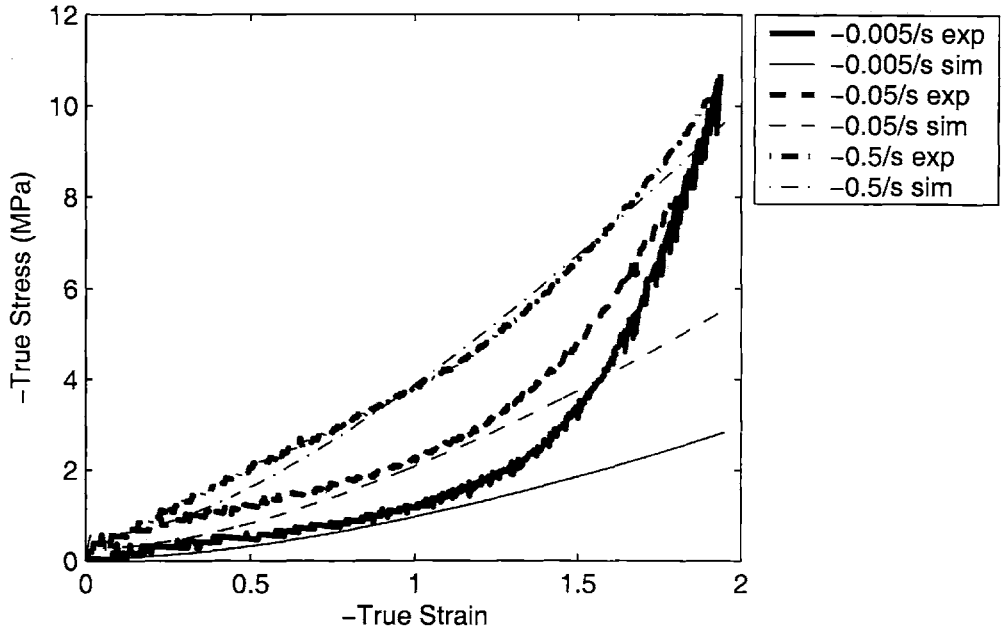

Figure 4-35: PETG Uniaxial compression, comparing simulation results with experimental data, Temperature = 110 ° C

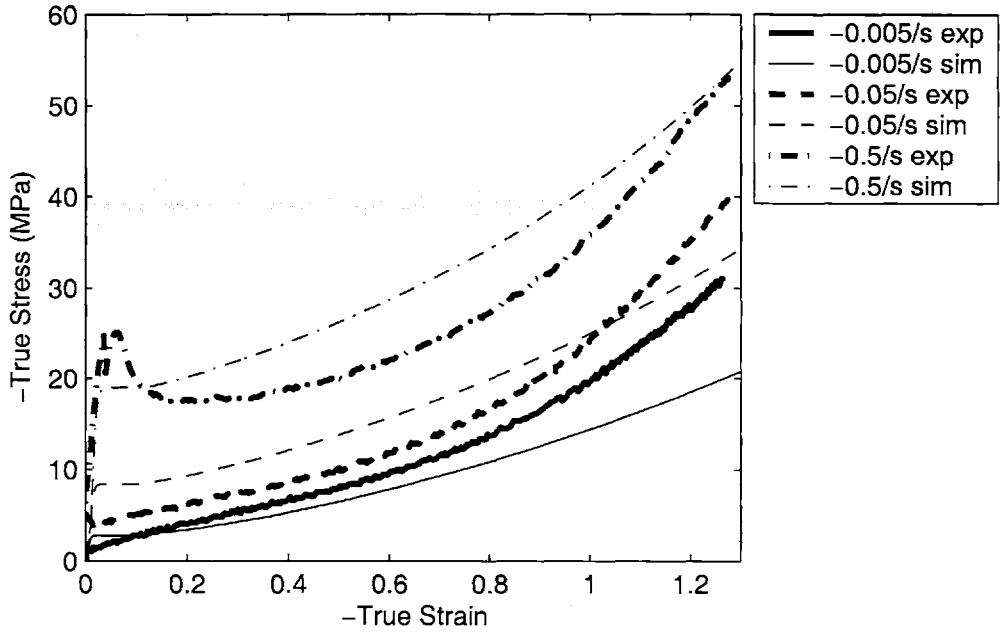

Figure 4-36: PETG Plane strain compression, comparing simulation results with experimental data, Temperature = 80 ° C

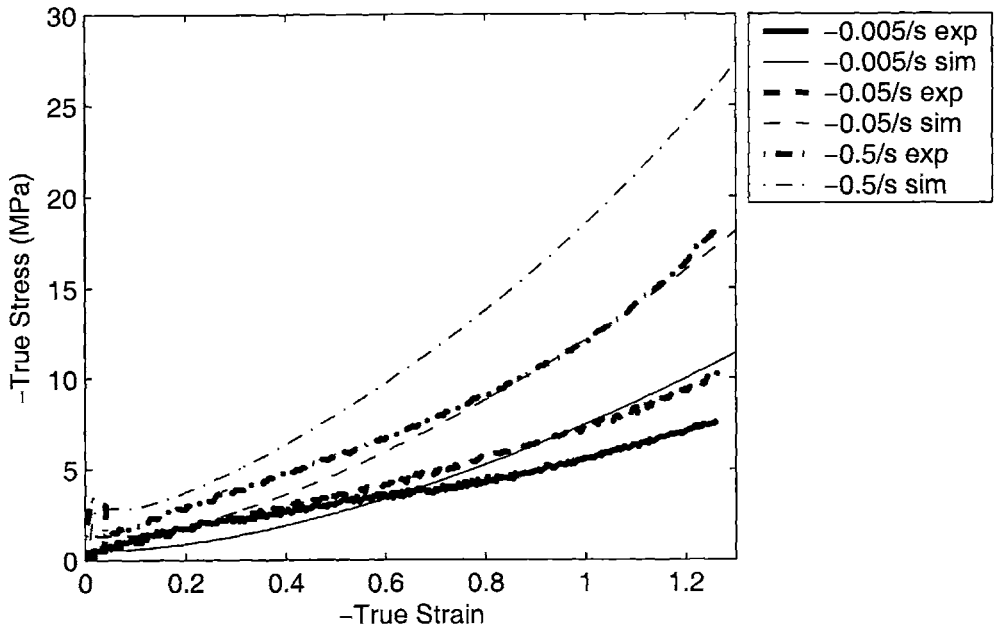

Figure 4-37: PETG Plane strain compression, comparing simulation results with experimental data, Temperature = 90 ° C

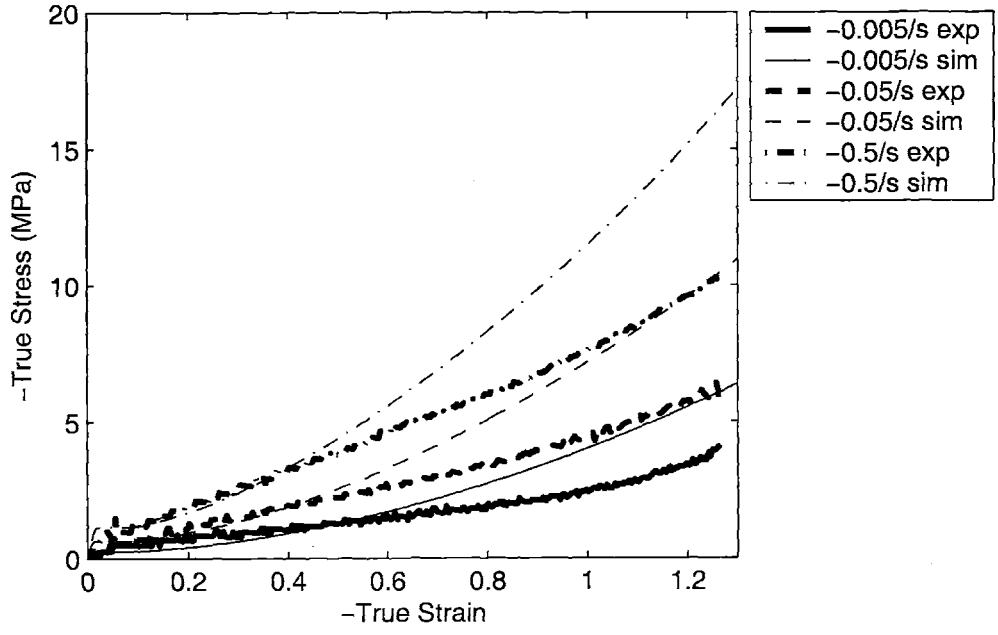

Figure 4-38: PETG Plane strain compression, comparing simulation results with experimental data, Temperature = 100 ° C

Table 4.1: PETG Error values for uniaxial and plane strain compression simulations

Strain State	Temperature	Strain Rate	$\bar{y}$, full range	$\bar{y}$, up to $\varepsilon = 1.0$
Uniaxial	80 ° C	-0.005/sec	.1945	.0777
Uniaxial	80 ° C	-0.05/sec	.1869	.0612
Uniaxial	80 ° C	-0.5/sec	.2269	.3037
Uniaxial	90 ° C	-0.005/sec	.2901	.3724
Uniaxial	90 ° C	-0.05/sec	.1102	.1095
Uniaxial	90 ° C	-0.5/sec	.1420	.1267
Uniaxial	100 ° C	-0.005/sec	.2705	.3050
Uniaxial	100 ° C	-0.05/sec	.1412	.1683
Uniaxial	100 ° C	-0.5/sec	.1368	.1380
Uniaxial	110 ° C	-0.005/sec	.4199	.3889
Uniaxial	110 ° C	-0.05/sec	.2580	.2953
Uniaxial	110 ° C	-0.5/sec	.0995	.1475
Plane Strain	80 ° C	-0.005/sec	.2217	.1943
Plane Strain	80 ° C	-0.05/sec	.2949	.3520
Plane Strain	80 ° C	-0.5/sec	.1977	.2301
Plane Strain	90 ° C	-0.005/sec	.3007	.2808
Plane Strain	90 ° C	-0.05/sec	.4659	.3975
Plane Strain	90 ° C	-0.5/sec	.4563	.4410
Plane Strain	100 ° C	-0.005/sec	.3955	.3414
Plane Strain	100 ° C	-0.05/sec	.3507	.2707
Plane Strain	100 ° C	-0.5/sec	.2905	.2165

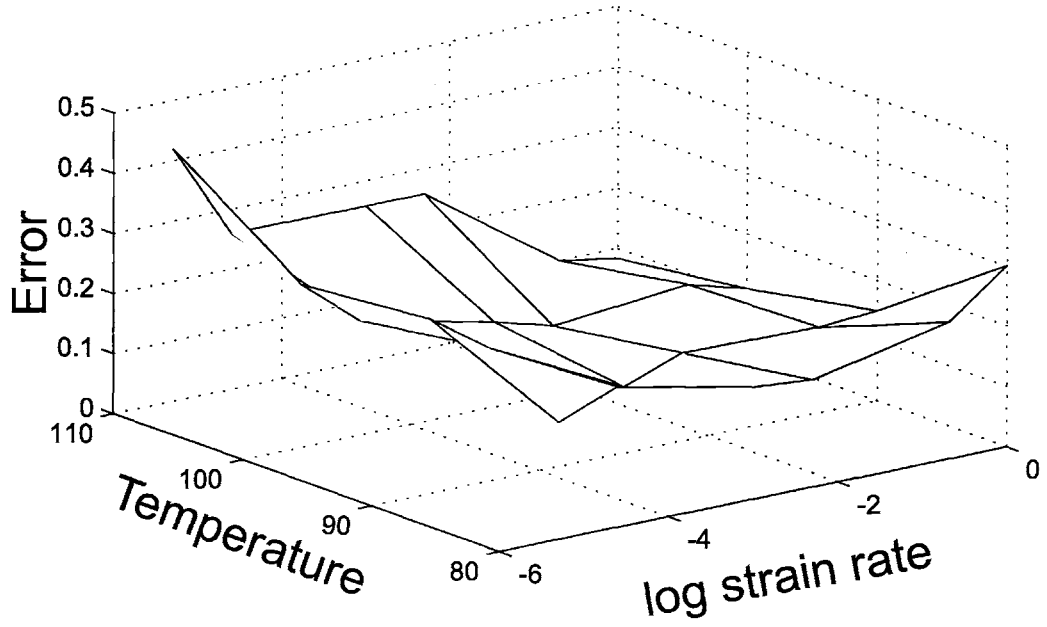

Figure 4-39: PETG Uniaxial compression error values

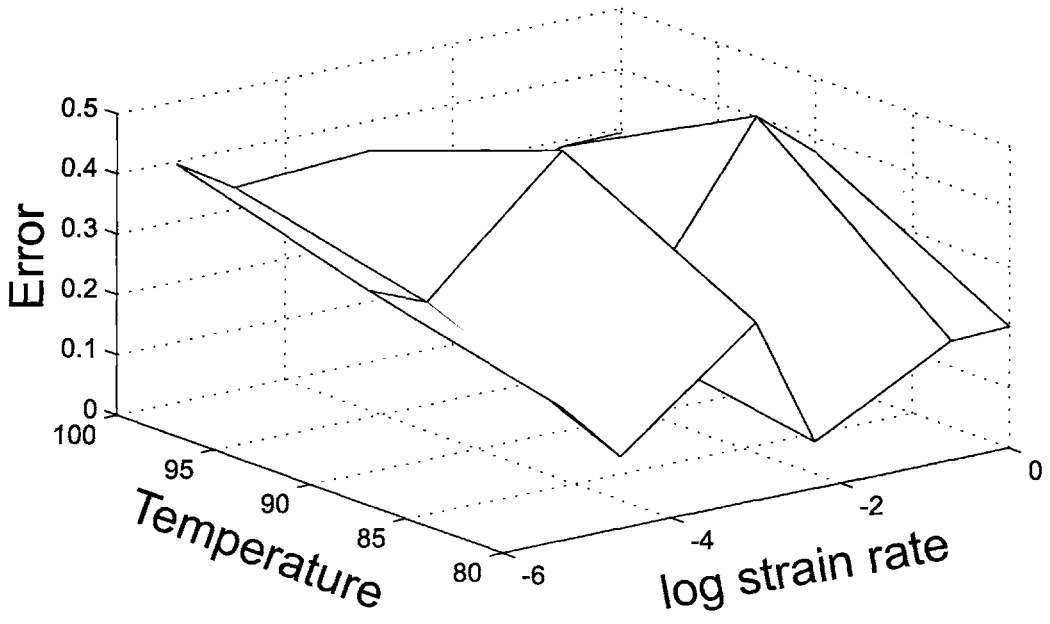

Figure 4-40: PETG Plane strain compression error values

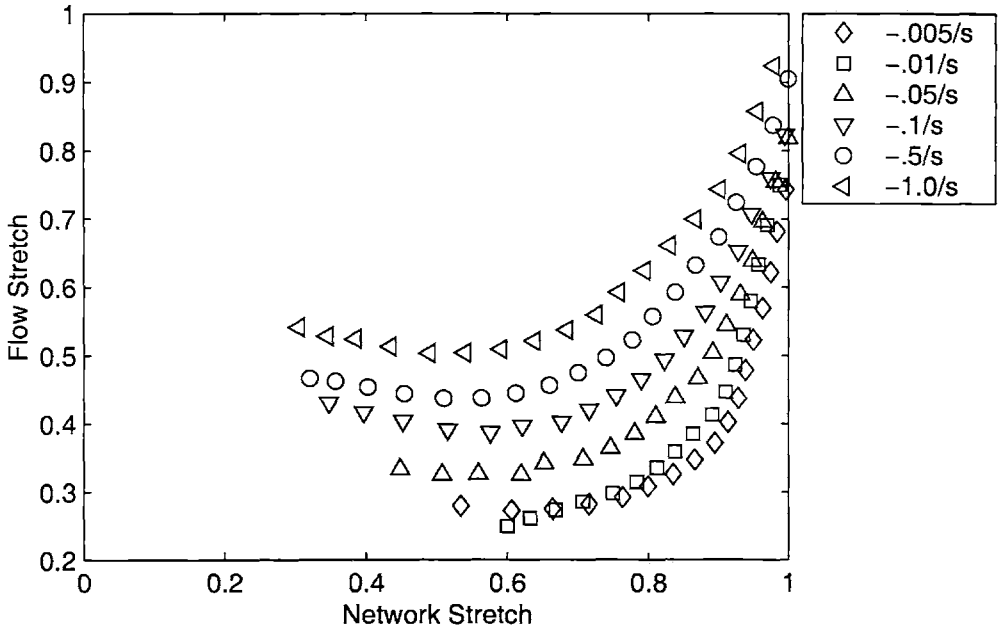

Figure 4-41: PETG Network stretch-flow stretch, uniaxial compression, T = 90 ° C, experimental data alone

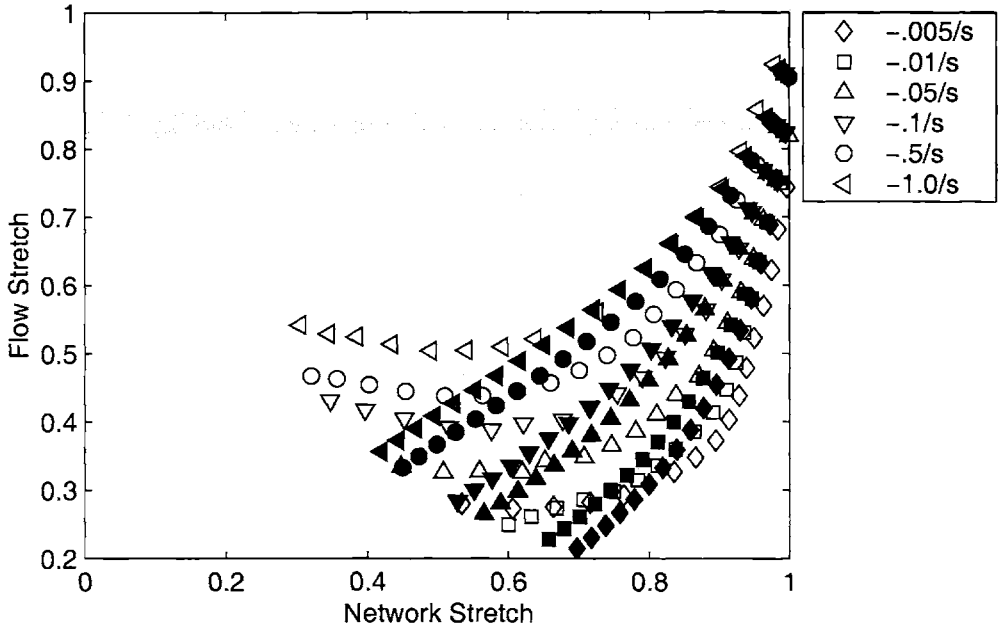

Figure 4-42: PETG Network stretch-flow stretch, uniaxial compression, T = 90 ° C (open symbols are experimental data; filled symbols are from computer simulations)

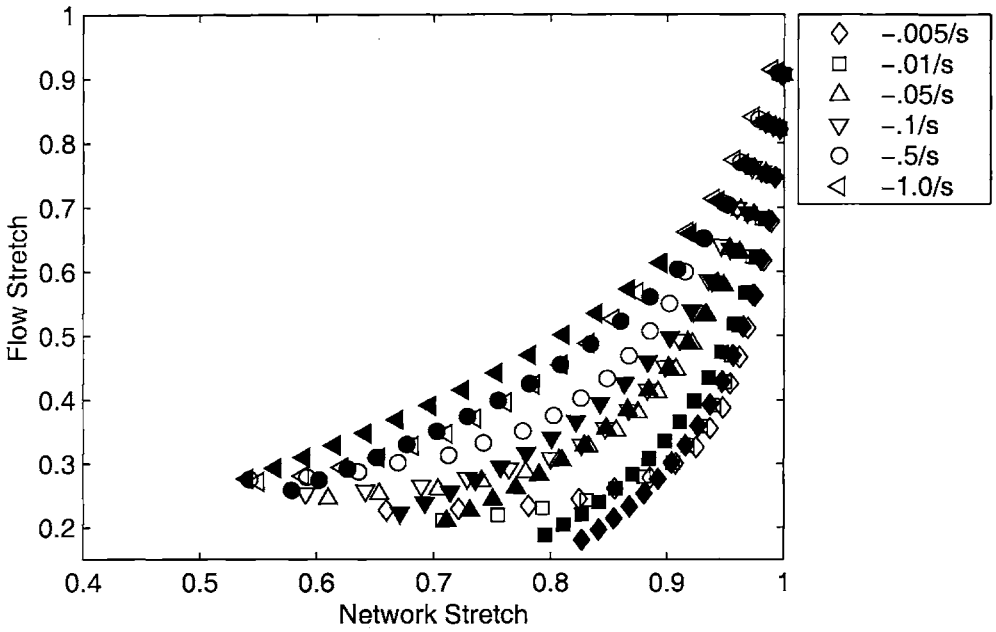

Figure 4-43: PETG Network stretch-flow stretch, uniaxial compression, T = 100 ° C (open symbols are experimental data; filled symbols are from computer simulations)

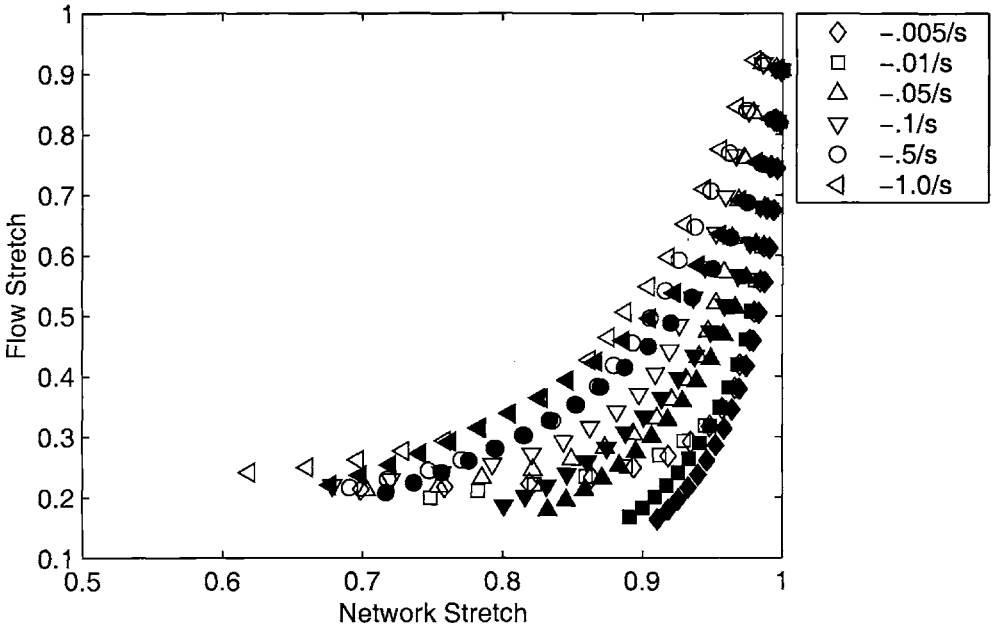

Figure 4-44: PETG Network stretch-flow stretch, uniaxial compression, T = 110 ° C (open symbols are experimental data; filled symbols are from computer simulations)

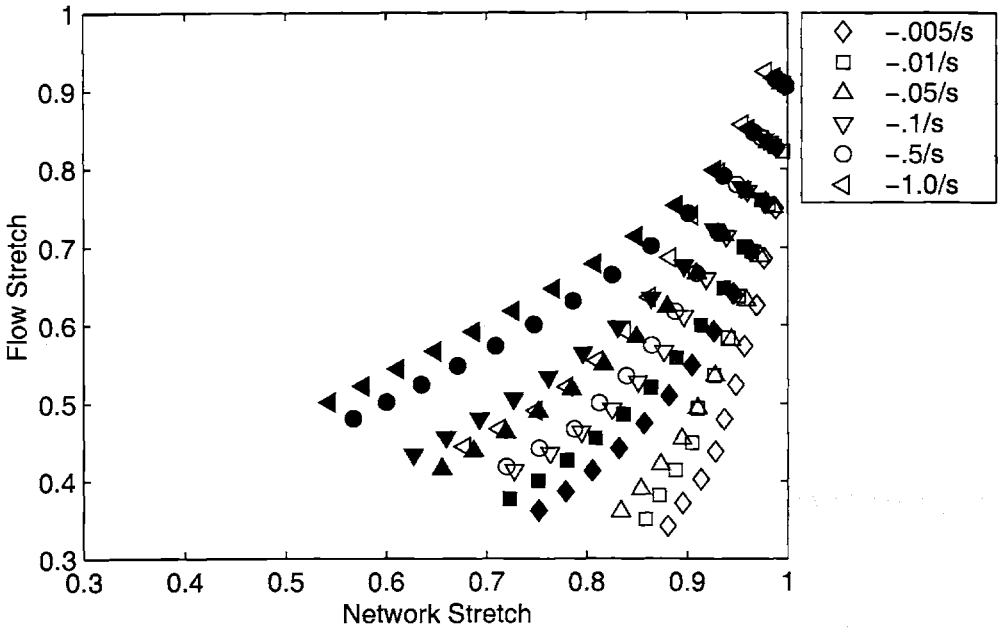

Figure 4-45: PETG Network stretch-flow stretch, plane strain compression, T = 90 ° C (open symbols are experimental data; filled symbols are from computer simulations)

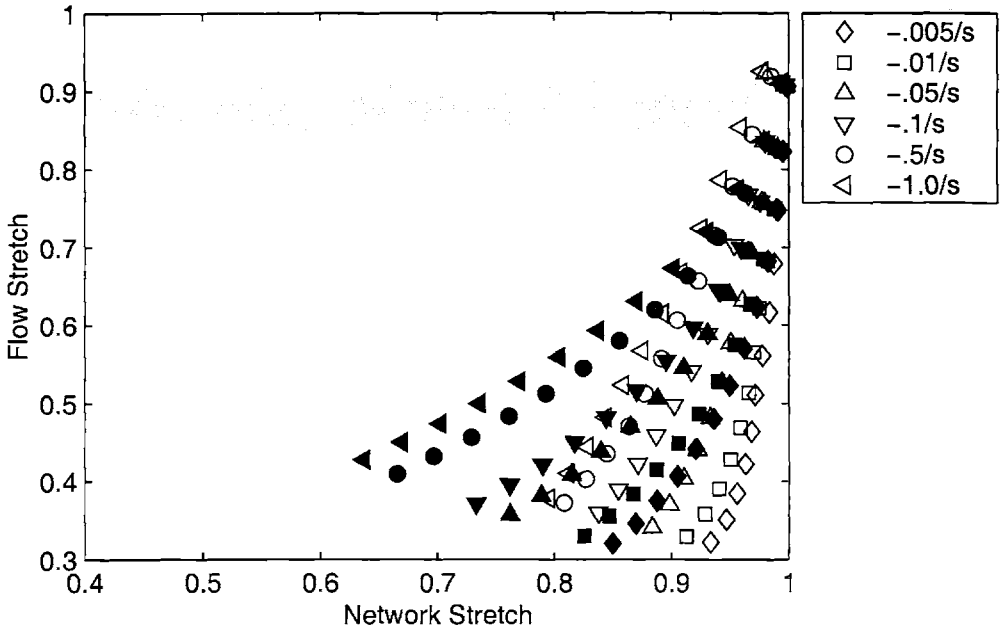

Figure 4-46: PETG Network stretch-flow stretch, plane strain compression, T = 100 ° C (open symbols are experimental data; filled symbols are from computer simulations)

4.5 Improvements to the Model

4.5.1 Cessation of Flow

To account for the cessation of flow at large network stretch, the model is modified using the same approach as Adams et al. (2000). Equation 4.23 is modified to be:

$$\dot{\gamma}_B^F = C\frac{(\bar{\lambda}_{NC} - \lambda_N)}{(\bar{\lambda}_{NC} - 1)}\left[\left(\frac{1}{\lambda_F - 1}\right)\tau_B\right]^3 \tag{4.36}$$

where $\bar{\lambda}_{NC}$ is a critical network stretch where molecular orientation causes molecular relaxation to cease. This provides the functionality that as the network stretch, λ_N, approaches $\bar{\lambda}_{NC}$, the flow strain rate, $\dot{\gamma}_B^F$, goes to zero. When this occurs, all subsequent straining is accommodated by the network stretch and orientation element of Resistance B.

The temperature and strain-rate dependence of $\bar{\lambda}_{NC}$ is modeled phenomenologically based on the uniaxial compression data in a similar manner to Boyce et al. (2000)

$$\bar{\lambda}_{NC} = \bar{\lambda}^* + m\log_{10}(\dot{\gamma}_A^p/0.0173) \tag{4.37}$$

where

$$\lambda^* = \lambda_a^* + \lambda_b^*(\theta - \theta^*) + \lambda_c^*(\theta - \theta^*)^2 \tag{4.38}$$

$$m = m_a + m_b(\theta - \theta^*) + m_c(\theta - \theta^*)^2 \tag{4.39}$$

where λ_a^*, λ_b^*, λ_c^*, m_a, m_b, and m_c are fitting parameter as follows:

$$\begin{aligned}
\lambda_a^* &= 1.06 \\
\lambda_b^* &= -.0035/\mathrm{K} \\
\lambda_c^* &= .00005/\mathrm{K}^2 \\
m_a &= .06 \\
m_b &= .0065/\mathrm{K}
\end{aligned}$$

$$m_c = -.00035/\mathrm{K}^2$$

and $\theta^* = 363\mathrm{K}$.

The computer simulation with this modification to the material model is illustrated in the following figures. Figures 4-47 through 4-56 show the results for uniaxial compression and figures 4-57 and 4-59 show the results for plane strain compression. These figures illustrate that the model still captures the strain and temperature dependence of the initial modulus, flow stress, and initial hardening modulus of the PETG. In addition, the model is now capable of predicting the large upswing in stress at large strains.

Figures 4-60 through 4-66 show the comparison of simulation with experiment. Error values for these curves are shown in Table 4.2 and are represented graphically in figures 4-67 and 4-68. It can be seen that the uniaxial compression experiments are much better approximated with the new model, particularly at large strains. The 80 ° C data shows especially good agreement at all strain rates, even though the model was not specifically fit to this data. The model also captures the behavior at 90 ° C and at 100 ° C quite well. At 110 ° C the fit is not quite as good, but is still better than without the added flow cutoff features. The plane strain simulations still rise above the plane strain compression data, as was anticipated from the results of the previous section.

Figures 4-69 through 4-73 again show the network stretch versus flow stretch for the experimental data and for the computer model at various temperatures and in both deformation modes. These plots demonstrate that this form for the molecular relaxation cessation captures the flow cutoff quite well in uniaxial compression. For example, in figure 4-69 the -1.0 sec^{-1} simulation, indicated by filled triangles pointing left, lies virtually on top of the data for this strain rate, indicated by the open left pointing triangles. Similar corellation occurs at other strain rates and temperatures for the uniaxial compression experiments and simulations. In plane strain, the agreement is not as good, and ways to improve upon this will be addressed in the next section.

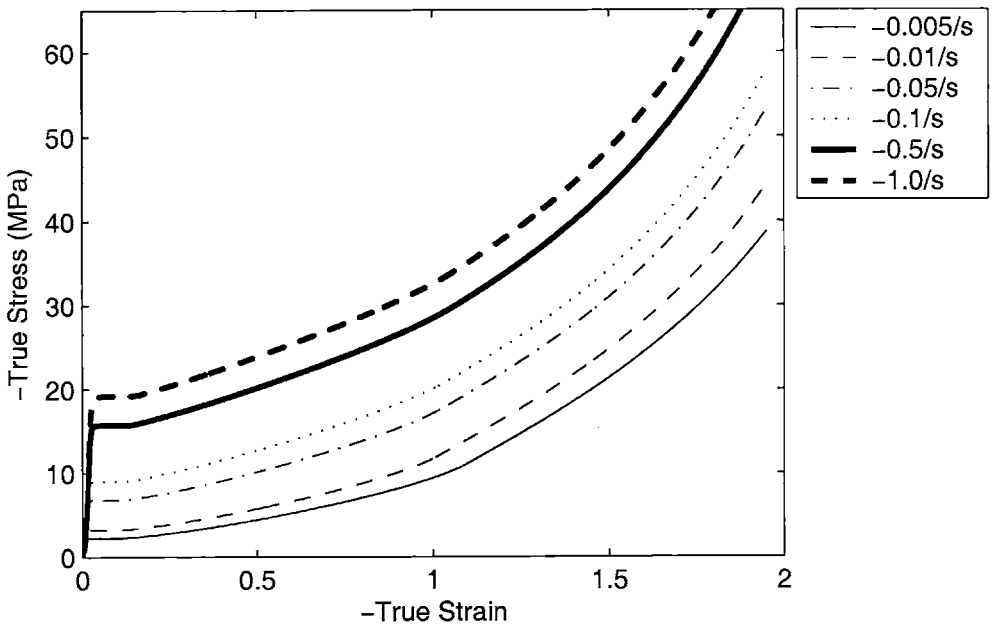

Figure 4-47: Uniaxial compression simulation, Temperature = 80 ° C

Overall, this series of experiments and simulations indicates the many features of the model adequately represent the mechanical behavior of PETG. The initial modulus is captured well, as is verified by both DMA experiments and uniaxial and plane strain compression experiments. The initial flow stress is captured very well using the thermally-activated mechanism. The Arruda-Boyce model captures the strain state dependence of the hardening curve, and the molecular relaxation expressions provide a good representation of the temperature and rate dependent large strain behavior.

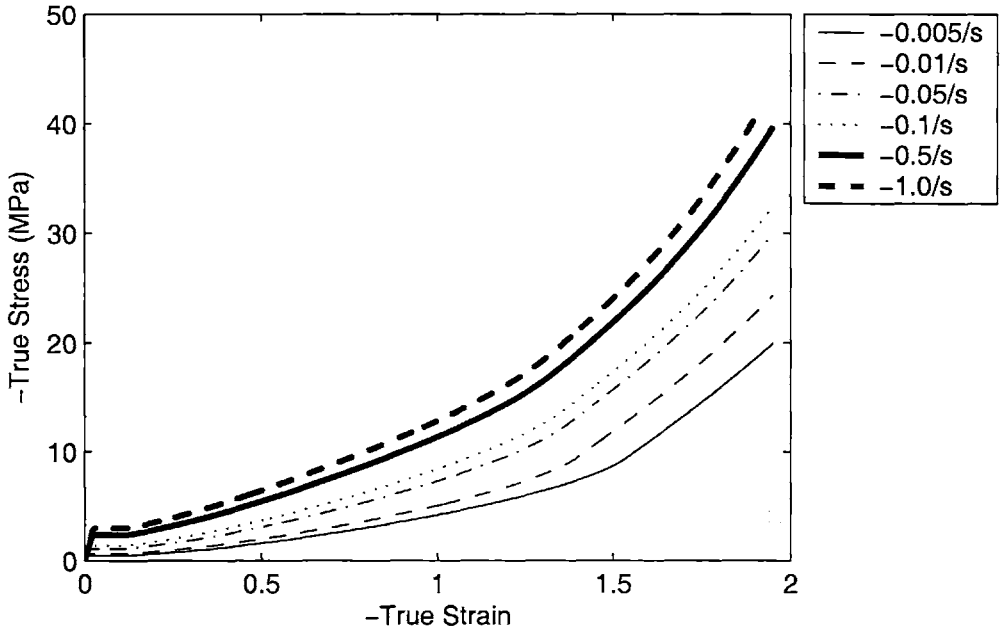

Figure 4-48: Uniaxial compression simulation, Temperature = 90 ° C

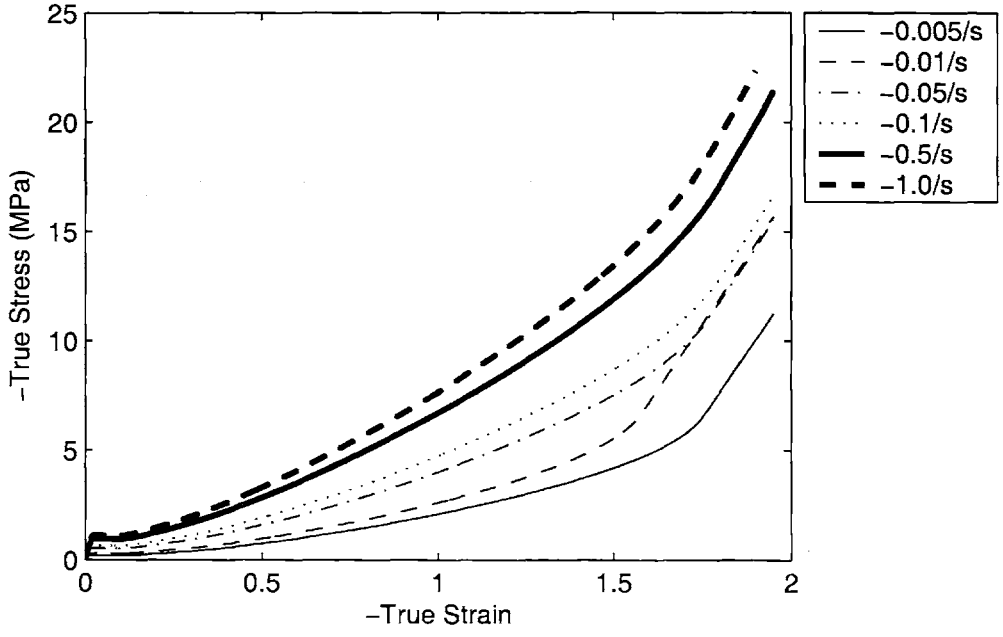

Figure 4-49: Uniaxial compression simulation, Temperature = 100 ° C

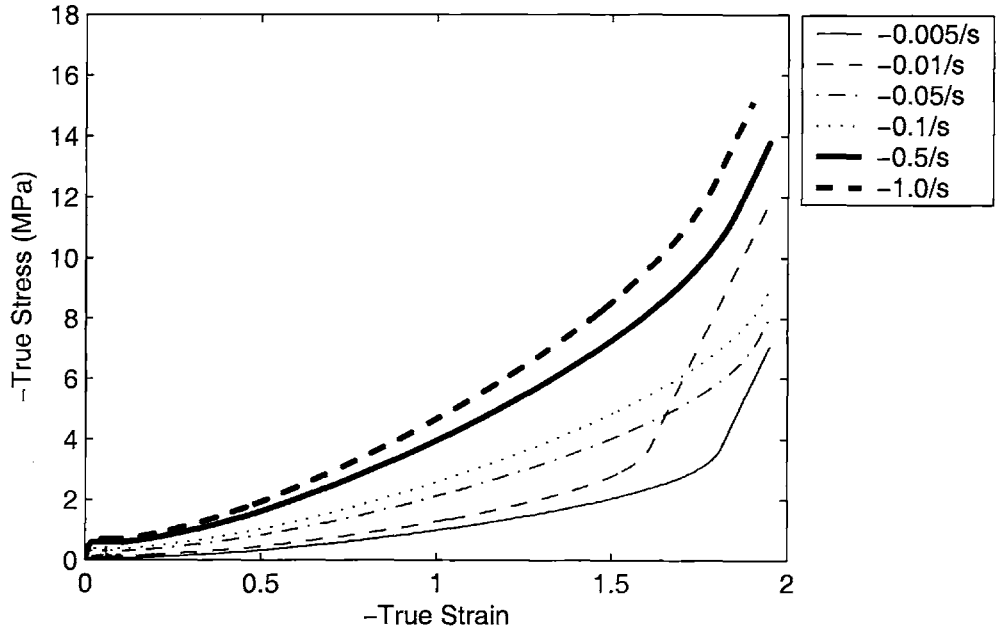

Figure 4-50: Uniaxial compression simulation, Temperature = 110 ° C

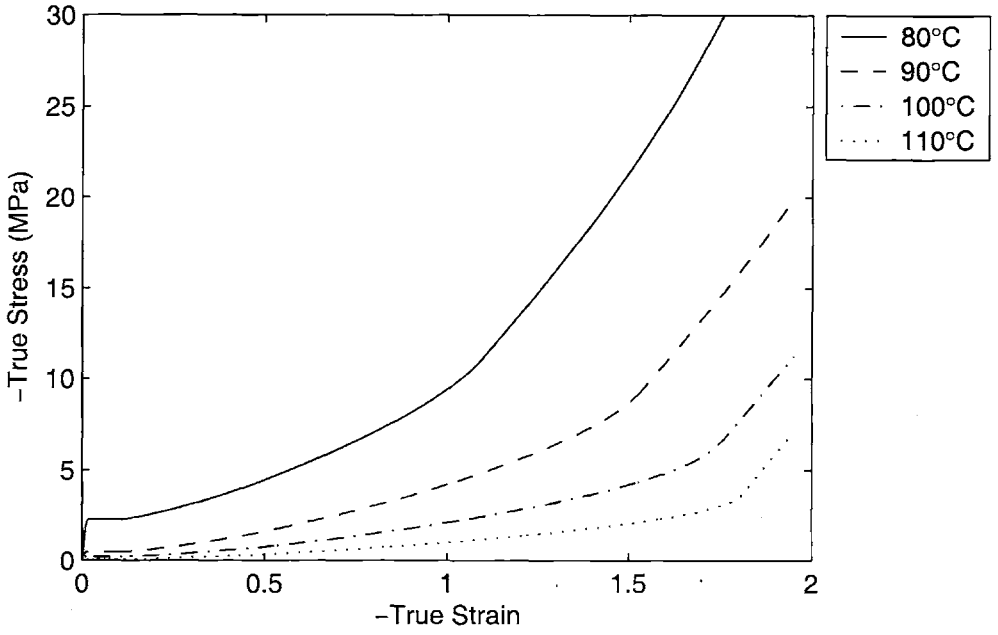

Figure 4-51: Uniaxial compression simulation, $\dot{\varepsilon}$ = -.005/s

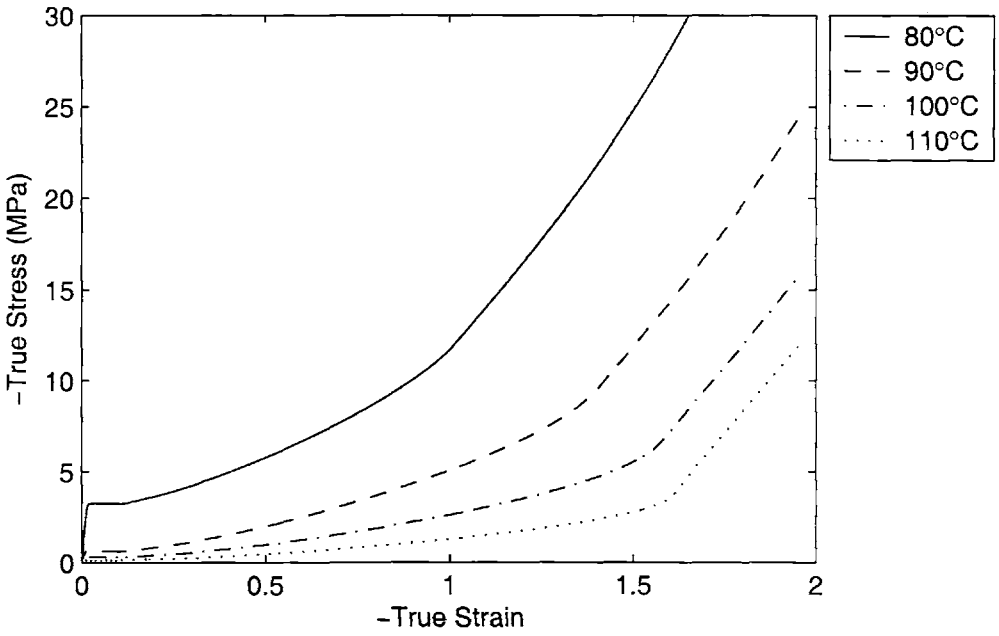

Figure 4-52: Uniaxial compression simulation, $\dot{\varepsilon}$ = -.01/s

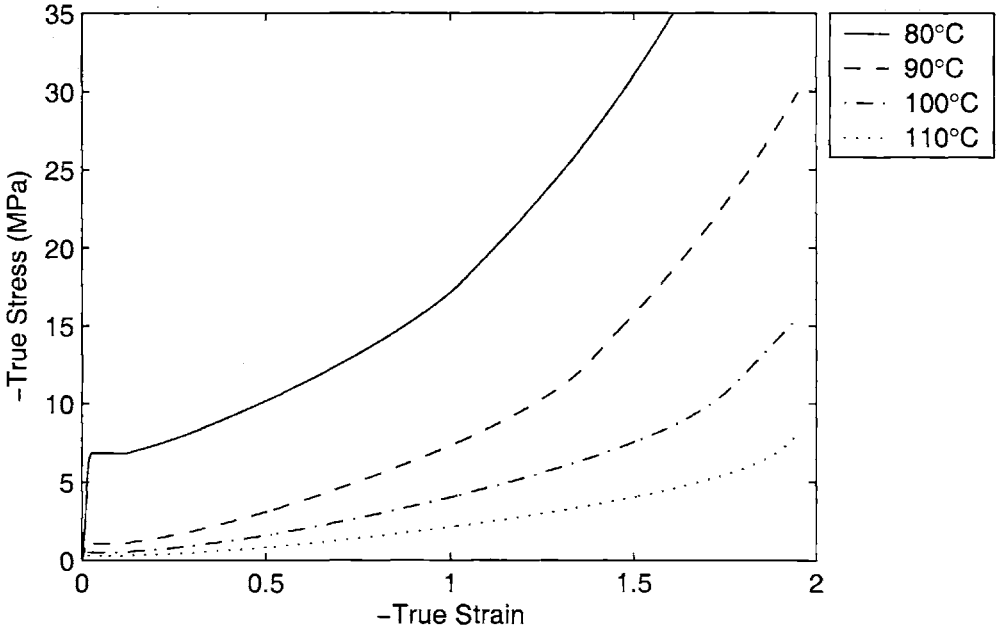

Figure 4-53: Uniaxial compression simulation, $\dot{\varepsilon}$ = -.05/s

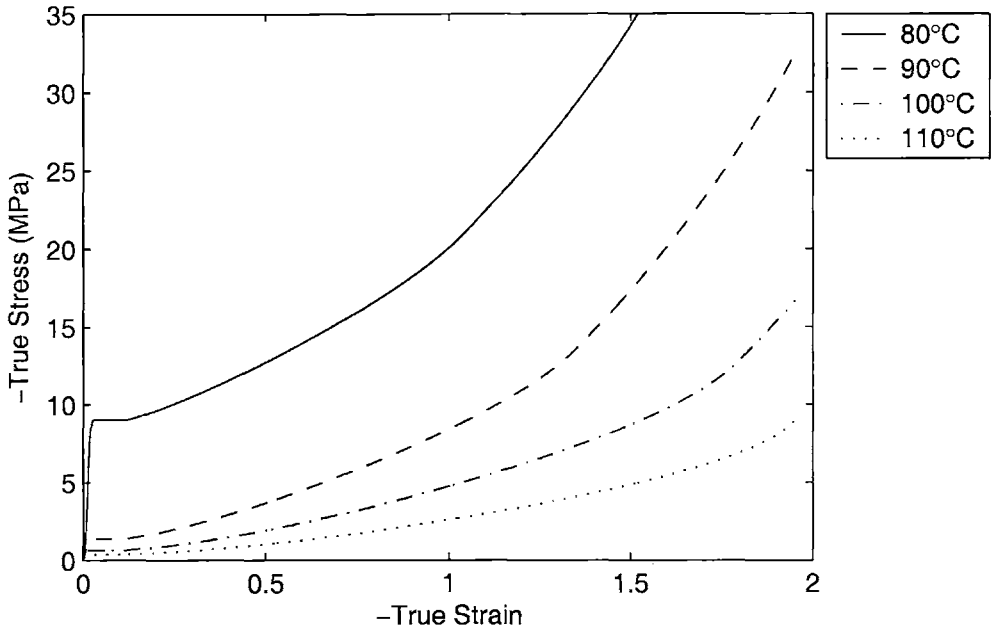

Figure 4-54: Uniaxial compression simulation, $\dot{\varepsilon}$ = -.1/s

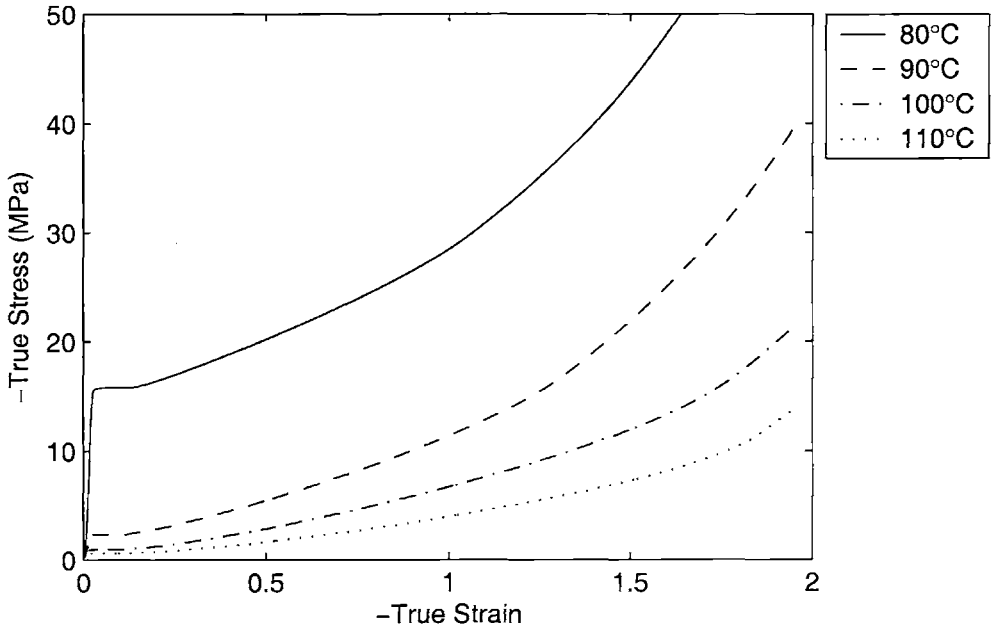

Figure 4-55: Uniaxial compression simulation, $\dot{\varepsilon}$ = -.5/s

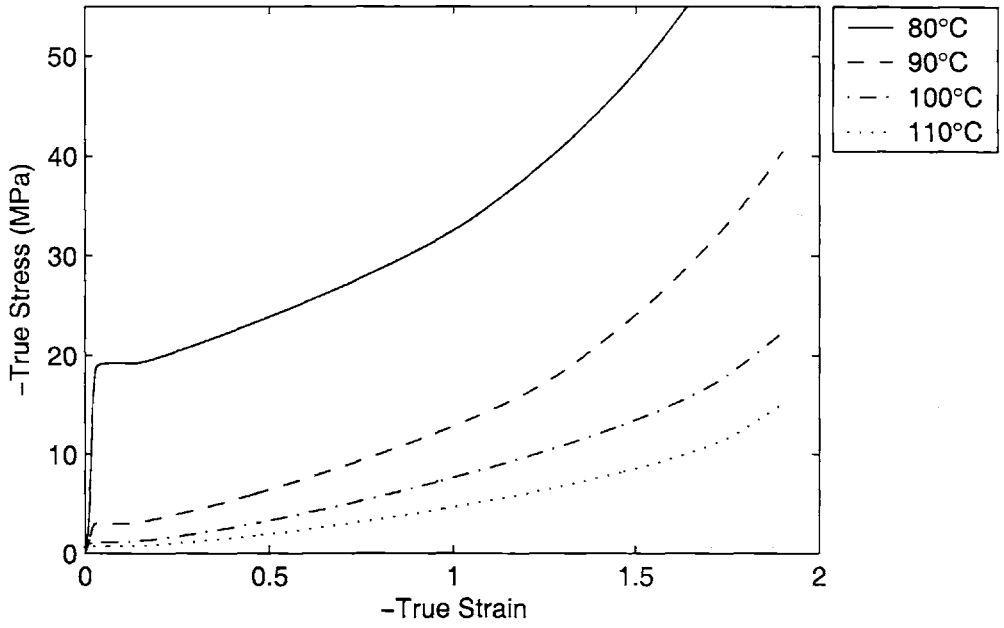

Figure 4-56: Uniaxial compression simulation, $\dot{\varepsilon}$ = -1.0/s

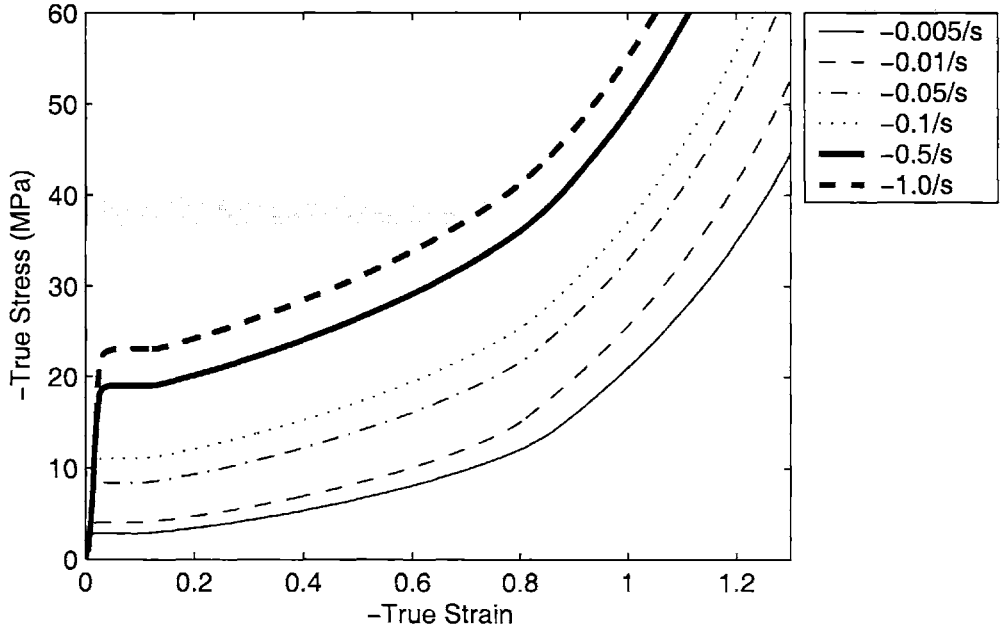

Figure 4-57: Plane strain compression simulation, Temperature = 80 ° C

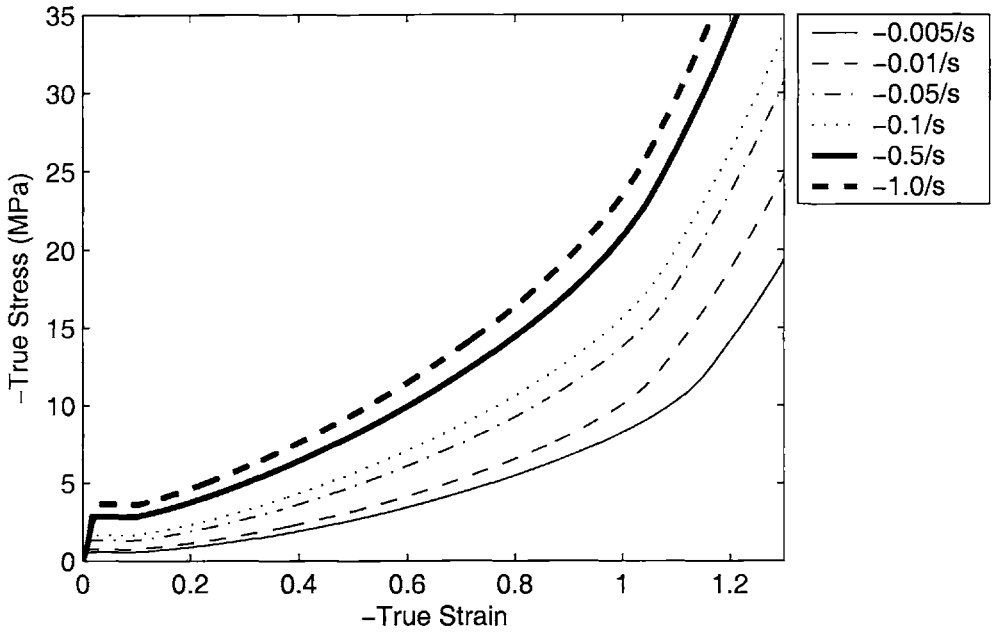

Figure 4-58: Plane strain compression simulation, Temperature = 90 ° C

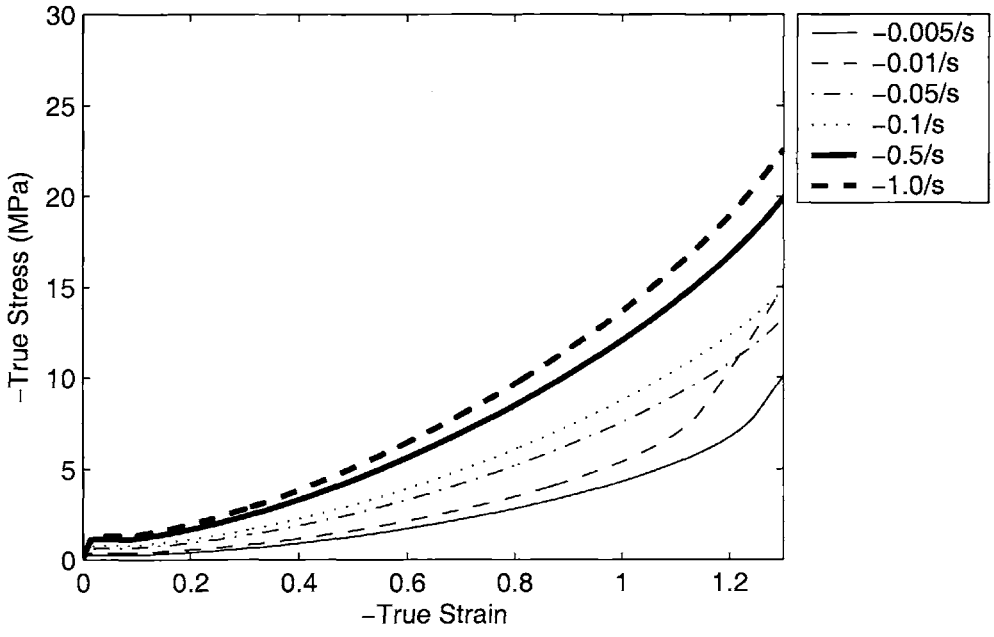

Figure 4-59: Plane strain compression simulation, Temperature = 100 ° C

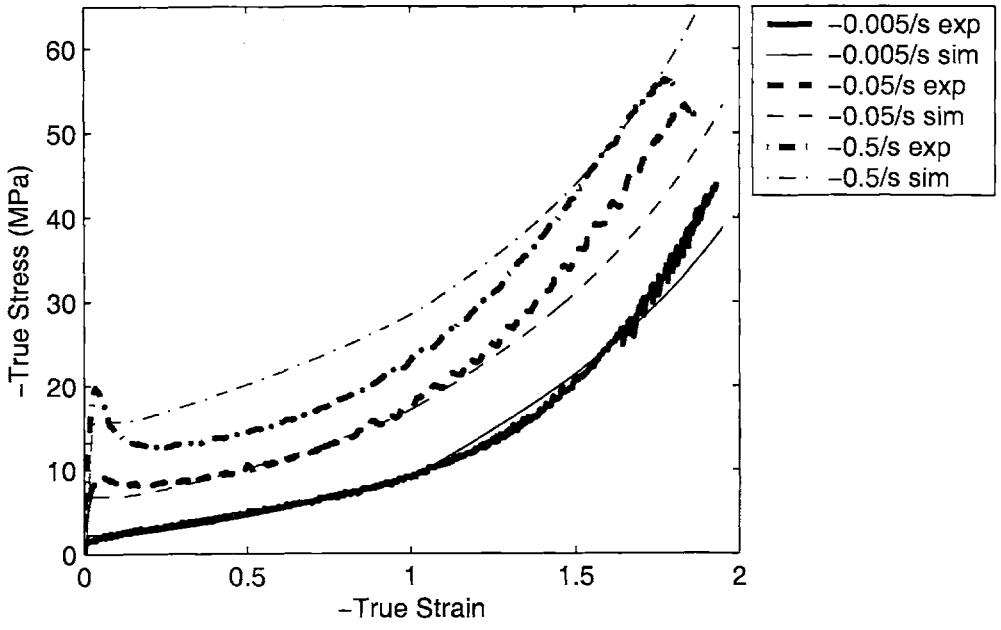

Figure 4-60: PETG Uniaxial compression, comparing simulation results with experimental data, Temperature = 80 ° C

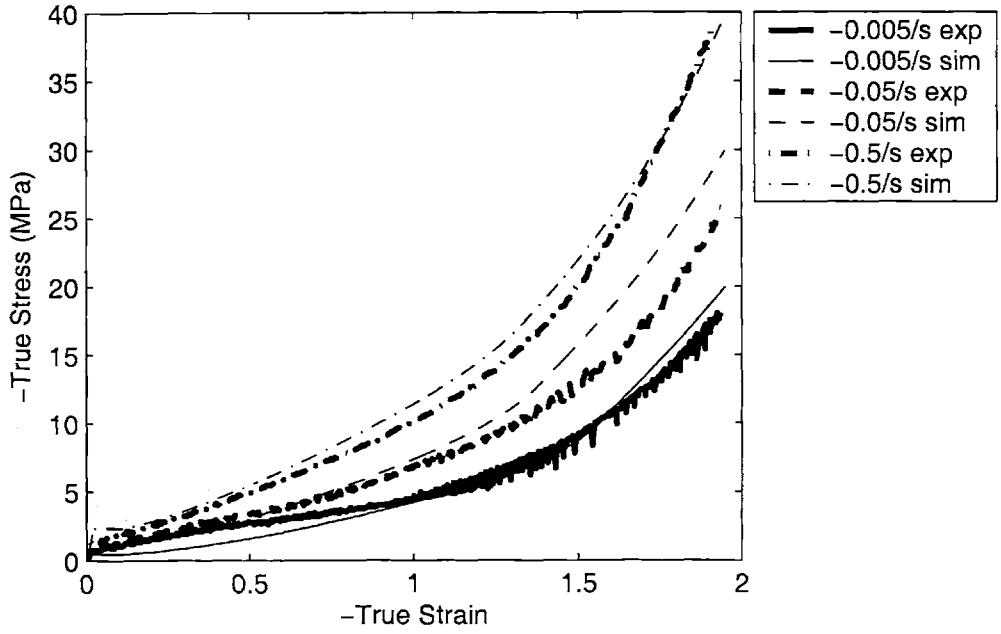

Figure 4-61: PETG Uniaxial compression, comparing simulation results with experimental data, Temperature = 90 ° C

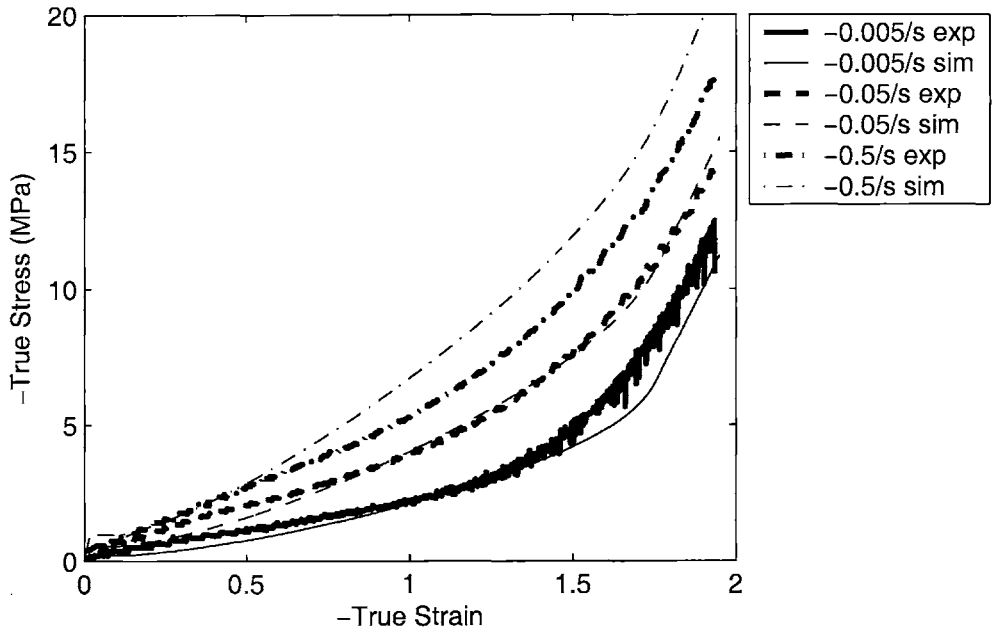

Figure 4-62: PETG Uniaxial compression, comparing simulation results with experimental data, Temperature = 100 ° C

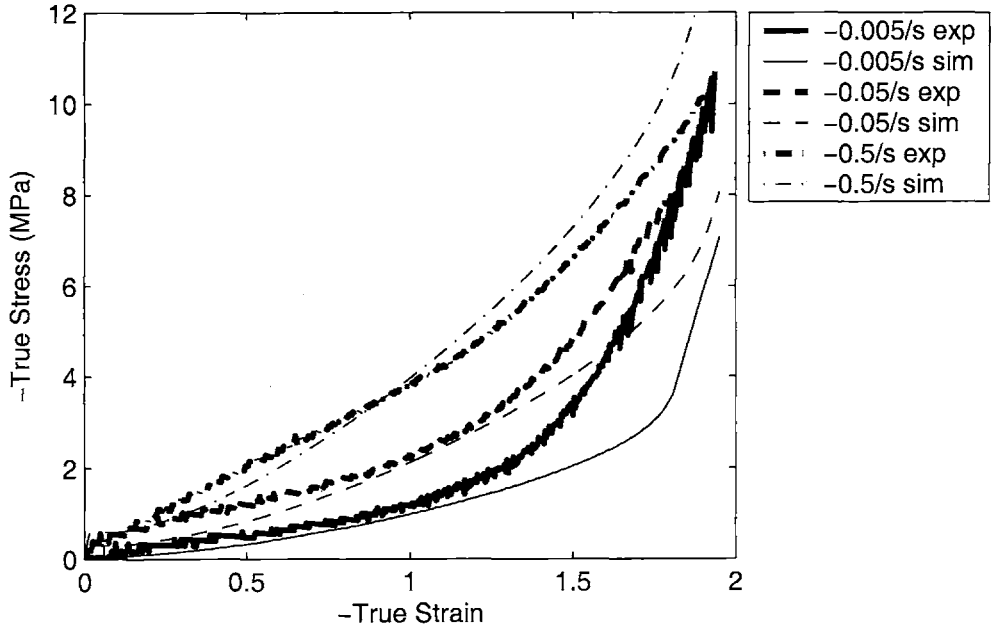

Figure 4-63: PETG Uniaxial compression, comparing simulation results with experimental data, Temperature = 110 ° C

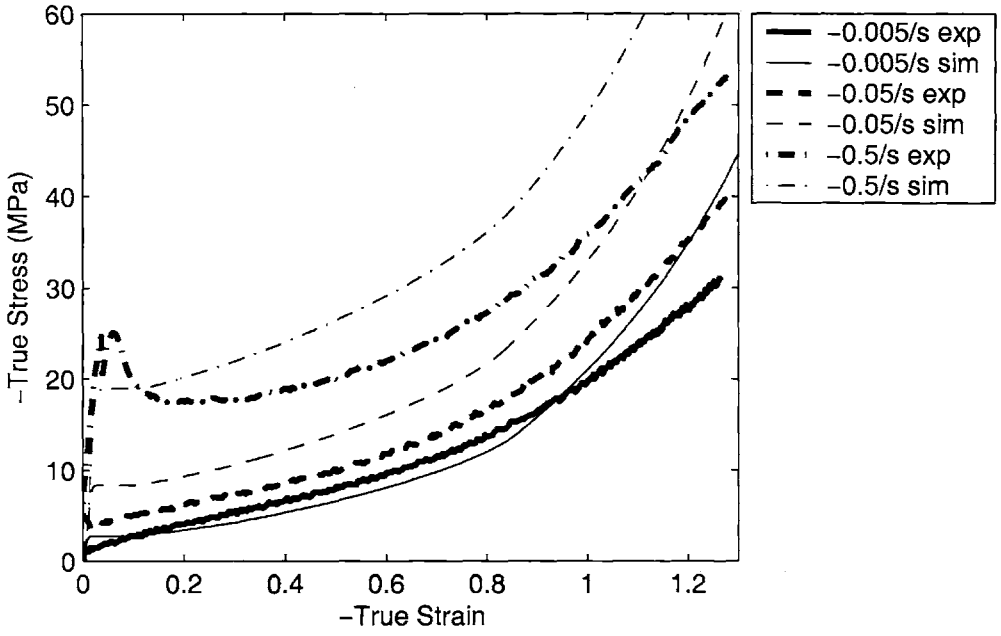

Figure 4-64: PETG Plane strain compression, comparing simulation results with experimental data, Temperature = 80 ° C

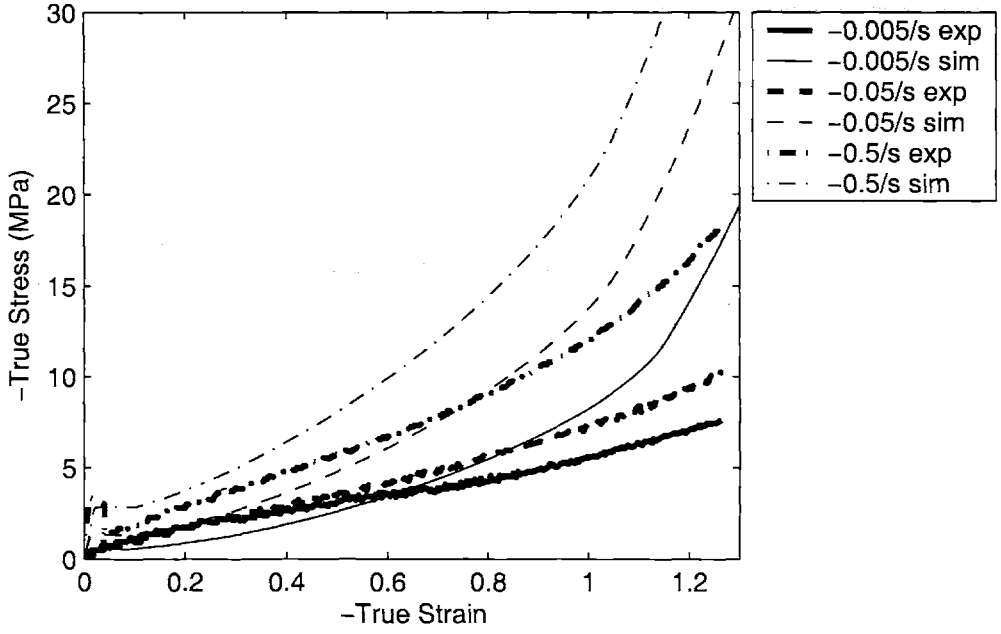

Figure 4-65: PETG Plane strain compression, comparing simulation results with experimental data, Temperature = 90 ° C

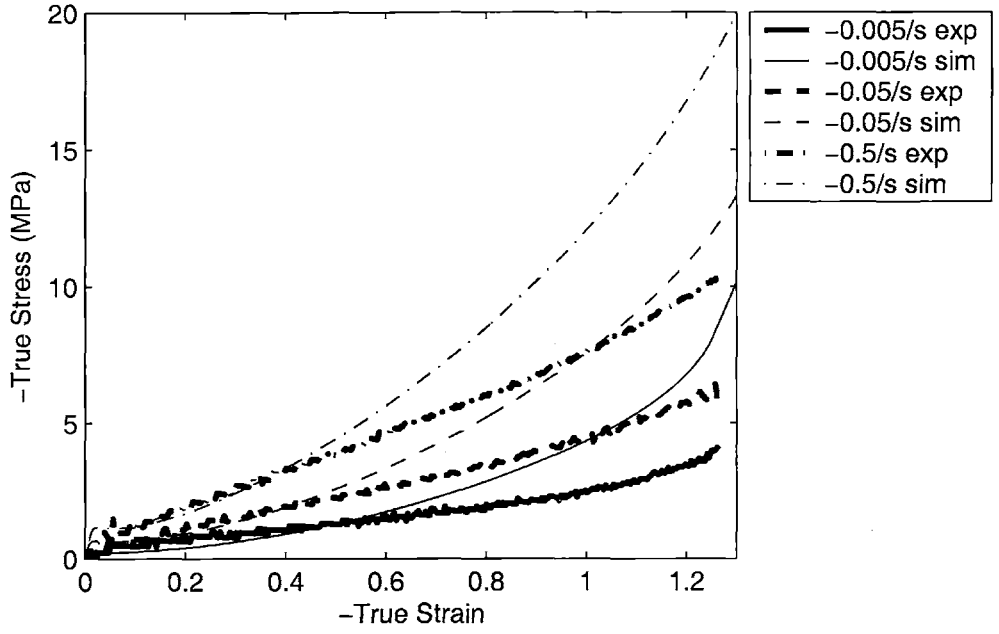

Figure 4-66: PETG Plane strain compression, comparing simulation results with experimental data, Temperature = 100 ° C

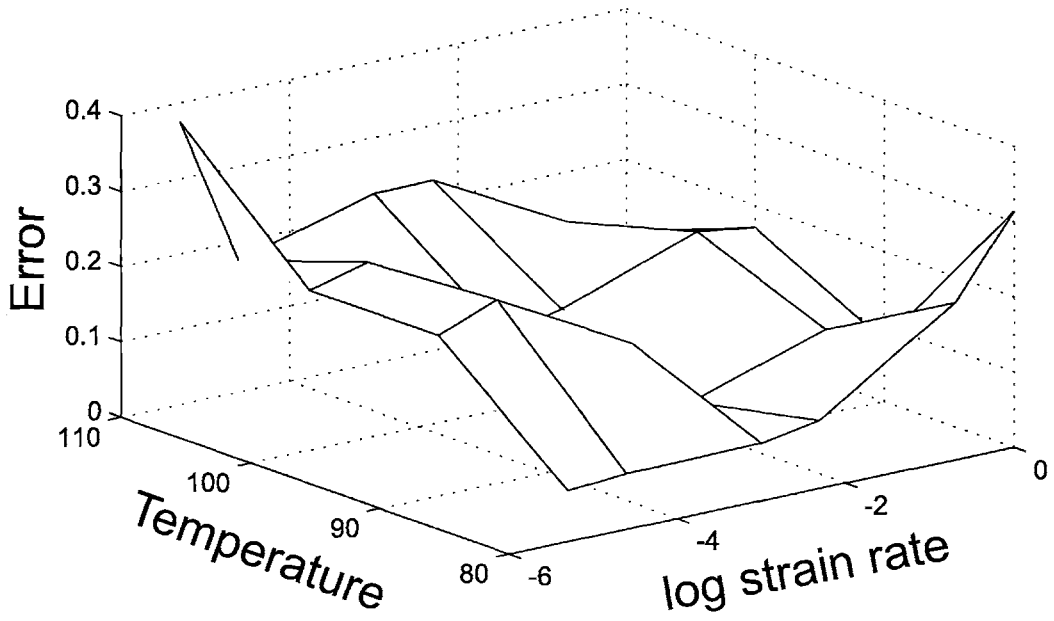

Figure 4-67: PETG Uniaxial compression error values with flow cutoff

Table 4.2: PETG Error values for uniaxial and plane strain compression simulations with flow cutoff

Strain State	Temperature	Strain Rate	$\bar{y}$, full range	$\bar{y}$, up to $\varepsilon = 1.0$
Uniaxial	80 ° C	-0.005/sec	.0675	.0668
Uniaxial	80 ° C	-0.05/sec	.0763	.0559
Uniaxial	80 ° C	-0.5/sec	.2093	.3156
Uniaxial	90 ° C	-0.005/sec	.2127	.3650
Uniaxial	90 ° C	-0.05/sec	.1474	.1195
Uniaxial	90 ° C	-0.5/sec	.1118	.1393
Uniaxial	100 ° C	-0.005/sec	.2124	.3004
Uniaxial	100 ° C	-0.05/sec	.0984	.1649
Uniaxial	100 ° C	-0.5/sec	.1819	.1449
Uniaxial	110 ° C	-0.005/sec	.3755	.3809
Uniaxial	110 ° C	-0.05/sec	.2259	.2933
Uniaxial	110 ° C	-0.5/sec	.1334	.1456
Plane Strain	80 ° C	-0.005/sec	.1521	.1417
Plane Strain	80 ° C	-0.05/sec	.4132	.4160
Plane Strain	80 ° C	-0.5/sec	.3041	.2702
Plane Strain	90 ° C	-0.005/sec	.3982	.3042
Plane Strain	90 ° C	-0.05/sec	.6230	.4419
Plane Strain	90 ° C	-0.5/sec	.5794	.4805
Plane Strain	100 ° C	-0.005/sec	.4705	.3655
Plane Strain	100 ° C	-0.05/sec	.4004	.2898
Plane Strain	100 ° C	-0.5/sec	.3305	.2330

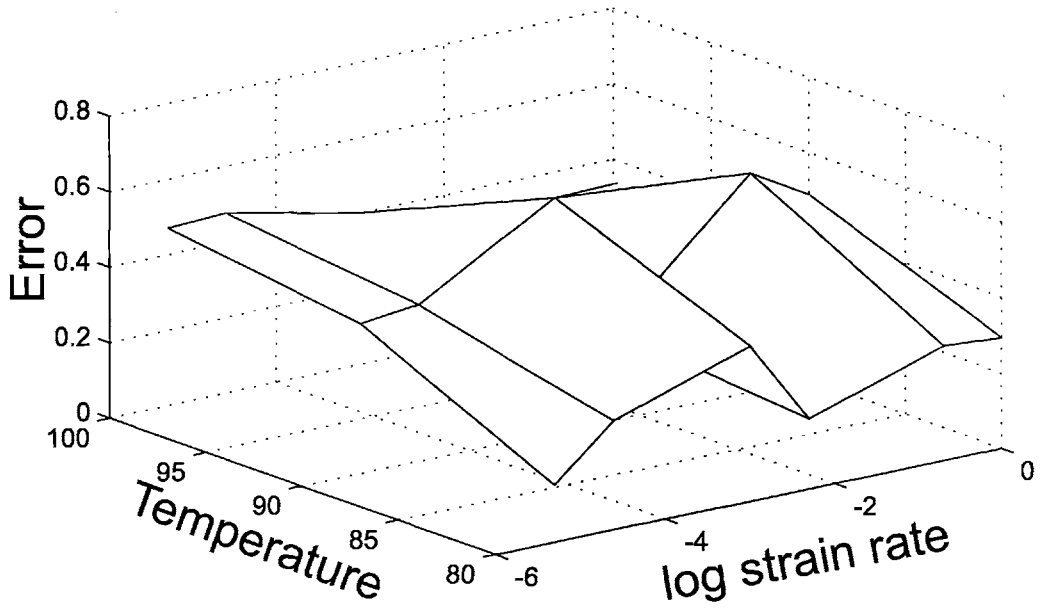

Figure 4-68: PETG Plane strain compression error values with flow cutoff

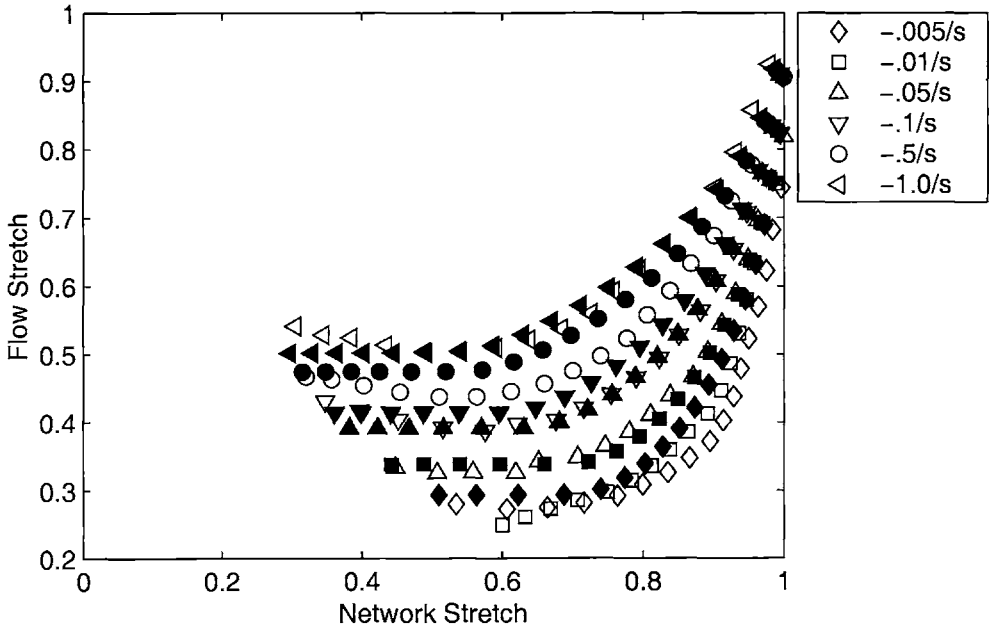

Figure 4-69: PETG Network stretch-flow stretch, uniaxial compression, T = 90 ° C (open symbols are experimental data; filled symbols are computer simulations)

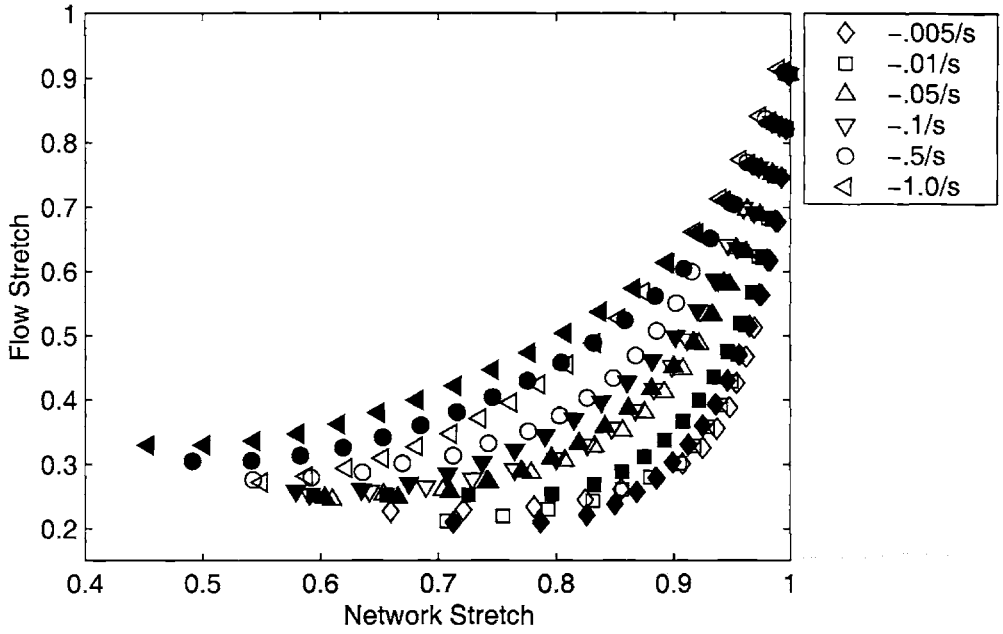

Figure 4-70: PETG Network stretch-flow stretch, uniaxial compression, T = 100 ° C (open symbols are experimental data; filled symbols are computer simulations)

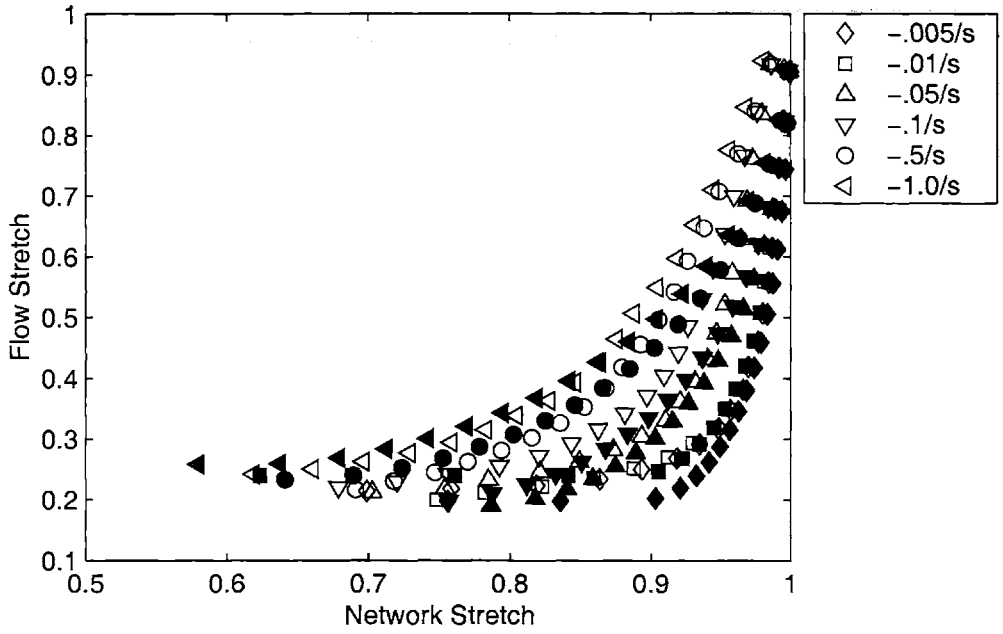

Figure 4-71: PETG Network stretch-flow stretch, uniaxial compression, T = 110 ° C (open symbols are experimental data; filled symbols are computer simulations)

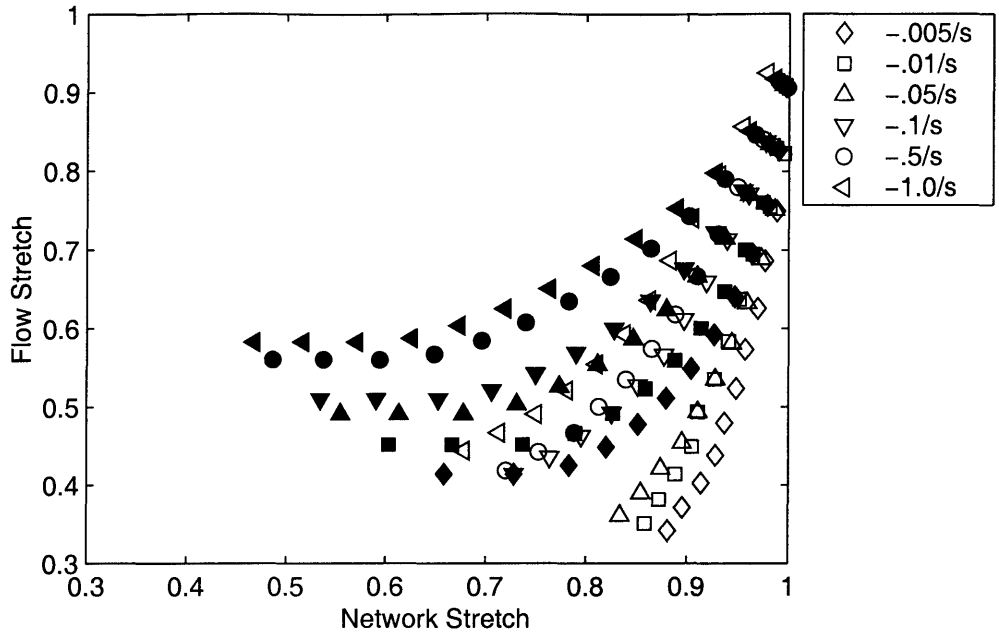

Figure 4-72: PETG Network stretch-flow stretch, plane strain compression, T = 90 ° C (open symbols are experimental data; filled symbols are computer simulations)

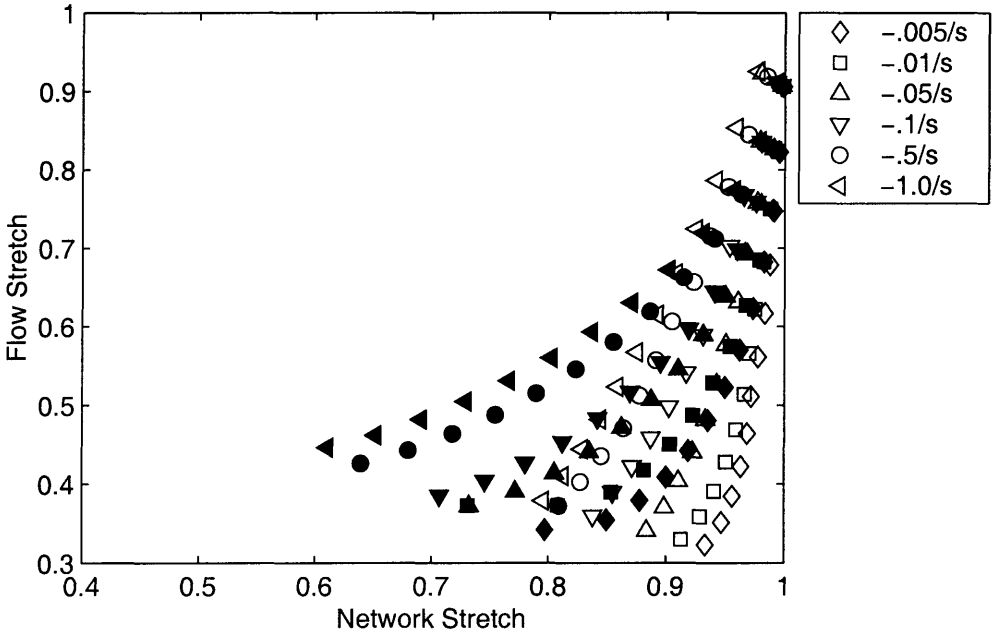

Figure 4-73: PETG Network stretch-flow stretch, plane strain compression, T = 100 ° C (open symbols are experimental data; filled symbols are computer simulations)

4.5.2 Orientation Angle Parameter and a New Approach to Reptation

From the results in the previous section, it is clear that the model is inadequate at predicting how the material behavior depends on the state of strain. The model can capture uniaxial compression data very well, but is unable to capture the large strain behavior in plane strain compression. An alternate approach to modeling molecular relaxation will be presented in this section, which is shown to capture both uniaxial and plane strain compression quite well for PETG, and which requires fewer fitting parameters than the previous model.

As molecular relaxation is, in effect, a viscous flow problem, we begin by looking at an effective "viscosity" of the polymer. To do this, we take a set of stress-strain curves over a range of strain rates, remove that portion of the behavior which is associated with intermolecular interactions (initial modulus and flow stress) and extract data at a constant level of strain (see figure 4-74.) Each data point at a particular strain level is a point along a stress-strain rate curve. This can also be represented as a viscosity-strain rate curve since the definition of viscosity is simply stress divided by strain rate:

$$\tau = \eta\dot{\gamma} \ , \ \eta = \frac{\tau}{\dot{\gamma}} \tag{4.40}$$

Plotting one of these stress-strain rate curves (and the corresponding viscosity-strain rate curve) at a given level of strain, we obtain a plot as shown in figure 4-75. The viscosity-strain rate plot is even more descriptive if it is drawn using a log-log scale as shown in figure 4-76. We see that log viscosity and log strain rate are linearly related.

If we plot viscosity versus strain rate at several different strain levels, we find that the curves are parallel straight lines, as shown in figure 4-77. When plane strain data at the same temperature is plotted along with the uniaxial data, it appears that the data for corresponding axial strain levels lies very nearly on top of each other. (see figure 4-78).

However, axial strain is not a particularly good measure for developing a constitutive model, as it is a function of the testing conditions and would be rather difficult

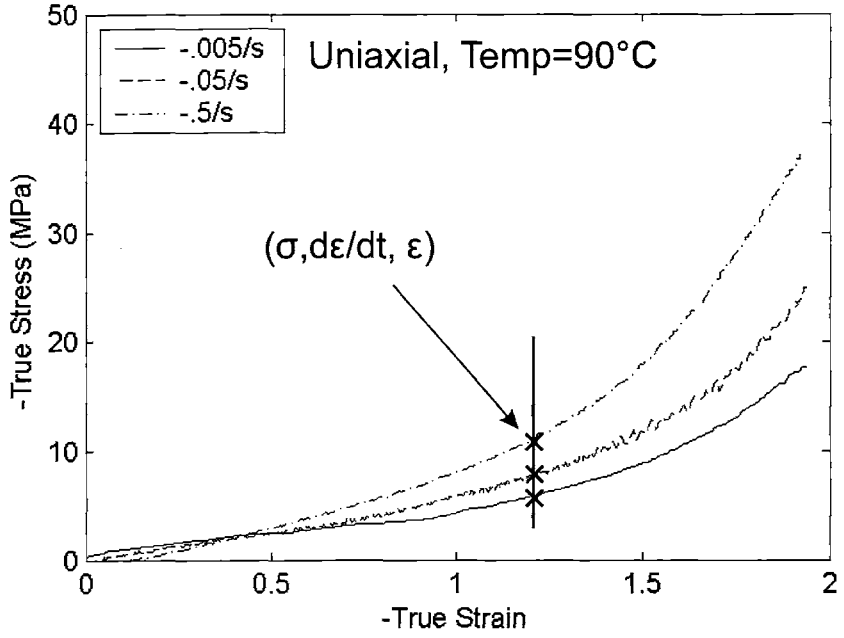

Figure 4-74: Extracting data for viscosity calculation

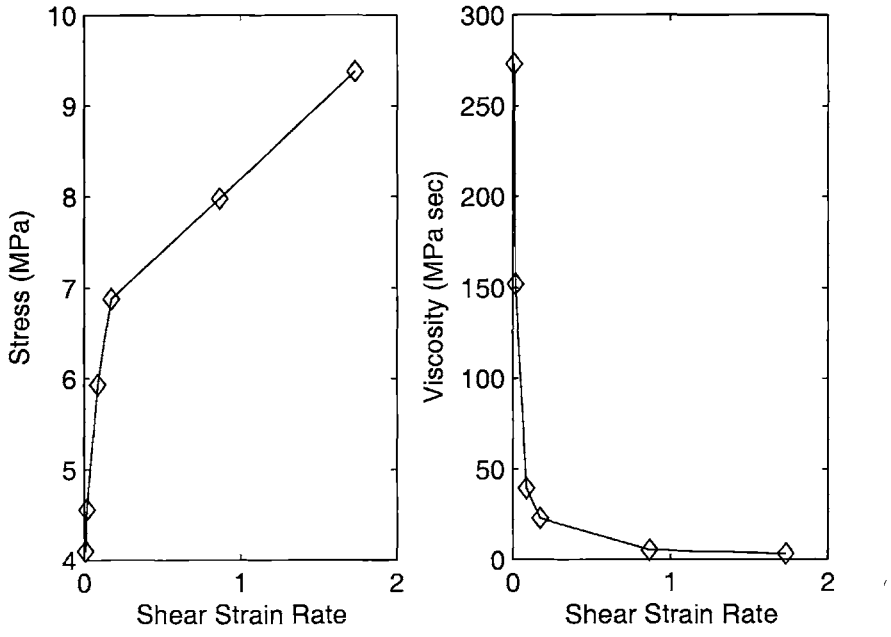

Figure 4-75: Stress versus strain rate and viscosity versus strain rate curves, PETG uniaxial compression, T=90 ° C, $\varepsilon = 1.0$

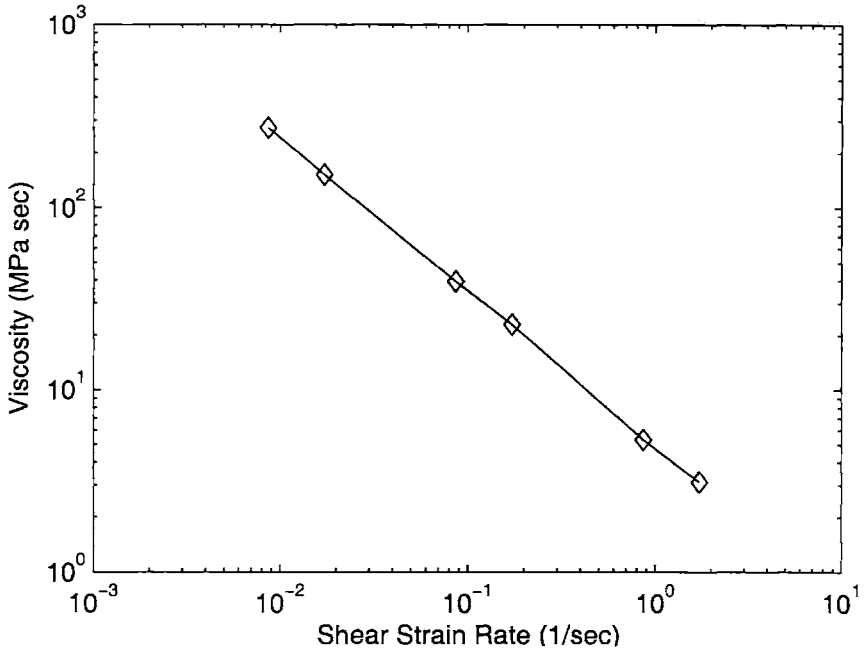

Figure 4-76: Viscosity versus strain rate on a log-log plot, PETG uniaxial compression, T=90 ° C, $\varepsilon = 1.0$

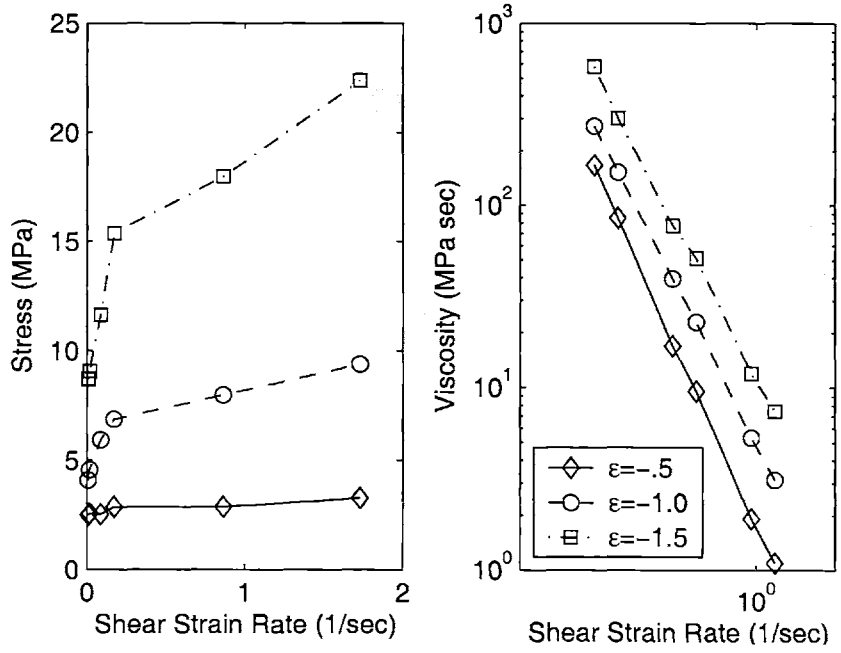

Figure 4-77: Stress versus strain rate and viscosity versus strain rate on a log-log plot, PETG uniaxial compression, T=90 ° C

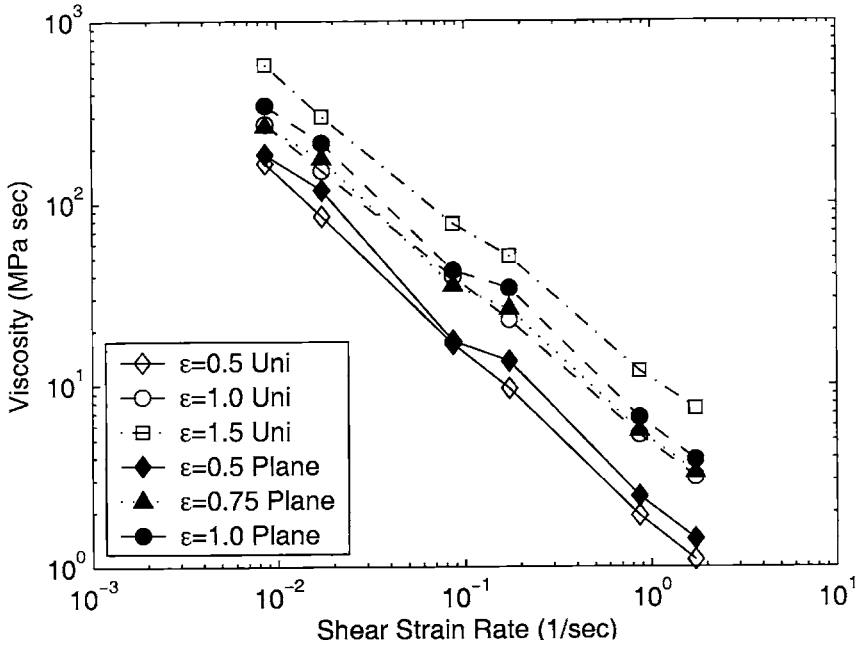

Figure 4-78: Stress versus strain rate and viscosity versus strain rate on a log-log plot, PETG uniaxial and plane strain compression, T=90 ° C

to extend to general three-dimensional loading configurations. Instead, we seek a more physically-based parameter which is able to capture the behavior of both plane strain and uniaxial compression data. One such candidate which is found to work well is what we will term an orientation angle or orientation parameter, α. This can be thought of microstructurally by thinking back to the 8-chain model (figure 4-79), in which the stress was related to the stretch of a chain due to deformation. During deformation, the chains also rotate and align in the direction of flow, so another parameter which can be useful to look at is the angle these chains make with a given axis, or with each other.

If we consider a unit cube with a chain extending from its center to one of the corners (figure 4-80), the vector describing this chain can be expressed by direction cosines (cosines of the angles between the vector and each of the coordinate axes, α_1, α_2, α_3). Initially, each of these angles will have the same value, 54.7 ° , or 0.9553 radians. As the deformation continues, the angles between the three principal stretch axes will no longer be equal. It would appear that the maximum of these angles (which

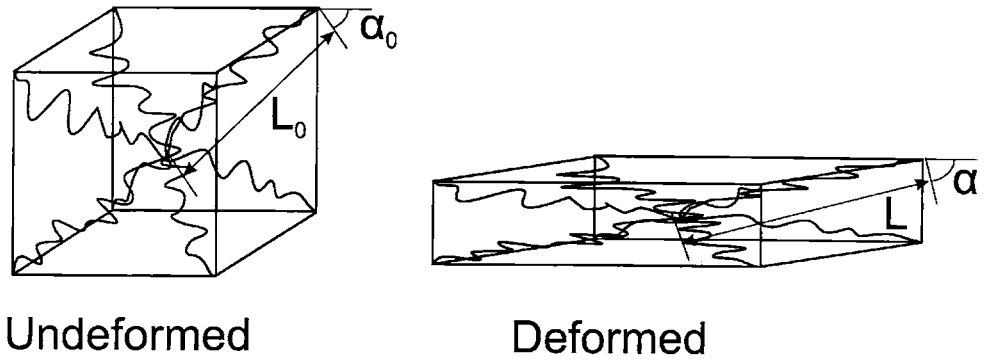

Figure 4-79: Schematic illustrating the 8-chain model

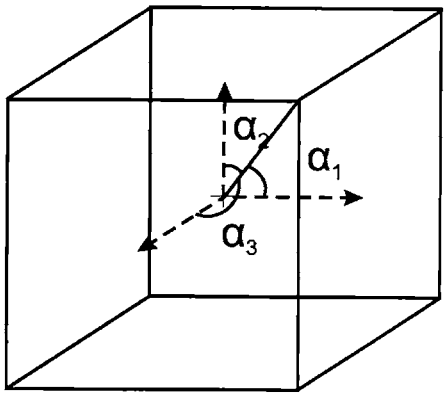

Figure 4-80: Illustration of the unit cube and the angles between a chain and the principal axes

is a measure of how far the chains are getting from a particular axis or alternatively of how well aligned the chains are getting with each other) should be of interest. If we plot instead of stress-strain curves, stress versus maximum angle curves (shown in figure 4-83), we find that the plane strain and uniaxial compression data collapses quite nicely and that all curves tend to reach their limiting extensibility at a common value of the maximum angle. The orientation angle at which this occurs may be thought of as some indication of registry or meso-order.

It should be interesting to consider how this orientation angle is related to something measurable, such as the Hermans orientation function: $\frac{1}{2}(3 < \cos^2\phi > -1)$, where ϕ represents the angle between the axis of a polymer chain and the axis of

deformation, as in the case of uniaxial tension. If we assume affine deformation and use Gaussian chain statistics, this orientation function is related to the elongational stretch as:

$$\frac{3 < \cos^2 \phi > -1}{2} = \frac{1}{5}\left(\lambda^2 - \frac{1}{\lambda}\right) \tag{4.41}$$

This relation between angle ϕ and stretch λ is shown in figure 4-81. Also plotted, for comparison, is the minimum angle obtained using the 8-chain geometric construction. As the deformation mode is uniaxial tension, the angle ϕ obtained from the Hermans orientation function should correspond to a minimum angle (α_{min}) which decreases with deformation, instead of a maximum angle. This could be computed in two ways: (1) as the minimum of the three angles between the chain and the principal stretch axes (shown as a dashed line in figure 4-81) or (2) as the complement of α_{max} computed above (shown as the dash-dotted line in figure 4-81). Later in this chapter, we will adopt the second definition for α_{min}. It should be noted that for either choice, the curve illustrating the relation between angle and stretch has a decidedly different shape than the angle in the Hermans orientation function, reminiscent of the difference between affine deformation and pseudo-affine deformation, as described in Ward (1975) and as illustrated in figure 4-82.

We can again plot viscosity-strain rate curves, but this time at constant angle, instead of at constant axial strain. This is shown in figures 4-84 and 4-85. It can be seen that the viscosity-strain rate curves at a given value of maximum angle coincide for plane strain and uniaxial compression data over all angles.

Since the viscosity versus strain-rate curves give straight lines, it seems simple enough to use a power-law model for the material behavior at a particular strain level:

$$\tau = \eta\dot{\gamma} = m\dot{\gamma}^n \ , \ \eta = \hat{\eta}(\dot{\gamma}) \tag{4.42}$$

where m and n are constants. Rearranging, we obtain

$$\dot{\gamma} = C\tau^{(1/n)} \tag{4.43}$$

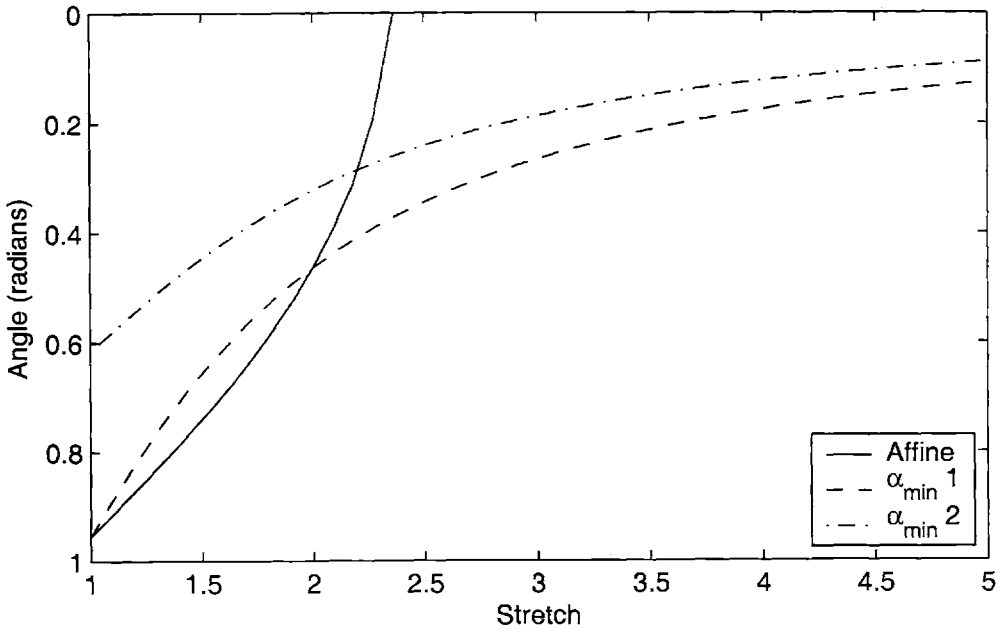

Figure 4-81: Relation between stretch and orientation angle parameters

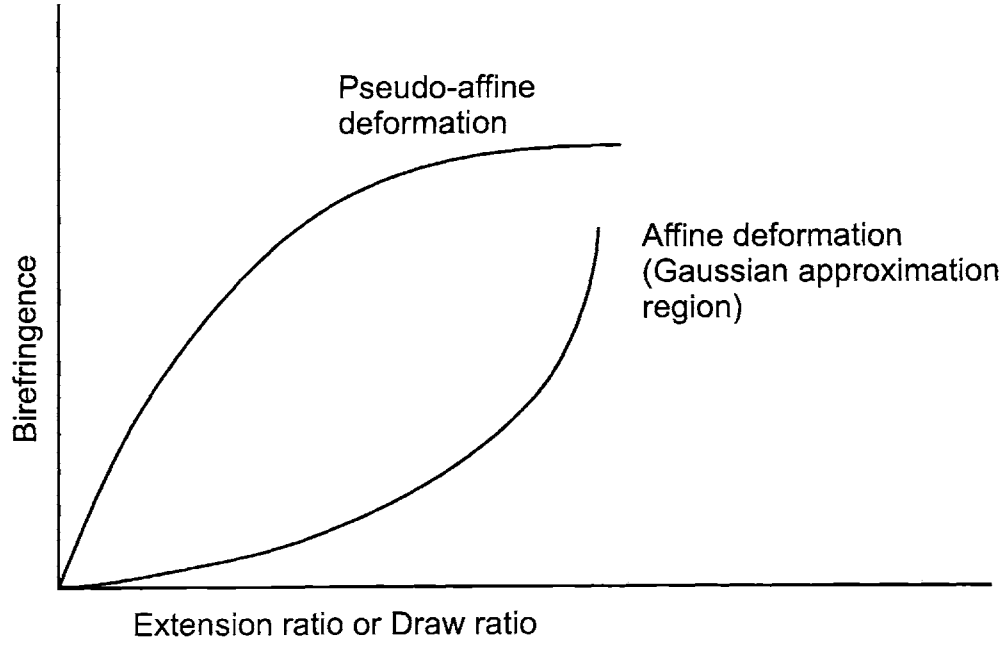

Figure 4-82: Affine versus pseudo-affine deformation (from Ward (1975))

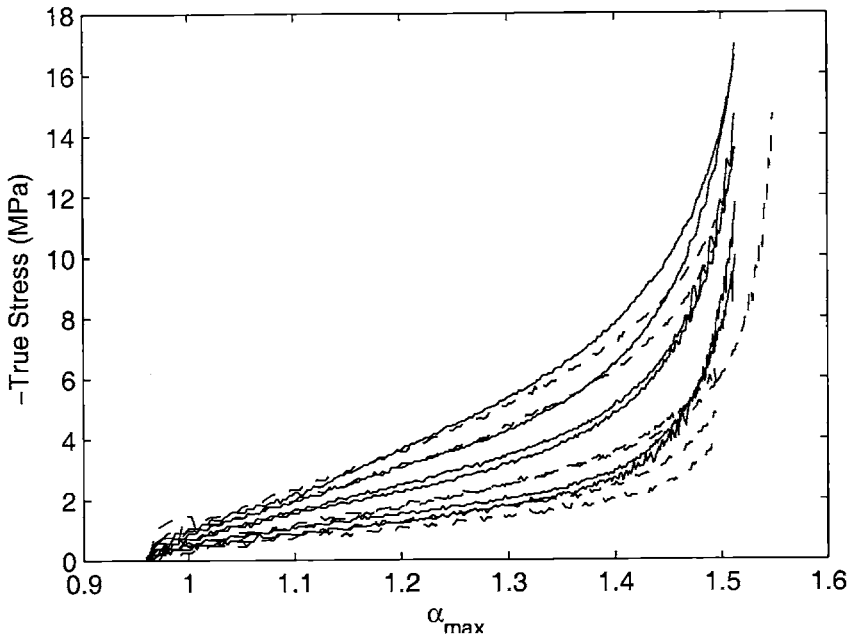

Figure 4-83: Stress versus maximum angle (in radians), PETG uniaxial compression and plane strain compression, Temperature=90 ° C

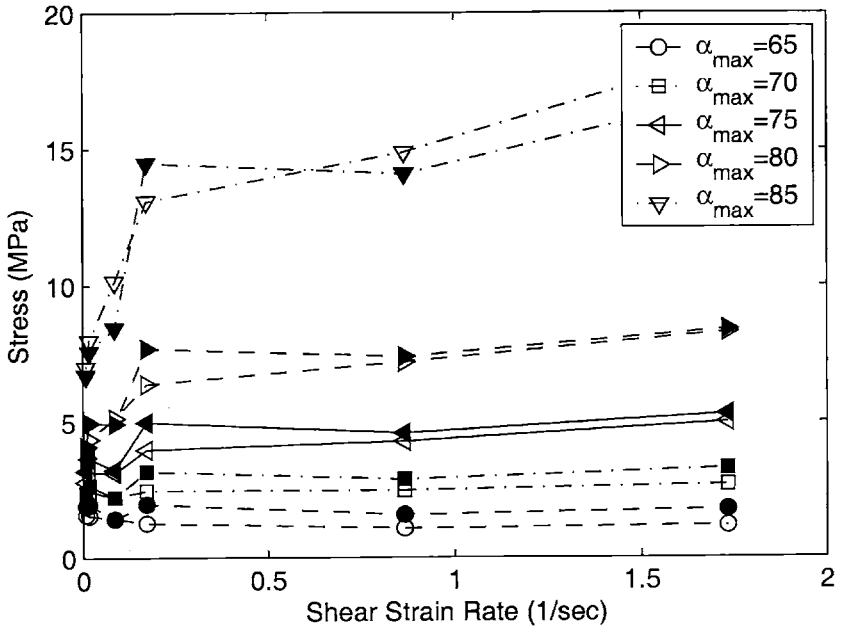

Figure 4-84: Stress versus strain rate, PETG uniaxial compression and plane strain compression, Temperature=90 ° C, angles in degrees

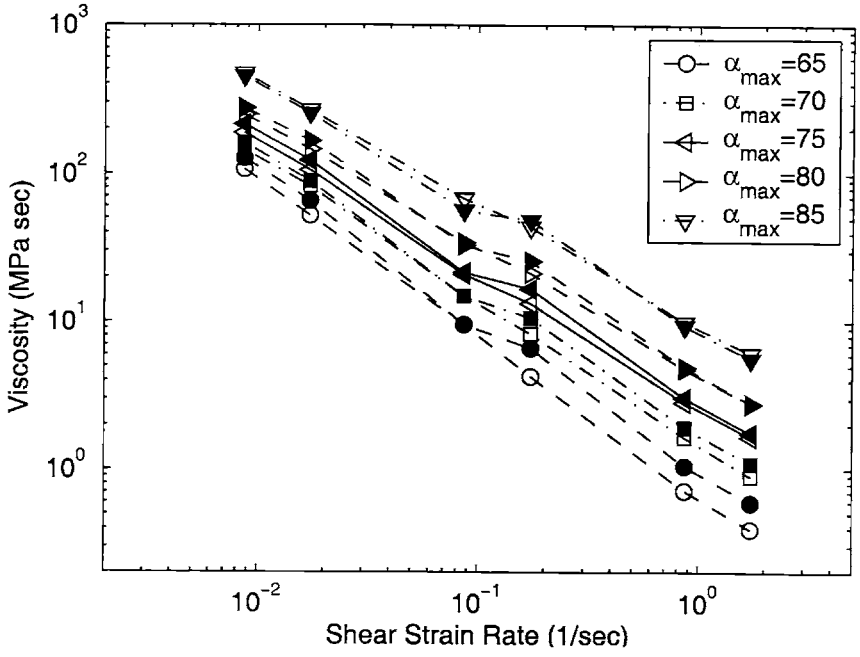

Figure 4-85: Viscosity versus strain rate on a log-log plot, PETG uniaxial compression and plane strain compression, T=90 ° C, angles in degrees

where $C = (1/m)^{(1/n)}$. The power-law exponent, n, is obtained from the slope of the curves on the log viscosity-log strain rate plot, which is constant with angle, α. The curve fit gives 1/n = 6.67, which is a reasonable value for the power-law exponent. The parameter C is a measure of the shift in the log viscosity-log strain rate curve, and is therefore a function of angle, α. A curve fit gives the following expression:

$$C = \hat{C}(\alpha_{max}) = g(\alpha_{max})^{-38} \tag{4.44}$$

where α_{max} is the value of the maximum angle between a chain and the principal stretch axes, in radians. The exponential value of -38 is not very convenient, numerically, nor is it very physical, so we instead cast the equations in terms of the complement of α_{max}, which we will call α_{min}. Physically, α_{min} is proportional to how closely aligned two of the neighboring eight chains have become. If we use this

formulation, equation 4.44 becomes:

$$C = \hat{C}(\alpha_{min}) = h(\alpha_{min})^{6.67} \tag{4.45}$$

With this formulation the exponent obtained is identical to the power-law exponent obtained before, suggesting that this orientation parameter represented by α_{min} is fundamentally related to the mechanism involved in molecular relaxation. [4]

The constants g and h in equations 4.44 and 4.45 are temperature dependent as in the previous model:

$$h = D \exp\left(-\frac{Q}{R\theta}\right) \tag{4.46}$$

Again, we find that this formulation under-predicts the material behavior at very large strains and thus need to incorporate a cessation to flow:

$$\dot{\gamma} = \left(\frac{\frac{\alpha_{min}}{\alpha_c} - 1}{\frac{\alpha_0}{\alpha_c} - 1}\right) C\tau^{1/n} \tag{4.47}$$

where α_0 is the initial value of the complement to the maximum angle (α_0=90 ° - 54.7 ° = 35.3 ° = .616 rad). α_c is determined by a curve fit and is found to be 0.05 rad = 2.9 °. The same value of α_c is obtained at every temperature and strain rate considered, thus eliminating the need for complicated temperature and rate-dependence fitting constants (as compared with the expressions in equations 4.38 and 4.39). This rate and temperature independence of α_c lends confidence to the concept that the orientation parameter is the governing variable in this molecular relaxation mechanism, and particularly to the cessation of flow.

For incorporation in the constitutive model previously developed, equation 4.47 becomes:

$$\dot{\gamma}_B^F = \left(\frac{\frac{\alpha_{min}}{\alpha_c} - 1}{\frac{\alpha_0}{\alpha_c} - 1}\right) h(\alpha_{min}\tau_B)^{1/n} \tag{4.48}$$

[4]Returning to the original power-law viscosity formulation, we have $\tau = \eta(\dot{\gamma})\dot{\gamma} = m\dot{\gamma}^n$. If we want to add a dependence on strain, it could be done as follows: $\tau = m\dot{\gamma}^n f(\varepsilon)$. Rearranging, we obtain $\dot{\gamma} = (\tau/(mf(\varepsilon)))^{1/n}$, which from above yields $f(\varepsilon) = 1/\alpha_{min}$. This indicates that the viscosity is inversely proportional to the orientation parameter α_{min}

which can be rewritten in a non-dimensional form as:

$$\dot{\gamma}_B^F = h \left(\frac{\frac{\alpha_{min}}{\alpha_c} - 1}{\frac{\alpha_0}{\alpha_c} - 1} \right) \left(\frac{\alpha_{min}}{\alpha_c} \frac{\tau_B}{\nu k \theta} \right)^{1/n} \tag{4.49}$$

with

$$\begin{aligned} \alpha_c &= 0.05 \text{ rad} \\ \alpha_0 &= 0.616 \text{ rad} \\ \nu k\theta &= 8.5 \text{ MPa} \end{aligned}$$

and the temperature dependence is as follows:

$$\begin{aligned} h(90\,^\circ C) &= 0.0290 \text{ sec}^{-1} \\ h(100\,^\circ C) &= 4.4716 \text{ sec}^{-1} \end{aligned}$$

giving

$$\begin{aligned} D &= 1.25 \times 10^{80} \text{ sec}^{-1} \\ Q/R &= 6.823 \times 10^4 \text{ K} \end{aligned}$$

Using this new approach, the following simulation results are obtained. Figures 4-86 through 4-95 show the results for uniaxial compression and figures 4-96 and 4-98 show the results for plane strain compression. These figures illustrate that the model still captures the strain and temperature dependence of the initial modulus, flow stress, and initial hardening modulus of the PETG. In addition, the model is now capable of predicting the large upswing in stress at large strains.

Figures 4-99 through 4-105 show the comparison of simulation with experiment. Error values for these curves are tabulated in Table 4.3 and are shown graphically in figures 4-106 and 4-107. It can be seen that the uniaxial compression experiments are very well approximated with the new model at all strain levels, strain rates and

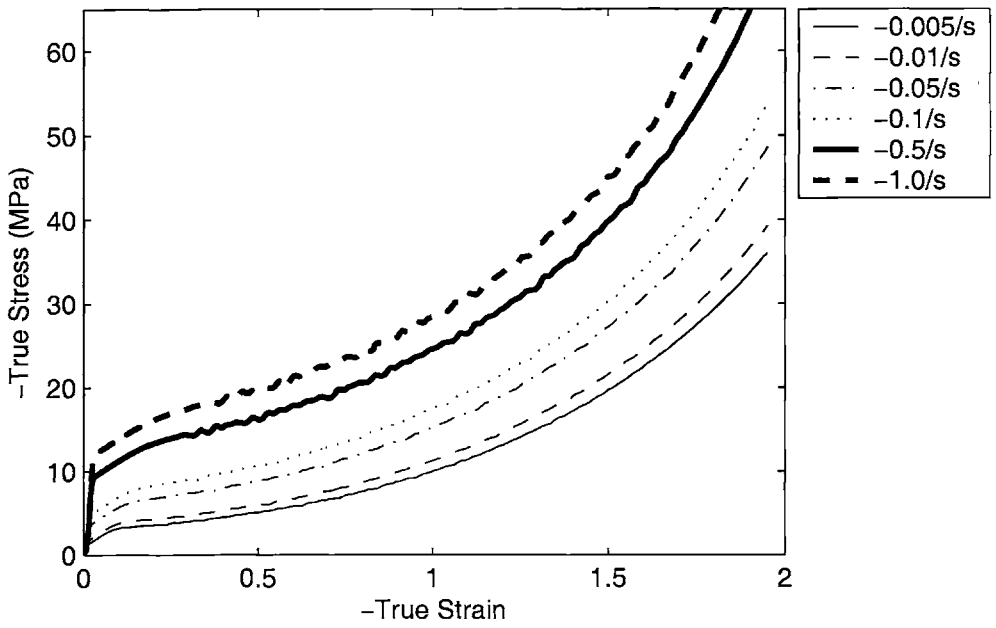

Figure 4-86: Uniaxial compression simulation, Temperature = 80 ° C

temperatures. Plane strain behavior is predicted quite well with the new model, as well.

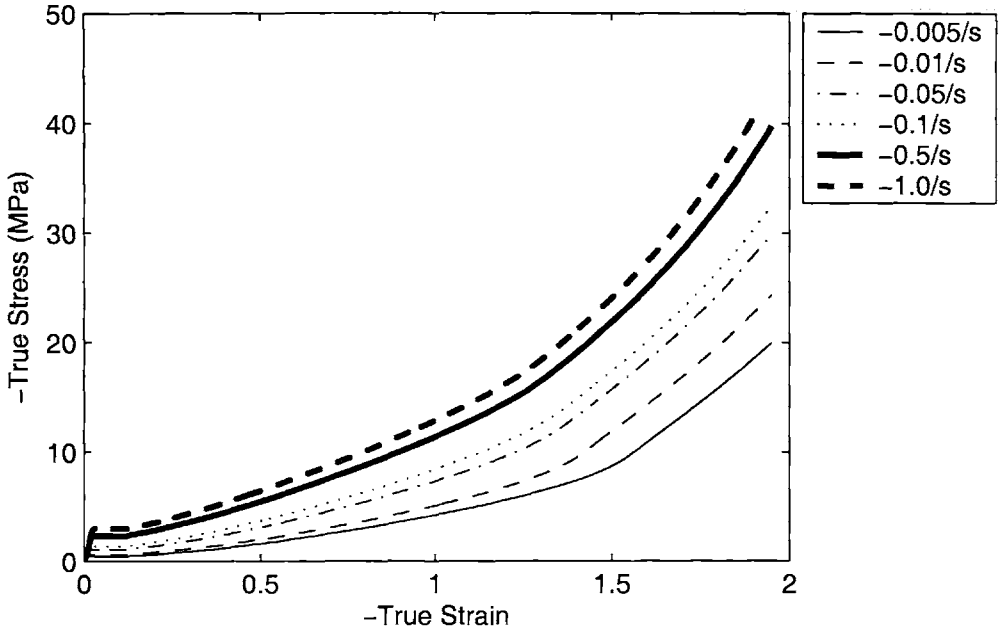

Figure 4-87: Uniaxial compression simulation, Temperature = 90 ° C

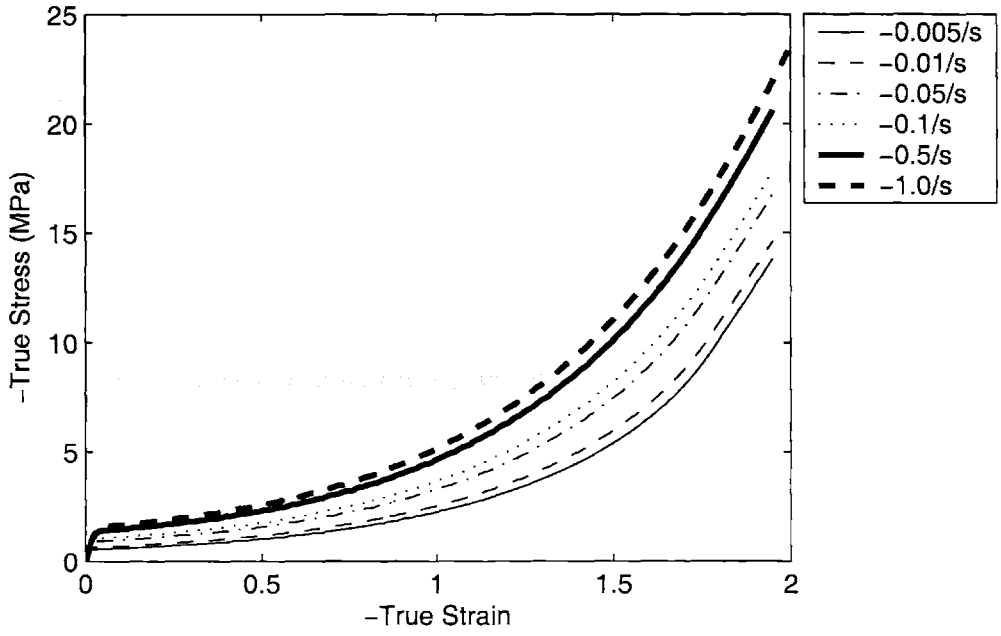

Figure 4-88: Uniaxial compression simulation, Temperature = 100 ° C

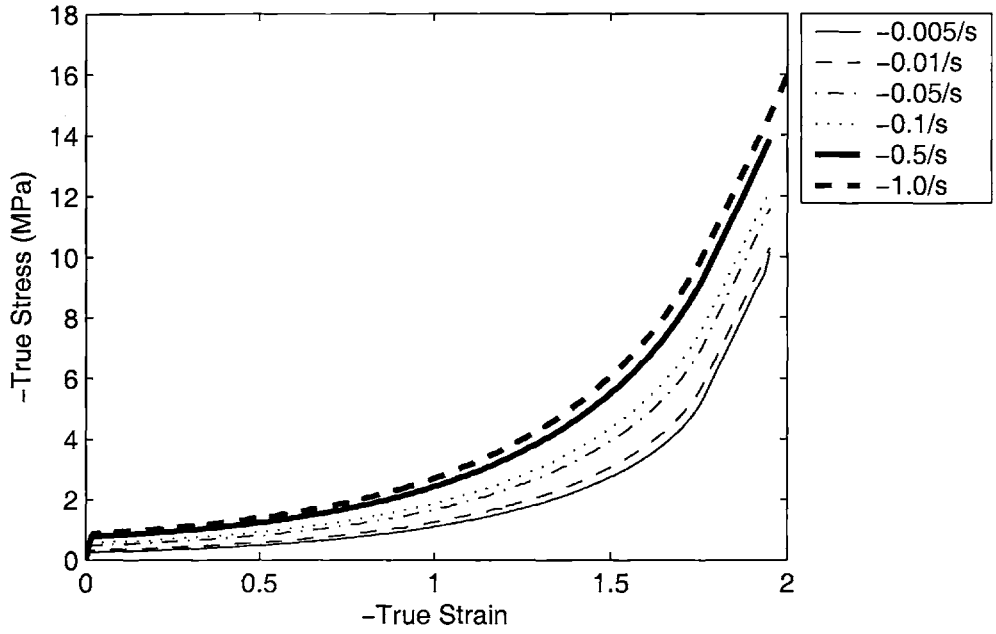

Figure 4-89: Uniaxial compression simulation, Temperature = 110 ° C

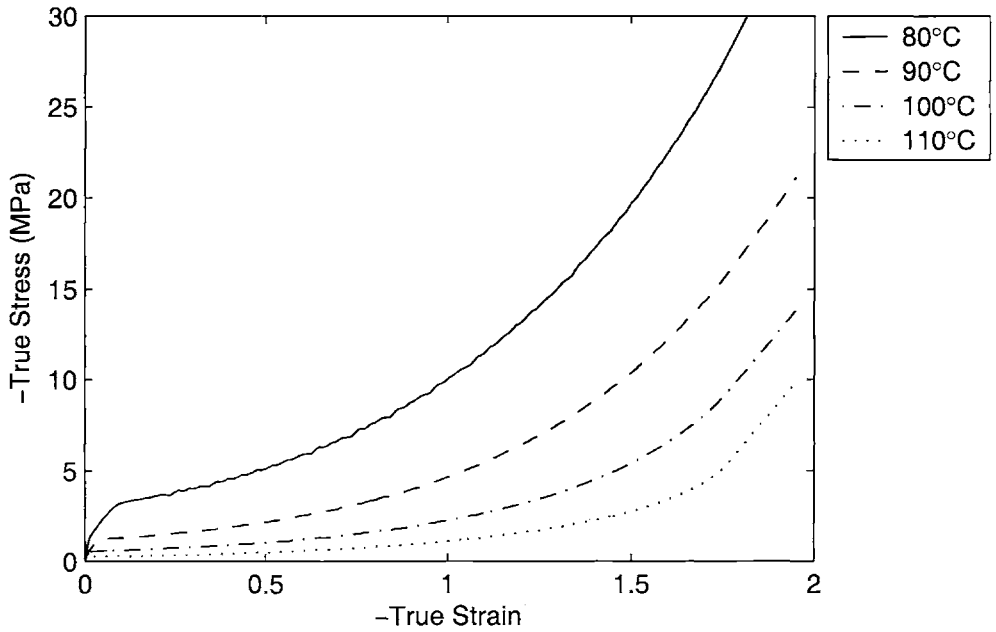

Figure 4-90: Uniaxial compression simulation, $\dot{\varepsilon}$ = -.005/s

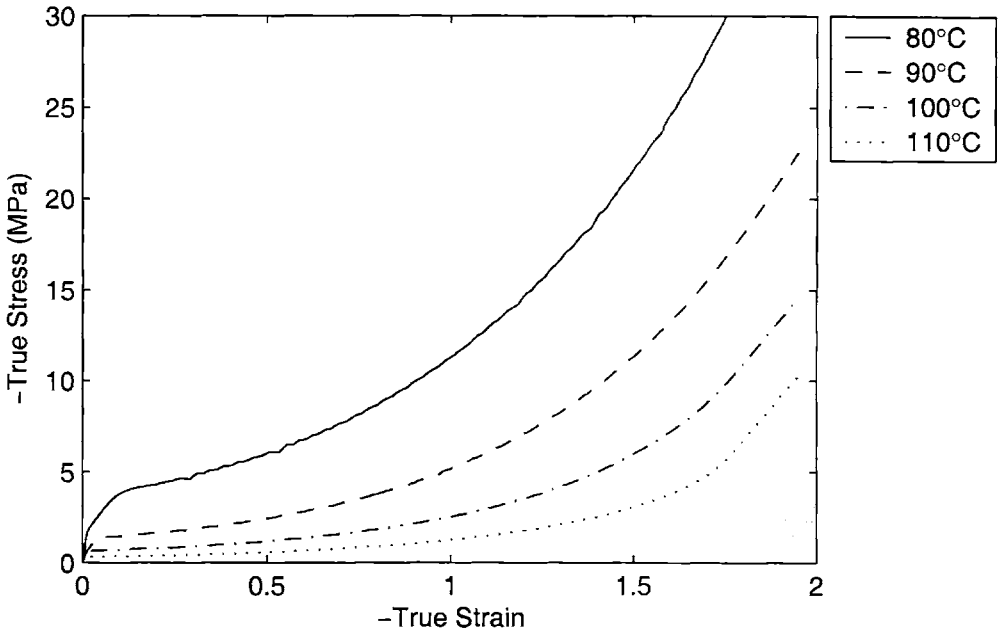

Figure 4-91: Uniaxial compression simulation, $\dot{\varepsilon}$ = -.01/s

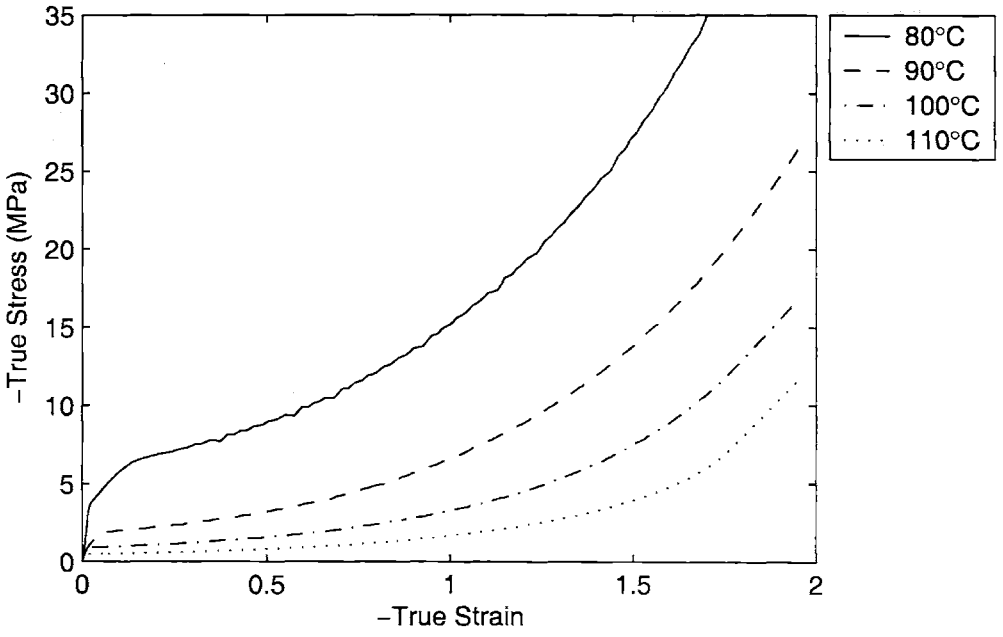

Figure 4-92: Uniaxial compression simulation, $\dot{\varepsilon}$ = -.05/s

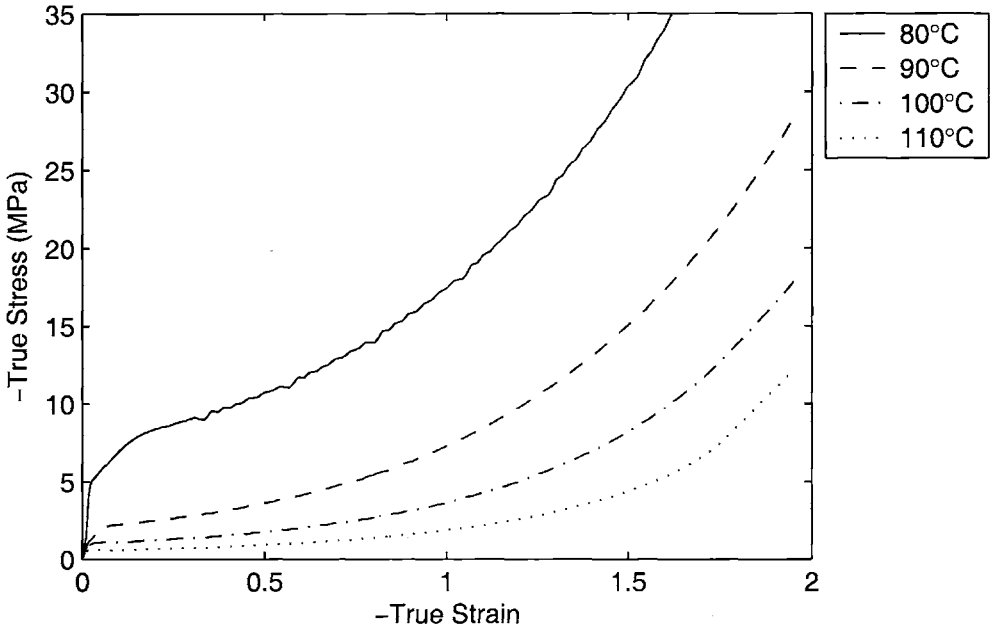

Figure 4-93: Uniaxial compression simulation, $\dot{\varepsilon}$ = -.1/s

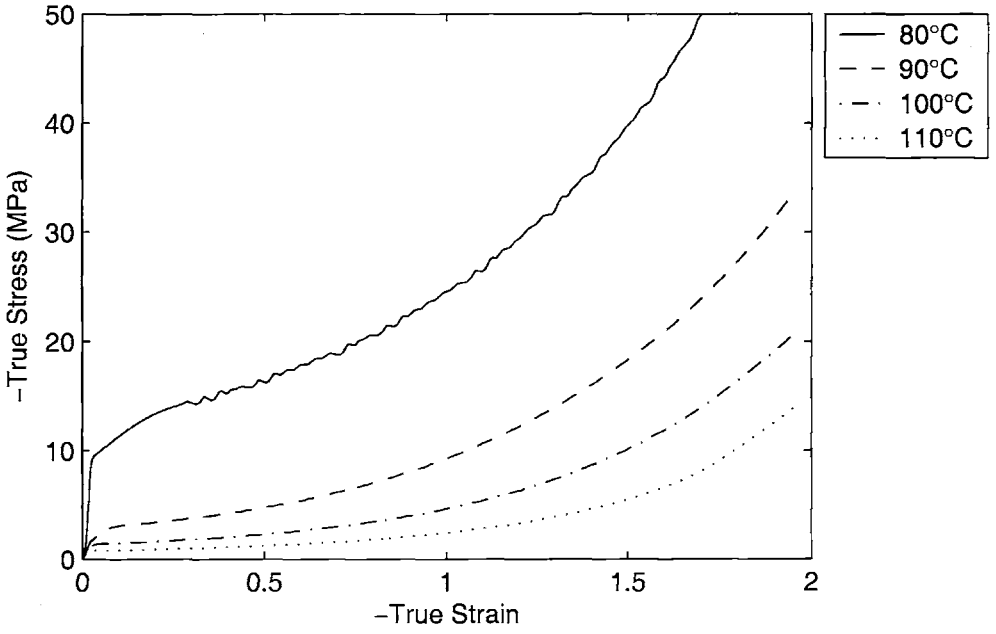

Figure 4-94: Uniaxial compression simulation, $\dot{\varepsilon}$ = -.5/s

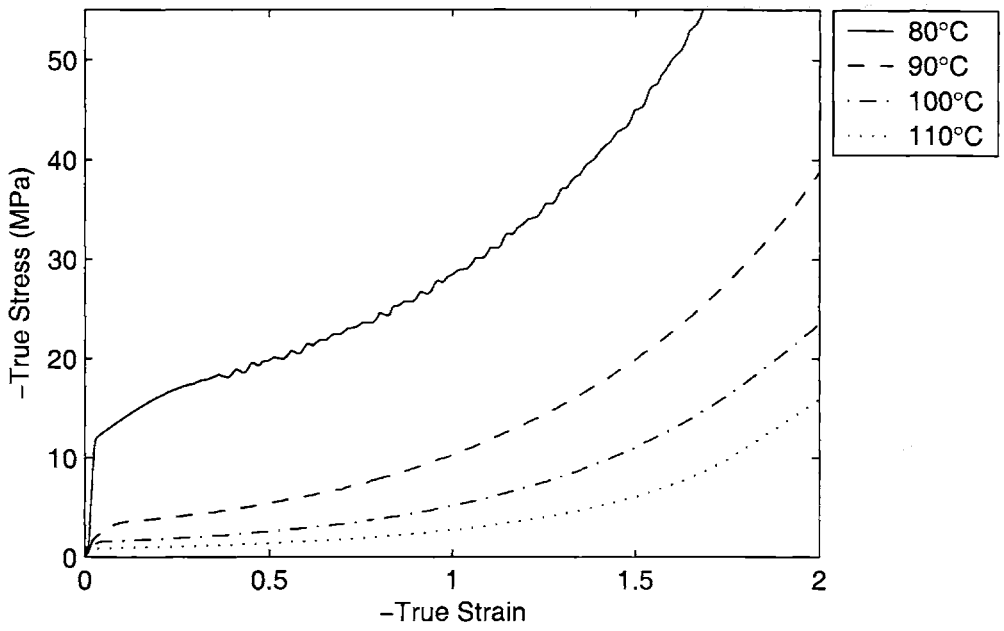

Figure 4-95: Uniaxial compression simulation, $\dot{\varepsilon}$ = -1.0/s

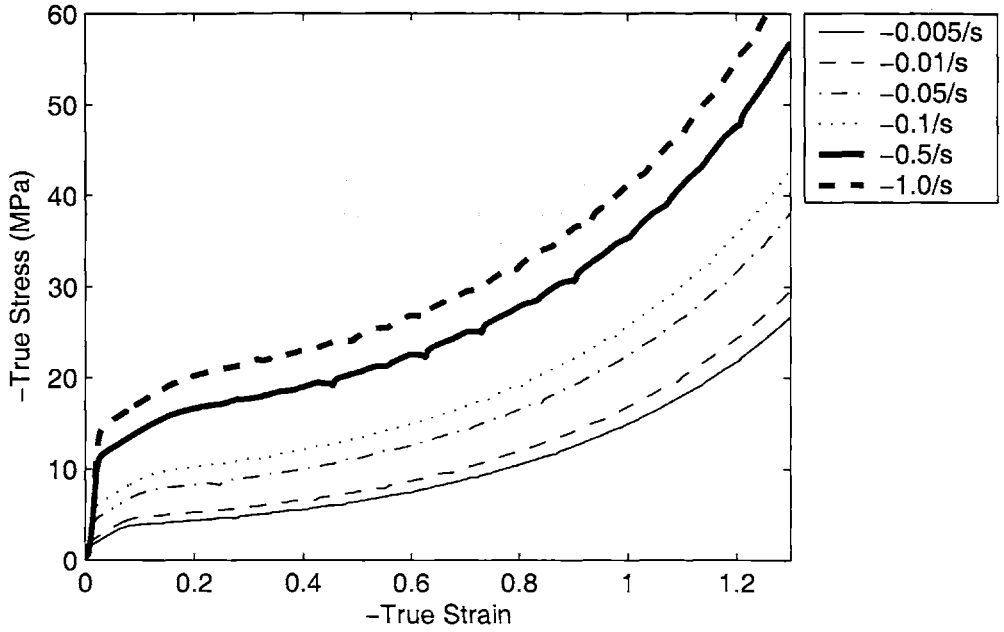

Figure 4-96: Plane strain compression simulation, Temperature = 80 ° C

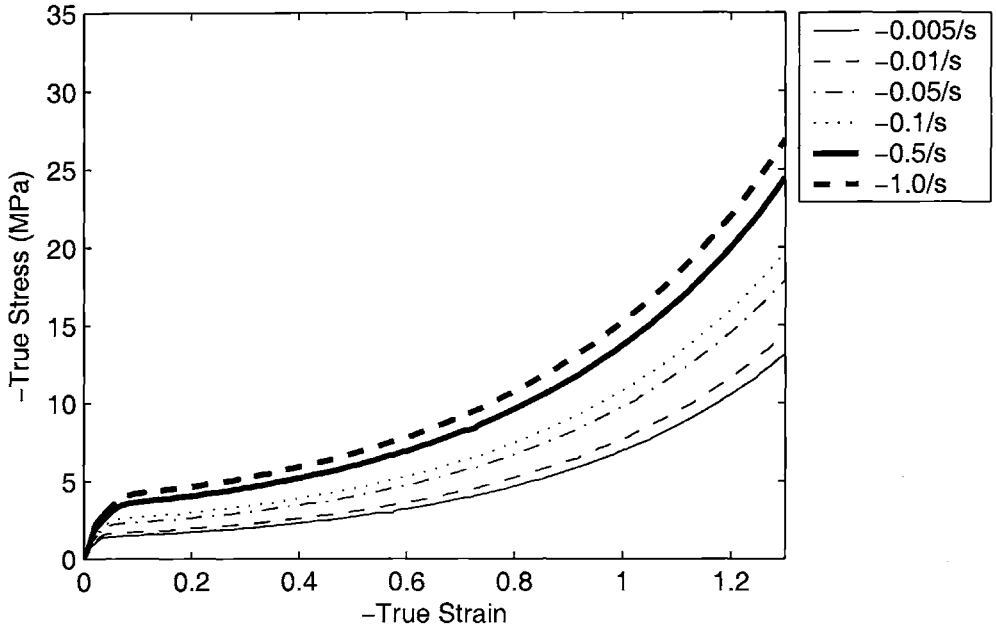

Figure 4-97: Plane strain compression simulation, Temperature = 90 ° C

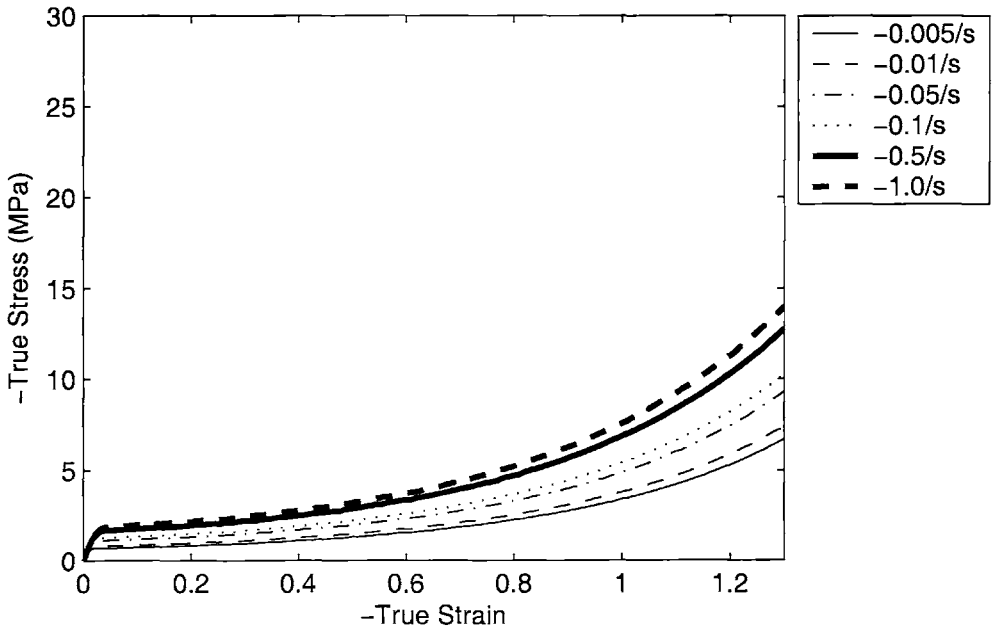

Figure 4-98: Plane strain compression simulation, Temperature = 100 ° C

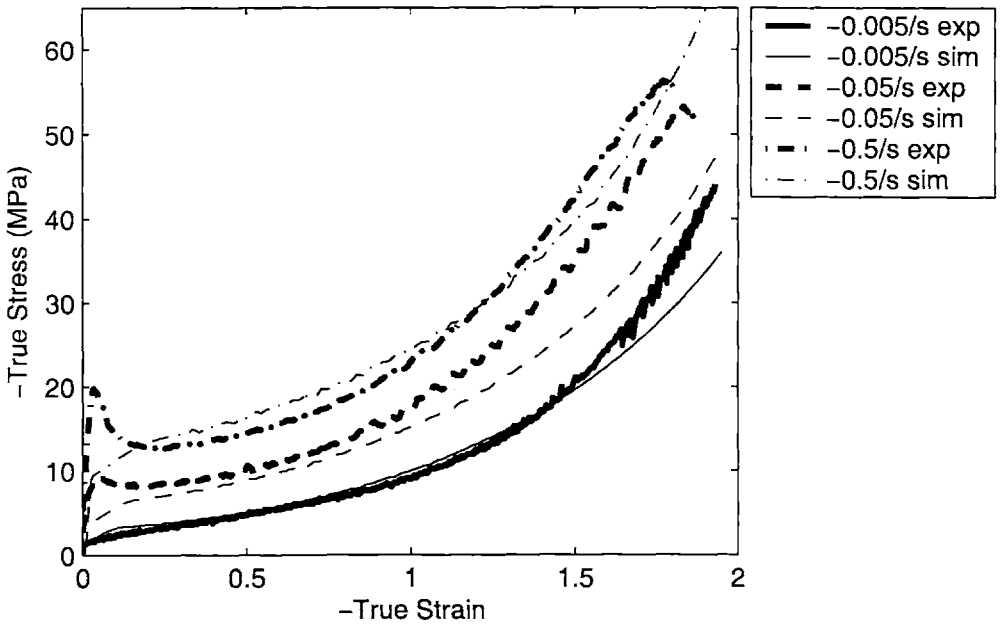

Figure 4-99: PETG Uniaxial compression, comparing simulation results with experimental data, Temperature = 80 ° C

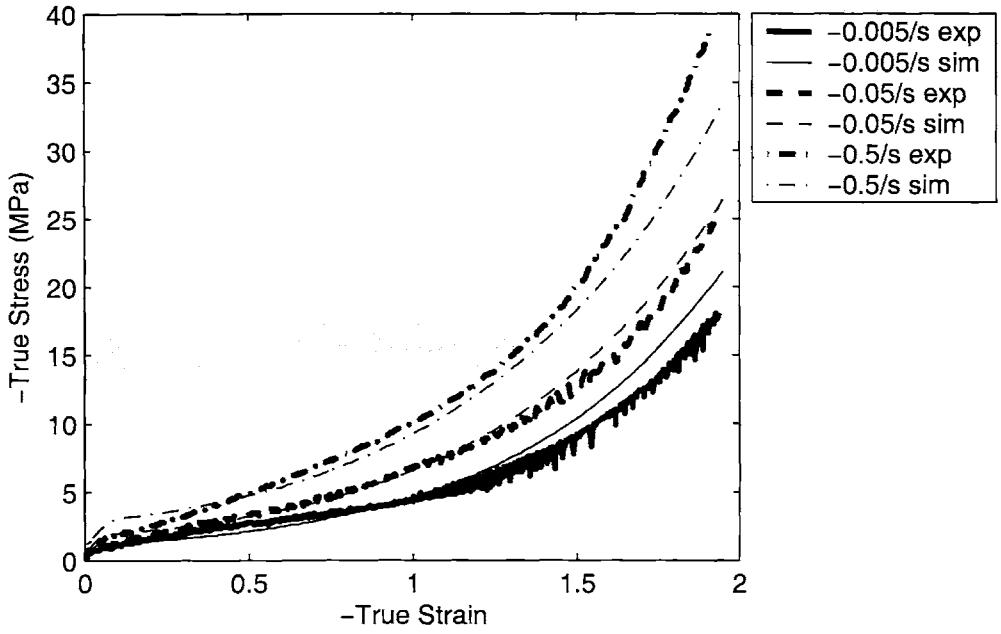

Figure 4-100: PETG Uniaxial compression, comparing simulation results with experimental data, Temperature = 90 ° C

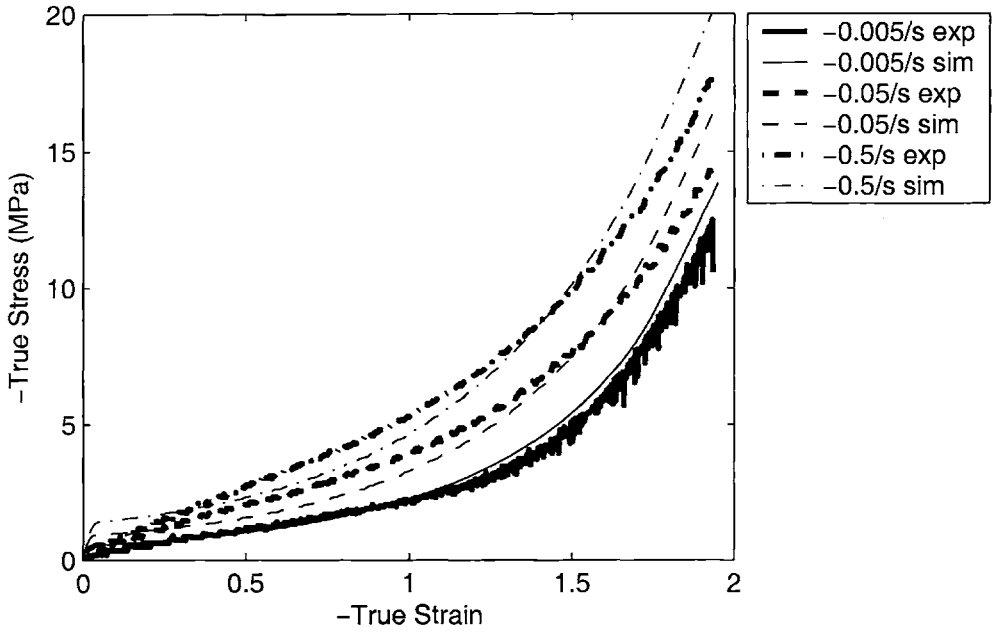

Figure 4-101: PETG Uniaxial compression, comparing simulation results with experimental data, Temperature = 100 ° C

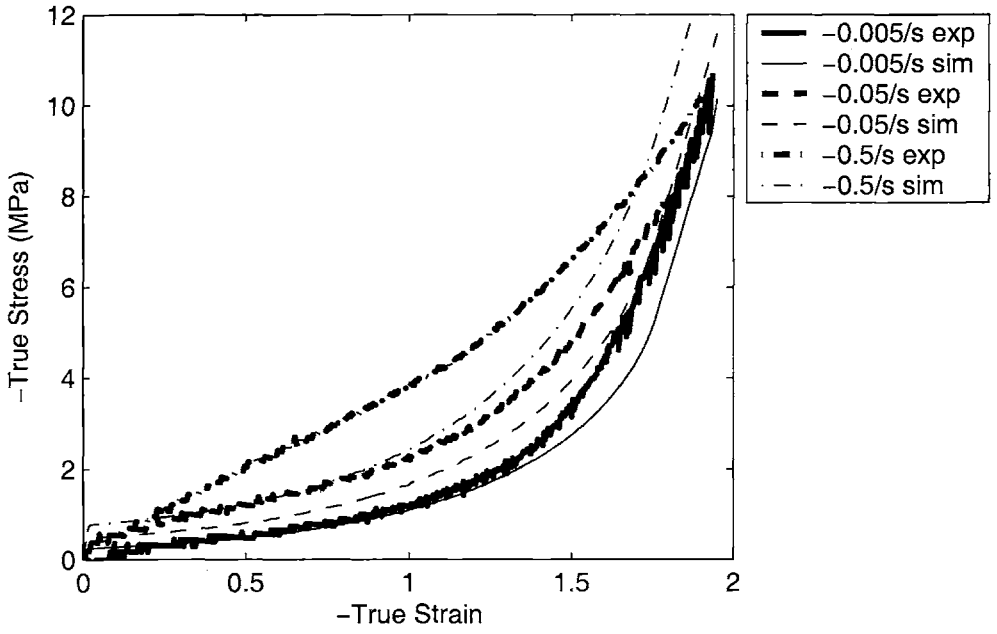

Figure 4-102: PETG Uniaxial compression, comparing simulation results with experimental data, Temperature = 110 ° C

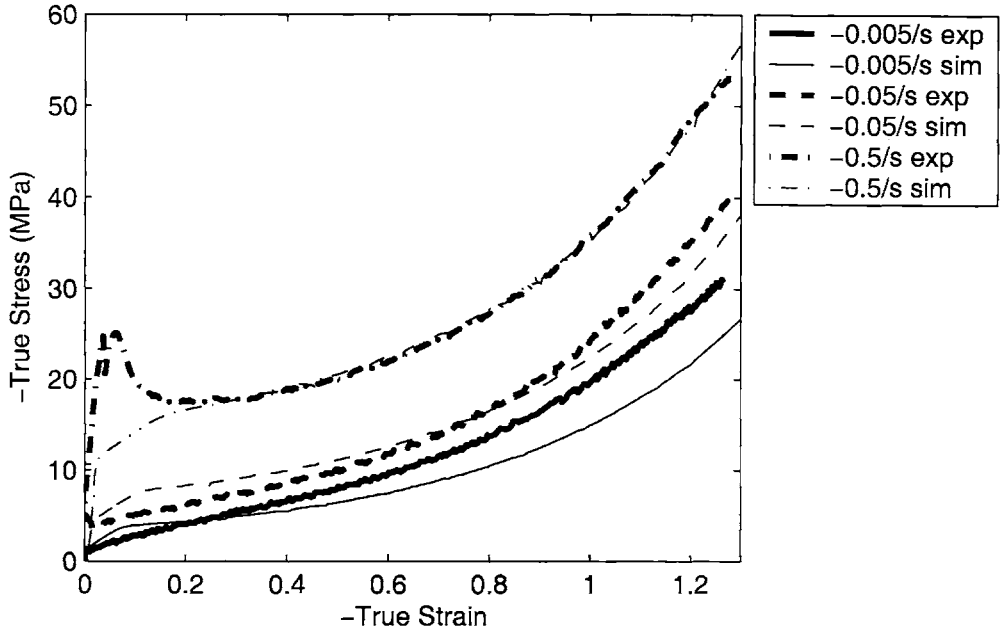

Figure 4-103: PETG Plane strain compression, comparing simulation results with experimental data, Temperature = 80 ° C

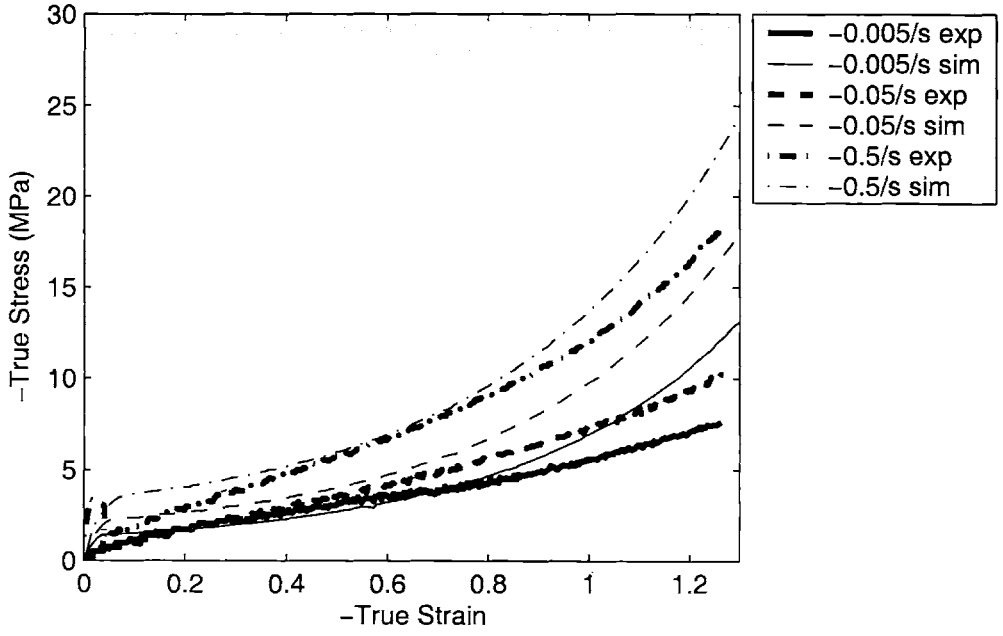

Figure 4-104: PETG Plane strain compression, comparing simulation with experimental data, Temperature = 90 ° C

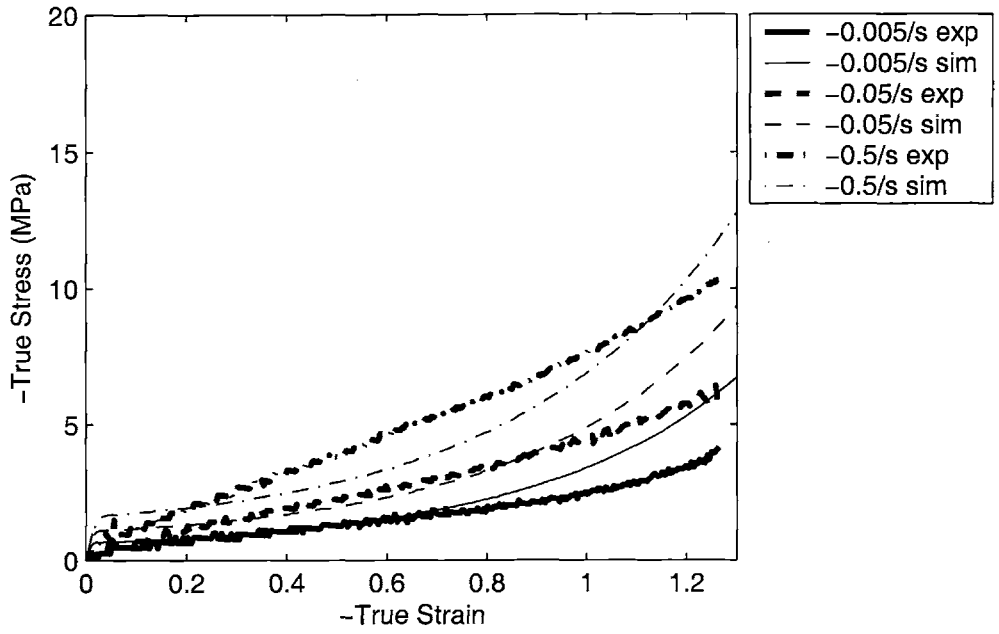

Figure 4-105: PETG Plane strain compression, comparing simulation with experimental data, Temperature = 100 ° C

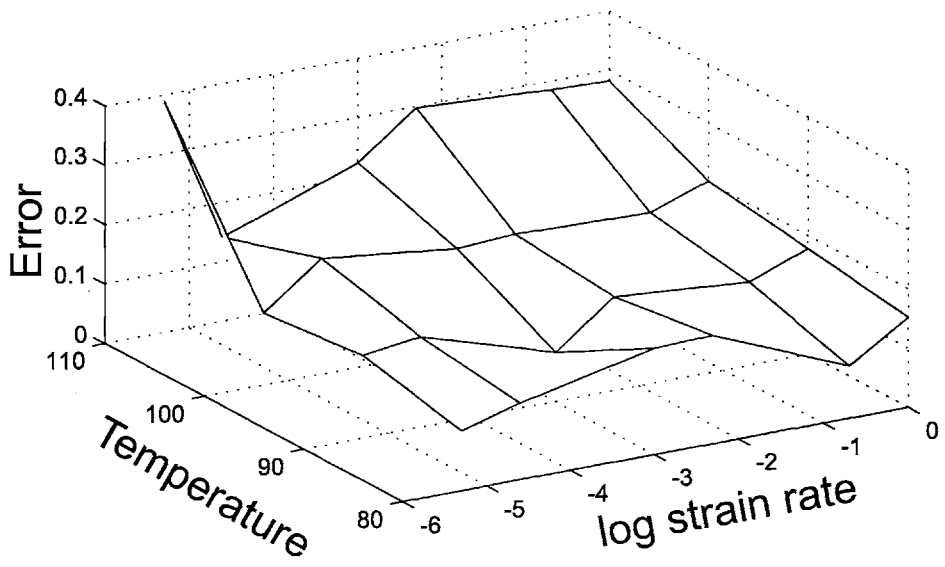

Figure 4-106: PETG Uniaxial compression error values with flow cutoff and viscosity representation

Table 4.3: PETG Error values for uniaxial and plane strain compression simulations with flow cutoff and viscosity representation

Strain State	Temperature	Strain Rate	$\bar{y}$, full range	$\bar{y}$, up to $\varepsilon = 1.0$
Uniaxial	80 ° C	-0.005/sec	.1017	.1196
Uniaxial	80 ° C	-0.05/sec	.1799	.1533
Uniaxial	80 ° C	-0.5/sec	.0884	.1237
Uniaxial	90 ° C	-0.005/sec	.1393	.1301
Uniaxial	90 ° C	-0.05/sec	.0828	.1018
Uniaxial	90 ° C	-0.5/sec	.1404	.1748
Uniaxial	100 ° C	-0.005/sec	.1219	.1514
Uniaxial	100 ° C	-0.05/sec	.1683	.2339
Uniaxial	100 ° C	-0.5/sec	.1676	.2522
Uniaxial	110 ° C	-0.005/sec	.3896	.2284
Uniaxial	110 ° C	-0.05/sec	.2235	.2838
Uniaxial	110 ° C	-0.5/sec	.2855	.3625
Plane Strain	80 ° C	-0.005/sec	.2122	.2094
Plane Strain	80 ° C	-0.05/sec	.1408	.1522
Plane Strain	80 ° C	-0.5/sec	.0430	.0507
Plane Strain	90 ° C	-0.005/sec	.1996	.1465
Plane Strain	90 ° C	-0.05/sec	.4133	.3834
Plane Strain	90 ° C	-0.5/sec	.2101	.2090
Plane Strain	100 ° C	-0.005/sec	.2295	.1553
Plane Strain	100 ° C	-0.05/sec	.1791	.1662
Plane Strain	100 ° C	-0.5/sec	.1995	.2367

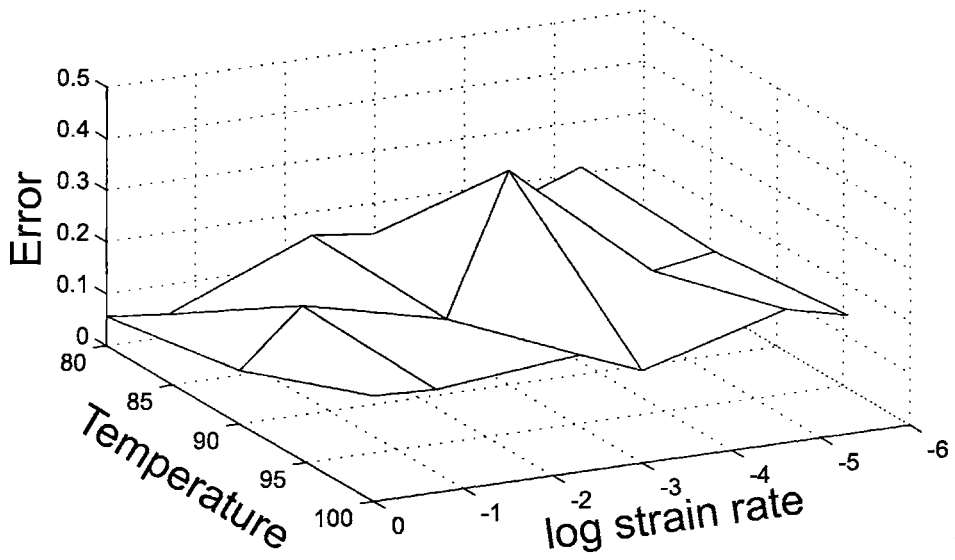

Figure 4-107: PETG Plane strain compression error values with flow cutoff and viscosity representation

4.5.3 Comparison with the Doi-Edwards Model

As the molecular relaxation model previously developed is intended to capture the phenomenon of chain reptation, it should be interesting to compare the results to the theory of Doi and Edwards (1978, 1980, 1986). To do this, we make use of the equations contained in reference (Doi and Edwards 1978). The components of the stress tensor as a function of time are taken to be:

$$\sigma_{\alpha\beta}(t) = G_0 \int_{-\infty}^{t} dt' \mu'(t-t') Q_{\alpha\beta}[\mathbf{F}(t,t')] \tag{4.50}$$

where

$$\mu'(t) = \sum_{p\ odd} \frac{8}{p^2\pi^2\tau_p} \exp\left(\frac{-t}{\tau_p}\right) \tag{4.51}$$

or

$$\mu'(t) = \sum_{p\ odd} \frac{8}{\pi^2 T_d} \exp\left(-\frac{t}{T_d}p^2\right) \tag{4.52}$$

is a relaxation modulus, τ_p or T_d being a time constant.[5]

Also,

$$G_0 = 3ck\theta\left(\frac{L}{a}\right) \tag{4.53}$$

where c is the number of molecules per unit volume, L is the contour length, and a is the length of a primitive chain segment. Thus,

$$c\left(\frac{L}{a}\right) = \nu \tag{4.54}$$

which is the chain density used previously in the 8-chain model (refer to equation 4.17.) Additional variables are $\mathbf{F}$, the deformation gradient; $\sigma_{\alpha\beta}$, the components of the Cauchy stress tensor; $\mathbf{u}$, the unit tangent vector to the polymer chain

[5]In models such as the Doi-Edwards model, the phenomenon of reptation is generally interpreted as a relaxation or softening of the material's modulus with time (as in a stress-relaxation experiment); hence μ' is a function of time and for a given deformation $\mathbf{F}$ the stress will relax over time through the change in modulus. This is in contrast to the solid mechanics approach, in which the modulus is independent of time, but the deformation is decomposed into an elastic and viscous (plastic) part ($\mathbf{F} = \mathbf{F}^e\mathbf{F}^v$). Only the elastic part gives rise to stress in the material. Over time, viscoplastic relaxation is interpreted as a decrease in the portion of deformation which is elastic ($\mathbf{F}^e$) and a corresponding increase in the viscous deformation ($\mathbf{F}^v$).

segment; t, the current time; t', a reference time in the past; k, Boltzmann's constant; θ, temperature; and $Q_{\alpha\beta}$ is given by:

$$Q_{\alpha\beta}(\mathbf{F}) = \left\langle \frac{(\mathbf{F}\cdot\mathbf{u})_\alpha(\mathbf{F}\cdot\mathbf{u})_\beta}{|\mathbf{F}\cdot\mathbf{u}|^2} - \frac{1}{3}\delta_{\alpha\beta} \right\rangle_0 \tag{4.55}$$

$$\equiv \int_S \frac{d^2\mathbf{u}}{4\pi} \left\{ \frac{(\mathbf{F}\cdot\mathbf{u})_\alpha(\mathbf{F}\cdot\mathbf{u})_\beta}{|\mathbf{F}\cdot\mathbf{u}|^2} - \frac{1}{3}\delta_{\alpha\beta} \right\} \tag{4.56}$$

where $\langle\ \rangle_0$ indicates a volume average and the integral in equation 4.56 is over the surface of a unit sphere. This is essentially an orientation tensor which accounts for the deformation gradient operating on the unit vector along the chain backbone.

For the specific case of uniaxial deformation in the 3-direction,

$$\mathbf{F} = \begin{bmatrix} \frac{1}{\sqrt{\lambda}} & 0 & 0 \\ 0 & \frac{1}{\sqrt{\lambda}} & 0 \\ 0 & 0 & \lambda \end{bmatrix} \tag{4.57}$$

and

$$\mathbf{Q} = \begin{bmatrix} Q_{xx} & 0 & 0 \\ 0 & Q_{yy} & 0 \\ 0 & 0 & Q_{zz} \end{bmatrix} \tag{4.58}$$

also, $Q_{xx} = Q_{yy}$ because of symmetry. The quantity of interest is therefore $Q_{zz} - Q_{xx}$, which from above is a function of λ:

$$Q_{zz} - Q_{xx} = F_3(\lambda) \equiv \left\langle \frac{\lambda^2 u_z^2 - \lambda^{-1} u_x^2}{\lambda^2 u_z^2 + \lambda^{-1}(u_x^2 + u_y^2)} \right\rangle_0 \tag{4.59}$$

The integral which is represented by this averaging can be evaluated analytically using spherical coordinates for $\mathbf{u}$ and by computing the average over the surface of a unit sphere. The derivation is shown in Appendix A. The resulting equations given

by eqns A.7, A.10, and A.15 are repeated here as equation 4.60:

$$F_3(\lambda) \equiv Q_{zz} - Q_{xx} = \begin{cases} \frac{3}{2}\frac{\lambda^3}{1-\lambda^3}\left(\frac{\tanh^{-1}(\sqrt{1-\lambda^3})}{\sqrt{1-\lambda^3}} - 1\right) - \frac{1}{2} & : \quad \lambda^3 - 1 < 0 \\ 0 & : \quad \lambda^3 - 1 = 0 \\ \frac{3}{2}\frac{\lambda^3}{\lambda^3-1}\left(1 - \frac{\tan^{-1}(\sqrt{\lambda^3-1})}{\sqrt{\lambda^3-1}}\right) - \frac{1}{2} & : \quad \lambda^3 - 1 > 0 \end{cases} \tag{4.60}$$

To calculate the stress during uniaxial deformation, we proceed as follows:

$$\begin{aligned} \sigma_{zz} - \sigma_{xx} &= G_0 \int_{-\infty}^{t} dt' \mu'(t,t') Q_{zz} - G_0 \int_{-\infty}^{t} dt' \mu'(t,t') Q_{xx} \\ &= G_0 \int_{-\infty}^{t} dt' \mu'(t,t') \left[Q_{zz} - Q_{xx}\right] \\ &= G_0 \int_{-\infty}^{t} dt' \sum_{p \ odd} \frac{8}{p^2\pi^2\tau_p} \exp\left(-\frac{(t-t')}{\tau_p}\right) \left[Q_{zz} - Q_{xx}\right] \\ &= G_0 \sum_{p \ odd} \frac{8}{p^2\pi^2\tau_p} \int_{-\infty}^{t} dt' \exp\left(-\frac{(t-t')}{\tau_p}\right) F_3\left(\lambda(t,t')\right) \end{aligned} \tag{4.61}$$

Note that

$$\lambda(t,t') = \exp\left(\int_{t'}^{t} dt'' \dot{\varepsilon}(t'')\right) \tag{4.62}$$

For loading at a constant strain rate starting at t=0,

$$\lambda(t,t') = \begin{cases} \exp\left(\dot{\varepsilon}t\right) & : \quad t' < 0 \\ \exp\left(\dot{\varepsilon}(t-t')\right) & : \quad t' \geq 0 \end{cases} \tag{4.63}$$

Equation 4.61 becomes:

$$\begin{aligned} \sigma_{zz} - \sigma_{xx} &= G_0 \sum_{p \ odd} \frac{8}{p^2\pi^2\tau_p} \int_{-\infty}^{t} dt' \exp\left(-\frac{(t-t')}{\tau_p}\right) F_3\left(\lambda(t,t')\right) \\ &= Z \int_{-\infty}^{t} dt' \exp\left(-\frac{(t-t')}{\tau_p}\right) F_3\left(\lambda(t,t')\right) \\ &= Z \left[\int_{-\infty}^{0} dt' \exp\left(-\frac{(t-t')}{\tau_p}\right) F_3\left(\lambda(t,t')\right) \right. \\ &\qquad \left. + \int_{0}^{t} dt' \exp\left(-\frac{(t-t')}{\tau_p}\right) F_3\left(\lambda(t,t')\right)\right] \end{aligned}$$

$$
\begin{aligned}
&= Z\left[\int_{-\infty}^{0} dt' \exp\left(-\frac{(t-t')}{\tau_p}\right) F_3\left(\exp\left(\dot{\varepsilon}t\right)\right)\right. \\
&\qquad \left. + \int_{0}^{t} dt' \exp\left(-\frac{(t-t')}{\tau_p}\right) F_3\left(\exp\left(\dot{\varepsilon}(t-t')\right)\right)\right] \\
&= ZF_3\left(\exp\left(\dot{\varepsilon}t\right)\right) \int_{-\infty}^{0} dt' \exp\left(-\frac{(t-t')}{\tau_p}\right) \\
&\qquad + Z\int_{0}^{t} dt' \exp\left(-\frac{(t-t')}{\tau_p}\right) F_3\left(\exp\left(\dot{\varepsilon}(t-t')\right)\right) \qquad (4.64)
\end{aligned}
$$

The first integral can be solved analytically:

$$
\begin{aligned}
\int_{-\infty}^{0} dt' \exp\left(-\frac{(t-t')}{\tau_p}\right) &= \int_{-\infty}^{0} dt' \exp\frac{-t}{\tau_p} \exp\frac{t'}{\tau_p} \\
&= \exp\frac{-t}{\tau_p} \int_{-\infty}^{0} dt' \exp\frac{t'}{\tau_p} \qquad (4.65)
\end{aligned}
$$

Substituting $u = t'$:

$$
\begin{aligned}
\int_{-\infty}^{0} dt' \exp\left(-\frac{(t-t')}{\tau_p}\right) &= \exp\frac{-t}{\tau_p} \int_{0}^{\infty} ds \exp\frac{-s}{\tau_p} \\
&= \tau_p \exp\frac{-t}{\tau_p} \qquad (4.66)
\end{aligned}
$$

The second integral cannot be solved analytically, but may be simplified by the substitution $s = t - t'$:

$$
\int_{0}^{t} dt' \exp\left(-\frac{(t-t')}{\tau_p}\right) F_3\left(\exp\left(\dot{\varepsilon}(t-t')\right)\right) = \int_{0}^{t} ds \exp\left(\frac{-s}{\tau_p}\right) F_3\left(\exp\left(\dot{\varepsilon}s\right)\right) \qquad (4.67)
$$

Finally,

$$
\sigma_{zz} - \sigma_{xx} = ZF_3\left(\exp\left(\dot{\varepsilon}t\right)\right)\tau_p \exp\frac{-t}{\tau_p} + Z\int_{0}^{t} ds \exp\left(\frac{-s}{\tau_p}\right) F_3\left(\exp\left(\dot{\varepsilon}s\right)\right) \qquad (4.68)
$$

where

$$
Z = G_0 \sum_{p\ odd} \frac{8}{p^2\pi^2\tau_p} \qquad (4.69)
$$

Using equation 4.68, the stress can be calculated as a function of time for a given strain rate. Figure 4-108 shows stress-strain curves calculated from equation 4.68

for a variety of strain rates under conditions of uniaxial compression. The following constants were used:

$$T_d = 40 \text{ sec}$$
$$\nu k\theta = 8.5 \text{ MPa}$$

and only one term was included in the summation over p. Including additional terms serves to soften the rollover portion of the stress-strain curve. As in the proposed model, this data can again be converted into log viscosity-log strain rate curves. This is shown in figure 4-109. And we can similarly plot these curves at various values of the orientation parameter. Figure 4-110 shows this, comparing the Doi-Edwards model to the model proposed in section 4.5.2. A few differences are readily apparent. (1) The slope of the Doi-Edwards model curves is slightly steeper than in the proposed model. This slope can be adjusted somewhat. Decreasing the time constant, T_d, leads to a slight decrease in slope. Alternately, increasing the number of terms which are retained tends to make the curves slightly more shallow as adding terms smoothes out the transition from below T_d to above T_d. Even incorporating both these changes the Doi-Edwards model is still incapable of reaching the same slope as in the proposed model. A reptation model which includes effects of chain stretching may better capture this trend as chain stretch would cause an increase in viscosity at higher strain rates as compared with a model witout chain stretch, thus leading to a decrease in slope.

(2) The Doi-Edwards model departs from linearity at a strain rate of approximately 0.025 sec^{-1}. This corresponds to the reciprocal of the selected time constant, T_d, which in this case was 40 sec. A higher time constant, on the order of 1000 sec would provide for a linear curve through the range of strain rates considered. (3) In the Doi-Edwards model, the curves become much closer together as the orientation parameter decreases. This is in contrast to the proposed model, as well as in contrast to the data, which does not show such a trend. This can be explained as being due to the inability of the Doi-Edwards model to capture strain hardening. In figure 4-108 it

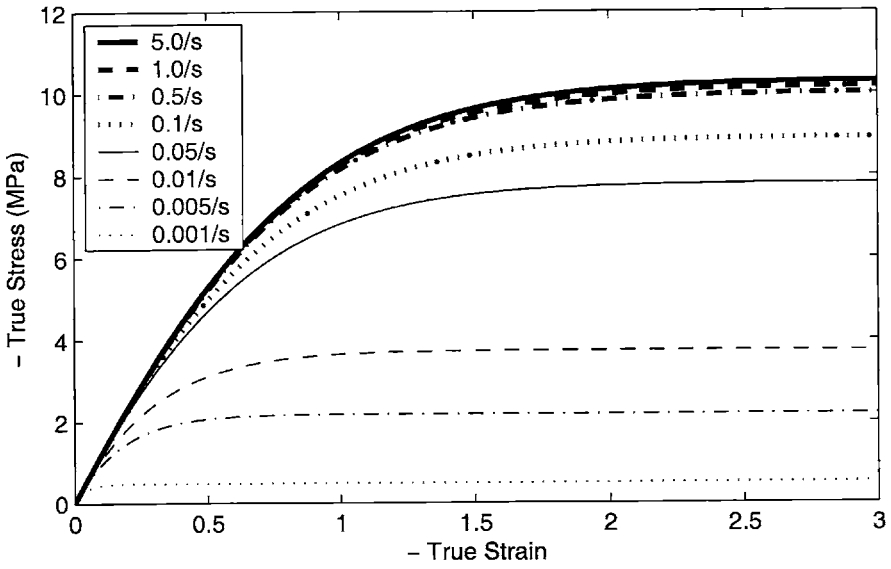

Figure 4-108: Stress-strain curves from Doi-Edwards model

is clear that at large strains the curves level off and show no strain hardening at very large strains. More recent models incorporate means of capturing strain hardening by including finite extensibility of the polymer chains (see, for example Ianniruberto and Marrucci (2001), Bhattacharjee, et al. (2002), or McLeish (2002).)

4.6 PETG Model Summary

The model developments presented in this chapter were progressively able to capture the features of the mechanical behavior of PETG above the glass transition temperature. The final model consists of four basic elements: (1) a linear-elastic spring to capture the rate and temperature dependence of the initial modulus; (2) a thermally-activated flow rule, to account for the rate and temperature dependent rollover to flow; (3) an 8-chain network model, to account for strain hardening due to molecular stretching and orientation; and (4) an element to account for molecular relaxation, which provides for a rate and temperature dependence of strain hardening. The molecular relaxation model is found to depend on an orientation angle parameter. Additionally, once the orientation parameter reaches a critical value, which is found

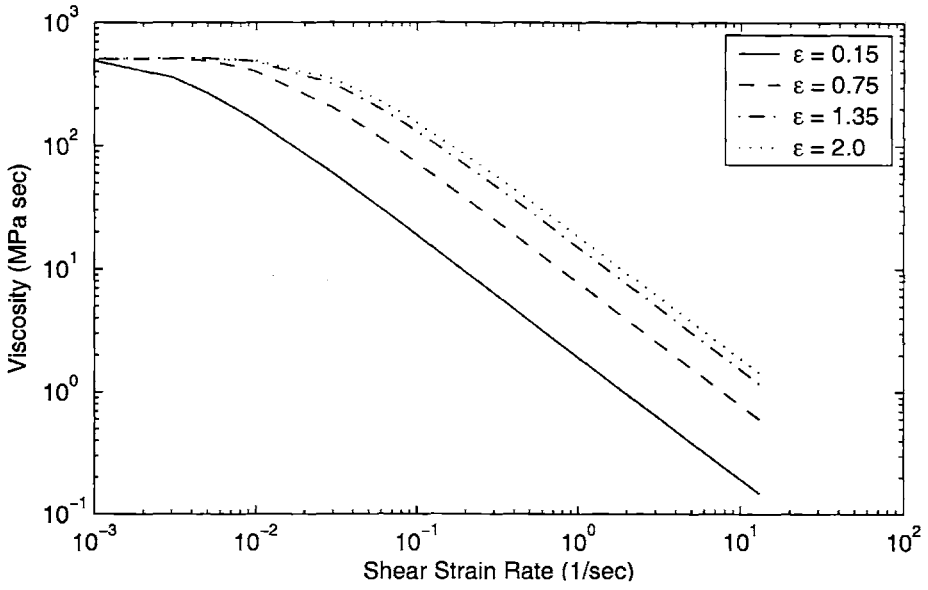

Figure 4-109: Log viscosity versus log strain rate curves from Doi-Edwards model

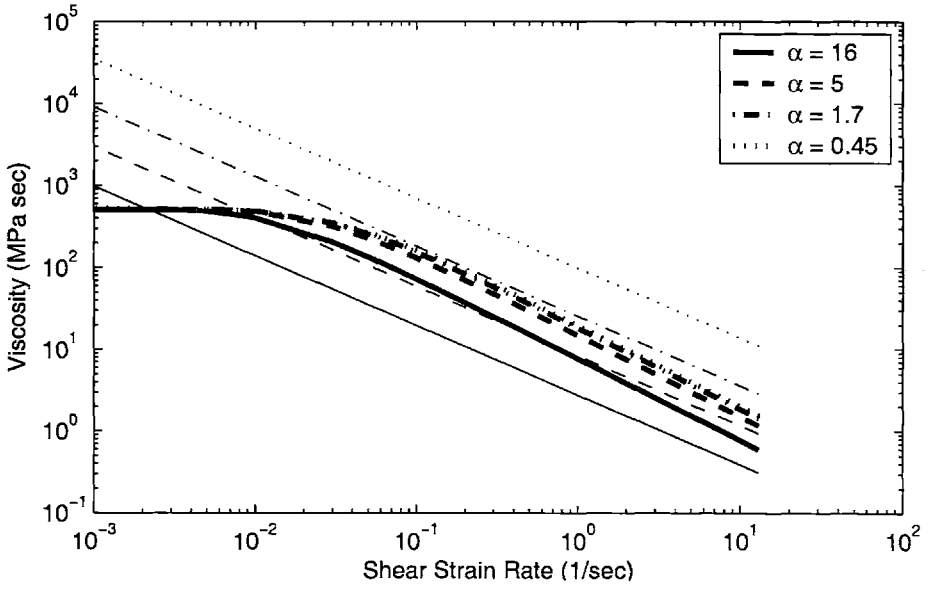

Figure 4-110: Log viscosity versus log strain rate curves from Doi-Edwards Model, curves plotted at constant value of the orientation parameter, α (in radians), compared with the model from section 4.5.2 (thick lines are the Doi-Edwards model, thin lines are the proposed model)

to be independent of rate and temperature, molecular relaxation ceases.

The model is very successful at capturing the trends observed in the experimental data of Chapter 2. Improvements to previous models came primarily in the implementation of the molecular relaxation model. In order to capture the strain state dependence of the material behavior, a new orientation parameter was developed. Not only was this approach successful in capturing the behavior of the material in both plane strain and uniaxial compression, but it also provided a convenient measure for flow cessation at large deformations. Previous models (Adams et al. 2000; Boyce et al. 2000) identified the need to incorporate flow cessation in the model in order to capture large strain hardening in PET. This was attributed to the onset of strain-induced crystallization. The same cessation is needed in order to capture stress-strain trends in PETG, where it is known that crystallization does not occur. This suggests that the cessation of molecular relaxation is due to orientation of the chains, and not solely to strain-induced crystallization. The same previous models used a critical value of network stretch to identify the point at which molecular relaxation would cease; this value was found to depend on rate and temperature. Using the newly-defined orientation angle parameter, molecular relaxation is found to cease at a value of 0.05 radians, a value which is independent of rate and independent of temperature.

This new molecular relaxation model is expressed in a form which can be easily compared to other models from the field of non-Newtonian fluid mechanics. It is found to give good agreement with the model of Doi and Edwards (1978, 1980), in terms of the slope of the power-law region of the curve, provided the correct constants are used in the Doi-Edwards model. A major discrepancy exists between the models in terms of the shift in the viscosity-strain rate curves with increasing strain (decreasing α_{min}). The stress (viscosity) in the Doi-Edwards model levels off as strain level increases, in sharp contrast to the actual material behavior. It is suggested that a polymer viscosity model which includes chain stretching may be able to better capture the trends observed in the experimental data. This will be an interesting subject for future work.

Chapter 5

Constitutive Model applied to PET

5.1 Review of the Model

We begin by summarizing the final model obtained for PETG, which will be compared with data for PET.

The constitutive response is interpreted as two mechanisms which resist deformation in the presence of an applied load: a resistance due to intermolecular forces and a network resistance due to molecular stretching and orientation. This is shown schematically in figure 5-1 with the two distinct resistances represented as A and B.

Resistance A arises due to the intermolecular resistance between neighboring polymer segments. This gives the material its initial stiffness and results in a finite stress at which the polymer will flow, termed the flow stress. In resistance B, network stretching and orientation of the polymer chains causes the polymer to stiffen and strain harden at large strains. The nonlinear dashpot allows for molecular relaxation at higher temperatures and lower strain rates. The two resistances are modeled as being in parallel, so the deformation gradient in each network is equal to the total deformation gradient,

$$\mathbf{F}_A = \mathbf{F}_B = \mathbf{F} \tag{5.1}$$

The descriptions of the intermolecular (A) and intramolecular (B) resistances are summarized below.

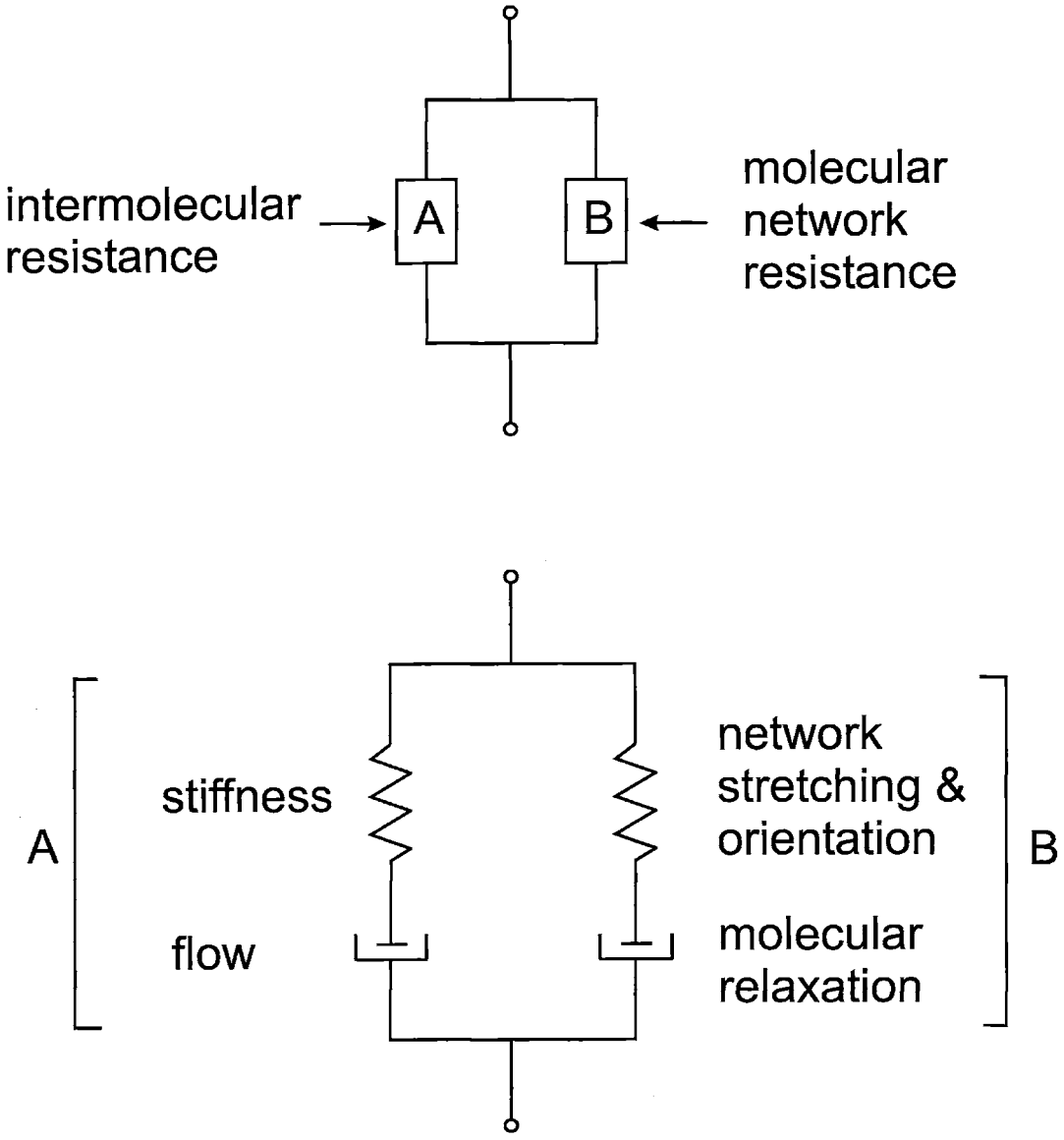

Figure 5-1: Schematic representation of the constitutive model

5.1.1 Resistance A: Intermolecular Interactions

The deformation gradient of resistance A is decomposed into elastic and plastic components in a multiplicative manner

$$\mathbf{F}_A = \mathbf{F}_A^e \mathbf{F}_A^p \tag{5.2}$$

and is then decomposed into stretch and rotation components

$$\mathbf{F}_A^e = \mathbf{V}_A^e \mathbf{R}_A^e \tag{5.3}$$

$$\mathbf{F}_A^p = \mathbf{V}_A^p \mathbf{R}_A^p \tag{5.4}$$

The rate kinematics are described by the velocity gradient, $\mathbf{L}_A$

$$\mathbf{L}_A = \dot{\mathbf{F}}_A \mathbf{F}_A^{-1} \tag{5.5}$$

By substitution of the elastic and plastic contributions to the deformation gradient this becomes

$$\mathbf{L}_A = \dot{\mathbf{F}}_A^e \mathbf{F}_A^{e-1} + \mathbf{F}_A^e \dot{\mathbf{F}}_A^p \mathbf{F}_A^{p-1} \mathbf{F}_A^{e-1} = \mathbf{L}_A^e + \tilde{\mathbf{L}}_A^p \tag{5.6}$$

where $\tilde{\mathbf{L}}_A^p = \tilde{\mathbf{D}}_A^p + \tilde{\mathbf{W}}_A^p$. The representation is made unique by prescribing the spin to be zero: $\tilde{\mathbf{W}}_A^p = 0$.

The rate of stretching is constitutively described by

$$\tilde{\mathbf{D}}_A^p = \dot{\gamma}_A^p \mathbf{N}_A \tag{5.7}$$

$\mathbf{N}_A$ is the normalized deviatoric stress in resistance A

$$\mathbf{N}_A = \frac{1}{\sqrt{2}\tau_A} \mathbf{T}'_A \tag{5.8}$$

$$\tau_A = \left[\frac{1}{2} \mathbf{T}'_A \mathbf{T}'_A \right]^{1/2} \tag{5.9}$$

$\mathbf{T}_A$ is related to the elastic deformation gradient by the constitutive relation

$$\mathbf{T}_A = \frac{1}{J_A}\mathscr{L}^e[\ln \mathbf{V}_A^e] \tag{5.10}$$

where $J_A = \det \mathbf{F}_A^e$ is the volume change, $\mathscr{L}^e$ is the fourth order tensor of elastic constants, and $\ln \mathbf{V}_A^e$ is the Hencky strain. The plastic strain rate, $\dot{\gamma}_A^p$, is assumed to follow a thermally activated process

$$\dot{\gamma}_A^p = \dot{\gamma}_{0A} \exp\left[-\frac{\Delta G(1-\tau_A/s)}{k\theta}\right] \tag{5.11}$$

where $\dot{\gamma}_{0A}$ is the pre-exponential factor, ΔG is the activation energy which must be overcome for flow to begin, s is the shear resistance, taken to be $.15\mu$ (μ is the shear modulus), k is Boltzmann's constant, and θ is the absolute temperature.

Equations 5.1 to 5.11 complete the constitutive prescription for resistance A.

5.1.2 Resistance B: Network Interactions

Two mechanisms are involved in the deformation of resistance B: first, the stretching and orientation of the polymer chain network and second, molecular relaxation. Resistance B can be thought of as a non-linear spring in series with a viscous element (see figure 5-1). As such, the deformation of this element can also be multiplicatively decomposed into a network and flow portion:

$$\mathbf{F}_B = \mathbf{F}_B^N \mathbf{F}_B^F \tag{5.12}$$

The velocity gradient is then

$$\mathbf{L}_B = \dot{\mathbf{F}}_B \mathbf{F}_B^{-1} \tag{5.13}$$

$$\mathbf{L}_B = \dot{\mathbf{F}}_B^N \mathbf{F}_B^{N-1} + \mathbf{F}_B^N \dot{\mathbf{F}}_B^F \mathbf{F}_B^{F-1} \mathbf{F}_B^{N-1} = \mathbf{L}_B^N + \tilde{\mathbf{L}}_B^F \tag{5.14}$$

Again, $\tilde{\mathbf{L}}_B^F = \tilde{\mathbf{D}}_B^F + \tilde{\mathbf{W}}_B^F$ is made unique by setting the spin to zero, $\tilde{\mathbf{W}}_B^F = 0$.

The Arruda-Boyce eight-chain rubber elasticity model (1993b, 1993a) is used to prescribe the stress arising from the network orientation of the polymer. The stretch

of each chain in the network is given by an effective chain stretch, or the root-mean square of the distortional applied stretch: $\bar{\lambda}_N = [\frac{1}{3} tr(\bar{\mathbf{B}}^N)]^{1/2}$, where $\bar{\mathbf{B}}^N = \bar{\mathbf{F}}_B^N \bar{\mathbf{F}}_B^{NT}$, $\bar{\mathbf{F}}_B^N = (J_B)^{-1/3} \mathbf{F}_B^N$, and $J_B = \det \mathbf{F}_B^N$. The relationship between the chain stretch and the network stress is then

$$\mathbf{T}_B = \frac{1}{J_B} \frac{\nu k\theta}{3} \frac{\sqrt{N}}{\bar{\lambda}_N} \mathscr{L}^{-1} \left[\frac{\bar{\lambda}_N}{\sqrt{N}} \right] [\bar{\mathbf{B}}^N - (\bar{\lambda}_N)^2 \mathbf{I}] \tag{5.15}$$

The parameters in this expression are as follows: ν is the chain density, N is the number of rigid links between entanglements, and $\nu k\theta$ is a rubbery modulus, which is proportional to the initial hardening modulus of the strain hardening curve, or the initial slope of the stress-strain curve at the onset of flow, before much hardening has occurred. $\mathscr{L}^{-1}$ is the inverse Langevin function given by $\mathscr{L}(\beta) = \coth(\beta) - (1/\beta)$. This derives from a non-Gaussian probability function which accounts for the fact that the chains have a finite extensibility. $\mathscr{L}^{-1}[\bar{\lambda}_N/\sqrt{N}]$ provides the functionality that as $\bar{\lambda}_N$ approaches $\sqrt{N}$, the stress rises dramatically.

The rate of molecular relaxation is given by

$$\tilde{\mathbf{D}}_B^F = \dot{\gamma}_B^F \mathbf{N}_B \tag{5.16}$$

where $\mathbf{N}_B$ is

$$\mathbf{N}_B = \frac{1}{\sqrt{2}\tau_B} \mathbf{T}'_B \tag{5.17}$$

$$\tau_B = \left[\frac{1}{2} \mathbf{T}'_B \mathbf{T}'_B \right]^{1/2} \tag{5.18}$$

and $\mathbf{T}_B$ is prescribed using the Arruda-Boyce model. The only remaining unknown is the rate of relaxation, $\dot{\gamma}_B^F$. The assumed mechanism is chain reptation, the physical picture being one of polymer chains sliding through tube-like paths created by the entangled chains around them. The model used is that which was developed in section 4.5.2:

$$\dot{\gamma}_B^F = \left(\frac{\frac{\alpha_{min}}{\alpha_c} - 1}{\frac{\alpha_0}{\alpha_c} - 1} \right) C \left(\frac{\tau_B}{\nu k\theta} \right)^{1/n} \tag{5.19}$$

$$C = h\left(\frac{\alpha_{min}}{\alpha_c}\right)^{1/n} \tag{5.20}$$

where the relaxation temperature dependence is captured by an exponential expression for h

$$h = D\exp\left(-\frac{Q}{R\theta}\right) \tag{5.21}$$

Equations 5.1 and 5.12 through 5.21 describe the constitutive behavior of resistance B.

The total stress acting on the system is the sum of the stress in the two resistances

$$\mathbf{T} = \mathbf{T}_A + \mathbf{T}_B \tag{5.22}$$

5.2 Model Compared to PET Using PETG Material Constants

To begin to understand the differences between the constitutive behavior of PET and PETG, we superimpose the model previously obtained and fit to PETG onto the data for PET. This is shown in Figures 5-2 to 5-8. Error values for these curve fits are shown in Table 5.1 and are graphically represented in figures 5-9 and 5-10. It can be seen that overall good agreement is obtained, with no modification to the PETG material constants. By looking at figure 5-9 it is clear that the error becomes worse as the temperature increases. Also, by examining figures 5-3, 5-4, and 5-5, it appears that it is the temperature-dependence of molecular relaxation which is not being captured with the current material parameters. In the next section, the corresponding material constants are adjusted to obtain a better fit to the PET data. The strain state dependence of PET is fairly well captured, with the exception of the behavior in plane strain compression at very large strains. As the stress at this temperature rises very dramatically at large strains, it is suggested that strain-induced crystallization may be playing a role at this temperature in plane strain compression.

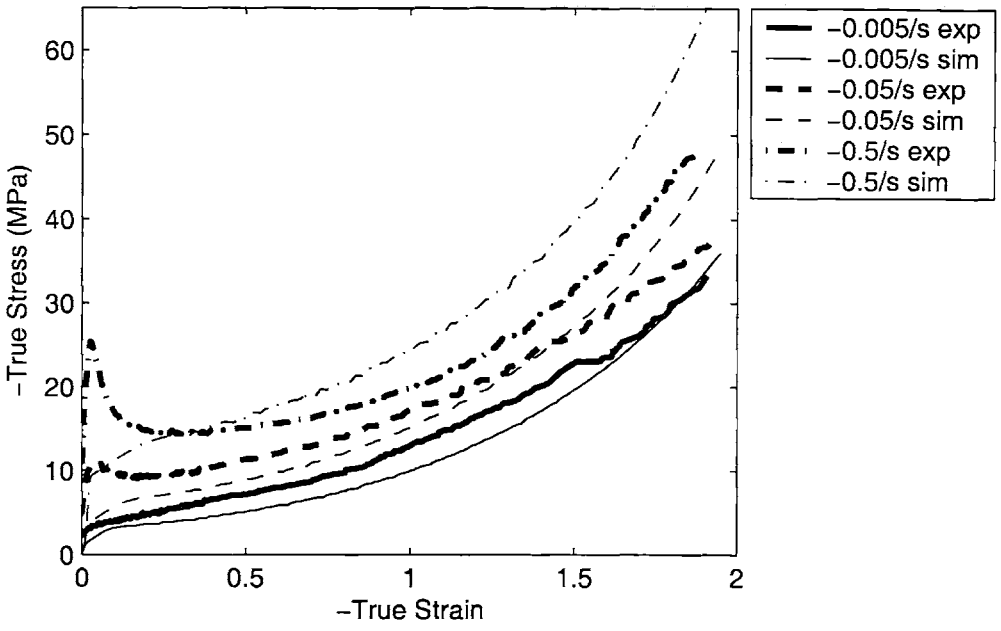

Figure 5-2: PET Uniaxial compression, comparing simulation results with experimental data, Temperature = 80 ° C

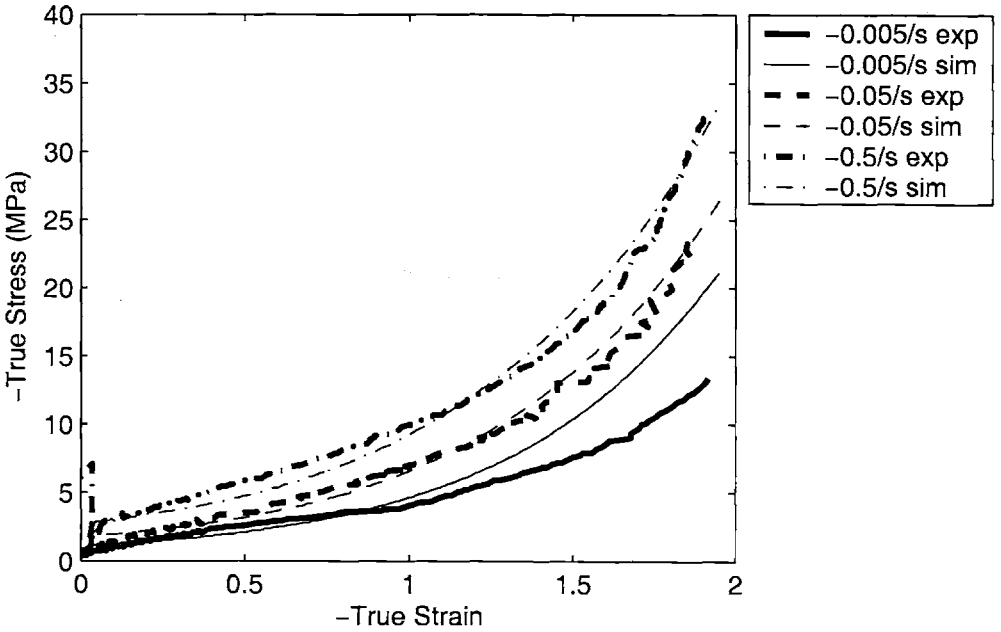

Figure 5-3: PET Uniaxial compression, comparing simulation results with experimental data, Temperature = 90 ° C

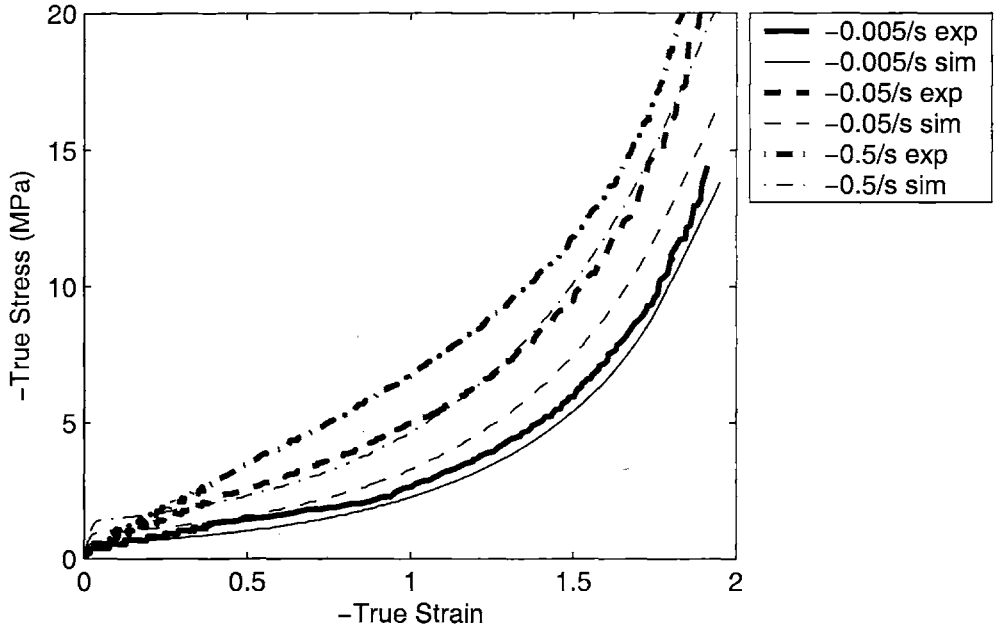

Figure 5-4: PET Uniaxial compression, comparing simulation results with experimental data, Temperature = 100 ° C

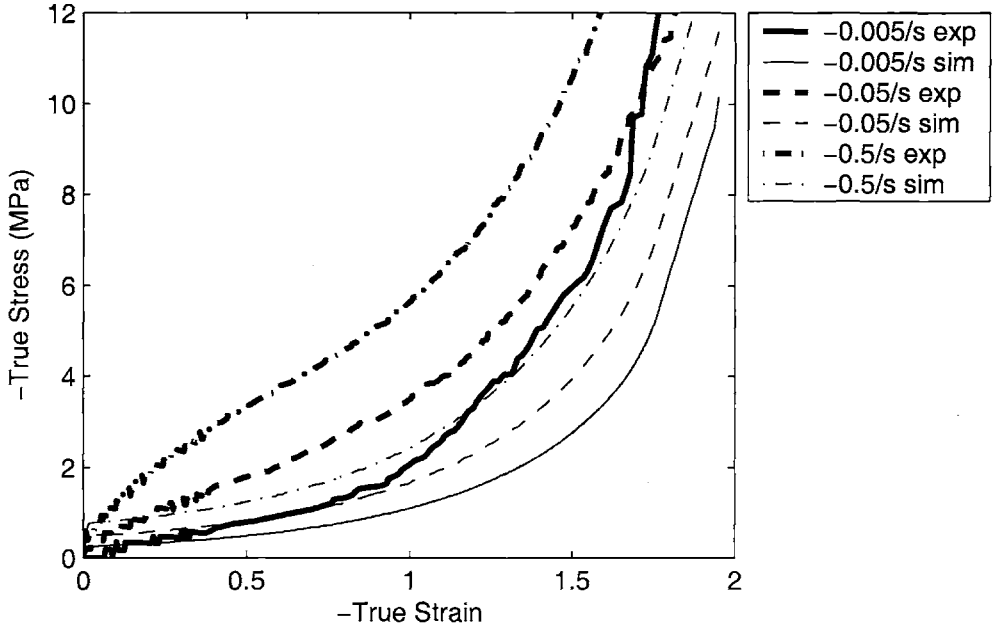

Figure 5-5: PET Uniaxial compression, comparing simulation results with experimental data, Temperature = 110 ° C

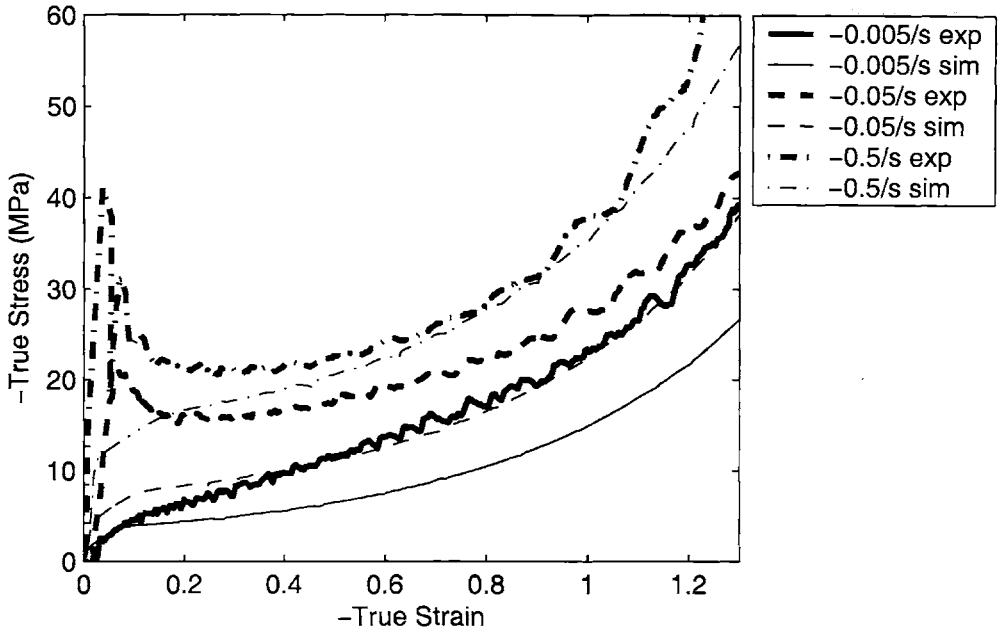

Figure 5-6: PET Plane strain compression, comparing simulation results with experimental data, Temperature = 80 ° C

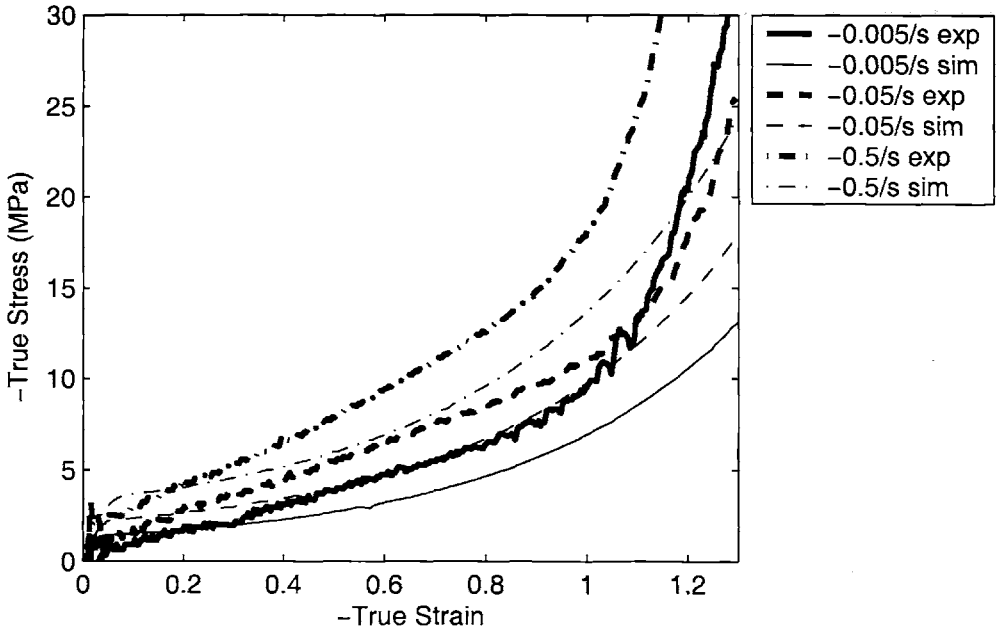

Figure 5-7: PET Plane strain compression, comparing simulation results with experimental data, Temperature = 90 ° C

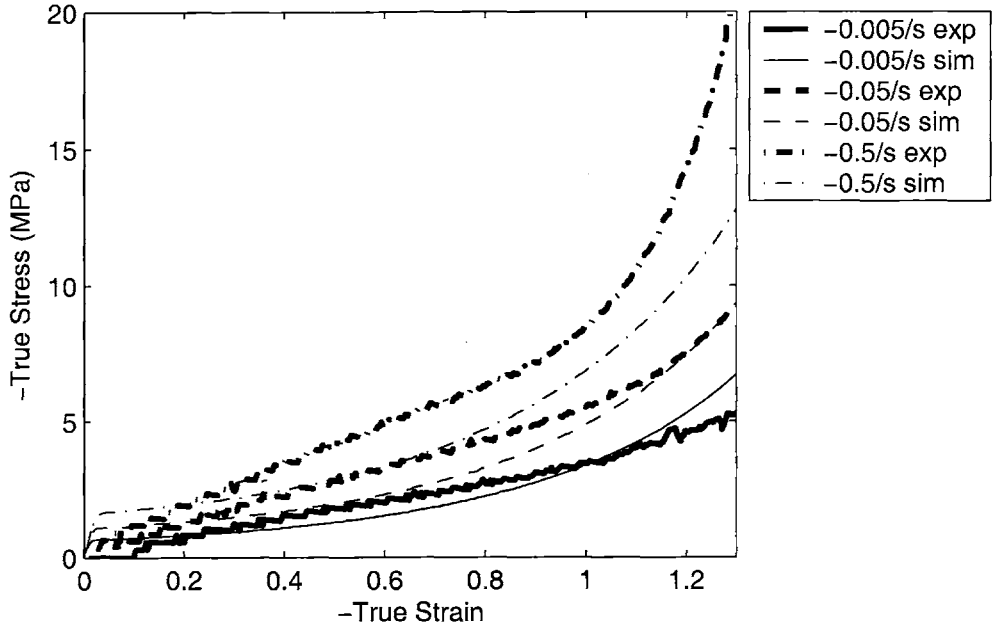

Figure 5-8: PET Plane strain compression, comparing simulation results with experimental data, Temperature = 100 ° C

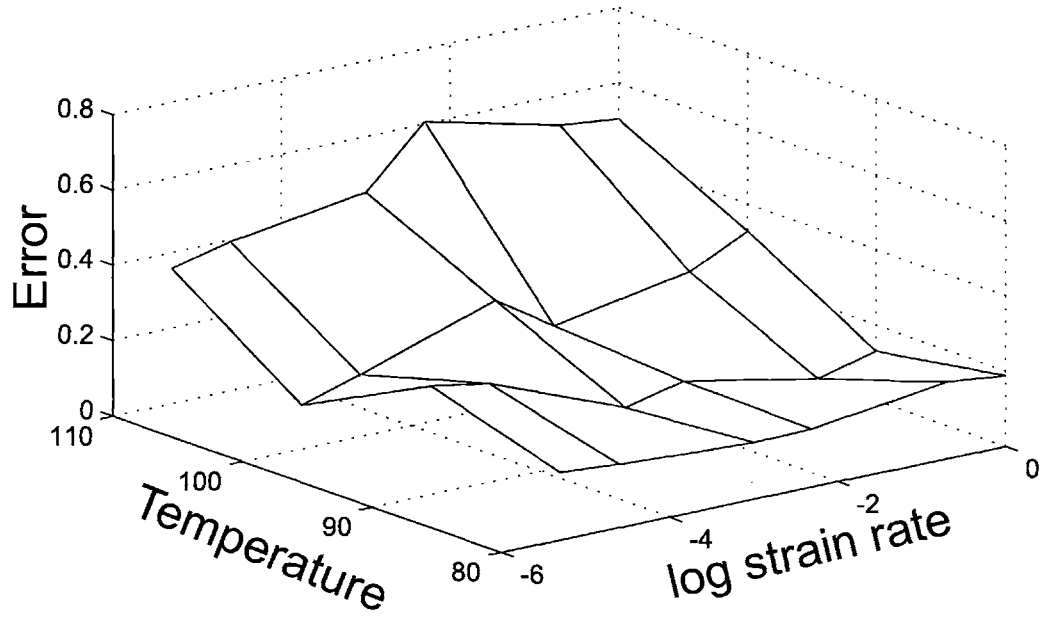

Figure 5-9: Uniaxial compression error values for PET using PETG constants

Table 5.1: Error values for uniaxial and plane strain compression simulations, PET data with PETG material constants

Strain State	Temperature	Strain Rate	$\bar{y}$, full range	$\bar{y}$, up to $\varepsilon = 1.0$
Uniaxial	80 ° C	-0.005/sec	.1800	.2540
Uniaxial	80 ° C	-0.05/sec	.1512	.2085
Uniaxial	80 ° C	-0.5/sec	.2033	.1517
Uniaxial	90 ° C	-0.005/sec	.2878	.1309
Uniaxial	90 ° C	-0.05/sec	.1219	.1013
Uniaxial	90 ° C	-0.5/sec	.0892	.1253
Uniaxial	100 ° C	-0.005/sec	.1170	.1754
Uniaxial	100 ° C	-0.05/sec	.2840	.3272
Uniaxial	100 ° C	-0.5/sec	.2522	.3141
Uniaxial	110 ° C	-0.005/sec	.3579	.3365
Uniaxial	110 ° C	-0.05/sec	.4511	.4740
Uniaxial	110 ° C	-0.5/sec	.5201	.5544
Plane Strain	80 ° C	-0.005/sec	.3604	.3680
Plane Strain	80 ° C	-0.05/sec	.3220	.3690
Plane Strain	80 ° C	-0.5/sec	.1234	.1305
Plane Strain	90 ° C	-0.005/sec	.3211	.2933
Plane Strain	90 ° C	-0.05/sec	.2087	.2319
Plane Strain	90 ° C	-0.5/sec	.2464	.2088
Plane Strain	100 ° C	-0.005/sec	.1850	.2285
Plane Strain	100 ° C	-0.05/sec	.2530	.3312
Plane Strain	100 ° C	-0.5/sec	.2733	.2800

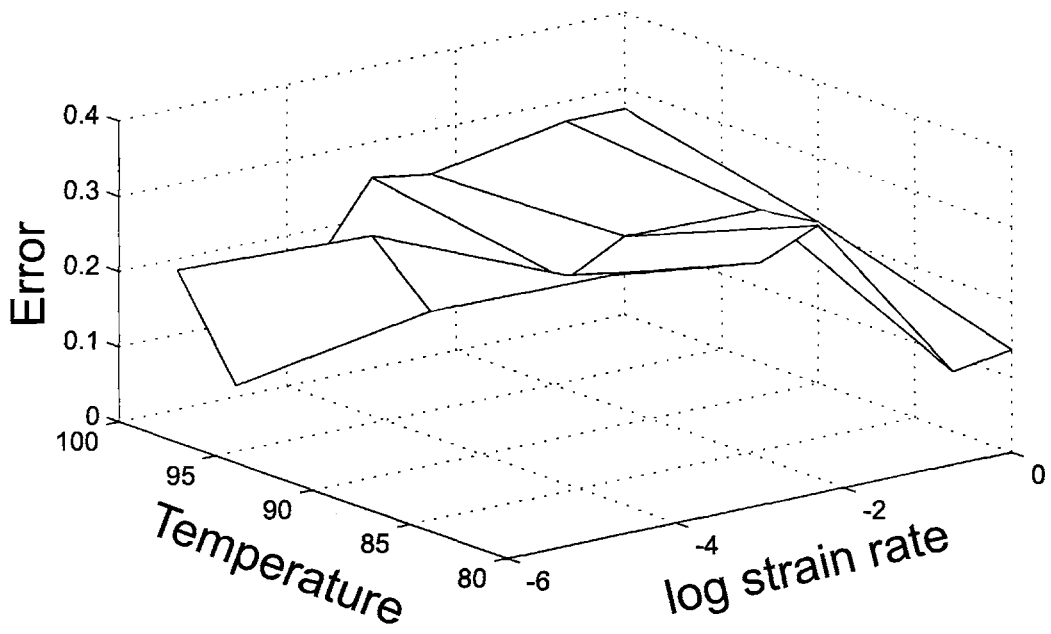

Figure 5-10: Plane strain compression error values for PET using PETG constants

5.3 Material Constants Fit to PET

The material constants are next adjusted to better capture the behavior of PET, as listed in table 5.2. Those constants which have been modified are indicated in boldface. The results of modifying the constants is shown in Figures 5-11 to 5-15. Error values for these curve fits are shown in Table 5.2 and are represented graphically in figures 5-16 to 5-17.

5.4 Results and Discussion

The model is able to capture many of the features of the PET data, including the initial modulus, rollover to flow, the gradual strain hardening, and the start of dramatic strain hardening at large strains. It is especially able to capture the dependence on strain rate, temperature and strain state. This is significant in that it indicates that strain-induced crystallization must play a minor role, if any, in the deformation behavior of PET during compressive loading. One area where crystallization, or at the least,

Table 5.2: Material constants for PETG and PET

Material Property	Symbol	PETG Value	PET Value	Units
Glassy Modulus	G_{gl}	455	455	MPa
Rubbery Modulus	G_r	15	15	MPa
Temperature Shift	$\Delta\theta$	30	30	K
Transition Slope	X_g	-2.0×10^{-5}	-2.0×10^{-5}	MPa K^{-1}
First Rate Shift Factor	a	3	3	K
Second Rate Shift Factor	b	1.226	1.226	K
Bulk Modulus	B	1.25	1.25	GPa
Pre-exponential Factor	$\dot{\gamma}_{0A}$	2.0×10^{12}	2.0×10^{12}	sec^{-1}
Activation Energy	ΔG	1.8×10^{-19}	1.8×10^{-19}	J
Rubbery Orientaion Modulus	C_R	8.5	8.5	MPa
Entanglement Density	N	7.0	7.0	
Temperature Coefficient	**D**	$\mathbf{1.25\times10^{80}}$	$\mathbf{4.147\times10^{36}}$	$\mathbf{sec^{-1}}$
Second Temperature Parameter	**Q/R**	$\mathbf{6.823\times10^{4}}$	$\mathbf{3.183\times10^{4}}$	**K**
Power-law Exponent	n	6.67	6.67	
Cutoff Orientation	α_c	0.05	0.05	

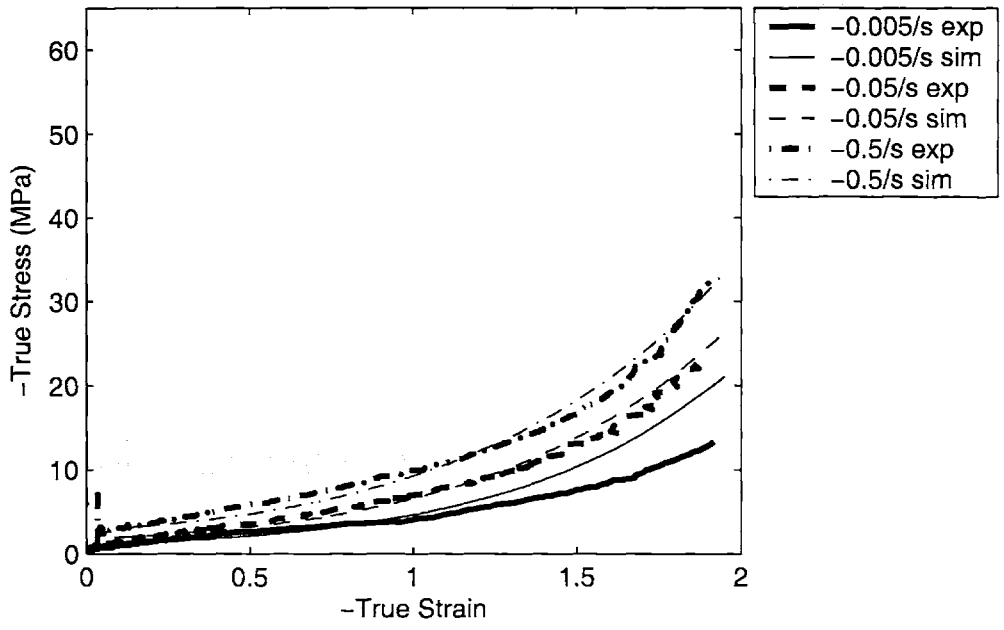

Figure 5-11: PET Uniaxial compression, comparing simulation results with experimental data, Temperature = 90 ° C

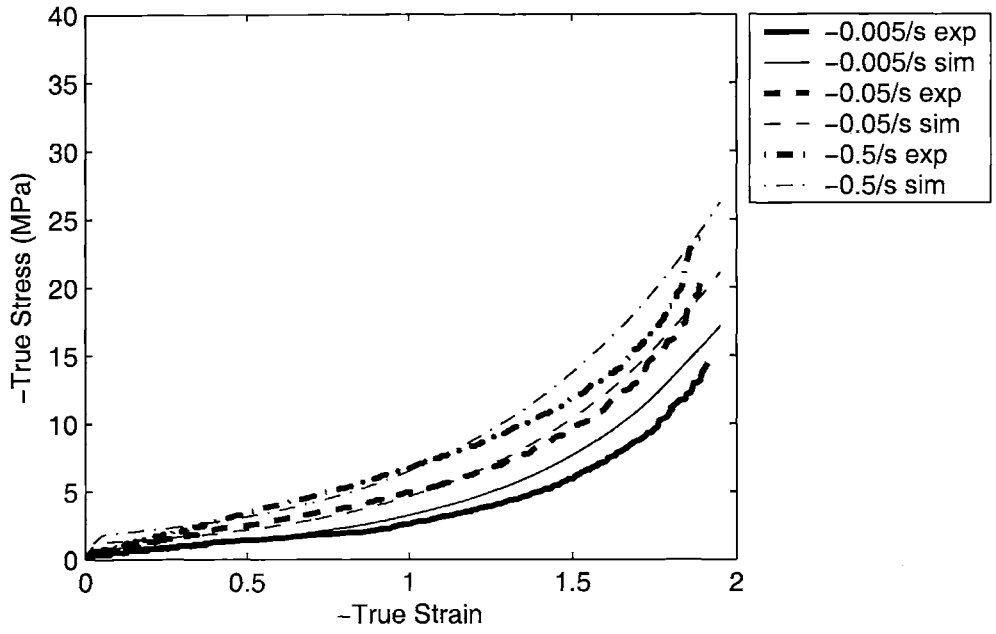

Figure 5-12: PET Uniaxial compression, comparing simulation results with experimental data, Temperature = 100 ° C

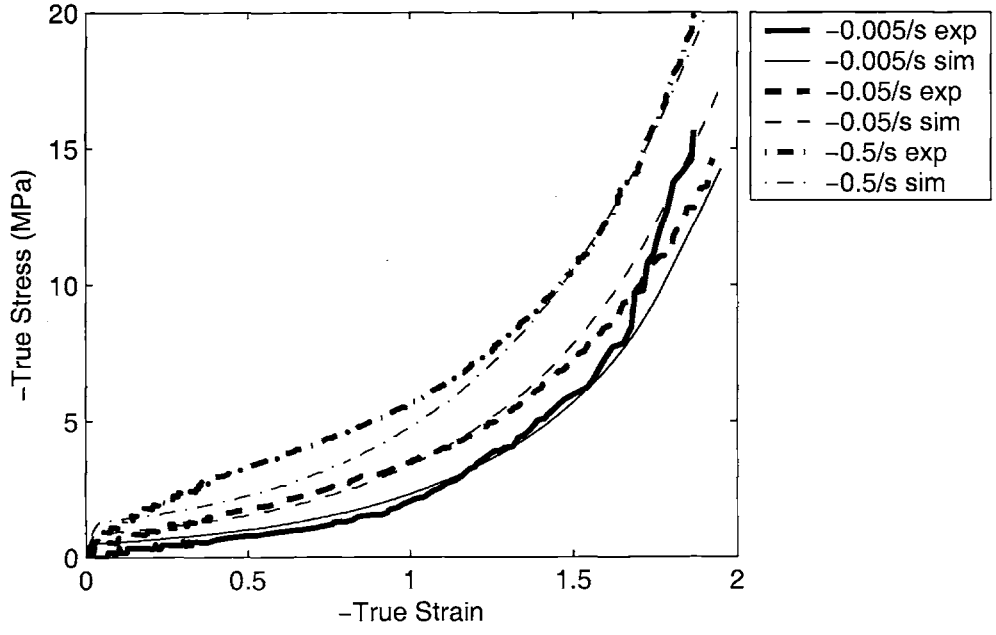

Figure 5-13: PET Uniaxial compression, comparing simulation results with experimental data, Temperature = 110 ° C

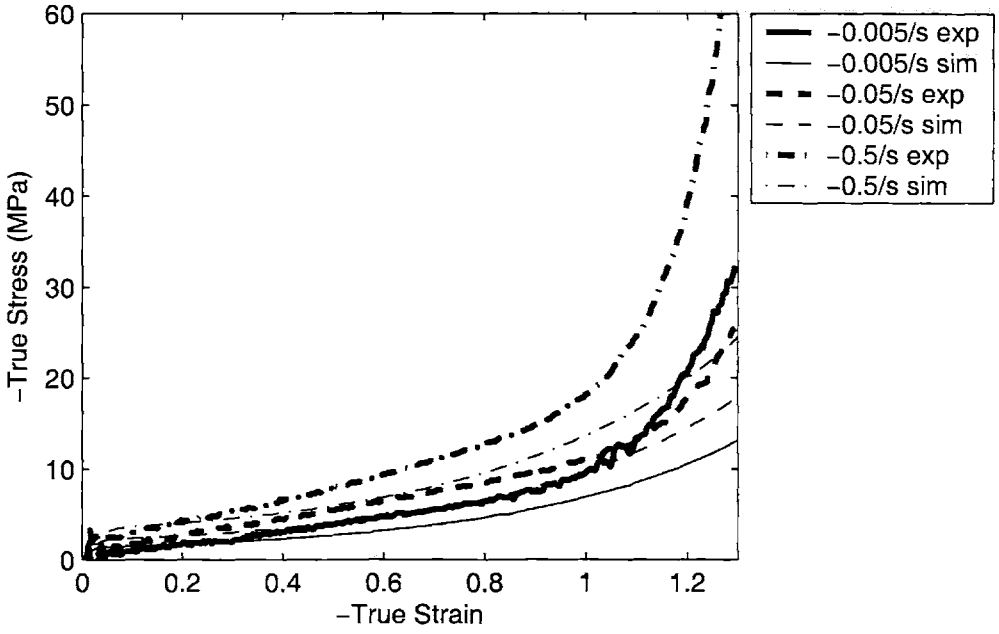

Figure 5-14: PET Plane strain compression, comparing simulation results with experimental data, Temperature = 90 ° C

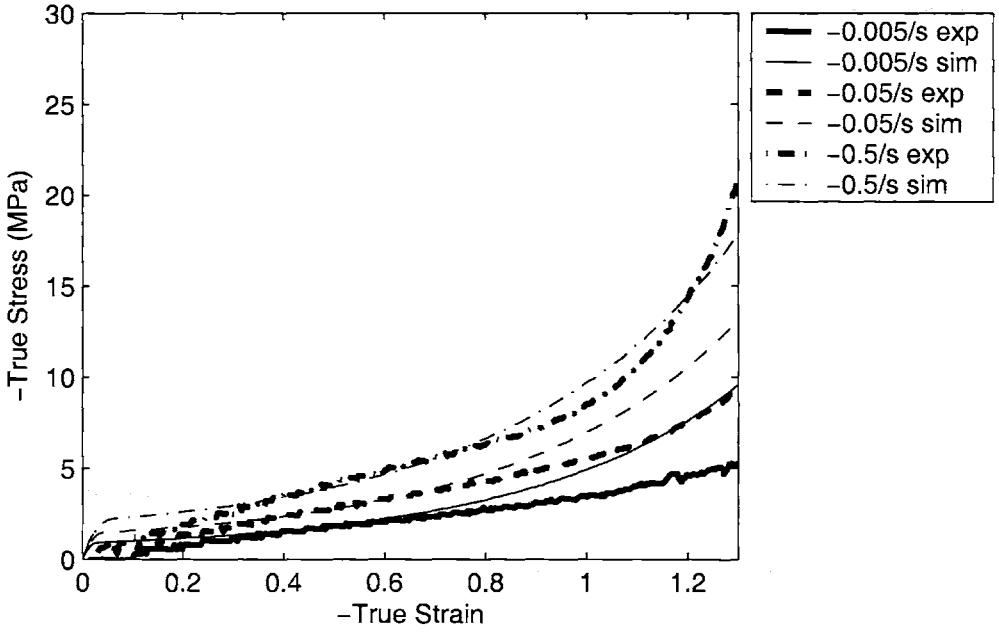

Figure 5-15: PET Plane strain compression, comparing simulation resultswith experimental data, Temperature = 100 ° C

Table 5.3: Error values for uniaxial and plane strain compression simulations PET data with fit constants

Strain State	Temperature	Strain Rate	$\bar{y}$, full range	$\bar{y}$, up to $\varepsilon = 1.0$
Uniaxial	90 ° C	-0.005/sec	.2837	.1312
Uniaxial	90 ° C	-0.05/sec	.1216	.1015
Uniaxial	90 ° C	-0.5/sec	.0891	.1258
Uniaxial	100 ° C	-0.005/sec	.2823	.2371
Uniaxial	100 ° C	-0.05/sec	.1210	.1825
Uniaxial	100 ° C	-0.5/sec	.1720	.2264
Uniaxial	110 ° C	-0.005/sec	.4525	.6382
Uniaxial	110 ° C	-0.05/sec	.1152	.1399
Uniaxial	110 ° C	-0.5/sec	.1495	.2438
Plane Strain	90 ° C	-0.005/sec	.3216	.2937
Plane Strain	90 ° C	-0.05/sec	.2093	.2324
Plane Strain	90 ° C	-0.5/sec	.2471	.2095
Plane Strain	100 ° C	-0.005/sec	.3337	.2970
Plane Strain	100 ° C	-0.05/sec	.3137	.3276
Plane Strain	100 ° C	-0.5/sec	.1960	.2234

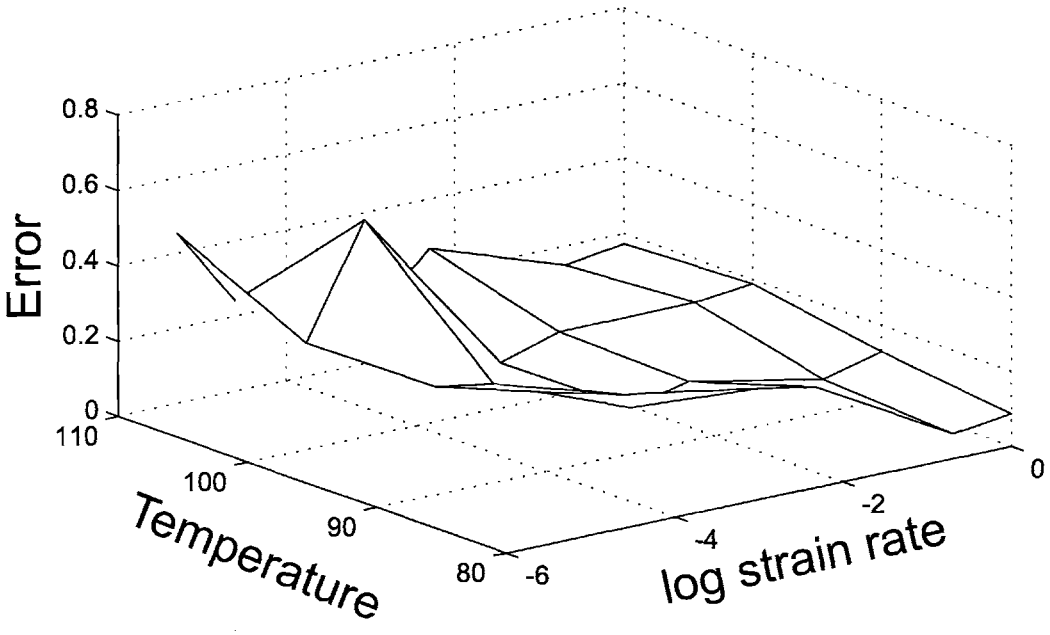

Figure 5-16: PET Uniaxial compression error values using fit constants

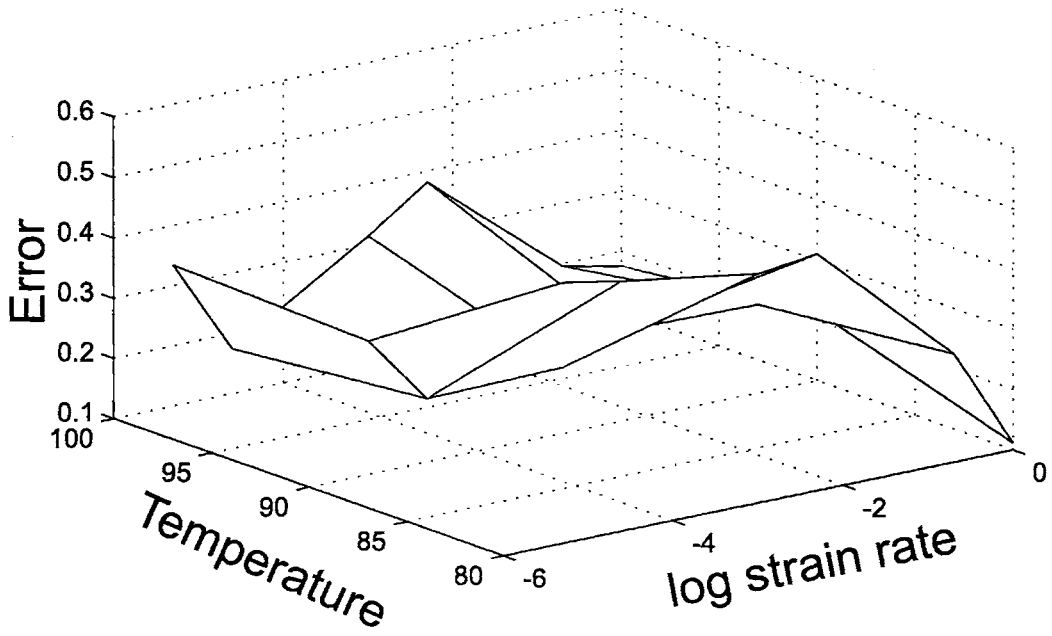

Figure 5-17: PET Plane strain compression error values using fit constants

the development of a highly ordered mesophase, may be occurring in PET, causing a discrepancy at very large strains in plane strain compression. That this discrepancy between the simulation and experimental data would occur only in plane strain compression, and most notably at 90 ° C (see figure 5-11) is due to the highly ordered state the polymer is in in this deformation state and at this temperature. At higher temperatures, molecular relaxation plays a larger role, and in uniaxial compression the molecules are oriented in a plane, but not as preferentially in one direction as in plane strain compression. It is expected that the addition of a crystallization criteria accounting for very large states of orientation in PET could capture this large upturn in stress, which the model is currently unable to capture. For the vast majority of the experimental data considered, however, the model provides very good agreement (see figure 5-16). It should be noted that in a deformation process such as stretch blow molding, the deformation mode is primarily biaxial in nature, corresponding to a deformation state similar to that for uniaxial compression. The good agreement obtained to the uniaxial compression experiments therefore lends confidence to the ability of this model to give insight to reheat stretch blow molding simulations.

Chapter 6

Model Extension Using Anisotropic 8-chain Model

6.1 Difference between Orientation Angle Parameter and Molecular Chain Angle

In section 4.5.2, we developed an orientation angle parameter which was found to be an excellent measure to account for how molecular relaxation, and particularly the cessation of molecular relaxation, depend on strain and strain state. This development was motivated by the construction of the 8-chain model. The orientation angle parameter was taken to be the complement of the angle between one of the 8 'chains' and the most distant principal deformation axis (see figure 6-1, α_{min} is the orientation angle parameter). The orientation angle parameter was then calculated from the principal stretches of the deformation gradient in resistance B, λ_1, λ_2, and λ_3. The principal stretches are computed by performing an eigenvalue decomposition on the stretching portion of $\mathbf{F}_B$, which is denoted by $\mathbf{V}_B$. Equivalently, the principal stretches can be computed by finding the eigenvalues of $\mathbf{V}_B^2 = \mathbf{F}_B\mathbf{F}_B^T = \mathbf{B}_B$, which eigenvalues are the squares of the principal stretches. The orientation angle

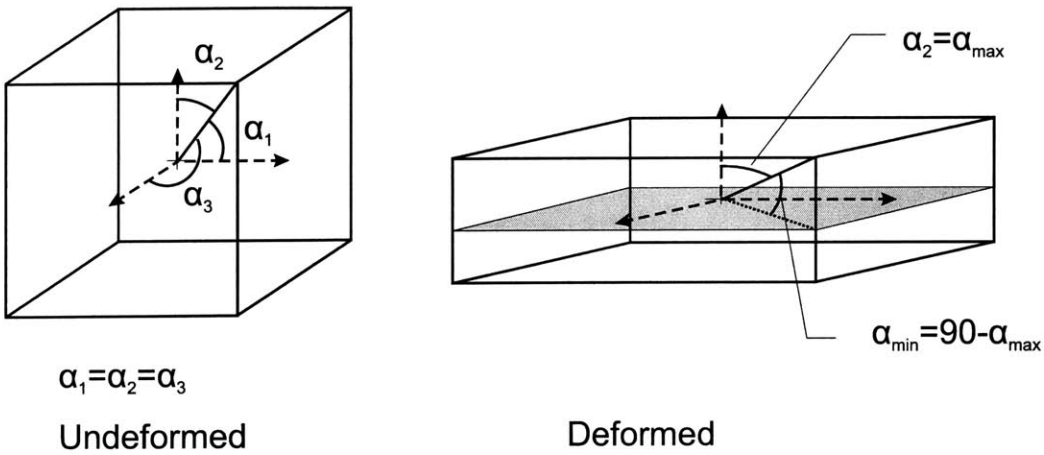

Figure 6-1: Schematic illustrating the orientation angle parameter

parameter, α_{min} is then:

$$\alpha_{min} = \frac{\pi}{2} - \cos^{-1}\left(\frac{\lambda_{min}}{\sqrt{3}\lambda_T}\right) = \frac{\pi}{2} - \cos^{-1}\left(\frac{\lambda_{min}}{\sqrt{\lambda_1^2 + \lambda_2^2 + \lambda_3^2}}\right) \tag{6.1}$$

where λ_{min} is the minimum of the three principal stretches. In the model presented thus far, the elastic-plastic decomposition provides that stress is generated due to elastic deformation. In other words, the only portion of the deformation which goes into deforming the 8-chain model and thus in generating stress via network stretching and orientation is $\mathbf{F}_B^N$. Thus, if one were to calculate the chain angle imposed on the 8-chain model at a particular point in the deformation, it would be decidedly different from the orientation angle parameter calculated above, as the 8-chain model is deformed by $\mathbf{F}_B^N$ whereas the orientation angle parameter is calculated from $\mathbf{F}_B$. This is a subtle point which deserves further elaboration.

Figure 6-2 shows the kinematical description of a general elastic-plastic decomposition. Under the influence of a deformation gradient, $\mathbf{F}$, a body is deformed from its configuration at time t=0, denoted by $\mathcal{B}_0$, to a new configuration at time t, denoted by $\mathcal{B}_t$. We can imagine that if we were to elastically unload the body, by applying an inverse elastic deformation gradient, $\mathbf{F}^{e-1}$, all that would remain would be the plastic deformation, $\mathbf{F}^p$. Thus, $\mathbf{F} = \mathbf{F}^e\mathbf{F}^p$ is the elastic-plastic decomposition.

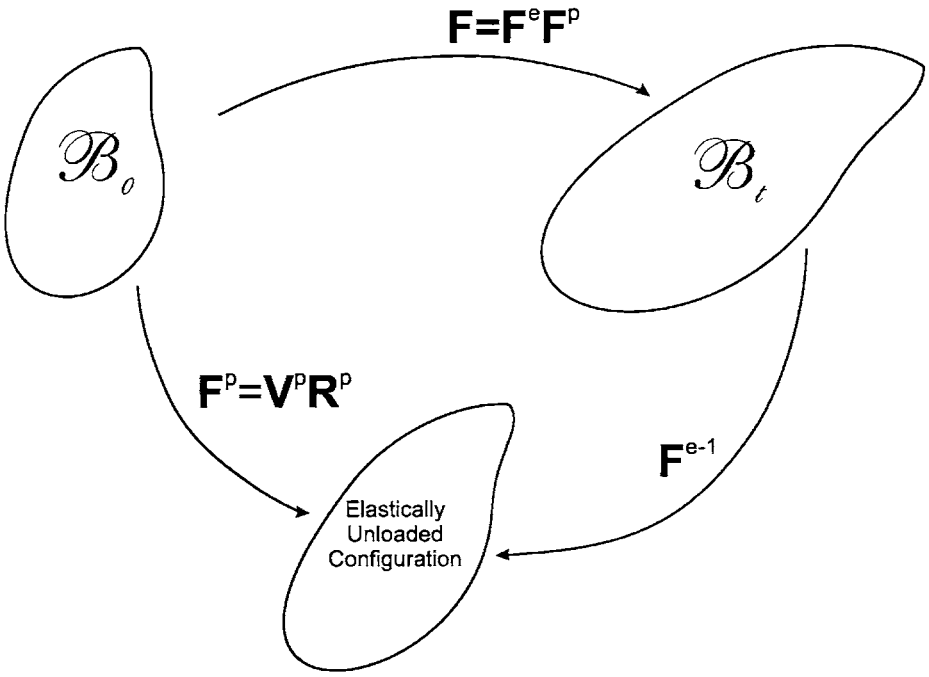

Figure 6-2: Kinematical description of elastic-plastic decomposition

This decomposition is simple to understand for a polycrystalline material, such as a metal. Figure 6-3 illustrates the concept of the combination of elastic and plastic deformation to the underlying crystal lattice. Elastic deformation is the result of lattice deformations (bonds stretching and rotating), and is completely reversible (a). Plastic deformation, on the other hand, is accommodated by dislocation motion, which occurs in the presence of the underlying elastically-stretched lattice. Upon elastic unloading, the lattice stretching is recovered, but the plastic deformation remains (b).

An analagous decomposition was used for the polymeric material in Chapter 4, as is conventional in the literature. The analog is illustrated in figure 6-4. Elastic deformation is accommodated by stretching and orientation of the polymer network (here represented by the 8-chain unit cube) and this stretching is what generates stress in the material. Plastic deformation, on the other hand, does not stretch the network, but is rather a stress-induced, rate-dependent flow, driven by stress but providing no increase in stress. Upon elastic unloading, the network returns to its

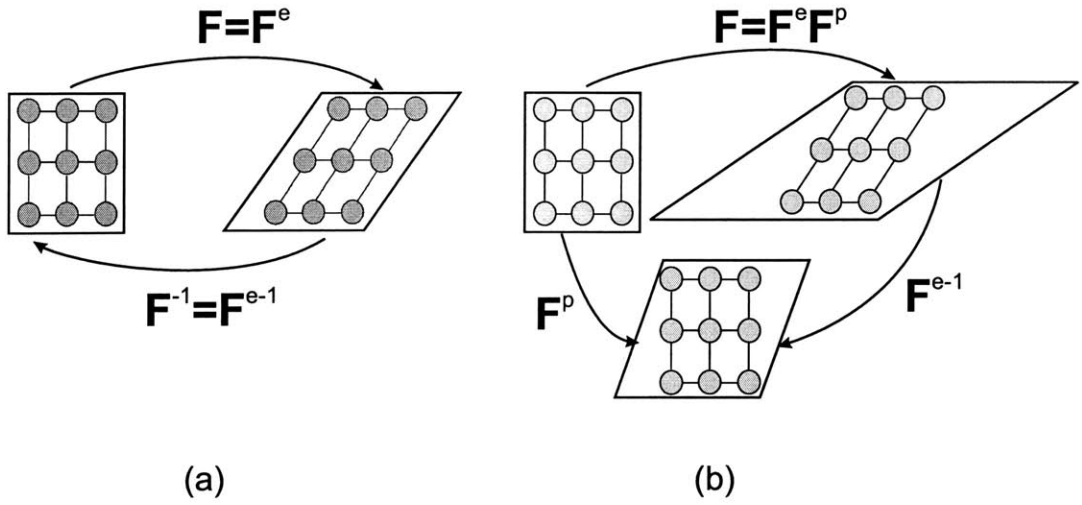

Figure 6-3: Elastic-plastic decomposition for a polycrystalline material

isotropic state and only the plastic deformation is permanent. Thus, the polymer network only undergoes a deformation equal to $\mathbf{F}^e$ (or $\mathbf{F}_B^N$ in our model) and the chain angles calculated from the 8-chain network deformation will also be related to $\mathbf{F}_B^N$.

If we wish to tie the orientation angle parameter mentioned previously to the angle of a chain in the polymer network description, a different modeling approach must be adopted such that the natural state of the polymer is allowed to evolve during plastic deformation. In such an approach, the network model will deform affinely with the macroscopic deformation (thus tieing chain angle to the macroscopic orientation angle parameter), and plastic deformation will serve to evolve the elastically unloaded configuration, such that the stress-free unloaded state will no longer be isotropic. This is illustrated in figure 6-5, where $\mathcal{B}_{sf}$ denotes the stress-free, or elastically unloaded configuration. In such a formulation, the original 8-chain model is no longer useful, as it would give a non-zero stress state for any anisotropic unloaded configuration. We therefore proceed to investigate incorporating an anisotropic 8-chain model into this new model formulation.

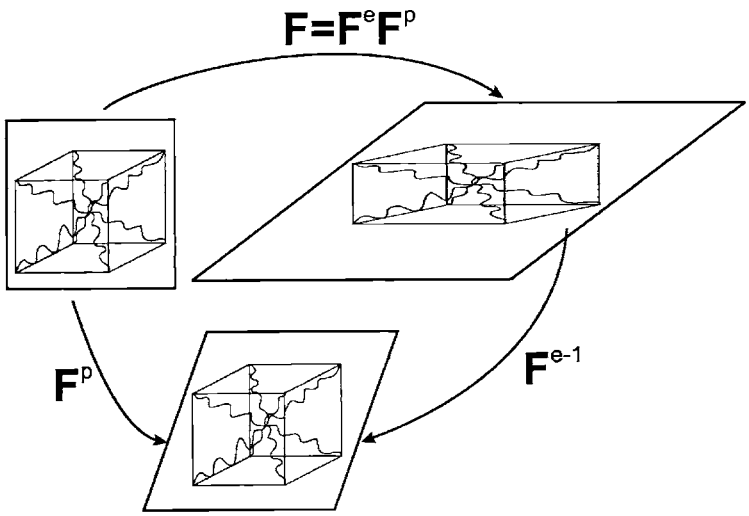

Figure 6-4: Elastic-plastic decomposition for a polymeric material

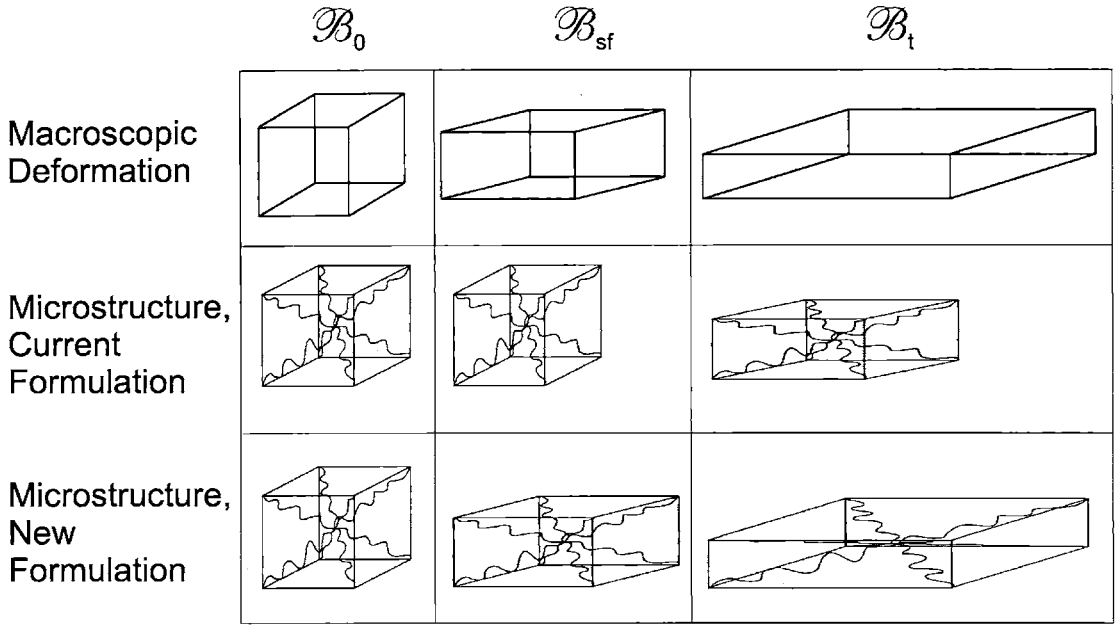

Figure 6-5: Comparing two elastic-plastic decomposition microstructural pictures

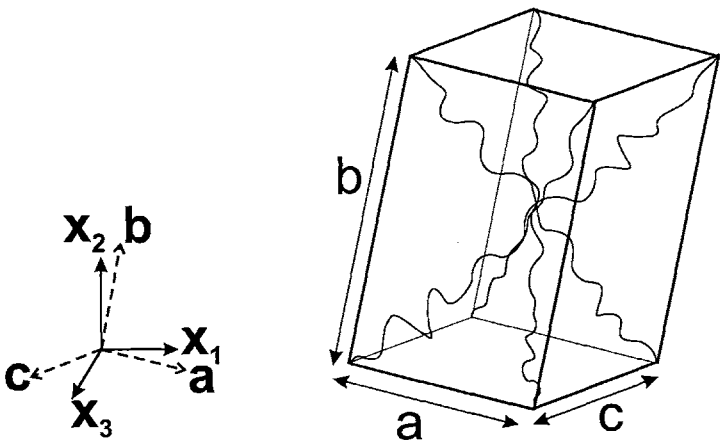

Figure 6-6: Unit cell for the orthotropic model

6.2 Description of the 8-chain Anisotropic Model

The anisotropic constitutive model development follows the details of Bischoff, Arruda, and Grosh (2000). The unit cell is taken to be orthotropic, with dimensions a, b, and c, as shown in figure 6-6. The material axes, **a**, **b**, and **c** are required to be orthogonal, but may be rotated relative to a reference coordinate system, $\mathbf{X_1}$, $\mathbf{X_2}$, $\mathbf{X_3}$. The vector description of each of the 8 chains is given by:

$$\mathbf{P}^{(1)} = -\mathbf{P}^{(5)} = \frac{a}{2}\mathbf{a} + \frac{b}{2}\mathbf{b} + \frac{c}{2}\mathbf{c}$$
$$\mathbf{P}^{(2)} = -\mathbf{P}^{(6)} = \frac{a}{2}\mathbf{a} + \frac{b}{2}\mathbf{b} - \frac{c}{2}\mathbf{c}$$
$$\mathbf{P}^{(3)} = -\mathbf{P}^{(7)} = \frac{a}{2}\mathbf{a} - \frac{b}{2}\mathbf{b} + \frac{c}{2}\mathbf{c}$$
$$\mathbf{P}^{(4)} = -\mathbf{P}^{(8)} = \frac{a}{2}\mathbf{a} - \frac{b}{2}\mathbf{b} - \frac{c}{2}\mathbf{c}$$

And the length of each undeformed chain is:

$$P = \frac{1}{2}\sqrt{a^2 + b^2 + c^2} \tag{6.2}$$

This undeformed chain length is related to the rms length of a chain, so P = $\sqrt{N}$, and N is related to the unit cell dimensions by:

$$\sqrt{N} = \frac{1}{2}\sqrt{a^2 + b^2 + c^2} \tag{6.3}$$

Assuming affine deformation, the lengths, $\rho^{(i)}$, of the deformed chains are given by:

$$\rho^{(i)} = \sqrt{\mathbf{P}^{(i)T} \cdot \mathbf{C} \cdot \mathbf{P}^{(i)}} \tag{6.4}$$

summation over i not assumed. $\mathbf{C} = \mathbf{F}^T\mathbf{F} = 2\mathbf{E} + \mathbf{I}$ is the right Cauchy-Green strain tensor, $\mathbf{I}$ is the identity tensor, and $\mathbf{E}$ is the Lagrangian strain field.

The two components of strain energy which contribute in the deformation of the unit cell are a contribution due to entropy:

$$w_{entropy} = w_0 + 2k\theta N \sum_{i=1}^{4} \left[\frac{\rho^{(i)}}{N} \beta_\rho^{(i)} + \ln \frac{\beta_\rho^{(i)}}{\sinh \beta_\rho^{(i)}} \right] \tag{6.5}$$

and a contribution due to repulsion:

$$w_{repulsion} = \frac{8k\theta\sqrt{N}\beta_P}{a^2 + b^2 + c^2} \ln \lambda_a^{a^2} \lambda_b^{b^2} \lambda_c^{c^2} \tag{6.6}$$

where w_0 is a constant related to the nonzero entropy in the undeformed state, k is Boltzmann's constant, θ is absolute temperature, N is a chain parameter related to crosslink density, $\beta_P = \mathscr{L}^{-1}[P/N]$, and $\beta_\rho^{(i)} = \mathscr{L}^{-1}[\rho^{(i)}/N]$, with $\mathscr{L}(x) = \coth x - 1/x$. Also, $\lambda_a = \sqrt{\mathbf{a}^T \cdot \mathbf{C} \cdot \mathbf{a}}$, $\lambda_b = \sqrt{\mathbf{b}^T \cdot \mathbf{C} \cdot \mathbf{b}}$, and $\lambda_c = \sqrt{\mathbf{c}^T \cdot \mathbf{C} \cdot \mathbf{c}}$, which are the stretches along the principal material axes.

Assuming a chain density of ν and noting that there are eight chains per cell, the strain energy per unit volume is:

$$W(\mathbf{x}) = \frac{\nu}{8}(w_{entropy} + w_{repulsion}) \tag{6.7}$$

An additional term can be added to account for compressibility, but if we assume

incompressibility, the final form of the strain energy function is:

$$W(\mathbf{x}) = W_0 + \frac{\nu k\theta}{4}\left(N\sum_{i=1}^{4}\left[\frac{\rho^{(i)}}{N}\beta_\rho^{(i)} + \ln\frac{\beta_\rho^{(i)}}{\sinh\beta_\rho^{(i)}}\right] - \frac{\beta_P}{\sqrt{N}}\ln\lambda_a^{a^2}\lambda_b^{b^2}\lambda_c^{c^2}\right) \tag{6.8}$$

From this strain energy function, one can calculate the second Piiola-Kirchhoff stress tensor as $\tilde{\mathbf{T}} = \partial W/\partial \mathbf{E}$:

$$\tilde{T}_{jk} = \frac{\nu k\theta}{4}\left[\sum_{i=1}^{4}\frac{P_j^{(i)}P_k^{(i)}}{\rho^{(i)}}\beta_\rho^{(i)} - \frac{\beta_P}{\sqrt{N}}\left(\frac{a^2}{\lambda_a^2}a_j a_k + \frac{b^2}{\lambda_b^2}b_j b_k + \frac{c^2}{\lambda_c^2}c_j c_k\right)\right] \tag{6.9}$$

The details of the differentiation are included in Appendix B. The Cauchy stress can then be calculated as:

$$\mathbf{T} = \frac{1}{J}\mathbf{F}\tilde{\mathbf{T}}\mathbf{F}^T \tag{6.10}$$

where J = det$\mathbf{F}$.

If we consider only triaxial states of deformation in which the material axes are aligned with the coordinate system, the expression for the Cauchy stress becomes:

$$\begin{aligned}
T_{11} &= \frac{\nu k\theta a^2}{4J}\left[\frac{\lambda_1^2\beta_\rho}{\rho} - \frac{\beta_P}{\sqrt{N}}\right] \\
T_{22} &= \frac{\nu k\theta b^2}{4J}\left[\frac{\lambda_2^2\beta_\rho}{\rho} - \frac{\beta_P}{\sqrt{N}}\right] \\
T_{33} &= \frac{\nu k\theta c^2}{4J}\left[\frac{\lambda_3^2\beta_\rho}{\rho} - \frac{\beta_P}{\sqrt{N}}\right] \\
T_{12} &= T_{21} = T_{13} = T_{31} = T_{23} = T_{32} = 0
\end{aligned} \tag{6.11}$$

with λ_1, λ_2, and λ_3 being the components of the deformation gradient:

$$\mathbf{F} = \begin{bmatrix} \lambda_1 & 0 & 0 \\ 0 & \lambda_2 & 0 \\ 0 & 0 & \lambda_3 \end{bmatrix} \tag{6.12}$$

Also, ρ here is defined as $\rho = \sqrt{a^2\lambda_1^2 + b^2\lambda_2^2 + c^2\lambda_3^2}$.

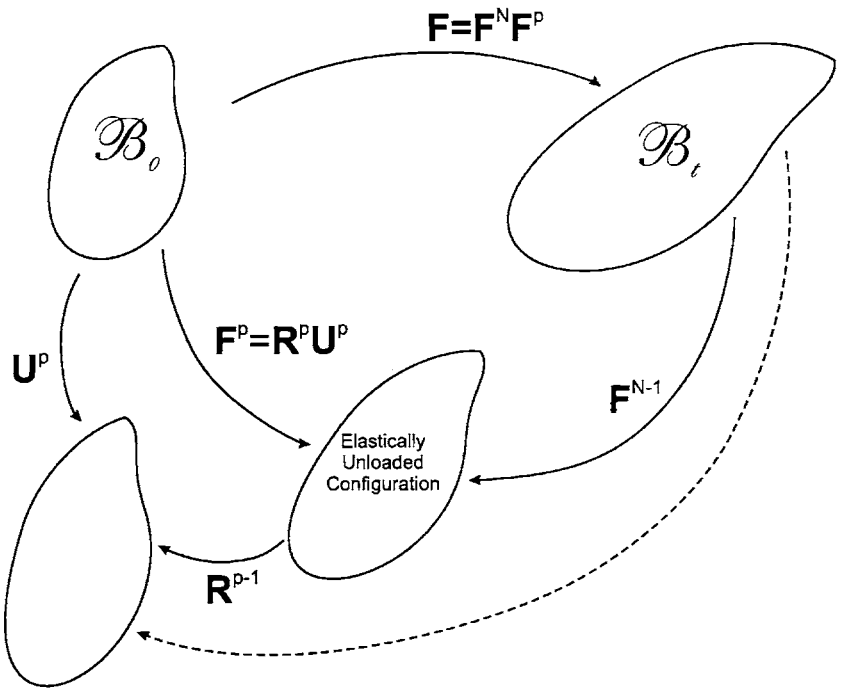

Figure 6-7: Kinematics involved in incorporating the anisotropic model

6.3 Incorporation of the Anisotropic Model in the PETG Model

In order to incorporate the anisotropic model into the model for PETG, we need to calculate the evolving natural state of the polymer. In other words, we need to find the new unit material vectors **a**, **b**, and **c** and the new dimensions of the unit cell, a, b, and c in order to compute the stress. Once these have been obtained, the stress can be calculated from equation 6.11 for triaxial deformation or from equation 6.9 more generally. Note that the network deformation gradient, $\mathbf{F}_B^N$, is used to compute **C** above and λ_1, λ_2, λ_3 would correspond to the diagonal components of $\mathbf{F}_B^N$ in the case of triaxial deformation.

To obtain the new natural state, we return to the kinematics associated with the deformation (see figure 6-7). The deformation of resistance B is multiplicatively

decomposed into a network and flow portion:

$$\mathbf{F}_B = \mathbf{F}_B^N \mathbf{F}_B^F \tag{6.13}$$

The velocity gradient is

$$\mathbf{L}_B = \dot{\mathbf{F}}_B \mathbf{F}_B^{-1} \tag{6.14}$$

$$\mathbf{L}_B = \dot{\mathbf{F}}_B^N \mathbf{F}_B^{N-1} + \mathbf{F}_B^N \dot{\mathbf{F}}_B^F \mathbf{F}_B^{F-1} \mathbf{F}_B^{N-1} = \mathbf{L}_B^N + \tilde{\mathbf{L}}_B^F \tag{6.15}$$

$$\tilde{\mathbf{L}}_B^F = \tilde{\mathbf{D}}_B^F + \tilde{\mathbf{W}}_B^F \tag{6.16}$$

We choose to make the representation unique by setting the plastic spin to zero, $\tilde{\mathbf{W}}_B^F = 0$.

We can use the polar decomposition of $\mathbf{F}_B^F$ to separate it into its stretch and rotation components:

$$\mathbf{F}_B^F = \mathbf{R}_B^F \mathbf{U}_B^F \tag{6.17}$$

and an eigenvalue decomposition of $\mathbf{U}_B^F$ will yield the directions and magnitudes of the principal flow stretches λ_{1F}, λ_{2F}, λ_{3F}:

$$(\mathbf{U}_B^F)^2 = \mathbf{C}_B^F = \sum_{i=1}^{3} \lambda_{iF}^2 \hat{\mathbf{n}}_i \otimes \hat{\mathbf{n}}_i \tag{6.18}$$

where λ_{iF} is an eigenvalue of $\mathbf{U}_B^F$, termed a principal flow stretch, $\mathbf{C}_B^F$=$(\mathbf{F}_B^F)^T \mathbf{F}_B^F$ is the Right Cauchy-Green strain tensor, and $\hat{\mathbf{n}}_i$ is an eigenvector[1] of $\mathbf{C}_B^F$. The vectors ($\mathbf{a}$, $\mathbf{b}$, and $\mathbf{c}$) and lengths (a, b, and c) representing the orthotropic unit cell can be obtained from the principal flow stretch values λ_{1F}, λ_{2F}, λ_{3F} and their corresponding eigenvectors $\hat{\mathbf{n}}_1$, $\hat{\mathbf{n}}_2$, $\hat{\mathbf{n}}_3$ as:

$$\mathbf{a} = \hat{\mathbf{n}}_1 \tag{6.19}$$

$$\mathbf{b} = \hat{\mathbf{n}}_2 \tag{6.20}$$

$$\mathbf{c} = \hat{\mathbf{n}}_3 \tag{6.21}$$

[1] $\hat{\mathbf{n}}_i$ is also an eigenvector of $\mathbf{U}_B^F$

and

$$a = a_0 \lambda_{1F} \tag{6.22}$$

$$b = a_0 \lambda_{2F} \tag{6.23}$$

$$c = a_0 \lambda_{3F} \tag{6.24}$$

where a_0 is the initial size of the isotropic unit cube prior to deformation, related to the initial number of rigid links between entanglements, N_0, by:

$$a_0 = \frac{2}{\sqrt{3}} \sqrt{N_0} \tag{6.25}$$

Recall from equation 6.3 another expression relating the number of rigid links between entanglements to the size of the unit cell:

$$\sqrt{N} = \frac{1}{2} \sqrt{a^2 + b^2 + c^2} \tag{6.26}$$

Substituting in from eqns. 6.22 to 6.24 we obtain

$$\sqrt{N} = \frac{1}{2} a_0 \sqrt{\lambda_{1F}^2 + \lambda_{2F}^2 + \lambda_{3F}^2} \tag{6.27}$$

which indicates that N will vary from N_0 with deformation. This means that through flow, the polymer chains essentially reptate or slip through their entanglements, causing there to be more rigid links between two neighboring entanglements, a result which is rather intuitive. Note that conservation of mass requires that the product of N and ν remain constant, so that the evolution of N

$$\frac{N}{N_0} = \frac{\lambda_{1F}^2 + \lambda_{2F}^2 + \lambda_{3F}^2}{3} \tag{6.28}$$

necessitates an evolution of ν

$$\frac{\nu}{\nu_0} = \frac{3}{\lambda_{1F}^2 + \lambda_{2F}^2 + \lambda_{3F}^2} \tag{6.29}$$

Once the material directions **a**, **b**, and **c** have been calculated from the above equations, they need to be rotated by $\mathbf{R}_B^F$ to bring the orthotropic cell into the elastically unloaded configuration. Then the stress can then be calculated directly from equation 6.9 or from the simplified form for triaxial deformation in equation 6.11.

This completes the modifications to the model framework to include the anisotropic model.

6.4 Comparison with Experimental Data

Using this new approach, the following simulation results are obtained. Figures 6-8 through 6-17 show the results for uniaxial compression and figures 6-18 and 6-20 show the results for plane strain compression. These figures illustrate that the model is able to capture the trends of strain rate, strain state, and temperature dependence of the initial modulus, flow stress, initial hardening modulus, and the dramatic hardening at large strains for PETG.

Figures 6-21 through 6-27 show the comparison of simulation with experiment. Error values for these curves are tabulated in Table 6.1 and are shown graphically in figures 6-28 and 6-29. It can be seen that all experiments are very well approximated and are even slightly better approximated than in the previous model. This is especially clear in uniaxial compression at higher strain rates (see figure 6-28).

6.5 A Comment on Shear Behavior

An interesting sidetrack relating to this anisotropic model arises if we look at the limit of a = b = c = a_0. Going through the math, it becomes clear that for triaxial deformation along the material axes, the anisotropic model yields the same result as the isotropic model. However, if there is any shear deformation involved, the anisotropic model no longer reduces to the isotropic 8-chain model for a = b = c = a_0. This can be explained by noting that for the isotropic model, the model depends simply on an effective chain stretch, and the symmetry of the model makes the result inde-

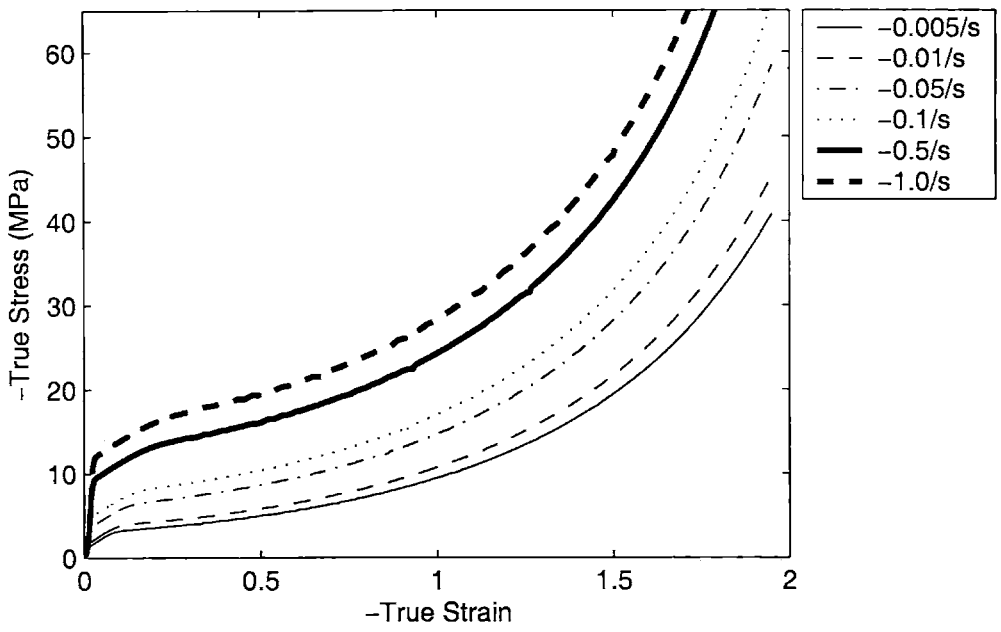

Figure 6-8: Uniaxial compression simulation, Temperature = 80 ° C

pendent of the spatial orientation of the unit cube. In the anisotropic model, on the other hand, the material directions are explicitly included in the constitutive equation, hence causing the results to depend on the choice of material orientation, even in the isotropic limit. For cases of triaxial deformation and when the material axes of the anisotropic cell coincide with the principal axes of deformation, the anisotropic model gives the same result as the isotropic model. In shear deformations, this is not the case. In order to use the model obtained in this chapter for arbitrary deformations, this issue of material-orientation dependence must be dealt with appropriately. It is proposed that a way to address the issue is to take an average of the response over several different material orientations. The implementation of such an averaging approach is left to future work.

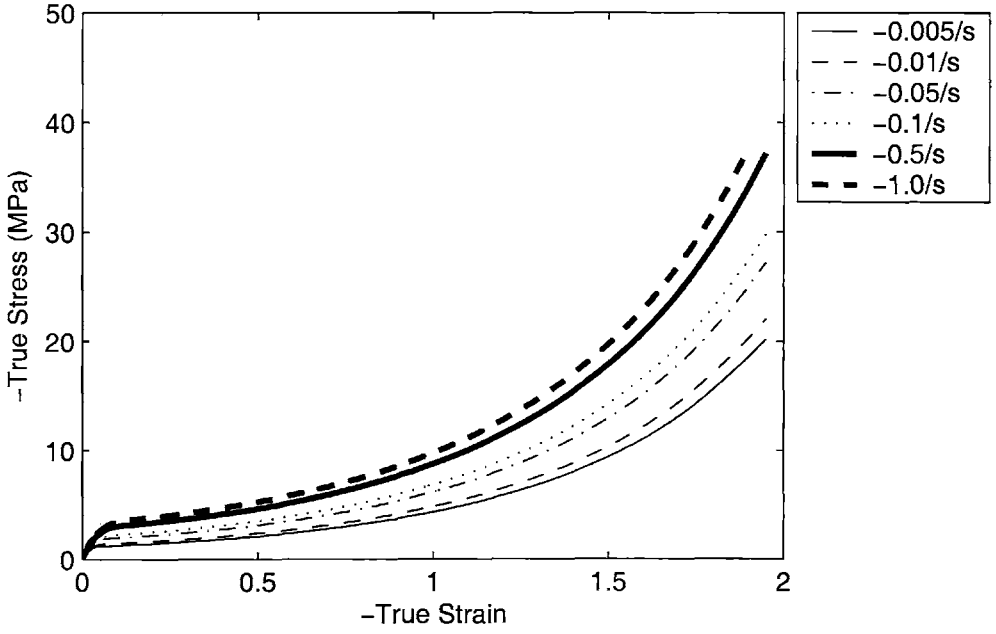

Figure 6-9: Uniaxial compression simulation, Temperature = 90 ° C

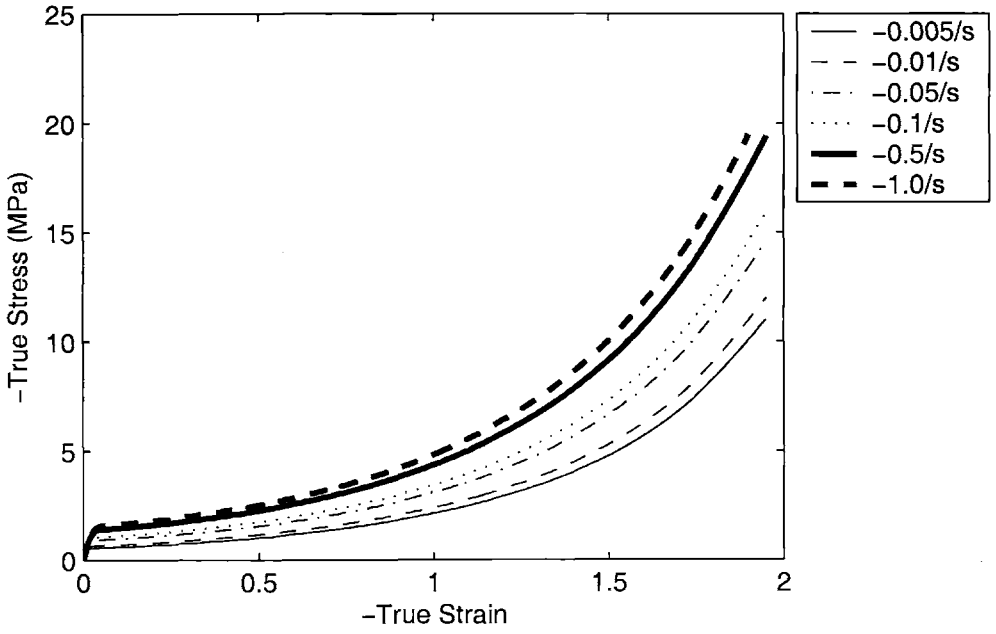

Figure 6-10: Uniaxial compression simulation, Temperature = 100 ° C

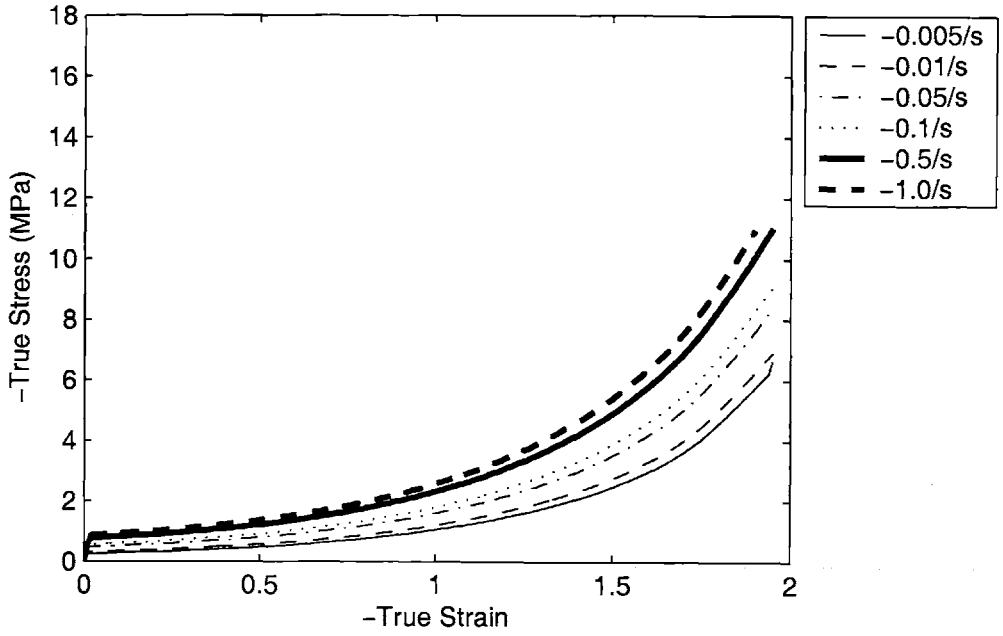

Figure 6-11: Uniaxial compression simulation, Temperature = 110 ° C

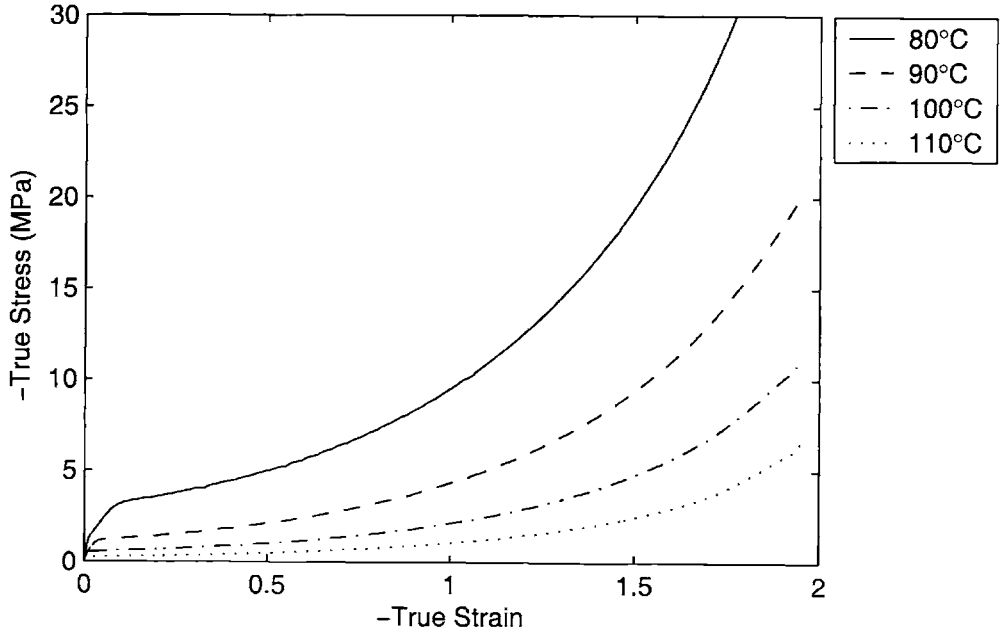

Figure 6-12: Uniaxial compression simulation, $\dot{\epsilon}$ = -.005/s

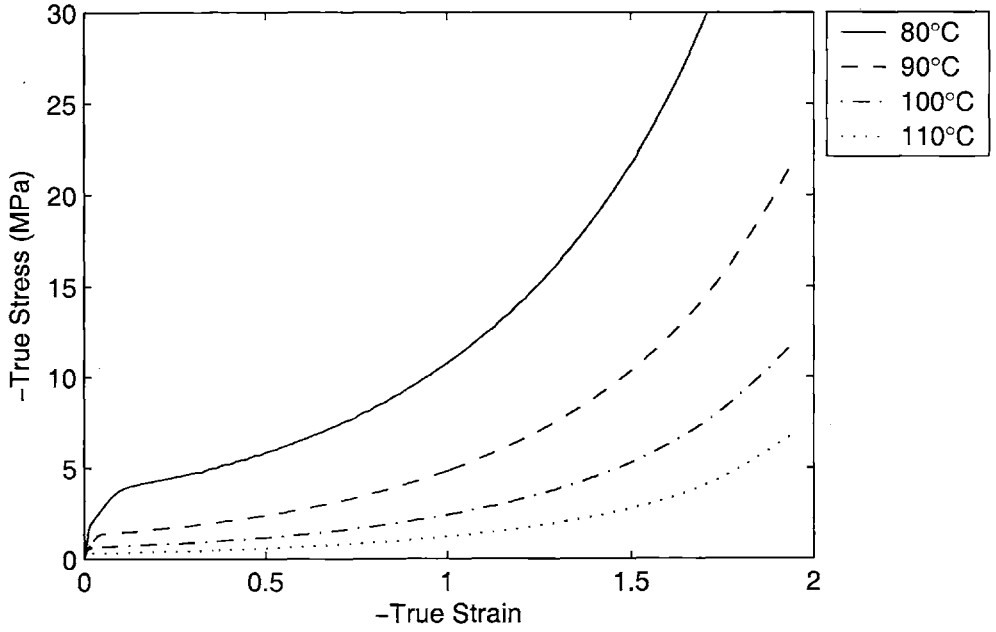

Figure 6-13: Uniaxial compression simulation, $\dot{\varepsilon}$ = -.01/s

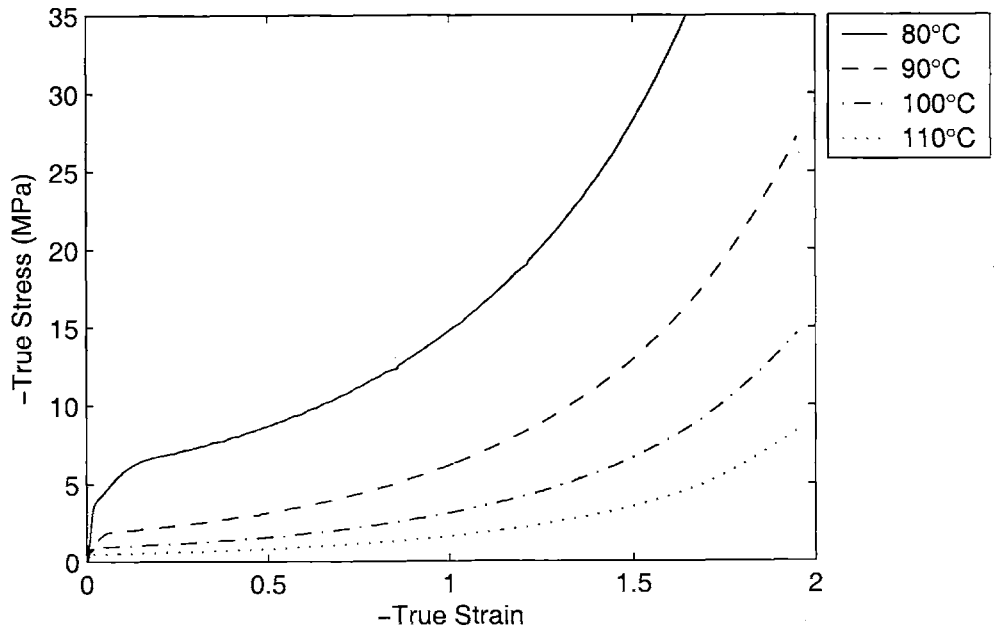

Figure 6-14: Uniaxial compression simulation, $\dot{\varepsilon}$ = -.05/s

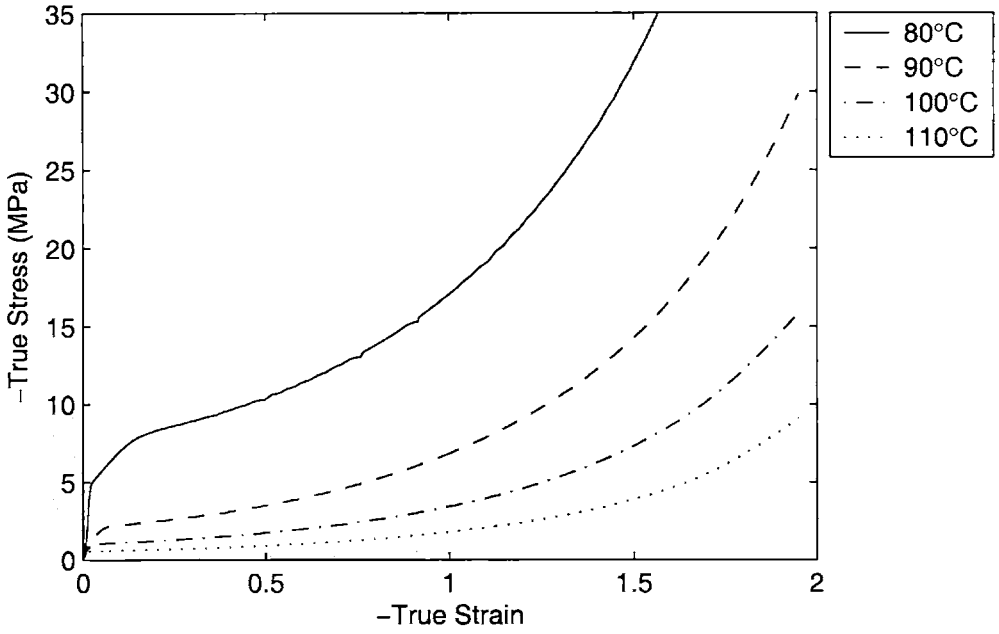

Figure 6-15: Uniaxial compression simulation, $\dot{\epsilon}$ = -.1/s

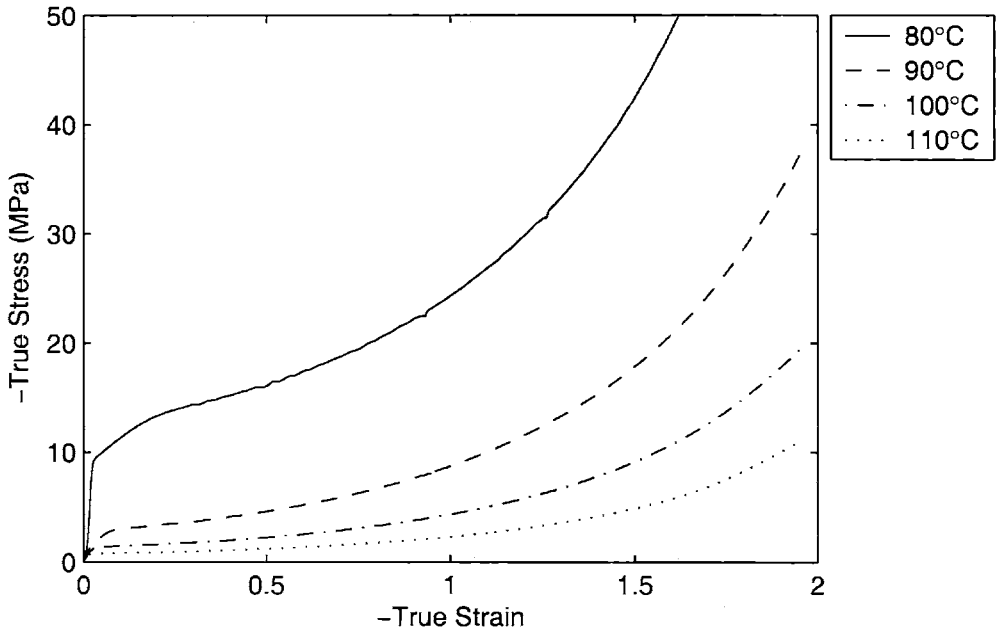

Figure 6-16: Uniaxial compression simulation, $\dot{\epsilon}$ = -.5/s

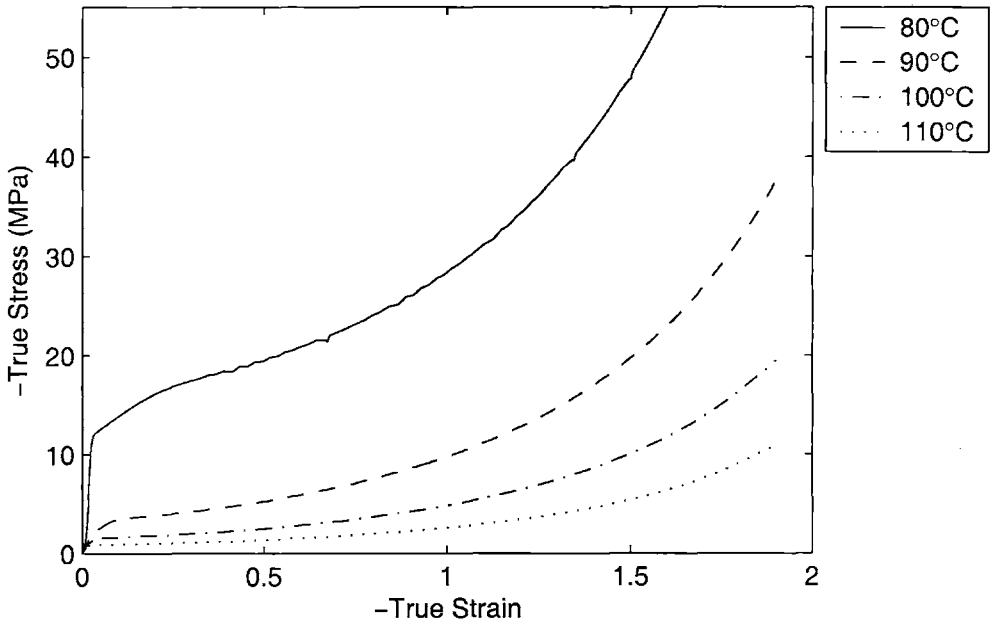

Figure 6-17: Uniaxial compression simulation, $\dot{\varepsilon}$ = -1.0/s

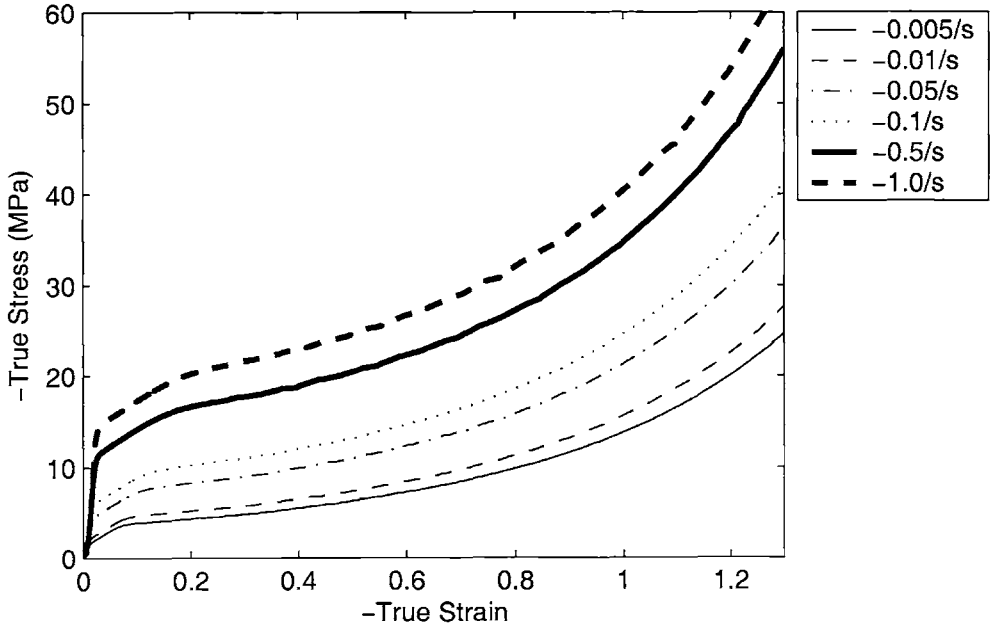

Figure 6-18: Plane strain compression simulation, Temperature = 80 ° C

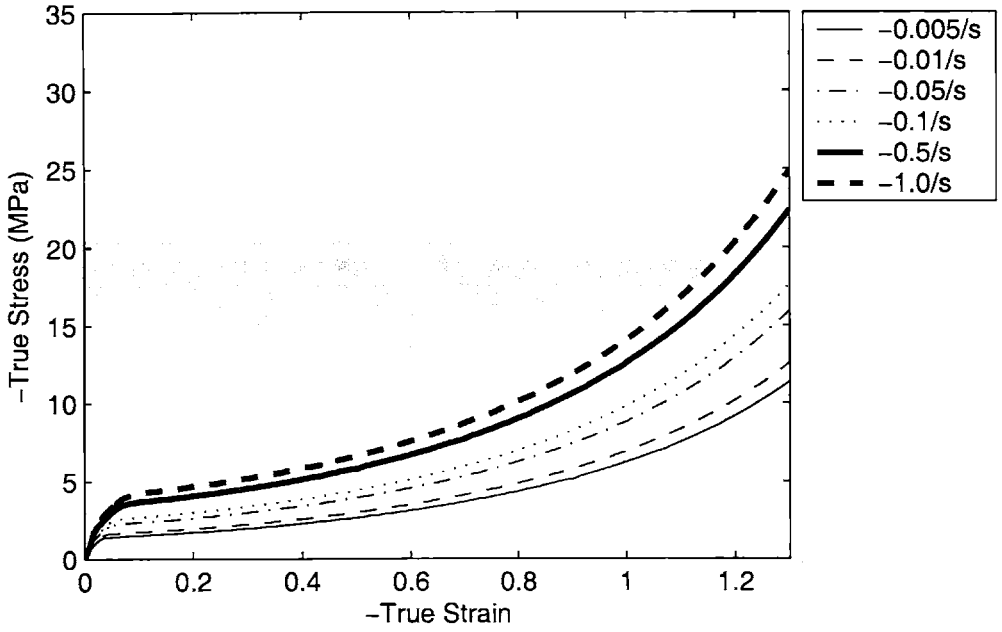

Figure 6-19: Plane strain compression simulation, Temperature = 90 ° C

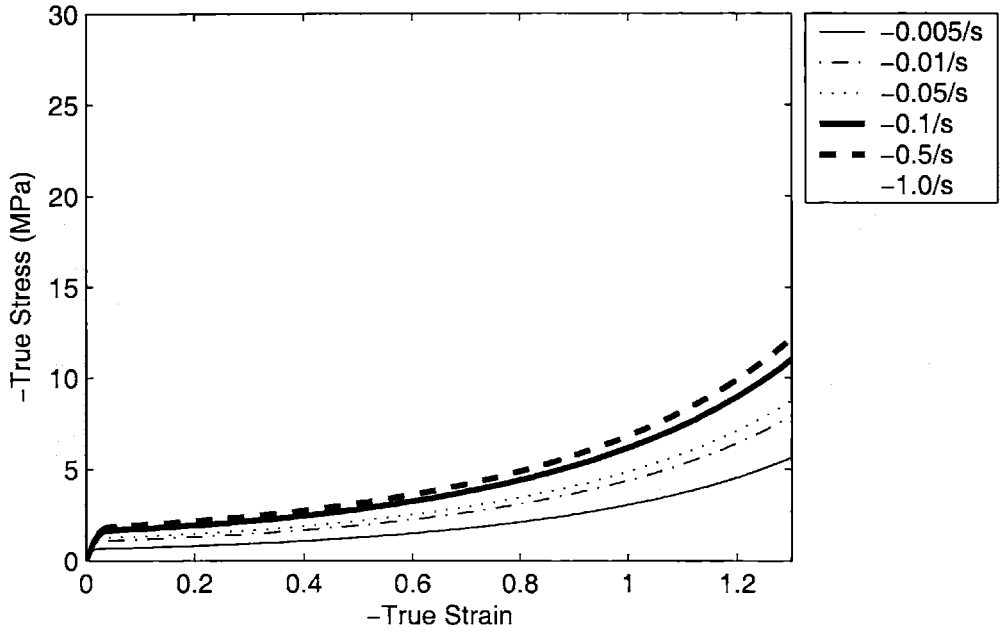

Figure 6-20: Plane strain compression simulation, Temperature = 100 ° C

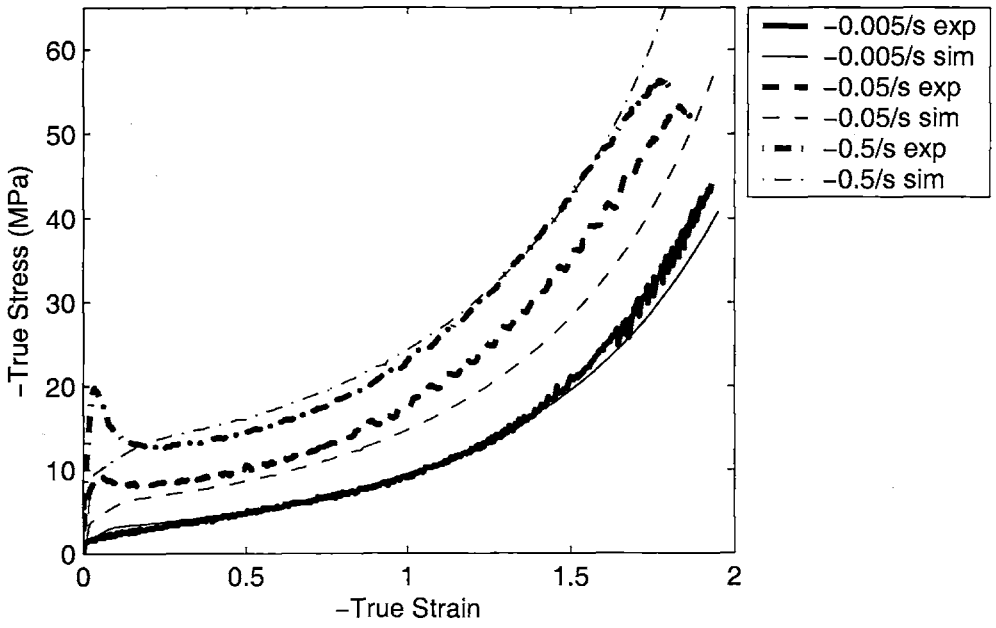

Figure 6-21: PETG Uniaxial compression, comparing simulation results with experimental data, Temperature = 80 ° C

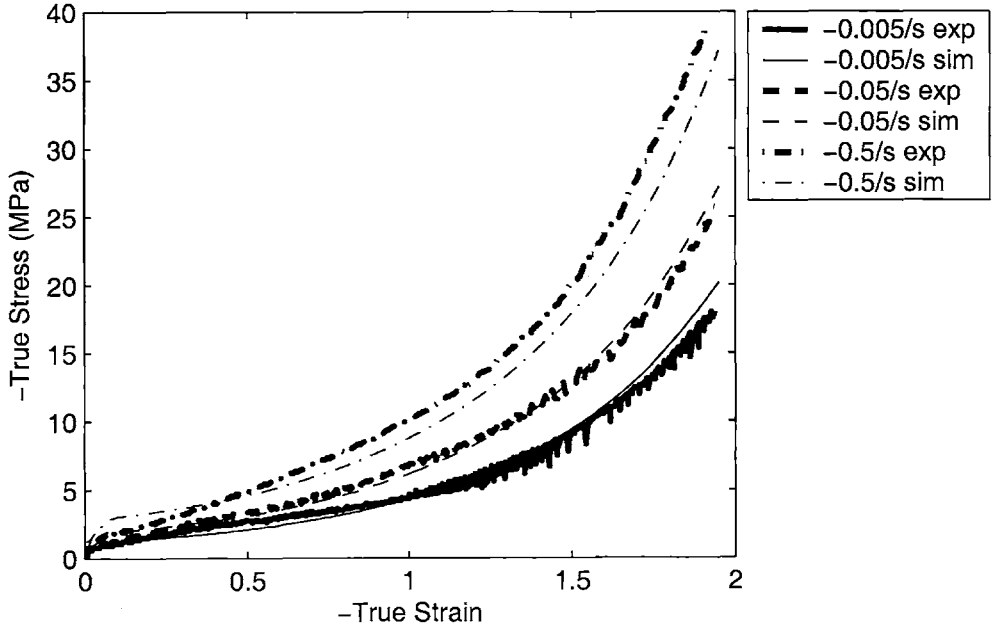

Figure 6-22: PETG Uniaxial compression, comparing simulation results with experimental data, Temperature = 90 ° C

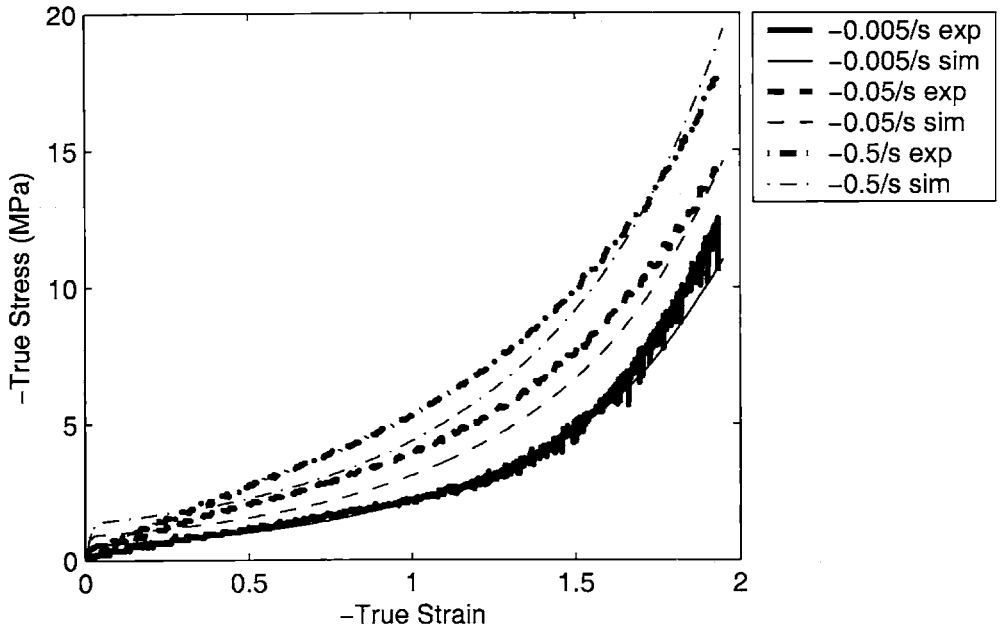

Figure 6-23: PETG Uniaxial compression, comparing simulation results with experimental data, Temperature = 100 ° C

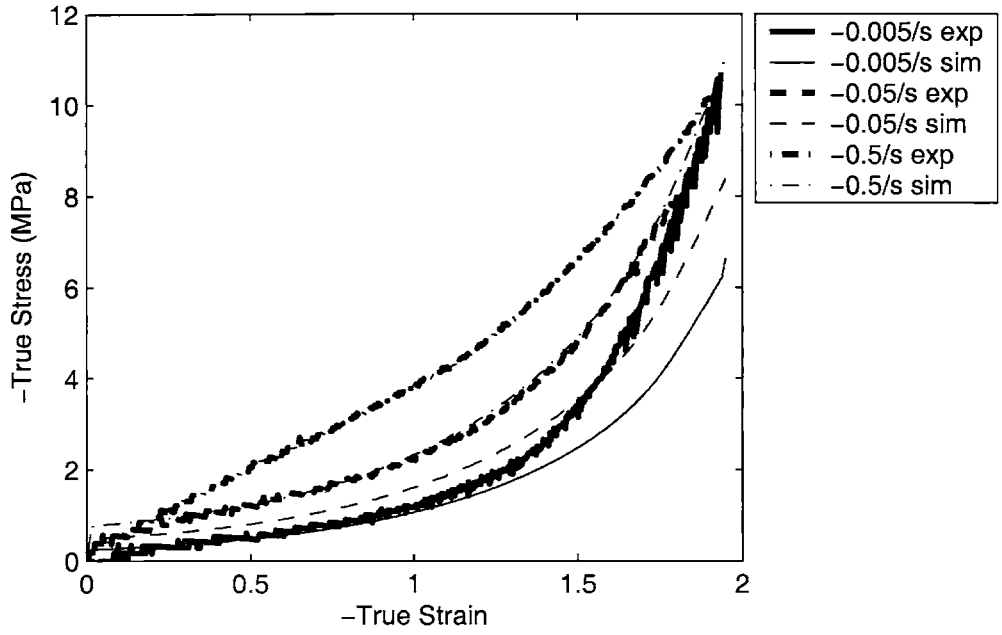

Figure 6-24: PETG Uniaxial compression, comparing simulation results with experimental data, Temperature = 110 ° C

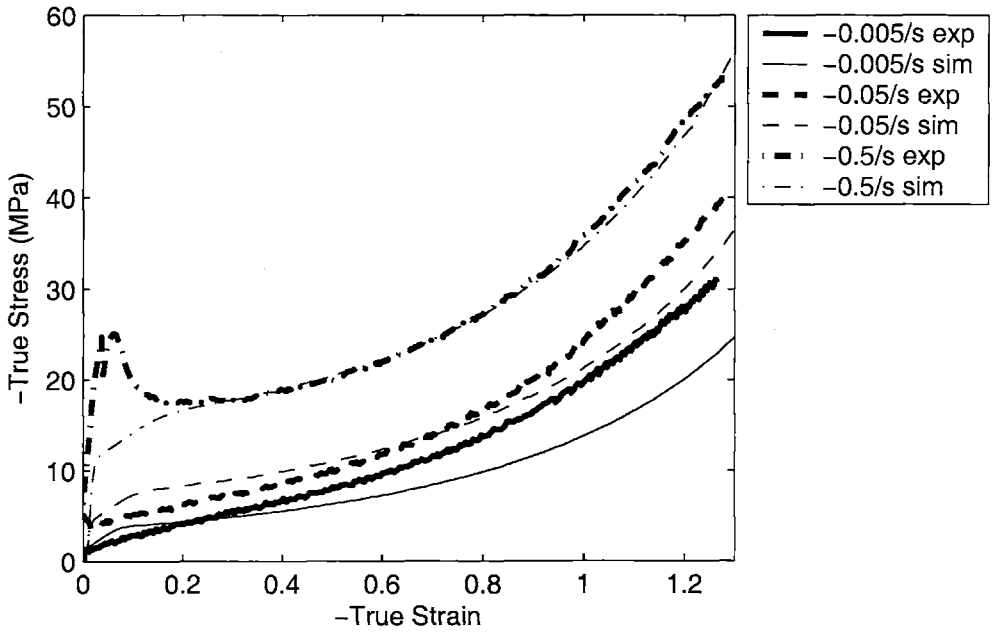

Figure 6-25: PETG Plane strain compression, comparing simulation results with experimental data, Temperature = 80 ° C

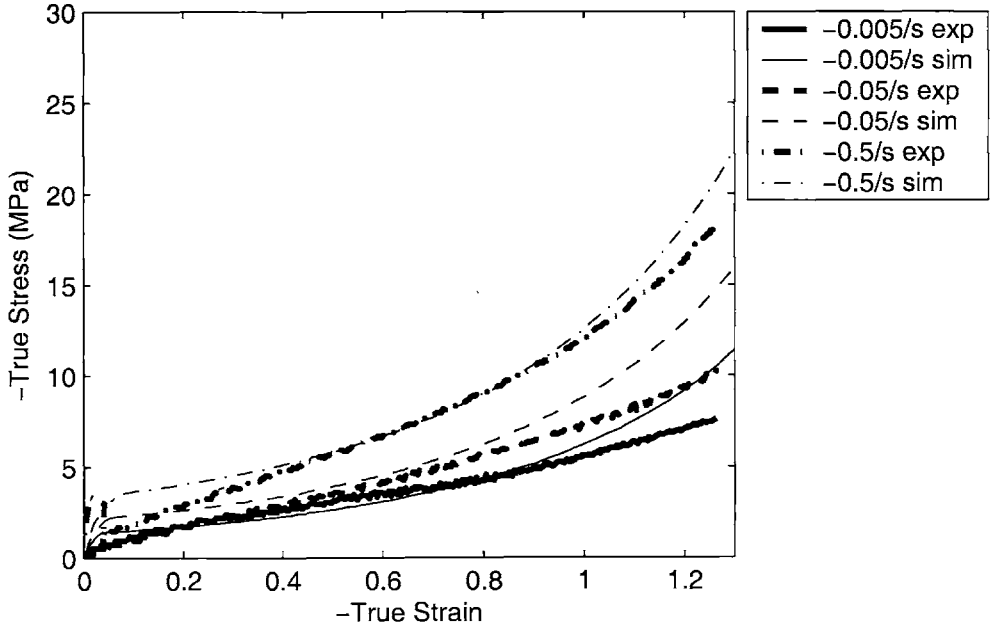

Figure 6-26: PETG Plane strain compression, comparing simulation results with experimental data, Temperature = 90 ° C

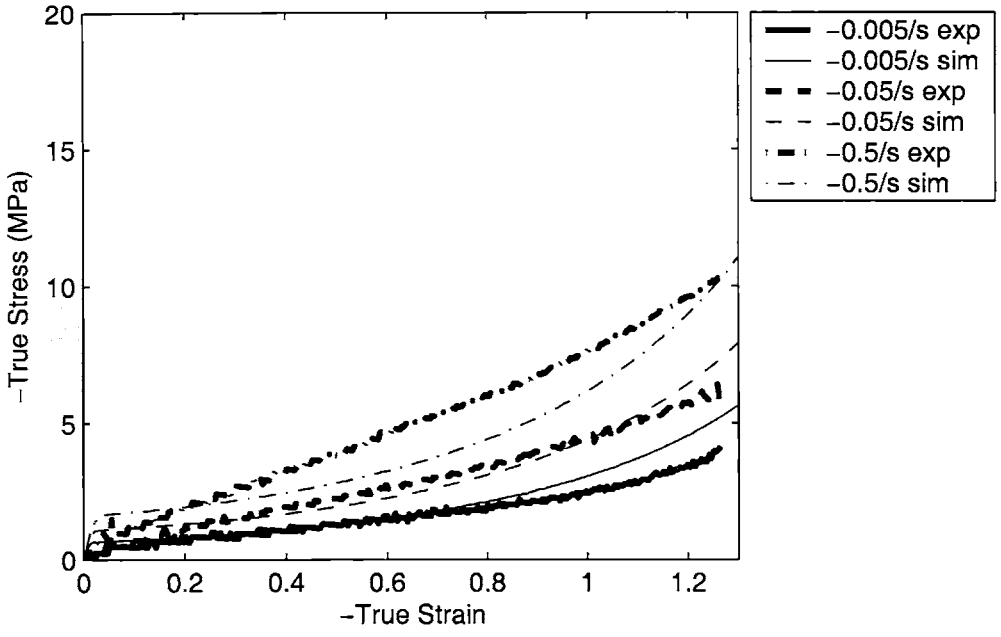

Figure 6-27: PETG Plane strain compression, comparing simulation results with experimental data, Temperature = 100 ° C

Table 6.1: PETG Error values for uniaxial and plane strain compression simulations using anisotropic model

Strain State	Temperature	Strain Rate	$\bar{y}$, full range	$\bar{y}$, up to $\varepsilon = 1.0$
Uniaxial	80 ° C	-0.005/sec	.0708	.0886
Uniaxial	80 ° C	-0.05/sec	.1749	.1724
Uniaxial	80 ° C	-0.5/sec	.0773	.1124
Uniaxial	90 ° C	-0.005/sec	.1060	.1482
Uniaxial	90 ° C	-0.05/sec	.0856	.1246
Uniaxial	90 ° C	-0.5/sec	.1557	.1912
Uniaxial	100 ° C	-0.005/sec	.1037	.1642
Uniaxial	100 ° C	-0.05/sec	.1992	.2484
Uniaxial	100 ° C	-0.5/sec	.1846	.2686
Uniaxial	110 ° C	-0.005/sec	.4431	.2376
Uniaxial	110 ° C	-0.05/sec	.2726	.2919
Uniaxial	110 ° C	-0.5/sec	.3124	.3712
Plane Strain	80 ° C	-0.005/sec	.2430	.2325
Plane Strain	80 ° C	-0.05/sec	.1529	.1516
Plane Strain	80 ° C	-0.5/sec	.0456	.0490
Plane Strain	90 ° C	-0.005/sec	.1510	.1289
Plane Strain	90 ° C	-0.05/sec	.3451	.3389
Plane Strain	90 ° C	-0.5/sec	.1654	.1793
Plane Strain	100 ° C	-0.005/sec	.1656	.1256
Plane Strain	100 ° C	-0.05/sec	.1612	.1826
Plane Strain	100 ° C	-0.5/sec	.2312	.2626

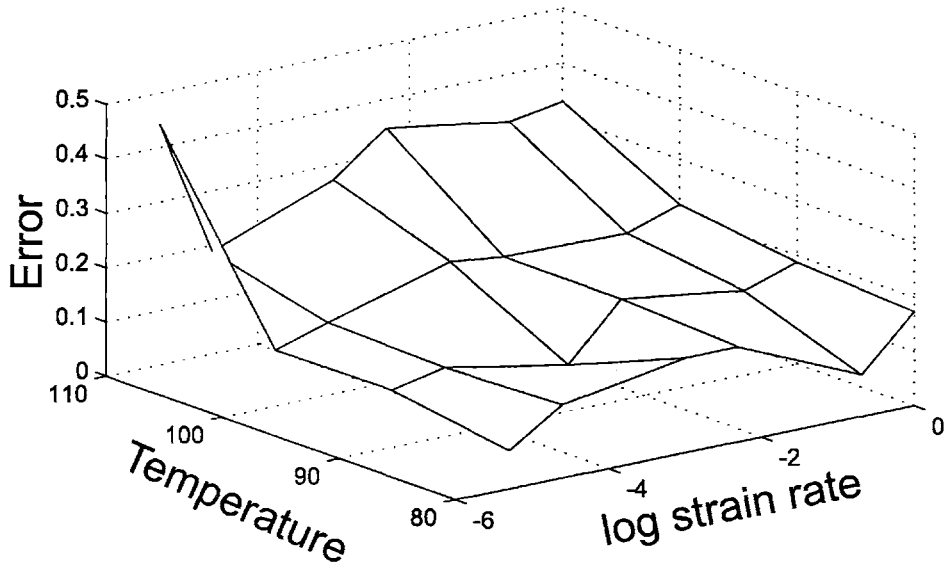

Figure 6-28: PETG Uniaxial compression error values using anisotropic model

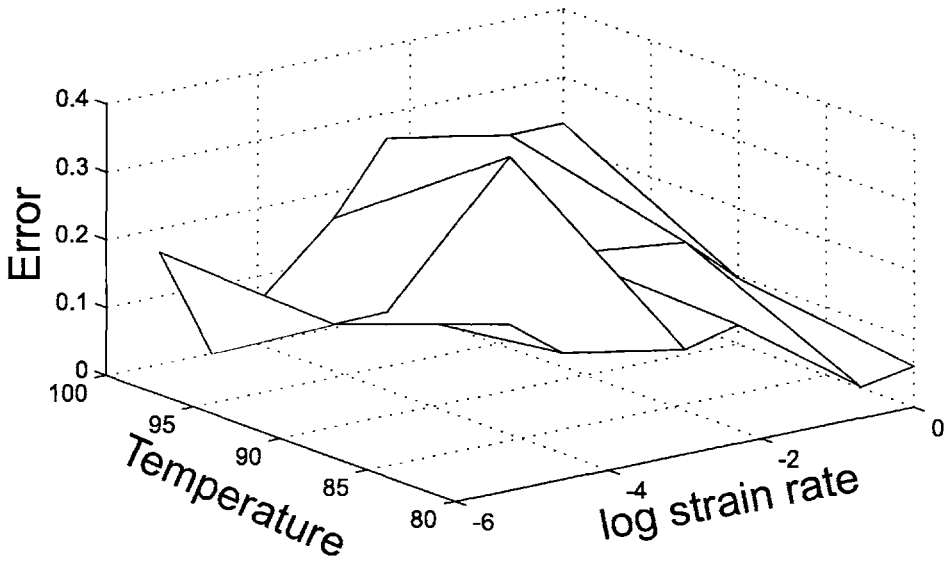

Figure 6-29: PETG Plane strain compression error values using anisotropic model

Chapter 7

Blow Molding Simulations

A primary motivation for developing the constitutive models presented in this thesis was for the application to industrial processes. One prominent example is the process of reheat stretch blow molding. In this chapter, we discuss the design challenges associated with this process and present the results of finite element simulations using the model for PETG from Chapter 4.

7.1 Introduction

The reheat stretch blow molding process is illustrated in figure 7-1. A preform is first injection molded. Later, the preform is reheated to approximately 15-30 degrees above the glass transition temperature. It is then stretched by an axial rod and a pressure is applied inside the preform to inflate the bottle. As the preform makes contact with the mold, it cools and solidifies. Once the bottle has cooled, it is ejected from the mold.

7.2 Experimental Blow Molding Parameters

Several factors significantly affect the final bottle product. The aim is, of course, to reduce costs by using the least amount of material and by blowing bottles as quickly as possible. However, this drive to reduce cost is checked by several important

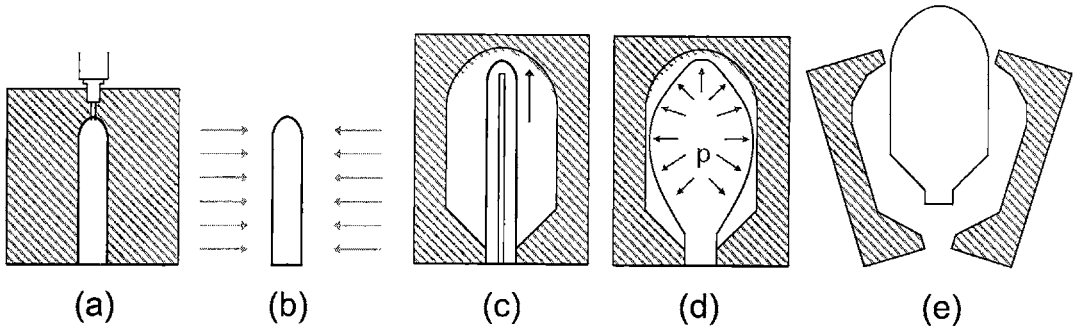

Figure 7-1: The reheat stretch blow molding process: (a) injection mold preform (b) reheat preform above θ_g (c) stretch preform with axial rod (d) apply pressure to inflate preform (e) cool and eject from mold

product features. One of these is shelf life. Since many bottles will contain carbonated beverages, it is desired that the bottles be highly impermeable to gasses, so that carbonation loss is as slow as possible. A bottle which has a very thin wall may save money by requiring less material, but if the wall is too thin, the beverage will lose carbonation too quickly for a realistic shelf life. A second important feature is the optical clarity of the bottle walls. Ideally, customers desire a clear, transparent bottle. If the bottle is processed at an inappropriate temperature or speed, processes referred to as pearling and hazing may occur, causing the bottles to become opaque. Pearling indicates the bottle was blown at too cold a temperature, inducing chain scission. Hazing, on the other hand, results from blowing the bottle at too high a temperature, leading to larger crystallites and a hazy appearance to the bottle.

We can identify several key manufacturing parameters which need to be appropriately specified: (1) Preform and mold geometries must be designed in such a way that the polymer reaches its natural draw ratio before contacting the mold. In such a design, any neck caused by an imperfection in the preform will propagate along the length of the preform before contact with the mold cools the material. This gives the bottle a very uniform wall thickness. Other geometric design issues include prescribing proper taper angles on the preform and the bottle mold to ensure proper mold release, both of the preform after it has been injection molded, and of the final bottle from its mold. Proper design of the preform base is needed so that excess material is

not wasted in an overly thick base. More complex design issues continually arise as customers demand new products which are no longer simple axisymmetric geometries.

(2) Reheat time and furnace configuration are critical in achieving the correct bottle temperature, temperature profile along the length, and temperature profile through the bottle thickness. As mentioned above, blowing the bottle too hot or too cold results in opacity in the bottle walls. Additionally, thicker sections in the preforms generally require higher temperatures to blow properly. Due to a combination of different heat transfer effects during the preform heating stage, the inner and outer surfaces of the preform tend to be at different temperatures when blowing begins. If properly controlled, this can work to the advantage of the designer. During inflation, the inner surface experiences a larger strain than the outer surface. Thus, it is generally desirable to have the inner surface at a slightly higher temperature than the outer surface. This slight temperature difference can be controlled by appropriately specifying the reheat time.

(3) Stretch rod geometry and velocity (force) must be specified. The stretch rod is generally driven by a hydraulic pressure, so that it applies an approximately constant force to the bottom of the preform. One of its main purposes is to stretch the material in the base of the preform prior to inflating the bottle, since directly applying a pressure will generally not create sufficient stretching in the base of the bottle. Another purpose is to center the preform in the mold as it is inflated. It additionally creates a more complex stretch history for the bottle sidewalls than in a simple inflation process, something which is important to understand in order to correctly predict bottle blowing behavior and final bottle properties.

(4) The magnitude and duration of the pressure must be specified. Often, the pressure is applied in two stages. First a lower (preblow) pressure is applied prior to stretching with the axial rod, in order to prevent the preform from touching off on the stretch rod. A larger pressure is then applied to inflate the bottle. This pressure is generally specified as a constant value, but in reality the pressure felt by the preform is determined by hydraulic relationships. First, when the pressure is applied, it rises quite rapidly in a fairly linear ramp. As the bottle begins to inflate, the pressure

subsequently drops due to the increase in volume. The pressure again rises according to the air flow rate provided by the system.

Each of these design issues and challenges can be studied using computer simulations, a sampling of which will be addressed in the next section.

7.3 Description of the Finite Element Model

In this section some simple finite element simulations are set up to try to understand some of the variables which affect bottle blowing. The preform geometry which has been studied is shown in figure 7-2. This geometry is represented in figure 7-3 by a mesh consisting of quadratic axisymmetric elements (ABAQUS element type CAX8H) constrained by a symmetry boundary condition at the bottom and by a constraint in the 1- and 2- directions at the top. The upper boundary condition is, in fact, rather difficult to prescribe without initiating numerical problems at this location. As a result, two acceptable methods were found to achieve the desired constraint for free blows (simulations without a mold): (1) a pseudo-rigid element with rotations and contractions allowed at the top and (2) a contacting rigid element to provide a smooth boundary condition for the nodes near the top. These are illustrated in figures 7-4 and 7-5, respectively.

For boundary condition (1), the following constraint equations were applied to the nodes along the top of the preform:

$$
\begin{aligned}
u_1^{(3)} &= 0.0 \\
u_2^{(3)} &= 0.0 \\
u_1^{(2)} &= 0.5u_1^{(1)} \\
u_2^{(2)} &= 0.5u_2^{(1)} \\
u_1^{(4)} &= -u_1^{(2)} \\
u_2^{(4)} &= -u_2^{(2)} \\
u_1^{(5)} &= -u_1^{(1)}
\end{aligned}
$$

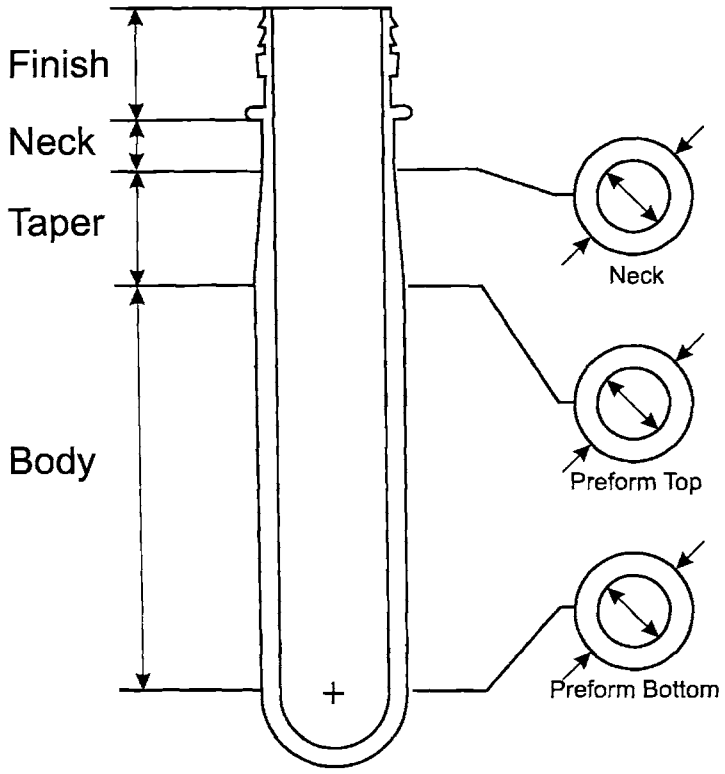

Figure 7-2: Preform used for bottle simulations

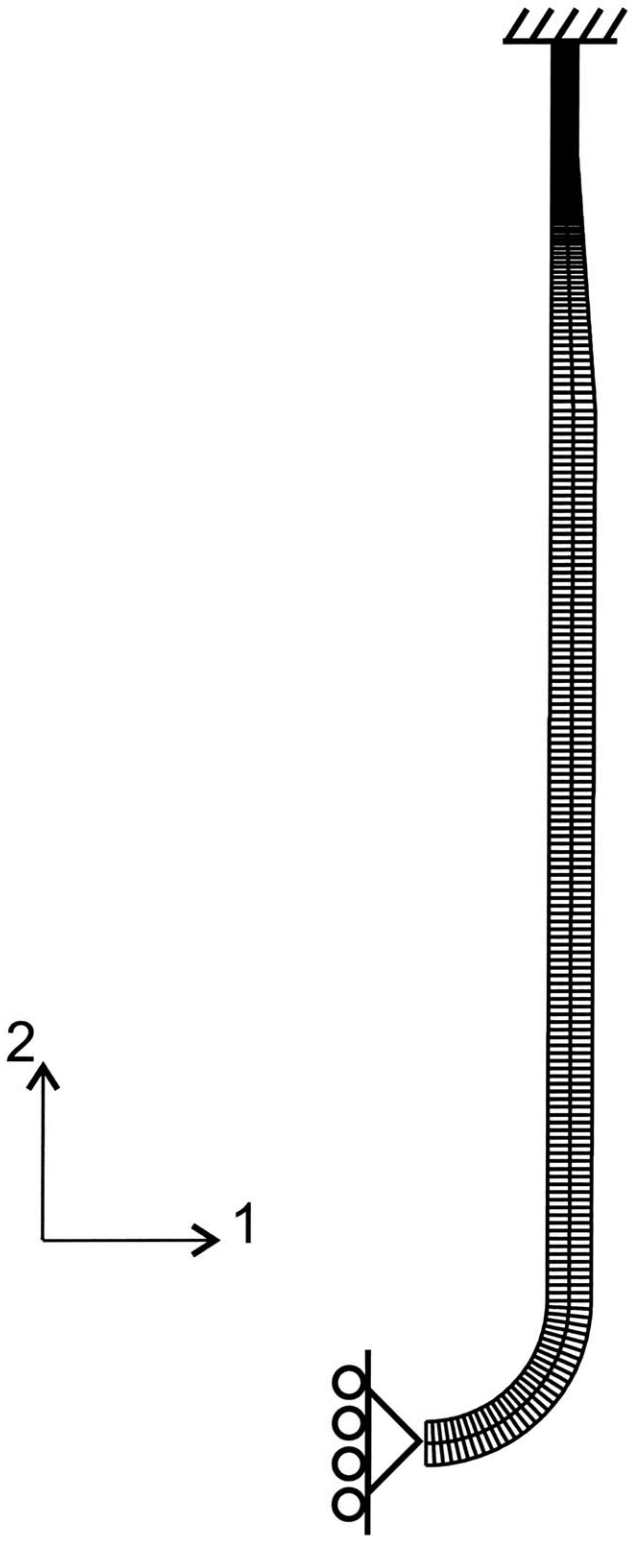

Figure 7-3: Finite element mesh for bottle simulations

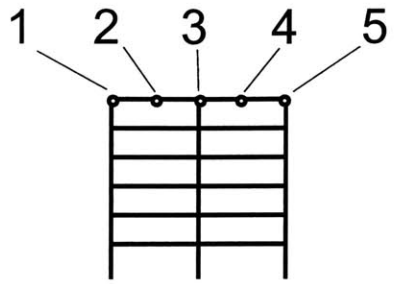

Figure 7-4: Boundary condition (1)

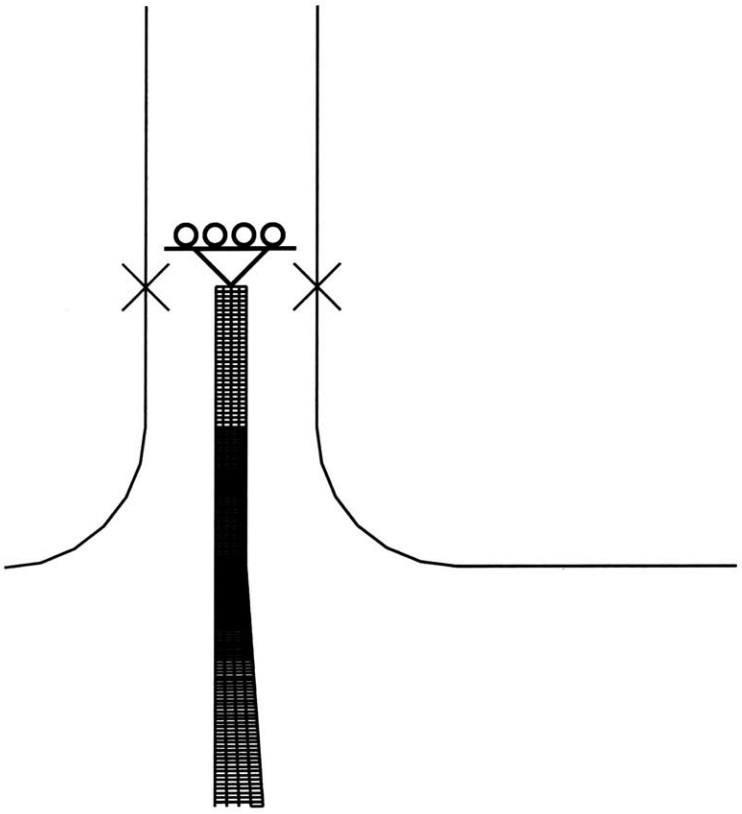

Figure 7-5: Boundary condition (2)

$$u_2^{(5)} = -u_2^{(1)} \tag{7.1}$$

where $u_j^{(i)}$ denotes the displacement of node i in the j-direction. These constraints essentially tie the nodes along the top of the preform to remain along a straight line, allowing that line to both rotate and contract with deformation.

For boundary condition (2), the nodes along the top of the preform were constrained to have no displacement in the 2-direction and were held in place in the 1-direction by bringing the curved rigid surfaces into contact with the preform. The rigid surfaces were prevented from translating and from rotating. Several different friction and contact conditions were specified, in an effort to find the most stable boundary condition to use.

7.4 Simulation Results and Discussion

A free blow simulation using boundary condition 2 is shown in figure 7-6, with the time shown underneath each snapshot. In this simulation, the entire preform was at a temperature of 100 ° C. The pressure was applied to the inner surface of the preform along a linear ramp from 0 to 0.5 MPa over the course of 10 sec. It can be seen that the preform did not sustain any appreciable deformation up to a pressure of about 0.293 MPa, corresponding to a time of 5.87 sec. Once this pressure was reached, the deformation proceeded very rapidly. Deformation began in the thinnest section of the preform (near the top) and then started to propagate down the length of the preform.

From this simulation, some interesting parameters can be monitored. A sampling of these is given in the following figures. Figure 7-7 shows how the orientation parameter, α_{min}, varies with time along the length of the bottle. The cutoff value of α_{min} is 0.05 rad (2.9 °), so it appears that in this simulation the top portion of the bottle has just reached the cutoff point. Figure 7-8 shows how the plastic shear rate in resistance B (molecular relaxation) varies with time along the length of the bottle. This parameter indicates where the material is actively deforming at that instant in the process. Figure 7-9 shows how planar stretch ratio (PSR), a design parameter

used in bottle production, varies with time along the length of the bottle. PSR is defined as:

$$PSR = \lambda_1 \times \lambda_2 \tag{7.2}$$

where λ_1 and λ_2 are the two largest principal stretches. The bottle simulated here was designed for a PSR of 11, indicating the bulk of the preform should reach this value before contacting the mold wall. It can be seen that the simulation falls short of this point. This may be because the simulations were run using the material model for PETG. In blowing an actual bottle, it is very difficult to blow a bottle made of PETG without rupture of the bottle occuring. Additionally, figure 7-9 showed that the plastic shear rate had decreased in the highly stretched region of the bottle, indicating that in PET, crystallization might start to occur at this point in the deformation. Crystallization would stabilize the deformation and could explain why PET will form, but PETG will not. Figure 7-10 shows how the bottle wall thickness varies with time along the length of the bottle. In an ideal bottle, the thickness should be fairly uniform along the length of the bottle. Figure 7-11 shows how chain stretch evolves during processing.

For comparison, a simulation was performed using a temperature profile along the length of the bottle. The temperature profile is shown in figure 7-12 and the deformation progression is shown in figure 7-13. It can be seen that the deformation progresses through much more of the bottle using a temperature profile such as this. Figure 7-14 shows how the orientation parameter, α_{min}, varies with time along the length of the bottle. Clearly, much more of the bottle wall has started to experience strain hardening than in the previous simulation. Figure 7-15 shows how the plastic shear rate varies with time along the length of the bottle and indicates that plastic flow is moving from one section of the bottle to another. Figure 7-16 shows how PSR varies with time along the length of the bottle. Again, the bottle, in spite of having the correct overall shape, falls short of the design PSR by a factor of 2. Figure 7-17 shows how the bottle wall thickness varies with time along the length of the bottle. In this simulation, a much more uniform wall thickness is obtained. Figure 7-18 shows

how chain stretch evolves during blowing.

Additional simulations have been performed to incorporate the effects of using a stretch rod and effects of blowing a bottle inside a mold. The stretch rod was simulated as a cylindrical rigid body with a spherical head of radius 4.5 mm. Blowing inside a mold was simulated using a mold geometry supplied by Eastman Chemical. Rather than simulating the complex thermal effects of cooling upon contact with the mold, a no-slip boundary condition was specified for the mold-bottle interface. Some results using the mold and rod are shown in figures 7-19 and 7-21, with their corresponding pressure-time and stretch rod displacement-time curves shown in figures 7-20 and 7-22. For the simulation with the mold, the simulation was run with a preform temperature of 90 $^{\circ}$ C. This is a rather low temperature to blow a bottle, the temperature partially accounting for the inability of the bottle to fill the mold entirely. Adding a stretch rod would also help the bottle to fill the mold more fully. In bottle forming processes, a stretch rod has several purposes: (1) the rod helps to center the expanding preform inside the mold, inhibiting a lop-sided deformation in which the bottle could touch off on one side early in the deformation; (2) the rod extends the bottle to the length of the mold, helping to prevent short-shot bottles, or bottles which did not form to the appropriate length; and (3) the rod alters the stretch history of the bottle, causing the material in the sidewalls to be stretched first in the longitudinal direction before being inflated biaxially. In the simulation with the stretch rod, the same temperature profile was used as in the simulation shown in figures 7-12 through 7-17. Even though the stretch rod did not deform the entire length of the bottle, it is clear that the stretch rod should be able to cause a bottle to attain a more elongated shape than without.

In summary, a few example blow molding simulations have been illustrated to show the ability of the model to simulate complex industrial processes. A complete parametric study to investigate the effect of variations in key parameters can be conducted using the model to aid in design. It should be noted that the model developed so far does not account for strain-induced crystallization. Future work to add a simple crystallization criteria is needed to capture the behavior of PET under

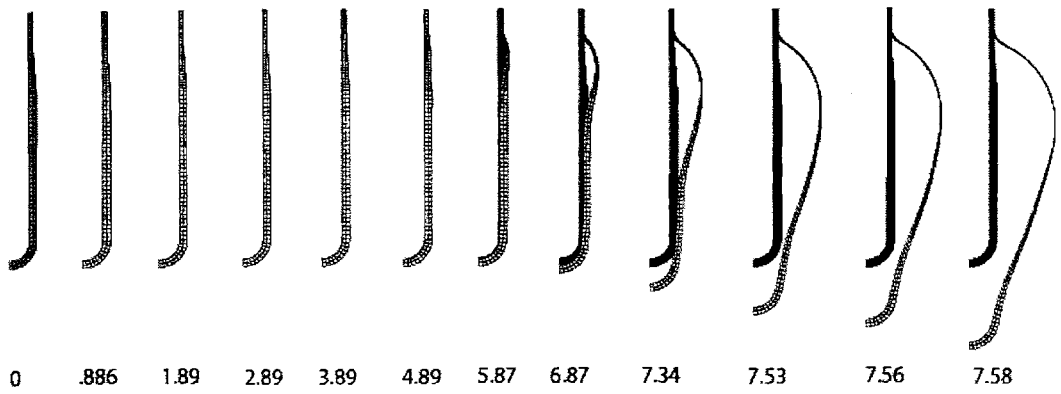

Figure 7-6: Deformed shape, T = 100 ° C

conditions where portions of the geometry experience periods of zero strain rate. In fact, to correctly capture the behavior during stretch blow molding of PET, it is likely such a criteria needs to be added. It is observed that during bottle formation, one area will begin to deform first until it starts to strain harden, at this point the deformation moves to another region of the bottle. If the strain rate falls below a critical level when the deformation leaves a region which has been strained to a large degree, strain-induced crystallization is likely to occur. Incorporating this in the model by means of a stiffening mechanism, possibly anisotropic, should prove useful, also for determining final bottle properties upon cooling. Another area for future work is to address the need to accurately model the pressure history felt by the bottle during the blow molding process. The pressure is not constant, but rather decreases as the bottle experiences an increase in volume. Employing a user-defined volume element and prescribing the pressure to respond appropriately to changes in volume should improve the predictive ability of simulations.

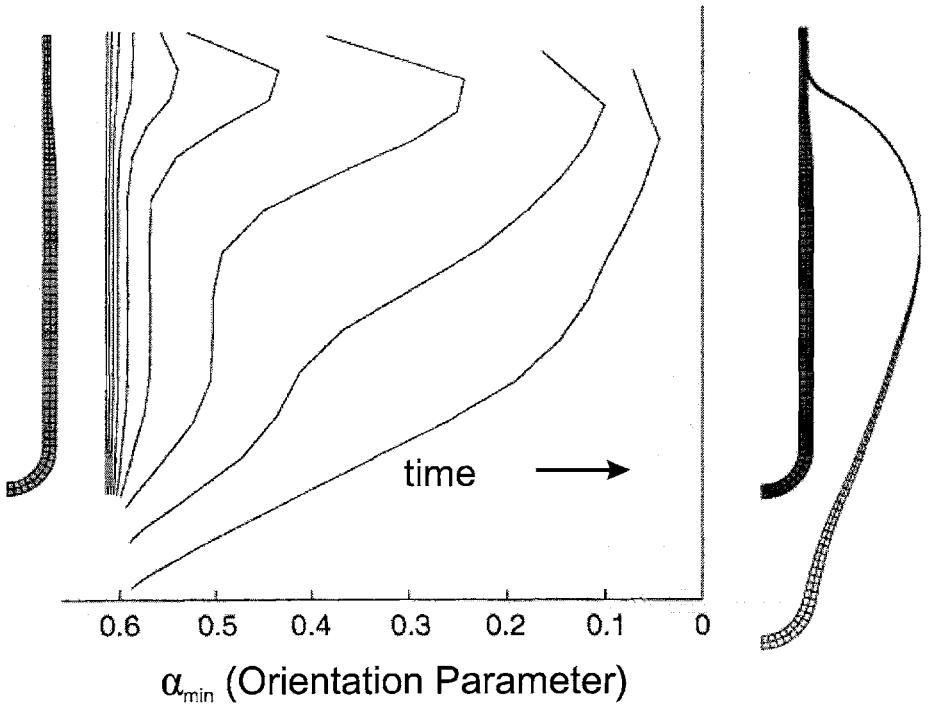

Figure 7-7: Orientation parameter, T = 100 ° C

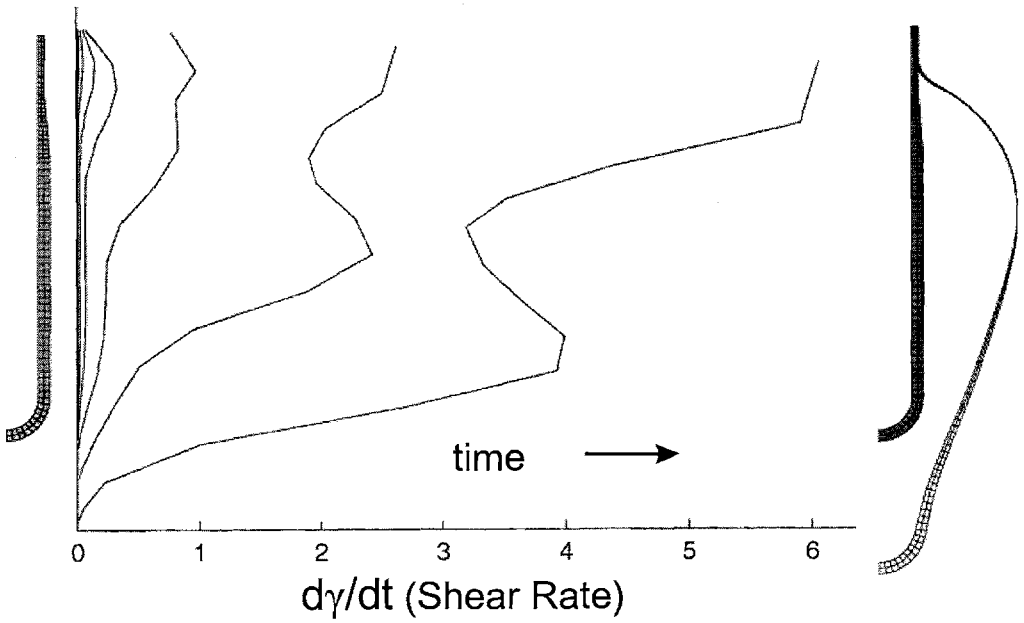

Figure 7-8: Shear rate, T = 100 ° C

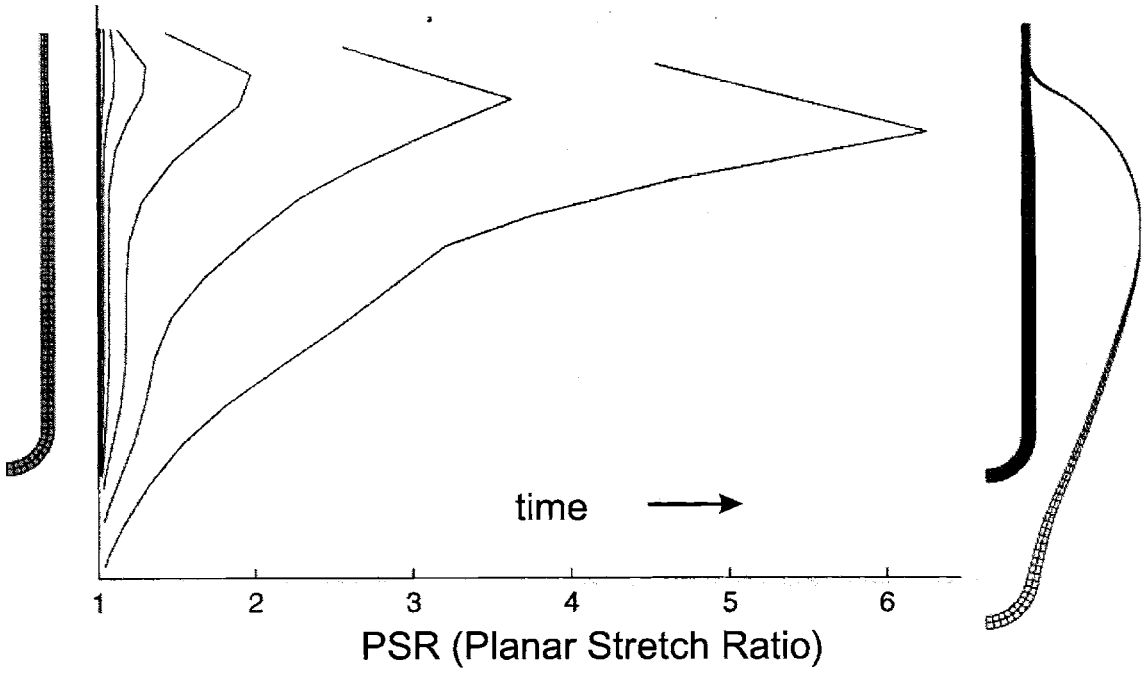

Figure 7-9: Orientation parameter, T = 100 ° C

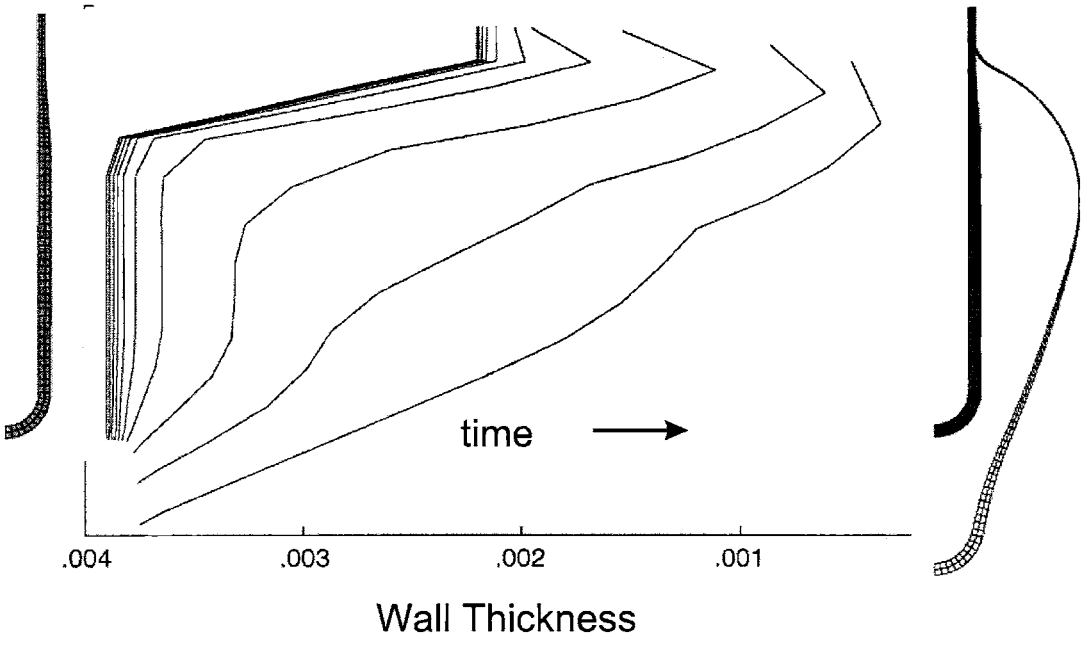

Figure 7-10: Shear rate, T = 100 ° C

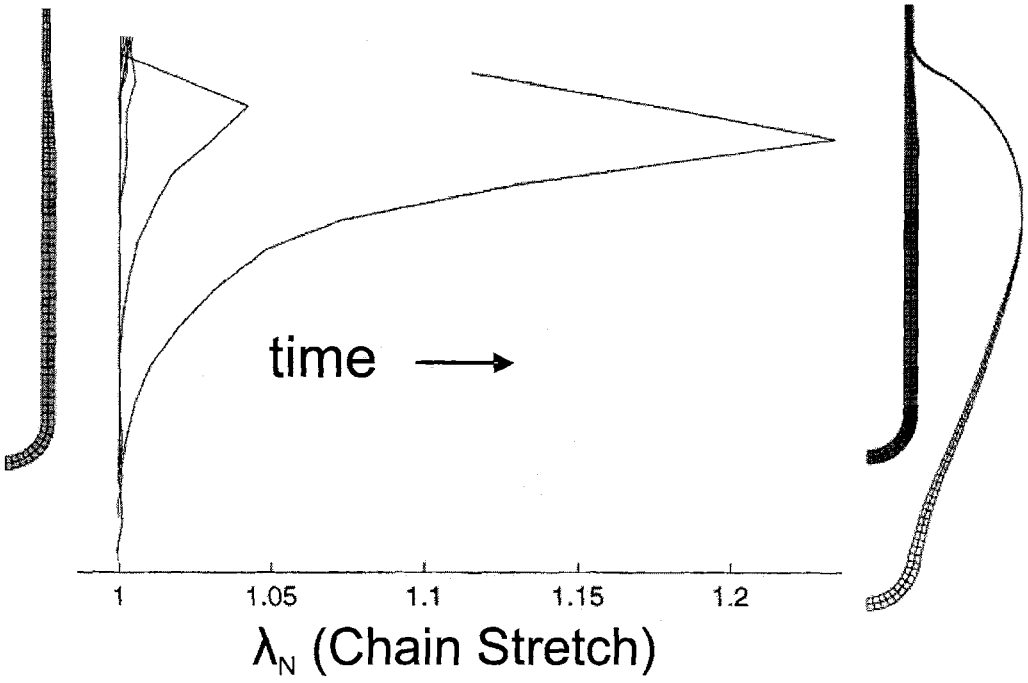

Figure 7-11: Chain Stretch, T = 100 ° C

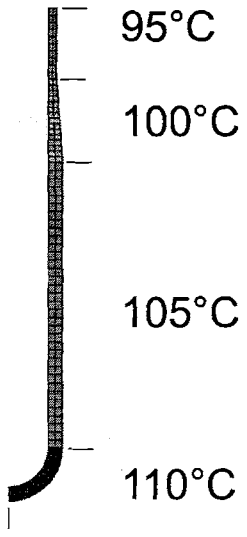

Figure 7-12: Temperature profile for blow molding simulation

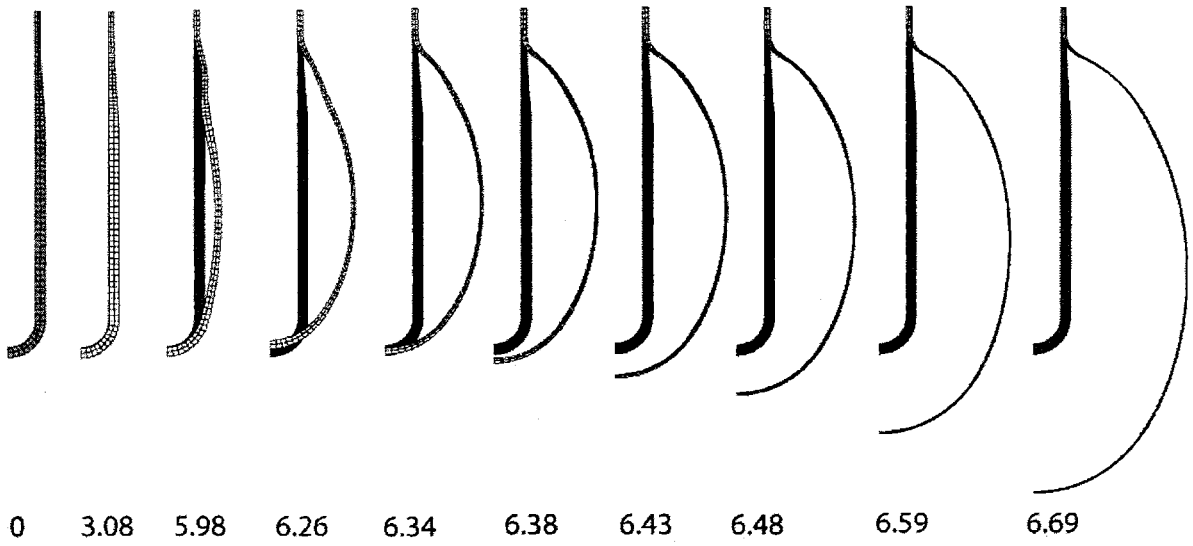

Figure 7-13: Deformed shape, temperature profile

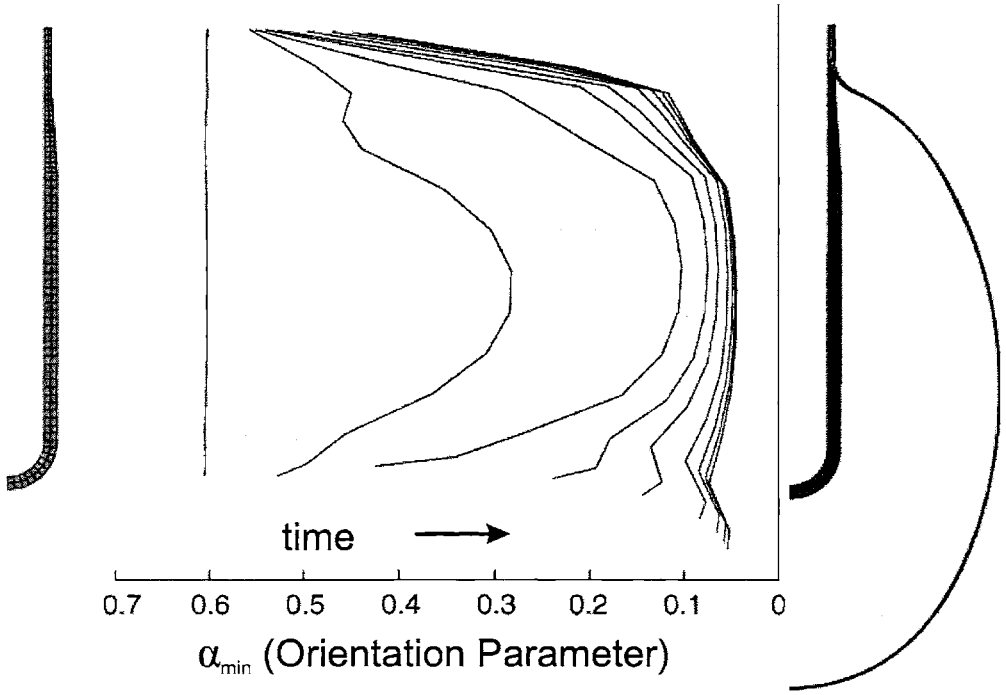

Figure 7-14: Orientation parameter, temperature profile

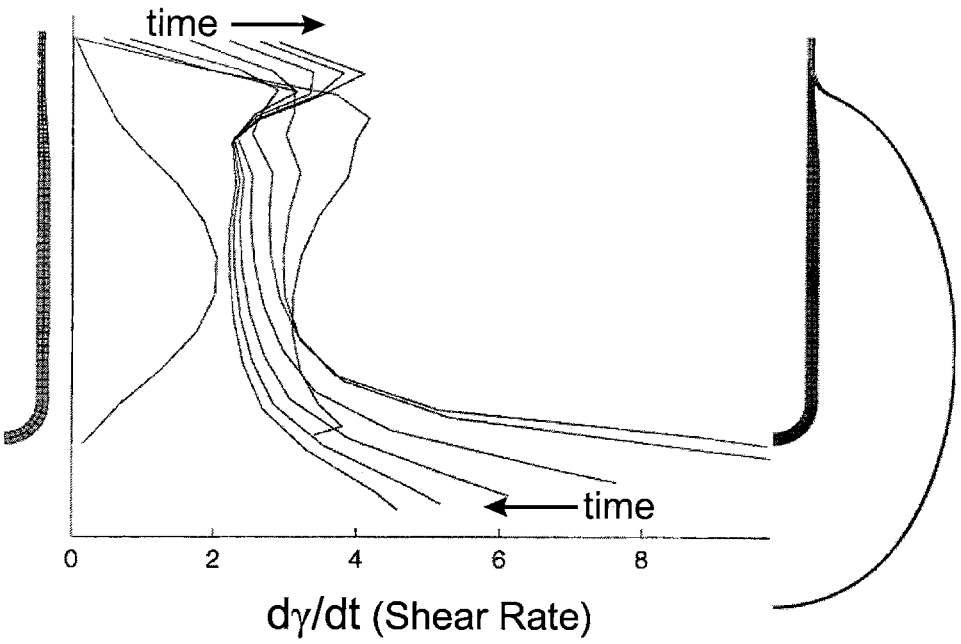

Figure 7-15: Shear rate, temperature profile

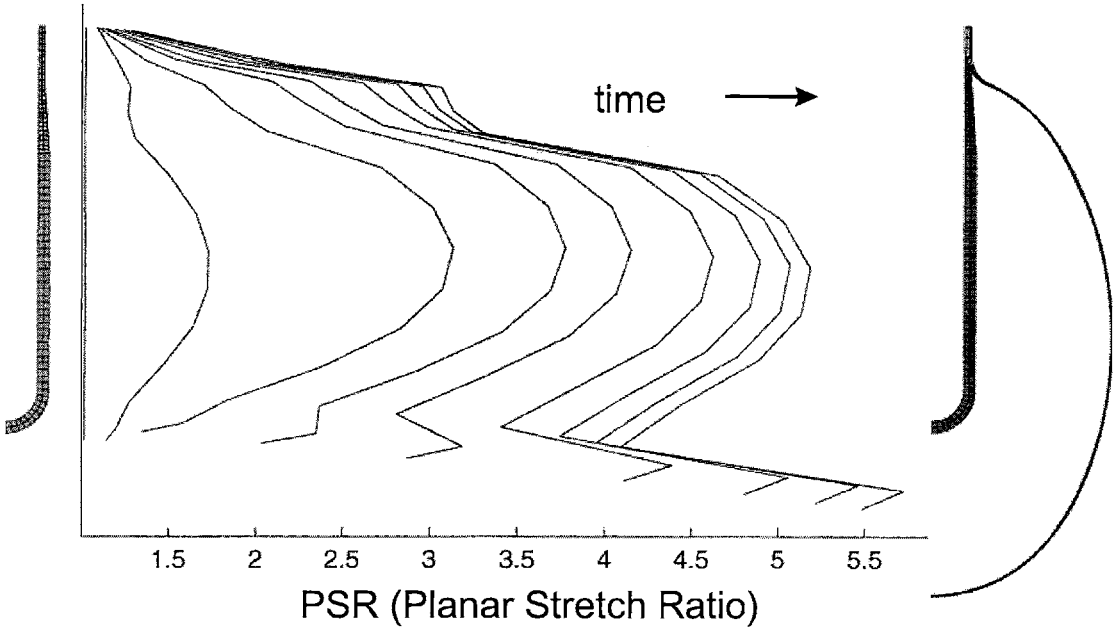

Figure 7-16: Orientation parameter, temperature profile

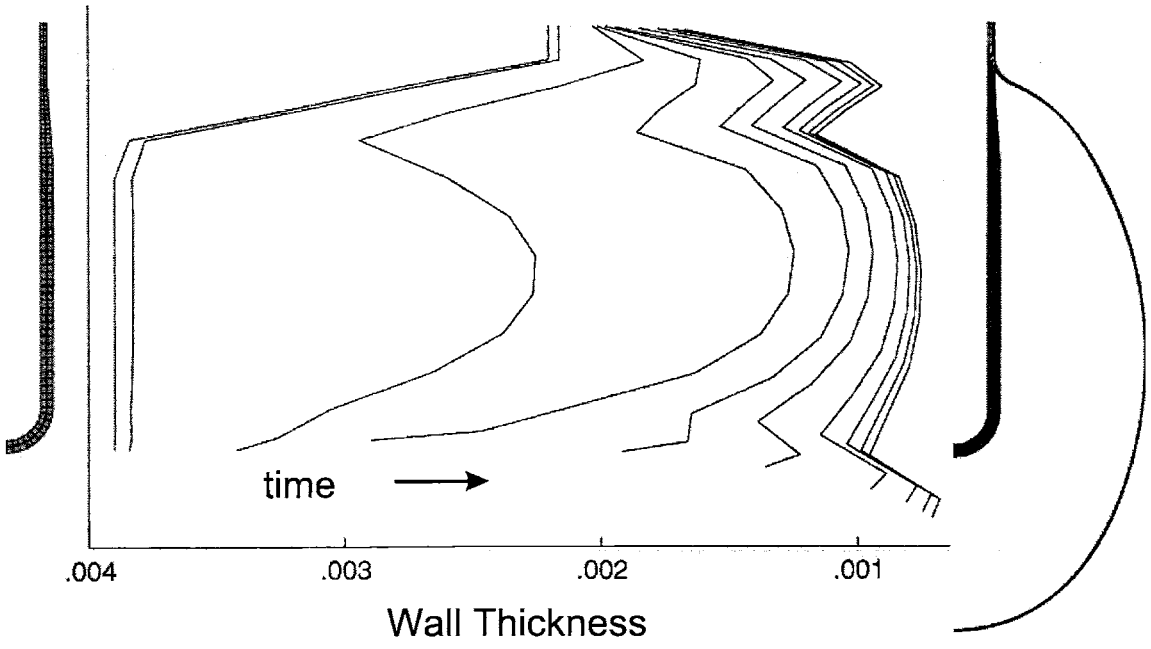

Figure 7-17: Shear rate, temperature profile

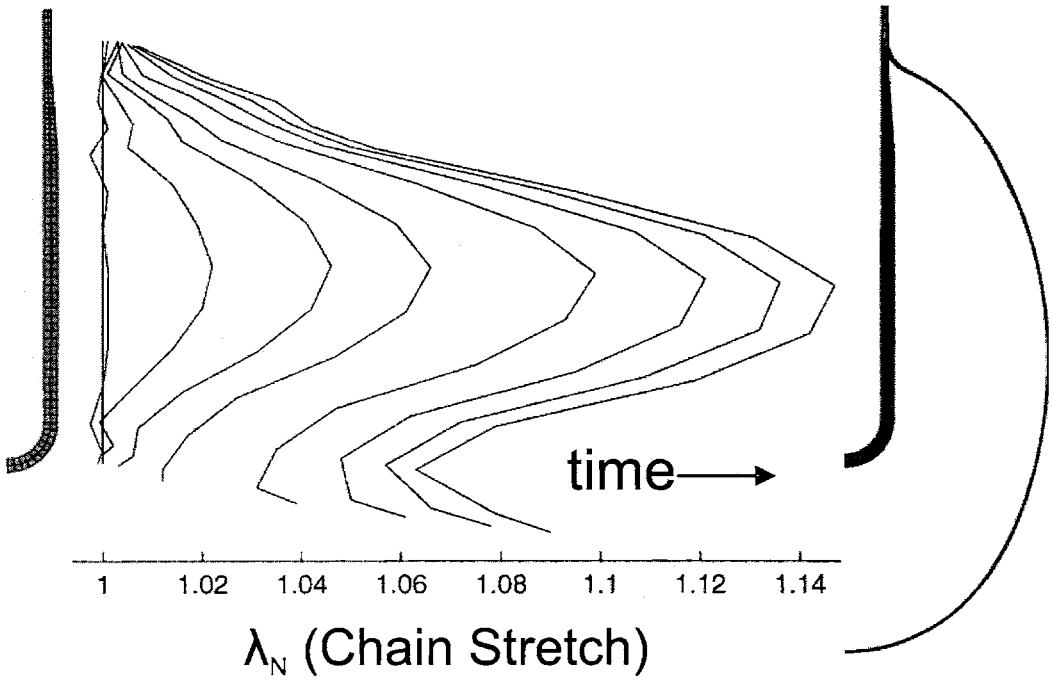

Figure 7-18: Chain Stretch, temperature profile

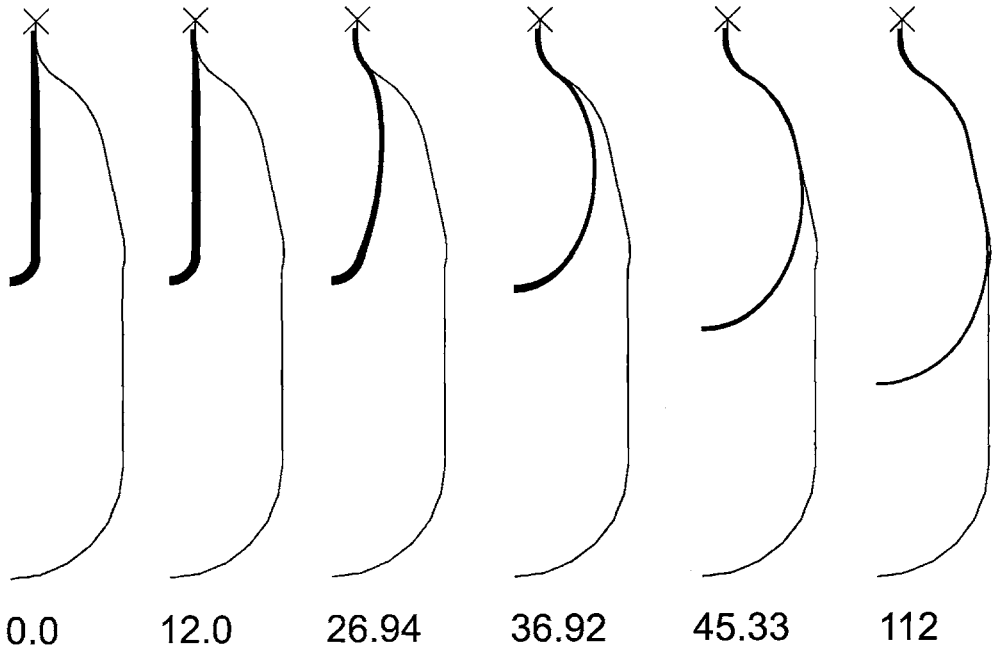

Figure 7-19: Finite element simulation, blowing inside a mold, temperature=90 ° C

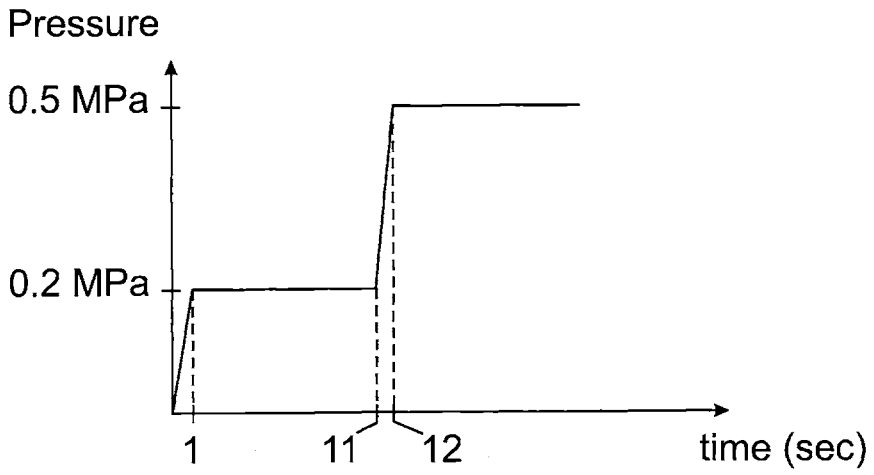

Figure 7-20: Pressure-time curve for the simulation shown in figure 7-19

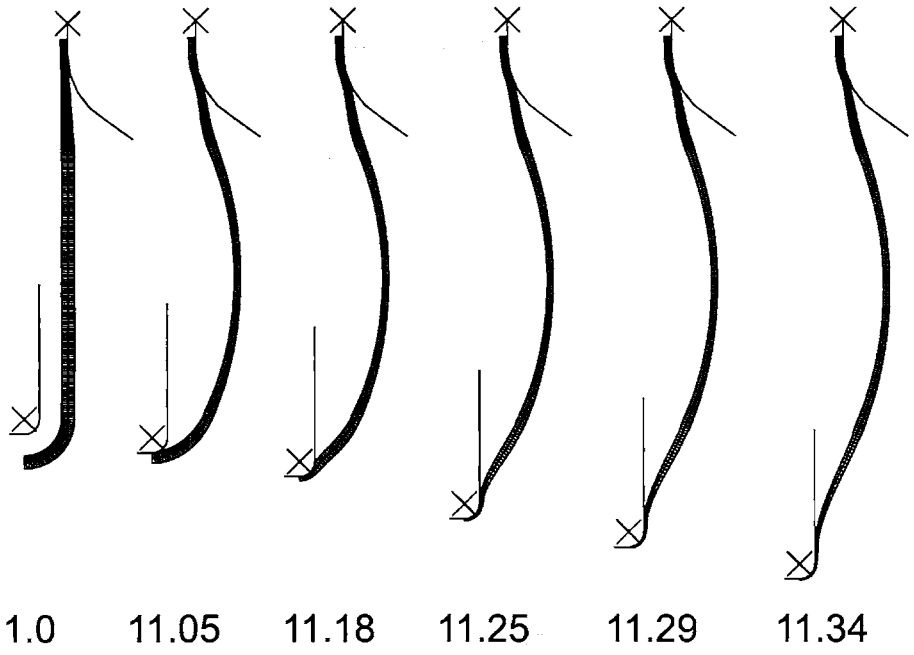

Figure 7-21: Finite element simulation, using an axial stretch rod, temperature profile

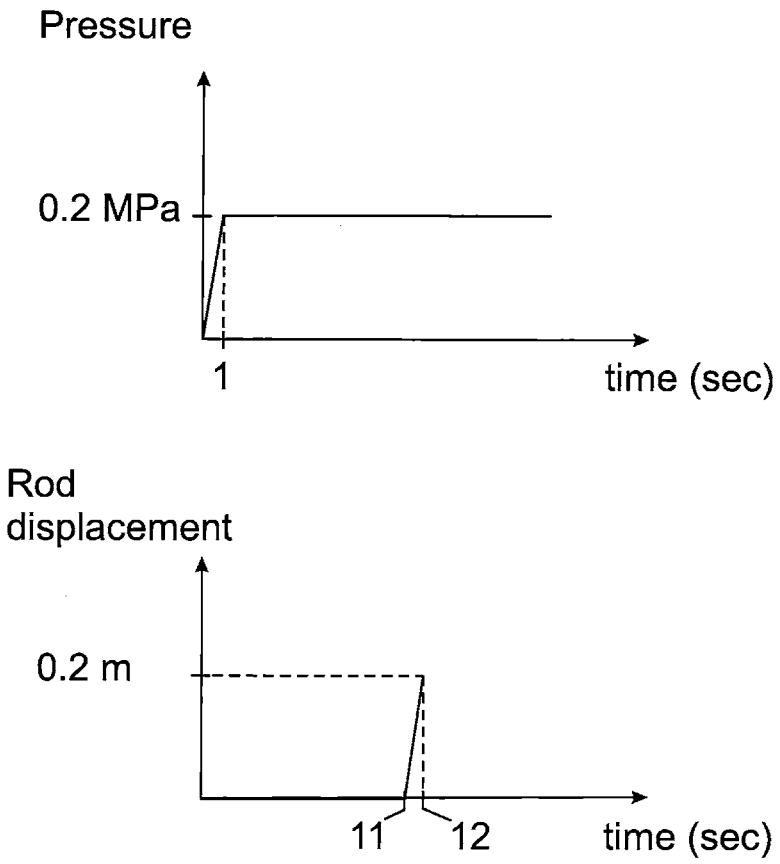

Figure 7-22: Pressure-time curve and displacement-time curve for the simulation shown in figure 7-21

Chapter 8

Conclusions and Future Work

The aim of this work has been to better understand the mechanical behavior of PET above the glass transition temperature. The approach followed was to compare the behavior of PET with PETG, a random amorphous copolymer of PET. While PET crystallizes very easily when deformed at these processing temperatures, PETG is nearly impossible to crystallize. The goal was to be able to isolate the precise effects of crystallization on the stress-strain behavior of PET by comparing the behavior exhibited by the two polymers.

Several important conclusions can be drawn from this work as well as various areas where future work can shed even greater insights. The data gathered and presented in Chapter 2 is one of the first comprehensive collections of data on PETG. The general trends of the stress-strain behavior are characteristic of polymers in the rubbery regime. The stress-strain curves contain four general features: a relatively stiff initial modulus, a rollover to flow at a rather low stress level on the order of 1-2 MPa, a gradual strain hardening at moderate strain levels, and a dramatic upturn in stress at very large strains. Each of these features depends strongly on temperature and strain rate. With increasing temperature of deformation, the initial modulus decreases, the flow stress decreases, the initial hardening modulus decreases, and the strain level at which the dramatic hardening occurs shifts to larger strains. A decrease in strain rate has the same effect on the stress-strain behavior as increasing the temperature. DMA data is used to characterize the effects of strain rate and temperature on the elastic

modulus through the glass transition region. In particular, the rate dependence of the glass transition temperature is found to be an important factor, leading to a sharp increase in modulus at moderately high strain rates. Due to the rates and temperatures used in warm deformation processing of PET, careful modeling of rate dependence near the glass transition is crucial.

State of strain dependence is also investigated by comparing the behavior in uniaxial compression with plane strain compression expreiments. In plane strain compression, the material exhibits a slightly stiffer initial modulus, increased flow stress and increased strain hardening. Also, the dramatic upturn in stress occurs at lower axial strain levels in plane strain compression.

In Chapter 3, the mechanical behavior of PET is investigated in parallel with that of PETG. The same trends exist for PET almost word for word. The same level of dramatic strain hardening exists in both materials, suggesting that a large amount of the strain hardening which occurs in PET is due only to molecular orientation, and not to strain-induced crystallization, as was believed previously. One area where a difference is discernible between the two materials is in plane strain compression, most notably at 90 $^{\circ}$ C. At this temperature, the PET plane strain stress-strain curve rises very abruptly at a strain level of approximately -1.25. This additional strain hardening which is not as evident in PETG is likely due to either a crystallization event, or to a meso-ordering of the PET chain segments which causes the material response to stiffen dramatically.

In Chapter 4 a constitutive model was presented to capture the stress-strain behavior of PETG above the glass transition temperature. This model takes the resistance of the polymer to deformation to consist of two separate resistances which act in parallel: an intermolecular resistance to flow, and a resistance due to stretching and orientation of a molecular network. The intermolecular portion accounts for the initial modulus and rollover to flow at small strains. The network resistance accounts for strain hardening, with a viscous dashpot allowing for molecular relaxation through reptation or chain slip to occur at higher temperatures and lower strain rates. Through developing the model, it was found that the model can only capture the large

strain hardening behavior of PETG by incorporating a criteria to halt the molecular relaxation process once a particular level of stretch or orientation is achieved. This halt to molecular relaxation had previously been observed in PET and was then attributed to the onset of strain-induced crystallization. As this phenomenon is also observed in PETG, it suggests that molecular relaxation can be halted solely by a high degree of molecular order or alignment.

In trying to capture the state of strain dependence of PETG, it is found that previously used models for molecular relaxation were inadequate. To correct for these inadequacies, a new orientation parameter is developed. This orientation parameter is found not only to capture the state of strain dependence of molecular relaxation remarkably well, but also to be an excellent measure of the point at which molecular relaxation ceases. Fitting the model to data for PETG yields the critical value of the orientation parameter where molecular relaxation ceases to be 2.9 degrees (.05 rad). This critical value is found to be independent of rate, temperature, and strain state, further motivating the conclusion that this parameter is physically related to the orientation of the molecular network and is in fact a key variable in the mechanism of molecular relaxation. The orientation parameter developed here is qualitatively related to other orientation factors used in polymer physics, such as the Hermans orientation function. Quantitatively, there are some differences, as was noted in section 4.5.2, as this model follows the trend of a pseudo-affine model. Future work can further investigate the relation between the orientation parameter developed in this work and other, more experimentally-based measures of orientation.

Parallels are also drawn between the newly proposed molecular relaxation model and the original Doi-Edwards reptation model, an effort which forms the basis for the start of a link between the often disconnected branches of polymer solid mechanics and polymer fluid mechanics. Differences are identified between the Doi-Edwards model and the proposed molecular relaxation model and it is suggested that the discrepancies could be overcome by using newer reptation models, such as that of Marrucci and Ianniruberto (?) which incorporate effects of chain stretching on the polymer viscosity. Future work is needed in this area.

In comparing the constitutive model results with experimental results, an error parameter has been defined to quantify the level of agreement between simulation and experiment. This error parameter is easy to compute and can be an aid in evaluating whether one model is better than another at capturing a particular set of data. An additional use for this parameter is in understanding the range of use for a particular model. If error values are plotted against temperature, strain rate, etc. the designer can easily see where the model error exceeds a preset tolerance. If it is determined that the model is not sufficiently precise in the operating range for a particular process, the designer can then either look for a different model or recompute the fitting parameters so that the error is lower in that strain rate and temperature regime.

Chapter 5 extends the model to PET. It is found that only two of the material constants need to be varied in order to capture the behavior of PET quite successfully over the temperature range and strain rate regimes tested. The two material constants are those related to the temperature dependence of molecular relaxation. One area where the model is unable to fully capture the behavior of PET is at very large strains in plane strain compression. This is to be expected since this is where the experimental data of PET deviated from the behavior observed for PETG. It is suggested that the discrepancy is only evident in plane strain compression since in this deformation mode, the molecules all become oriented in a uniaxial manner, thus facilitating formation of a meso-ordered structure.

Initial blow molding simulations are performed to look at how temperature affects such parameters as wall thickness, orientation parameter, planar stretch ratio, chain stretch, and plastic shear rate. It is anticipated that the model can be used to investigate additional parameters and to perform a complete parametric study of the blow molding process.

Future experimental work centering around comparing the behavior of PET and PETG in biaxial extension should prove valuable. In the preliminary experiments conducted here, it appears that there is more difference between the materials in tension than in compression, but it is unclear whether this is due to a difference in

the inherent pressure dependence of the stress-strain behavior of the two materials, or if it is instead due to a different fracture toughness between the two materials, causing PETG to fracture before dramatic hardening can be seen. Additional experiments which take in-situ measurments of structural properties (such as crystallinity and birefringence) would be helpful to better understand these differences. In-situ experiments could also further validate the conclusions drawn here in which strain hardening in these materials is related primarily to the development of molecular orientation rather than to strain-induced crystallization.

Additionally, in compression experiments, final strains are limited by the experimental setup to true strains of -2.0 in uniaxial compression and to -1.3 in plane strain compression. These values correspond to biaxial planar stretch ratios ($\lambda_1 \times \lambda_2$) of 7.39 and 3.67, respectively. In biaxial extension, on the other hand, dramatic strain hardening does not begin to appear until the material reaches a planar stretch ratio on the order of 9.0 and even higher stretch ratios are seen in processes. In stretch blow molding of PET, for example, planar stretch ratios are on the order of 11.0. Future work should investigate ways to obtain compression data to larger strains to determine whether sharp, dramatic hardening as seen in plane strain compression can also be achieved in uniaxial compression experiments.

Future modeling work can be done to address incorporation of strain induced crystallization upon unloading of the material, or after a brief halt in deformation. This will likely give improvements in blow molding simulations, as during these processes flow may momentarily stop at various locations along the bottle when deformation propagates to another region. Additionally, the incorporation of an anisotropic 8-chain model in Chapter 6 can be extended to tie in with other work, such as in the field of biological materials. Biological materials are particularly challenging to model due to the evolution of their natural states (due to growth, for example). It is hoped that the approach taken in Chapter 6, where the natural state of the polymer was made to evolve and become anisotropic with deformation (thus influencing the final state and mechanical properties of the material) could be extended to model more complicated problems with evolving natural states.

Appendix A

Mathematical details of the averaging required for the Doi-Edwards Model

Using the coordinate system shown in figure A-1 we have:

$$\begin{aligned} u_x &= \sin\theta\cos\phi \\ u_y &= \sin\theta\sin\phi \\ u_z &= \cos\theta \end{aligned}$$

and equation 4.59 becomes:

$$\begin{aligned} Q_{zz} - Q_{xx} &= \int\int \frac{1}{4\pi}\sin\theta \frac{\lambda^2\cos^2\theta - \frac{1}{\lambda}\sin^2\theta\cos^2\phi}{\lambda^2\cos^2\theta + \frac{1}{\lambda}[(\sin\theta\sin\phi)^2 + (\sin\theta\cos\phi)^2]} d\phi d\theta \\ &= \int_0^{\pi}\int_0^{2\pi} \frac{1}{4\pi}\sin\theta \frac{\lambda^3\cos^2\theta - \sin^2\theta\cos^2\phi}{\lambda^3\cos^2\theta + \sin^2\theta} d\phi d\theta \\ &= \int_0^{\pi} \frac{1}{4\pi}\sin\theta \frac{1}{\lambda^3\cos^2\theta + \sin^2\theta}\Big[\int_0^{2\pi} \lambda^3\cos^2\theta \\ &\qquad - \sin^2\theta\cos^2\phi d\phi\Big] d\theta \\ &= \int_0^{\pi} \frac{1}{4\pi}\sin\theta \frac{1}{\lambda^3\cos^2\theta + \sin^2\theta}\Big[(\lambda^3\cos^2\theta)\phi \\ &\qquad - [\frac{1}{2}(\sin^2\theta)\phi + \frac{1}{4}\sin^2\theta\sin 2\phi]\Big]_{\phi=0}^{\phi=2\pi} d\theta \end{aligned}$$

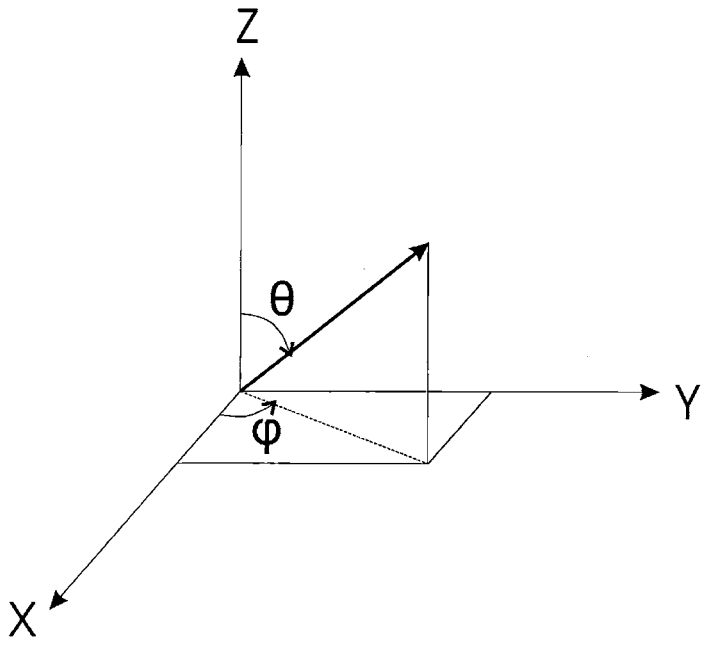

Figure A-1: Coordinate system for polar angle conversion

$$
\begin{aligned}
&= \int_0^{\pi} \frac{1}{2} \sin\theta \frac{\lambda^3 \cos^2\theta - \frac{1}{2}\sin^2\theta}{\lambda^3 \cos^2\theta + \sin^2\theta} d\theta \\
&= \frac{1}{4} \int_0^{\pi} \frac{2\lambda^3 \cos^2\theta - \sin^2\theta}{\lambda^3 \cos^2\theta + \sin^2\theta} \sin\theta d\theta \\
&= \frac{1}{4} \int_0^{\pi} \frac{2\lambda^3 \cos^2\theta - (1 - \cos^2\theta)}{\lambda^3 \cos^2\theta + (1 - \cos^2\theta)} \sin\theta d\theta \\
&= \frac{1}{4} \int_0^{\pi} \frac{\cos^2\theta(2\lambda^3 + 1) - 1}{\cos^2\theta(\lambda^3 - 1) + 1} \sin\theta d\theta
\end{aligned} \tag{A.1}
$$

Using the following substitution

$$
\begin{aligned}
w &= \cos\theta \\
dw &= -\sin\theta d\theta \\
w &= 1 \text{ when } \theta = 0 \\
w &= -1 \text{ when } \theta = \pi
\end{aligned}
$$

we obtain:

$$\begin{aligned} Q_{zz} - Q_{xx} &= -\frac{1}{4}\int_{1}^{-1} \frac{u^2(2\lambda^3+1)-1}{u^2(\lambda^3-1)+1} du \\ &= \frac{1}{4}\int_{-1}^{1} \frac{u^2(2\lambda^3+1)-1}{u^2(\lambda^3-1)+1} du \\ &= \frac{1}{4}\int_{-1}^{1} \frac{u^2(2\lambda^3+1)}{u^2(\lambda^3-1)+1} du - \frac{1}{4}\int_{-1}^{1} \frac{1}{u^2(\lambda^3-1)+1} du \end{aligned} \tag{A.2}$$

The solution to this problem will fall into three categories: (1) $\lambda^3 - 1 < 0$, (2) $\lambda^3 - 1 = 0$, and (3) $\lambda^3 - 1 > 0$, each of which will be solved separately

Case 1: $\lambda^3 - 1 < 0$

It is helpful to recall from calculus:

$$\int \frac{du}{1-u^2} = \tanh^{-1} u + C \ , \ |u| < 1 \tag{A.3}$$

Now the second term of equation A.2 is,

$$\begin{aligned} \int \frac{1}{1+w^2(\lambda^3-1)} dw &= \int \frac{1}{1-w^2(1-\lambda^3)} dw \\ &= \frac{\tanh^{-1}(w\sqrt{1-\lambda^3})}{\sqrt{1-\lambda^3}} \end{aligned} \tag{A.4}$$

For the first term,

$$\begin{aligned} \int \frac{w^2(2\lambda^3+1)}{1+w^2(\lambda^3-1)} dw &= \int \frac{w^2(2\lambda^3+1)}{1-w^2(1-\lambda^3)} dw \\ &= \frac{2\lambda^3+1}{(1-\lambda^3)} \int \frac{(1-\lambda^3)w^2}{1-w^2(1-\lambda^3)} dw \end{aligned} \tag{A.5}$$

Substitute

$$\begin{aligned} w\sqrt{1-\lambda^3} &= \tanh\phi \\ \sqrt{1-\lambda^3} dw &= \operatorname{sech}^2\phi \, d\phi \\ 1 - w^2(1-\lambda^3) &= 1 - \tanh^2\phi = \operatorname{sech}^2\phi \end{aligned}$$

and equation A.5 becomes

$$\begin{aligned}
\int \frac{w^2(2\lambda^3+1)}{1+w^2(\lambda^3-1)}dw &= \int \frac{2\lambda^3+1}{(1-\lambda^3)\sqrt{1-\lambda^3}}\frac{\tanh^2\phi}{\operatorname{sech}^2\phi}\operatorname{sech}^2\phi\, d\phi \\
&= \frac{2\lambda^3+1}{(1-\lambda^3)\sqrt{1-\lambda^3}}\int \tanh^2\phi\, d\phi \\
&= \frac{2\lambda^3+1}{(1-\lambda^3)\sqrt{1-\lambda^3}}(\phi-\tanh\phi) \\
&= \frac{2\lambda^3+1}{(1-\lambda^3)\sqrt{1-\lambda^3}}\Big(\tanh^{-1}(w\sqrt{1-\lambda^3}) \\
&\qquad - w\sqrt{1-\lambda^3}\Big) \qquad \text{(A.6)}
\end{aligned}$$

Combining,

$$\begin{aligned}
Q_{zz}-Q_{xx} &= \frac{1}{4}\Bigg[\frac{2\lambda^3+1}{(1-\lambda^3)\sqrt{1-\lambda^3}}\Big(\tanh^{-1}(w\sqrt{1-\lambda^3})-w\sqrt{1-\lambda^3}\Big) \\
&\qquad - \frac{\tanh^{-1}(w\sqrt{1-\lambda^3})}{\sqrt{1-\lambda^3}}\Bigg]_{-1}^{1} \\
&= \frac{1}{2}\Bigg[\frac{2\lambda^3+1}{(1-\lambda^3)\sqrt{1-\lambda^3}}\Big(\tanh^{-1}\sqrt{1-\lambda^3}-\sqrt{1-\lambda^3}\Big) \\
&\qquad - \frac{\tanh^{-1}\sqrt{1-\lambda^3}}{\sqrt{1-\lambda^3}}\Bigg] \\
&= \frac{1}{2}\frac{(2\lambda^3+1)-(1-\lambda^3)}{(1-\lambda^3)\sqrt{1-\lambda^3}}\tanh^{-1}\sqrt{1-\lambda^3}-\frac{\lambda^3+\frac{1}{2}}{1-\lambda^3} \\
&= \frac{1}{2}\frac{3\lambda^3}{(1-\lambda^3)\sqrt{1-\lambda^3}}\tanh^{-1}\sqrt{1-\lambda^3}-\frac{\lambda^3+\frac{1}{2}}{1-\lambda^3} \\
&= \frac{3}{2}\frac{\lambda^3}{1-\lambda^3}\left(\frac{\tanh^{-1}(\sqrt{1-\lambda^3})}{\sqrt{1-\lambda^3}}\right)-\frac{\lambda^3+\frac{1}{2}}{1-\lambda^3} \\
&= \frac{3}{2}\frac{\lambda^3}{1-\lambda^3}\left(\frac{\tanh^{-1}(\sqrt{1-\lambda^3})}{\sqrt{1-\lambda^3}}-1\right)+\frac{\frac{3}{2}\lambda^3}{1-\lambda^3}-\frac{\lambda^3+\frac{1}{2}}{1-\lambda^3} \\
Q_{zz}-Q_{xx} &= \frac{3}{2}\frac{\lambda^3}{1-\lambda^3}\left(\frac{\tanh^{-1}(\sqrt{1-\lambda^3})}{\sqrt{1-\lambda^3}}-1\right)-\frac{1}{2} \qquad \text{(A.7)}
\end{aligned}$$

Case 2: $\lambda^3 - 1 = 0$

The two terms in equation A.2 become simply

$$\int \frac{1}{w^2(\lambda^3-1)+1} dw = \int dw = w \tag{A.8}$$

$$\int \frac{w^2(2\lambda^3+1)}{w^2(\lambda^3-1)+1)} dw = \int 3w^2 dw = w^3 \tag{A.9}$$

Evaluating the limits of the integral, we obtain

$$\begin{aligned} Q_{zz} - Q_{xx} &= \frac{1}{4}w^3 - \frac{1}{4}w\Big|_{-1}^{1} = \frac{1}{4} - \frac{1}{4} - \left(-\frac{1}{4} + \frac{1}{4}\right) = 0 \\ Q_{zz} - Q_{xx} &= 0 \end{aligned} \tag{A.10}$$

Case 3: $\lambda^3 - 1 > 0$

Recall from calculus:

$$\int \frac{du}{1+u^2} = \tan^{-1} u + C \tag{A.11}$$

The second term of equation A.2 is,

$$\int \frac{1}{w^2(\lambda^3-1)+1} dw = \frac{\tan^{-1}(w\sqrt{\lambda^3-1})}{\sqrt{\lambda^3-1}} \tag{A.12}$$

For the first term,

$$\int \frac{w^2(2\lambda^3+1)}{w^2(\lambda^3-1)+1} dw = \frac{2\lambda^3+1}{\lambda^3-1} \int \frac{w^2(\lambda^3-1)}{w^2(\lambda^3-1)+1} dw \tag{A.13}$$

Substitute

$$\begin{aligned} w\sqrt{\lambda^3-1} &= \tan\phi \\ \sqrt{\lambda^3-1}\, dw &= \sec^2\phi \, d\phi \\ 1 + w^2(\lambda^3-1) &= 1 + \tan^2\phi = \sec^2\phi \end{aligned}$$

$$\begin{aligned}
\int \frac{w^2(2\lambda^3+1)}{w^2(\lambda^3-1)+1}dw &= \int \frac{2\lambda^3+1}{(\lambda^3-1)\sqrt{\lambda^3-1}}\frac{\tan^2\phi}{\sec^2\phi}\sec^2\phi\, d\phi \\
&= \frac{2\lambda^3+1}{(\lambda^3-1)\sqrt{\lambda^3-1}}\int \tan^2\phi\, d\phi \\
&= \frac{2\lambda^3+1}{(\lambda^3-1)\sqrt{\lambda^3-1}}(\tan\phi-\phi) \\
&= \frac{2\lambda^3+1}{(\lambda^3-1)\sqrt{\lambda^3-1}}\Big(w\sqrt{\lambda^3-1} \\
&\qquad -\tan^{-1}(w\sqrt{\lambda^3-1})\Big) \qquad \text{(A.14)}
\end{aligned}$$

$$\begin{aligned}
Q_{zz}-Q_{xx} &= \frac{1}{4}\Bigg[\frac{2\lambda^3+1}{(\lambda^3-1)\sqrt{\lambda^3-1}}\Big(w\sqrt{\lambda^3-1}-\tan^{-1}(w\sqrt{\lambda^3-1})\Big) \\
&\qquad -\frac{\tan^{-1}(w\sqrt{\lambda^3-1})}{\sqrt{\lambda^3-1}}\Bigg]_{-1}^{1} \\
&= \frac{1}{2}\Bigg[\frac{2\lambda^3+1}{(\lambda^3-1)\sqrt{\lambda^3-1}}\Big(\sqrt{\lambda^3-1}-\tan^{-1}\sqrt{\lambda^3-1}\Big) \\
&\qquad -\frac{\tan^{-1}\sqrt{\lambda^3-1}}{\sqrt{\lambda^3-1}}\Bigg] \\
&= \frac{\lambda^3+\frac{1}{2}}{\lambda^3-1}-\frac{1}{2}\frac{(2\lambda^3+1)+(\lambda^3-1)}{(\lambda^3-1)\sqrt{\lambda^3-1}}\tan^{-1}\sqrt{\lambda^3-1} \\
&= \frac{\lambda^3+\frac{1}{2}}{\lambda^3-1}-\frac{1}{2}\frac{3\lambda^3}{(\lambda^3-1)\sqrt{\lambda^3-1}}\tan^{-1}\sqrt{\lambda^3-1} \\
&= \frac{3}{2}\frac{\lambda^3}{\lambda^3-1}\left(-\frac{\tan^{-1}(\sqrt{\lambda^3-1})}{\sqrt{\lambda^3-1}}\right)+\frac{\lambda^3+\frac{1}{2}}{\lambda^3-1} \\
&= \frac{3}{2}\frac{\lambda^3}{\lambda^3-1}\left(1-\frac{\tan^{-1}(\sqrt{\lambda^3-1})}{\sqrt{\lambda^3-1}}\right)-\frac{\frac{3}{2}\lambda^3}{\lambda^3-1}+\frac{\lambda^3+\frac{1}{2}}{\lambda^3-1} \\
Q_{zz}-Q_{xx} &= \frac{3}{2}\frac{\lambda^3}{\lambda^3-1}\left(1-\frac{\tan^{-1}(\sqrt{\lambda^3-1})}{\sqrt{\lambda^3-1}}\right)-\frac{1}{2} \qquad \text{(A.15)}
\end{aligned}$$

The expressions which have been derived for $Q_{zz}-Q_{xx}$ in equations A.7, A.10, and A.15 are the same as those found in reference (Doi and Edwards 1978).

Appendix B

Derivative of the Strain-Energy Function

We start with the strain energy function for the anisotropic 8-chain model (refer to Eqn. 6.8),

$$W(\mathbf{x}) = W_0 + \frac{\nu k\theta}{4}\left(N\sum_{i=1}^{4}\left[\frac{\rho^{(i)}}{N}\beta_\rho^{(i)} + \ln\frac{\beta_\rho^{(i)}}{\sinh\beta_\rho^{(i)}}\right] - \frac{\beta_P}{\sqrt{N}}\ln\lambda_a^{a^2}\lambda_b^{b^2}\lambda_c^{c^2}\right) \tag{B.1}$$

Note that the deformed length of chain i, $\rho^{(i)}$, is defined as:

$$\rho^{(i)} = \sqrt{\mathbf{P}^{(i)T}\cdot\mathbf{C}\cdot\mathbf{P}^{(i)}} \tag{B.2}$$

which can be expressed in indicial notation as

$$\begin{aligned}\rho^{(i)} &= \sqrt{P_l^{(i)}C_{lm}P_m^{(i)}} \\ &= \sqrt{P_l^{(i)}[2E_{lm}+\delta_{lm}]P_m^{(i)}}\end{aligned} \tag{B.3}$$

with summation over l and m implied and δ_{lm} representing the Kronecker delta:

$$\delta_{lm} = \begin{cases} 1 & : \quad l = m \\ 0 & : \quad l \neq m \end{cases} \tag{B.4}$$

Differentiating Eqn. B.3 with respect to E_{jk} yields:

$$\begin{aligned}\frac{\partial \rho^{(i)}}{\partial E_{jk}} &= \frac{P_l^{(i)} P_m^{(i)}}{2\sqrt{P_l^{(i)}[2E_{lm}+\delta_{lm}]P_m^{(i)}}} \frac{\partial}{\partial E_{jk}}(2E_{lm}+\delta_{lm}) \\ &= \frac{1}{2\rho^{(i)}} P_l^{(i)} P_m^{(i)} \times 2\delta_{lj}\delta_{mk} \\ &= \frac{P_j^{(i)} P_k^{(i)}}{\rho^{(i)}} \end{aligned} \tag{B.5}$$

Also, the stretch in the **a**-direction, λ_a, is defined as:

$$\lambda_a = \sqrt{\mathbf{a}^T \cdot \mathbf{C} \cdot \mathbf{a}} \tag{B.6}$$

and by the same process as above, we obtain:

$$\frac{\partial \lambda_a}{\partial E_{jk}} = \frac{a_j a_k}{\lambda_a} \tag{B.7}$$

To evaluate $\partial W/\partial E_{jk}$, we take one term at a time. As W_0 is a constant, the derivative of the first term in Eqn. B.1 is 0. From the second term, we obtain by the product rule:

$$\begin{aligned}\frac{\partial}{\partial E_{jk}}\left(\frac{\rho(i)}{N}\beta_\rho^{(i)}\right) &= \frac{1}{N}\left[\rho^{(i)}\frac{\partial \beta_\rho^{(i)}}{\partial E_{jk}} + \frac{\partial \rho^{(i)}}{\partial E_{jk}}\beta_\rho^{(i)}\right] \\ &= \frac{\rho^{(i)}}{N}\frac{\partial \beta_\rho^{(i)}}{\partial E_{jk}} + \frac{\beta_\rho^{(i)}}{N}\frac{P_j^{(i)} P_k^{(i)}}{\rho^{(i)}} \end{aligned} \tag{B.8}$$

From the third term, using the chain rule:

$$\begin{aligned}\frac{\partial}{\partial E_{jk}}\left(\ln\frac{\beta_\rho^{(i)}}{\sinh\beta_\rho^{(i)}}\right) &= \frac{\sinh\beta_\rho^{(i)}}{\beta_\rho^{(i)}} \times \frac{\partial}{\partial E_{jk}}\left(\frac{\beta_\rho^{(i)}}{\sinh\beta_\rho^{(i)}}\right) \\ &= \frac{\sinh\beta_\rho^{(i)}}{\beta_\rho^{(i)}} \times \frac{\sinh\beta_\rho^{(i)}\frac{\partial\beta_\rho^{(i)}}{\partial E_{jk}} - \beta_\rho^{(i)}\cosh\beta_\rho^{(i)}\frac{\partial\beta_\rho^{(i)}}{\partial E_{jk}}}{\sinh^2\beta_\rho^{(i)}} \\ &= \frac{\partial\beta_\rho^{(i)}}{\partial E_{jk}}\left[\frac{1}{\beta_\rho^{(i)}} - \coth\beta_\rho^{(i)}\right] \end{aligned}$$

$$
\begin{aligned}
&= -\frac{\partial \beta_\rho^{(i)}}{\partial E_{jk}} \mathscr{L}\left(\beta_\rho^{(i)}\right) \\
&= -\frac{\partial \beta_\rho^{(i)}}{\partial E_{jk}} \frac{\rho^{(i)}}{N}
\end{aligned} \tag{B.9}
$$

Combining Eqns. B.8 and B.9:

$$
\frac{\partial}{\partial E_{jk}}\left(\frac{\rho(i)}{N}\beta_\rho^{(i)} - \ln\frac{\beta_\rho^{(i)}}{\sinh\beta_\rho^{(i)}}\right) = \frac{\beta_\rho^{(i)}}{N}\frac{P_j^{(i)}P_k^{(i)}}{\rho^{(i)}} \tag{B.10}
$$

From the last term in Eqn. B.1:

$$
\begin{aligned}
\frac{\partial}{\partial E_{jk}}\left(\frac{\beta_P}{\sqrt{N}}\ln\left[\lambda_a^{a^2}\lambda_b^{b^2}\lambda_c^{c^2}\right]\right) &= \frac{\beta_P}{\sqrt{N}}\frac{1}{\lambda_a^{a^2}\lambda_b^{b^2}\lambda_c^{c^2}} \\
&\quad \times\left[a^2\lambda_a^{a^2-1}\frac{\partial\lambda_a}{\partial E_{jk}}\lambda_b^{b^2}\lambda_c^{c^2}\right. \\
&\quad + b^2\lambda_b^{b^2-1}\frac{\partial\lambda_b}{\partial E_{jk}}\lambda_a^{a^2}\lambda_c^{c^2} \\
&\quad \left. + c^2\lambda_c^{c^2-1}\frac{\partial\lambda_c}{\partial E_{jk}}\lambda_a^{a^2}\lambda_b^{b^2}\right] \\
&= \frac{\beta_P}{\sqrt{N}}\left[\frac{a^2}{\lambda_a}\frac{\partial\lambda_a}{\partial E_{jk}} + \frac{b^2}{\lambda_b}\frac{\partial\lambda_b}{\partial E_{jk}} + \frac{c^2}{\lambda_c}\frac{\partial\lambda_c}{\partial E_{jk}}\right] \\
&= \frac{\beta_P}{\sqrt{N}}\left[\frac{a^2}{\lambda_a}a_j a_k + \frac{b^2}{\lambda_b}b_j b_k + \frac{c^2}{\lambda_c}c_j c_k\right]
\end{aligned} \tag{B.11}
$$

Combining Equations B.10 and B.11 yields

$$
\frac{\partial W}{\partial E_{jk}} = \frac{\nu k\theta}{4}\left[\sum_{i=1}^{4}\frac{P_j^{(i)}P_k^{(i)}}{\rho^{(i)}}\beta_\rho^{(i)} - \frac{\beta_P}{\sqrt{N}}\left(\frac{a^2}{\lambda_a^2}a_j a_k + \frac{b^2}{\lambda_b^2}b_j b_k + \frac{c^2}{\lambda_c^2}c_j c_k\right)\right] \tag{B.12}
$$

which is the same as Equation 6.9.

Appendix C

Time-integration Procedure for the Constitutive Model

This appendix summarizes the time-integration procedure which is used to incorporate the constitutive model into a finite element analysis.

(1) From the current time step the following quantities are known: $\mathbf{F}(t)$, $\mathbf{F}_A^p(t)$, $\mathbf{F}_B^F(t)$, $\dot{\mathbf{F}}_A^p(t)$, $\dot{\mathbf{F}}_B^F(t)$, $\dot{\gamma}_A^p(t)$, and $\dot{\gamma}_B^F(t)$.

(2) The following are given by the finite element routine for the new time step: $\mathbf{F}(\tau)$,Δt, and the quantity $(t + \Delta t)$ will be denoted by τ.

(3) The following quantities need to be calculated for the new time step: $\mathbf{T}(\tau)$, $\mathbf{T}_A(\tau)$, $\mathbf{T}_B(\tau)$, $\mathbf{F}_A^p(\tau)$, $\mathbf{F}_B^F(\tau)$, $\dot{\mathbf{F}}_A^p(\tau)$, $\dot{\mathbf{F}}_B^F(\tau)$, $\dot{\gamma}_A^p(\tau)$, and $\dot{\gamma}_B^F(\tau)$.

Resistance A

(1) The plastic deformation gradient is updated explicitly:

$$\mathbf{F}_A^p(\tau) = \mathbf{F}_A^p(t) + \dot{\mathbf{F}}_A^p(t)\Delta t \tag{C.1}$$

(2) Since $\mathbf{F}(\tau) = \mathbf{F}_A(\tau) = \mathbf{F}_B(\tau)$ the elastic deformation gradient is computed as:

$$\mathbf{F}_A^e(\tau) = \mathbf{F}(\tau)(\mathbf{F}_A^p(\tau))^{-1} \tag{C.2}$$

(3) Using the polar decomposition,

$$\mathbf{V}_A^e(\tau) = \mathbf{F}_A^e(\tau)(\mathbf{R}_A^e(\tau))^{-1} \tag{C.3}$$

(4) The Cauchy stress is then:

$$\mathbf{T}_A(\tau) = \frac{1}{J_A(\tau)} \mathscr{L}^e[\ln \mathbf{V}_A^e(\tau)] \tag{C.4}$$

with

$$J_A(\tau) = \det \mathbf{F}_A^e(\tau) \tag{C.5}$$

The material constants in the fourth-order tensor of elastic constants ($\mathscr{L}^e$) are determined from equations 4.26 and 4.28, using $\dot{\gamma}_A^p(t)$ to calculate θ_g.

(5) The shear stress is:

$$\tau_A(\tau) = \left[\frac{1}{2}\mathbf{T}'_A(\tau)\mathbf{T}'_A(\tau)\right]^{1/2} \tag{C.6}$$

$$\mathbf{N}_A(\tau) = \frac{1}{\sqrt{2}\tau_A(\tau)}\mathbf{T}'_A(\tau) \tag{C.7}$$

where $\mathbf{T}'_A(\tau)$ is the deviatoric portion of $\mathbf{T}_A(\tau)$.

(6) From the flow rule:

$$\dot{\gamma}_A^p(\tau) = \dot{\gamma}_{0A} \exp\left[-\frac{\Delta G(1 - \tau_A(\tau)/s)}{k\theta}\right] \tag{C.8}$$

(7) If the plastic shear rate has changed too much (i.e. if the ratio $\dot{\gamma}_A^p(\tau)/\dot{\gamma}_A^p(t)$ differs greatly from 1.0), then the increment is repeated with a smaller time step.

(8) Provided the change in $\dot{\gamma}_A^p$ is not too great, the rate of stretching is calculated as

$$\tilde{\mathbf{D}}_A^p(\tau) = \dot{\gamma}_A^p(\tau)\mathbf{N}_A(\tau) \tag{C.9}$$

with

$$\mathbf{L}_A = \dot{\mathbf{F}}_A^e\mathbf{F}_A^{e-1} + \mathbf{F}_A^e\dot{\mathbf{F}}_A^p\mathbf{F}_A^{-1} = \mathbf{L}_A^e + \tilde{\mathbf{L}}_A^p \tag{C.10}$$

$$\tilde{\mathbf{L}}_A^p = \tilde{\mathbf{D}}_A^p + \tilde{\mathbf{W}}_A^p \tag{C.11}$$

and prescribing $\tilde{\mathbf{W}}_A^p = 0$, we obtain $\dot{\mathbf{F}}_A^p(\tau)$:

$$\dot{\mathbf{F}}_A^p(\tau) = (\mathbf{F}_A^e(\tau))^{-1}\tilde{\mathbf{D}}_A^p(\tau)\mathbf{F}_A(\tau) \tag{C.12}$$

Resistance B

(1) The plastic deformation gradient is updated explicitly:

$$\mathbf{F}_B^F(\tau) = \mathbf{F}_B^F(t) + \dot{\mathbf{F}}_B^F(t)\Delta t \tag{C.13}$$

(2) The elastic deformation gradient is then computed as:

$$\mathbf{F}_B^N(\tau) = \mathbf{F}(\tau)(\mathbf{F}_B^F(\tau))^{-1} \tag{C.14}$$

(3) The following quantities are needed to calculate the stress:

$$J_B(\tau) = \det \mathbf{F}_B^N(\tau) \tag{C.15}$$

$$\bar{\mathbf{F}}_B^N(\tau) = (J_B(\tau))^{-1/3}\mathbf{F}_B^N(\tau) \tag{C.16}$$

$$\bar{\mathbf{B}}^N(\tau) = \bar{\mathbf{F}}_B^N(\tau)(\bar{\mathbf{F}}_B^N(\tau))^T \tag{C.17}$$

$$\bar{\lambda}_N(\tau) = [\frac{1}{3}\mathrm{tr}(\bar{\mathbf{B}}^N)(\tau)]^{1/2} \tag{C.18}$$

(4) Then the stress is calculated using the 8-chain model:

$$\mathbf{T}_B(\tau) = \frac{1}{J_B(\tau)}\frac{\nu k\theta}{3}\frac{\sqrt{N}}{\bar{\lambda}_N(\tau)}\mathscr{L}^{-1}\left[\frac{\bar{\lambda}_N(\tau)}{\sqrt{N}}\right][\bar{\mathbf{B}}^N(\tau) - (\bar{\lambda}_N(\tau))^2\mathbf{I}] \tag{C.19}$$

(5) The shear stress is:

$$\tau_B(\tau) = \left[\frac{1}{2}\mathbf{T}'_B(\tau)\mathbf{T}'_B(\tau)\right]^{1/2} \tag{C.20}$$

$$\mathbf{N}_B(\tau) = \frac{1}{\sqrt{2}\tau_B(\tau)}\mathbf{T}'_B(\tau) \tag{C.21}$$

where $\mathbf{T}'_B(\tau)$ is the deviatoric portion of $\mathbf{T}_B(\tau)$.

(6) The different constitutive expressions employed for the plastic shear rate are:

$$\dot{\gamma}_B^F(\tau) = C\left(\frac{1}{\lambda_F(\tau)-1}\right)\tau_B(\tau) \tag{C.22}$$

$$\dot{\gamma}_B^F(\tau) = C\left[\left(\frac{1}{\lambda_F(\tau)-1}\right)\tau_B(\tau)\right]^3 \tag{C.23}$$

$$\dot{\gamma}_B^F(\tau) = C\frac{(\bar{\lambda}_{NC}-\lambda_N(\tau))}{(\bar{\lambda}_{NC}-1)}\left[\left(\frac{1}{\lambda_F(\tau)-1}\right)\tau_B(\tau)\right]^3 \tag{C.24}$$

$$\dot{\gamma}_B^F(\tau) = h\left(\frac{\frac{\alpha_{min}(\tau)}{\alpha_c}-1}{\frac{\alpha_0}{\alpha_c}-1}\right)\left(\frac{\alpha_{min}(\tau)}{\alpha_c}\frac{\tau_B(\tau)}{\nu k\theta}\right)^{1/n} \tag{C.25}$$

In equation C.24, the strain-rate dependence of $\bar{\lambda}_{NC}(\tau)$ is calculated using $\dot{\gamma}_B^F(t)$ in equation 4.37. Also,

$$\lambda_F(\tau) = [\frac{1}{3}\mathrm{tr}\{\mathbf{F}_B^F(\tau)(\mathbf{F}_B^F(\tau))^T\}]^{1/2} \tag{C.26}$$

and α_{min} is calculated as follows

$$\mathbf{B}_B(\tau) = \mathbf{F}_B(\tau)(\mathbf{F}_B(\tau))^T \tag{C.27}$$

$$\mathbf{B}_B(\tau) = \sum_{i=1}^{3}\lambda_i(\tau)^2\hat{\mathbf{n}}_i(\tau)\otimes\hat{\mathbf{n}}_i(\tau) \tag{C.28}$$

$$\lambda_{min}(\tau) = \min(\lambda_i(\tau)) \tag{C.29}$$

$$\alpha_{min}(\tau) = \frac{\pi}{2} - \cos^{-1}\left(\frac{\lambda_{min}(\tau)}{\sqrt{\lambda_1(\tau)^2+\lambda_2(\tau)^2+\lambda_3(\tau)^2}}\right) \tag{C.30}$$

(7) If the plastic shear rate has changed too much (i.e. if the ratio $\dot{\gamma}_B^F(\tau)/\dot{\gamma}_B^F(t)$ differs greatly from 1.0), then the increment is repeated with a smaller time step.

(8) Provided the change in $\dot{\gamma}_B^F$ is not too great, the rate of stretching is calculated as

$$\tilde{\mathbf{D}}_B^F(\tau) = \dot{\gamma}_B^F(\tau)\mathbf{N}_B(\tau) \tag{C.31}$$

Prescribing $\tilde{\mathbf{W}}_B^F = 0$, we obtain as in Resistance A:

$$\dot{\mathbf{F}}_B^F(\tau) = (\mathbf{F}_B^N(\tau))^{-1}\tilde{\mathbf{D}}_B^F(\tau)\mathbf{F}_B(\tau) \tag{C.32}$$

(9) The total stress is the sum of the stress in the two resistances:

$$\mathbf{T}(\tau) = \mathbf{T}_A(\tau) + \mathbf{T}_B(\tau) \tag{C.33}$$

Anisotropic Model Changes

Using the anisotropic model, the time-integration procedure is unchanged for Resistance A. The procedure for Resistance B changes as follows, with changes appearing in steps (2a), (3), (4), and (6):

(1) The plastic deformation gradient is updated explicitly:

$$\mathbf{F}_B^F(\tau) = \mathbf{F}_B^F(t) + \dot{\mathbf{F}}_B^F(t)\Delta t \tag{C.34}$$

(2) The elastic deformation gradient is then computed as:

$$\mathbf{F}_B^N(\tau) = \mathbf{F}(\tau)(\mathbf{F}_B^F(\tau))^{-1} \tag{C.35}$$

(2a) To calculate the parameters for the anisotropic model, we need

$$\begin{aligned}
\mathbf{F}_B^F(\tau) &= \mathbf{R}_B^F(\tau)\mathbf{U}_B^F(\tau) && \text{(C.36)}\\
\mathbf{C}_B^F(\tau) &= (\mathbf{F}_B^F(\tau))^T\mathbf{F}_B^F(\tau) && \text{(C.37)}\\
\mathbf{C}_B^F(\tau) &= \sum_{i=1}^{3}(\lambda_{iF}(\tau))^2\hat{\mathbf{n}}_i(\tau)\otimes\hat{\mathbf{n}}_i(\tau) && \text{(C.38)}\\
\mathbf{a}(\tau) &= \hat{\mathbf{n}}_1(\tau) && \text{(C.39)}\\
\mathbf{b}(\tau) &= \hat{\mathbf{n}}_2(\tau) && \text{(C.40)}\\
\mathbf{c}(\tau) &= \hat{\mathbf{n}}_3(\tau) && \text{(C.41)}\\
a(\tau) &= a_0\mathbf{R}_B^F(\tau)\lambda_{1F}(\tau) && \text{(C.42)}\\
b(\tau) &= a_0\mathbf{R}_B^F(\tau)\lambda_{2F}(\tau) && \text{(C.43)}\\
c(\tau) &= a_0\mathbf{R}_B^F(\tau)\lambda_{3F}(\tau) && \text{(C.44)}\\
\frac{N(\tau)}{N_0} &= \frac{\lambda_{1F}(\tau)^2+\lambda_{2F}(\tau)^2+\lambda_{3F}(\tau)^2}{3} && \text{(C.45)}\\
\frac{\nu(\tau)}{\nu_0} &= \frac{3}{\lambda_{1F}(\tau)^2+\lambda_{2F}(\tau)^2+\lambda_{3F}(\tau)^2} && \text{(C.46)}
\end{aligned}$$

Rotating $\mathbf{a}(\tau)$, $\mathbf{b}(\tau)$, and $\mathbf{c}(\tau)$ by $\mathbf{R}_B^F(\tau)$ brings the orthotropic unit cell into the elastically unloaded configuration

(3) The following additional quantities are needed to calculate the stress:

$$J_B(\tau) = \det \mathbf{F}_B^N(\tau) \tag{C.47}$$

$$\mathbf{C}_B^N(\tau) = (\mathbf{F}_B^N(\tau))^T \bar{\mathbf{F}}_B^N(\tau) \tag{C.48}$$

(4) The stress is calculated using the anisotropic 8-chain model:

$$\tilde{T}_{jk} = \frac{\nu(\tau)k\theta}{4}\left[\sum_{i=1}^{4}\frac{P_j^{(i)}P_k^{(i)}}{\rho^{(i)}}\beta_\rho^{(i)} - \frac{\beta_P}{\sqrt{N(\tau)}}\left(\frac{a^2}{\lambda_a^2}a_j a_k + \frac{b^2}{\lambda_b^2}b_j b_k + \frac{c^2}{\lambda_c^2}c_j c_k\right)\right] \tag{C.49}$$

$$\mathbf{T}_B(\tau) = \frac{1}{J_B(\tau)}\mathbf{F}_B^N(\tau)\tilde{\mathbf{T}}(\mathbf{F}_B^N(\tau))^T \tag{C.50}$$

where the values of $\mathbf{P}_j^{(i)}$, $\rho^{(i)}$, $\beta_\rho^{(i)}$, a, a_i, λ_a, etc. are calculated using the appropriate expressions in Chapter 6 and using values at the new time step for all quantities which change in time.

(5) The shear stress is:

$$\tau_B(\tau) = \left[\frac{1}{2}\mathbf{T}'_B(\tau)\mathbf{T}'_B(\tau)\right]^{1/2} \tag{C.51}$$

$$\mathbf{N}_B(\tau) = \frac{1}{\sqrt{2}\tau_B(\tau)}\mathbf{T}'_B(\tau) \tag{C.52}$$

where $\mathbf{T}'_B(\tau)$ is the deviatoric portion of $\mathbf{T}_B(\tau)$.

(6) The constitutive expression for the plastic shear rate is:

$$\dot{\gamma}_B^F(\tau) = h\left(\frac{\frac{\alpha_{min}(\tau)}{\alpha_c} - 1}{\frac{\alpha_0}{\alpha_c} - 1}\right)\left(\frac{\alpha_{min}(\tau)}{\alpha_c}\frac{\tau_B(\tau)}{\nu k\theta}\right)^{1/n} \tag{C.53}$$

and α_{min} is calculated as follows

$$\mathbf{B}_B(\tau) = \mathbf{F}_B(\tau)(\mathbf{F}_B(\tau))^T \tag{C.54}$$

$$\mathbf{B}_B(\tau) = \sum_{i=1}^{3}\lambda_i(\tau)^2\hat{\mathbf{n}}_i(\tau)\otimes\hat{\mathbf{n}}_i(\tau) \tag{C.55}$$

$$\lambda_{min}(\tau) = \min(\lambda_i(\tau)) \tag{C.56}$$

$$\alpha_{min}(\tau) = \frac{\pi}{2} - \cos^{-1}\left(\frac{\lambda_{min}(\tau)}{\sqrt{\lambda_1(\tau)^2 + \lambda_2(\tau)^2 + \lambda_3(\tau)^2}}\right) \tag{C.57}$$

(7) If the plastic shear rate has changed too much (i.e. if the ratio $\dot{\gamma}_B^F(\tau)/\dot{\gamma}_B^F(t)$ differs greatly from 1.0), then the increment is repeated with a smaller time step.

(8) Provided the change in $\dot{\gamma}_B^F$ is not too great, the rate of stretching is calculated as

$$\tilde{\mathbf{D}}_B^F(\tau) = \dot{\gamma}_B^F(\tau)\mathbf{N}_B(\tau) \tag{C.58}$$

Prescribing $\tilde{\mathbf{W}}_B^F = 0$, we obtain as in Resistance A:

$$\dot{\mathbf{F}}_B^F(\tau) = (\mathbf{F}_B^N(\tau))^{-1}\tilde{\mathbf{D}}_B^F(\tau)\mathbf{F}_B(\tau) \tag{C.59}$$

(9) The total stress is the sum of the stress in the two resistances:

$$\mathbf{T}(\tau) = \mathbf{T}_A(\tau) + \mathbf{T}_B(\tau) \tag{C.60}$$

Bibliography

Adams, A. M., Buckley, C. P., and Jones, D. P. (1998). Biaxial hot-drawing of poly(ethylene terephalate): dependence of yield stress on strain-rate ratio. Polymer 39 (23), 5761–5763.

Adams, A. M., Buckley, C. P., and Jones, D. P. (2000). Biaxial hot drawing of poly(ethylene terephthalate): measurements and modelling of strain-stiffening. Polymer 41 (2), 771–786.

Ahzi, S., Makradi, A., Gregory, R. V., and Edie, D. D. (2002). Modeling of deformation behavior and strain-induced crystallization during hot drawing of PET. In Abstracts of Papers of the American Chemical Society, Volume 223, pp. 095–PMSE Part 2.

Ajji, A., Guevremont, J., Cole, K. C., and Dumoulin, M. M. (1994). Orientation, mechanical, and thermal characterization of drawn PET. In Annual Technical Conference–ANTEC, Conference Proceedings, pp. 1421–1423.

Anand, L. (1979). On H. Hencky's approximate strain energy function for moderate deformations. Journal of Applied Mechanics 46, 78–82.

Arruda, E. M. and Boyce, M. C. (1993a). Evolution of plastic anisotropy in amorphous polymers during finite straining. International Journal of Plasticity 9 (6), 697–720.

Arruda, E. M. and Boyce, M. C. (1993b). A three-dimensional constitutive model for the large stretch behavior of rubber elastic materials. Journal of the Mechanics and Physics of Solids 41 (2), 389–412.

Axtell, F. H. and Haworth, B. (1993). An investigation of the parison sagging behaviour during the extrusion blow moulding of copoplyester PETG. Journal of the Science Society of Thailand 19, 25–36.

Axtell, F. H. and Haworth, B. (1994). Elongational deformation and stretch blow moulding of poly(ethylene terephthalate). Plastics, Rubber, and Composites Processing and Applications 22 (3), 127–136.

Ball, R. C., Doi, M., Edwards, S. F., and Warner, M. (1981). Elasticity of entangled networks. Polymer 22, 1010–1018.

Bellare, A., Cohen, R. E., and Argon, A. S. (1993). Development of texture in poly(ethylene terephthalate) by plane-strain compression. Polymer 34 (7), 1393–1403.

Bergstrom, J. S. and Boyce, M. C. (1998). Constitutive modeling of the large strain time-dependent behavior of elastomers. Journal of the Mechanics and Physics of Solids 46 (5), 931–954.

Bhattacharjee, P. K., Oberhauser, J. P., McKinley, G. H., Leal, L. G., and Sridhar, T. (2002). Extensional rheometry of entangled solutions. Macromolecules 35, 10131–10148.

Bird, R. B., Armstrong, R. C., and Hassager, O. (1987). Dynamics of Polymeric Liquids, Volume 1: Fluid Mechanics. John Wiley and Sons.

Bird, R. B., Curtiss, C. F., Armstrong, R. C., and Hassager, O. (1987). Dynamics of Polymeric Liquids, Volume 2: Kinetic Theory. John Wiley and Sons.

Bischoff, J. E., Arruda, E. M., and Grosh, K. (2000). Finite element modeling of human skin using an isotropic, nonlinear elastic constitutive model. Journal of Biomechanics 33, 645–652.

Blundell, D. J., MacKerron, D. H., Fuller, W., Mahendrasingam, A., Martin, C., Oldman, R. J., Rule, R. J., and Riekel, C. (1996). Characterization of strain-induced crystallization of poly(ethylene terephthalate) at fast draw rates using synchrotron radiation. Polymer 37 (15), 3303–3311.

Blundell, D. J., Mahendrasingam, A., Martin, C., Fuller, W., Mackerron, D. H., Harvie, J. L., Oldman, R. J., and Riekel, C. (2000). Orientation prior to crystallization during drawing of poly(ethylene terephthalate). Polymer 41, 7793–7802.

Blundell, D. J., Oldman, R. J., Fuller, W., Mahendrasingam, A., Martin, C., MacKerron, D. H., Harvie, J. L., and Riekel, C. (1999). Orientation and crystallization mechanisms during fast drawing of poly(ethylene terephthalate). Polymer Bulletin 42, 357–363.

Bonnebat, C., Roullet, G., and deVries, A. J. (1981). Biaxially oriented poly(ethylene terephthalate) bottles: effects of resin molecular weight on parison stretching behavior. Polymer Engineering and Science 21 (4), 189–195.

Bower, D. I. and Ward, I. M. (1982). Quantitative characterization of orientation in PET fibres by Raman spectroscopy. Polymer 23 (5), 645–649.

Boyce, M. C. and Arruda, E. M. (2000). Constitutive models of rubber elasticity: a review. Rubber Chemistry and Technology 73 (3), 504–523.

Boyce, M. C., Parks, D. M., and Argon, A. S. (1988). Large inelastic deformation of glassy polymers. Part I: Rate dependent constitutive model. Mechanics of Materials 7, 15–33.

Boyce, M. C., Socrate, S., and Llana, P. G. (2000). Constitutive model for the finite deformation stress-strain behavior of poly(ethylene terephthalate) above the glass transition. Polymer 41 (6), 2183–2201.

Brown, R. A. (2000). Large strain deformation of PETG at processing temperatures. Master's thesis, MIT.

Buckley, C. P. and Jones, D. C. (1995). Glass-rubber constitutive model for amorphous polymers near the glass transition. Polymer 36 (17), 3301–3312.

Buckley, C. P., Jones, D. C., and Jones, D. P. (1996). Hot-drawing of poly(ethylene terephthalate) under biaxial stress: application of a three-dimensional glass-rubber constitutive model. Polymer 37 (12), 2403–2414.

Buckley, C. P. and Salem, D. R. (1987). High-temperature viscoelasticity and heat-setting of poly(ethylene terephthalate). Polymer 28, 69–85.

Cakmak, M., Spruiell, J. E., and White, J. L. (1984). A basic study of orientation in poly(ethylene terephthalate) stretch-blow molded bottles. Polymer Engineering and Science 24 (18), 1390–1395.

Cakmak, M., Spruiell, J. E., White, J. L., and Lin, J. S. (1987). Small angle and wide angle x-ray pole figure studies on simultaneous biaxially stretched poly(ethylene terephthalate) (PET) films. Polymer Engineering and Science 27 (12), 893–905.

Cakmak, M., White, J. L., and Spruiell, J. E. (1985a). An investigation of the kinematics of stretch blow molding poly(ethylene terephthalate) bottles. Journal of Applied Polymer Science 30, 3679–3695.

Cakmak, M., White, J. L., and Spruiell, J. E. (1985b). Structure development in stretch blow molding polyethylene terephthalate bottles. In ANTEC '85, pp. 912–915. ANTEC.

Cakmak, M., White, J. L., and Spruiell, J. E. (1986). Structural characterization of crystallinity and crystalline orientation in simultaneously biaxially stretched and annealed polyethylene terephthalate films. Journal of Polymer Engineering 6, 291–312.

Cakmak, M., White, J. L., and Spruiell, J. E. (1989). Optical properties of simultaneous biaxially stretched poly(ethylene terephthalate) films. Polymer Engineering and Science 29 (21), 1534–1543.

Caldicott, R. J. (1999). The basics of stretch blow molding PET containers. Plastics Engineering, 35–39.

Chandran, P. and Jabarin, S. (1993a). Biaxial orientation of poly(ethylene terephthalate). Part I: Nature of the stress-strain curves. Advances in Polymer Technology 12 (2), 119–132.

Chandran, P. and Jabarin, S. (1993b). Biaxial orientation of poly(ethylene tereph-

thalate). Part II: The strain-hardening parameter. Advances in Polymer Technology 12 (2), 133–151.

Chandran, P. and Jabarin, S. (1993c). Biaxial orientation of poly(ethylene terephthalate). Part III: Comparative structure and property changes resulting from simultaneous and sequential orientation. Advances in Polymer Technology 12 (2), 153–165.

Chen, L. P., Yee, A. F., Goetz, J. M., and Schaefer, J. (1998). Molecular structure effects on the secondary relaxation and impact strength of a series of polyester copolymer glasses. Macromolecules 31, 5371–5382.

Chen, L. P., Yee, A. F., and Moskala, E. J. (1999). The molecular basis for the relationship between the secondary relaxation and mechanical properties of a series of polyester copolymer glasses. Macromolecules 32, 5944–5955.

Ching, E. C. Y., Li, R. K. Y., and Mai, Y.-W. (2000). Effects of gauge length and strain rate on fracture toughness of polyethylene terephthalate glycol (PETG) film using the essential work of fracture analysis. Polymer Engineering and Science 40 (2), 310–319.

Choi, K., Spruiell, J. E., and White, J. L. (1989). Orientation and crystalline morphology of blow molded polyethylene bottles. Polymer Engineering and Science 29 (7), 463–470.

Chung, T. S. (1983). Principles of preform design for stretch blow molding process. Polymer-Plastics Technology and Engineering 20 (2), 147–160.

Clauss, B. and Salem, D. R. (1992). Characterization of the non-crystalline phase of oriented poly(ethylene terephthalate) by chain-induced fluorescence. Polymer 33 (15), 3193–3202.

Clauss, B. and Salem, D. R. (1995). A chain-intrinsic fluorescence study of orientation-strain behavior in uniaxially drawn poly(ethylene terephthalate) film. Macromolecules 28, 8328–8333.

Cole, K. C., Ajji, A., and Pellerin, E. (2002). New insights into the development

of ordered structure in poly(ethylene terephthalate). 1. results from external reflection infrared spectroscopy. Macromolecules 35 (3), 770–784.

Coppola, S., Grizzuti, N., and Maffettone, P. L. (2001). Microrheological modeling of flow-induced crystallization. Macromolecules 34, 5030–5036.

Dargent, E., Grenet, J., and Auvray, X. (1994). Thermal behaviour of drawn semi-crystalline poly(ethylene terephthalate) films. Journal of Thermal Analysis 41, 1409–1415.

Dargent, E., Grenet, J., Dahoun, A., Aubert, A., and G'Sell, C. (1999). Evolution of the microstructure of poly(ethylene terephthalate) sheets submitted to a thermomechanical treatment. I. microstructure-thermal properties relationships. Revue de Metallurgie 96 (2), 1501–1509.

de Gennes, P. G. (1979). Scaling Concepts in Polymer Physics. Cornell University Press.

Debbaut, B., Homerin, O., and Jivraj, N. (1999). A comparison between experiments and predictions for the blow molding of an industrial part. Polymer Engineering and Science 39 (9), 1812–1822.

deP. Daubeny, R., Bunn, C. W., and Brown, C. J. (1954). The crystal structure of polyethylene terephthalate. Proceedings of the Royal Society of London: A 226 (1167), 531–542.

Doi, M. (1980). A constitutive equation derived from the model of Doi and Edwards for concentrated polymer solutions and polymer melts. Journal of Polymer Science: Polymer Physics Edition 18, 2055–2067.

Doi, M. and Edwards, M. F. (1986). The theory of polymer dynamics. Oxford University Press.

Doi, M. and Edwards, S. F. (1978). Dynamics of concentrated polymer systems. Part 3 - the constitutive equation. Journal of the Chemical Society - Faraday Transactions II 74, 1818–1832.

Dooling, P. J., Buckley, C. P., and Hinduja, S. (1998). The onset of nonlinear viscoelasticity in multiaxial creep of glassy polymers: a constitutive model and its application to PMMA. Polymer Engineering and Science 38 (6), 892–904.

Doufas, A. K., Dairanieh, I. S., and McHugh, A. J. (1999). A continuum model for flow-induced crystallization of polymer melts. Journal of Rheology 43 (1), 85–109.

Doufas, A. K. and McHugh, A. J. (2001a). Simulation of film blowing including flow-induced crystallization. Journal of Rheology 45 (5), 1085–1104.

Doufas, A. K. and McHugh, A. J. (2001b). Simulation of melt spinning including flow-induced crystallization. Part III. quantitative comparisons with PET spinline data. Journal of Rheology 45 (2), 403–420.

Doufas, A. K., McHugh, A. J., and Miller, C. (2000). Simulation of melt spinning including flow-induced crystallization Part I. model development and predictions. Journal of Non-Newtonian Fluid Mechanics 92, 27–66.

Doufas, A. K., McHugh, A. J., Miller, C., and Immaneni, A. (2000). Simulation of melt spinning including flow-induced crystallization Part II. quantitative comparisons with industrial spinline data. Journal of Non-Newtonian Fluid Mechanics 92, 81–103.

Duckett, R. A., Rabinowitz, S., and Ward, I. M. (1970). The strain-rate, temperature and pressure dependence of yield of isotropic poly(methylmethacrylate) and poly(ethylene terephthalate). Journal of Materials Science 5, 909–915.

Edwards, S. F. and Vilgis, T. (1986). The effect of entanglements in rubber elasticity. Polymer 27 (4), 483–492.

Erwin, L., Pollock, M. A., and Gonzalez, H. (1983). Blowing of oriented PET bottles: predictions of free blown size and shape. Polymer Engineering and Science 23 (15), 826–829.

Fischer, E. W. and Fakirov, S. (1976). Structure and properties of polyethyleneterephthalate crystallized by annealing in the highly oriented state

Part I: Morphological structure as revealed by small angle x-ray scattering. Journal of Materials Science 11, 1041–1065.

Flory, P. J. (1947). Thermodynamics of crystallization in high polymers. I. crystallization induced by stretching. Journal of Chemical Physics 15 (6), 397–408.

Flory, P. J. (1956). Role of crystallization in polymers and proteins. Science 124, 53.

Flory, P. J. (1985). Molecular theory of rubber elasticity. Polymer Journal 17 (1), 1–12.

Flory, P. J. and Rehner, J. (1943). Statistical mechanics of cross-linked polymer networks. The Journal of Chemical Physics 11 (11), 512–520.

Foot, J. S. and Ward, I. M. (1975). The cold drawing of amorphous polyethylene terephthalate. Journal of Materials Science 10, 955–960.

Gerlach, C., Buckley, C. P., and Jones, D. P. (1998). Development of an integrated approach to modelling of polymer film orientation processes. Chemical Engineering Research and Design Part A 76, 38–44.

Giesekus, H. (1982). A simple constitutive equation for polymer fluids based on the concept of deformation-dependent tensorial mobility. Journal of Non-Newtonian Fluid Mechanics 11, 69–109.

Gohil, R. M. and Salem, D. R. (1993). Orientation distribution in the noncrystalline regions of biaxially drawn poly(ethylene terephthalate) film: a chain-intrinsic fluorescence study. Journal of Applied Polymer Science 47, 1989–1998.

Gordon, D. H., Duckett, R. A., and Ward, I. M. (1994). A study of uniaxial and constant-width drawing of poly(ethylene terephthalate). Polymer 35 (12), 2554–2559.

Gorlier, E., Agassant, J., Haudin, J., and Billon, N. (2000). Experimental and theoretical study of the uni-axial deformation of amorphous PET above the glass transition temperature. In 11th International Conference on Deformation,

Yield, and Fracture of Polymers, Churchill College, Cambridge, UK, pp. 351–354.

Gorlier, E., Haudin, J. M., and Billon, N. (2001). Strain-induced crystallization in bulk amorphous PET under uni-axial loading. Polymer 42, 9541–9549.

Greener, J., Blanton, T. N., Tsou, A. H., and Mosehauer, G. (1995). The heat-setting of PET films: a morphological study. In ANTEC '95, pp. 1464–1467. ANTEC.

G'Sell, C., Hiver, J. M., Elkoun, S., Vigny, M., Cabot, C., Aubert, A., and Dahoun, A. (2000). Plane strain deformation mechanisms of PET in the rubbery state. In 11th International Conference on Deformation, Yield, and Fracture of Polymers, Churchill College, Cambridge, UK, pp. 375–378.

Guan, J. Y., Saraf, R. F., and Porter, R. S. (1987). Evaluation of free and hydrostatic equibiaxial deformation of poly(ethylene terephthalate) by trirefringence measurement. Journal of Applied Polymer Science 33, 1517–1523.

Guan, J. Y., Wang, L., and Porter, R. S. (1992). Planar deformation of amorphous poly(ethylene terephthalate) by stretching and forging. Journal of Polymer Science: Part B: Polymer Physics 30 (7), 387–391.

Ianniruberto, G. and Marrucci, G. (2001). A simple constitutive equation for entangled polymers with chain stretch. Journal of Rheology 45 (6), 1305–1318.

Jabarin, S. A. (1984). Orientation studies of poly(ethylene terephthalate). Polymer Engineering and Science 24 (5), 376–384.

Jabarin, S. A. (1992). Strain-induced crystallization of poly(ethylene terephthalate). Polymer Engineering and Science 32 (18), 1341–1348.

Jog, J. P. (1995). Crystallization of polyethyleneterephthalate. Journal of Macromolecular Science–Reviews of Macromolecular Chemical Physics C35 (3), 531–553.

Kattan, M., Dargent, E., and Grenet, J. (2002). Three phase model in drawn thermoplastic polyesters: comparison of differential scanning calorimetry and ther-

mally stimulated depolarisation current experiments. Polymer 43 (4), 1399–1405.

Kattan, M., Dargent, E., Ledru, J., and Grenet, J. (2001). Strain-induced crystallization in uniaxially drawn PETG plates. Journal of Applied Polymer Science 81, 3405–3412.

Kim, G. H., Kang, C., Chang, C. G., and Ihm, D. W. (1997). Molecular orientation angle of biaxially stretched poly(ethylene terephthalate) films. European Polymer Journal 33, 1633–1638.

Kim, S. L. (1984). Effect of preheat time on the morphological and oxygen barrier properties of reheat blown PET containers. Polymer Engineering Reviews 4 (4), 239–254.

Kim, S. L. (1985). Effect of equilibration time on the properties of reheat blown 2L PET bottles. Journal of Polymer Engineering 5 (2), 125–134.

LeBourvellec, G., Monnerie, L., and Jarry, J. P. (1986). Amorphous orientation and induced crystallization in uniaxially stretched poly(ethylene terephthalate glycol). Polymer 27, 856–860.

LeBourvellec, G., Monnerie, L., and Jarry, J. P. (1987). Kinetics of induced crystallization during stretching and annealing of poly(ethylene terephthalate) films. Polymer 28, 1712–1716.

Lee, C. H., Saito, H., Inoue, T., and Nojima, S. (1996). Time-resolved small-angle x-ray scattering studies on the crystallization of poly(ethylene terephthalate). Macromolecules 29, 7034–7037.

Lee, E. H. (1969). Elastic-plastic deformation at finite strains. Journal of Applied Mechanics 36, 1–6.

Liu, S. J. (1999). Computer simulation of the inflation process in blow molding. Journal of Reinforced Plastics and Composites 18 (8), 759–774.

Llana, P. G. (1998). The mechanics of strain-induced crystallization in poly(ethylene terephthalate). Master's thesis, MIT.

Llana, P. G. and Boyce, M. C. (1999). Finite strain behavior of poly(ethylene terephthalate) above the glass transition temperature. Polymer 40 (24), 6729–6751.

Lodge, A. S. (1964). Elastic Liquids. Academic Press.

Long, S. D. and Ward, I. M. (1991a). Shrinkage force studies of oriented polyethylene terephthalate. Journal of Applied Polymer Science 42, 1921–1929.

Long, S. D. and Ward, I. M. (1991b). Tensile drawing behaviour of polyethylene terephthalate. Journal of Applied Polymer Science 42, 1911–1920.

Lu, X. F. and Hay, J. N. (2001). Crystallization orientation and relaxation in uniaxially drawn poly(ethylene terephthalate). Polymer 42, 8055–8067.

Mahendrasingam, A., Martin, C., Fuller, W., Blundell, D. J., Oldman, R. J., Harvie, J. L., MacKerron, D. H., Riekel, C., and Engstrom, P. (1999). Effect of draw ratio and temperature on the strain-induced crystallization of poly (ethylene terephthalate) at fast draw rates. Polymer 40 (20), 5553–5565.

Mahendrasingam, A., Martin, C., Fuller, W., Blundell, D. J., Oldman, R. J., MacKerron, D. H., Harvie, J. L., and Riekel, C. (2000). Observation of a transient structure prior to strain-induced crystallization in poly(ethylene terephthalate). Polymer 41 (3), 1217–1221.

Marckmann, G., Verron, E., and Penseux, B. (2001). Finite element analysis of blow molding and thermoforming using a dynamic explicit procedure. Polymer Engineering and Science 41 (3), 426–439.

Marshall, I. and Thompson, A. B. (1954). The drawing of 'Terylene'. Journal of Applied Chemistry 4, 145–153.

Matthews, R. G., Ajji, A., Dumoulin, M. M., and Prud'homme, R. E. (1999). The effects of roll drawing on the structure and properties of oriented poly(ethylene terephthalate). Polymer Engineering and Science 39 (12), 2377–2388.

Matthews, R. G., Duckett, R. A., Ward, I. M., and Jones, D. P. (1997). The biaxial drawing behaviour of poly(ethylene terephthalate). Polymer 38 (19),

4795–4802.

McEvoy, J. P., Armstrong, C. G., and Crawford, R. J. (1998). Simulation of the stretch blow molding process of PET bottles. Advances in Polymer Technology 17 (4), 339–352.

McHugh, A. J. and Doufas, A. K. (2001). Modeling flow-induced crystallization in fiber spinning. Composites Part A: Applied Science and Manufacturing 32, 1059–1066.

McLeish, T. C. B. (2002). Tube theory of entangled polymer dynamics. Advances in Physics 51 (6), 1379–1527.

Menary, G. H., Armstrong, C. G., and Crawford, R. J. (1999). Computer aided design of preforms for injection stretch blow moulding. In Annual Technical Conference–ANTEC, Conference Proceedings, Volume 1, pp. 988–992.

Menary, G. H., Armstrong, C. G., Crawford, R. J., and McEvoy, J. P. (2000). Modelling of poly(ethylene terephthalate) in injection stretch-blow moulding. Plastics, Rubber, and Composites 29 (7), 360–370.

Middleton, A. C., Duckett, R. A., Ward, I. M., Mahendrasingam, A., and Martin, C. (2001). Real-time FTIR and WAXS studies of drawing behavior of poly(ethylene terephthalate) films. Journal of Applied Polymer Science 79, 1825–1837.

Misra, A. and Stein, R. S. (1979). Stress-induced crystallization of poly(ethylene terephthalate). Journal of Polymer Science: Polymer Physics Edition 17, 235–257.

Mooney, M. (1940). NEED TO LOOK UP TITLE. Journal of Applied Physics 11, 582.

Moskala, E. J. (1996). Fatigue resistance of impact-modified thermoplastic copolyesters. Journal of Material Science 31 (2), 507–511.

Ogden, R. W. (1972). Large deformation isotropic elasticity–on the correlation of theory and experiment for incompressible rubberlike solids. Proceedings of the

Royal Society of London: A 326, 565–584.

Papadopoulou, C. P. and Kalfoglou, N. K. (1997). Compatibility behavior of blends of poly(ethylene terephthalate) with an amorphous copolyester. Polymer 38 (3), 631–637.

Patton, R. L. (1998). Rate and temperature dependent stress-strain behavior of amorphous PET in uniaxial and plane strain compression. Report from an undergraduate research project at MIT.

Peszkin, P. N. and Schultz, I. M. (1986). Kinetics of fiber heat treatment II. Poly(ethylene terephthalate) fibers. Journal of Polymer Science: Part B: Polymer Physics 24, 2591–2616.

Petermann, J. and Rieck, U. (1987). Morphologies and mechanical properties of PET films crystallized under high strain rate. Journal of Polymer Science: Part B: Polymer Physics 25 (2), 279–293.

Pinnock, P. R. and Ward, I. M. (1966). Stress-optical properties of amorphous polyethylene terephthalate fibres. Journal of the Chemical Society Faraday Transactions I 62, 1308–1320.

Purvis, J., Bower, D. I., and Ward, I. M. (1973). Molecular orientation in PET studied by polarized raman scattering. Polymer 14 (8), 398–400.

Rietsch, F., Duckett, R. A., and Ward, I. M. (1979). Tensile drawing behavior of poly(ethylene terephthalate). Polymer 20, 1133–1142.

Rivlin, R. S. (1948). Large elastic deformations of isotropic materials IV further developments of the general theory. Philolophical Transactions of the Royal Society of London: A 241 (835), 379–397.

Roland, C. M. and Sonnenschein, M. F. (1991). The onset of orientational crystallization in poly(ethylene terephthalate) during low temperature drawing. Polymer Engineering and Science 31 (19), 1434–1439.

Salem, D. R. (1992a). Crystallization kinetics during hot-drawing of poly(ethylene

terephthalate) film: strain-rate/draw-time superposition. Polymer 33, 3189–3192.

Salem, D. R. (1992b). Development of crystalline order during hot-drawing of poly(ethylene terephthalate) film: influence of strain rate. Polymer 33 (15), 3182–3188.

Salem, D. R. (1994). Crystallization during hot-drawing of poly(ethylene terephthalate) film: influence of temperature on strain-rate/draw-time superposition. Polymer 35 (4), 771–776.

Salem, D. R. (1995). Crystallization during hot-drawing of poly(ethylene terephthalate) film: influence of the deformation mode. Polymer 36 (18), 3605–3608.

Salem, D. R. (1998). Microstructure development during constant-force drawing of poly(ethylene terephthalate) film. Polymer 39 (26), 7067–7077.

Salem, D. R. (1999). Orientation and crystallization in poly(ethylene terephthalate) during drawing at high temperatures and strain rates. Polymer Engineering and Science 39 (12), 2419–2430.

Schmidt, F. M., Agassant, J. F., and Bellet, M. (1998). Experimental study and numerical simulation of the injection stretch/blow molding process. Polymer Engineering and Science 38 (9), 1399–1412.

Schrauwen, B. A. G., Rastogi, S., Govaert, L. E., and Meijer, H. E. H. (2000). Wide- and small-angle x-ray scattering studies on the deformation behaviour of PET. In 11th International Conference on Deformation, Yield and Fracture of Polymers, Churchill College, Cambridge UK, pp. 367–370.

Siegmann, A. (1980). Melting and crystallization of poly(ethylene terephthalate) under pressure. Journal of Polymer Science: Polymer Physics Edition 18, 2181–2196.

Sun, T., Pereira, J., and Porter, R. S. (1984). Crystallization kinetics for poly(ethylene terephthalate) oriented by solid-state coextrusion. Journal of Polymer Science: Part B: Polymer Physics Edition 22, 1163–1171.

Sweeney, J., Shirataki, H., Unwin, A. P., and Ward, I. M. (1999). Application of a necking criterion to PET fibers in tension. Journal of Applied Polymer Science 74, 3331–3341.

Sweeney, J. and Ward, I. M. (1995). Rate dependent and network phenomena in the multiaxial drawing of poly(vinyl chloride). Polymer 36 (2), 299–308.

Tassin, J., Vigny, M., and Veyrat, D. (1999). Biaxial stretching of PET films: a molecular description. Macromolecular Symposia 147, 209–220.

Thompson, A. B. (1959). Strain-induced crystallization in polyethylene terephthalate. Journal of Polymer Science 34, 741–760.

Treloar, L. R. G. (1943). NEED TO LOOK UP THE TITLE. Transactions of the Faraday Society 39, 241.

Treloar, L. R. G. (1975). The Physics of Rubber Elasticity (3rd ed.). Oxford: Clarendon Press.

Treloar, L. R. G. (1976). The mechanics of rubber elasticity. Proceedings of the Royal Society of London: A 351 (1666), 301–322.

Valanis, K. C. and Landel, R. F. (1967). The strain-energy function of a hyperelastic material in terms of the extension ratios. Journal of Applied Physics 38 (7), 2997–3002.

Venkateswaran, G., Cameron, M. R., and Jabarin, S. A. (1998a). Effects of temperature profiles through preform thickness on the properties of reheat-blown PET containers. Advances in Polymer Technology 17 (3), 237–249.

Venkateswaran, G., Cameron, M. R., and Jabarin, S. A. (1998b). Prediction of PET container properties using film data. Advances in Polymer Technology 17 (3), 217–235.

Vigny, M., Aubert, A., Hiver, J. M., Aboulfaraj, M., and G'Sell, C. (1999). Constitutive viscoplastic behaviour of amorphous PET during plane-strain tensile stretching. Polymer Engineering and Science 39 (12), 2366–2376.

Vigny, M., Tassin, J. F., and Lorentz, G. (1999). Study of the molecular structure of pet films obtained by an inverse stretching process Part 2: crystalline reorganization during longitudinal drawing. Polymer 40, 397–406.

Vries, A. J. D., Bonnebat, C., and Beautemps, J. (1977). Uni- and biaxial orientation of polymer films and sheets. Journal of Polymer Science Part C: Polymer Symposium 58, 109–156.

Wang, M. C. and Guth, E. (1952). Statistical theory of networks of non-Gaussian flexible chains. The Journal of Chemical Physics 20 (7), 1144–1157.

Wang, S., Makinouchi, A., Okamoto, M., Kotaka, T., Maeshima, M., Ibe, N., and Nakagawa, T. (2000). Viscoplastic material modeling for the stretch blow molding simulation. International Polymer Processing 15 (2), 166–175.

Ward, I. M. (1967). The mechanical behavior of poly(ethylene terephthalate). Journal of Macromolecular Science - Physics B1 4, 667–694.

Ward, I. M. (1975). Structure and Properties of Oriented Polymers. Applied Science Publishers.

Ward, I. M. (1983). Mechanical Properties of Solid Polymers (2nd ed.). New York: Wiley.

Wiest, J. M. (1989). A differential constitutive equation for polymer melts. Rheologica Acta 28, 4–12.

Zaroulis, J. S. and Boyce, M. C. (1997). Temperature, strain rate, and strain state dependence of the evolution in mechanical behaviour and structure of poly(ethylene terephthalate) with finite strain deformation. Polymer 38 (6), 1303–1315.